The Dissertation Committee for Bo Gao Certifies that this is the approved version of the following dissertation:

DEVELOPMENT OF A NOVEL EOR SURFACTANT AND DESIGN OF AN ALKALINE/SURFACTANT/POLYMER FIELD PILOT

Committee:

Mukul M. Sharma, Supervisor

Gary A. Pope

Chun Huh

Kishore K. Mohanty

Keith P. Johnston

DEVELOPMENT OF A NOVEL EOR SURFACTANT AND DESIGN OF AN ALKALINE/SURFACTANT/POLYMER FIELD PILOT

by

Bo Gao, B.E.; M.E.

Dissertation

Presented to the Faculty of the Graduate School of

The University of Texas at Austin

in Partial Fulfillment

of the Requirements

for the Degree of

Doctor of Philosophy

The University of Texas at Austin

December 2012

Dedication

To my beloved wife, Qianqian, for her love, patience and support.

To my parents, Chengyou and Xiaotang, for inspiring me to strive to achieve my dreams.

To all other family members, for their devoted and endless love.

Acknowledgements

I would like to express my deepest gratitude to my supervisor, Dr. Mukul M. Sharma, for his guidance throughout my study at UT. He has always been keen on sharing his experience and suggesting ever more fascinating and challenging ideas and concepts to work on. It has been a great honor and truly enjoyable experience to work under his supervision. Dr. Gary A. Pope must also be acknowledged for his invaluable contributions throughout the course of this work. I would also like to extend my appreciation to my other committee members: Dr. Huh, Dr. Mohanty and Dr. Johnston, for sound suggestions and comments in the dissertation and the final defense. Insightful inputs from Dr. Weerasooriya, Dr. Menger (Emory), Dr. Shi (Princeton) and Dr. Delshad regarding surfactant synthesis and UTCHEM simulation are also gratefully acknowledged.

The multiple challenges of graduate school were greatly facilitated thanks to the day-to-day contributions from Jin Lee, Glen Baum, Gary Miscoe, Frankie Hart, and Roger Terzian, whose dedication to the success of students is remarkable.

I am indebted to many of my friends and colleagues who through their sincere suggestions and fruitful discussions shaped this dissertation in so many ways. In particular I would like to thank Qing Tao, Tie Sun, and Tina Zhang, whose moral support has been crucial in the final stretch of the dissertation, as well as Chicheng Xu, Haiyang Yu, Jun Lu, Junhao Zhou, Guangwei Ren, Peila Chen, Zhitao Li, Shan Huang, Wei Yu, Sahil Malhotra, Trevor Pollock, Lionel Ribeiro, Ripudaman Manchanda, Somnath Mondal, Kyunghaeng Lee and many others whom I did not cite explicitly.

Development of a Novel EOR Surfactant and Design of an Alkaline/Surfactant/Polymer Field Pilot

Bo Gao, Ph.D.

The University of Texas at Austin, 2012

Supervisor: Mukul M. Sharma

Surfactant related recovery processes are of increasing interest and importance because of high oil prices and the urge to meet energy demand. High oil prices and the accompanying revival of EOR operations have provided academia and industry with great opportunities to test alkaline surfactant polymer (ASP) methods on a field scale and to develop novel surfactant systems that can improve the performance of such EOR processes. This dissertation intends to discuss both opportunities through two unique projects, the development of novel surfactants for EOR applications and the design for an alkaline/surfactant/polymer (ASP) field pilot.

In Section I of this dissertation, a novel series of anionic Gemini surfactants are carefully synthesized and systematically investigated. The remarkable abilities of Gemini surfactants to influence oil-water interfaces and aqueous solution properties are fully demonstrated. These surfactants are shown to have great potential for application in EOR processes.

A wide range of Gemini structures (C_{14} to C_{24} chain length, -C_2- and -C_4- spacers, sulfate and carboxylate head groups) was synthesized and shown to have high aqueous solubility, with Krafft points below 20˚C. The critical micelle concentrations (CMC) for these new molecules are measured to be orders of magnitude lower than their

conventional counterparts. The significantly more negative Gibbs free energy for Gemini surfactant drives the micellization process and results in ultralow CMC. An adsorption study of Gemini surfactants at air-water and solid-water interfaces shows their superior surface activity from tighter molecular packing, and attractive characteristics of low adsorption loss at the solid surface.

All anionic Gemini surfactants synthesized have an extraordinary tolerance to salinity and/or hardness. No phase separation or precipitation occurs in the aqueous stability tests, even in the presence of extremely high concentrations of mono- and/or di-valent ions. Moreover, ultra-low IFT values are reached under these conditions for Type I microemulsion systems, at very low surfactant concentrations. The stronger molecular interaction between the Gemini and conventional surfactants offers synergy that promotes aqueous stability and interfacial activity. Gemini molecules with short spacers are capable of giving rise to high viscosities at fairly low concentrations. The rheological behavior can be explained by changes in the micellar structure.

A molecular thermodynamic model is developed to study anionic Gemini surfactants aggregation behavior in solution. The model takes into account of the head group-counter-ion binding effect and utilizes two simplified solutions to the Poisson-Boltzmann equation. It properly predicts the CMC of the surfactants synthesized and can be easily expanded to investigate other factors of interest in the micellization process.

Section II of this dissertation studies chemical formulation design and implementation for an oilfield where an alkaline/surfactant/polymer (ASP) pilot is being carried out. A four-step systematic design approach, composed of a) process and material selection; b) formulation optimization; c) coreflood validation; 4) lab-scale simulation, was successfully implemented and could be easily transferred to other EOR projects. The optimal chemical formulation recovered over 90% residual oil from Berea coreflood.

Lab-scale simulation model accurately history matches the coreflood experiment and sets the foundation for pilot-scale numerical study. Different operating strategies are investigated using a pilot-scale model, as well as the sensitivities of project economics to various design parameters. A field execution plan is proposed based on the results of the simulation study. A surface facility conceptual design is put together based on the practical needs and conditions in the field. Key lessons learned throughout the project are summarized and are invaluable for planning and designing future pilot floods.

Table of Contents

List of Tables

List of Figures

SECTION I: LABORATORY DEVELOPMENT OF GEMINI SURFACTANTS FOR CHEMICAL EOR PROCESSES

Chapter 1: Introduction

1.1 SURFACTANT EOR BASICS

It is generally considered that only about one third of the petroleum present in known reservoirs is economically recoverable with established technology, i.e., primary recovery methods utilizing gas pressure and other natural forces in the reservoir and secondary recovery by waterflooding. The largest onshore oil reserves in the US are the discovered mature oilfields that have been produced by primary and secondary recovery but still contain over 60% of the original oil in place. This represents a large amount of oil that is not recoverable by traditional methods. It has long been an objective of the industry to develop improved processes to increase overall recovery. However, the low oil prices which prevailed from the mid-1980's until recently provided little inventive for research on enhanced oil recovery (EOR), especially various chemical EOR processes with substantial initial investments.

In tertiary, or enhanced, oil recovery one generally attempts to reduce the capillary forces restraining the oil and/or alter viscosity of the displacing fluid in order to modify the viscous forces being applied to drive oil out of the pores. The ratio of viscous forces to capillary forces actually correlates well with the residual oil saturation and is termed the capillary number. One formulation of the capillary number is (Foster, 1973):

$$N_c = \frac{\mu v}{\gamma \phi} \tag{1.1}$$

Where μ and v are the viscosity and Darcy velocity of the displacing fluid, γ is the interfacial tension (IFT) and ϕ is the porosity. The more general proposal of trapping number (Pope *et al.*, 2000) that consists of the capillary and Bond number has recently been shown to successfully describe the phenomena of the residual oil.

To keep things simple, higher N_c implies a smaller capillary trapping force, and therefore results in higher recovery. Typical the capillary number for secondary waterflooding is on the order of 10^{-7} to 10^{-5}, and the corresponding residual oil saturation is oftentimes quite substantial (0.3 to 0.45). Additional oil recovery requires increasing the capillary number at least several orders of magnitude. This can be done by raising the viscous forces, i.e. viscosity and velocity, but practical limitations on the size of pumps and the need to avoid inducing fractures in the reservoir prevent one from using these factors to achieve the needed orders of magnitude increase. But, by adding a suitable surfactant to the water one can readily decrease the interfacial tension to an ultralow level ($\sim 10^{-3}$mN/m), which can in turn recover oil from much smaller pores and improve displacement efficiency (Stegemeier, 1977; Pope *et al.*, 2000). This important observation forms the basis for surfactant based chemical EOR processes.

Surfactants are widely used and find a very large number of applications because of their remarkable ability to influence the properties of surfaces and interfaces. For the oil and gas industry, surfactants may be applied or encountered at all stages in petroleum recovery and processing, from drilling, production, and surface plant processes, to pipeline and transportation. With the current higher prices and accompanying revival of interest in EOR it seems appropriate to research and develop novel surfactant systems, and examine their prospects for surfactant EOR.

1.2 RESEARCH ADVANCES IN EOR SURFACTANTS

The use of surfactants for oil recovery has been well studied for over 80 years. Water-soluble surfactants, such as polycyclic sulfonate and wood sulfate, were described (De Groote, 1929 and 1930) as an aid to improve oil recovery in patents filed in late 1920's. Blair and Lehmann (1942) invented a well stimulation process, in which the

injection of transparent emulsions was used to remove waxy solids. Holbrook (1958) suggested the use of fatty acid soaps, polyglycol ether, and salts of fatty acids for surfactant flooding, based on reduced IFT and enhanced oil recovery observed in the lab. Injected by itself, surfactant might suffer from severe retention in the reservoir. Reisberg and Doscher (1956), using a California crude and surfactant solutions containing NaOH, demonstrated in the lab that the addition of alkali produced interfacial activity related to certain components in the crude oil and that the addition of surfactant could enhance this activity. Nelson *et al.* (1984) proposed injection of a solution containing both surfactant and alkali for EOR. The primary role of the alkali in a surfactant flooding process is to reduce adsorption of the surfactant during displacement through the formation and sequester divalent ions. Such processes, described as alkaline surfactant processes, have attracted and continue to attract considerable interest.

The surfactants used in the 1960's (Hirasaki *et al.*, 2011) were made either by direct sulfonation of aromatic groups in refinery streams or crude oils, or by organic synthesis of alkyl/aryl sulfonates. Throughout the 1970's and early 1980's, extensive research, field testing and implementation were triggered by an expectation of high oil prices and especially in the US, by a decline of overall oil production. Petroleum sulfonates (together with an alcohol co-solvent in most cases) gained in popularity during this time. A series of systematic studies (Taber, 1969; Foster, 1973, Melrose, 1974; Stegemeier, 1977) have led to the recognition that the capillary number controlled the amount of residual oil remaining after flooding an oil-containing core. These studies revealed that at typical reservoir fluid velocities, the crude oil-brine IFT had to be reduced from crude oil-brine values of 20-30mN/m to values in the range of 0.001-0.01mN/m to achieve low values of residual oil saturation. Gale and Sandvik (1973) proposed four criteria for selecting a surfactant for a tertiary oil-recovery process: i) low

oil-water interfacial tension; ii) low adsorption; iii) compatibility with reservoir fluids; and iv) low cost.

Given the low oil prices from late 1980's to early 2000's, the number of chemical EOR projects especially saw a sharp decline during this period. However, recent oil price developments combined with the evolution of advanced technologies and current outlook on supply/demand forecasts have resulted in a new emphasis on improving recovery factors through implementation of EOR processes, including various surfactant related processes. Plenty of studies and applications (Barnes *et al.*, 2008; Zhao *et al.*, 2008; Flaaten *et al.*, 2008; Levitt *et al.*, 2009) have used ethoxylated and propoxyated sulfates / sulfonates, as well as internal olefin sulfonates (IOS). Researchers at the University of Texas have been conducting extensive and productive research (Levitt, 2006; Jackson *et al.*, 2006; Flaaten, 2007; Zhao *et al.*, 2008; Flaaten *et al.*, 2008; Levitt *et al.*, 2009; Sahni, 2009; Yang *et al.*, 2010; Dean, 2011; Solairaj, 2011; Walker, 2011) on testing new generations of high-performance and low-cost chemical systems (surfactant, co-surfactant, co-solvent, alkali, polymer and electrolyte) for a wide range of reservoir conditions. The microemulsion phase behavior procedure and screening criteria (Yang *et al.*, 2010; Salairaj *et al.*, 2012a) been widely applied for light oils and is being successfully expanded to viscous and even heavy oils. This "phase behavior approach" has now evolved into an essential pathway to identify optimum chemical formulations, instead of being just a simple surrogate for interfacial tension (IFT) measurements since it provides much more information than just IFT and these other data such as viscosity are as important to success as IFT (Solairaj, 2011).

There have been tremendous advances in EOR surfactant development during the past few years to address the compelling need for high molecular weight surfactants as chemical EOR is targeting more difficult resources (high temperature, high salinity, and

highly viscous oil). Researchers at The University of Texas have been making major strides towards a new generation of "heavy EOR surfactants" (Liyanage *et al.*, 2012). Adkins *et al.* (2010) proposed a relatively inexpensive way to prepare Guerbet alkoxy sulfates (GAS) with large hydrophobes and demonstrated that these surfactants exhibited good performance under a wide range of conditions. She also showed that the sulfates can be stabilized at high temperature at optimal pH conditions (~10), which greatly broadens the application scope of these molecules. Solairaj (2011) demonstrated through a series of coreflood experiments the stability and effectiveness of GAS surfactants under high temperature conditions. An interesting but rather revealing conclusion was that large hydrophobe surfactant was actually needed for a low viscosity oil that behaves like an oil with high EACN number. This again shows the complexity of the crude oil systems and the necessity of developing new surfactant systems.

The stability issue with GAS surfactants requires the use of alkali to raise pH. There are, however, circumstances when that is not practical (Lu *et al.*, 2012a). Therefore, in a follow-up study, Adkins *et al.* (2012) showed that Guerbet alkoxy carboxylates (GAC) can also be made with large branched hydrophobes and with a wide range of propylene oxide (PO) and ethylene oxide (EO) groups added for HLB adjustment. GAC surfactants open doors to applications when gypsum or anhydrite is present in the reservoir rock or when soft water is unavailable for injection. These surfactants have been tested for a wide variety of crude oils under a large range of reservoir conditions (Lu *et al.*, 2012a): high salinity, high hardness, and high temperature, with or without alkali, sandstone and carbonate, active and inactive oils. Promising results were also observed when applied on a naturally fracture reservoir (Lu *et al.*, 2012b). In an effort to bring in diversity and reduce the associated risk in raw material supply, Liyanage *et al.* (2012) have developed and tested another novel class of large

hydrophobe surfactants based on commercially available tristyrylphenol (TSP). These surfactants are very attractive in applications involving heavier crude oils, because of the enhanced solubility of heavy components by the benzene rings in the hydrophobe.

Built upon an extensive and high-quality data set of so many new surfactants with diverse structures and successful formulations with a wide range of reservoir conditions, a new correlation (Solairaj *et al.*, 2012a) has recently been developed to study the surfactant structure – performance relationship (Salager *et al.*, 1979) and to help identify the most important variables affecting the optimum surfactant selection. This correlation is a great advance in optimizing CEOR processes and will greatly increases the commercial potential of chemical enhanced oil recovery.

Petroleum industry has long been known for its interdisciplinary nature and is always striving for innovative ways to utilize technologies from other industries. Guerbet alkoxy surfactants (GAS and GAC) recently invented at the University of Texas (Adkins *et al.*, 2010 & 2012) are perfect demonstration to this point where the Guerbet reaction from alcohol industry is used to create large hydrophobe surfactants. A new class of surfactants know as Gemini surfactants, has recently appeared in the chemistry literature (Zana *et al.*, 1993; Menger *et al.*, 1993 & 2000; and Rosen *et al.*, 1993 & 1998). These molecules have been shown to be endowed with some interesting properties with potential for application in the petroleum industry. Investigating new molecules in this family of surfactants specifically for EOR is the main motivation for our research.

1.3 RESEARCH ADVANCES IN GEMINI SURFACTANTS

The first report on Gemini surfactants dates back to 1946 when Bersworth (1946) prepared a series of new compounds for detergent and water treatment applications, including a Gemini surfactant with carboxylate head groups. Dow Chemical initiated a

new line of chemicals in 1960's for special applications, e.g. disulfonated Gemini surfactant (trademark DOWFAX). The first report on Gemini surfactants in the scientific literature is that by Bunton *et al.* (1971). These authors reported the synthesis of dimeric cationic surfactants with an alkylene or 2-butynylene spacer group and their use in micelle catalysis. This work was followed by that of Devinsky *et al.* (1986) who reported on the relationship between the structure and surface activity of four series of cationic dimeric surfactants and on their high antimicrobial activity. Since early 1990's, research groups from the US (Menger *et al.*, 1993 & 2000; Rosen *et al.*, 1993 & 1998), France (Zana *et al.*, 1993, 1995, 1998 & 2002), and Japan (Okahara *et al.*, 1990, 1991, 1992 & 1993) have prepared numerous Gemini surfactants and studied their unique properties (surface activity and molecular aggregation). Their work and efforts have increased the interest in Gemini surfactants in both industrial and academic research organizations.

1.3.1 Gemini Surfactant Basics

Gemini (also called dimeric) surfactants represent a new class of surfactants made up of two amphiphilic moieties (identical or different) connected at the level of head groups or very close to the head groups by a spacer group of varied nature (see a and b in Figure 1.1). A popular notation in Gemini literature is *m*-*s*-*m*, where *m* and *s* represent the number of carbon atoms in the tail and spacer groups for the molecule, respectively. It must be stressed here that it is essential to have the spacer as close as possible to the head groups. Surfactants where the spacer connects the amphiphilic moieties towards the end of the alkyl chains are in fact bola-form surfactants (c in Figure 1.1) with a branched alkyl chain, and they do not show many interesting properties.

For Gemini surfactants, the hydrocarbon tails can vary in length; the spacer group can be flexible or rigid, hydrophilic or hydrophobic; and the polar group can be anionic,

cationic, nonionic or zwitterionic. It is their unique and versatile structures of Gemini surfactants that have recently attracted considerable interest from the academic and industrial communities.

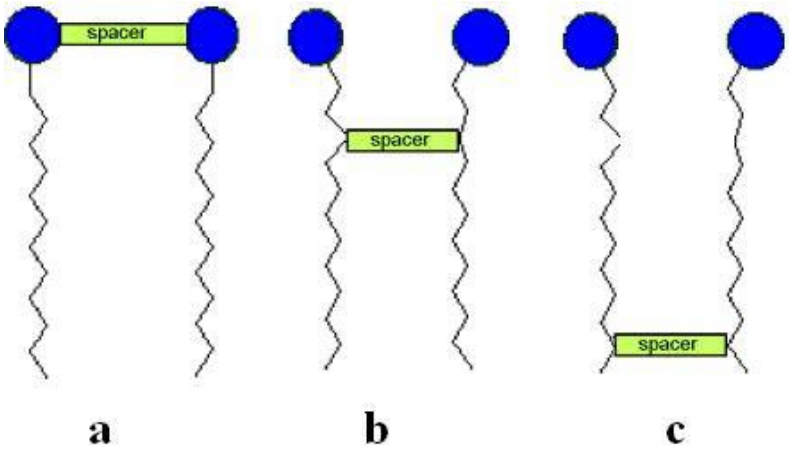

Figure 1.1: Schematic Drawing of Gemini (a & b) and Bola-form (c) Surfactants. Joints position: a) between polar head groups, Gemini surfactant; b) close to head groups, Gemini surfactant, c) towards the end of alkyl chains, bolaform surfactant.

Anionic Geminis, in particular, have significant water solubility, form micelles and substantially lower surface tension compared to conventional anionic homologues (Shukla *et al.*, 2006). Because of their ultralow critical micelle concentration (CMC) and high surface activity, anionic Geminis can potentially be used as emulsifiers, dispersants or hydrotropic agents in washing and cleaning technologies, laundry and detergent formulations, soil clean up, and enhanced oil recovery.

1.3.2 Synthesis of Anionic Gemini Surfactants

Menger (1991) synthesized a phosphate Gemini surfactant by reacting α,α'-dibromo-*p*-xylene with a monoalkyl phosphate anion. The benzene ring was introduced into the structure as a rigid spacer group, as shown in Figure 1.2.

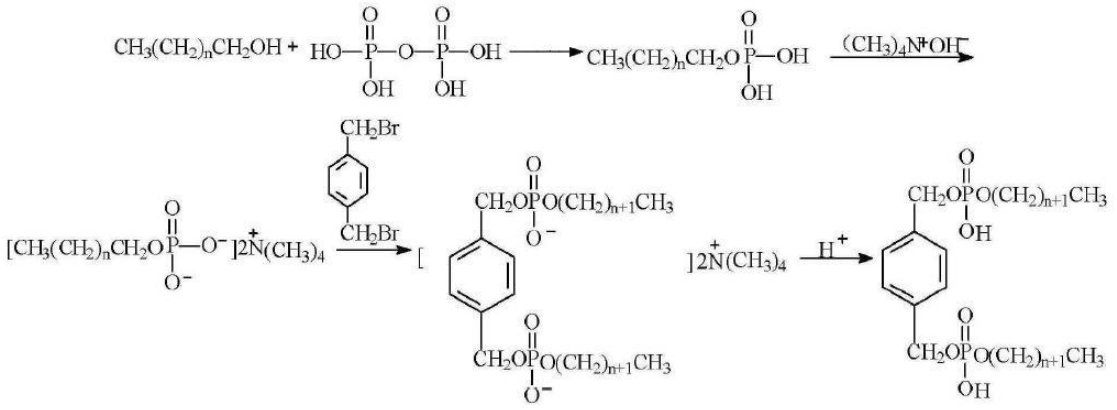

Figure 1.2: Phosphate Gemini Surfactant Synthesis (Menger *et al.*, 1991).

Duivenvoorde (1997) also synthesized a bis-phosphate Gemini surfactant, but using the hydrophobic polymethylene group as spacer. The reaction scheme is shown in Figure 1.3.

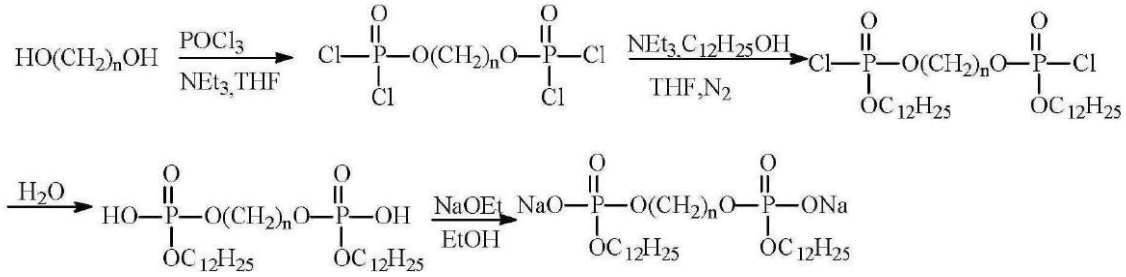

Figure 1.3: Phosphate Gemini Surfactant with Hydrophobic Spacer (Duivenvoorde *et al.*, 1997).

Okahara and Zhu (1991-1993) prepared a series of anionic Gemini surfactants, including sulfates, sulfonates, phosphates, and carboxylates by utilizing a three-functional epichlorohydrin, as shown in Figure 1.4. This scheme actually involves one more pre-reaction (Okahara *et al.*, 1985, not included in Figure 1.4), which makes it a three-step reaction with final yield normally below 25% and takes more than one week to finish.

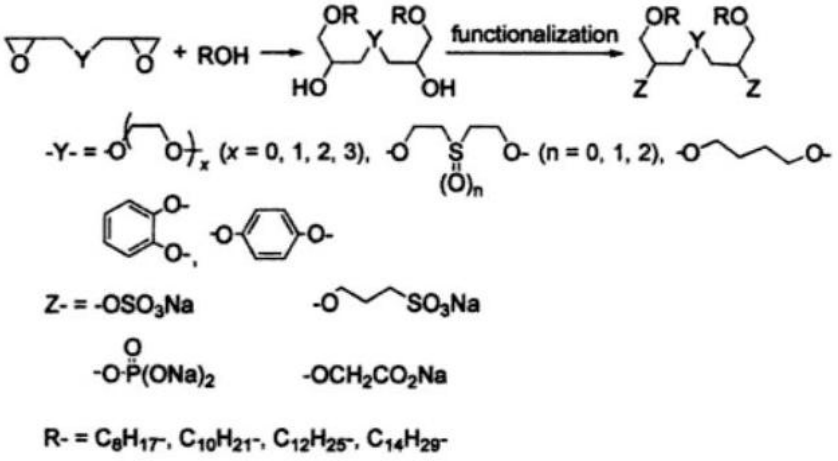

Figure 1.4: Anionic Gemini Surfactant Synthesized from Diglycidyl Ethers (Okahara, *et al.*, 1990-1993).

Rist and Carlsen (1999) reported a two-step and more general reaction scheme (shown in Figure 1.5) for selective synthesis of sulfate/sulfanote Gemini surfactants, with EO units (-CH_2CH_2O-) as spacer groups. Generally, this route offers higher yield (~45%) and requires less laboratory operations and reaction time. Therefore, this reaction scheme has been adopted as the base route in the current study, as will be discussed in detail in Chapter 2.

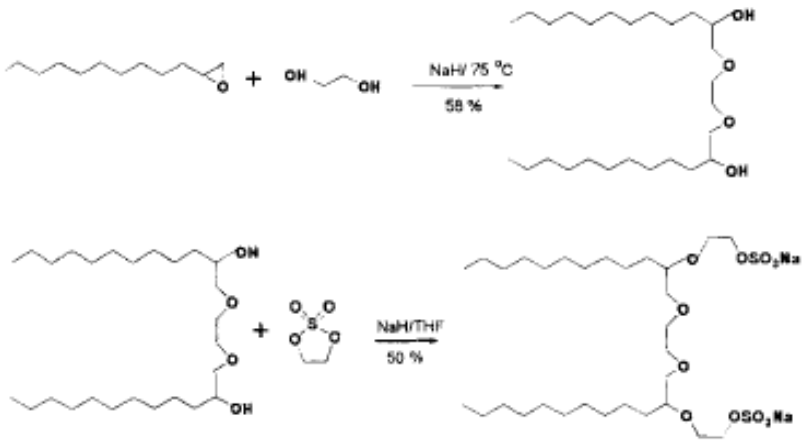

Figure 1.5: Sulfate Gemini Surfactant Synthesis (Rist *et al.*, 1999).

1.3.3 Distinct Characteristics of Gemini Surfactants

There are several reasons for the current interest in Gemini surfactants in both academic and industrial circles working on surfactants.

Critical Micelle Concentration

A key property of all surfactants is their critical micelle concentrations (CMC). The CMC is the concentration above which monomeric surfactant molecules assemble into aggregates called micelles. If the micelles are small (e.g. 10 molecules) then the CMC may embody a concentration range, if the micelles are a more usual size of 50-100 molecules, then the CMC is indeed sharply defined owing to the highly cooperative nature of the aggregation process. The CMC is useful as it reveals the propensity of surfactants to assemble in water. Usually, the longer the surfactants tail, the lower the CMC. Hydrophobic forces, opposed by electrostatic repulsion among the ionic head groups at the micelle surface, drive the micellization. Micelles are known to be disorganized assemblies with interiors consisting of mobile, nonlinear hydrocarbon chains (Tanford, 1973; and Menger, 1979).

Table 1.1 CMC Values for Anionic Gemini and Conventional Surfactants (Rosen and Tracy, 1998).

Compound	CMC (mM)
$[C_{10}H_{21}OCH_2CH(SO_4^-Na^+)CH_2OCH_2]_2$	0.013
$C_{12}H_{25}SO_4^-Na^+$	8.2
$[C_{10}H_{21}OCH_2CH(OCH_2CH_2CH_2SO_3^-Na^+)CH_2]_2O$	0.033
$C_{12}H_{25}SO_3^-Na^+$	9.8
$[C_{10}H_{21}OCH_2CH(OCH_2COO^-Na^+)CH_2]_2O$	0.084
$C_{11}H_{23}COO^-Na^+$	20.0
$C_{12}H_{25}OPO_2^-O\text{-}(CH_2)_6\text{-}OPO_2^-OCH_{12}H_{25}\ 2Na^+$	0.4
$C12H25N^+(CH_3)_2(CH_2)_nN^+(CH_3)_2C_{12}H_{25}\ 2Br^-$	1.0

The CMC of Geminis can be conveniently measured using different techniques. Surface tension is probably the most common method of determining the CMC. Anionic Gemini surfactants have lower CMC than their cationic counterparts. The CMC of anionic Geminis also decreases with increasing spacer length (Hait *et al.*, 2002). CMC values of some anionic Gemini are listed in Table 1.1, together with those of some conventional anionic surfactants for comparison purposes. Interesting generalizations emerge from the numbers: i) anionic Gemini surfactants have remarkably low CMCs when compared with corresponding surfactants of equivalent chain length; ii) anionic Geminis have somewhat lower CMC values than their cationic counterparts.

Surface Activity

The surface tension of water (72mN/m at 25^{o}C) is typically reduced to 30 to 40mN/m at the CMC of a surfactant. Surface activity has a close connection to the wide-ranging applications of surfactants in virtually every major industry. A known means of reporting the surface activity is in terms of C_{20} values. It corresponds to the surfactant concentration that reduces the surface tension by 20mN/m. C_{20} values of some anionic Geminis are given in Table 1.2.

Table 1.2 CMC Values for Anionic Gemini and Conventional Surfactants (Rosen and Tracy, 1998).

Compound	C_{20} Value (mM)
$[C_{10}H_{21}OCH_2CH(SO_4^-Na^+)CH_2OCH_2]_2$	0.001
$C_{12}H_{25}SO_4^-Na^+$	3.1
$[C_{10}H_{21}OCH_2CH(OCH_2CH_2CH_2SO_3^-Na^+)CH_2]_2O$	0.008
$C_{12}H_{25}SO_3^-Na^+$	4.4
$[C_{10}H_{21}OCH_2CH(OCH_2COO^-Na^+)CH_2]_2O$	0.004
$C_{11}H_{23}COO^-Na^+$	5.0

Anionic Gemini surfactants have low C_{20} values compared with corresponding single chain surfactants of equivalent chain length. The surface activity of short alkyl chain (8-12) Geminis with either rigid and hydrophobic or flexible and hydrophilic spacers increases regularly with an increase in the alkyl chain length of the hydrophobic group. Geminis with a flexible hydrophilic spacer appear to aggregate more readily than those with a rigid hydrophobic one (Song and Rosen, 1996). The higher surface activity of these Geminis leads to requirement of fewer raw materials for synthesis.

Quite a few qualitative explanations have been proposed, as to why are Geminis so prone to adsorb at the air/water interface. Rosen (1993) ascribed these effects to a stronger distortion of the water structure by the two hydrophobic groups of a Gemini molecule. Migration of surfactants to the air-water interface is thereby promoted. Menger (2000) further connected this with closer interfacial packing of Geminis. Apparently, the Gemini spacer forces the pair of ionic groups to reside in a smaller space filling geometry relative to that of two ordinary surfactants. And the resulting smaller cross-sectional area-per-molecule promotes the formation of a more coherent interfacial film. Anionic Geminis have wide applications due to their high surface activity. They have mature applications in industry for detergency and emulsification.

Solubility in Water

The Krafft point temperature is the characteristic temperature at which the solubility of a surfactant becomes equal to CMC. For surfactant to be considered soluble, their Krafft point temperature has to be below room temperature. Various anionic Gemini surfactants, including disulfonate, disulfate, and diphosphate, have been synthesized and investigate, especially by the group of Okahara and Ikeda in Osaka University (Okahara *et al.*, 1990, 1991, 1992 & 1993). The Krafft points of all these anionic Gemini surfactants have been reported below those of comparable conventional surfactants. The water solubility of some dicarboxylate anionic Gemini surfactants in hard water has been reported to be greater than that of comparable sodium carboxylates (Shukla *et al.*, 2006).

Micelle Shape & Rheology

Single-chained amphiphiles form, in aqueous solution, spherical aggregates called micelles. Ionic head groups lie near the water, whereas the hydrocarbon tails project inward. If there are two chains per head group, as in a phospholipid, then the head group and chains are of roughly equal diameter and the compound can pack into a parallel array, e.g. a bilayer. Micellar shape in Geminis is a complicated matter as it depends on not only surfactant structure but also on solution conditions such as concentration, temperature, and ionic strength. It affects rheological and solubilization properties, which are important issues from a practical standpoint.

Aqueous solutions of some Gemini surfactants with a short spacer can have a very high viscosity at a relatively low surfactant concentration, whereas the viscosity of the solution of the corresponding monomeric surfactant solution normally remains low (Kern *et al.*, 1994). Aggregation behavior of a given surfactant can be predicted using the surfactant packing parameter introduced by Israelachvili (1976). Based on the packing parameter, Danino *et al.* (1995) proposed that a bimodal head group distance distribution

and the effect of the chemical link between head groups on the packing of surfactant alkyl chains in the micelle core are expected to strongly affect the curvature of surfactant layers, and thus the micelle shape and the properties of the solution.

Most experimental studies, however, have been conducted using cationic Gemini surfactants. Cryo-transmission electron microscopy (Cryo-TEM) studies (Zana *et al.*, 1995) on cationic *12-s-12* and *16-s-16* Geminis have produced photos with the following morphologies: a) giant, entangled, wormlike micelles with *12-2-12* and *12-3-12* (consistent with an observed viscoelasticity at higher concentrations); b) spherical micelles for *12-s-12* (s=4,8,12); c) vesicles of *12-16-12*; d) vesicles, membrane fragments.

Oda *et al.* (1997) discovered that in the absence of any added salt, solutions of less than 2wt% *12-2-12* display low viscosities. Above 2wt%, however, the viscosity rises abruptly due to formation of wormlike micelles. The average length of the worms, and hence the viscosity is affected by two opposing forces: a) electrostatic repulsive energy among the cationic nitrogen atoms that favors scission of the worms; and b) end-cap energy that favors micelle growth by minimizing the number of high energy termini. At elevated *12-2-12* concentrations, electrostatic interactions become screened, end-cap energy assumes a more dominant role, and the micelles grow into semi-flexible worms. It is interesting that micelles can be forced to grow even at lower *12-2-12* concentrations by an applied shear that exceeds a certain critical shear rate. The tendency to form worm-like structures increases as the spacer length decreases and the chain length decreases.

Solubilization

Solubilization is an important phenomenon required in tertiary oil recovery and detergency. Many organic compounds that are normally insoluble in water, or only

slightly soluble, dissolve to a greater extent in the presence of a micellar surfactant. The increased solubility is called solubilization. A few aspects of solubilization for conventional surfactant systems are compiled here (Menger *et al.*, 2000):

- The location within the micelle of a solubilized compound depends upon its structure. Saturated hydrocarbons concentrate at the micellar core. Even nonpolar aromatic moieties prefer this to the interfacial region.
- Increase in the surfactant chain length increases the solubilization power.
- Branching of the surfactant chain length tends to diminish solubilization power.
- For a given chain length solubilization by micelles of different charge types usually follows the sequence nonionic>cationic>anionic (Saito, 1967).

Solubilization in Gemini micelles has not been examined in detail. The one exception involved the determination of the solubility of toluene and *n*-hexane in aqueous solutions of cationic Geminis (Dam *et al.*, 1996). The experiments were carried out by shaking 3ml of hydrocarbon with 30ml of aqueous surfactant for many hours until clarity was achieved. Analysis of the water layer for hydrocarbon provided the solubilization power of the surfactant. It was found that, in the words of the authors, "the propensity of Gemini micelles for oil solubilization is significantly better than of conventional surfactants; this is true on a molar basis as well as a weight basis". For example, *12-2-12* gave a [toluene]/[surfactant] ratio of 3.8 compared to 0.78 for CTAB. However, the Geminis showed a distinct preference for solubilizing toluene over n-hexane. *10-2-10* and *12-2-12* led to [*n*-hexane]/[surfactant] ratios of only 0.29 and 0.99, respectively. It is proposed that the enhanced solubilization power of Geminis may be related to tubular shapes of their aggregates.

Synergy between Anionic Geminis and Conventional Surfactants

Because of the double charge on ionic Geminis, they interact more strongly with oppositely charged surfactants at interfaces or in mixed micelles than single charged surfactants. In many practical applications, surfactants are used in formulations containing mixtures of different compounds, and synergism can often be observed. Synergism is defined here as the condition in which the properties of a mixture are better than those attainable with the individual components separately. An important mixed system is that includes ionic Gemini surfactants and conventional ionic surfactants with the same charge. In most practical applications, e.g., in cosmetic products, mixing an ionic surfactant with another surfactant bearing the same change is common.

Tsubone *et al.* (2003) investigated molecular interaction in two mixtures of an anionic Gemini $(CH_2)_2[N(COC_{11}H_{23})CH(COOH)CH_2(COOH)]_2$ 2NaOH (GA) and a conventional anionic surfactant in 0.1M NaCl at pH 5.0 and to search for synergism. The stronger interaction for GA/SDS (sodium dodecyl sulfate) mixture may be caused by the combination of the smaller minimum area per molecule at the air/water interface of the head groups in the GA molecule and larger in the SDS molecule. In case of cationic Gemini surfactants (bis-ammonium Gemini), Sugihara *et al.* (2003) investigated the mixed micellization and mixed adsorbed film formation for the combination of a Gemini type cationic surfactant and a nonionic surfactant mixture: bis-trimethyl ammonium Gemini (BAGTB) and *n*-decanoy-N-glucamide (MEGA-10). They determined the critical micelle concentration (CMC), minimum surface tension at CMC (γ_{CMC}), surface excess (Γ), mean surface area occupied by a molecule and parameters related to the synergism in surface activity such as pC_{20} and CMC/C_{20}. They observed that the synergism in surface tension reduction was weak in the mixed micelle formation. It would appear from these results that the existence of synergism depends heavily on the specifics of a particular

surfactant mixture, and it is difficult to draw any conclusion before detailed tests are conducted.

1.4 APPLICATIONS OF GEMINI SURFACTANTS IN THE PETROLEUM INDUSTRY

Gemini surfactants are remarkably superior to conventional surfactants in characteristic features. They have a much lower CMC, much lower values of the C_{20}, and lower Krafft temperature. In terms of concentration, they are about three orders of magnitude more efficient at reducing the surface tension of water and more than two orders of magnitude more efficient in interfacial activity than conventional surfactants. Therefore, a small quantity of Gemini surfactant can have a dramatic effect on IFT and may be useful in EOR applications. Theses advantages led many scientists, researchers, and manufacturers to develop new varieties of Gemini surfactants for industrial, agricultural, biological, or daily uses. Many patents cover the manufacture and applications of anionic, cationic, zwitterionic, and nonionic Gemini surfactants. Some Gemini surfactants with specific performances have been introduced in markets as commercial products, individually or blended with other surfactants (Zana and Xia, 2004). In this section in particular, some of the potential areas in petroleum industry where Gemini surfactants can be used are discussed and summarized. However, most studies in the past were conducted using cationic Gemini surfactants.

1.4.1 Corrosion Inhibition

Gemini surfactant series *m-2-m* (cationic) has been investigated as potential inhibitor of corrosion of iron in 1M HCl by different techniques (Achouri *et al.*, 2001). The results showed that the Gemini surfactants act mainly as cathodic inhibitors by adsorbing on the electrode surface and forming a protective layer. The results also indicated that the added surfactants do not change the proton reduction mechanism and

that the inhibition efficiency increases with the number of carbon atoms in the alkyl chain (*m*), with increasing surfactant concentration and are a maximum near CMC.

The sequence of *m-2-m* surfactants according to their increasing efficiency in inhibiting iron corrosion is the same as the sequence of increasing adsorption of the surfactant at the air-water interface: *10-2-10* < *12-2-12* < *14-2-14*. The inhibition efficiency versus concentration curves are S-shape. The efficiency plateau at high concentration is attributed to the formation of a full bimolecular surfactant layer on the iron surface.

1.4.2 Antimicrobial Activity

Dicationic *m-s-m* surfactants with a short spacer show high antimicrobial activity, up to 100 times larger than the commonly used germicides (Masuyama *et al.*, 2000). The dicationic Gemini surfactants $[C_{12}H_{25}N^{+}(CH_3)_2CH_2CONH]_2Y\ 2Cl^{-}$ [with $Y=(CH_2)_4$ or $(CH_2)_2SS(CH_2)_2$] were found to be more effective against many micro-organisms other than CTAB (Diz *et al.*, 1994). Arginie-based Gemini surfactants have been shown to possess a broad range of antimicrobial activity, and they also have low toxicity (Perez *et al.*, 1996).

1.4.3 Environmental Surfactant

The quantity of Gemini surfactants used for a given application being much lower than that of conventional surfactants, this reduces the load of waste-water treatment. Moreover, environmental surfactants, such as disulfonate or dicarboxylate Geminis containing C=C groups in the hydrophobic moiety or spacer are cleaved by ozone. Their degradability is much higher than for conventional surfactants such as LAS, SDS, for instance (Masuyama *et al.*, 2000).

1.4.4 Gelator of Organic Solvents and Water

The self-assembly of small molecules in solution into very elongated aggregates is necessary for gel formation (Zana and Xia, 2004). The formation of wormlike micelles and tubules is easy in aqueous solutions of Geminis with a short spacer. This also allows Gemini surfactants to gel organic solvents if they assemble into aggregates similar to those formed in water. The cationic Gemini surfactants 16-2-16, with tartrate counterions can gel organic solvents containing traces of water (Oda *et al.*, 1998). Gelling is already effective with a surfactant concentration as low as 10mM. TEM imaging revealed the presence of long entangled helical fibers. These surfactants can gel chlorinated solvents such as CH_2Cl_2, $CHCl_3$, and $Cl_2CHCHCl_2$. Gelation of water was reported to occur with bis-urea dicarboxylic acid Gemini surfactants (Estroff *et al.*, 2000). Scanning electron microscopy also revealed the presence of entangled fibers.

1.4.5 EOR Surfactant

Despite the fact that Gemini surfactants are potential game changers in chemical EOR practices, research into their application in petroleum related areas is very limited.

Zaitoun *et al.* (2003) reported the effects of ANTISORBTM 1416 (a sulfonate oligomeric polymer) on adsorption reduction and high salt (salinity and hardness) tolerance at low concentration, which is of particular interest to operations that might be otherwise be uneconomical because of water treatment and handling cost. Berger *et al.* (2002) reported further improvement of these effects by attaching the sulfonate group to the end of the alkyl chain rather than to the aromatic ring. The other important properties, such as surface activity, interfacial tension and rheology, have not been well examined.

Researchers in China have shown great interest in the application of Gemini surfactants to the petroleum industry (Wang *et al.*, 2003 & 2007; Yue *et al.*, 2008). Research groups of Luo (2004, 2005 & 2008) and Pu (2005 & 2006) synthesized two

series of cationic Gemini surfactants with different tail lengths and spacer groups. Ultralow interfacial tension values were observed with certain crude oil systems. Clearly the application of these cationic surfactants is limited by adsorption/retention in porous media. Tang *et al.* (2007) reported some preliminary coreflooding tests using cationic Gemini surfactants. Due to the retention of cationic molecules and poor screening and design, incremental oil recovery after waterflooding was found to be only 7.7 % of OOIP.

Zhu *et al.* (2006 & 2007) investigated the synergism between a synthetic sulfonate Gemini surfactant and petroleum sulfonate. With low surfactant concentration, the mixture gave superior performance to conventional petroleum sulfonates in terms of CMC and IFT values. Tan *et al.* (2003 & 2006) synthesized several sulfonate Gemini surfactants and studied their interfacial properties. The IFT between crude oil and aqueous surfactant solution prepared in high salinity brine could reach ultralow values, indicating the usage of Gemini surfactants in harsh water environments is promising. However, these studies were all based on a trial and error process without a full appreciation of Gemini structure-performance relationships. If these types of surfactants are to be used for EOR applications, a more fundamental understanding of solution behavior of these novel molecules needs to be gained with carefully designed and implemented experiments.

1.5 RESEARCH OBJECTIVES FOR SECTION I

Because of the enormous variety in their structure, and their superior interfacial activity, Gemini surfactants have the potential of being utilized in chemical EOR. It is, therefore, our main objective in Section I of this dissertation to systematically test EOR relevant (interfacial and rheological) properties, and gain a better fundamental understanding of the solution behavior of anionic Gemini surfactants, and finally lay a

firm foundation for more concrete applications in chemical EOR operations. The specific objectives can be further broken down as follows:

- To seek convenient and reliable synthesis routes for targeted anionic Gemini surfactants, based on considerations of raw material availability, final product structure and process complexity.
- To study the basic solution and interfacial properties of synthesized Gemini surfactants, such as critical micelle concentration, surface tension reduction at an air-water interface, and adsorption behavior at a solid-liquid interface; and to gain fundamental insights into the micellization in aqueous solution and adsorption at air-water interface by determining the relevant thermodynamic parameters.
- To examine the EOR potential of Gemini surfactants using a systematic approach: experimentally, conducting aqueous stability, phase behavior tests, interfacial tension (IFT) and rheology measurements; theoretically, modifying existing and/or developing new theoretical models for better understanding the interfacial and solubilization behaviors of Gemini surfactants.
- To fundamentally understand the superior solution properties of Gemini surfactants from a molecular thermodynamic viewpoint by improving on the existing models for conventional surfactants; to establish prediction capability for aggregation behavior for anionic Gemini surfactants in aqueous solution.

1.6 CHAPTER OUTLINE FOR SECTION I

Section I of this dissertation is organized into seven chapters, with this Introduction serving as **Chapter 1**.

Chapter 2 describes in detail the synthesis of the anionic Gemini surfactants of interest in the current study. In addition to the description of the general reaction scheme,

more detailed experimental sections for two sample Gemini molecules are also included. NMR characterization results confirming the targeting structures are tabled for future reference.

In **Chapter 3**, the critical micelle concentration (CMC) and degree of ionization of the synthesized Gemini molecules in aqueous solution are determined using electrical conductivity measurements. And based on experimental results, the thermodynamic parameters of micellization are derived, which offer fundamental insights into the solution behavior of Gemini surfactants. More specifically, the entropy of micellization is used to demonstrate the superior ability of Gemini surfactants to reduce oil/water interfacial tension.

In **Chapter 4**, the adsorption behavior of Gemini surfactants at air-water and solid-liquid interfaces are studied by surface tension and static adsorption tests. Thermodynamic properties of Gemini adsorption process of Gemini surfactants at air-water interface are derived and compared with those of conventional surfactants. The adsorption of synthesized anionic Gemini surfactants onto Berea core materials are determined by static adsorption tests. More specifically, the impacts of liquid/solid ratio, equilibration time, brine salinity, pH, and surfactant structure are systematically studied.

In **Chapter 5**, the interfacial tension (IFT) reduction potential of Gemini surfactant is systematically examined for solution systems containing hydrocarbon, Gemini surfactant, and electrolytes. More specifically, the effects of different variables on the interfacial tension are investigated, including surfactant concentration, tail chain length, mono- and divalent ion concentration, etc. A thermodynamic treatment is adopted to predict the interfacial tension measured for an example system. The model also sheds light on whether an IFT minimum is possible or not for such a system.

Chapter 6 deals with solutions of anionic Gemini surfactants with a short spacer, since these molecules represent the most interesting rheological properties. Viscosity measurements are carried out on aqueous solutions of the anionic Gemini surfactants synthesized in-house. Effects of surfactant structure and concentration, temperature, additives, and shear rate are investigated.

In **Chapter 7**, a predictive model of surfactant self-assembly in aqueous solution is developed to study the micellization properties of the synthesized Gemini surfactants. The model is then used to predict the CMC values for surfactants of varying tail lengths. The effects of temperature and salinity on Gemini micellization are also investigated.

Chapter 2: Synthesis of Anionic Gemini Surfactants

2.1 INTRODUCTION

Gemini surfactants are defined as surfactants that are made up of two amphiphilic moieties connected at the level of, or close to, the head groups by a spacer group. In the past two decades, many different types of Gemini surfactants have been synthesized due to their unique properties in aqueous solution. At first, however, studies on catalysis of chemical reactions by micelles of cationic Gemini surfactants and on the use of these surfactants as bactericidal and fungicidal agents were reported (Bunton *et al.*, 1971; Devinsky *et al.*, 1986). It might have been recognized at that time that cationic surfactants showed unique micelle-forming and surface-adsorbing properties when connecting them two by two to generate Gemini surfactants. Later, unique properties concerning not only surface activity but also molecular aggregation were evidenced. Recently, Gemini surfactants have attracted much attention as potential agents in various industrial applications, and thus the relationship between structure and properties of Gemini surfactants is under careful examination. The activity in the synthesis of these surfactants has shifted in recent years from simple Gemini surfactants to multi-armed, poly-ionic, or even oligo-meric Geminis (Zana and Xia, 2004), as well as developing new types of hydrophilic group, hydrophobic chain, spacer and counter-ion.

In general, cationic Gemini surfactants can be readily synthesized by heating a mixture of the reagents in dry ethanol under reflux for two or three days and purifying the product by recrystallization (Menger *et al.*, 2000). For EOR applications, cationic surfactants are generally used as co-surfactants in surfactant flooding or chemical agents for wettability alteration. However, their application is limited due to high retention in most sandstone reservoirs. On the contrary, anionic surfactants consistently show low

adsorption at neutral to high pH on both sandstones and carbonates. Therefore, in the current study, efforts will be focused on anionic Gemini surfactants.

The first report showing the universal relationship between the properties and structures of anionic Gemini surfactants was published in 1990 (Zhu *et al.*, 1990). Since then, many anionic Gemini surfactants, including sulfates, sulfonates, carboxylates, and phosphates (Okahara *et al.*, 1990, 1991, 1992 & 1993) were prepared by utilizing a three-functional epichlorohydrin (ECH), as shown in Figure 2.1 below.

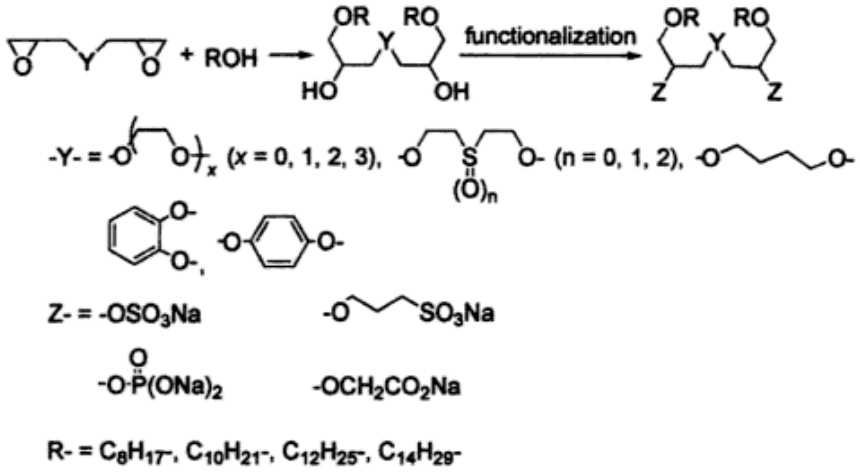

Figure 2.1: Anionic Gemini Surfactants Synthesized from Diglycidyl Ethers (Okahara *et al.*, 1990).

Epoxyalkane was used to synthesize a disulfate Gemini, as shown in Figure 2.2 (Zana *et al.*, 1997). Anionic Gemini surfactants of varied structures have been prepared, because many kinds of starting material other than epichlorohydrin and epoxyalkane, are available for synthesis. For instance, from diphenyl ether and olefin, benzenesulfonate Gemini surfactants are prepared as the components of a mixture product, which has been offered commercially for years (DOWFAX). The isolated benzenesulfonate Gemini

surfactants were confirmed to show excellent detergency (Rosen *et al.*, 2001). All these approaches involve, however, multi-step slow reactions with low final yield.

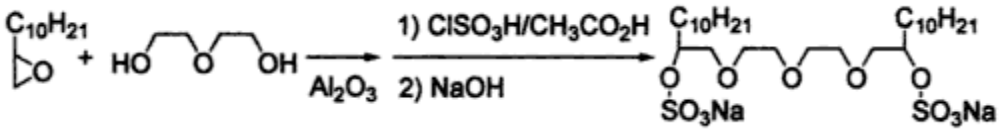

Figure 2.2: Anionic Gemini Surfactants Synthesized from Epoxyalkane (Zana *et al.*, 1997).

2.2 REACTION SCHEME FOR CURRENT STUDY

Rist *et al.* (1999) proposed a general reaction scheme for the selective synthesis of new, pure single-component Gemini surfactants. Gemini surfactants of different types (both ionic and non-ionic) were successfully synthesized with decent yield. Following Rist's approach, Tan *et al.* (2006) synthesized a series of anionic Gemini surfactants with different tail chain lengths. However, the surface-chemical properties of these molecules were not fully characterized, not to mention any EOR related properties.

By referencing the prior art, a two-step stable reaction route has been adopted for the current study. As a general feature, the synthesized molecules contain multiple chains each consisting of hydrophobic alkyl chains that are terminated by sulfate (-$CH_2CH_2OSO_3Na$), or carboxylate (-CH_2COONa) head groups. The chains are interconnected by alkyloxy spacer groups.

The first step (as shown in Figure 2.3) in the synthetic scheme towards the target Gemini molecules deals with the introduction of the flexible spacers. The corresponding diol *3* can be readily obtained by the coupling of two 1,2-epoxyalkane *1* with one short chain diol (e.g. ethylene glycol, or 1,4-butanediol) *2*, in the presence of catalytic amounts

of base (e.g. sodium hydride, or potassium hydroxide). Compound *3* is vacuum dried and isolated after reaction work-up and recrystallization.

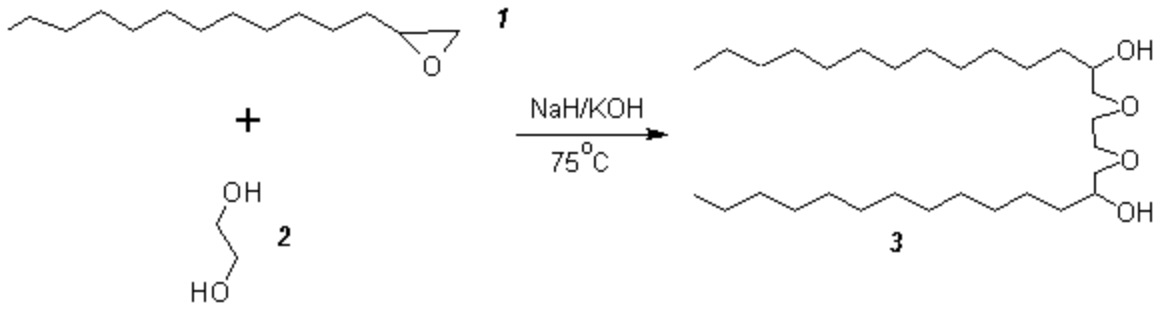

Figure 2.3: Reaction I for the Synthesis of Intermediate Diol Compound, *3*.

The sulfate head groups are then introduced by reacting diol *3* with ethylene sulfate *4* (or propylene sulfonate for sulfonate Geminis) in THF in the presence of an excess of base (shown in Figure 2.4). The pure Gemini disulfate surfactant *5* was vacuum dried and isolated after recrystallization.

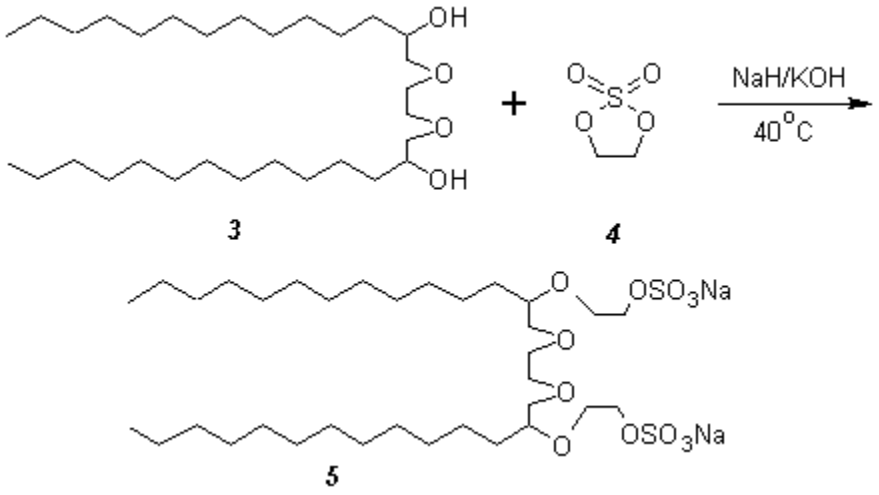

Figure 2.4: Reaction II for the Synthesis of the Sulfate Gemini Surfactant, *5*.

The carboxylate head groups can be introduced by reacting diol *3'* with sodium hydroxide, and followed by a reaction of the product *6* with sodium monochloroacetate *7*, as shown in Figure 2.5. The pure Gemini dicarboxylate surfactant *8* was vacuum dried and isolated after recrystallization.

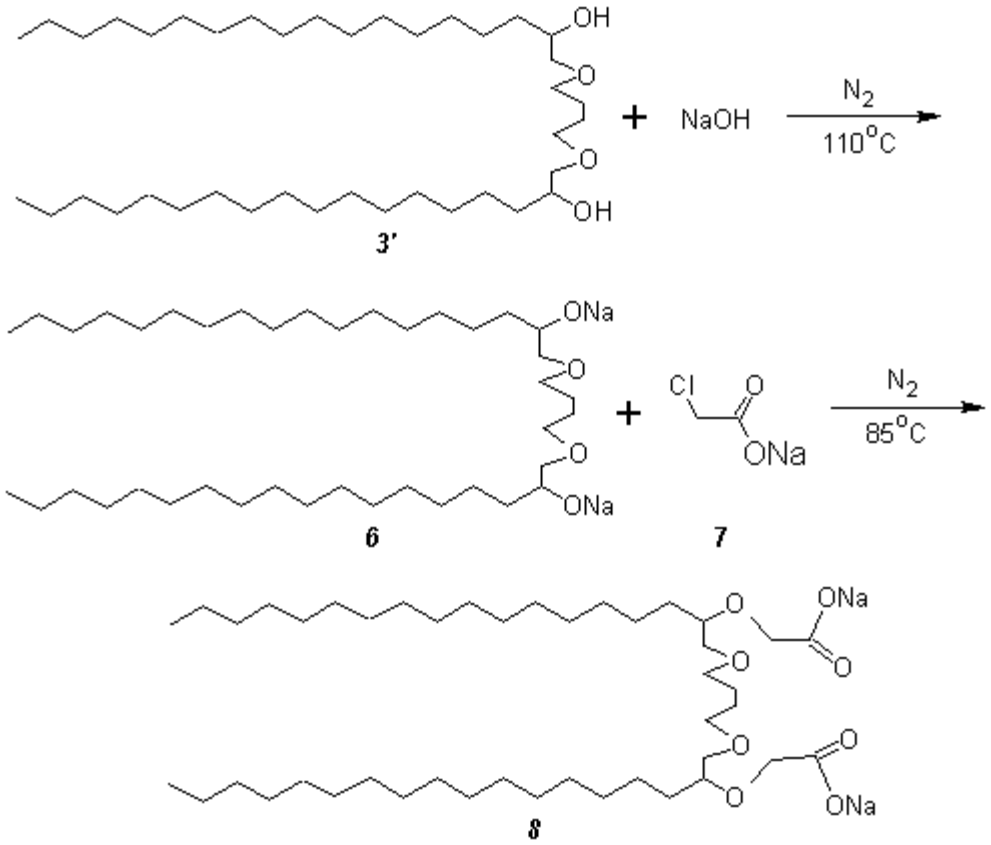

Figure 2.5: Reaction III for the Synthesis of the Carboxylate Gemini Surfactant, *8*.

The proton (^{1}H) and carbon (^{13}C) NMR spectra were registered on a Varian Inova 500 spectrometer using deuterated chloroform ($CDCl_3$) or deuterated water (D_2O) as solvent, and tetramethylsilane (TMS) as internal standard. All products exhibited spectroscopic properties that were in agreement with those expected for the desired structures.

2.3 MATERIALS AND INSTRUMENTS

2.3.1 Materials / Reagents

Table 2.1: Materials / Reagents Used in Gemini Surfactant Synthesis.

Name	Molecular Formula	Assay	Source
Sodium Hydride	NaH	60% dispersion in mineral oil	Sigma-Aldrich
Ethylene Glycol	$HOCH_2CH_2OH$	99.8%	Sigma-Aldrich
1,4-Butanediol	$HO(CH_2)_4OH$	99%	Sigma-Aldrich
1,2-Epoxytetradecane	$C_{14}H_{28}O$	technical grade, 85%	Sigma-Aldrich
1,2-Epoxyhexadecane	$C_{16}H_{32}O$	technical grade, 85%	Sigma-Aldrich
1,2-Epoxyoctadecane	$C_{18}H_{36}O$	>95%	Arkema Inc.
1,2-Epoxyalkane	$C_{20\text{-}30}H_{40\text{-}60}O$	Mixture	Arkema Inc.
Ethylene Sulfate	$CH_2CH_2SO_4$	98%	Sigma-Aldrich
Sodium Monochloroacetate	$ClCH_2COONa$	98%	Sigma-Aldrich
Potassium Hydroxide in MeOH	KOH	1N	Fisher Scientific
Hydrochloric Acid	HCl	1M	Fisher Scientific
Diethyl Ether	$CH_3CH_2OCH_2CH_3$	99.5%	Acros Organics
Deuterated Chloroform	$CDCl_3$	99.8%	Cambridge Isotope Laboratories
Phosphomolybdic Acid (PMA)	$12MoO_3 \cdot H_3PO_4$	10-30%	Sigma-Aldrich
Tetrahydrofuran	C_4H_8O	99.5%	Acros Organics
Dichloromethane	CH_2Cl_2	99.9%	Acros Organics
Sodium Sulfate Anhydrous	Na_2SO_4	99.3%	Fisher Scientific
Acetone	CH_3COCH_3	99.6%	Acros Organics

2.3.2 Instruments / Facilities

Table 2.2: Instruments / Facilities Used in Gemini Surfactant Synthesis.

Name	Manufacturer	Specifications
Stirring Hotplate	Fisher Scientific Isotemp	Ambient to 540˚C 60 to 1200rpm
Heat Gun	Wagner Spray Tech Milwaukee	Ambient to 540˚C
Rotary Evaporator	Buchi R-114	5 to 240rpm
Water Bath	Buchi B-480	20 to 100˚C
Immersion Circulator	B Braun Biotech Inc.	50 to 250˚C 13L/min
Refrigerated Open Bath	Fisher Scientific Isotemp	0 to 70˚C 13 L reservoir
Duo Seal Vacuum Pump	The Welch Scientific Company	
Digital Balance Scale	Mettler PL200	0.001g
TLC Silica Gel	EMD	100 Glass plates 2.5 × 7.5cm
NMR Spectroscopy	Varian Inova 500	500MHz

2.4 SYNTHESIS OF SAMPLE MOLECULES

The general reaction scheme outlined in the previous section was successfully employed in our lab to synthesize a series of Gemini surfactants of different tail and spacer length. Table 2.3 below is a complete list of Gemini surfactants synthesized.

The experimental details for two example molecules, one sulfate (*14-2-14*) and one carboxylate (*18-4-18*) are described in this section. The experimental operations for several key synthesis techniques, including reaction monitoring using TLC, reaction work-up, and NMR sample preparation, are included in Appendix A.

Table 2.3: Anionic Gemini Surfactants Synthesized in Our Lab.

Molecular formula	Notation	Starting Materials
$(n\text{-}C_{14}H_{28})_2(OCH_2CH_2O)$-$(OCH_2CH_2SO_4Na)_2$	*14-2-14*	1,2-epoxytetradecane ethylene glycol ethylene sulfate
$(n\text{-}C_{18}H_{36})_2(OCH_2CH_2O)$-$(OCH_2CH_2SO_4Na)_2$	*18-2-18*	1,2-epoxyoctadecane ethylene glycol ethylene sulfate
$(n\text{-}C_{20+}H_{40+})_2(OCH_2CH_2O)$-$(OCH_2CH_2SO_4Na)_2$	20^+-2-20^+	mixture of epoxyalkanes ethylene glycol ethylene sulfate
$(n\text{-}C_{14}H_{28})_2(OCH_2CH_2CH_2CH_2O)$-$(OCH_2CH_2SO_4Na)_2$	*14-4-14*	1,2-epoxytetradecane 1,4-butanediol ethylene sulfate
$(n\text{-}C_{16}H_{32})_2(OCH_2CH_2CH_2CH_2O)$-$(OCH_2CH_2SO_4Na)_2$	*16-4-16*	1,2-epoxyhexadecane 1,4-butanediol ethylene sulfate
$(n\text{-}C_{18}H_{36})_2(OCH_2CH_2CH_2CH_2O)$-$(OCH_2CH_2SO_4Na)_2$	*18-4-18*	1,2-epoxyoctadecane 1,4-butanediol ethylene sulfate
$(n\text{-}C_{20+}H_{40+})_2(OCH_2CH_2CH_2CH_2O)$-$(OCH_2CH_2SO_4Na)_2$	20^+-4-20^+	mixture of epoxyalkanes 1,4-butanediol ethylene sulfate
$(n\text{-}C_{18}H_{36})_2(OCH_2CH_2CH_2CH_2O)$-$(OCH_2COONa)_2$	*18-4-18 2COONa*	1,2-epoxyoctadecane 1,4-butanediol sodium chloroacetate
$(n\text{-}C_{20+}H_{40+})_2(OCH_2CH_2CH_2CH_2O)$-$(OCH_2COONa)_2$	20^+-4-20^+ *2COONa*	mixture of epoxyalkanes 1,4-butanediol sodium chloroacetate

2.4.1 *14-2-14* Sulfate Gemini

Intermediate Diol Compound

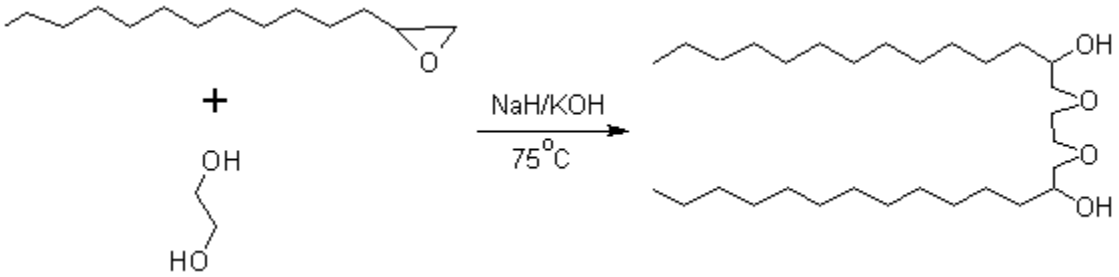

Sodium hydride (60% dispersion in mineral oil; 0.376g, 9.4mmol) was placed in a 100ml 3-neck flask under N_2 protection. Ethylene glycol (99.8% 1.113g/ml; 5.25ml, 0.094mmol) was added through a septum, followed by 1,2-epoxytetradecane (85% 0.845g/ml; 55.59ml, 0.188mmol). The resulting reaction mixture was stirred at 75˚C. The conversion was monitored by thin layer chromatography (TLC). After approximately 48 hours, only trace amounts of the epoxide could be detected, and the reaction mixture was then cooled to room temperature and quenched with water and 1M hydrochloric acid (9.4ml). The mixture was then transferred to a separatory funnel and subjected to continuous extraction with ether/water (150ml/50ml). The combined organic phase was dried over Na_2SO_4 (anhydrous). The solvent was removed by rotary evaporation. The crude product was recrystallized twice in diethyl ether at 5˚C. The product was isolated by filtration and vacuum dried for 2 hours.

^{1}H-NMR ($CDCl_3$): δ 0.85~0.89 (6H, terminal methyl groups), 1.30~1.50 (44H, methylene groups in two tails), 2.75~2.79 (2H, terminal hydroxyl groups), 3.29~3.35 (2H, hydrogen attached to the hydroxyl-carbon), 3.52~3.83 (8H, methylene groups

connected to oxygen) ppm. ^{13}C-NMR ($CDCl_3$): δ 14.5, 23.1, 25.8, 26.0, 29.7, 30.0, 30.0, 30.1, 32.3, 33.4, 70.6, 70.6, 70.9, 76.4ppm.

Target Gemini Surfactant

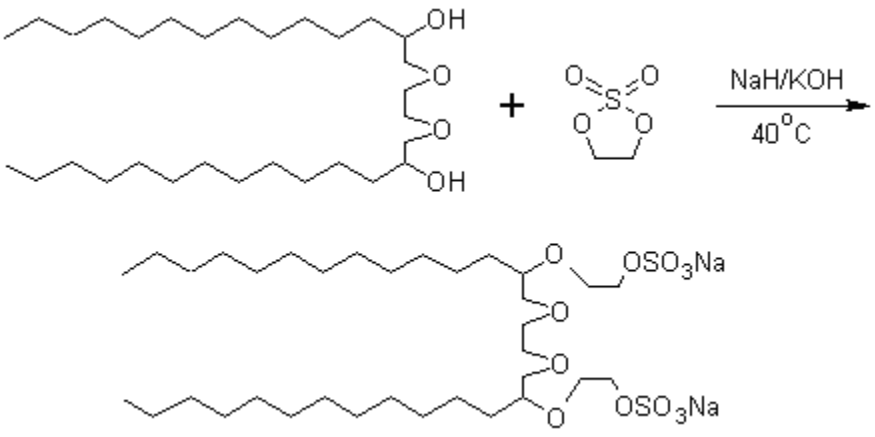

Diol compound (1.217g, 2.50mmol) and ethylene sulfate (98%; 0.633g, 5.0mmol) in 50 ml of dry THF was placed in a 100 ml flask under N_2 protection. The reaction was cooled in an ice bath and sodium hydride (60% dispersion in mineral oil; 0.2g, 5.0mmol) was added portion-wise over a 15min period. The temperature was then allowed to reach 40˚C. The progress of the reaction was monitored by TLC. After approximately 44 hours the substrate was fully consumed. The reaction mixture was then cooled down in an ice bath, quenched with water and the solvent removed under reduced pressure using a rotary evaporator. The crude product was then subjected to continuous extraction with 60ml of butanol/50ml water. The solvent was removed again by evaporation under reduced pressure. The crude product was washed with ice-cold acetone (50ml), and then recrystallized from ethanol (80ml).

It is probably worth mentioning that sulfonate Gemini can be readily synthesized by substituting propylene sulfonate for ethylene sulfate in the final step. Due to the high

toxicity of propylene sulfonate, however, very limited work was done on sulfonate molecules.

^{1}H-NMR (D_2O): δ 0.87~0.92 (6H, terminal methyl groups), 1.20~1.40 (44H, methylene groups in two tails), 1.97~2.04 (4H, methylene groups connected to SO_4), 2.94~3.0 (4H, the rest methylene groups in head), 3.38~3.7ppm (14H, the rest hydrogen atoms).

Catalytic Base Selection

Sodium hydride (NaH) was adopted based on past work in the literature (Rist *et al.*, 1999; Tan *et al.*, 2006) as the catalyst base material for the reaction. This material, however, needs special handling and storage due to the high tendency to ignite, especially upon contact with water (or moisture). Therefore, in the experiments sodium hydride was used in the form of dispersion in oil, which can be exposed to air for a short period of time. In order to address the safety issue and simplify the experimental procedure, the more commonly used bases, sodium hydroxide (NaOH) and potassium hydroxide (KOH), were tried out for reactions (see Table 2.4 below). Sodium hydroxide, because of its solid form, even after grinding still slows down the reaction significantly. Potassium hydroxide, on the other hand, can be used in the form of a methanol solution at high concentration. Therefore, it can be easily handled and injected into the reaction system. And the solvent itself could be readily removed by evaporation. As shown in Table 2.4, for the first reaction, with a catalytic amount of KOH (in methanol) at 120˚C, a final yield of 65% was achieved after 44 hours. This use of KOH has reduced the complexity of running the experiments. All reactions (both steps for all surfactants) were, therefore, run with KOH as the catalyst and base.

Table 2.4: Trial Reactions Run for Catalytic Base Selection.

RXN #	Base	RXN Temp. (˚C)	Yield	Time (hrs)	Description
I	NaH, catalytic amount	85	31%	48	confirmed by NMR
II	NaH, catalytic amount	85	40.6%	48	confirmed by NMR
III	KOH (methanol), 1 g	85	NA	--	dark colored mixture; purification failed
IV	KOH (methanol), 500 mg	75	NA	--	
V	KOH (methanol), 250 mg	65	NA	--	
VI	KOH (methanol), catalytic amount	120	65%	44	confirmed by NMR

2.4.2 *18-4-18* Carboxylate Gemini

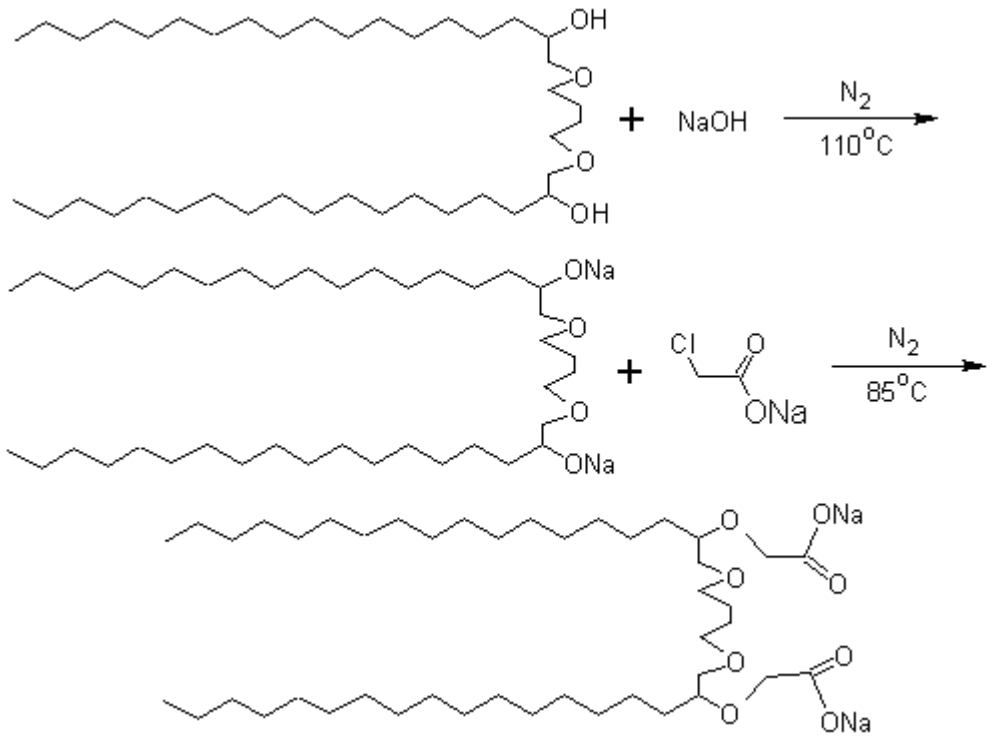

Diol *18-4-18* (1.565g, 2.50mmol) in 50ml of dry THF and sodium hydroxide (0.200g, 5.0mmol) was placed in a 100 ml flask under a N_2-atmosphere. The temperature was then heated up to 110˚C. The progress of the reaction was monitored by TLC and pH drop. After approximately 12 hours, sodium monochloroacetate (98%, 0.594g, 5.0mmol) was added into the reaction mixture and the temperature was reduced to 85^{o}C for 20 hours. The reaction mixture was then cooled down to room temperature and quenched with water and the solvent removed under reduced pressure using a rotary evaporator. The crude product was then subjected to continuous extraction with 60ml of DCM/50ml water. The solvent was removed again by evaporation under reduced pressure. The crude product was then recrystallized from dichloromethane (80ml).

^{1}H-NMR (D_2O): δ 0.87~0.92 (6H, terminal methyl groups), 1.20~1.55 (60H, methylene groups in two tails), 3.40~3.89 (10H), 4.25~4.32ppm (4H).

2.5 NMR CHARACTERIZATION

Table 2.5 below demonstrates the corresponding relationship between chemical shift on ^{1}H-NMR spectrum and atomic environment of different hydrogen in *14-2-14* diol compound. Figure 2.6 shows the corresponding proton NMR spectrum.

Table 2.5: Atomic Environment for Hydrogen Atoms in *14-2-14* Diol.

Chemical Environment	**a**	**b**	**c**	**d**	**e**
Chemical Shift	0.85~0.89	1.30~1.50	2.75~2.79	3.29~3.35	3.52~3.83
Type of Hydrogen Atom	$-CH_3$	$-CH_2-$	-OH	-CH-	$-CH_2-$
Number of Hydrogen	6	44	2	2	8
Location in the Structure	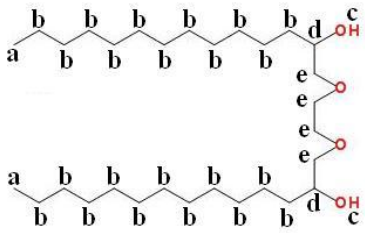				

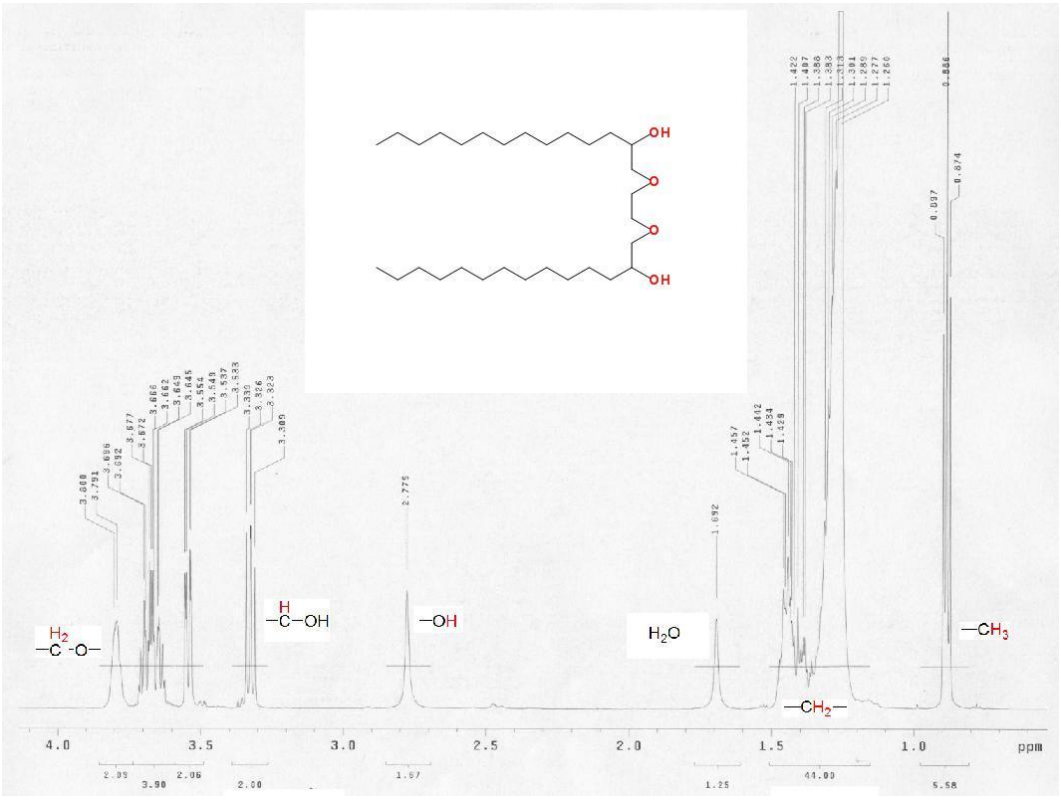

Figure 2.6: ^{1}H NMR Spectrum of *14-2-14* Diol Compound.

Figure 2.7 below is the proton NMR spectrum of the *14-2-14* sulfate Gemini molecule.

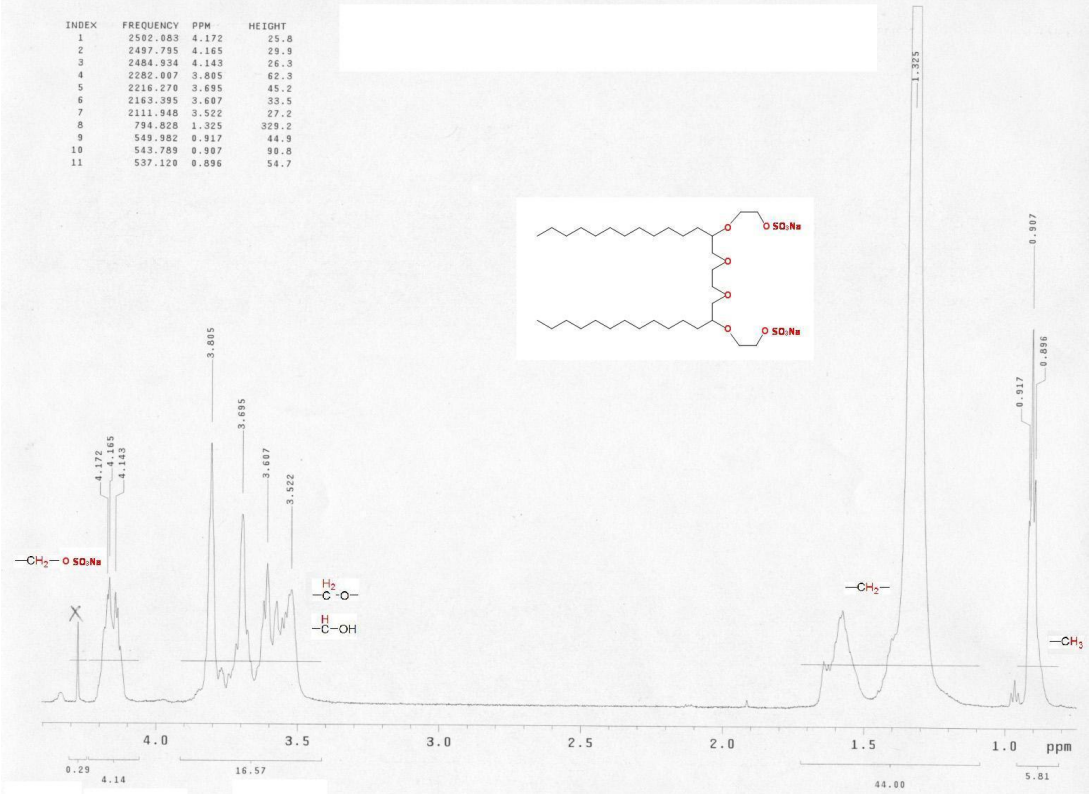

Figure 2.7: ^{1}H NMR Spectrum of *14-2-14* Sulfate Gemini Surfactant.

Figure 2.8 and Figure 2.9 are the 2D and 3D representations of this surfactant using a ball-and-stick model. Although the carbon chains look straight and stiff in the figure, they are actually fairly flexible and can take on more complex configurations.

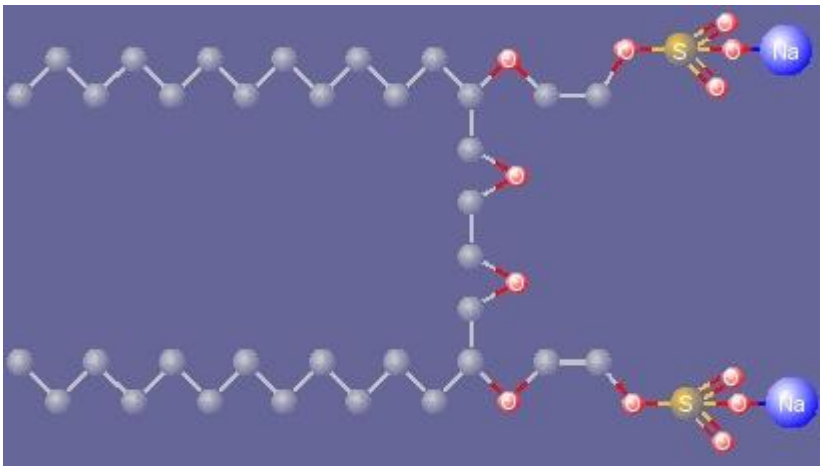

Figure 2.8: 2D Ball-and-Stick Model for *14-2-14* Sulfate Gemini Surfactant.

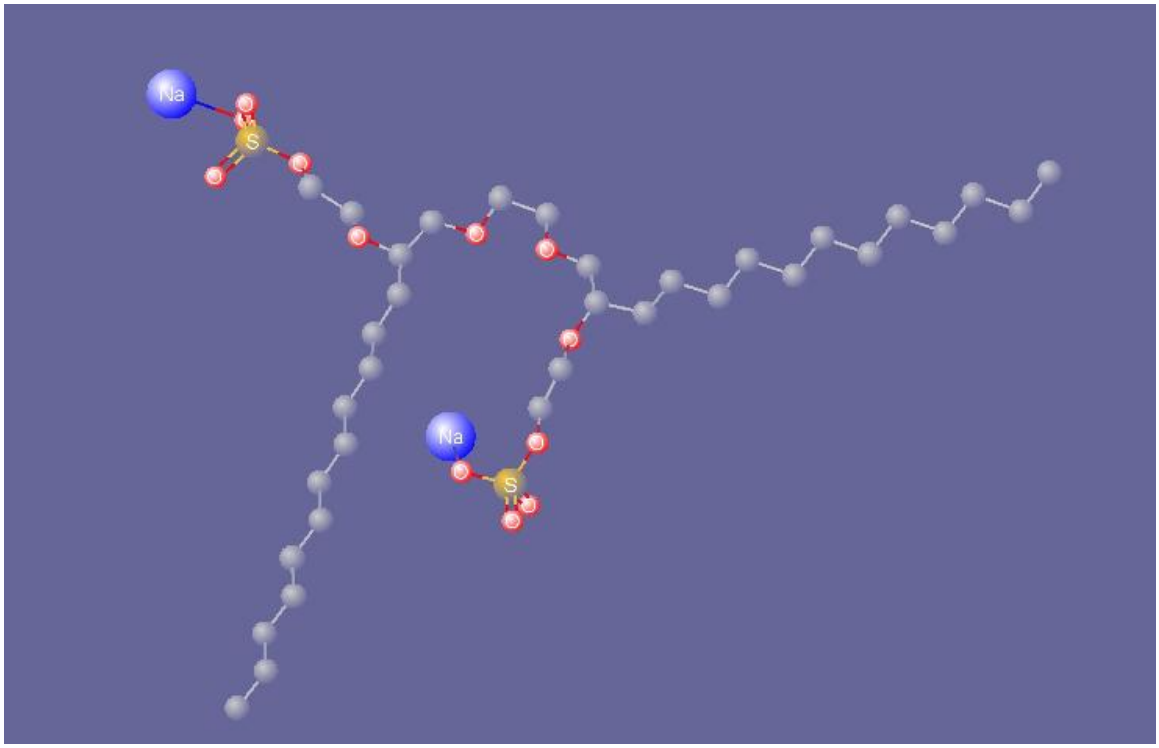

Figure 2.9: 3D Ball-and-Stick Model for *14-2-14* Sulfate Gemini Surfactant (flexible spacer).

Table 2.6 and Table 2.7 summarize the ^{1}H-NMR spectra for all the intermediate diol compounds and their corresponding sulfate Gemini molecules.

Table 2.6: ^{1}H-NMR Data for Intermediate Diol Compounds.

Diol Compound	**^{1}H-NMR ($CDCl_3$), δ**
$(n\text{-}C_{14}H_{28})_2(OCH_2CH_2O)(OH)_2$	0.85~0.89 (6H), 1.30~1.50 (44H), 2.75~2.79 (2H), 3.29~3.35 (2H), 3.52~3.83 (8H)
$(n\text{-}C_{18}H_{36})_2(OCH_2CH_2O)(OH)_2$	0.83~0.87 (6H), 1.24~1.41 (60H), 2.50~2.53 (2H), 3.26~3.32 (2H), 3.49~3.78 (8H)
$(n\text{-}C_{20+}H_{40+})_2(OCH_2CH_2O)(OH)_2$	0.86~0.90 (6H), 1.26~1.49 (84H), 2.84~2.87 (2H), 3.27~3.36 (2H), 3.50~3.81 (8H)
$(n\text{-}C_{14}H_{28})_2(OCH_2CH_2CH_2CH_2O)(OH)_2$	0.83~0.88 (6H), 1.23~1.39 (44H), 1.62~1.66 (4H), 2.29 (2H), 3.19~3.25 (2H), 3.40~3.49 (6H), 3.73~3.75 (2H)
$(n\text{-}C_{16}H_{32})_2(OCH_2CH_2CH_2CH_2O)(OH)_2$	0.87~0.93 (6H), 1.27~1.40 (52H), 1.59~1.63 (4H), 2.32 (2H), 3.22~3.29 (2H), 3.45~3.56 (6H), 3.82~3.83 (2H)
$(n\text{-}C_{18}H_{36})_2(OCH_2CH_2CH_2CH_2O)(OH)_2$	0.85~0.92 (6H), 1.25~1.45 (60H), 1.58~1.64 (4H), 2.25 (2H), 3.12~3.2 (2H), 3.33~3.41 (6H), 3.67~3.71 (2H)
$(n\text{-}C_{20+}H_{40+})_2(OCH_2CH_2CH_2CH_2O)(OH)_2$	0.92~0.98 (6H), 1.30~1.41 (84H), 1.67~1.78 (4H), 2.34 (2H), 3.28~3.37 (2H), 3.56~3.68 (6H), 3.83~3.89 (2H)

Table 2.7: ^{1}H-NMR Data for Sulfate Gemini Surfactants.

Gemini Surfactant	^{1}H-NMR ($CDCl_3$), δ
14-2-14 $(n\text{-}C_{14}H_{28})_2(OCH_2CH_2O)$-$(OCH_2CH_2SO_4Na)_2$	0.87~0.92 (6H), 1.20~1.40 (44H), 1.97~2.04 (4H), 2.94~3.0 (4H), 3.38~3.7 (14H)
18-2-18 $(n\text{-}C_{18}H_{36})_2(OCH_2CH_2O)$-$(OCH_2CH_2SO_4Na)_2$	0.75~0.79 (6H), 1.15~1.35 (60H), 1.82~1.89 (4H), 2.78~2.80 (4H), 3.37~3.51 (14H)
20^+-2-20^+ $(n\text{-}C_{20+}H_{40+})_2(OCH_2CH_2O)$-$(OCH_2CH_2SO_4Na)_2$	0.74~0.75 (6H), 1.01~1.39 (60H), 1.84~1.86 (4H), 2.77~2.84 (4H), 3.20~3.53 (14H)
14-4-14 $(n\text{-}C_{14}H_{28})_2(OCH_2CH_2CH_2CH_2O)$-$(OCH_2CH_2SO_4Na)_2$	0.72~0.74 (6H), 1.15~1.49 (46H), 1.81~1.86 (6H), 2.75~2.80 (4H), 3.32~3.48 (14H)
16-4-16 $(n\text{-}C_{16}H_{32})_2(OCH_2CH_2CH_2CH_2O)$-$(OCH_2CH_2SO_4Na)_2$	0.73~0.75 (6H), 1.17~1.38 (54H), 1.82~1.87 (6H), 2.77~2.84 (4H), 3.30~3.52 (14H)
18-4-18 $(n\text{-}C_{18}H_{36})_2(OCH_2CH_2CH_2CH_2O)$-$(OCH_2CH_2SO_4Na)_2$	0.75 (6H), 1.15~1.39 (62H), 1.82~1.89 (6H), 2.78~2.80 (4H), 3.37~3.51 (14H)
20^+-4-20^+ $(n\text{-}_{20+}H_{40+})_2(OCH_2CH_2CH_2CH_2O)$-$(OCH_2CH_2SO_4Na)_2$	0.75~0.77 (6H), 1.15~1.37 (86H), 1.84~1.88 (6H), 2.79~2.84 (4H), 3.41~3.53 (14H)

2.6 SUMMARY

Synthesis of new Gemini surfactants is described in this Chapter. By utilizing a two-step stable reaction scheme, a new series of anionic Gemini surfactants with varying spacers, hydrophobic chain lengths and head groups were successfully synthesized in our lab. Experimental details for two sample molecules were included as reference for future studies. ^{1}H and ^{13}C NMR spectroscopy is employed for chemical characterization. All products exhibited spectroscopic properties that were in agreement with those expected for the desired structures.

Chapter 3: Critical Micelle Concentration of Gemini Surfactants by Conductivity Measurements

3.1 INTRODUCTION

One of the most important properties of surface active materials is their ability to spontaneously assemble into higher order structures. This process, commonly known as self-assembly, usually involves molecules featuring two or more components with distinctive chemical and physical properties. Everyday examples include soaps, which contain molecules composed of hydrophobic organic chains and a hydrophilic polar head. These types of molecules are referred to as amphiphiles (or surfactants, examples shown in Figure 3.1).

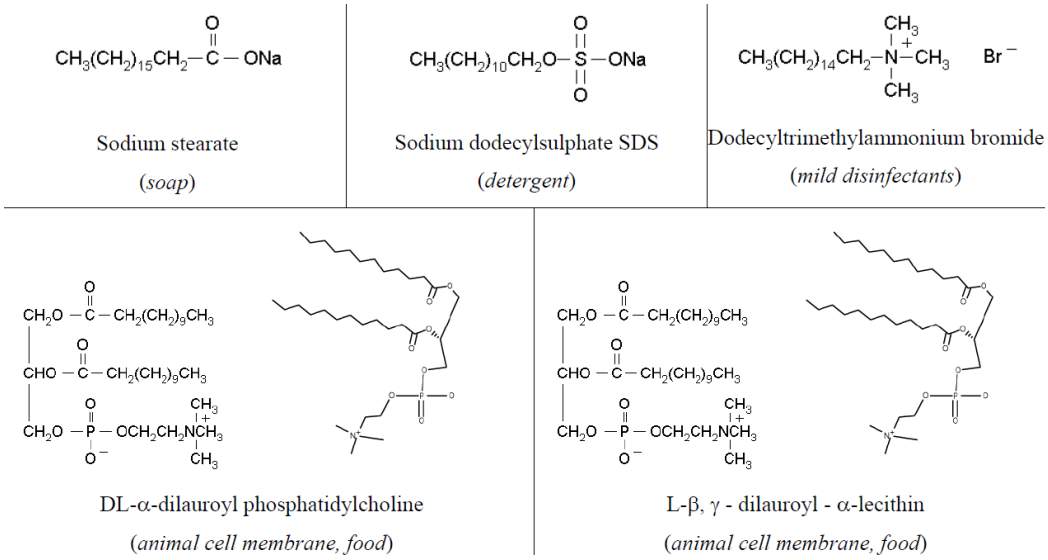

Figure 3.1: Examples of Commonly Used Surfactants (Jones, 2002).

In aqueous solutions, the surfactant system will tend to maximize the hydration of the polar heads and minimize the contact of water molecules with the hydrophobic chains. Organized structures can thus be generated as those illustrated in Figure 3.2.

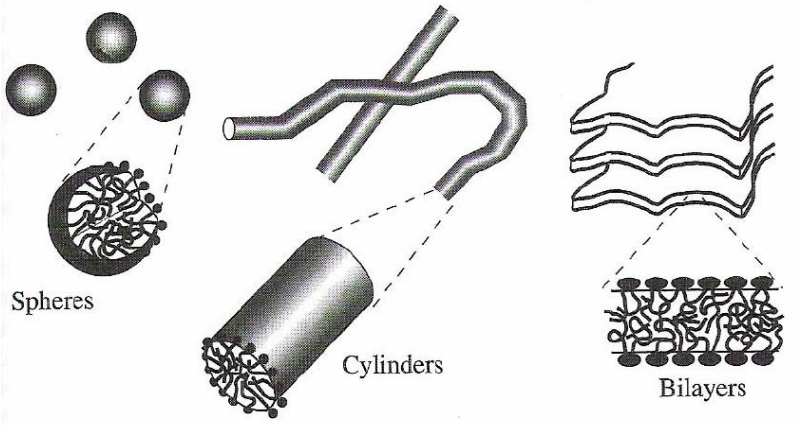

Figure 3.2: Self-Assembly of Surfactant Molecules (Jones, 2002).

Despite the complexity of these structures, the physics underlying these processes can be interpreted in terms of a relatively simple model. The basic driving force for the self-assembly is the need to minimize the Gibbs free energy *G*, by minimizing the degree of mixing between the hydrophobic tails of the surfactant with water and keeping the hydrophilic head in contract with water. In bulk liquid water, each water molecule is hydrogen bonded to 3.4 molecules on average. The hydrophobic tail of surfactants strongly disrupts the structure of water, forcing rearrangement in order to maximize the number of H-bonds around the solute. This process leads to a decrease of the entropy as the number of configurations of water molecules is restricted in contact with the hydrophobic molecule.

In the presence of a certain number of surfactant molecules, the aggregation will take place in well defined assemblies according to the structure and properties of the molecules. The most common structure of all is spherical micelles. The formation of spherical micelles arises from collective interactions of *n* number of surfactants. The

optimum aggregation number in a micelle n^o, which in general is of the order of 50 to 100 molecules, represents a fine balance of several interactions:

i. $n<n^o$, the area of the micelle per head group is too large, allowing energetically costly contact between water and the hydrophobic core;
ii. $n>n^o$, the area of the micelle per head group is too small, generating repulsion between the charged heads. In addition, the difficulty of packing hydrophobic chains at constant density will force head groups inside the hydrophobic core.

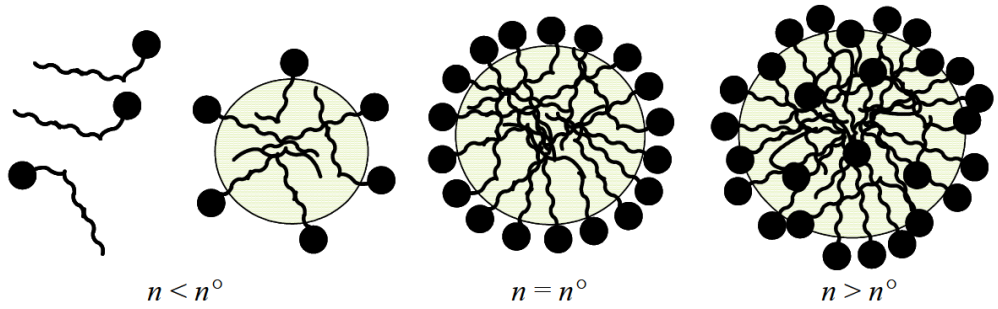

Figure 3.3: Schematic Illustration of Micelle Formation and the Concept of CMC.

The interaction between micelles is determined by electrostatic repulsion induced by the head groups. The polar heads are randomly oriented at the surface of the micelle generating an electrical double layer. The close pack array of polar heads generates a charged plane (Stern layer) where water dipoles are oriented according to the charges of the surfactant head. The charge of the Stern layer induces an image charge of mobile counter-ions. When two micelles are in close contact, the electrostatic repulsion induced by the Stern layer will repel them from each other. Based on this balance of forces, it could be assumed that micelles form at a given condition of temperature and ionic strength will exhibit a relatively narrow size distribution.

Gemini surfactants are known for the superior tendency to self-assemble and give rise to well-developed aggregates possessing interesting structures. Studies concerning Gemini surfactants are focused on the relationship between surfactant structure and the critical micelle concentration. The present chapter examines the critical micelle concentration, the micellar degree of ionization and the free energy of micellization for Gemini surfactants in aqueous solutions.

3.2 THEORETICAL BASIS

3.2.1 Electrical Conductivity of Aqueous Solution

The electrical resistance of an electrolyte solution is fundamentally determined by the motion of the ionic species. The transition from surfactant monomers to micelles involves a dramatic change in the size of the mobile charged species, and this effect will manifest itself in the resistance of the electrolyte. This phenomenon can be monitored by conductance measurements, where the conductance G is defined as the inverse of the resistance R. The conductance of a system is dependent of the cell geometry employed for the measurements,

$$G = \frac{\sigma A}{l} \tag{3.1}$$

Where A is the area of the electrodes and l is the distance of separation. The parameter σ is defined as the conductivity (or specific conductance). The unit is Siemens per meter (S/m). l / A is defined as the electrode cell constant, and typically expressed in cm^{-1}.

The conductivity of a solution depends on the concentration of free ions; consequently the conductivity is often expressed as molar conductivity, λ ($S \cdot m^2/mol$),

$$\lambda = \frac{\sigma}{C} \tag{3.2}$$

where C is the molar concentration of the ion. λ measures the efficiency with which a given electrolyte conducts electricity in solution. In infinitely diluted electrolyte solutions, a limiting molar conductivity λ^o is directly determined by summation of the limiting ionic conductivities of the cations and anions present in the electrolyte. Taking λ_+^o and λ_-^o as the limiting values for the cations and anions respectively, the law of the independent migration of ion states,

$$\lambda^o = \nu_+ \lambda_+^o + \nu_- \lambda_-^o \tag{3.3}$$

where ν_+ and ν_- are the numbers of cations and anions pre formula unit of electrolyte (e.g. ν_+=1 and ν_-=2 for $CaCl_2$). This rather simple expression allows predicting the value of λ^o for any electrolyte salt for which the limiting ionic conductivities are known. Table 3.1 below provides typical values of λ^o for various ions.

Table 3.1: Limiting Ionic Conductivities in Water at 298 K.

Ion	**λ^o (mS·m^2/mol)**	**Ion**	**λ^o (mS·m^2/mol)**
H^+	34.96	OH^-	19.91
Na^+	5.01	Cl^-	7.63
K^+	7.35	Br^-	7.81
Zn^{2+}	10.56	SO_4^{2-}	16.00

3.2.2 CMC Determination by Conductivity

In the case of ionic micelles, a typical plot of conductivity as a function of the surfactant concentration is characterized by a clear change in slope as a result of the transition from surfactant monomers (strong electrolytes) to micelles (partially ionized). The point at which the slope drastically changes corresponds to the CMC. Let us first consider a simple case of SDS under two conditions.

Below the CMC

It is accepted that no micelles are formed and the SDS molecules are considered to be a fully dissociated 1:1 strong electrolyte. Under this circumstance and assuming that ionic molar conductivities are independent of concentration, the specific conductance of aqueous SDS solution consists of independent contributions from C_{14}-SO_4^- (SD^-) anions and Na^+ cations can be computed as:

$$\sigma = \lambda \cdot C \approx \lambda^o \cdot C = \left(\lambda_{Na^+} + \lambda_{SD^-}\right)\left[SDS\right]_t = m_1\left[SDS\right]_t \tag{3.4}$$

Where m_1 is the slope of the plot of σ vs. $[SDS]_t$ below the CMC.

Above the CMC

The conductivity of ionic surfactants such as SDS usually decreases. This is explained by the inclusion within the micelles of the ions of opposite charge (counter-ions) to the long-chain anions. The percentage of counter-ions in relation to the number of long-chain ions in the micelle (the aggregation number n^o) is called the fraction of micellar charge neutralized β; then α (=1-β) is the degree of micelle ionization. Therefore, the concentration of free counter-ions (Na^+, in the case of SDS surfactant) is given by,

$$\left[Na^+\right]_{\text{free}} = CMC + \alpha\left[SDS\right]_m \tag{3.5}$$

Where $[SDS]_m$=$[SDS]_t$-CMC is the concentration of surfactant molecules incorporated into the micelles. The conductivity of an aqueous SDS solution at concentrations above the CMC may be regarded as divisible into three components: that due to the single ions (Na^+ and SD^-) at the CMC, that due to the micellar ions and that due to the Na^+ in excess.

The conductivity of a SDS micellar solution may be written in the form,

$$\sigma = \left(\lambda_{Na^+} + \lambda_{SD}\right) CMC + \lambda_{Na^+} \alpha \left[SDS\right]_m + \lambda_{mic} \left[micelles\right] \tag{3.6}$$

Taking into account that [micelles]=$[SDS]_m/n^o$ and assuming that the contribution of the micelle to the conductance is the same as that of an equivalent number of monomeric ions, the sum of whose charges equals the micellar charge $\lambda_{mic}=\alpha n^o \lambda_{SD}$, then,

$$\sigma = \left(\lambda_{Na^+} + \lambda_{SD}\right) CMC\left(1-\alpha\right) + \left(\lambda_{Na^+} + \lambda_{SD}\right) \alpha \left[SDS\right]_t = \sigma_o + m_2 \left[SDS\right]_t \tag{3.7}$$

Where m_2 ($=m_1\alpha$) is the slope of the linear plot of σ vs. $[SDS]_t$ above the CMC, and σ_o is the corresponding intercept.

The CMC value can, therefore, be determined from the intercept of the straight line obtained above the CMC (eq.(3.7)) together with the values of the slope m_2 and the fractional micellar ionization α, which can then be obtained as the ratio of the slopes of conductivity vs. [SDS] above and below the CMC; that is:

$$\alpha = m_2 / m_1 = \left(\frac{d\sigma}{dC}\right)_{C>CMC} \Bigg/ \left(\frac{d\sigma}{dC}\right)_{C<CMC} \tag{3.8}$$

The exact same analysis can be applied to Gemini surfactant solutions, with a special emphasis made on the definition of degree of ionization. We denote β as the percentage of micellar charge (the aggregation number n^o, total negative charge $-2n^o$) neutralized by Na^+. And α ($=1-\beta$) is the degree of micelle ionization, defined by percentage of surfactant charges R^{2-}, rather than counter-ions Na^+. For Gemini surfactants, eqs. (3.4) and (3.7) can be written as:

$$\sigma = \lambda \cdot C \approx \lambda^o \cdot C = \left(2\lambda_{Na^+} + \lambda_{R^{2-}}\right)\left[\text{surf.}\right]_t = m_1 \left[\text{surf}\right]_t \tag{3.9}$$

$$\sigma = \left(2\lambda_{Na^+} + \lambda_{R^{2-}}\right) CMC\left(1-\alpha\right) + \left(2\lambda_{Na^+} + \lambda_{R^{2-}}\right) \alpha \left[\text{surf}\right]_t = \sigma_o + m_2 \left[\text{surf}\right]_t \tag{3.10}$$

Obviously, the value of conductivity of a Gemini micellar solution would be different from that of the SDS solution, but the degree of ionization α can still be estimated by the same token. This clarification is necessary for thermodynamic modeling later on to define the micellar surface charge density (as will be see in Chapter 7).

3.2.3 Thermodynamics of Micelle Formation

Conventional Ionic Surfactants

The process of micelle formation in aqueous solution occurs when the concentration of free surfactants reaches CMC. As we mentioned before, this process is spontaneous, which implies that the Gibbs free energy of formation is negative. For simplicity, let us first consider a conventional anionic surfactant, sodium dodecyl sulfate (SDS). The micelle equilibrium can be expressed as:

$$nSD^- + (n-p)Na^+ \rightleftharpoons \left(SD_nNa_{n-p}\right)^{p-} \tag{3.11}$$

where (n-p) is the number of counter-ions binding to the micelle and p is the charge of the micelle. In the case that no additional electrolyte is present in the system, the corresponding monomer-micelle equilibrium constant, K_m, can be expressed as,

$$K_m = \frac{\left[\left(SD_nNa_{n-p}\right)^{p-}\right]}{\left[SD^-\right]^n\left[Na^+\right]^{n-p}} \tag{3.12}$$

where the brackets represent the molar concentrations. $[(SD_nNa_{n-p})^{p-}]$ is the molar micelle concentration. Normally, the CMC is sufficiently low so that the ionic activity coefficients can be safely approximated by 1. The change in Gibbs free energy (ΔG_M^o) is related to the micelle formation constant by,

$$-\Delta G_M^o = RT \ln K_m \tag{3.13}$$

We can also define the Gibbs free energy as the differential work for inserting a surfactant molecule into a micelle as:

$$\Delta G_S^o = \frac{\Delta G_M^o}{n} = -\frac{RT}{n} \ln\left[\left(SD_n Na_{n-p}\right)^{p-}\right] + RT \ln\left[SD^-\right] + (1-\alpha)RT \ln\left[Na^+\right] \tag{3.14}$$

in which $\alpha=p/n=1-\beta$ is the micellar degree of ionization. Considering that i) n is a relatively large number, and ii) when the surfactant concentration is close to the CMC, the molar micelle concentration is very small compared to [SD^-] and [Na^+], as a result, the first term on the right-hand side of eq. (3.14) is negligible and [SD^-]≈[Na^+]≈CMC. In all the derivations that follow, we try to be consistent with literature and denote ΔG_S^o by ΔG_M^o. Finally, eq. (3.14) can be written as,

$$\Delta G_M^o = (2-\alpha)RT \ln CMC \tag{3.15}$$

This relationship is commonly used for conventional ionic surfactants with monovalent counter-ions. α values for sodium alkyl sulfate surfactants (Stache, 1995) at room temperature are listed below in Table 3.2.

Table 3.2: α Values for Several Alkyl Sulfate Surfactants at 30˚C.

Alkyl Chain	**Counter-ion**	α
Octyl, C_8-	Na^+	0.42
Decyl, C_{10}-	Na^+	0.25
Dodecyl, C_{12}-	Na^+	0.21
Tetradecyl, C_{14}-	Na^+	0.17
Hexadecyl, C_6-	Na^+	0.11

The relationship in eq. (3.15) provides the means to obtain the standard Gibbs free energy of micellization from the experimentally assessable CMC and α. In surfactant literature (Zana and Xia, 2004), two different representation are used for the CMC and

thus calculate ΔG_M^o using eq. (3.15), i) CMC in *moles of surfactant* and ii) CMC in *mole fraction of surfactant*. For dilute solutions (near CMC), the mole faction can be taken as CMC/55.6. Going from concentration to mole fraction at T=298K and α=0.2 makes the free energy more negative by -(2-α)RTln55.5≈-17.91kJ/mol. For simplicity and self-consistency, we adopt the first approach by using molar concentration throughout.

Invoking the Gibbs-Helmholtz equation,

$$\Delta H_M^o = -T^2 \frac{\partial\left(\Delta G_M^o / T\right)}{\partial T} \tag{3.16}$$

thus,

$$\Delta H_M^o \approx -RT^2\left[\left(2-\alpha\right)\frac{\partial \ln CMC}{\partial T} - \frac{\partial \alpha}{\partial T}\ln CMC\right] \tag{3.17}$$

The dependence of α on the temperature is usually neglected for the calculations of thermodynamic parameters associated with micellar systems (Kang *et al.*, 2001). For conventional surfactants, ln*CMC* in eq. (3.17) can be estimated using the following fitting equation proposed by Kim and Lim (2004),

$$\ln CMC = A + BT + C/T \tag{3.18}$$

Thus eq. (3.17) can be simplified as,

$$\Delta H_M^o = -\left(2-\alpha\right)RT^2\left(B - \frac{C}{T^2}\right) \tag{3.19}$$

The entropy of micellization can then be obtained by,

$$\Delta S_M^o = \frac{\Delta H_M^o - \Delta G_M^o}{T} \tag{3.20}$$

Gemini Surfactants

Let us now consider the more complicated case of Gemini surfactant micellization near the critical micelle concentration (at the onset of micellization), and assume that only a small portion, ε, of the surfactants is involved in the process described by:

$$\begin{array}{lccccc} & nR^{2-} & + & 2n\beta Na^{+} & \rightleftharpoons & \left(R_n Na_{2n\beta}\right)^{2n(1-\beta)-} \\ \text{t=0} & CMC & & 2CMC & & 0 \\ \text{t=t}_e & CMC(1-\varepsilon) & & 2CMC(1-\beta\varepsilon) & & CMC\cdot\varepsilon/n \end{array} \tag{3.21}$$

Here, R^{2-} refers to the Gemini surfactant anion; n is the micelle aggregation number; β refers to the fraction of micellar charge neutralized. The equilibrium constant K_m of eq. (3.21) can be expressed as:

$$K_m = \frac{CMC\cdot\varepsilon/n}{\left[CMC(1-\varepsilon)\right]^n\cdot\left[CMC(2-2\beta\varepsilon)\right]^{2n\beta}} = \frac{\varepsilon\cdot CMC^{\left[1-n(1+2\beta)\right]}}{n\cdot(1-\varepsilon)^n\cdot(2-2\beta\varepsilon)^{2n\beta}} \tag{3.22}$$

The change in Gibbs free energy (ΔG_S^o) is calculated by,

$$\begin{aligned} \Delta G_M^o &= -\frac{\Delta G_M^o}{n} = -\frac{RT\ln K_m}{n} = -\frac{RT}{n}\ln\left[\frac{\varepsilon\cdot CMC^{\left[1-n(1+2\beta)\right]}}{n\cdot(1-\varepsilon)^n\cdot(2-2\beta\varepsilon)^{2n\beta}}\right] \\ &= \left(1+2\beta\right)RT\ln CMC + \frac{RT}{n}\ln\frac{n}{\varepsilon} - \frac{RT}{n}\ln CMC \\ &\quad + RT\ln(1-\varepsilon) + 2\beta RT\ln(2-2\beta\varepsilon) \end{aligned} \tag{3.23}$$

n is a relatively large number, whereas ε is very small, eq. (3.23) can be simplified as:

$$\begin{aligned} \Delta G_M^o &= \left(1+2\beta\right)RT\ln CMC + 2\beta RT\ln 2 \\ &= 2\left(1.5-\alpha\right)RT\ln CMC + 2(1-\alpha)RT\ln 2 \end{aligned} \tag{3.24}$$

In eq.(3.24), ΔG_M^o is the free energy of micellization per mole of Gemini surfactant containing two alkyl chains. The CMC is again expressed in molar concentration. And

eq. (3.18) is used here to evaluate ln*CMC* for Gemini surfactants. ΔH_M^o and ΔS_M^o can be calculated based on eqs. (3.16) and (3.20),

$$\Delta H_M^o = -2\left(1.5-\alpha\right)RT^2\frac{\partial \ln\left(CMC\right)}{\partial T} = -2\left(1.5-\alpha\right)RT^2\left(B-\frac{C}{T^2}\right) \tag{3.25}$$

$$\Delta S_M^o = \frac{\Delta H_M^o - \Delta G_M^o}{T} \tag{3.26}$$

Zana (1996) first proposed a relationship between CMC and ΔG_M^o for a general type of ionic surfactant, made up of a surfactant ion containing *i* polar groups of valency z_s bonded to *j* alkyl chains, with counter-ions of valency z_c

$$\Delta G_{M\_\text{alkyl}}^o = RT\left(\frac{1}{j}+\beta\frac{i}{j}\left|\frac{z_s}{z_c}\right|\right)\ln CMC_{\text{alkyl}} + RT\left(\beta\frac{i}{j}\left|\frac{z_s}{z_c}\right|\ln\frac{i}{j}\left|\frac{z_s}{z_c}\right| - \frac{\ln j}{j}\right) \tag{3.27}$$

Note that in eq. (3.27) Zana expresses CMC in mole of alkyl chain, $\text{CMC}_{\text{alkyl}}$. ΔG_M^o is also expressed for single alkyl chain.

For conventional single chain surfactant, $i=j=1$, $|z_s|=|z_c|=1$, eq. (3.27) reduces to the same form as eq. (3.15). For Gemini surfactants, $i=j=2$, $|z_s|=|z_c|=1$, therefore eq. (3.27) can be simplified as:

$$\Delta G_{M\_\text{alkyl}}^o = RT\left(1.5-\alpha\right)\ln \text{CMC}_{\text{alkyl}} - \left(RT/2\right)\ln 2 \tag{3.28}$$

Here, $\text{CMC}_{\text{alkyl}}=2\text{CMC}$, and $G_M^o = 2\Delta G_{M\_\text{alkyl}}^o$ is the free energy per mole of surfactant molecules.

$$\begin{aligned}\Delta G_M^o &= 2RT\left(1.5-\alpha\right)\ln 2\text{CMC} - 2\left(RT/2\right)\ln 2 \\ &= 2RT\left(1.5-\alpha\right)\ln CMC + 2\left(1-\alpha\right)\ln 2\end{aligned} \tag{3.29}$$

which is of the same form as eq. (3.24) derived above.

3.3 MATERIALS AND METHODS

The critical micelle concentration of the Gemini surfactants was obtained from conductivity measurements conducted as described in this section. From studies performed at various temperatures, several thermodynamic parameters associated with the micelle formation will be discussed. Gemini surfactants *m-s-m*, were prepared in house with reactions described in Chapter 2. The product was purified by recrystallization. Thin layer chromatography and NMR analysis confirmed sample identity.

The Oakton® ECTestr 11+ multi-range (200μS/cm, 2000μS/cm, and 20mS/cm), waterproof portable conductivity tester with 11+ series electrode sensor was used for the conductivity measurements (cell constant = 1cm^{-1}). The values of critical micelle concentration were calculated as the intersection of linear parts in the dependence conductivity vs. surfactant concentration. The degree of ionization α was calculated as the ratio of slopes above and below the CMC in the plot.

3.4 EXPERIMENTAL SECTION

The detailed experimental procedure is described below:

1. Prepare 100ml 0.02mM Gemini surfactant solution (0.02M in case of SDS) from a 1M stock solution. A clean weighting boat is used for accurately measuring the calculated quantity. Ultrapure milli-Q water is used for the solution making.
2. Introduce 20ml of the Gemini solution (50ml in case of SDS) into a 100ml beaker and put it into the water batch at desired temperature. Fill a clean flask with milli-Q water and place it in the water bath too. Allow 30min for thermal equilibrium. Measure the conductivity of the surfactant solution. Dilute the surfactant solution by adding 20ml (10ml in case of SDS) of milli-Q water at

the same temperature and stir the solution with a clean glass stirrer. Allow a couple minutes for equilibration and record the conductivity. Repeat the diluting and measuring steps until the total volume reaches 100ml.

3. Introduce 20ml (50ml in case of SDS) of the final volume from step 2 into a clean and dry beaker of 100 ml. Follow the same experimental procedure as in step 2 until the total volume is 100ml.
4. Transfer 20ml (50ml in case of SDS) of the final volume in step 3 into a clean and dry beaker of 100ml. Repeat as in step 3 until a final dilution of 100ml.
5. Transfer 20ml (50ml in case of SDS) of the final volume in step 4 into a clean and dry beaker of 100ml. Repeat as in step 4 until a final dilution of 100ml.
6. Finally, repeat the measurements at other designed temperatures.

3.5 SOLUBILITY OF GEMINI SURFACTANTS

Surfactants are useful and can be utilized only if they are sufficiently soluble in an aqueous phase. The solubility of ionic surfactants is commonly characterized by the Krafft temperature T_K, which is the minimum temperature at which surfactants form micelles. It is a point of phase change below which the surfactant remains in crystalline form, even in aqueous solution. Surfactants in such a crystalline state will only solubilize and form micelles if another surfactant assists it in overcoming the forces that keep it crystallized, or if the temperature increases, thus causing entropy to have a stronger force and encouraging the crystalline structure to break apart.

Anionic Gemini surfactants synthesized in current study have sulfate head groups. Two different spacer groups (-C_2- & -C_4-) were used. Alkyl chain lengths were varied 14 to ~23. As described by Hato (1973), aqueous solutions of all disulfate Geminis were prepared at room temperature of 20˚C (or 68˚F), and at a concentration of 1wt%. Upon

sufficient mixing, all solutions were visually examined to be clear and homogeneous Therefore, the Krafft temperatures of these surfactants are lower than 20˚C. Comparably low Krafft temperatures were reported in many other studies (Zhu *et al.*, 1990, 1991, 1992, & 1993).

The low Krafft temperatures of these surfactants can be attributed to the hydrophilic nature of the spacer and head groups. The hydrophilic-lipophilic balance (HLB) (Becher, 1984) of a surfactant is a measure of the degree to which it is hydrophilic or lipophilic, determined by calculating values for the different regions of the molecule. The empirical HLB number for a given surfactant is computed by adding 7 to the algebraic sum of the group numbers g_i (values for some functional groups are listed in Table 3.3): $HLB=7+\Sigma g_i$.

Table 3.3: g_i Values of Some Functional Groups (Sjoblom, 2001).

Group	g_i	Group	g_i
$-SO_4Na$	38.7	-OH (free)	1.9
-COOK	21.1	-O-	1.3
-COONa	19.1	$-(CH_2-CH_2-O)-$	0.33
Sulfonate	~11.0	-CH-, $-CH_2-$, $-CH_3$, -CH=	-0.475
-COOH	2.1	$-(CH_2-CH_2-CH_2-O)-$	-0.15

Therefore, for a conventional surfactant molecule STS (sodium tetradecyl sulfate), the HLB number will be calculated as: $HLB=7+38.7+14\times(-0.475)=39.05$. The HLB of Gemini surfactant *14-2-14* Gemini surfactant can also be estimated as: $HLB=7+38.7\times2+1.3\times4+(2\times14+2\times2+2)\times(-0.475)=73.45$. Table 3.4 is a complete summary of the Krafft points and HLB values for all sulfate Gemini molecules synthesized in this study, compared in parallel with four conventional sodium alkylsulfate surfactants (O'Lenick). Although having the same alkyl chain and head group, the

Gemini surfactant shows a much higher HLB value and thus correspondingly higher water solubility, compared to its conventional counterpart.

Table 3.4: Krafft Points and HLB Values for Gemini Surfactants.

Surfactants	Krafft Point (˚C)	HLB
14-2-14	<20	73.45
14-4-14	<20	72.5
16-4-16	<20	70.6
18-2-18	<20	69.65
18-4-18	<20	68.7
20^{+}-2-20^{+}	<20	64.9
20^{+}-4-20^{+}	<20	63.95
C_{12}-$SO_4^-Na^+$	16	40
C_{14}-$SO_4^-Na^+$	28	39.05
C_{16}-$SO_4^-Na^+$	45	38.1
C_{18}-$SO_4^-Na^+$	56	37.15

3.6 CONDUCTIVITY MEASUREMENT RESULTS

3.6.1 Validation Measurements using SDS

Figure 3.4 shows results obtained working with aqueous solutions of SDS at three different temperatures. The experimental procedures have been described in a previous section. The CMC, slopes of curves within and beyond CMC, and degrees of ionization at 30˚C, 40˚C, and 60˚C are summarized in Table 3.5.

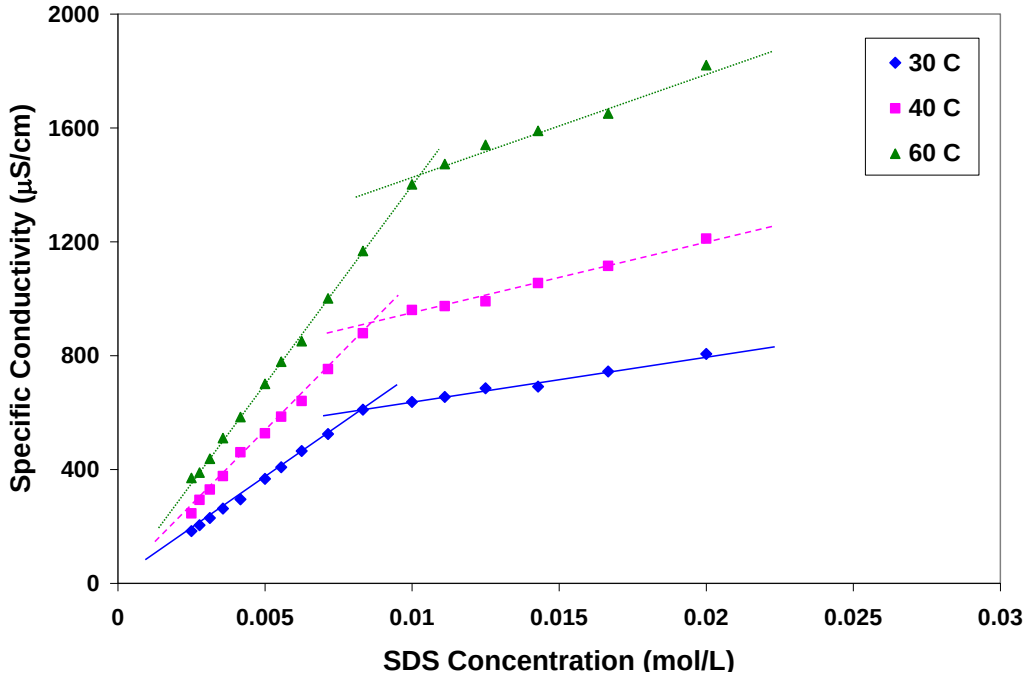

Figure 3.4: Electrical Conductivity (in μS/cm) vs. SDS Concentration.

Table 3.5: Critical Micelle Concentration (CMC) of SDS at Various Temperatures.

Temp.	CMC (mM)		m_1 ($S \cdot cm^2/mol$)	m_2 ($S \cdot cm^2/mol$)	α
	Exp.	NIST			
30˚C	8.33	8.23	73.447	16.10	0.2192
40˚C	8.64	8.60	105.40	25.47	0.2415
60˚C	10.3	10.16	140.13	36.77	0.2623

Notice that in Table 3.5, the experimental CMC values are compared side by side with data obtained from the NIST CMC database (Mukerjee *et al.*, 1971). The two sets of data are in good agreement. Furthermore, the α value of 0.2192 is in line with the reported value cited in Table 3.2. These two points serve as double validations of the current method of CMC determination by conductivity. Based on eqs. (3.15) through (3.20), the thermodynamic parameters for SDS micellization can be calculated, as listed below in Table 3.6 and depicted in Figure 3.5.

Table 3.6: Thermodynamic Parameters of SDS Micellization at Different Temperatures.

Temp.	In(CMC)		ΔG_M^o	ΔH_M^o	ΔS_M^o	$T \cdot \Delta S_M^o$
	Exp.	eq. (3.18)	(kJ/mol)	(kJ/mol)	(J/mol/K)	(kJ/mol)
30˚C	-4.788	-4.792	-21.49	-4.64	55.59	16.85
40˚C	-4.751	-4.745	-21.75	-8.63	41.91	13.13
60˚C	-4.576	-4.578	-22.02	-16.92	15.32	5.10

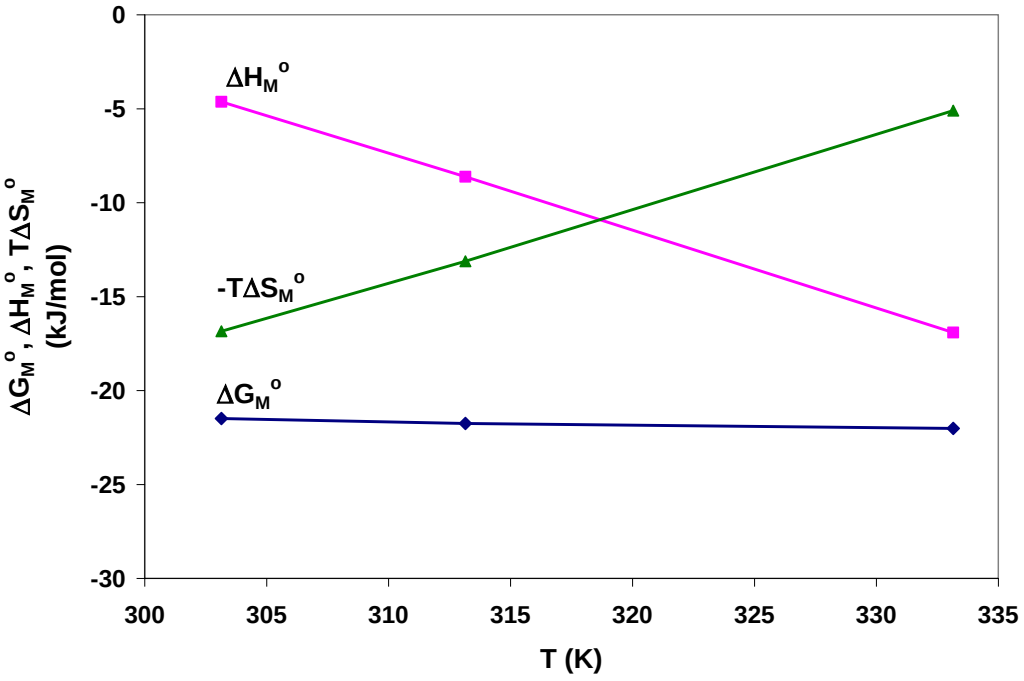

Figure 3.5: Thermodynamic Parameters (ΔG_M^o , ΔH_M^o , and $-T \cdot \Delta S_M^o$) vs. Temperature.

Note that the value of ΔG_M^o at 30˚C is -21.49kJ/mol is almost identical to the value of -21.2kJ/mol obtained by Benrraou *et al*. (2003) and also close to the one reported by Aniansson *et al.* (-22.6kJ/mol, 1976). This comparison serves once again as a validation of the accuracy of our measurements. Over the temperature range investigated, ΔG_M^o remains negative while ΔS_M^o remains positive, confirming that micelle formation occurs spontaneously when surfactant concentration reaches the CMC value.

Furthermore, the constancy in the ΔG_M^o reveals the cancellation effects between ΔH_M^o and $-T \cdot \Delta S_M^o$ at all temperatures. Larger linear changes in ΔH_M^o and ΔS_M^o compensate each other. Based on the absolute value, it is clear that the SDS micellization is an entropy driven process at low temperatures and an enthalpy driven process at higher temperatures.

3.6.2 Measurements with Gemini Surfactant *14-2-14*

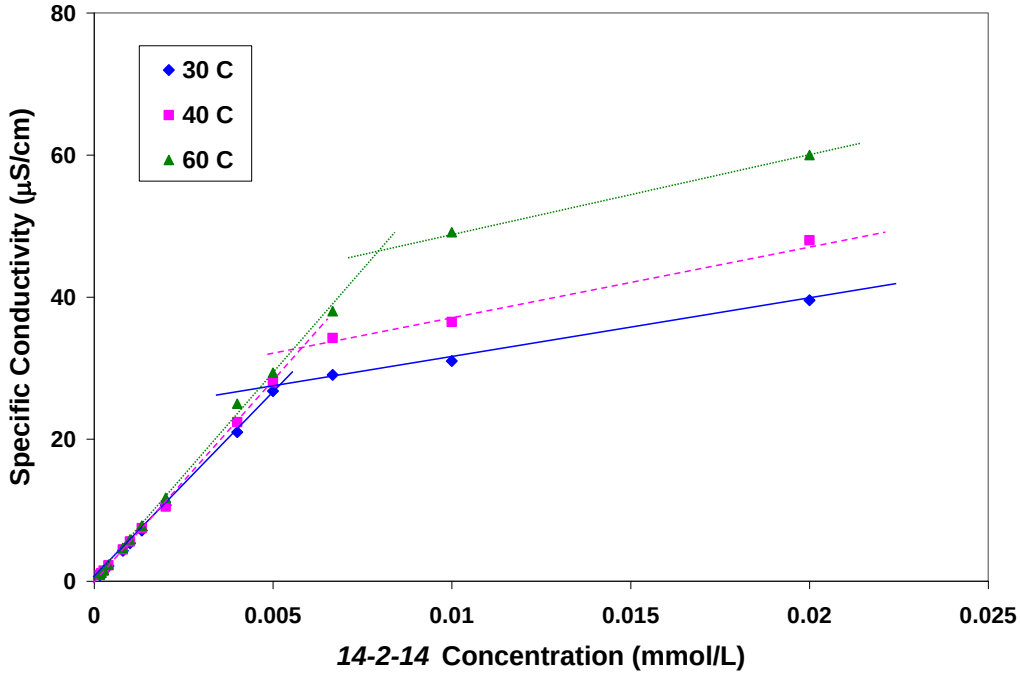

Figure 3.6: Electrical Conductivity (in μS/cm) v.s. *14-2-14* Concentration.

Figure 3.6 shows results obtained working with aqueous solutions of *14-2-14* Gemini surfactant at three different temperatures. As done for the SDS case, CMC, slopes of curves within and beyond CMC, and degrees of ionization are summarized in Table 3.7. The thermodynamic parameters of *14-2-14* micellization process can be calculated, as listed below in Table 3.8.

Table 3.7: CMC of *14-2-14* at Various Temperatures.

Temp.	CMC (10^{-3} mM)	m_1 (mS·cm^2/mol)	m_2 (mS·cm^2/mol)	α
30˚C	5.1	5354.17	851.93	0.1591
40˚C	6.0	5599.06	957.54	0.1710
60˚C	8.0	5869.48	1087.01	0.1852

Table 3.8: Thermodynamic Parameters of *14-2-14* at Different Temperatures.

Temp.	In(CMC)		ΔG_M^o	ΔH_M^o	ΔS_M^o	$T \cdot \Delta S_M^o$
	Exp.	eq. (3.18)	(kJ/mol)	(kJ/mol)	(J/mol/K)	(kJ/mol)
30˚C	-12.186	-12.171	-79.43	-22.56	187.59	56.87
40˚C	-12.024	-12.047	-80.21	-29.52	161.89	50.70
60˚C	-11.736	-11.728	-82.35	-44.05	114.96	38.30

The magnitudes of the above energy terms are in line with reported values for cationic Gemini surfactants (Grosmaire *et al.*, 2002). The significantly more negative ΔG_M^o (as compared to values listed in Table 3.6) is apparently the driving force for *14-2-14* micellization. And the ultralow CMC values are a direct result of the huge negative Gibbs free energies.

Another key characteristic of *14-2-14* micellization process is that this is primarily an entropy driven process (comparing Figure 3.5 and Figure 3.7). This is intuitively understandable considering the much larger disruption to the water structure caused by double tail groups from a Gemini surfactant. This will lead to negative entropy and positive Gibbs free energy changes, which apparently cannot occur spontaneously. A stronger tendency to micellization can help effectively counteract such a disruption. It should be noted here that the calculated values of ΔH_M^o and $-T \cdot \Delta S_M^o$ from eqs. (3.25) and (3.26) depends on the accuracy of using eq. (3.18) for approximate $\ln CMC$ for Gemini surfactants. The difference, however, will only be a constant.

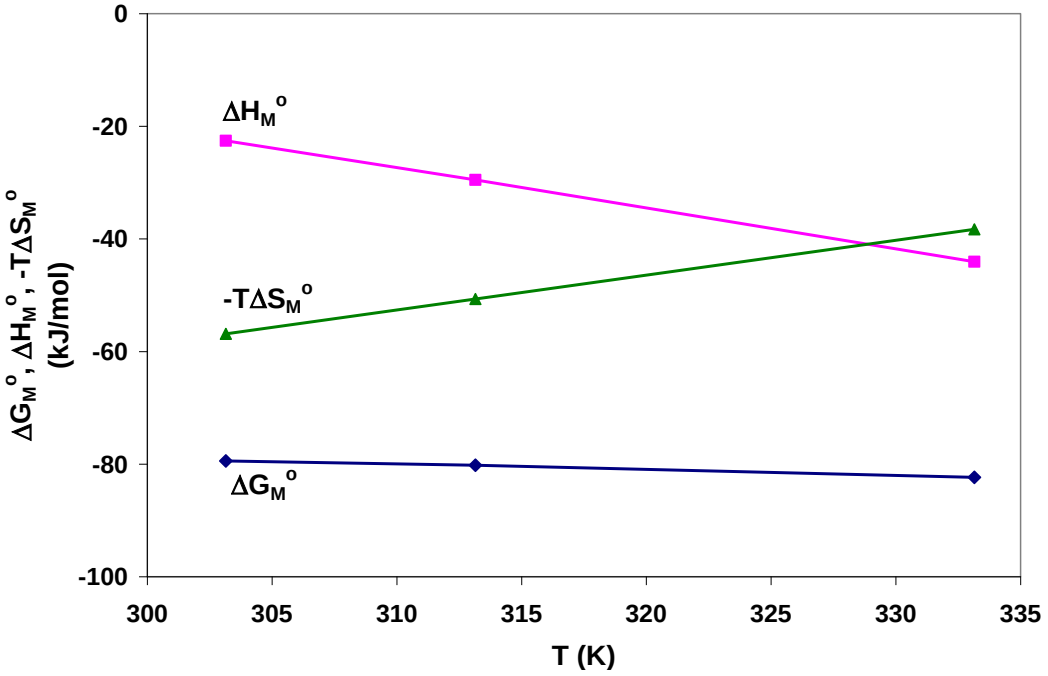

Figure 3.7: Thermodynamic Parameters (ΔG_M^o , ΔH_M^o , and $-T \cdot \Delta S_M^o$) vs. Temperature.

The detailed experimental results of the other Gemini surfactants are not included in this chapter, bur deferred to the Appendix B. The results are organized in the same manner as Figure 3.6, Table 3.7, and Table 3.8.

3.7 RESULTS AND DISCUSSION

Table 3.9, Table 3.10 and Table 3.11 below summarize all the critical micelle concentrations, degrees of ionization and thermodynamic parameters for the current series of Gemini surfactants at three different temperatures. For comparison, CMC values for C_{12}-, C_{14}-, and C_{16}- sodium sulfates (Mukerjee *et al.*, 1971) are listed in Table 3.12.

CMC values for Gemini surfactants reported here are apparently two to three orders of magnitude lower than those for the conventional molecules. These CMC measurements fully demonstrate the strong tendency of Gemini surfactants to self-

aggregate and form micellar structures in aqueous solutions at ultralow concentrations. In this section, the effects of the surfactant alkyl chain, spacer, head group, and temperature on CMC and α will be discussed.

Table 3.9: Summary of Results for Gemini Surfactants at 30˚C.

Surfactant	**CMC (10^{-3} mM)**	α	ΔG_M^o **(kJ/mol)**	ΔH_M^o **(kJ/mol)**	ΔS_M^o **(J/mol/K)**
14-2-14	5.1	0.1591	-79.43	-22.56	187.59
14-4-14	4.8	0.1815	-78.54	-1.05	255.59
16-4-16	2.3	0.1566	-84.97	-7.76	254.7
18-2-18	1.5	0.1138	-90.61	-21.31	228.58
18-4-18	1.2	0.1345	-90.82	-19.78	234.34
20^+-2-20^+	0.63	0.099	-97.68	-35.47	205.23
20^+-4-20^+	0.53	0.1254	-97.07	-0.28	319.29
18-4-18 2COONa	8.7	0.6401	-49.26	2.43	170.48
20^+-2-20^+ 2COONa	2.7	0.5705	-58.57	-5.08	176.47

Table 3.10: Summary of Results for Gemini Surfactants at 40˚C.

Surfactant	**CMC (10^{-3} mM)**	α	ΔG_M^o **(kJ/mol)**	ΔH_M^o **(kJ/mol)**	ΔS_M^o **(J/mol/K)**
14-2-14	6	0.1708	-80.21	-29.52	161.89
14-4-14	5.1	0.1999	-79.61	-6.64	233.01
16-4-16	2.5	0.1628	-86.79	-13.93	232.68
18-2-18	1.8	0.1269	-91.42	-28.37	201.35
18-4-18	1.4	0.147	-91.88	-26.67	208.26
20^+-2-20^+	0.9	0.1095	-97.58	-43.48	172.76
20^+-4-20^+	0.56	0.137	-99.05	-6.1	296.84
18-4-18 2COONa	9.1	0.65967	-49.56	-1.05	154.94
20^+-2-20^+ 2COONa	3.0	0.5794	-59.44	-9.29	160.16

Table 3.11: Summary of Results for Gemini Surfactants at 60˚C.

Surfactant	CMC (10^{-3} mM)	α	ΔG_M^o (kJ/mol)	ΔH_M^o (kJ/mol)	ΔS_M^o (J/mol/K)
14-2-14	8	0.1846	-82.35	-44.05	114.96
14-4-14	5.5	0.2191	-82.94	-18.12	194.55
16-4-16	2.9	0.1713	-90.67	-26.78	191.77
18-2-18	2.3	0.139	-94.58	-43.21	154.17
18-4-18	1.8	0.1602	-94.95	-41.1	161.65
20^+-2-20^+	1.2	0.1202	-100.83	-60.37	121.43
20^+-4-20^+	0.6	0.1424	-104.45	-18.23	258.8
18-4-18 2COONa	9.3	0.6694	-52.04	-8.12	131.84
20^+-2-20^+ 2COONa	3.4	0.5890	-61.97	-18.02	131.91

Table 3.12: CMC Values for Single Chain Sodium Alkyl Sulfates.

Surfactant	CMC (mM)		
	30˚C	40˚C	60˚C
C_{12}-$SO_4^-Na^+$	8.23	8.6	10.16
C_{14}-$SO_4^-Na^+$	2.08	2.21	2.77
C_{16}-$SO_4^-Na^+$	---	0.58	---

3.7.1 Critical Micelle Concentration (CMC)

Effect of Alkyl Chain Length

In the case of conventional surfactants, the log of the CMC (Preiss *et al.*, 2009) varies linearly with the carbon number *m* of the surfactant alkyl chain. Variations of Gemini CMC (measured at 30˚C) with *m* for two different spacers (*s*=2, and 4) are presented in Figure 3.8. Longer alkyl chains make the surfactant molecule more hydrophobic in general and thus results in lower CMC values.

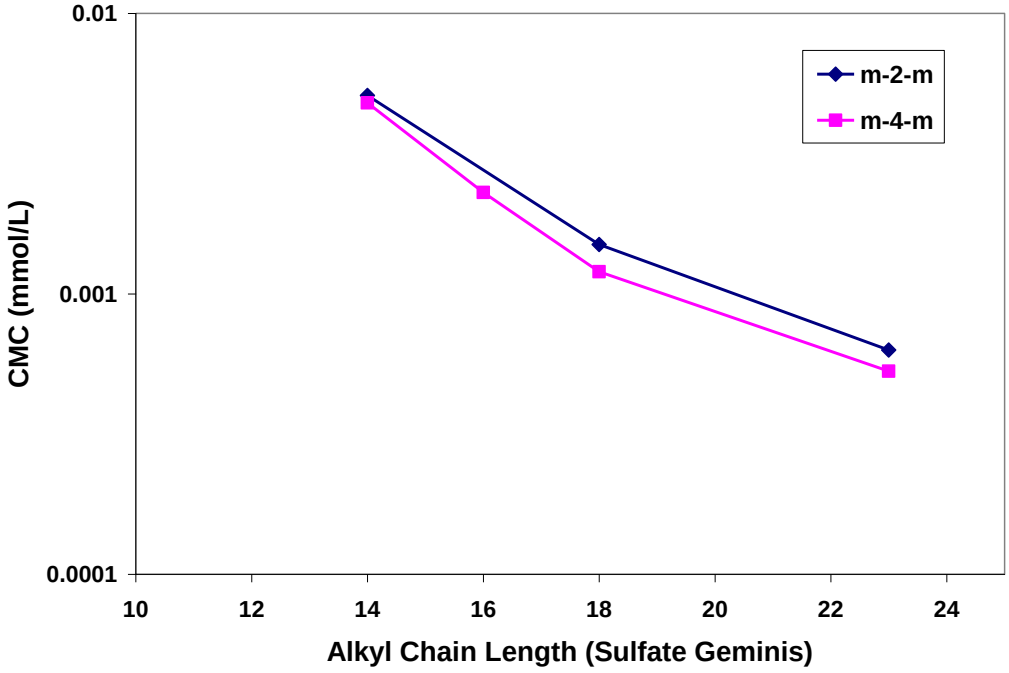

Figure 3.8: Effect of Alkyl Chain Length on Critical Micelle Concentration (30˚C).

The correlation between CMC and alkyl chain length is well known (Klevens *et al.*, 1953) and for conventional surfactants can be generalized as:

$$\log CMC = A - Bm \tag{3.30}$$

where A is a specific constant for the particular homologous series and temperature. B (Okano *et al.*, 1996) represents the energy contribution of one methylene group.

For our case, linear regression renders the following correlations:

$$m-2-m \text{ group:} \quad \log CMC = -0.9414 - 0.0999m, \; R^2 = 0.9740 \tag{3.31}$$

$$m-4-m \text{ group:} \quad \log CMC = -0.9577 - 0.1013m, \; R^2 = 0.9556 \tag{3.32}$$

B values obtained in the current study are smaller than most reported values for cationic Gemini surfactants, which are all around 0.43 (Zana *et al.*, 2004). This suggests that

anionic Gemini micelles have a relatively weaker cohesive force or a stronger electrical repulsive force. From a hydrophilic-lipophilic balance point of view, the two sulfate head groups of synthesized surfactants are extremely hydrophilic and thus exhibit very strong electrical interactions, as compared to weaker interaction between ammonium ions in most cationic Geminis.

Effect of Spacer Group

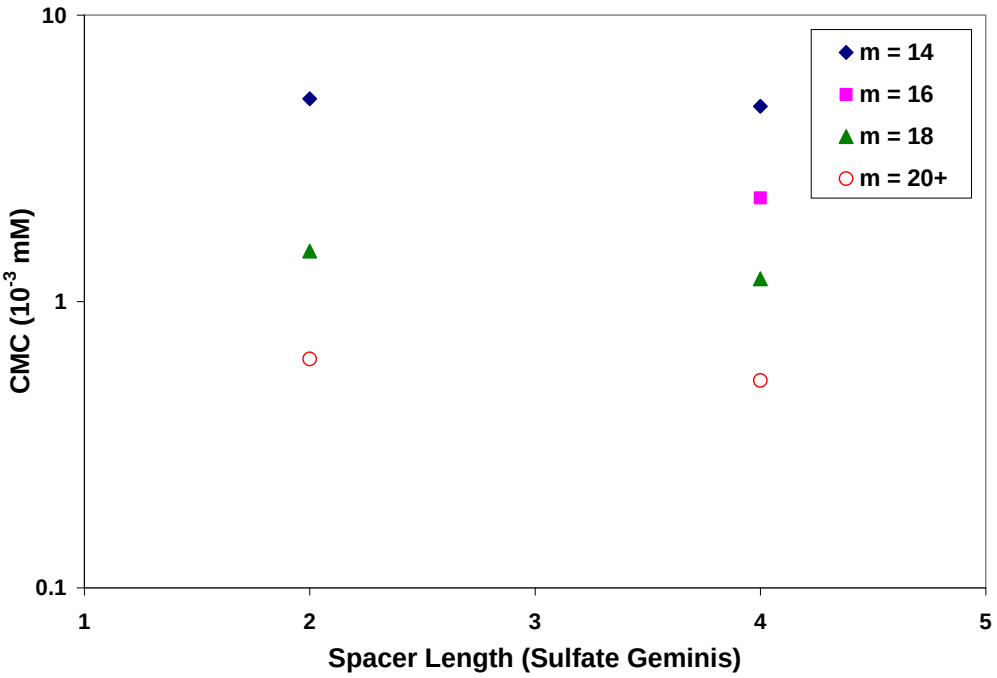

Figure 3.9: Effect of Spacer Length on Critical Micelle Concentration (30˚C).

Table 3.13: Effect of Spacer Group on CMC (30°C).

Alkyl Chain, *m*	**CMC (10^{-3} mM)**	
	***s*=2**	***s*=4**
14	5.1	4.8
16	---	2.3
18	1.5	1.2
20^{+}	0.63	0.53

Longer spacer further reduces the CMC of Gemini surfactants, possibly due to increasing hydrophobicity. It should probably be pointed out that the variations of the CMC with the spacer length are insignificant (in Figure 3.9), as compared to those with alkyl chain length. This fact is important in the uses and applications of Gemini surfactants because it indicates that the properties of a Gemini surfactant can be potentially modified by acting on the spacer group, without affecting the CMC substantially.

Effect of Head group

Table 3.14: CMCs of Geminis with Different Head Groups (30^{o}C, s=4).

Head Group	**CMC (10^{-3} mM)**	
	***m*=18**	***m*=20^{+}**
-SO_4^-	1.2	0.53
COO^-	8.7	2.7

Comparing Gemini molecules with carboxylate and sulfate head groups from the above table, it seems that carboxylate Geminis have much higher CMC values, indicating their weaker tendency to aggregate and form micellar structures. This is self-consistent with the observations that degrees of ionization of carboxylate molecules are much larger than sulfate molecules, which results in larger electrostatic repulsion forces (less screening) and impedes the formation and growth of micelles.

From a HLB balance viewpoint, however, carboxylate head group tends to make the Gemini molecule more hydrophobic and thus should give rise to lower CMC values. Such contradictory results seem to arise from the weak acid-strong base nature of the carboxylate-sodium (head group-counter-ion) combination. This will be discussed in more detail in Chapter 4 where we compare the CMC values from two different measurements, conductivity and surface tension.

Effect of Temperature

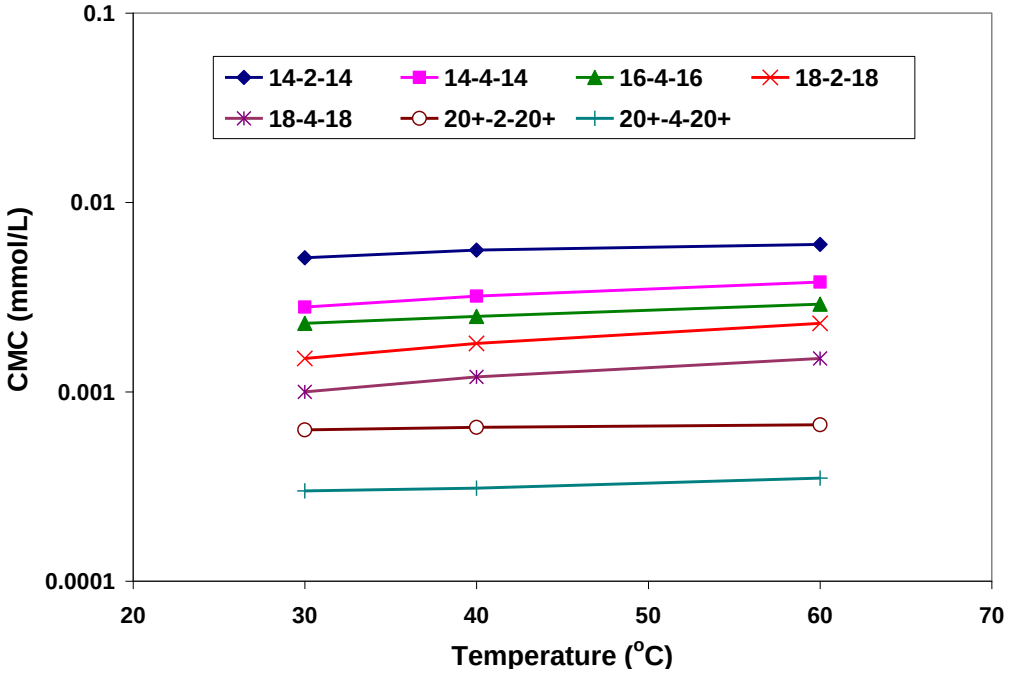

Figure 3.10: Effect of Temperature on CMC.

As shown in Figure 3.10, higher temperature promotes solubility of Gemini surfactants in aqueous solution, and thus increases CMC, but only slightly as shown on the log scale.

3.7.2 Degree of Ionization α

Effect of Alkyl Chain Length

As can be seen in Figure 3.11, a general trend of decreasing α with m is obtained. This is also seen in the results for cationic Gemini surfactants (Wettig *et al.*, 2001). A similar behavior was reported (Zana, 1980) for conventional quaternary ammonium surfactants as well. Such a decrease of α upon increasing surfactant chain length is in line with the corresponding decrease of CMC and increase of micelle size.

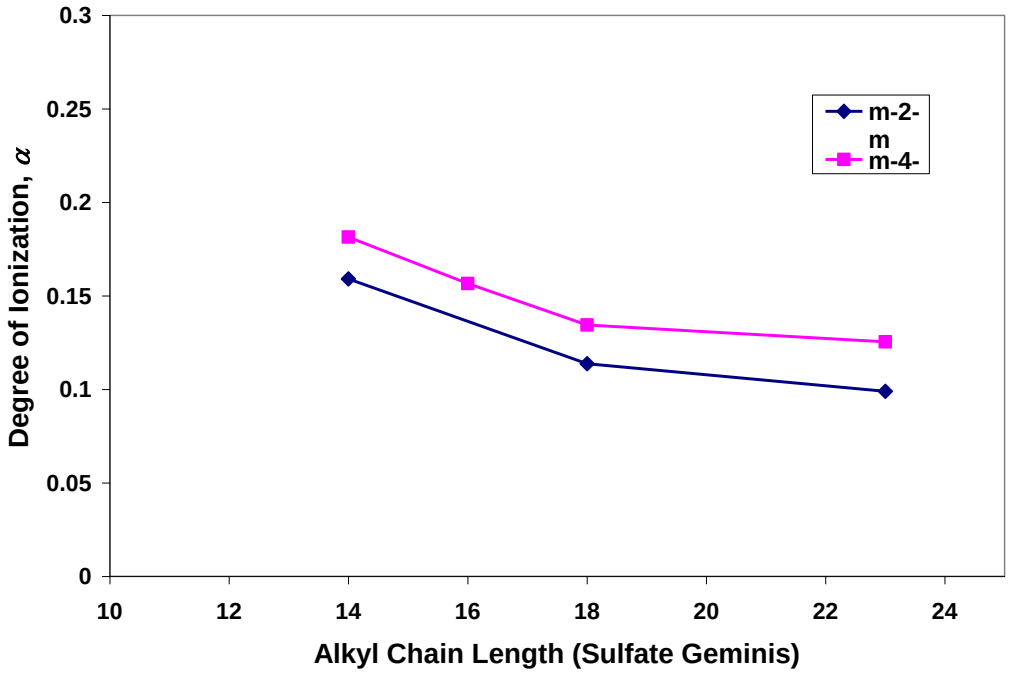

Figure 3.11: Effect of Alkyl Chain Length on Degree of Ionization (30˚C).

Effect of Spacer Group

An increase of α with spacer length can be seen from Table 3.15. This was also reported for the micelles of the cationic Gemini surfactants *16-s-16* (Aswal *et al.*, 1998), as well as for the micelles of the anionic Gemini surfactants *16-s-16,* $2Na^+$ (Aswal *et al.*, 1999) that have a polymethylene spacer and sodium phosphate head groups.

Table 3.15: Effect of Spacer Group on Degree of Ionization (30^oC).

Alkyl Chain, *m*	***α***	
	***s*=2**	***s*=4**
14	0.1591	0.1815
16	---	0.1566
18	0.1138	0.1345
20^+	0.099	0.1254

Effect of Head Group

As can be seen in Table 3.16, the degrees of ionization for carboxylate Geminis are apparently much greater than those of sulfate Geminis.

Table 3.16: Effect of Head Group on Degree of Ionization (30°C, s=4).

Head Group	α	
	***m*=18**	***m*=20$^+$**
-SO_4^-	0.1345	0.1245
COO^-	0.6401	0.5705

This is again suspected to be caused by the weak acid-strong base nature of the carboxylate-sodium head group-counter-ion combination. Such a combination might result in an increase of hydroxyl ion concentration in the solution during the protonation process described in Figure 3.12.

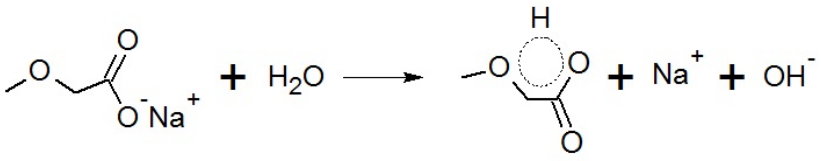

Figure 3.12: Hydrogen Bonding between the Protonated Carboxylate Group and a Neighboring Ether Oxygen

Effect of Temperature

Similar to the case of CMC, higher temperature promotes the disassociation and movement of the ions in the solution, therefore, renders a higher degree of ionization.

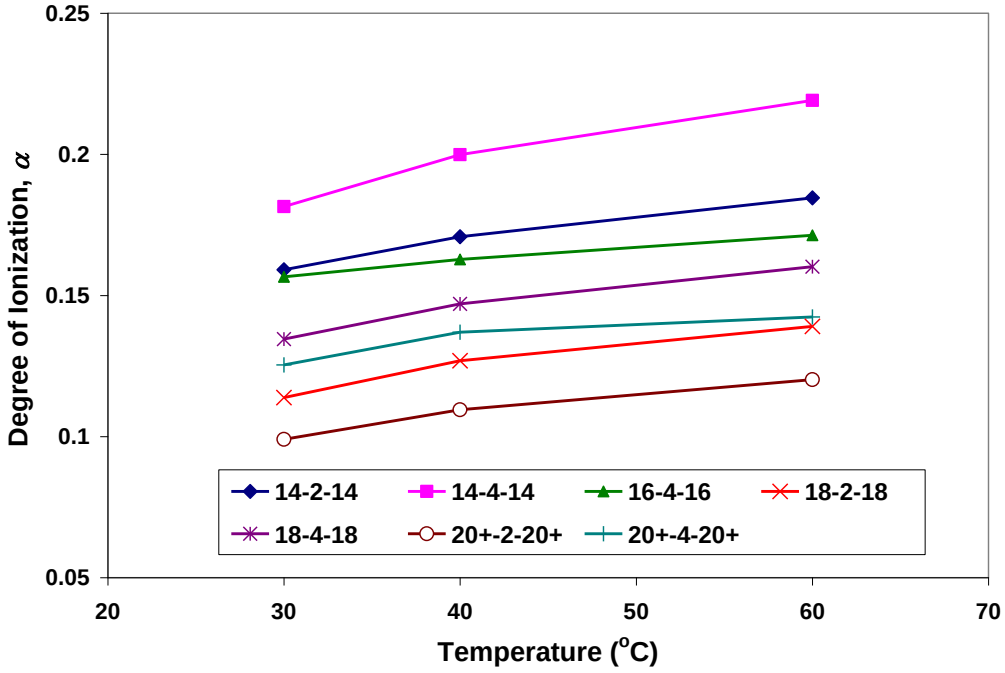

Figure 3.13: Effect of Temperature on Degree of Ionization.

3.7.3 Thermodynamic Parameters ΔG_M^o, ΔH_M^o and ΔS_M^o

The calculated thermodynamic parameters are listed in tables below.

Table 3.17: Thermodynamic Parameters of -C_2- Group at 30˚C.

Surfactant	ΔG_M^o (kJ/mol)	ΔH_M^o (kJ/mol)	ΔS_M^o (J/mol/K)
14-2-14	-79.43	-22.56	187.59
18-2-18	-90.61	-21.31	228.58
20^+-2-20^+	-97.68	-35.47	205.23

Table 3.18: Thermodynamic Parameters of –C_4- Group at 30˚C.

Surfactant	ΔG_M^o (kJ/mol)	ΔH_M^o (kJ/mol)	ΔS_M^o (J/mol/K)
14-4-14	-78.54	-1.05	255.59
16-4-16	-84.97	-7.76	254.7
18-4-18	-90.82	-19.78	234.34
20^+-4-20^+	-97.07	-0.28	319.29

Table 3.19: Effect of Head Group on Thermodynamic Parameters at 30˚C.

Surfactant	ΔG_M^o (kJ/mol)	ΔH_M^o (kJ/mol)	ΔS_M^o (J/mol/K)
18-4-18 2SO$_4$Na	-90.82	-19.78	234.34
18-4-18 2COONa	-49.26	2.43	170.48
20$^+$-4-20$^+$ 2SO$_4$Na	-97.07	-0.28	319.29
20$^+$-4-20$^+$ 2COONa	-58.57	-5.08	176.47

From Table 3.17 and Table 3.18, it is evident that all the micellization free energy terms ΔG_M^o are negative and all the entropy contributions ΔS_M^o are positive. For the same spacer length, longer alkyl chain leads to even more negative free energy, which leads to the fact that Gemini surfactants with large hydrophobes will naturally have a higher tendency to form micelles in aqueous solution and thus lower CMC value. The primary contribution of the negative free energy comes from the entropy term, and therefore the micellization process is primarily entropy driven.

3.8 INTERFACIAL TENSION REDUCTION POTENTIAL BY GEMINI SURFACTANTS

Study of the micellization process is important for understanding the self-aggregation behavior of Gemini surfactant in aqueous solution. It has direct implications for microemulsion formation and thus oil solubilization in the surfactant flooding process. Therefore, in this section, we try to establish a connection between the micellization and solubilization processes and obtain, as a first order of approximation, some qualitative estimates of interfacial tension between a microemulsion phase and excess dispersed phase.

In order to build such a connection, we assume the microemulsion phase contains spherical globules (of uniform radius r_e) dispersed in a continuous medium. Ruckenstein (1981) proposed a treatment based on such an assumption and established a relationship between the interfacial tension γ at the surface of the globule and the derivative, with

respect to the radius, of the entropy of dispersion of the globules in the continuous medium,

$$\gamma\left(r_e\right)=\frac{r_e^2}{3\phi_v}\left(\frac{d\Delta f_e}{dr}\right)_{r_e} \tag{3.33}$$

Here, r_e is the equilibrium globule radius corresponding to the minimum Helmholtz free energy of the system; ϕ_v is the volume fraction of the dispersed phase per unit microemulsion volume. Δf_e is a free energy for the entropy of dispersion of the globules in the continuous phase, per unit microemulsion volume.

The key assumption in deriving eq. (3.33) is that the van der Waals and electrostatic interactions between globules are negligible compared to the entropy term, which Ruckenstein claimed to be the case at least for ϕ_v values that are not so large and at ionic sufficiently high ionic strength. This assumption seems to be in line with our observation that Gemini micellization process is primarily entropy driven. For some conventional surfactants, however, this might not be the case for certain conditions (Figure 3.5).

On the basis of a lattice model (Ruckenstein *et al.*, 1975), Ruckenstein *et al.* estimated the lower and upper bounds, as well as average value for the entropy of dispersion S_d of the globules in the continuous medium of the microemulsion. The free energy associated with the average S_d has the form:

$$\Delta f_{e,a}=-T\Delta S_{d,a}=-\frac{3\phi_v kT}{4\pi r^3}\ln\left(\frac{4\pi r^3}{3\phi_v v_c}\right) \tag{3.34}$$

where v_c is the molecular volume of the continuous phase (water or oil). Using eq. (3.34) for Δf_e, eq. (3.33) leads to,

$$\gamma = \frac{3kT}{4\pi r_e^2}\left[\ln\left(\frac{4\pi r_e^3}{3\phi_v v_c}\right) - 1\right] \tag{3.35}$$

If we assume that the surfactant concentration in the solution is low (near CMC), then a very limited amount of oil will be solubilized by the aggregation of surfactant molecules (ϕ_v is very small). The microemulsion droplets behave more like swollen micelles with very limited oil solubilized, and thus it is safe to approximate at least the order of magnitude of S_d by that of ΔS_M^o obtained from the thermodynamic calculations. It should, however, be noted that S_d is expressed per unit microemulsion volume, whereas ΔS_M^o is expressed per mole of surfactants. The conversion between the two quantities must be implemented for consistency.

We now consider two cases of O/W (Type I) microemulsion, i) conventional single chain surfactant; ii) anionic Gemini surfactant. Since this is a qualitative analysis, we use the parameters listed in Table 3.20 as a first order approximation to capture the relative magnitudes of various quantities.

Table 3.20: Qualitative Evaluation of IFT for Conventional and Gemini Surfactants. To put things into perspective: 0.1mM of Petrostep S13-B (C_{13}-7PO-SO_4Na) corresponds to less than 0.01wt% of surfactant.

Parameters	**Case I Conventional Surfactant**	**Case II Gemini Surfactant**
ϕ_v	0.0001	0.0001
T (K)	303.15	303.15
$C_{\text{surf.}}$ (mM, near CMC)	0.1	0.005
$\Delta f_{e,a}$ (kJ/m^3 of ME phase)	-2.0	-0.2
$-T\Delta S_M^o$ (kJ/mol)	-20	-40
r_e (Å)	8.83	20.10
$\gamma(r_e)$ (dynes/cm)	16.38	3.772

The values used here are on the conservative side as can be seen in the table that CMC for conventional surfactant is twenty times (instead of 100X or even 1000X) of that for Gemini, and that the entropic term for conventional is one half (instead of one third or fourth) of that for Gemini. The addition of salt is essential to achieve high ionic concentration (for the electrostatic repulsion to be neglected), and it will also affect the CMC values and thus the calculations of entropic terms. A detailed calculation can be carried out following the same procedures as outlined in previous sections. But again as a qualitative analysis, we assume that the addition of salt will not cause an order of magnitude change in $-T\Delta S_M^o$. The results from Table 3.20 indicate that the Gemini surfactant will be able to lower the water-oil IFT substantially more than a conventional surfactant, at concentration levels near their respective CMCs. The reason for this comes clearly from the fact that Gemini surfactants are able to self-associate at extremely low concentration and give rise to a substantial entropic gain during this process. Comparing the equilibrium radius r_e for the two cases, it is apparent that Gemini surfactants are able to form larger-size aggregates and reduce the overall free energy of the system. It is worth nothing that r_e here only represents a characteristic length (Ruckenstein, 1981) of the aggregates formed in the solution. The detailed structure and shape of these aggregates need further investigation.

3.9 SUMMARY

A very important characteristic for surfactants, critical micelle concentration, was carefully examined in this chapter for our series of anionic Gemini surfactants, by electrical conductivity measurements. The CMC values for anionic Gemini surfactants are about two to three orders of magnitude lower than the corresponding conventional surfactants. It depends primarily on the surfactant tail length, and relatively little on the

length of spacer and solution temperature. Another important outcome is the degree of ionization derived from the conductivity measurements. As will be discussed in Chapter 7, this parameter describes the surface charge conditions at the micellar surface, which in turn is defined largely the electrostatic repulsion between head groups.

By considering the detailed thermodynamics involved in Gemini micellization process, important thermodynamic parameters, including Gibbs free energy, enthalpy and entropy ΔG_M^o, ΔH_M^o and ΔS_M^o during micellization, can be determined using the experimentally measured CMC and degree of ionization data. These parameters provide fundamental insights into the Gemini self-assembly process in aqueous solution. The significantly more negative ΔG_M^o for Gemini surfactants is the driving force for its micellization, and the ultralow CMC value is the direct result of this huge negative free energy. Moreover, the micellization process of Gemini surfactants is primarily entropy driven, as compared to that of conventional surfactants, where enthalpy and entropy have comparable contributions. This is due to the much larger disruption to the water structure caused by double tail groups from a Gemini surfactant.

The thermodynamic parameters, more specifically the entropy term can be utilized in a qualitative estimation of the interfacial tension between a microemulsion phase and excess dispersed phase. The results suggest that even at extremely low surfactant concentration (and thus low solubilization), Gemini surfactants are still capable of reducing the water/oil interfacial tension substantially, thanks to their superior tendency to self-aggregate.

Chapter 4: Adsorption Behavior of Anionic Gemini Surfactants at Air-Water and Solid-Water Interfaces

4.1 INTRODUCTION

4.1.1 Gemini Adsorption at Air-Water Interface

The molecules at the surface of a liquid have potential energies greater than those of similar molecules in the interior of the liquid. This is because attractive interactions of molecules at the surface with those in the interior of the liquid are greater than those with the widely separated molecules in the gas phase. As a direct result, an amount of work equal to this difference in potential energy must be expended to bring a molecule from the interior to the surface. The surface free energy per unit area, or surface tension, is a measure of this work. Although more correctly thought of as a surface free energy, surface tension is often conceptualized as a force per unit length at a right angle to the force required to pull apart the surface molecules in order to permit expansion of the surface by movement into it of molecules from the phase underneath it.

As a generalization, the interfacial free energy per unit area, γ_I, of the interface between two distinctive phases (as shown in Figure 4.1), is given by (Rosen, 2004):

$$\gamma_I = \gamma_a + \gamma_b - 2\gamma_{ab} \tag{4.1}$$

Where γ_a and γ_b are the surface free energies per unit area (the surface tensions) of the pure liquid *a* and *b* respectively, and γ_{ab} is the *a*-*b* interaction energy per unit area across the interface. In the case where one of the phases is a gas, the molecules in that phase are so far apart relative to those in the condensed phase that tensions produced by molecular interactions in that phase can be disregarded. Thus if phase *a* is gas, γ_a and γ_{ab} can be disregarded and $\gamma_I \approx \gamma_b$, the surface tension of liquid phase *b*.

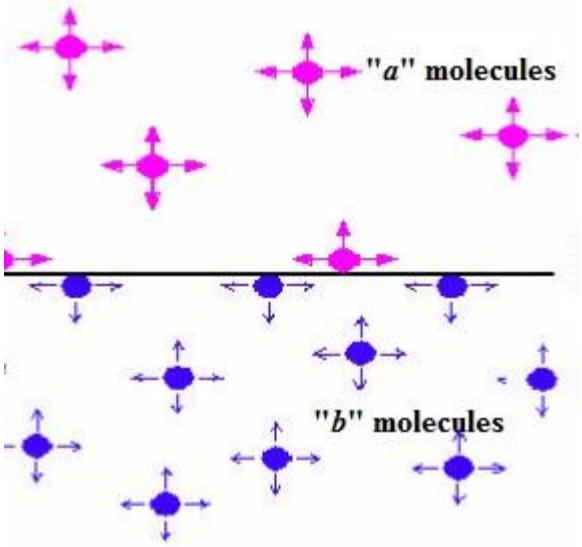

Figure 4.1: Interfacial Region between Two Adjacent Phases.

The aggregation behavior of Gemini surfactants at air-water, oil-water, and solid-water interfaces affects their ability to form stable foams, emulsions, and dispersions (Zana, 2002). More specifically, adsorption at aqueous solution surfaces determines the surface density, surface charge and surface tension properties. The first part of this chapter covers the experimental results for studying the surface tension behavior, showing surface properties of Gemini surfactants and contrasting them, when available, to those of similar monomeric surfactants. Generally, at the same molar concentrations, Gemini surfactants have far higher surface activities and lower surface tension than their monomeric counterparts. This is not surprising, as they have two hydrocarbon chains, making them more hydrophobic. Having two polar head groups makes them more hydrophilic than a double chain conventional surfactant with a single head group. This property introduces a higher solubility, which combined with the higher hydrophobicity, makes Geminis very efficient surfactants.

4.1.2 Gemini Adsorption at Solid-water Interface

Surfactants have a variety of applications in the petroleum industry especially for enhance oil recovery (EOR) processes. Loss of surfactant due to its interaction with reservoir rocks is always a key concern for economic reasons, especially when we consider the use of a low concentration Gemini surfactant slug in a flooding process. In the second part of this chapter, surfactant adsorption at solid-water interface will thus be the primary focus. The equilibrium adsorption of surfactants at the solid-water interface depends on the nature of surfactants and the absorbents (Paria and Khilar, 2004). The behavior of surfactants at solid-water interfaces is determined by a number of forces, including electrostatic attraction, covalent bonding, hydrogen bonding, and hydrophobic bonding, etc (Somasundaran and Huang, 2000).

Surfactant adsorption at solid-water interface has been studied for several decades. A number of studies have been conducted on ionic surfactants (Somasundaran *et al.*, 1983; Blokhus *et al.*, 1996; Somasundaran and Krishnakumar, 1997). The solid surfaces are either positively or negatively charged in the aqueous medium by ionization/dissociation of surface groups or by the adsorption of ions from solution onto a previously uncharged surface. At low surfactant concentrations, the charge on the electrical double layer of the solid surface largely determines the surfactant adsorption. However, as the surfactant concentrations increase other factors such as the tendency of the surfactant to aggregate, become significant (Somasundaran and Krishnakumar, 1997). The onset of hydrophobic interaction between the adsorbed surfactant molecules takes place, leading to a substantial increase in the adsorption that eventually levels off at the critical micelle concentration (Rosen, 2004).

The minerals present in most reservoir rocks are quartz, feldspars and clays such as Kaolinite, etc., which generally display a net negative charge at neutral pH. In order to

lower surface adsorption, negatively charged surfactants are usually considered to be better than cationic surfactants and so anionic surfactants have historically been the most used type of chemicals in surfactant flooding of sandstone oil reservoirs (Scamehorn *et al.*, 1982). The adsorption of surfactants from the solution will be affected by its physical-chemical properties such as temperature, electrolyte concentration, etc (Baviere *et al.*, 1993; Paria and Khilar, 2004).

Gemini surfactants attract attention due to their advantages of high salinity tolerance, (including multivalent cations), and low CMC. They have great potential of being applied in such harsh reservoir environments. The adsorption behavior of Geminis applied to EOR has not been fully investigated in the past. Mannhardt *et al.* (1992) carried out adsorption studies with several foam-forming surfactants on core samples of Berea sandstone. One surfactant blend investigated in their paper contained a DOWFAX® 3B2, a mixture of monoalkyl disulfonate and dialkyl disulfonate. Their results showed that the blend gave the lowest adsorption onto sandstone, and that the trends in adsorption can be explained on the basis of the interaction of the charge on the surfactant with changes in the solid surface.

In the current study, the adsorption data of synthesized anionic Gemini surfactants onto Berea core materials are determined by static adsorption tests and compared with results obtained from tests done on conventional EOR surfactants. The effects of different variables are systematically studied.

4.2 DETERMINATION OF SURFACE PROPERTIES

4.2.1 The Gibbs Adsorption Equation

A solute can exist in a different concentration at the surface/interface of a solvent than in its bulk phase. The surface excess density Γ (mol/m^2) represents excess of solute

per unit area of the surface over what would be present if the bulk concentration prevailed all the way to the surface. The surface density of adsorbed surfactant molecules, Γ_i, is related to the variation of the equilibrium surface tension with the chemical potential via the Gibbs adsorption equation, or "isotherm" (Adamson *et al.*, 1997):

$$d\gamma = -\sum \Gamma_i d\mu_i \tag{4.2}$$

Where $d\gamma$ is the change in surface or interfacial tension of the solvent; $d\mu_i$ represents the change in chemical potential of the component i of the system. This equation is fundamental to all adsorption processes where monolayers are formed. At equilibrium between the interfacial and bulk phase concentrations, $d\mu_i = RTd\ln a_i$, where a_i is the activity of component i in the bulk phase; R is the gas constant and T is the absolute temperature, thus,

$$d\gamma = -RT\sum \Gamma_i d\ln a_i = -RT\sum \Gamma_i d\ln\left(x_i f_i\right) \tag{4.3}$$

Where x_i is the mole fraction of component i and f_i its activity coefficient.

4.2.2 Surface Excess Concentration

For dilute ($\leq 10^{-2}$M) ionic surfactant solutions (Sandler, 2006), the activity of the solvent and the activity coefficient of the solute can both be considered to be constant and the mole fraction of the solute maybe replaced by its molar concentration C. Thus,

$$d\gamma \approx -nRT\Gamma d\ln C = -2.303nRT\Gamma d\log C \tag{4.4}$$

When γ is in dyne/cm (=ergs/cm^2) and R=8.314×10^{7}ergs/mol/K, then Γ is in mol/cm^2; when R=8.314J/mol/K, then Γ is in mol/10^{3}m^2. Based on eq. (4.4), Γ can be determined from the slope of the curve γ versus log$C$. The maximum (or saturated) value Γ_{max} is then:

$$\Gamma_{\max} = -\frac{1}{2.303nRT}\left[d\gamma/d\log C\right]_{\max} \quad (4.5)$$

Where n is a function of C, C_{add} (salt concentration), and the number of dissociated ionic species per molecule. For Geminis, various investigators have used 2 or 3 for n (Zana and Xia, 2004). In all calculations that follow, n=2 will be used based on the understanding that they are merely indicative of the change in Γ_{max} within the series of compounds.

4.2.3 Surface Area per Molecule

For surfactants, the surface excess concentration Γ can be considered to be equal to the actual surface concentration without significant error. The concentration of surfactant at the interface may, therefore, be calculated from surface or interfacial tension data by use of the appropriate Gibbs equation. The minimum area per molecule at the surface, $a_{\min}$ (in Å^2/molecule), is then given by:

$$a_{\min} = 10^{16}/N_{Av}\Gamma_{\max} \quad (4.6)$$

The values of $a_{\min}$ in aqueous solution without electrolyte are based upon n=2. With the presence of a large amount of electrolytes (>10^{-2}M NaCl), n=1 (Song *et al.*, 1996; Perez *et al.*, 1998; Tsubone *et al.*, 2003) is used and an accurate value of $a_{\min}$ can be calculated.

4.2.4 Efficiency of Adsorption at the Interface

In comparing the performance of surfactants at the interfaces, it is useful to have a parameter that measures the concentration of surfactant in the liquid phase required to produce a given amount of adsorption at the interface. A convenient measure of the efficiency of adsorption is the negative logarithm of the concentration of surfactant in the bulk phase required to produce a 20dynes/cm reduction in the surface or interfacial

tension of the solvent, pC_{20}=-logC_{20}. It can be calculated using the following equation (Rosen, 2004),

$$pC_{20} = -\log C_{20} = \frac{\pi_{CMC} - 20}{2.303nRT\Gamma_{max}} - \log CMC \tag{4.7}$$

where π is the surface pressure defined by,

$$\pi = \gamma_0 - \gamma \tag{4.8}$$

and π_{CMC} is the surface pressure at CMC. Eq. (4.7) is derived from eq. (4.5) and based on the assumptions that the point (-pC_{20}, γ_{C20}) lies on the linear portion of the log$C$ vs. γ plot and that Γ at C_{20} is close to its saturation value (Γ_{max}).

4.2.5 Thermodynamic Parameters of Adsorption

The standard free energies change upon adsorption ΔG_{ad}^0 tells us whether adsorption (in the standard state) is spontaneous (ΔG_{ad}^0 negative) or not and the magnitude of the driving force. Standard free energies at the air-water interface can be calculated from surface tension data in the vicinity of the CMC, where such data are commonly and conveniently taken, by use of equation (Rosen, 1981),

$$\Delta G_{ad}^0 = nRT \ln a_\pi - \pi A_{min} \tag{4.9}$$

Where a_π is the activity of the surfactant in the aqueous phase at a surface pressure of π (=γ_o-γ) in the region of surface saturation (i.e., where Γ=Γ_{max} and the molar area of the surfactant A_{min}). The standard state for the surface phase is a hypothetical monolayer of the surfactant at its closest packing (minimum surface area/molecule, i.e., Γ=Γ_{max}) but at a surface pressure of zero. For ionic surfactants at dilute concentrations ($\leq 10^{-2}$M) in the solution phase, we can substitute mole fractions for activities and the relation becomes,

$$\Delta G_{\text{ad}}^{0} = nRT \ln\left(C_{\pi}/\omega\right) - \pi A_{\min} \tag{4.10}$$

Where C_{π} is the molar concentration of surfactant in the aqueous phase at a surface pressure of π and ω is moles of water per liter. When C_{π} is in mol/L, π in dynes/cm, $a_{\min}$ in Å^2 per molecule, and R=8.314J/mol/K, this becomes,

$$\Delta G_{\text{ad}}^{0}\left(\text{in J/mol}\right) = 2.303nRT \log\left(C_{\pi}/\omega\right) - 6.023\pi a_{\min} \tag{4.11}$$

4.3 MATERIALS AND METHODS

Gemini surfactants *m-s-m*, were prepared in house with reactions described in Chapter 2. The product was purified by recrystallization from dichloromethane (DCM). Thin layer chromatography and NMR analysis confirmed sample identity. Sodium hexadecyl sulfate (SHS) was obtained from Sigma-Aldrich. Some commercial surfactants used in the adsorption tests, for instance Exxal TDA-9PO-Sulfate (Petrostep S13-C), were obtained from Stepan Company and used as received.

In this section, the critical micelle concentration of the Gemini surfactants will be derived from surface tension measurements and compared with results obtained from the previous chapter (conductivity method). Before reaching the CMC, the surface tension changes strongly with the concentration of the surfactant. When the CMC is reached, a further increase in surfactant concentration no longer has any appreciable influence on the surface tension. The CMC is obtained from the intersection of the straight lines for the linear concentration-dependent section and the concentration-independent section. A ring tensiometer (CSC DuNouy Tensiometer) based on the du Nouy method is used to measure the surface tension at surfactant solution surface. The detailed theory behind this method is included in Appendix C. Low concentration surfactant solutions were prepared

by continuous dilution of a 0.02mM stock solution (diluted from a 1M solution). All measurements were carried out at room temperature of 25˚C.

A static adsorption test was used for measuring surfactant adsorption at the solid-water interface. The experimental procedures are adopted from the study by Hanna and Somasundaran (1977). The adsorbents used for static adsorption tests were particles disaggregated from a Berea sandstone core and sieved through a 60 mesh screen (<320μm, medium-size sand and below). The use of 60 mesh screen is based on the consideration that a wider and thus more representative range of particle sizes could be included in the test. The adsorbents was heated in the oven overnight and cooled in a desiccator over Drierite^{TM} before use. Sands and sandstones typically have a specific surface area of 1 to 10m^2/g, and the clay content is responsible for most of that surface area. The disaggregation of any rock or mineral sample will typically result in material of higher surface area, and thus higher surface energy. As a result, the static adsorption tests often give higher values for adsorption than those observed in consolidated sandstones containing these materials (Jordan *et al.*, 1995). However, the important sensitivities to parameters like salinity and temperature will still be in the correct direction for predicting and analyzing consolidated core flooding experiments in reservoir cores.

4.4 EXPERIMENTAL DETAILS

4.4.1 Surface Tension Measurements

The tensiometer used for the determination of surface tensions was a du Nouy ring tensiometer supplied by CSC Scientific Company Inc. (shown in Figure 4.2). The ring, made of platinum-iridium alloy, had a mean circumference 6.02cm and a ratio of R/r=59.12. Ring was rinsed in chromic acid, then pure water and briefly heated to glowing by holding above a heat gun. The glass measuring vessels were similarly cleaned

and dried in an oven. They were filled with the appropriate liquid before measurements were made. The test results were read directly on the round dial on the front of the tensiometer. The surface tension of water at 25°C was measured to be 71.44mN/m, which is in good agreement with reported values (71.99mN/m, Pallas *et al.*, 1990).

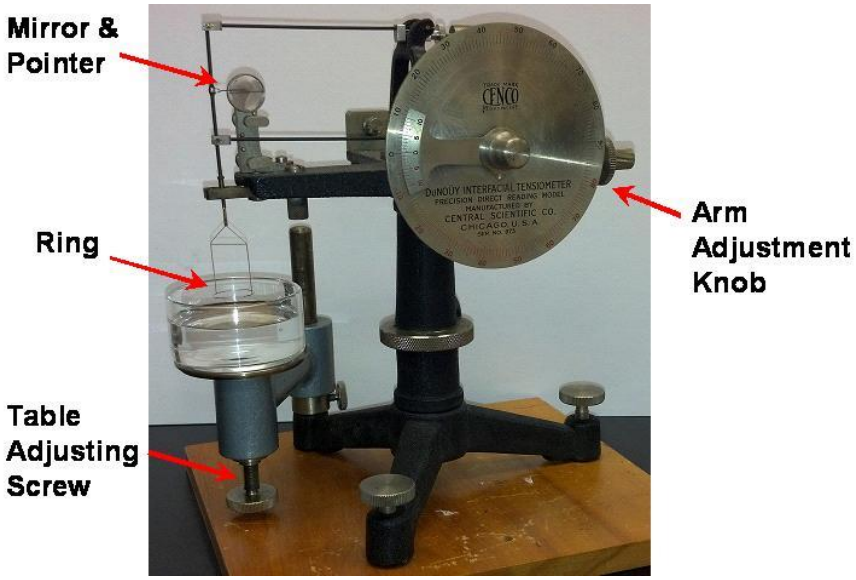

Figure 4.2: CSC du Nouy Ring Tensiometer.

To perform the test, there are few key parts of the instrument. The mirror and the pointer indicate the effect of surface tension forces on the ring as it passes the sample surface. The sample table adjusting screw moves the sample surface past the ring. The arm adjustment knob adjusts the arm pointer to offset the force required to pull the ring to surface and record the force on the front dial. Start the process with ring above the surface of the sample. The pointer should be at the line on the mirror. The next step is to immerse the ring below the surface of the sample. The pointer should still be at the line on the mirror. With the ring below the surface of the sample, begin to lower the sample table with the sample table adjusting screw. When the ring approaches the surface, the

pointer will move below the mirror line, at this point use the arm adjustment knob to move the pointer back to the mirror line. Repeat this process of slowly lowering the sample until the pointer moves below the mirror line and moving it back to the mirror line with the arm adjustment knob. With this process, the ring slowly pulls through the liquid surface, creating a meniscus. The process is repeated until the ring pops off and the pointer moves above the mirror line. This signals the end of the test process. At this point, the position of dial indicator is the surface tension in dynes per centimeter.

4.4.2 Static Adsorption Test

In the adsorption experiments, stock solutions containing Gemini surfactants were prepared in 10000ppm NaCl brine (base solution). The adsorption tests were carried out at 25^{o}C. A desired amount of adsorbent (typically 2g) was agitated (stirred) with the required volume of surfactant solution (typically 80ml) of different concentrations. The mixtures were stirred for 12 hours. After filtration at test temperature, the samples were centrifuged at 3000 rpm for 20 minutes. The supernatant liquid was filtered, diluted and analyzed for the residual concentration of the surfactant. The surfactant concentration was measured by Total Organic Carbon method, TOC, which represents the amount of total carbon in the sample, and is used in current study because of its simplicity. The collected samples needed to be diluted with brine so that the concentration could be in the detectable range of the TOC instrument (1 to 20ppm). Above 20ppm distortion of the peak and inaccurate results are likely to occur. Series of calibration samples with known concentrations was separately prepared and used to generate a calibration curve. Liquid standards and samples were prepared in 40 ml vials to have enough volume available to get at least 3 replicates per sample plus rinses of the tubing and reaction vessels. The

amount of surfactant adsorbed was determined by measuring difference in solution concentrations before and after contact with the adsorbents,

$$\Gamma = \frac{(C_o - C) \times V}{M} \tag{4.12}$$

Where Γ (mg/g) is the surfactant adsorption density on Berea core material; C_o and C (mg/L) are surfactant concentrations before and after adsorption tests; V (ml) is the volume of surfactant solution used in the test, and M (gram) is the mass of the adsorbents used in the test. A dimensionless quantity θ can be defined as follows:

$$\theta = \frac{\Gamma}{\Gamma_m} \tag{4.13}$$

in which Γ_m is the maximum or plateau adsorption density. Therefore, θ represents the fraction of surface area that is covered by surfactant.

4.5 SURFACE TENSION MEASUREMENTS

4.5.1 Validation Measurements using SDS

The semi-log plot Figure 4.3 shows surface tension measurements for a series of SDS aqueous solutions at 25^{o}C. The experimental procedures have been described in the previous section. The CMC, surface tension at CMC, and various surface properties described previously are summarized in Table 4.1.

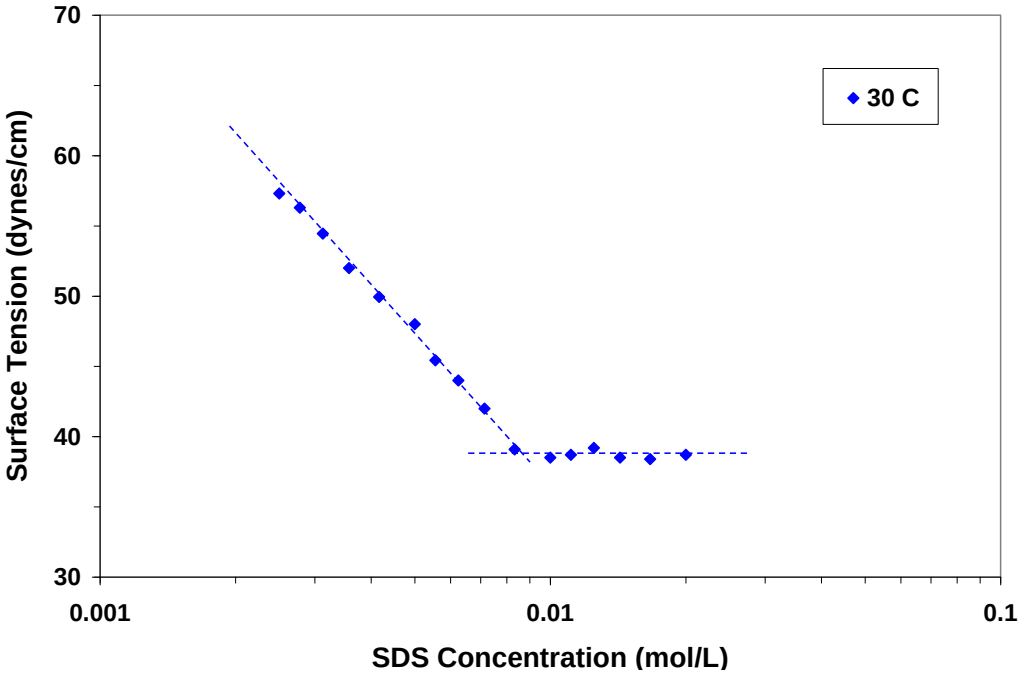

Figure 4.3: Surface Tension (in dynes/cm) vs. SDS Concentration (in M).

Table 4.1: Surface Properties of SDS in Water at 25°C.

CMC (mM)	γ_{CMC} **(dynes/cm)**	$\Gamma_{max} \times 10^{10}$ **(mol/cm^2)**	a_{min} **($\dot{A}^2$)**	pC_{20}	**CMC /C_{20}**	ΔG^0_{ad} **(kJ/mol)**
8.54	38.7	3.11	53	2.42	2.22	-54.7

The measured CMC value in Table 4.1 agrees well with the value of 8.33mM from Chapter 3 by conductivity measurement. Surface properties, Γ_{max}, a_{min}, pC_{20} and ΔG^0_{ad} are also close to the reported values by Rosen (2004). The CMC/C_{20} ratio is a measure of the tendency of surfactant molecule to form micelles relative to the tendency to adsorb at the air/water interface.

4.5.2 Measurements using Gemini Surfactant *14-2-14*

Figure 4.4 shows results obtained working with aqueous solutions of *14-2-14* Gemini surfactant at 25°C. As done for the SDS case, CMC, surface tension at CMC, and various surface properties are summarized in Table 4.2.

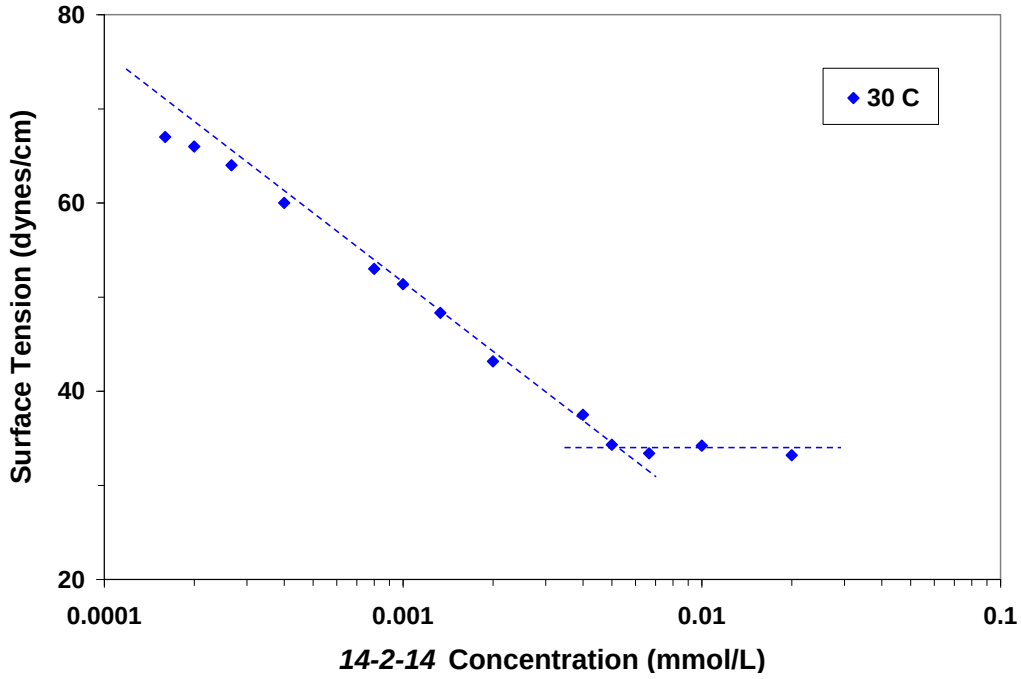

Figure 4.4: Surface Tension vs. *14-2-14* Concentration at 25°C.

Table 4.2: Surface Properties of *14-2-14* in Water at 25°C.

CMC (10^{-3} mM)	γ_{CMC} **(dynes/cm)**	$\Gamma_{max} \times 10^{10}$ **(mol/cm^2)**	a_{min} **($\dot{A}^2$)**	pC_{20}	**CMC /C_{20}**	ΔG^0_{ad} **(kJ/mol)**
5.3	33.7	2.1	79	5.99	5.22	-99.36

Once again, the CMC value in Table 4.2 agrees with the one obtained from conductivity measurement. The air/water surface tension is further reduced by 6.3dynes/cm for the *14-2-14* solution. Comparing surface excess density and area per molecule values between the SDS and *14-2-14* cases, Γ_{max} is more than one half of the

value for SDS, and a_{min} is less than two times as large as that for SDS. These two parameters indicate that the double chain molecules are somewhat more closely packed at the surface than the single-chain molecule, possibly due to the bonding by the short spacer group. pC_{20} and ΔG_{ad}^{0} values for *14-2-14* are much larger than those of SDS, representing the much higher surface activity and tendency to adsorb at the surface of these double-chain molecules.

The detailed experimental results of the other Gemini surfactants are not included in this chapter, and are presented in Appendix D. The results are organized in the same manner as Figure 4.4, and Table 4.2.

4.5.3 Results and Discussion

General Characteristics

Figure 4.5 and Figure 4.6 show the semi-log plots of γ vs. C at 25°C for all the synthesized sulfate Gemini surfactants, organized by spacer group (Figure 4.5 for *m-2-m*, and Figure 4.6 for *m-4-m*). The surface tension method can be used for checking the sample purity and the absence of a minimum is a good sign. The existence of the surface tension plateau, instead of a local minimum, is a good indication of the product purity. The samples used in the current study were carefully purified by recrystallization as discussed in Chapter 2.

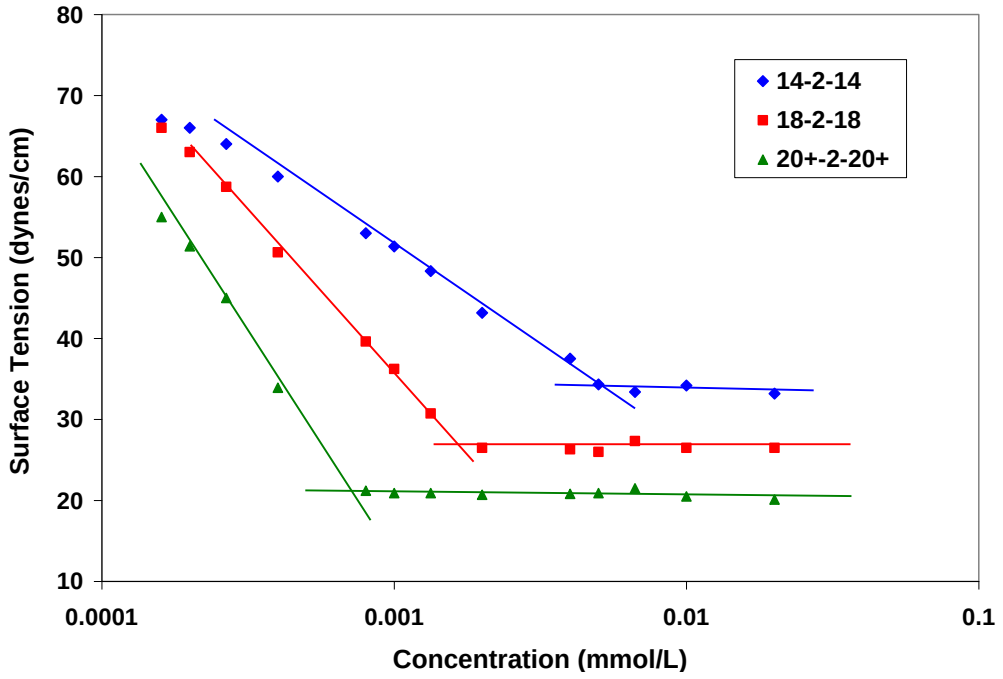

Figure 4.5: Surface Tension vs. Gemini Concentration at 25°C for *m-2-m* Series.

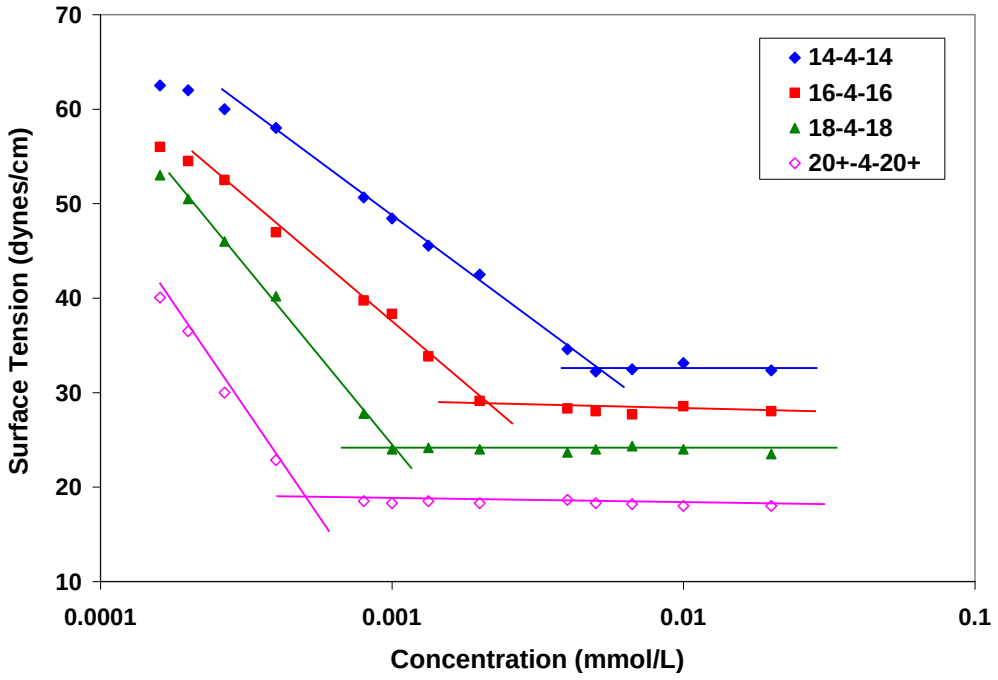

Figure 4.6: Surface Tension vs. Gemini Concentration at 25°C for *m-4-m* Series.

The break point for each molecule marks the critical micelle concentration. Various surface properties, e.g. Γ_{max}, a_{min}, pC_{20} and ΔG_{ad}^{0}, can be calculated from relevant equations outlined in previous sections. The results are listed in Table 4.3.

Table 4.3: Surface Properties of Sulfate Gemini Surfactants in Water at 25°C.

Surfactant	**CMC (10^{-3} mM)**	**γ_{CMC} (dynes/cm)**	**$\Gamma_{max}\times10^{10}$ (mol/cm^2)**	**a_{min} ($\dot{A}^2$)**	**pC_{20}**	**CMC/ C_{20}**	**ΔG_{ad}^{0} (kJ/mol)**
14-2-14	5.3	33.7	2.1	79	5.99	5.22	-99.36
14-4-14	4.9	32.56	1.98	84	6.12	6.47	-101.41
16-4-16	2.2	28.02	2.3	72	6.53	7.38	-104.71
18-2-18	1.7	26.5	3.45	48	6.39	4.14	-100.19
18-4-18	1.0	24.02	3.36	49	6.7	4.98	-103.96
20^+-2-20^+	0.67	20.91	5	33	6.7	3.33	-102
20^+-4-20^+	0.5	18.3	4.05	41	7	5.01	-106.47
SDS	*8540*	*38.7*	*3.11*	*53*	*2.42*	*2.22*	*-54.7*

As can be seen from Table 4.3, micellization of Gemini surfactants takes place at a concentration around 10^{-3}mM, about three orders of magnitude lower than that of SDS. The extraordinary ability to self-aggregate is a common feature for Gemini surfactants. Lower γ_{CMC} values than that of SDS are also observed. Recalling the results from Chapter 3, CMC values determined from both methods (conductivity and surface tension) are in decent agreement. It should be noted that CMC values in Chapter 3 were reported at a slightly different temperature of 30°C, while the surface tension measurements were conducted at 25°C due to the difficulties in adjusting the temperature on the ring tensiometer. It is, therefore, not a strict comparison. However, based on previous discussions temperature has only a small impact on CMC values, and thus such a comparison is still considered acceptable.

For ionic surfactant molecules in water, the micelle formation is a direct result of two opposing forces, an attractive force favoring aggregation and closer packing and a repulsive force that prevents larger size micelles. The attractive force arises from the hydrophobic effect (Tanford, 1973) acting upon the hydrocarbon chains of the surfactants. The hydrophobic effect is an entropic effect (Silverstein, 1998) originating from the disruption of highly dynamic hydrogen bonds between molecules of liquid water by the hydrocarbon chains. The repulsive force in micelle formation comes primarily from electrostatic interactions between the head groups. Longer hydrocarbon tails will thus induce stronger hydrophobic attraction which results in tighter packing and lower surface tension at air-water interface, provided that electrostatic repulsion remains unchanged.

Since surface tension reduction depends on the replacement of water molecules at the interface by surfactant molecules, the efficiency (e.g. γ_{CMC} and pC_{20}) of a surfactant should reflect the interface surfactant concentration relative to that of bulk liquid phase. The ratio of surfactant concentration at the surface to that in the bulk phase, C^S/C, is, therefore, a suitable measure. The surface concentration C^S (in mole/L) in turn can be related to the surface excess concentration Γ (in mole/cm^2) by the relation $C^S \approx 1000\Gamma/d$, where d (in cm) is the thickness of surface/interfacial region. $C^S/C = 1000\Gamma/Cd$. When the tension has been reduced by 20 dynes/cm, Γ is close to Γ_{max}, and most surfactant molecules are lying tilted to the surface/interface (Aguiar *et al.*, 2011). Assuming that the thickness of the interfacial region d is determined by the height of surfactant normal to the interface, then d is inversely proportional to the minimum surface area per molecule a_{min}; a larger value of a_{min} generally indicates a smaller angle of the surfactant with respect to the interface; a smaller value of a_{min} indicates an orientation of the surfactant more perpendicular to the interface.

All the above discussions explain why we see a general tend of decreasing γ_{CMC}, increasing Γ_{max}, and decreasing a_{min} as the hydrocarbon chain of Geminis becomes longer. The much higher pC_{20} values of Gemini surfactants over SDS represent the superior efficiency of Gemini molecules in reducing surface tension. The CMC/C_{20} ratios decease as the alkyl chain length increases. The standard free energies of adsorption ΔG_{ad}^{0} for all Gemini surfactants are negative; indicating that adsorption of these compounds at the aqueous air-water interface is spontaneous. Recalling from Chapter 3, we obtained the standard free energy of micellization, ΔG_{M}^{o}, for the synthesized Gemini surfactants. The values of ΔG_{M}^{o} and ΔG_{ad}^{0} are compared side by side in Table 4.4.

The negative values of both free energy terms illustrate once again the great potential for Gemini surfactants to form micelles in solution and to adsorb onto the air-water interface. The absolute values of ΔG_{M}^{o} are also smaller than those of ΔG_{ad}^{0}, indicating that the adsorption is promoted more than the micellization in all the series. This result is supported by the values of large pC_{20} as described above. And similar observations were made by Li *et al.* (2010) in their study of alkylamino ethane sulfonate Gemini surfactants.

Table 4.4: Standard Free Energy of Micellization and Adsorption of Gemini Surfactants.

Surfactant	ΔG_{M}^{o} **(kJ/mol)**	ΔG_{ad}^{0} **(kJ/mol)**
14-2-14	-79.43	-99.36
14-4-14	-78.54	-101.41
16-4-16	-84.97	-104.71
18-2-18	-90.61	-100.19
18-4-18	-90.82	-103.96
20^{+}-2-20^{+}	-97.68	-102
20^{+}-4-20^{+}	-97.07	-106.47

Effect of Alkyl Chain Length

Based on the experimental values listed in Table 4.3, the impacts of Gemini alkyl chain length on CMC and γ_{CMC} (plateau value of surface tension measurement) can be seen from Figure 4.7 and Figure 4.8 respectively. The data are organized by the length of the spacer group. Larger hydrophobes render the Gemini surfactants more hydrophobic and thus result in lower CMC values. Also seen in the figures are of course the effects of spacer group length on CMC and γ_{CMC}. The logarithm of CMC varies linearly with the carbon number *n* of the surfactant alkyl chain, just as what we have seen in Chapter 3.

$$m-2-m \text{ group:} \quad \log CMC = -0.9243 - 0.099m, \; R^2 = 0.9853 \tag{4.14}$$

$$m-4-m \text{ group:} \quad \log CMC = -0.9259 - 0.1065m, \; R^2 = 0.9229 \tag{4.15}$$

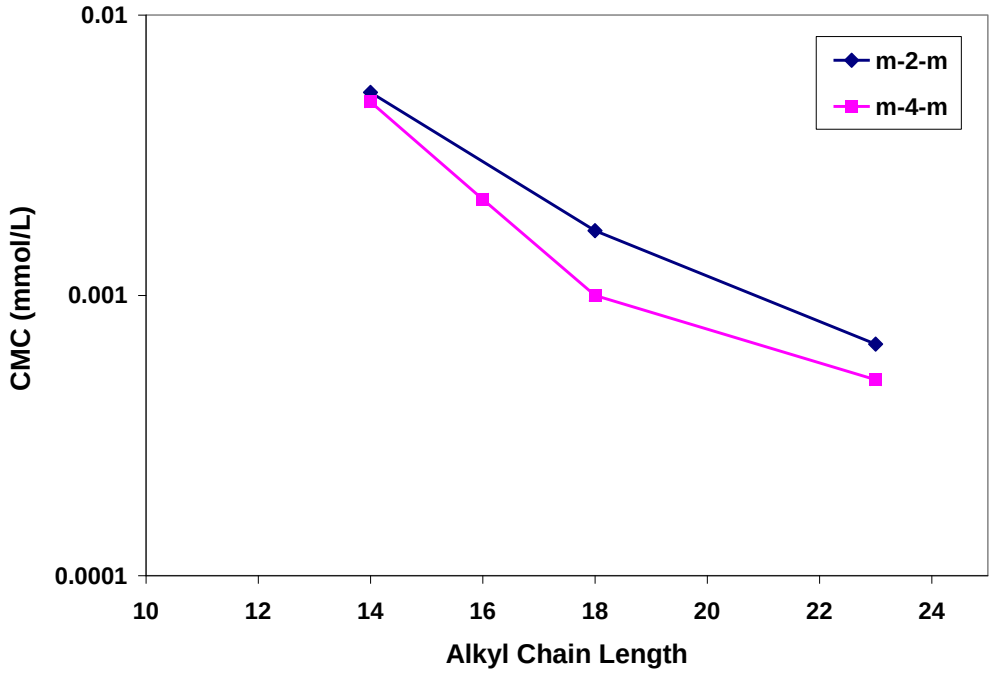

Figure 4.7: Effect of Alkyl Chain Length on CMC (25˚C).

The γ_{CMC} values also show good correlation with alkyl chain length in Figure 4.8:

$$m-2-m \text{ group: } \gamma_{CMC} = 52.863 - 1.4087m,\ R^2 = 0.9815 \quad (4.16)$$

$$m-4-m \text{ group: } \gamma_{CMC} = 53.113 - 1.5432m,\ R^2 = 0.9681 \quad (4.17)$$

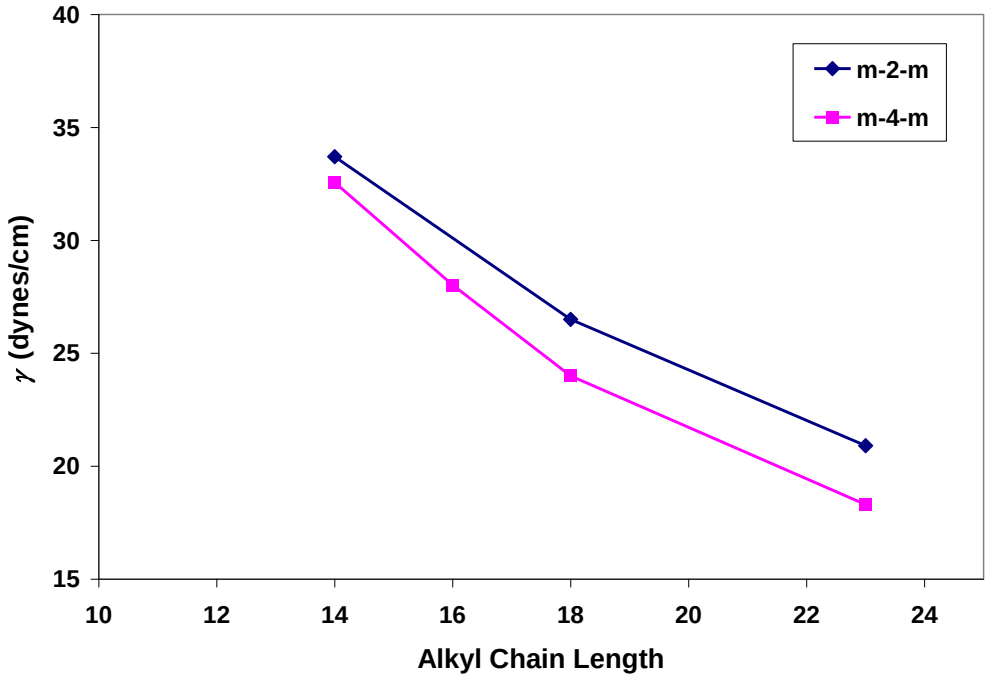

Figure 4.8: Effect of Alkyl Chain Length on γ_{CMC} Values (25˚C).

Effect of Electrolyte Concentration

The surface tension of aqueous solutions of *14-4-14* and *18-4-18* was also measured in the presence of 0.01M (0.058wt%) and 0.05M (0.287wt%) of NaCl as the electrolyte. The plots of surface tension vs. concentration for these two molecules are shown in Figure 4.9 and Figure 4.10, respectively. The corresponding CMC, γ_{CMC} and other surface properties calculated under these conditions are listed in Table 4.5 and

Table 4.6. Notice that in the presence of a large amount of electrolyte, ($\geq$0.01M NaCl), n=1 is used for calculating various surface properties.

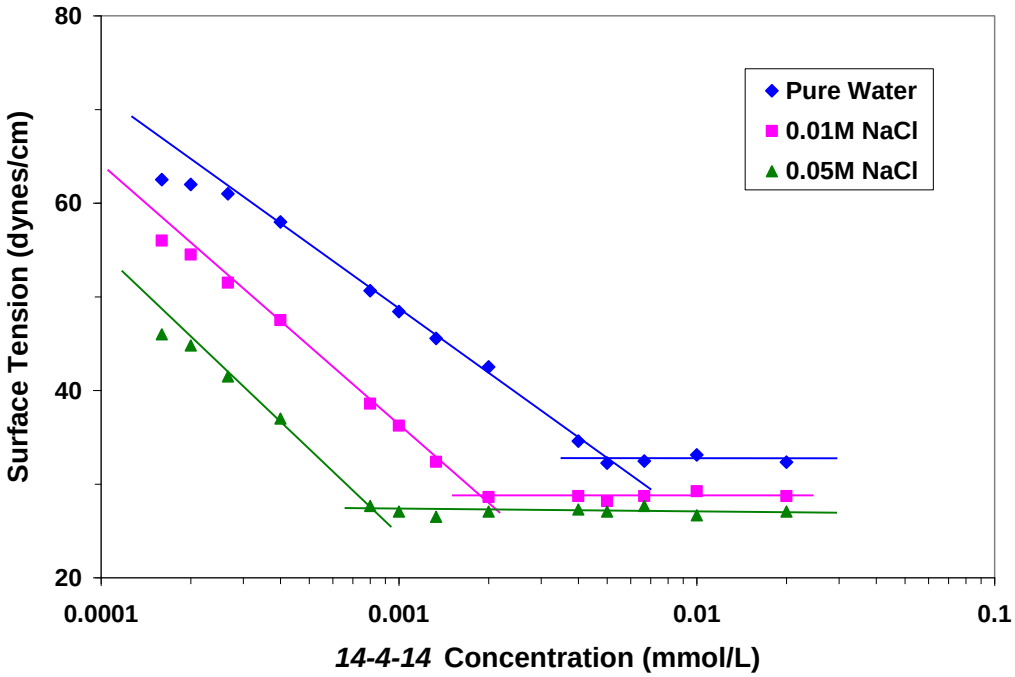

Figure 4.9: Effect of Electrolyte Concentration on Surface Tension Measurements of *14-4-14* Solution (25˚C).

Table 4.5: Surface Properties of *14-4-14* Molecule at Different Electrolyte (NaCl) Concentrations (25˚C).

NaCl Conc. (M)	**CMC (10^{-3} mM)**	γ_{CMC} **(dynes/cm)**	$\Gamma_{max} \times 10^{10}$ **(mol/cm^2)**	a_{min} **(nm^2)**	pC_{20}	**CMC /C_{20}**	ΔG^0_{ad} **(kJ/mol)**
0	4.9	32.56	1.98	0.84	6.12	6.47	-101.41
0.01	1.8	28.72	4.82	0.34	6.55	6.35	-52.28
0.05	0.82	27.07	5.17	0.32	6.89	6.37	-53.99

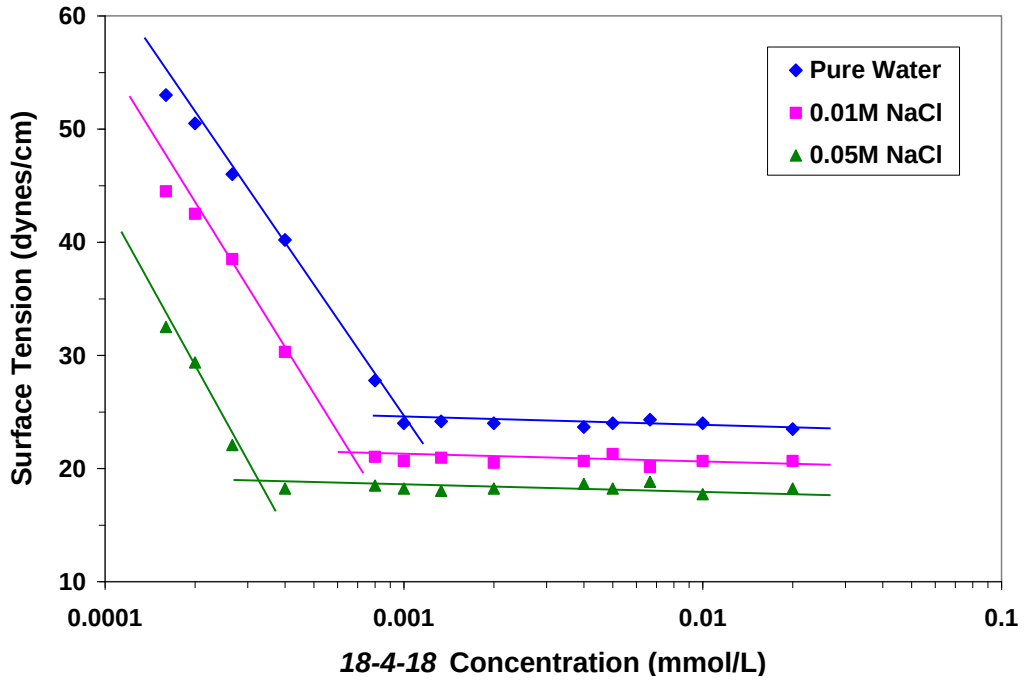

Figure 4.10: Effect of Electrolyte Concentration on Surface Tension Measurements of *18-4-18* Solution (25˚C).

Table 4.6: Surface Properties of *18-4-18* Molecule at Different Electrolyte (NaCl) Concentrations (25˚C).

NaCl Conc. (M)	**CMC (10^{-3} mM)**	γ_{CMC} **(dynes/cm)**	$\Gamma_{max} \times 10^{10}$ **(mol/cm^2)**	a_{min} **(nm^2)**	pC_{20}	**CMC /C_{20}**	ΔG^0_{ad} **(kJ/mol)**
0	1.0	24.02	3.36	0.49	6.7	4.98	-103.96
0.01	0.67	20.67	7.41	0.22	6.88	5.13	-52.79
0.05	0.34	18.23	7.92	0.21	7.19	5.21	-54.36

Because of the reduction in electrostatic repulsion between the ionic head group in the presence of NaCl, the CMC values of both surfactants are decreased dramatically as compared with those in the absence of NaCl. As a direct result, the surfactant molecules adsorbed at the surface feel less resistance to form closer packing. The pC_{20} values for each compound are larger in NaCl solution than in pure water, indicating greater tendency of Gemini surfactants to adsorb at air/water interface. The γ_{CMC} values

involve both CMC/C_{20} ratio and the a_{min} values. Gemini surfactants have apparently larger Γ_{max} values (and consequently lower a_{min} values) and larger CMC/C_{20} values in saline solution than in pure water, accounted for by the assumption that electrostatic repulsion in the adsorbed monolayer is reduced by the ionic strength effect. Notice, however, that a_{min} values for *14-4-14* with the presence of NaCl are considerably lower than the pure water case. Such extremely small a_{min} values probably indicate a surface structure more complicated than just a simple monolayer of surfactant molecules. The similar behavior was observed for some cationic Gemini surfactants (Rosen *et al.*, 1999), and the authors suggested the possibility that the longer-chain compounds form some type of multilayer structure. Even without adding NaCl, Gemini molecules with longer alkyl chains (C_{18} and C_{20+}) have much smaller a_{min} values than those of C_{14} and C_{16}.

The closer packing at the surface makes it much more difficult to insert any additional surfactant molecule into the surface region, and as a consequence, we see a drop in the magnitude of the adsorption free energy when electrolytes are present in aqueous solution (also n=1 is used in eq. (4.11) for ΔG_{ad}^{0} calculation).

Effect of Ionic Head Group

With identical tail chains and spacer group, Table 4.7 and Table 4.8 compare the surface properties of Geminis with sulfate ($-SO_4^-$) and carboxylate ($-COO^-$) head groups for two different surfactant backbones, *18-4-18* and *20^+-4-20^+*. Substituting the sulfate with carboxylate group makes the surfactant more efficient in reducing surface tension and accumulating at the air/water surface. The carboxylate molecule is less hydrophilic than its sulfate counterpart. This drives all the changes in surface properties. Figure 4.11 compares the critical micelle concentrations (CMC) determined from both conductivity and surface tension methods.

Table 4.7: Surface Properties of *18-4-18* Geminis with Different Head Groups (25˚C).

Head Group	**CMC (10^{-3} mM)**	γ_{CMC} **(dynes/cm)**	$\Gamma_{max} \times 10^{10}$ **(mol/cm^2)**	a_{min} **(nm^2)**	pC_{20}	**CMC/ C_{20}**	ΔG^0_{ad} **(kJ/mol)**
$-SO_4^-$	1.0	24.02	3.36	0.49	6.7	4.98	-103.96
$-COO^-$	0.93	23.27	3.45	0.48	6.73	5.00	-104.19

Table 4.8: Surface Properties of 20^+-*4*-20^+ Geminis with Different Head Groups (25˚C).

Head Group	**CMC (10^{-3} mM)**	γ_{CMC} **(dynes/cm)**	$\Gamma_{max} \times 10^{10}$ **(mol/cm^2)**	a_{min} **(nm^2)**	pC_{20}	**CMC/ C_{20}**	ΔG^0_{ad} **(kJ/mol)**
$-SO_4^-$	0.5	18.30	4.05	0.41	7.00	5.01	-106.47
$-COO^-$	0.35	17.03	4.22	0.39	7.15	4.97	-108.04

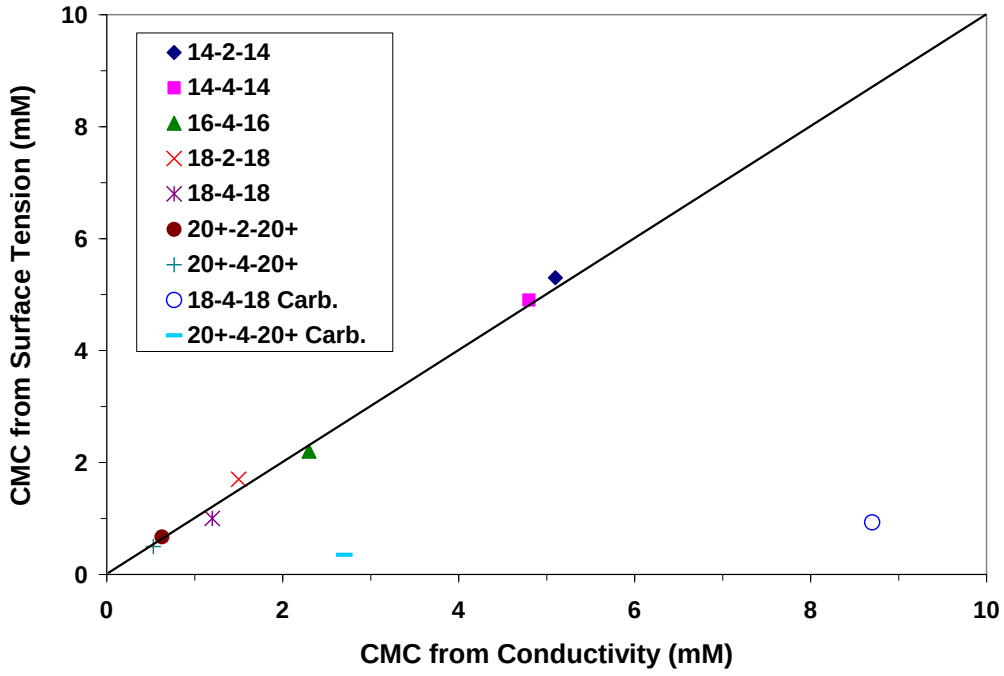

Figure 4.11: Comparison of CMC Obtained from Two Different Methods.

Apparently, for sulfate Gemini molecules, the data points (representing CMC values from both measurements) line up very nicely and follow the unit slope line. Notice, however, for carboxylate surfactants, the two entries (*18-4-18* Carb. and 20^{+}*-4-*20^{+} Carb.) deviate appreciably from the unit slope line. CMC values by the conductivity method are considerably larger than those obtained by the surface tension method.

A similar discrepancy was reported in a previous study (Rapaport, 1984) on conventional anionic surfactants containing *N*-dialkylamide and carboxylate groups. It was also observed that the order of the ratio of conductivity / surface tension CMC in those molecules was the same as that for their CMC/C_{20} ratio, which measures the tendency to adsorb at the air/water interface relative to the tendency to form micelles, and for their $a_{\min}$ values. This observation implied that some steric factor that inhibits micellization relative to adsorption was present in these compounds and was delaying the onset of the break in their conductivity plots. This order of increasing ratio of conductivity / surface tension CMC was also the order of increasing pH just above the CMC, indicating an increase of the hydroxyl ion concentration and release of Na^{+} during micellization. This pH behavior suggested that the reason for the difference in CMC measured by surface tension and by conductivity for these conventional anionic surfactants containing carboxylate groups may be that these anionics accept a proton and release Na^{+} during micellization. The steric factor inhibiting micellization may be H-bonded ring formation between the protonated carboxylate and the amide group, since such ring formation would increase the volume of the hydrophilic group. Murata *et al.* (1982) has described similar behavior for aqueous solutions of sodium deoxycholate showing increasing pH in the vicinity of CMC, the result of hydrogen bonding between the protonated carboxylate group and the hydroxyl group at the 3-position (as shown in Figure 4.12).

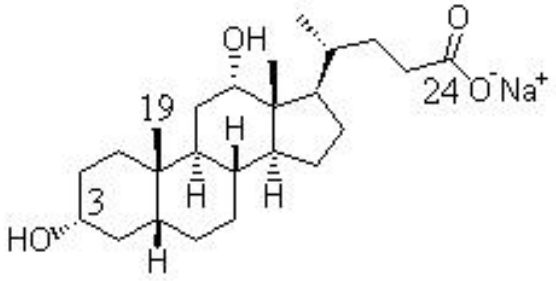

Figure 4.12: Molecular Structure of Sodium Deoxycholate (Numerals indicate the number assigned to respective carbons) (Murata et al., 1982).

CMC values obtained from conductivity and surface tension methods are listed in Table 4.9 below, together with the CMC ratios and a_{min} values. Apparently, the CMC ratio (conductivity / surface tension) for C_{18} molecule is greater than that of C_{20+} molecule, so as its corresponding a_{min}.

Table 4.9: Comparison between *18-4-18* and 20^{+}-*4*-20^{+} Carboxylate Geminis.

Surfactant	**CMC1 by Conductivity (10^{-3} mM)**	**CMC2 by Surface Tension (10^{-3} mM)**	**CMC1/ CMC2**	**CMC/ C_{20}**	a_{min} **(nm^2)**
18-4-18 –$(COO^{-})_2$	8.7	0.93	9.35	5.00	0.48
20^{+}-*4*-20^{+} –$(COO^{-})_2$	2.7	0.35	7.71	4.97	0.39

For the present case (see Figure 4.13), where there is at least one oxygen (excluding -O- bonds in the spacer group) in the vicinity of the carboxylate group in the same molecule, it is possible that proton uptake by the carboxylate group can occur. The resulting increase in hydroxyl ion concentration will result in an increase in its conductivity with increase in surfactant concentration. This effect may cause the delay of the break in the conductivity vs. molar concentration plot.

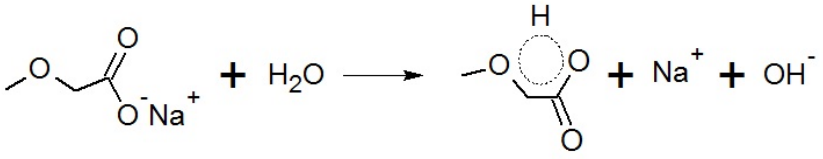

Figure 4.13: Hydrogen Bonding between the Protonated Carboxylate Group and Neighboring Ether Oxygen.

4.6 STATIC ADSORPTION TESTS

The adsorption of Geminis at air-water \interface was investigated in the first part of this chapter. In this section, we look into their behavior at the solid-water interface.

4.6.1 Equilibrium Adsorption Conditions

Adsorption results obtained for *16-4-16* molecule on Berea core material (sieved through 60 mesh screen) at different liquid/solid ratios (LSR) are shown in Figure 4.14.

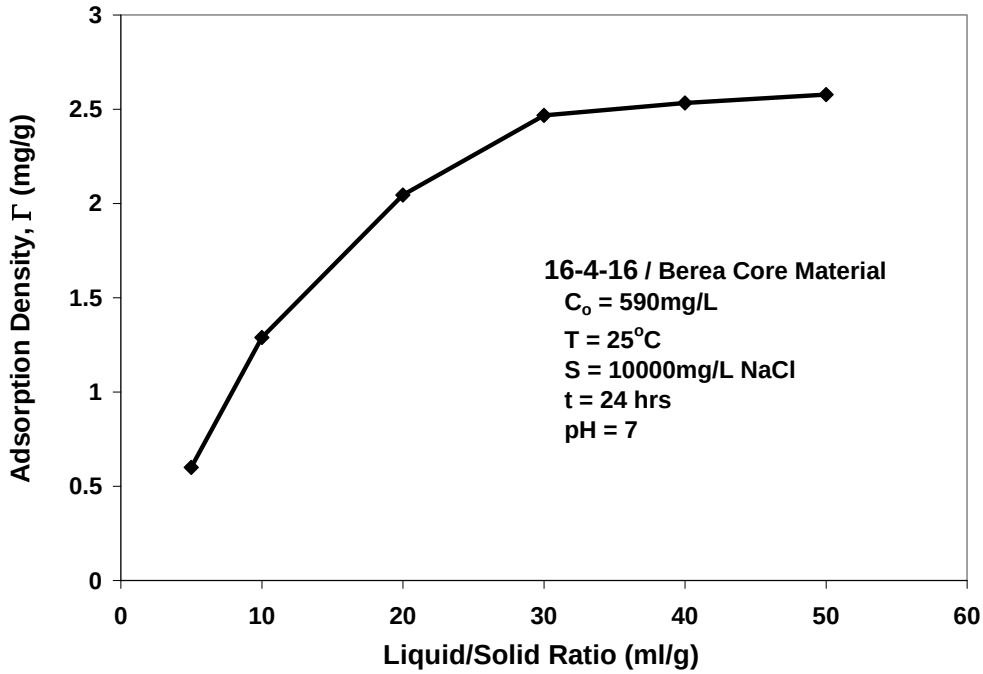

Figure 4.14: *16-4-16* Adsorption Density vs. Liquid/Solid Ratio.

All surfactant solutions were prepared in 10,000mg/L NaCl brine, with a constant concentration of 590mg/L. To ensure equilibration, the liquid-solid mixtures were agitated for 24 hours at 25°C. As shown in Figure 4.14, the amount of surfactant adsorbed starts to stabilize (or saturate) at LSR of 30, with a value of 2.467mg/g. The adsorption curve flattens out beyond this value. Ideally, for a well-defined system under equilibrium conditions there should be no effect of liquid/solid ratio (LSR) on adsorption results. Therefore a LSR value of 40 was selected in all the tests.

To ensure a true equilibrium adsorption, the progression of *16-4-16* adsorption level with time was recorded to identify a suitable duration for equilibration. The results are shown in Figure 4.15. The experimental conditions are also inserted into the figure.

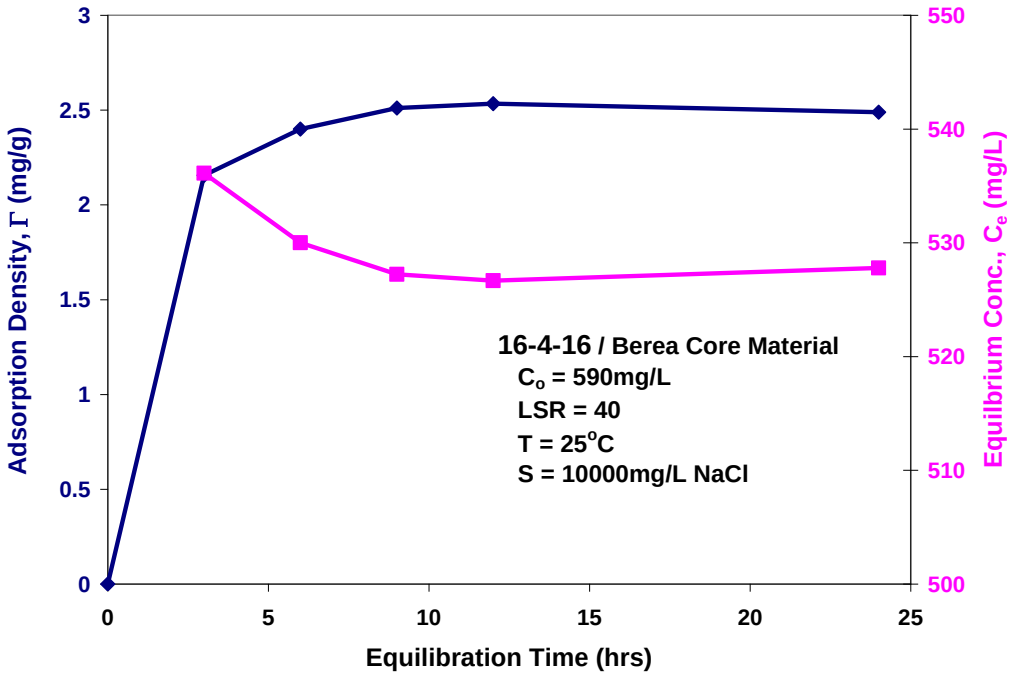

Figure 4.15: *16-4-16* Adsorption Density and Equilibrium Concentration vs. Time.

As can be seen in the figure, with 12 hours of agitation, the adsorption level reaches 2.533mg/g and does not change significantly with time afterwards. Therefore, an equilibrium adsorption time of 12 hours was chosen for all the adsorption tests in current study. Also shown in the plot is the equilibrium surfactant concentration measured from the supernatant liquid by TOC. After 12 hours of equilibration, *C* also reaches minimum that corresponds to the maximum adsorption density.

One thing worth noting in Figure 4.14 is the strong dependence of the adsorption results on liquid solid ratio used in the experiments. In all tests done in this section, a large LSR value of 40 was used to ensure true maximum adsorption, which is not affected by the choice of LSR or equilibration time (see Figure 4.15). A direct result to large LSR is the much larger (5 to 10 times) adsorption level observed in all our experiments, compared to what would typically be reported in petroleum literatures (Zhang, 2012). It is therefore very important in such comparisons that the results are obtained using similar experimental setup and under comparable conditions.

4.6.2 Adsorption Behavior of *16-4-16*

Adsorption Isotherm

With equilibrium experimental conditions identified, we measured the adsorption isotherm for *16-4-16* Gemini surfactant by progressively changing the initial surfactant concentration in the static test, and calculating the amount of surfactant adsorbed.

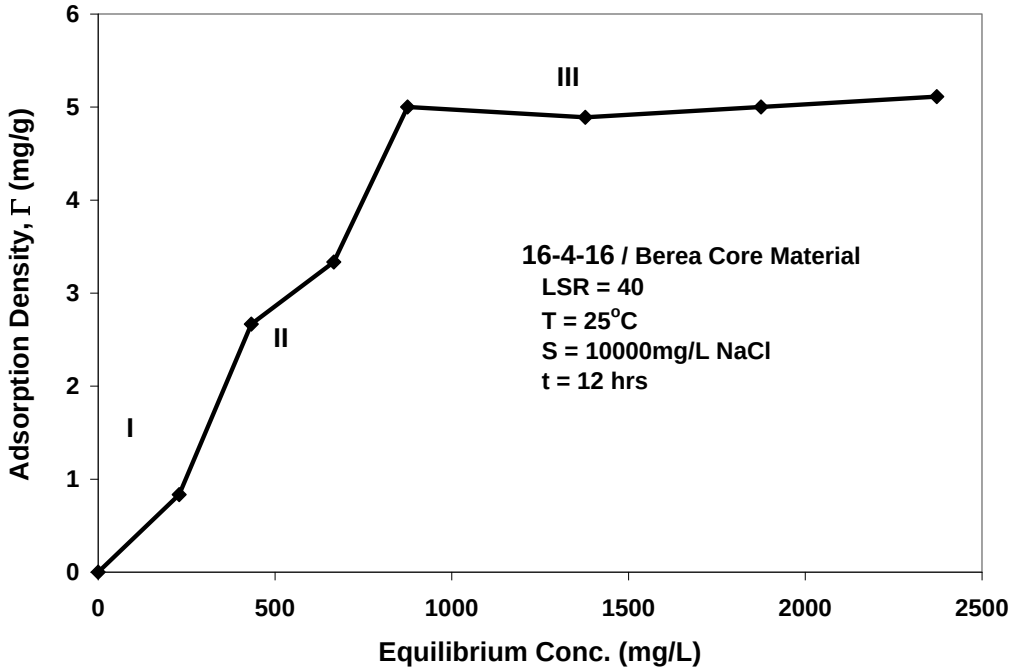

Figure 4.16: Adsorption Isotherm for *16-4-16* Surfactant.

The surfactant solutions were all prepared in the presence of 10,000mg/L NaCl. The liquid-solid mixtures at 40 LSR were agitated for 12 hours before TOC analysis. The isotherm is shown in Figure 4.16. Most adsorption studies have employed a similar method with the results being presented as isotherms which are plots of the amount of surfactant adsorbed per gram of solid versus the equilibrium surfactant concentration at a constant temperature. These plots can be used to obtain information over a wide range of surfactant concentrations, and they generally have four regions with noticeable slope changes as surfactant concentration increases (Paria and Khilar, 2004).

As shown in Figure 4.16, the adsorption process of *16-4-16* can be roughly divided into three regions. At low surfactant concentrations, designated as region I, the surfactant monomers get adsorbed as individual ions with no interactions between the adsorbed molecules (Bohmer *et al.*, 1992). The adsorption is due to electrostatic

interaction between the head groups and charged sites on the solid surface. This attraction obeys Henry's law that adsorption increases linearly with concentration (Paria and Khilar, 2004). The much faster increase of adsorption in region II was due to the association of the adsorbed surfactants at the solid-water interface (Wesson et al., 2000). These associations were attributed to lateral hydrophobic interactions between surfactant tails. This lateral attraction generates an additional driving force, and with the still existing electrostatic attraction, makes the adsorption isotherm curve in this stage exhibit a sharp increase. Adsorption of surfactant is proposed to occur with a reduced slope after region II, often referred to as region III (Paria and Khilar, 2004). Region III can be attributed to the surfactant ions having filled all of the surface sites by the end of region II with further adsorption being due to association between first and second layer hydrocarbon chain. Scamehorn *et al.* (1982) proposed that bilayer formation began in region II and continued into region III. This type of behavior is, however, not observed in Figure 4.16. The exact shape of the isotherm will depend on many different factors that could be unique in each adsorption test. Finally, a plateau of the adsorption isotherm, shown as region III, is characterized by little or no increase in adsorption with increasing surfactant concentration. In this region micelles start to form in bulk solution and act as a chemical potential sink for any additional surfactant added into the system.

The adsorption isotherm is re-plotted in Figure 4.17 by employing the dimensionless quantity θ (surface coverage) defined previously. A best fit of the Langmuir adsorption equation to the experimental data is also shown in the figure, with a R^2 value of 0.8354. Comparing the two curves, the Langmuir model is capable of capturing the general trend of the adsorption behavior of *16-4-16* onto Berea sands.

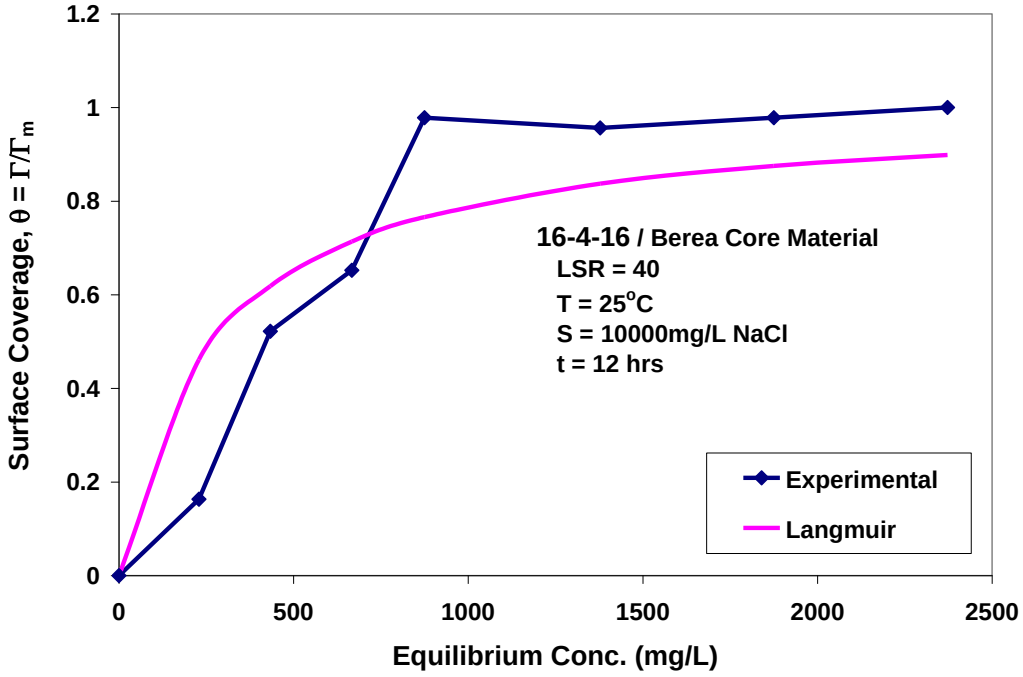

Figure 4.17: Adsorption Isotherms for *16-4-16* Surfactant from Experiments and the Langmuir Model.

Comparison with Conventional Surfactants

With all experimental conditions kept the same (10,000mg/L NaCl, LSR of 40, 12 hrs equilibration at 25°C), we compare the adsorption behavior of *16-4-16* Gemini with its single-chain counterpart SHS (sodium hexadecyl sulfate), as well as a commercial surfactant Petrostep S13-C (TDA-9PO-Sulfate). It can be seen from Figure 4.18 that maximum adsorption densities of the three surfactants follow the trend of *16-4-16* < SHS < S13-C. Possible explanations to the low adsorption of *16-4-16* include the hydrophilicity and the dual-head-group structure of Gemini surfactants.

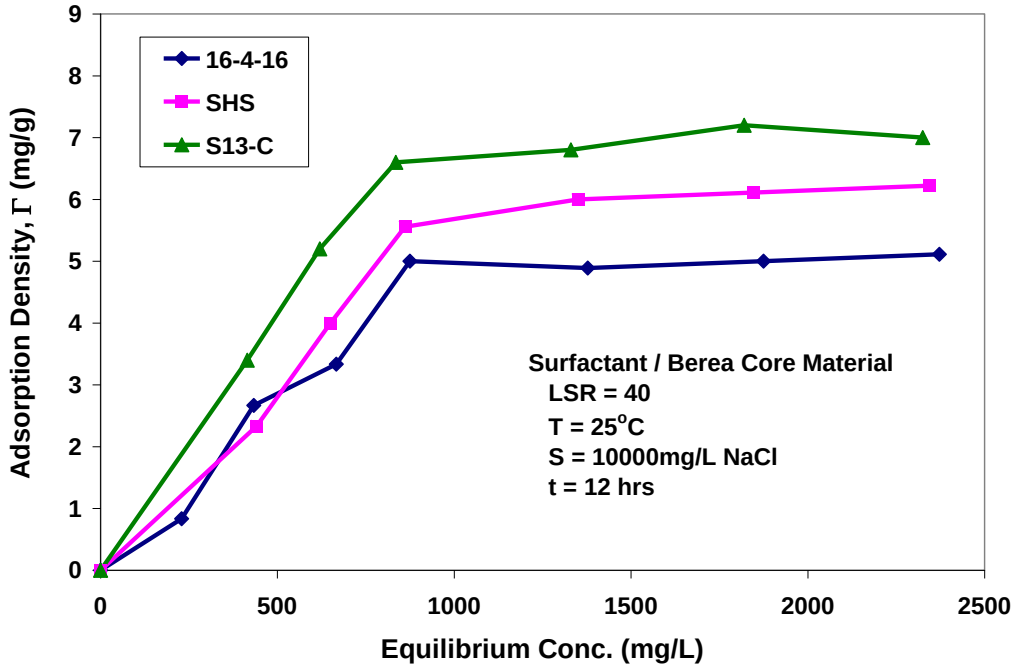

Figure 4.18: Adsorption Isotherm Comparison among *16-4-16*, STS and S13-C at 25°C.

First of all, Gemini surfactants are much more hydrophilic than their conventional counterparts. Therefore they will have higher tendency to go into the bulk aqueous phase than conventional surfactants, which makes it harder for Geminis to get adsorbed at the solid surface. Secondly, the two sulfate head groups in one molecule makes a Gemini effectively a bi-functional ion. Therefore, one Gemini molecule can potentially interact with more than two adsorption sites on the solid surface, and thus saturate the adsorption sites more efficiently. Oida et al. (2003) proposed that the bulkier structure of a Gemini surfactant, especially towards the head group end, could give rise to difficulty packing the surfactant molecules at the interface, which in effect reduces adsorption tendency. However, based on our results from surface tension experiments, Gemini surfactants are actually capable of packing together more tightly than conventional surfactants, at least at

the air-water interface. Considering, however, the difference between the adsorption conditions at solid-water and air-water interfaces, Oida's proposal could be true here.

By the same argument, S13-C, being the most hydrophobic molecule among the three, has a higher tendency to get adsorbed at the solid-water interface, resulting in the highest adsorption density. Moreover, SHS and S13-C are both monovalent surfactants. Assuming similar adsorption sites were provided in their respective test, the amount of surfactants adsorbed might be comparable at least on a molar basis. With S13-C being a higher MW molecule, it is not surprising to see a higher adsorption of S13-C by weight. Notice that the adsorption level of the commercial surfactant S13-C in Figure 4.18 is much higher the typical reported values for similar commercial surfactants. This is again due to the fact most static adsorption tests were conducted at a much lower liquid solid ratio where a truly saturated condition was not established on the solid surface.

Effect of Salinity

It was clearly shown in previous sections that the formation of surface aggregates has an important impact on the adsorption density of surfactants on the solid-water interface. Therefore, any factor that might affect the aggregation behavior is likely to cause changes in the adsorption behavior. Solution salinity is one such parameter. Three surfactant solutions of different salinities were prepared and mixed with the adsorbents. All other experimental conditions were kept the same. Figure 4.19 below shows a comparison between the three cases.

The adsorption density increases with solution salinity. This trend agrees with our intuition and can be explained at least three ways: i) the existence of a larger amount of sodium ions at higher salinities will significantly suppress the electrostatic interaction (repulsion) between the surfactant head group and the double layer on the solid surface;

ii) the addition of salt can promote the growth of various surface aggregates, into which more surfactant molecules will be incorporated; iii) higher salinity will also reduce the solubility (Somasundaran *et al*., 1998) of the surfactants in the aqueous phase and thus push them towards the solid-water interface.

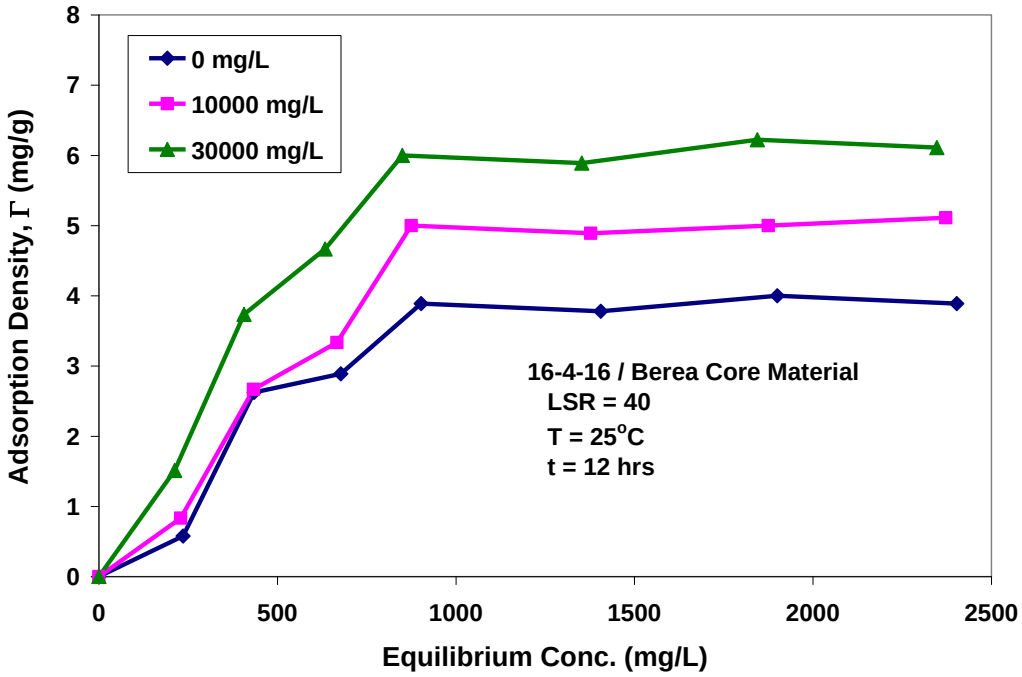

Figure 4.19: Effect of Salinity on the Adsorption of *16-4-16* Gemini.

Effect of Absorbents

Besides the Berea core material, we also used material collected from a field core plug (Brookshire Dome field). The same 60 mesh screen was used in the particle selection. To ensure the cleanness of the adsorbents, all the core plugs were first visually inspected and a clean one was chosen for disaggregation. The disaggregated particles were then washed with hexane and acetone before being oven dried overnight.

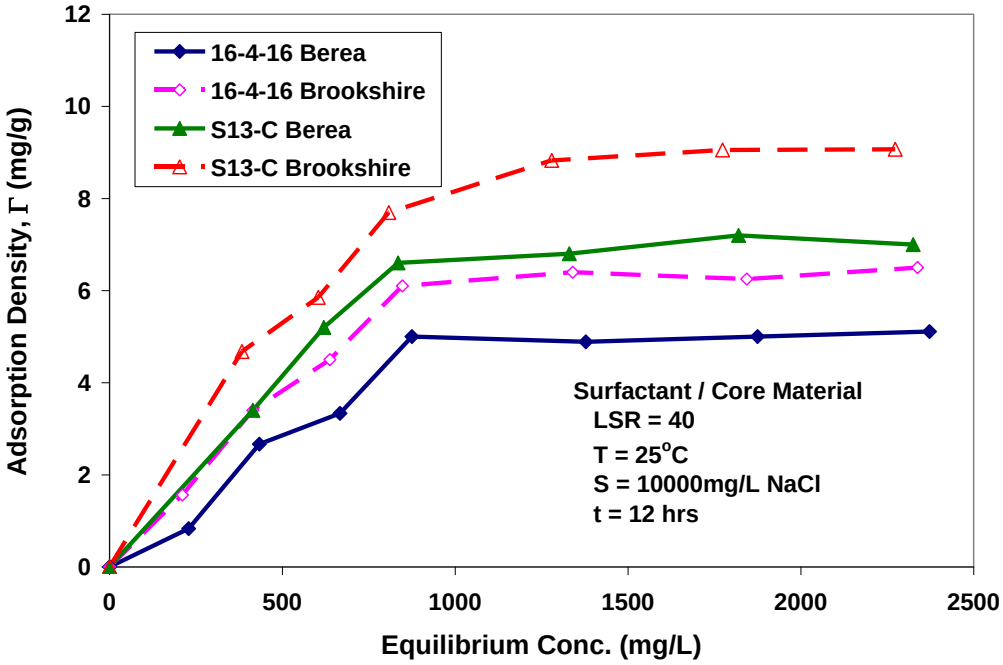

Figure 4.20: Effect of Core Material on the Adsorption of *16-4-16* Gemini.

The adsorption isotherms of *16-4-16* on Berea and Brookshire core materials are compared in Figure 4.20. The experimental conditions are also listed in the figure. The surfactants showed higher adsorption onto the field core material. Similar trend was also observed for the commercial surfactant Petrostep S13-C. The difference in adsorption density can probably be attributed to the difference in adsorbent size and thus total solid surface area. Although both cores were disaggregated in the same manner and filtered through the same 60 mesh screens, the difference in permeability (more details in Chapter 8) between the two core materials dictates their particle size distributions. For the lower permeability Brookshire material, there will be more particles of smaller sizes left after screening and these particles can create much larger surface area that contributes to higher adsorption values. We would, therefore, expect higher adsorption densities for other surfactants onto Brookshire core as well, based purely on a surface area argument.

4.6.3 Impact of Molecular Structure on Gemini Adsorption

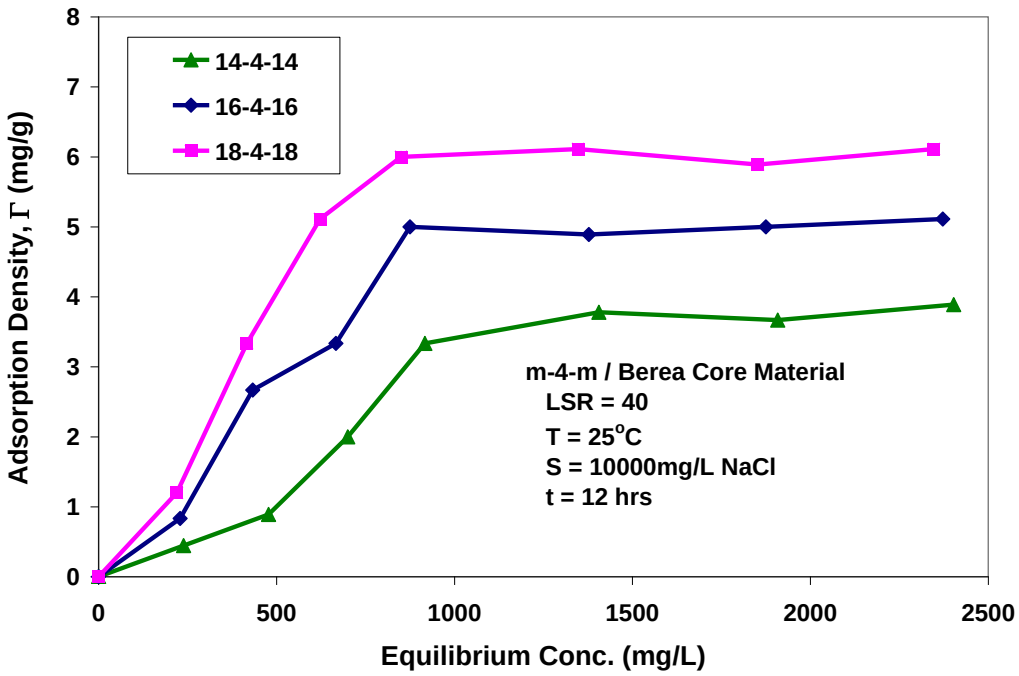

Figure 4.21: Effect of Alkyl Chain Length on the Adsorption of Geminis *m-4-m*.

An increase in the length of the non-polar part of a surfactant generally causes an increase in adsorption owing to increased lateral interactions between hydrocarbon chains. Results in Figure 4.21 for three Gemini surfactants of different tail lengths clearly indicate an increase in adsorption with an increase in chain length. Similar behavior (Esumi *et al.*, 1996; Li *et al.*, 2000; Rosen *et al.*, 2001) has been observed for many other surfactants (conventional and cationic Gemini) systems for the same reason. Longer hydrocarbon tails will also reduce the solubility of the Gemini molecule in bulk aqueous phase and thus tend to increase adsorption onto the solid-water interface. Also if a Langmuir monolayer adsorption was assumed to take place at the solid surface, the larger (or heavier) molecule will naturally show more adsorption on a mass basis (but similar adsorption level on a molar basis).

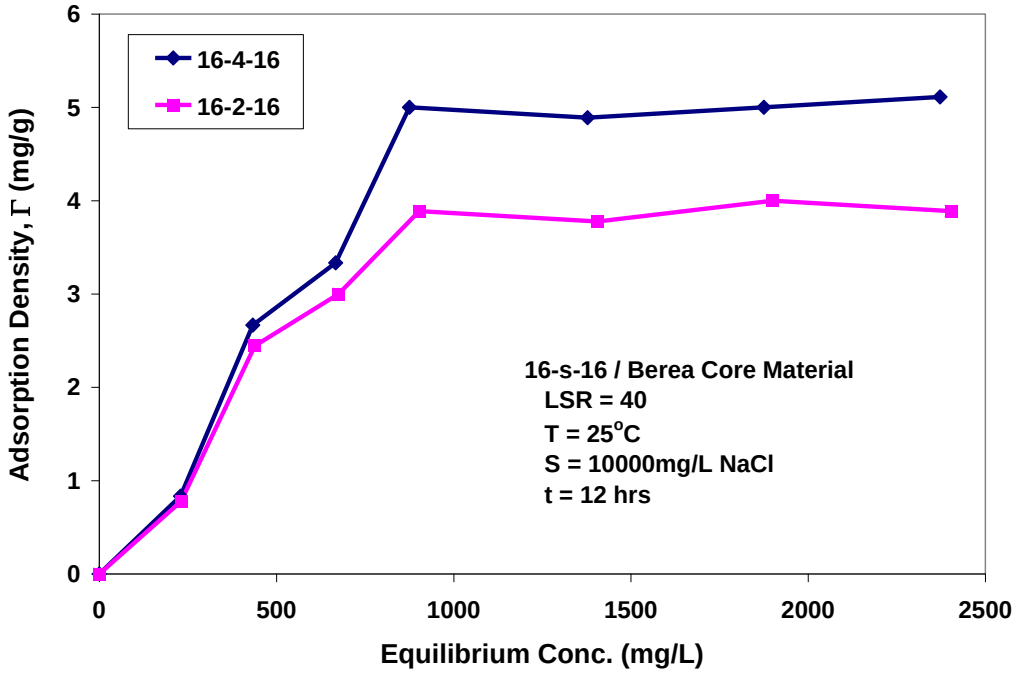

Figure 4.22: Effect of Spacer Length on the Adsorption of Geminis *16-s-16*.

Figure 4.22 shows the effect of spacer group length on the adsorption behavior of Gemini surfactants. As can be seen here, the molecule with a shorter spacer has a smaller plateau adsorption density for basically the same reason mentioned above, namely, stronger intermolecular interactions and reduced solubility. Again the difference in molecular weight can also be a contributor.

4.7 SUMMARY

A systematic study of the adsorption behavior of the current series of Gemini surfactants onto air-water and solid-water interfaces was conducted in this chapter. Overall, Gemini surfactants provide a new set of issues that control adsorbed layer density. In additional, they can also help modify the hydrophilicity or hydrophobicity of solid surfaces and their further adsorption capabilities.

1. The surface tension method was employed in this chapter to determine the critical micelle concentration (CMC) and other important surface properties of aqueous solutions for various Gemini surfactants. Results suggest that Gemini surfactants have CMC values two to three orders of magnitude lower than their single chain counterparts. They also exhibit better efficiency in reducing surface tension (γ_{CMC}, pC_{20}, and CMC/C_{20} values) and higher tendency to spontaneously adsorb at the air/water interface (Γ_{max}, a_{min}, and ΔG_{ad}^{0}). Longer alkyl chains help adjust the HLB balance, rendering a more hydrophobic surfactant and thus inducing a stronger hydrophobic interactions between neighboring molecules. Therefore, further improvements on adsorption properties were observed. A sudden increase in Γ_{max} and drop in a_{min} for C_{18} and C_{23+} Geminis are indications of the formation of possibly a multilayer structure at the surface, instead of the simple monolayer.
2. The addition of inorganic electrolytes, such as NaCl, increases the counter-ion concentration in the vicinity of ionic head groups. The attractive interactions between molecules at the surface are thus enhanced due to electrostatic screening of the ionic repulsion, resulting in closer molecular packing, lower γ_{CMC}, higher pC_{20} and surface excess density Γ_{max}. The correspondingly smaller a_{min} makes it harder to insert additional Gemini molecules into the surface layer and, therefore, reduces the absolute value of ΔG_{ad}^{0}. The more negative values of ΔG_{ad}^{0} than ΔG_{M}^{o} suggest that the adsorption is promoted more than the micellization for the current series of anionic Geminis.
3. The introduction of carboxylate head groups into the Gemini structure brings about more hydrophobicity of the molecule and thus better surface performance in terms of lowering surface tension and obtaining closer packing. One interesting observation regarding carboxylate Gemini is that CMC values determined from

conductivity and surface tension methods show substantial differences. The explanation lies in a chain of events taking place during the micellization of carboxylate Geminis in aqueous solution, namely protonation of the carboxylate group; hydrogen bond formation between the protonated carboxylate and nearby ether oxygen; hydroxyl ion concentration increase due to protonation of carboxylate and strong Na^+ release accompanying the process; proportional increase of conductivity to surfactant concentration resulting in a delay of the break in conductivity vs. concentration plot.

4. A series of static adsorption tests were conducted to study the adsorption behavior of Gemini surfactants onto solid-water interface. By utilizing disaggregated and screened Berea core material as adsorbents, adsorption plateau can be reached at a liquid-solid ratio of 40 (ml/g) and equilibration time of 12 hours. The Langmuir adsorption model is capable of capturing the general trend of the adsorption behavior of Gemini surfactant onto the adsorbents.
5. Gemini surfactants show a lower plateau adsorption density than conventional surfactants. Lower adsorption can be achieved by decreasing the solution salinity, based on the considerations of prohibiting surface aggregate growth and promoting electrostatic repulsion.
6. The surfactants showed higher adsorption density on a reservoir core material, due to possibly smaller adsorbent size from the low-perm rock. Longer alkyl chain and spacer group promote surfactant adsorption due to reduced solubility and stronger interactions with the solid surface.

Chapter 5: Reduction of Oil-Water Interfacial Tension by Anionic Gemini Surfactants

5.1 INTRODUCTION

The reduction of the tension at an interface by a surfactant in aqueous solution when a second liquid phase is present may be considerably more complex than when that second phase is absent, i.e., air-water interface discussed in Chapter 4. When the second liquid phase is a saturated hydrocarbon, the surfactant molecules will orient themselves at the interface, mainly with the hydrophilic group toward the water and hydrophobic group toward the hydrocarbon (Figure 5.1).

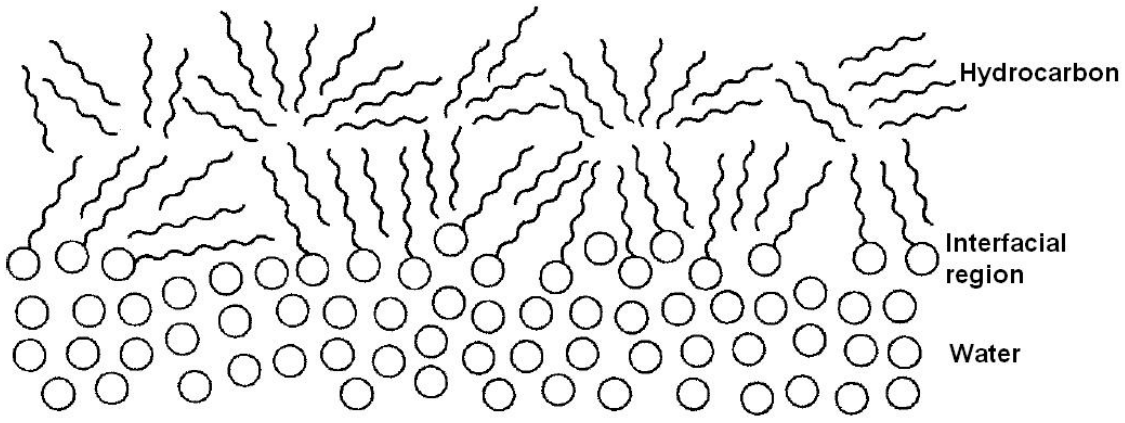

Figure 5.1 Schematic of Hydrocarbon-Water Interface with Adsorbed Surfactants.

When the surfactant molecules replace water and/or hydrocarbon molecules at the original interface, the interaction across the interface is now between the hydrophilic part of the surfactant and water molecules on one side, and between hydrophobic part of the surfactant and hydrocarbon on the other side of the interface. Since these interactions are now much stronger than the original interactions between the highly dissimilar

hydrocarbon and water molecules, the tension across the interface is significantly reduced by the presence of the surfactant.

We can see from this simple model why it is necessary for the surfactant molecule to have both hydrophilic and lipophilic portions. For significant surface activity, a proper balance between hydrophilic and lipophilic character in the surfactant is essential. Since the hydrophilic (or lipophilic) character of a particular structure group in the molecule varies with the chemical nature of the solvent and such conditions of the system as electrolyte concentration and temperature, the hydrophilic-lipophilic balance (HLB) of a particular surfactant varies with the system and the conditions of use.

The Winsor *R* ratio (Winsor, 1948 & 1968) is a more fundamental way of relating the aforementioned variables to interfacial tensions and for explaining them in terms of molecular interactions (Bourrel *et al.*, 1983). It is based on the dispersing tendencies of surfactant molecules (*C*) into oil (*O*) and water (*W*) phases at the interface (Bourrel *et al.*, 1988),

$$R = \frac{A_{CO} - A_{OO} - A_{ll}}{A_{CW} - A_{WW} - A_{hh}} \tag{5.1}$$

A_{CO} and A_{CW} are the cohesive energies (per unit interfacial area) of the surfactant with oil and water, promoting dispersion of surfactant into the respective phases; A_{OO} and A_{WW} are the cohesive energies of the solvent molecules in oil and water, opposing surfactant dispersion into them; A_{ll} and A_{hh} are the cohesive energies between the lipophilic and hydrophilic portions, also opposing dispersion. *R* ratio is, therefore, a semi-quantitative method of measuring the balance between the hydrophilic and lipophilic characters of the surfactant.

The formation of distinct and thermodynamically stable microemulsion phases in a surfactant-oil-brine mixture was first described by Winsor (1954). Using the R ratio, Winsor further characterized these microemulsions as being of three different types: i) $R<1$, the relative miscibility of surfactant C with water has increased, and thus the swollen micelles become convex toward water and an oil-in-water, or Type I microemulsion forms; ii) $R>1$, the aggregates become convex toward oil and a water-in-oil or Type II microemulsion forms; iii) $R \simeq 1$, no tendency for the interfacial layer to be preferentially convex toward either oil or water exists, and the optimum form is often assumed to be lamellar (Huh, 1979) or bicontinuous (Scriven, 1976; Evans *et al.*, 1994).

The interfacial tension (IFT) of interest for a Type I microemulsion is between the microemulsion and oil phases. The IFT value decreases as salinity is increased until the interface disappears at the Type III/Type II salinity boundary. Similarly, the IFT for a Type II microemulsion decreases as the salinity is decreased into the Type III region. Both the aqueous/microemulsion and microemulsion/oil interfaces exist in a Type III environment. The interfacial tensions of these two interfaces are equal at the optimal salinity. Determining this IFT value at optimal salinity is very important in surfactant selection. Huh (1979) derived a theoretical relationship between solubilization ratio and IFT at optimal salinity. A simplified form of his theory predicts that the IFT (γ) is inversely proportional to the square of the solubilization ratio (σ):

$$\gamma = \frac{C}{\sigma^2} \tag{5.2}$$

Here C is approximately 0.3dyne/cm and the σ is defined as the volume of oil or water solubilized divided by the volume of surfactant on a 100% active basis. Since, σ can be

more conveniently measured over time than interfacial tension and, therefore, used routinely as a surrogate for measuring IFT in the lab.

Although low liquid-liquid interfacial tension is important in promoting emulsification and in the removal of oily soil by detergents, advances in our knowledge of the factors governing the reduction at that interface stem from the intense interest in enhanced oil recovery by use of surfactant solutions. The 'surfactant flooding' process aims at producing the residual oil remained after secondary recovery with water flooding. For displacement of oil in the pores and capillaries of petroleum reservoir rock, it would appear that it is necessary to reduce interfacial tension between the oil and the slug of surfactant-bearing water to ultra-low ($<10^{-3}$dyne/cm) values (Stegemeier, 1977; Pope *et al.*, 2000). Such ultra-low interfacial tension (ULIFT), which can be achieved with suitable surfactants by adsorbing at the oil-water interface under pre-designed conditions, has made it possible to conduct displacements in the field at capillary number several orders of magnitude larger than those existing during water flooding.

Traditionally, the surfactants used for EOR applications were mixtures of petroleum sulfonates derived from crude oil (Hirasaki *et al.*, 2011). Later generations of commercial products (Barnes *et al.*, 2008; Zhao *et al.*, 2008; Flaaten *et al.*, 2008; Levitt *et al.*, 2006 & 2009) were typically poly-disperse in the propylene oxide (PO) and/or ethylene oxide (EO) groups, and mixtures of them are potential flooding chemicals. The latest studies on large hydrophobe surfactants (Adkins *et al.*, 2010 & 2012) are important advancement in EOR surfactant research, thanks to the great potential of applying these surfactants in more difficult reservoirs (Liyanage *et al.*, 2012; Lu *et al.*, 2012a & b). It has long been proposed (Gale *et al.*, 1973) that there exists a correlation between displacement efficiency and the equivalent weight (EW) of a sulfonate. A newly developed correlation (Salairaj *et al.*, 2012a) also shows that larger hydrophobes are

needed as either the temperature or EACN number of the oil increases. Chemical formulations are typically mixtures that differ in either alkyl chain length or number of embedded functional groups, and are usually treated as one pseudo-component. While high molecular weight (MW) surfactants cause the greatest reduction in IFT, the lower MW components serve as a sacrificial adsorbent or solubilizer for the high MW ones. During displacement in the reservoir, there is a possibility of selective adsorption or chromatographic separation (Miller *et al.*, 1991; Austad *et al.*, 1992; Fjelde *et al.*, 1995), which could alter both physical properties and effectiveness of the surfactant mixture. With stringent and careful screening criteria set in place, this can be successfully suppressed or even eliminated in laboratory design process (Salairaj *et al.*, 2012b). In the field, however, this undesired separation is still a legitimate concern for EOR operations. Hence, for the surfactant formulation design, there are two main concerns need to be carefully addressed: one is that the interfacial tension is not reduced sufficiently to mobilize the trapped oil; the other is that the surfactant slug does not maintain its integrity during displacement through the reservoir.

Gemini surfactants have great potential of being applied in surfactant flooding and help address the aforementioned issues, thanks to their unique properties of ultra-low critical micelle concentration and high efficiency in reducing the surface tension compared with conventional single-chain surfactants. Although a large amount of studies on surface tension of Gemini surfactant solutions have been reported (mostly for CMC determination of cationic Geminis), research on the liquid-liquid interfacial tension of Gemini surfactants is exceptionally rare. In this chapter, the interfacial behavior of Gemini surfactant / pure hydrocarbon / electrolyte system is experimentally studied.

5.2 MATERIALS AND METHODS

Gemini surfactants investigated in this study were again synthesized according to procedures previously described in Chapter 2. The purification of the Gemini surfactant is essential, particularly in the study of its interfacial properties, as the surface/interfacial tension is very sensitive to impurities. The samples used in the current study were purified by recrystallization of the crude products. And the product purity was verified in Chapter 4 with the existence of the surface tension plateaus. Some commercial surfactants used in the experiments, e.g. $C_{15\text{-}18}$ BABS (branched alkylbenzene sulfonate) and $C_{16\text{-}18}$ BABS, were samples obtained from Stepan Company and used as received.

Gemini surfactant solutions are prepared by weighing the surfactant in distilled water and stirring using a magnetic stirrer at the desired experimental temperature. The oil phase used in the current study is a pure hydrocarbon obtained from Sigma-Aldrich. The interfacial tension between oil and Gemini surfactant solutions are measured by the spinning drop tensiometer, Model 500. It has a wide range of measurements, 10^{-5} ~ 50dynes/cm, and is, therefore, a reasonable extension of the ring methods for measurements of low interfacial tension. The working principle of the spinning drop method is included in Appendix E. An outstanding advantage of the method is that an interface can be studied which is not in direct contact with any solid surface. The difficulties in using this method, on the other hand, include: i) the formation of artifacts, e.g. 'dumbell' shaped drops which can appear when the tension is low; and ii) the specification of criteria characteristic of true equilibrium. Drop shapes other than cylindrical can be avoided by increasing the rotation speed. As will be seen later, a reasonable test of equilibrium is the agreement (or otherwise) between tensions from phases that have been contacted prior to measurement and those obtained from system not originally at equilibrium.

5.3 EXPERIMENTAL SECTION

The spinning drop tensiometer consists of a high speed rotating capillary tube (2mm ID) open at one end. The tube in its housing is pivoted and sealed so that the closed end rotate inside the chamber and its middle section is observable through the windows. Illumination of the capillary is with a stroboscope 'in-phase' with the rotation of the tube. A microscope with a magnifying eyepiece is used to determine the drop diameter. Experimental procedures for measuring IFT using the spinning drop technique are summarized in Appendix E.

Phase behavior experiments offer a quick, economical method for estimating interfacial tension, as well as other microemulsion properties that are important in the screening process for commercial surfactant systems. Equipment used in phase behavior tests are listed in Table 5.1. Phase behavior tests are conducted following the experimental protocols recently developed at the University of Texas at Austin (Jackson, 2006; Levitt, 2006; Flaaten, 2007; Sahni, 2009; Yang, 2010; Dean, 2011; Solairaj, 2011; Walker, 2011), and the detailed experimental operations are also included in Appendix E.

Table 5.1 Equipment Used in Phase Behavior Experiments.

Name	Specifications
Fisherbrand® Borosilicate Serological Pipette	Standard 5ml; 5mm ID; 0.1ml markings.
Eppendorf Reperter® plus Pipette Dispenser	Accurate delivery between 25µl and 1ml.
TS99 Benzomatic® Torch	Work with a 14.1 oz MAPP gas canister; Melt the glass pipette in about 20 seconds.
Convection Oven	Incubate pipettes at desired temperature; Monitoring using temperature gauge.

5.4 INTERFACIAL TENSION MEASUREMENTS

The interfacial tension of a surfactant system is related to the adsorption of the surfactant at the oil-water interface (Rosen, 2004). There are many factors that affect this adsorption process, such as the nature of the surfactant, ionic strength of the solution, and temperature. In the current study, the effects of different variables such as surfactant concentration, tail chain length, mono- and di-valent ion concentration, and hydrocarbon type, etc. on the interfacial tensions of Gemini surfactant/pure hydrocarbon/electrolyte system are systematically investigated.

5.4.1 Surfactant Concentration

Surfactant molecules tend to accumulate at the oil-water interface where the hydrophilic and hydrophobic ends of the molecules can be in a minimum energy state. If the concentration of surfactants at the interface is very low, the molecules will lie flat on the surface (Aguiar *et al.*, 2011). As their concentration increases, the surfactant molecules begin to orient themselves at the interface, forming a monolayer. This increases the surface pressure and decreases both the interfacial energy and the interfacial tension. At a solution concentration about the same as the critical micelle concentration (CMC), surfactant monomers in solution begin to spontaneously associate into larger aggregates (or swollen micelles). At this point, no further adsorption at the interface will occur and, the interfacial tension reaches a final plateau value.

Aqueous samples of *14-4-14* and *18-4-18* Geminis at different surfactant concentrations were prepared in a 20wt% NaCl base solution. The interfacial tensions between these solutions and dodecane (n-$C_{12}H_{26}$) were measured at 55^{o}C. The first thing to note here is that the solution had a very high salinity (20wt% of NaCl). Even at this extremely high salinity, no phase separation or precipitation of any kind was observed for all the surfactant solutions prepared. All the Gemini surfactants synthesized in the current

study have shown their extraordinary tolerance to salinity indicating that they are very hydrophilic. The surface (ST) and interfacial tensions (IFT) vs. Gemini surfactant concentration plots for *14-4-14* and *18-4-18* are shown respectively in Figure 5.2 and Figure 5.3 below. The concentrations are expressed in mg/L (~ppm), as compared to mmol/L used in previous chapters. The break points in the figure mark the critical micelle concentrations of respective Gemini molecules under the current set of conditions (20wt% NaCl at 55^{o}C and dodecane as the oil phase).

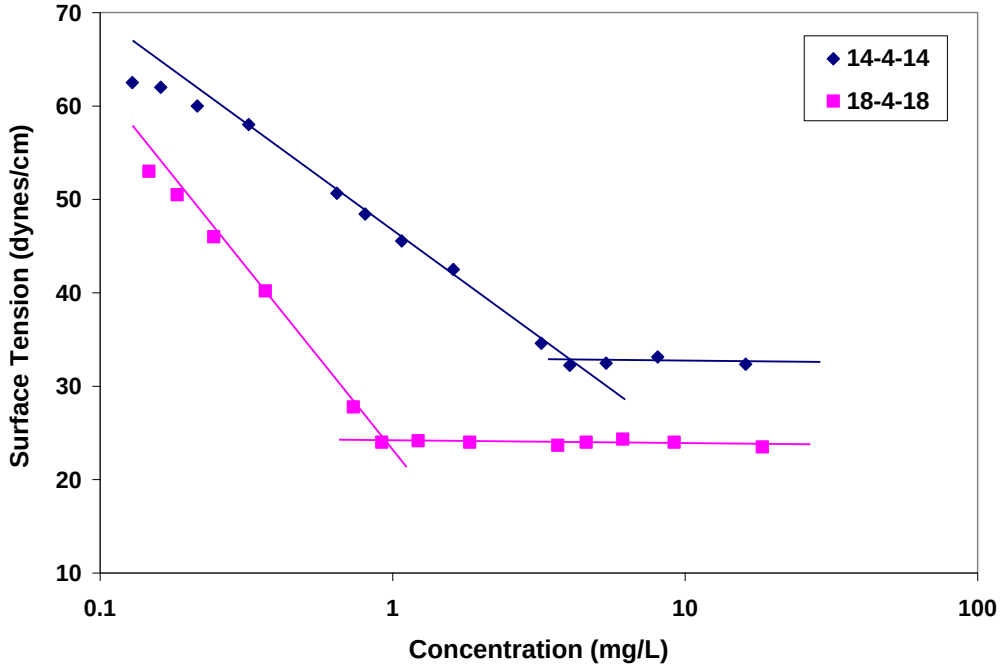

Figure 5.2 ST vs. Concentration for *14-4-14* and *18-4-18* in Pure Water at 25^{o}C.

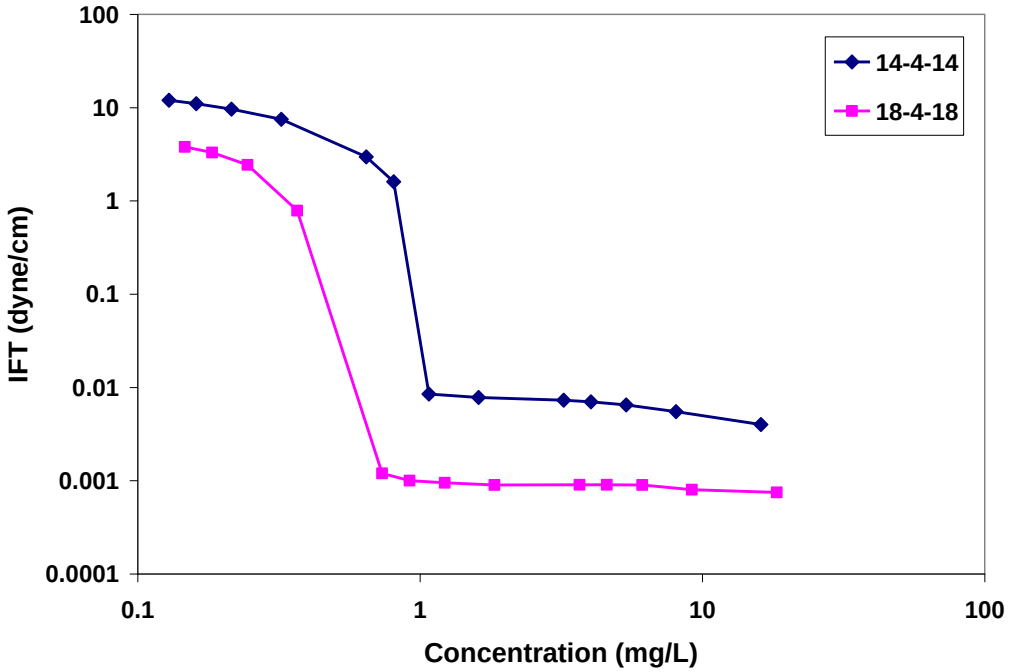

Figure 5.3 IFT vs. Concentration for *14-4-14* and *18-4-18* in 20wt% NaCl Base Solution at 55°C, with Dodecane (n-$C_{12}H_{26}$) as the Oil Phase.

CMC values obtained here by IFT measurements seem to be lower than those from the surface tension method. Ye *et al.* (2008) observed an opposite trend where CMC determined by IFT is greater than that by surface tension, from their measurements using cationic Gemini surfactants and a field crude oil. They attributed such a trend to the polar components in the oil phase. For current anionic Gemini and pure hydrocarbon systems, the experimental conditions (in terms of salinity and temperature) were quite different for surface tension and IFT measurements. A 20wt% NaCl concentration will cause a reduction in CMC, while an increase of temperature from 25°C to 55°C will shift CMC upwards, but possibly to a lesser extent (refer to discussions in Chapter 4). The end result is a smaller CMC by IFT than by surface tension measurements.

Obviously, even at this extremely low concentration level, Gemini surfactants (at least for the *18-4-18* molecule) are still capable of reducing the interfacial tension to

ultralow levels ($<10^{-3}$dyne/cm). In all measurements that follow, a surfactant concentration of 0.02wt% (~200mg/L) will be used to make sure we stay safely above the CMC, and in the meantime still remain much lower than that typically used for a conventional surfactant system (~0.2wt% to 2wt% total surfactant concentration).

5.4.2 Dynamic Response

Dynamic surface tension (DST) is critical in many industrial and biological processes (Chatterjee, 1998; Shahidzadeh, 2000). The dynamic progression of surface tension can be monitored by DST measurements (Rosen *et al.*, 1996). Similarly, on generation of a new liquid-liquid interface, the equilibrium interfacial tension (IFT) is not instantly reached. For the tension to reach its equilibrium value surfactant molecules must first diffuse onto the interface, then adsorb and orient themselves in the interfacial region. In the meantime, some of the adsorbed molecules will try to get desorbed and go back to the bulk aqueous phase under the influence of thermal motion. This is, therefore, a dynamic and competing process among diffusion, adsorption and desorption. At initial time, interface density is really low and adsorption dominates, which results in a steady reduction of IFT. As time goes on, more and more surfactant molecules accumulate at the interface, the adsorption rate decreases and gradually reaches equilibrium with desorption, and the IFT reaches a plateau value. Figure 5.4 is the plot of dynamic interfacial tension against time for 0.02wt% *16-4-16* and *18-4-18* solutions measured at temperatures of 55^{o}C and 85^{o}C.

It can be seen here that both surfactants are very efficient in reducing the interfacial tension between oil and water. Furthermore, *16-4-16* is more efficient than *18-4-18* in terms of the time needed for interfacial tension to reach equilibrium. At 55^{o}C, for *16-4-16*, it took about 10 minutes to reach equilibrium, in contrast to a much longer

period of 40 minutes for *18-4-18*. The dynamic behavior is closely related to the nature of the surfactant.

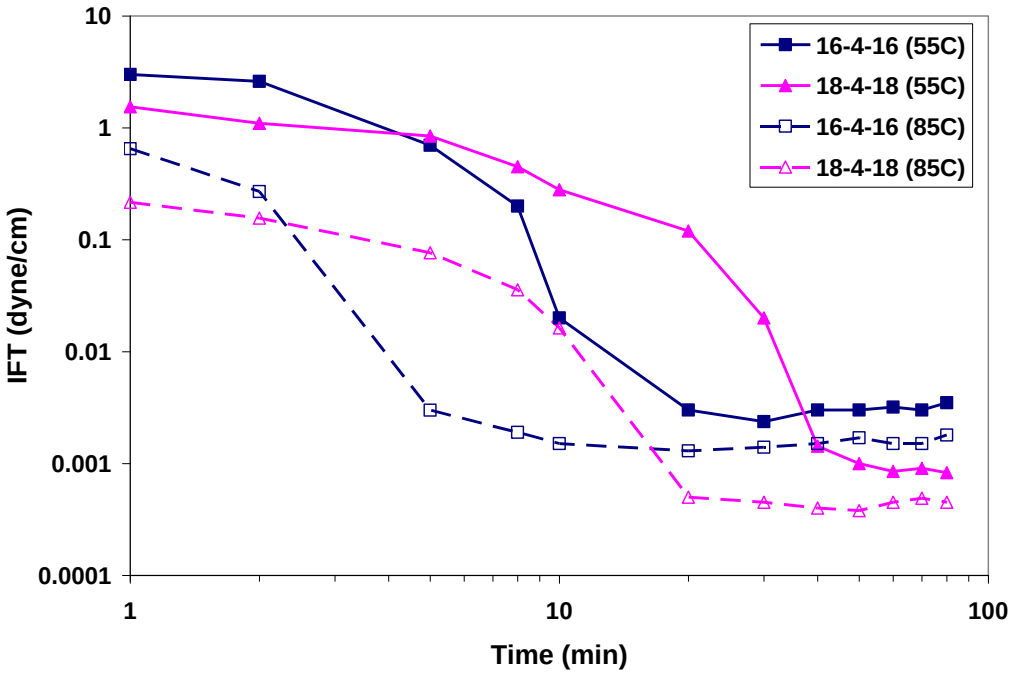

Figure 5.4 Dynamic IFT Response for 0.02wt% *16-4-16* and *18-4-18* in 20wt% NaCl Base Solution, with Dodecane (n-$C_{12}H_{26}$) as the Oil Phase.

Figure 5.4 also shows the effect of temperature on the dynamic interfacial tensions. Higher temperature apparently expedites the equilibrium process. For instance, at 85°C, it only took 15 minutes for the IFT of the *18-4-18* solution to stabilize. A higher temperature will affect the mutual solubility of the solvents, the CMC, and the adsorption kinetics of surfactant molecules, and the distribution of the surfactants between oil and water, and, therefore, the dynamic interfacial tension. It is crucial in all experiments to give every sample enough equilibration time to reach a true IFT plateau, and this can be accomplished by strictly following the equilibration criterion that requires three consecutive width readings from the tensiometer to agree to within ±0.001cm.

5.4.3 Comparison with Pre-Equilibrated System

In Figure 5.5, interfacial tension is plotted against the salt concentration for systems containing Gemini surfactant, NaCl and dodecane at 55°C. Included in the plot are values obtained in two different ways. First, results are shown for systems in which pure dodecane was introduced directly into an aqueous surfactant which has not previously been equilibrated with the oil phase. Initially, a coating was observed to form around the oil drop; the coating was quite fluid and the drop shape responded rapidly to changes in rotation speed of the tensiometer capillary. Eventually, the coating became detached from the drop leaving an apparently clean oil/water interface, and the drop radius became stable; tensions recorded were those for such clean interfaces.

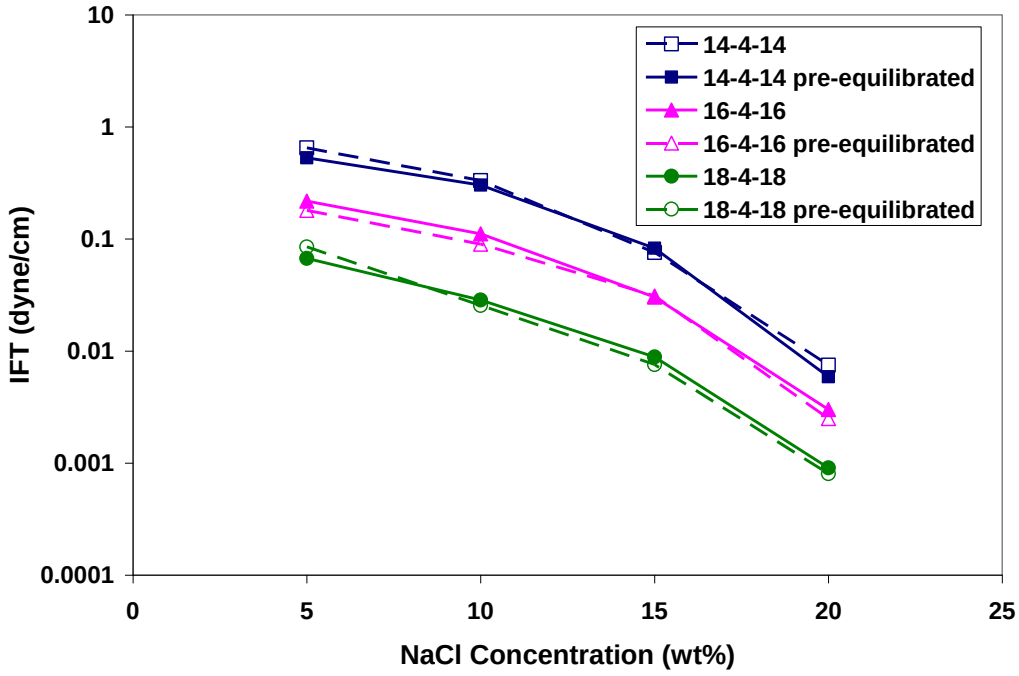

Figure 5.5 Comparison of IFT Values between Systems Containing Non-equilibrated (filled symbols) Phases and Pre-Equilibrated (open symbols) Phases for Three Gemini Surfactants at Different Salinities and 55°C, with Dodecane (n-$C_{12}H_{26}$) as the Oil Phase.

We also prepared equilibrium systems in which dodecane was mixed with aqueous surfactant in test vials and left in the oven at 55^{o}C for one week. Oil and aqueous phases on top and at the bottom were sampled and used for IFT measurements. It is apparent from Figure 5.5 that the tensions so obtained were in close agreement with those for the non-equilibrated systems described above. These results give us confidence in our IFT experimental procedures, especially regarding how to obtain true equilibrated IFT values. Similar agreements between IFT values obtained from non- and pre-equilibrated systems were also reported by Aveyand and Binks (1986 & 1988). They also used a surface light scattering technique to determine the tensions in equilibrated systems. All three sets of their data are in exceptional agreement.

5.4.4 Mixing with Polymer

Surfactant-based formulations often contain water-soluble polymers that improve the properties of the formulations. Therefore, it is important to study the interaction of Gemini surfactants with water-soluble polymers. The study of interactions between surfactants and polymers is an active field of interest in colloid science. We investigated the effect of adding 500ppm HPAM3330 on the dynamic interfacial tension between oil and Gemini surfactant solution.

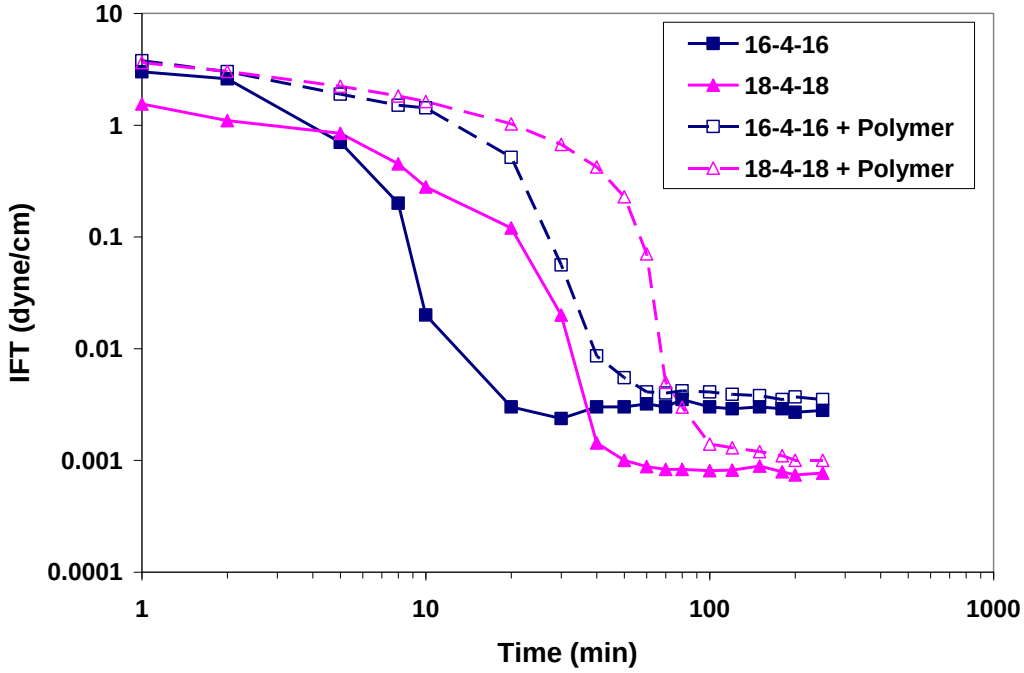

Figure 5.6 Dynamic IFT Response for 0.02wt% *16-4-16* and *18-4-18* in Base Solutions (containing 20wt% NaCl + 500ppm HPAM3330) at 55°C, with Dodecane (*n*-$C_{12}H_{26}$) as the Oil Phase.

It can be seen from Figure 5.6 that HPAM has a remarkable effect on the dynamic IFT response. It takes more time to reach the equilibrium interfacial tension with the addition of HPAM, but it has little effect on the equilibrium IFT values. This can be explained by the fact that the addition of HPAM will increase the viscosity of the solution, which in turn reduces the rate of diffusion of the surfactant molecules, thereby slowing down the adsorption of the surfactant onto the interface.

5.4.5 Effect of Alkyl Chain Length

As the alkyl chain gets longer, we see a gradual decrease in IFT in Figure 5.7, agreeing well with the trend observed for surface tension measurements in Chapter 4.

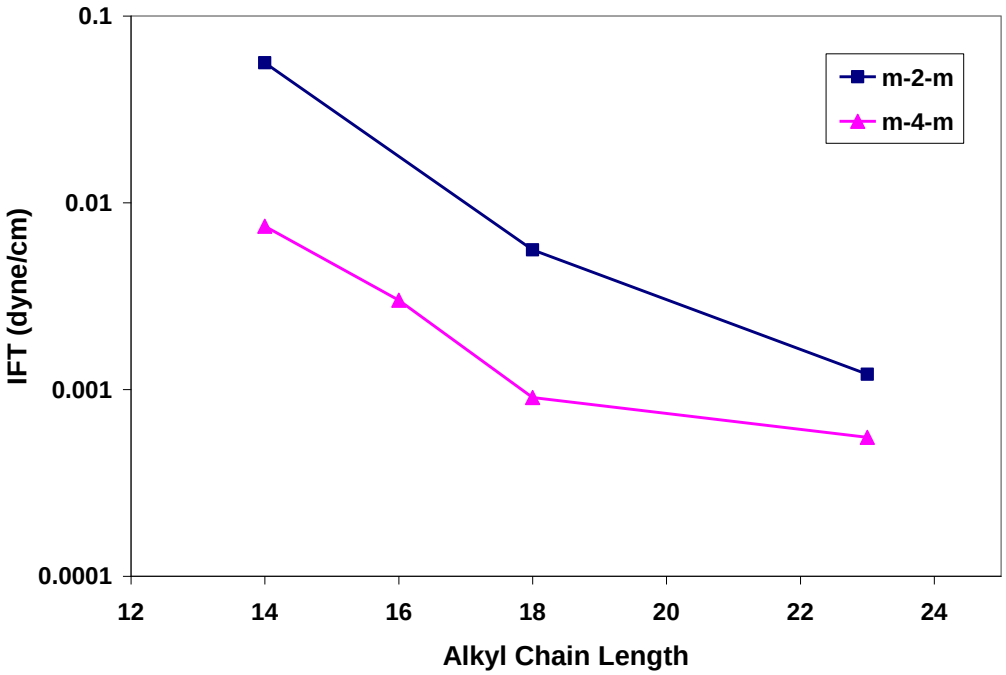

Figure 5.7 Impact of Alkyl Chain Length on IFT for 0.02wt% Geminis in 20wt% NaCl Base Solution at 55°C, with Dodecane (n-$C_{12}H_{26}$) as the Oil Phase.

Indeed, as the hydrophobe gets larger, the hydrophilic-lipophilic balance (HLB) is adjusted such that the surfactant molecules become more hydrophobic, and thus have a higher tendency to move from the bulk aqueous phase onto the oil-water interface. Once there, they can orient themselves so that the large hydrophobes point towards the oil phase to reduce the free energy of the system. All the Gemini molecules shown in Figure 5.7 have demonstrated their potential to effectively reduce oil-water IFT by several orders of magnitude (from the original ~50dynes/cm). Remarkably, this reduction occurs at very low surfactant concentrations (0.02wt%) as shown by our measurements. Ultralow interfacial tensions ($<10^{-3}$dyne/cm) were, however, only observed for Geminis with longer alkyl chain and spacer group, i.e. *18-4-18* and 20^{+}-*4*-20^{+}. These two molecules are better HLB balanced (more lipophilic) under this specific set of salinity (20wt% NaCl) and temperature (55°C) conditions.

The HLB calculation carried out earlier in Chapter 3 showed that all the Gemini surfactants synthesized are very hydrophilic. And while this hydrophilicity definitely helps out in dissolving these long chain surfactant molecules into aqueous solution even at extremely high salinity, it hurts their performance in reducing IFT. As can be seen from Figure 5.7, ultralow interfacial tensions were not obtained for some surfactants.

In order to further reduce the IFT, the HLB balance must be further adjusted. There are a few approaches to achieve this: (1) changes in aqueous solution condition, e.g. to increase electrolyte concentration in the solution and thus push the surfactant molecules onto oil-water interface; or raise the solution temperature and promote adsorption at the interface; (2) manipulations on the molecular structure, e.g. to make the surfactant more hydrophobic by introducing longer tail (as discussed in current section) and spacer groups, or switching to less hydrophilic head groups, such as carboxylates.

5.4.6 Effect of Monovalent Salt (NaCl) Concentration

Formation water is always salt-bearing, and, therefore, the interfacial tensions were measured between hydrocarbon and Gemini solutions with various amount of NaCl added. Results in Figure 5.8 show the positive impact of higher NaCl concentration on lowering the tension of an oil-water interface.

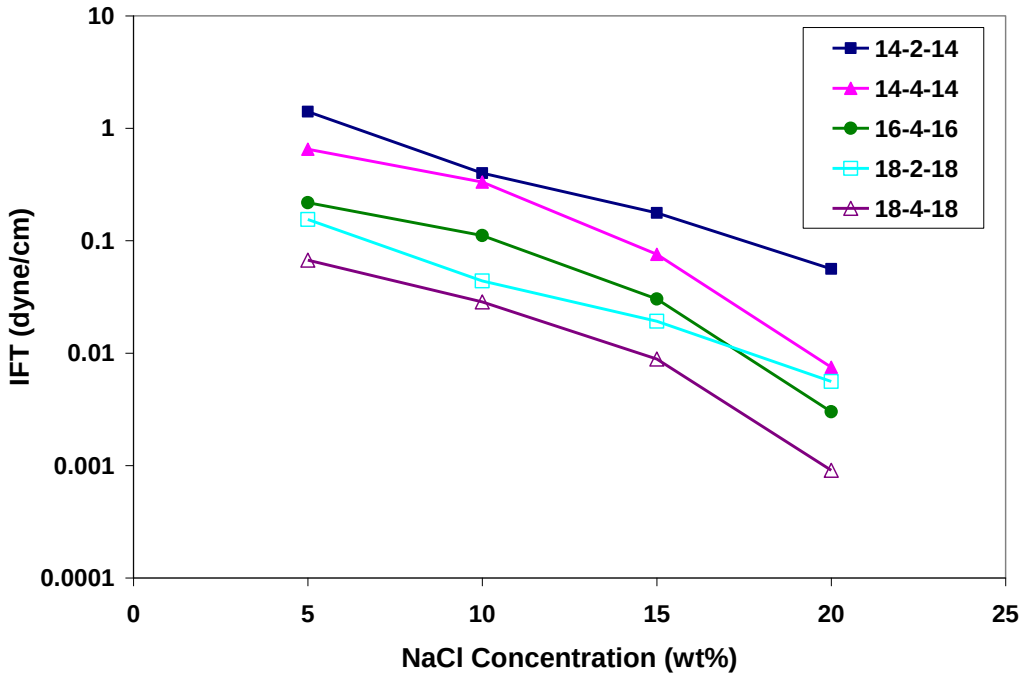

Figure 5.8 Impact of NaCl Concentration on IFT for 0.02wt% Gemini Solutions at 55°C, with Dodecane (n-$C_{12}H_{26}$) as the Oil Phase.

Again, shown here is firstly the great solubility of Gemini surfactants in highly saline solutions. As more and more NaCl is added, the interfacial tension steadily goes down. This is consistent with data for other surfactants and is to be expected. However, we did not observe any salting out of the surfactant indicating that Gemini surfactants show good salt tolerance. The increase in effectiveness of surfactant by the addition of salt is a result that has been well explained earlier through a modification of electrical double layer at the oil-water interface and the reduced hydrophilicity of the surfactant at high salinities due to ion binding at the surfactant head groups. Notice that, the lower IFT values were observed towards the higher end of the salinity range (15 to 20wt%) for Gemini surfactants. For conventional surfactants, on the other hand, the low interfacial tension usually exist at a narrow salinity window below a TDS of 100,000ppm (10wt%). Therefore, one potential area where Gemini surfactants can be used and may perform

better would be in high temperature, high salinity environments, which are commonly encountered in many oil reservoirs around the world. It should be noted that over the wide range of salinities examined in this section, we have yet to find a minimum of interfacial tension with regard to salinity. The existence of such minimum will be examined using a simplified thermodynamic treatment in a later section.

5.4.7 Effect of Divalent Salt ($CaCl_2$) Concentration

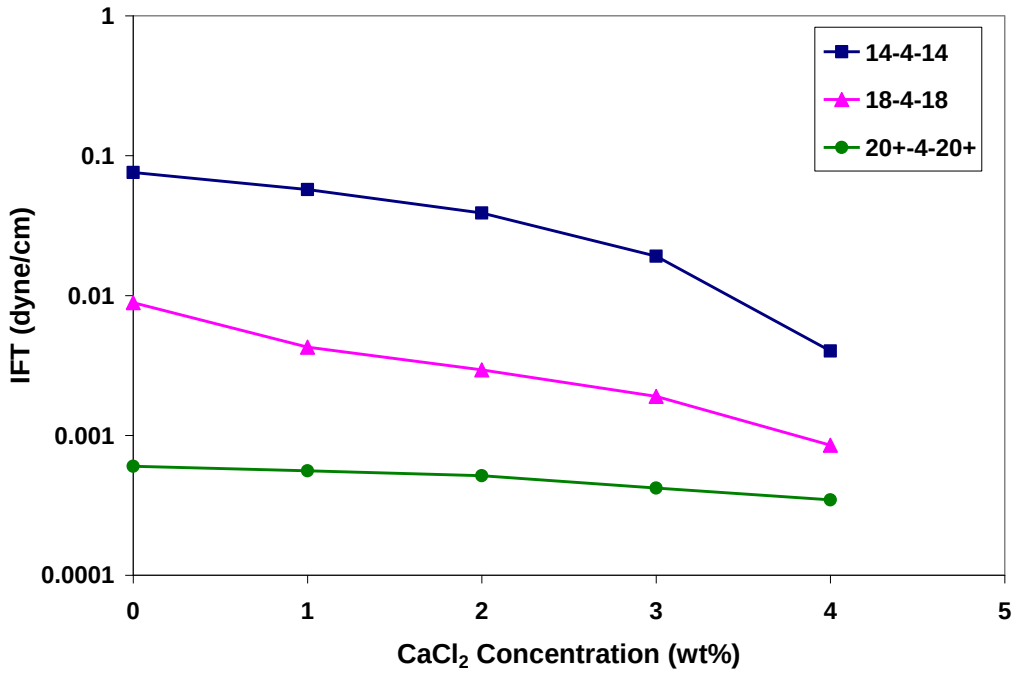

Figure 5.9 Impact of $CaCl_2$ Concentration on IFT for 0.02wt% Geminis in 15wt% NaCl Base Solution at 55°C, with Dodecane (n-$C_{12}H_{26}$) as the Oil Phase.

Divalent ions like Ca^{2+} and Mg^{2+} are more efficient in driving surfactant molecules onto the oil-water interface than monovalent ions. Most conventional surfactants do not work well with divalent ions, often showing precipitation or phase separation upon addition of Ca^{2+} and Mg^{2+} to their aqueous solutions. As shown earlier

Gemini surfactant solutions can withstand high concentrations of NaCl; it is thus natural to test the aqueous stability and IFT reduction capabilities of Gemini solutions under the influence of divalent ions. A series of 0.02wt% Gemini solutions (already containing 15wt% NaCl) were prepared with different amounts of $CaCl_2$ added and the IFT values were measured between these aqueous solutions and pure dodecane. The results are shown in Figure 5.9. First and most importantly, no solubility problems were encountered in these tests, even when the $CaCl_2$ concentration went as high as 4wt%. On the basis of 15wt% of NaCl, the addition of divalent ions helps further reduce the IFT and ultralow values were observed. Formation brines with TDS (mono- and di-valent ions together) in excess of 150,000ppm are generally considered to be difficult targets for EOR operations. Gemini surfactants are shown here to perform well (in terms of solubility and interfacial tension reduction) in such environments, which makes it possible to handle these difficult situations with simpler chemical systems.

5.4.8 Effect of Anionic Head group

As discussed in previous sections, the sulfate Gemini molecules are extremely hydrophilic, and the main reason for that is the inclusion of two sulfate head groups in one single molecule. One natural way to adjust the hydrophilic-lipophilic balance (HLB) is thus to introduce a more hydrophobic head group, for instance the carboxylate head group tested in current study. The hydrophobicity of carboxylate Geminis is confirmed by its lower CMC value compared with sulfate Geminis of the same alkyl chain length (results from Chapter 4). Figure 5.10 compares the IFT measurements of sulfate and carboxylate Gemini solutions at 85^{o}C. For both *18-4-18* and *20^{+}-4-20^{+}* Geminis, replacing the sulfate head groups with carboxylates indeed helps further reduce the interfacial tension. However for longer alkyl chain molecules (*20^{+}-4-20^{+}*) at higher

salinities, this reduction become less prominent, indicating that changing head groups might not be an efficient way to further reduce IFT under these conditions.

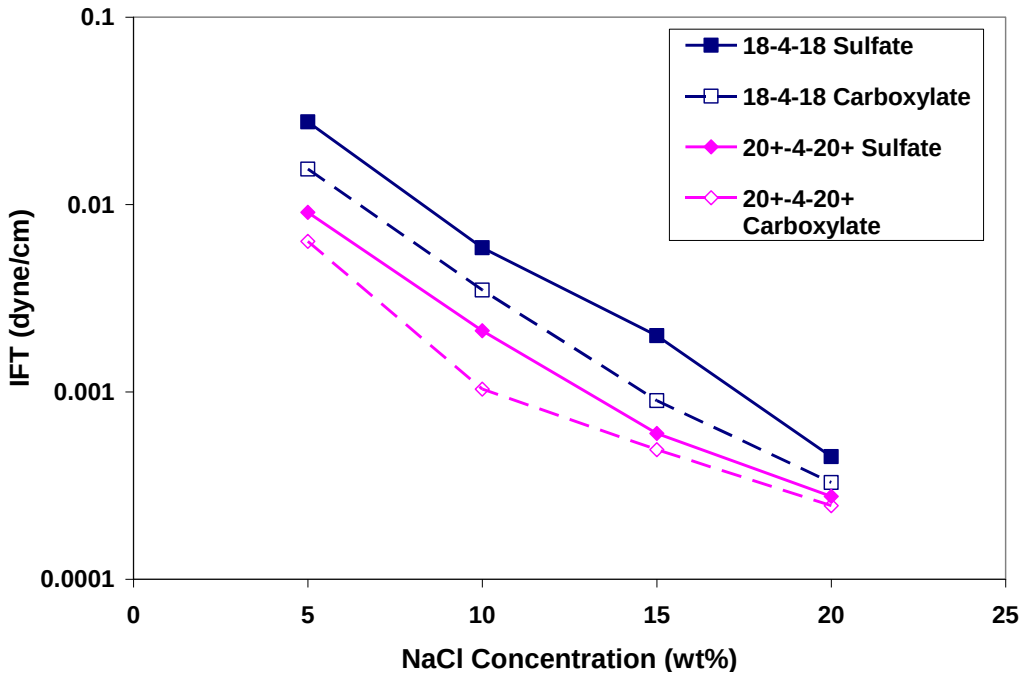

Figure 5.10 Impact of Anionic Head groups on IFT for 0.02wt% Gemini Aqueous Solutions at 85°C, with Dodecane (n-$C_{12}H_{26}$) as the Oil Phase.

5.4.9 Effect of Branching of Alkyl Chain

In an effort to further adjusting the HLB of the molecule, a polybutene epoxide (see Figure 5.11) with an average MW of 320 was obtained from Arkema Inc. and used to synthesize a corresponding sulfate Gemini surfactant *24-4-24*. Here the tail length of 24 is an estimate based on the average MW.

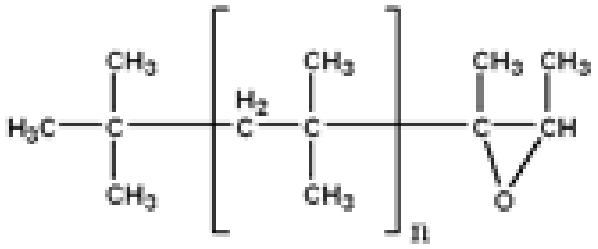

Figure 5.11 Structure of Epoxidized Polybutene Material (n=4 for our sample).

20^{+}*-4-20*$^{+}$ is another long chain sulfate Gemini synthesized in this study, from a mixture of epoxides of chain lengths ranging from 20 to 30. The weight-averaged chain length is 23 for this molecule. Therefore, *24-4-24* (from polybutene epoxide) and *20*$^{+}$*-4-20*$^{+}$ (from mixture of epoxides) have similar equivalent carbon chains, but different degrees of branching on the chains. Figure 5.12 shows the IFT measurement results.

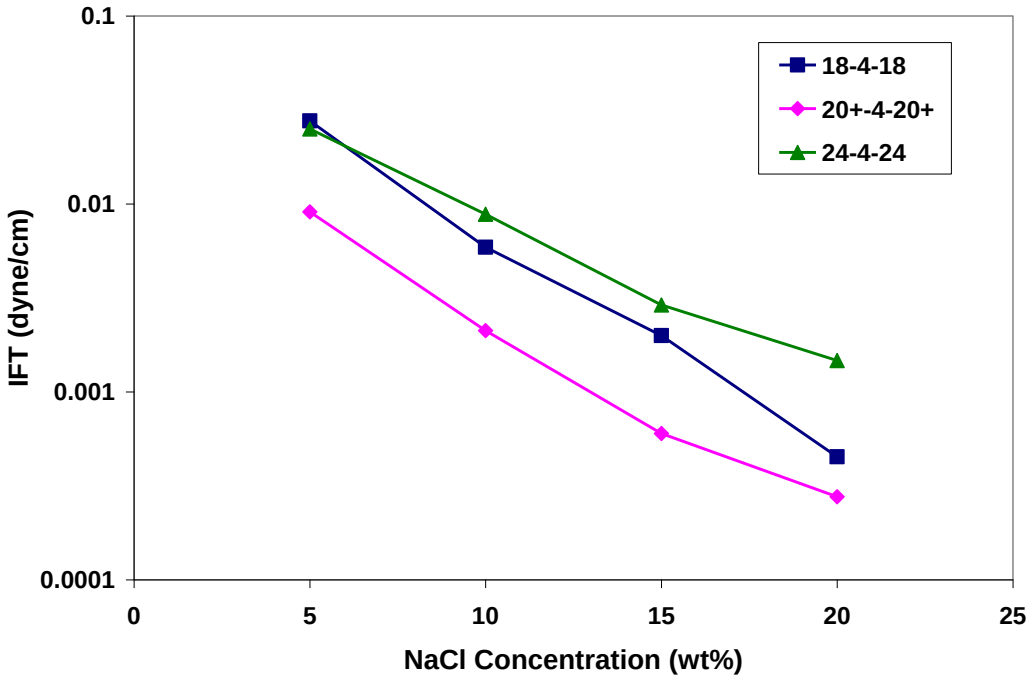

Figure 5.12 IFT Reduction by Long Chain Geminis (0.02wt%) at 85°C, with Dodecane (*n*-$C_{12}H_{26}$) as the Oil Phase.

Apparently, the more branched molecule *24-4-24* does not reduce the IFT down to the same level as the linear-chained 20^{+}-4-20^{+}. In fact, *18-4-18* molecule was able to lower the IFT more effectively than *24-4-24*, with ultra-low IFT (ULIFT) observed at higher salinities, whereas for *24-4-24*, no ULIFT was reached in the experiments. These results are actually consistent with observations made for conventional surfactants, where branching of the chain length tends to diminish solubilization and IFT reduction by the surfactant (Menger *et al.*, 2000). This is understandable considering the difficulty in packing the bulkier branched chains at the oil-water interface, as compared to the linear tail chains.

5.4.10 Hydrocarbon Type

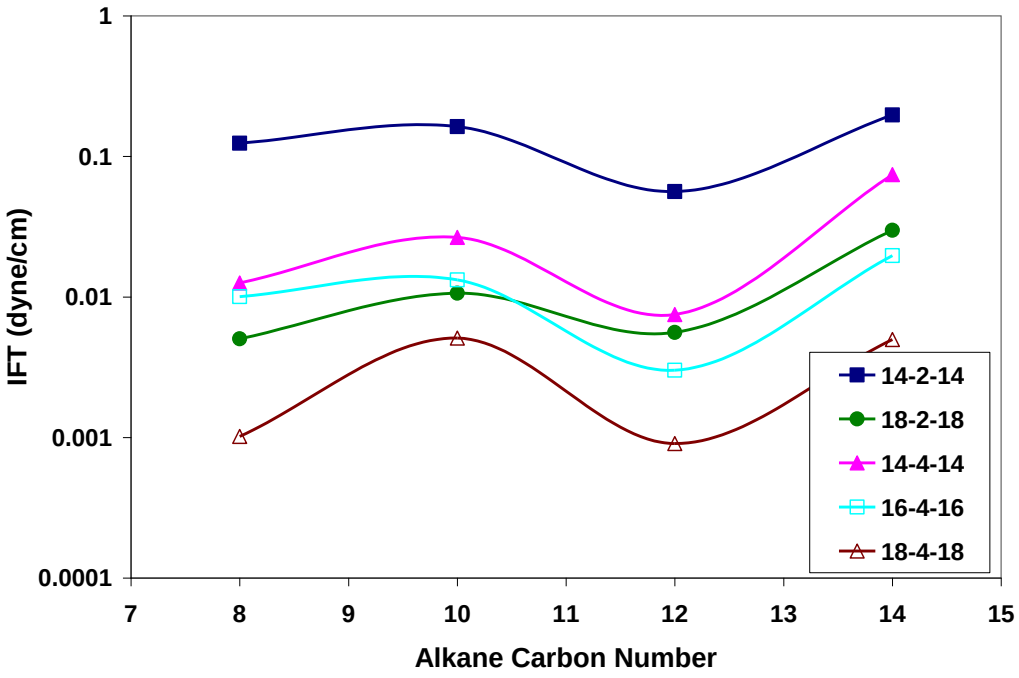

Figure 5.13 Effect of Alkane Carbon Number on IFT for 0.02wt% Geminis in 20wt% NaCl Base Solution at 55°C.

For conventional surfactant, the molecular interactions (Bourrel *et al.*, 1983 & 1987) taking place at the oil-water interface are strongly affected by the nature of the surfactant, the characteristics of the oil and solution conditions of the aqueous phase. And this is the fundamental reason why laboratory surfactant screening is always performed individually and customed to the specific oil and brine combination.

Figure 5.6 shows ACN (alkane carbon number) scans performed for five different Gemini surfactants, to investigate the effect of hydrocarbon type on IFT values. For conventional surfactants, there typically exists an optimum ACN number corresponding to a minimum IFT value (Bourrel *et al.*, 1987). For Gemini surfactants, the IFT results in Figure 5.13 do not show a strong preference to any particular hydrocarbon (at least for the oils tested here). There is, however, a local minimum at an ACN value of 12, e.g. dodecane for all the Geminis investigated, which is the reason why dodecane is used as the oil phase in most IFT measurements reported in this chapter. The absence of an optimal ACN number can be used to our advantage in the surfactant screening process, since Gemini surfactants can potentially be used for a range of different hydrocarbons. This is particular beneficial when dealing with crude oil systems, which are typically complex combinations of hydrocarbons of various ACN values. With Gemini surfactants, there is a better chance of finding a formulation that can be used for a wider range of oils.

5.4.11 Effect of Temperature

Temperature affects solubilities and interaction energies of hydrophobes and head groups in aqueous solution. As shown in Figure 5.14 higher temperature seems to promote adsorption of Gemini molecules onto water/oil interface and hence reduce the interfacial free energy or interfacial tension.

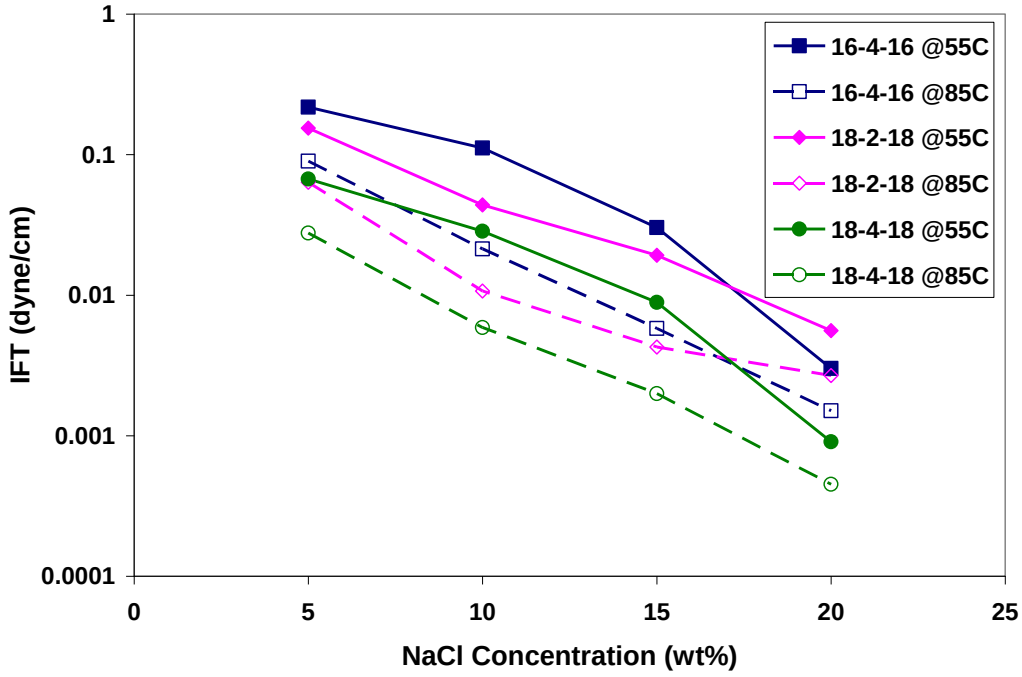

Figure 5.14 Effect of Temperature on IFT for 0.02wt% Gemini Aqueous Solutions, with Dodecane (n-$C_{12}H_{26}$) as the Oil Phase.

5.4.12 Synergy with Conventional Surfactants

In many practical applications, different types of surfactants are deliberately mixed together to improve the properties of the final product. In such cases, what is sought is synergism between the surfactant mixtures. The goal is to obtain properties of the mixture that are better than those attainable with the individual components by themselves. For example, a nonionic surfactant is often added to a phase behavior formulation based upon an anionic surfactant because the overall performance (aqueous stability and phase behavior) of the mixture is better than that of either surfactant by itself. It is evident to us that, in the future, the more hydrophilic Gemini surfactants will most likely be used in mixtures with conventional surfactants for both cost and performance considerations. The properties of such mixtures must, therefore, be investigated in order to better understand mixture behavior and properties.

In the current study, we investigate the synergy between Geminis and conventional surfactants in terms of IFT reduction. The conventional surfactants studied here are branched alkyl benzene sulfonates (BABS), i.e. Petrostep A1 (C_{15-18} BABS) and Petrostep M2 (C_{16-18} BABS). These surfactants are chosen because of their hydrophobic nature. Our expectation is that the strong hydrophilicity of Gemini surfactants at the water-oil interface might compensate for the relative lipophilicity of the other surfactant molecules. Figure 5.15 shows a concentration scan of Petrostep A1, conducted at 55°C and in aqueous solutions containing 0.02wt% Gemini and 15wt% NaCl.

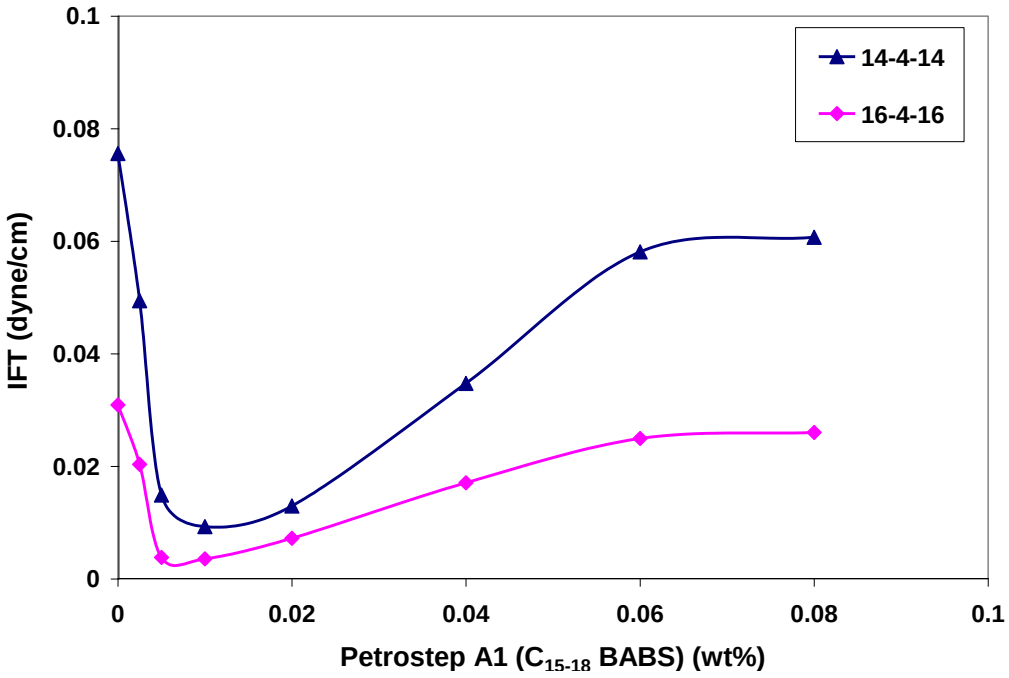

Figure 5.15 Synergy of Gemini (0.02wt%) with Petrostep A1, in 15wt% NaCl Solution at 55°C, with Dodecane (*n*-$C_{12}H_{26}$) as the Oil Phase.

With only about 0.01wt% of Petrostep A1 added, the interfacial tensions between aqueous solutions and dodecane were reduced to a minimum and were at ultralow levels ($<10^{-3}$ dyne/cm). Two points worth mentioning here are: i) the hydrophobic ABS type

surfactant, Petrostep A1, is stable and remains dissolved into an aqueous solution that contains 15wt% NaCl, due to the existence in solution of hydrophilic Geminis; ii) the interfacial tension from the surfactant mixture reaches ultralow levels, which is not achievable by the individual surfactant components. The molecular interaction between the Gemini and conventional surfactants provide mutual benefits that contribute to aqueous stability and interfacial activity. This leads to a new possibility of making use of Gemini surfactants. They can be used as co-solvents that help the solubility of the main surfactants, and as co-surfactants that help bring out the best performance of the surfactant mixture.

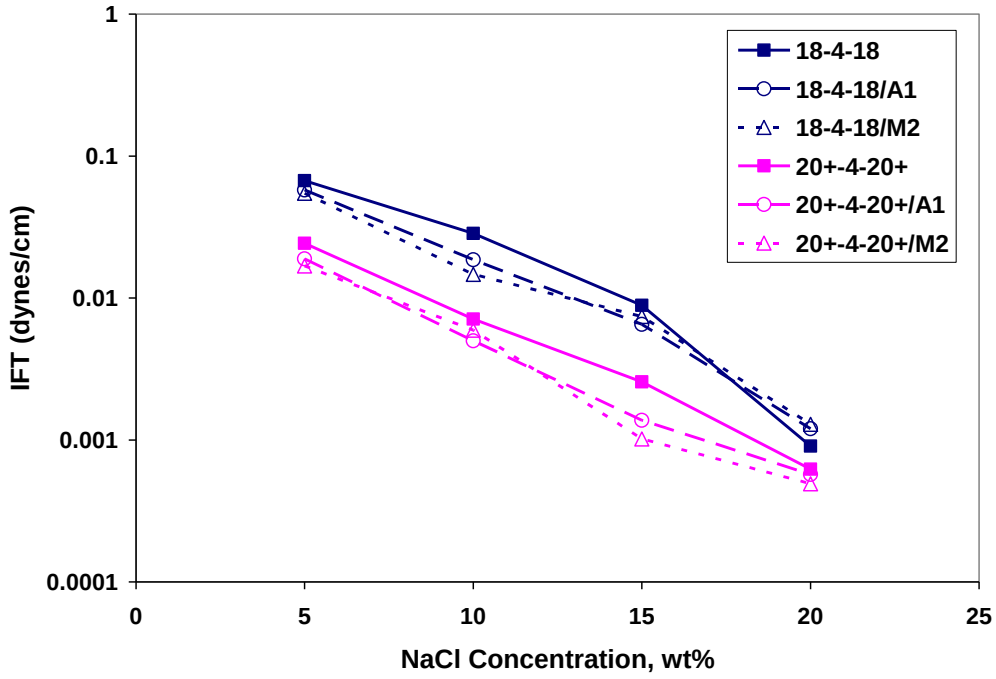

Figure 5.16 Synergism of Gemini (0.02wt%) with Petrostep A1/M2 (0.01wt%) at 55°C, with Dodecane (n-$C_{12}H_{26}$) as the Oil Phase.

Figure 5.16 shows the salinity scan results using surfactant mixtures with fixed composition. Lower interfacial tensions were observed after the ABS surfactant was

added into Gemini surfactant solutions, but only to a limited extent in some cases. The optimal concentration ratio between Gemini and conventional surfactants will depend on the specific structure of the molecules involved and solution conditions they are subject to. Nevertheless, all the surfactant mixtures are readily soluble in highly saline solutions, showing again that Gemini surfactants are able to help solubilize conventional surfactants at high salinity.

5.5 PHASE BEHAVIOR TESTS

Surfactant formulations for EOR applications are commonly characterized in phase behavior experiments by evaluating the microemulsion formed with hydrocarbon, water, and surfactant. In the current study, experiments were carried out to see if Gemini surfactants exhibit similar phase behavior to conventional single chain molecules. Table 5.2 below summarizes the experimental conditions examined in the phase behavior tests. Figure 5.17 shows the phase behavior pipettes prepared for 0.2wt% 20^{+}-4-20^{+} carboxylate Gemini surfactant.

Table 5.2 Experimental Conditions Examined in Phase Behavior Test.

	Surf. Conc. (wt%)	Temp. (^{o}C)	Scan Range	Oil Type
Group I Salinity	0.01, 0.02, 0.1, 0.2	45, 55, 85	up to 20wt% NaCl	C8, C10, C12, C14
Group II Hardness	0.01, 0.02, 0.1, 0.2	45, 55, 85	15wt% NaCl + up to 4wt% $CaCl_2$	C8, C10, C12, C14

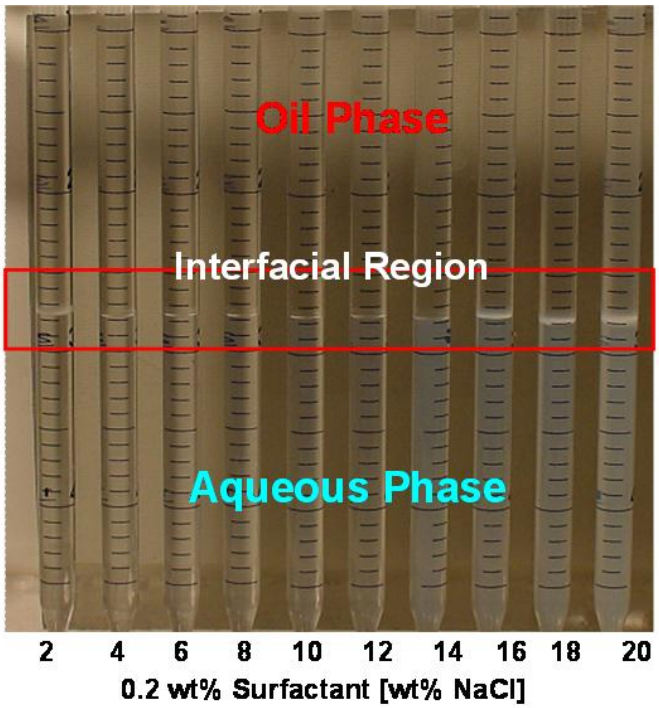

Figure 5.17 Test Pipettes Prepared for 20^{+}-4-20^{+} Carboxylate Gemini Surfactant (0.2wt%) Phase Behavior at 55°C, after 2 weeks.

The picture was taken after the pipettes were kept in a 55°C oven for two weeks. These pipettes actually represent very well what we would generally observe in phase behavior tests for Gemini surfactants under different conditions. A first common observation is that even with a salinity as high as 20wt%, no phase separation or precipitation take place, showing the superb salinity (and/or hardness) tolerance of this molecule. Another common observation across different tests is the absence of significant Type III middle phase. In fact, most test pipettes showed a Type I appearance even after an extended period of equilibration. On the other hand, ultra-low interfacial tensions (ULIFT) were indeed measured in some conditions corresponding to the phase behavior tests, as shown in the previous section. At first, this appears to be contradictory to the "common notion" that ultra-low interfacial tension and the presence of a Type III

microemulsion phase always go together. Fundamentally, however, IFT reduction and oil solubilization (Type III phase formation) are two separate phenomena, controlled by different mechanisms.

The interfacial tension of a surfactant system is greatly related to the adsorption of surfactant at the interface. ULIFT, as will be discussed in more detail in later sections, is caused by monolayer adsorption of surfactant molecules at the oil-water interface. The fact that Gemini surfactants can pack more closely at the interface helps the system to reach ULIFT despite a low solubilization ratio. On the other hand, conventional surfactants cannot form an interfacial packing as compact as Geminis. The closer packing by Gemini molecules can be ascribed to at least two facts: i) intramolecular level: the existence of the short spacer group chemically constrains the distance between the two tails; ii) intermolecular level: the extremely high salinity condition Gemini surfactants can withstand helps screen out the electrostatic repulsion between head groups and thus facilitate even closer packing.

Oil solubilization capability of a surfactant, on the other hand, is monitored by the minimization of the overall free energy of the hydrocarbon / surfactant (co-surfactant) / electrolyte system (Nagarajan *et al.*, 1991; Moreira *et al.*, 2010). For conventional surfactants at sufficiently high concentrations, the minimization of free energy requires the oil molecules be incorporated with surfactant molecules to form swollen micelles or even bicontinuous (middle phase) structures. Whereas for Gemini surfactants, due to their high tendency to self-aggregate, especially at higher concentration and with salt addition (more details in Chapter 6), it is possible that the free energy can be minimized by the Gemini molecules self-assemble, without solubilizing significant amount of oil molecules.

Although Type III systems are not generally observed in phase behavior experiments for Gemini surfactants, the success of applying Geminis in chemical EOR is still promising. Firstly, salinity and/or hardness tolerance is very important for applications in harsh reservoir conditions. Moreover, for conventional surfactant systems, low IFT can only be obtained in the Type III microemulsion window, in which case oil can be solubilized into a microemulsion phase. However, for Gemini surfactants, the ULIFT may be achieved at under-optimum conditions. Surfactant flooding under Type I phase behavior conditions but with ULIFT (Austad *et al.*, 2000) may have a huge advantage over a conventional (Type III) process since complicated phase behavior in the reservoir can be avoided and microemulsion trapping will no longer be an issue. Of course, all these need to be confirmed with further testing and core flood experiments.

5.6 ULTRALOW INTERFACIAL TENSION IN TWO-PHASE MICROEMULSION SYSTEMS

5.6.1 Ultralow Interfacial Tensions and Microemulsion Formation

Research related to microemulsions, formed by anionic surfactants, has been published regularly for many years. This body of work deals with phase diagrams and structural studies but also with interfacial tension between the microemulsion and the excess phase in two- and three-phase systems. The ultralow interfacial tension (ULIFT) observed in these cases are believed to be relevant to two mechanisms.

In three-phase systems, the very low tension is ascribed to a critical behavior of the microemulsion with respect to one of the excess phases (Cazabat *et al.*, 1982). The minimum in tension occurs under conditions around which a surfactant-rich third or "middle" phase is formed. The general features of the variation of ULIFT brought about by variations in salt concentration, temperature and changes in alkane chain length in systems containing a wide range of pure alkylbenzene sulfonates have been extensively

reported in a series of papers by Schechter and Wade (1978). These investigators have concentrated only on producing optimal conditions for ULIFT to occur. Hall (1980), using data obtained with a commercial surfactant mixture, argued that ULIFT in aqueous surfactant / hydrocarbon systems arise from the formation of a liquid crystal surfactant mesophase at the oil-water interface. Franses et al. (1980 & 1982) have studied systems containing pure *p*-(1-hetylnonyl) benzene sulfonate (often referred to as Texas 1). Their work was in accord with and extended the conclusions of Hall's. It was claimed that as the surfactant concentration in solution is increased, the interfacial tension attains a low, plateau value. Micelles are said not to be involved in the production of ULIFT, i.e. micelles are surface inactive since micelle formation is an alternative to adsorption. Similar conclusions (Puig *et al.*, 1985) have been arrived at using pure diethylhexyl sodium sulphosuccinate (AOT) as surfactant.

On the other hand, several authors found that dilute surfactant solution + oil two-phase systems could also display low interfacial tension provided that the CMC is reached in the aqueous phase. Chan and Shah (1980) have proposed a simple 'classical' picture of the occurrence of ULIFT in systems containing commercial anionic surfactant mixtures. It is believed that ULIFT is attained at the CMC of the surfactant in the aqueous phase, and is produced by monolayer adsorption. No mention is made of the production and role of a third phase. Minima in tensions observed as the surfactant concentration increases are attributed to the formation of mixed micelles and the ensuing reduction of monomer concentration. Interesting work has been done on the system SDS + aqueous NaCl + toluene + butonal (Cazabat *et al.*, 1982). In the two-phase regime the authors believe that ULIFT is associated with a 'very thin' adsorbed surfactant layer. Pouchelon *et al.* (1981) pointed out that a low interfacial tension is observed no matter what the concentration of the micelles. They proposed that this low interfacial tension is

due to the layer adsorbed at the interface. Aveyard *et al.* (1986 & 1988) presented interfacial tension measurements for systems containing pure alkane, aqueous sodium chloride, and a pure twin-tailed anionic surfactant (either AOT or p-dihexylbenzene sodium solfonate, DHBS). Their results support the claim that monolayer adsorption at the oil/water interface can produce ULIFT, and the presence at the interface of a third, surfactant-rich phase is not necessary.

5.6.2 Nature of Interface Exhibiting Low Tensions

In our current study, only two-phase systems (Type I microemulsions) were observed from most phase behavior tests for systems containing anionic Gemini surfactant, aqueous NaCl, and pure alkane. The experimentally measured interfacial tensions reached ultralow values under appropriate salinity and temperature conditions, therefore, monolayer adsorption of Gemini surfactants at the oil/water interface is proposed to be the main reason of ULIFT measured from these systems. This is very likely to be true considering the fact that Gemini surfactants are capable of forming a more condensed packing at the air-water interface (Chapter 4). The equilibrium aggregates in these systems are oil-in-water microemulsion droplets. And it should be noted that the droplets themselves are not surface active. The surfactant monolayer adsorbed at the drop surface is the real reason for the surface activity.

With regard to the precipitous fall in interfacial tension observed in systems containing Gemini surfactant *14-4-14* with dodecane and 20wt% NaCl, we have determined tensions ranging from 20 down to ~10^{-3}dyne/cm. These data are presented as interfacial tension versus surfactant concentration in Figure 5.18, and plotted in log-log scale it does appear that the IFT falls drastically just below the aggregation point. We have however obtained a number of IFTs between 5 and 10^{-3}dyne/cm and when these

data are plotted as γ versus C in a semi-log fashion a straight line results. As can be seen in Figure 5.18, at and above the aggregation point the tension remains constant in the range of surfactant concentration investigated. The plateau interfacial tension (surfactant concentration several times higher than CMC) is plotted against the salt concentration for systems containing Gemini surfactant, aqueous NaCl, and dodecane at 55°C in Figure 5.8. And a monotonically decreasing IFT trend was observed with increasing salinity.

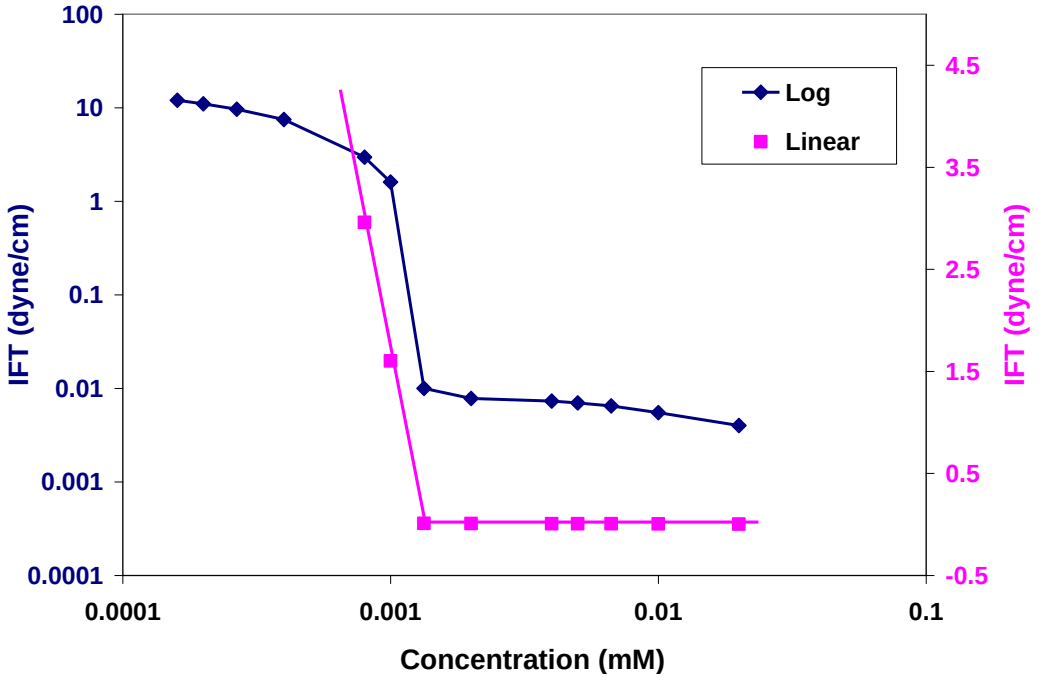

Figure 5.18 IFT vs. *14-4-14* Concentration in 20wt% NaCl Base Solution at 55°C, with Dodecane (n-$C_{12}H_{26}$) as the Oil Phase (log-log and semi-log plots).

The composition of the adsorbed surfactant layer can be determined from the slope of this straight line by Gibbs equation. When a large amount of salt exists in solution, we use the following equation to calculate interface excess,

$$\Gamma_{\max} = -\frac{1}{2.303RT}\left[d\gamma / d\log C\right]_{\max} \tag{5.3}$$

And the minimum area per molecule is,

$$a_{\min} = 10^{16} / N_{Av}\Gamma_{\max} \tag{5.4}$$

From the slope in Figure 5.18, the area per molecule obtained by use of Gibbs equation is found to be 0.75nm^2 for *14-4-14*. A molecular area of 0.66nm^2 was reported for the AOT molecule (Aveyard *et al.*, 1988). Considering the structures of these two molecules, our values reported here should be reasonable.

We concluded from the foregoing that the oil/water interfaces exhibiting ULT investigated here contain a saturated monolayer of surfactant and not a thick intervening layer of a third phase. It is relevant to note that if a third phase were to present the measured tension would presumably be close to the sum of the tensions between the third phase (*m*) and the oil phase (*o*), and the third phase and aqueous phase (*w*). For such systems at equilibrium Widom (1975) has shown that:

$$\gamma_{ow} \leq \gamma_{mo} + \gamma_{mw} \tag{5.5}$$

Thus if the "interface" contained a third phase at equilibrium and the measured tension $\gamma_{mo}+\gamma_{mw}$ were ultralow, it follows from eq. (5.5) that γ_{ow} must also be ultralow. Indeed, for systems consisting of SDS, NaCl, toluene and butanol, Cazabat *et al.* (1982) have shown that γ_{ow} is effectively equal to the higher of γ_{mo} and γ_{mw}, while the lower of the two being very low.

5.6.3 Relation between Aggregate Size and IFT

Assume that the surfactant aggregates consist of monodisperse oil droplets (of radius r_c) coated with an adsorbed monolayer of surfactant, then (Fletcher *et al.*, 1984; Aveyard *et al.*, 1988),

$$r_c = \frac{3Rv_o}{A_D} = r_h - t \tag{5.6}$$

where R=[Oil]/[Gemini] in water. It is assumed that all the surfactant in the bulk aqueous phase is adsorbed at droplet surfaces. The volume of an oil molecule is v_o (~0.376nm^3 for dodecane), and A_D is the area occupied by a surfactant molecule at the drop surface. The hydrodynamic radius r_h, of the droplet differs from r_c by an amount t which is expected to be approximately equal to the surfactant molecular length (~1.9nm for *14-4-14*). If we take A_D to be the area occupied in a close-packed monolayer at the oil/water interface (0.75nm^2 for *14-4-14*), and at 20wt% NaCl roughly 0.02ml of oil has been solubilized into the aqueous phase (from phase behavior test), then R can be calculated as,

$$R = \frac{[\text{Oil}]}{[\text{Gemini}]} = \frac{0.02 \times 0.75/170}{0.2\% \times 2 \times 1/806} \approx 17.8 \tag{5.7}$$

Then r_c=3×17.8×0.376/0.75=26.8nm, so that r_h is calculated to be 28.7nm. This value seems to be in line with literature reported droplet sizes for Type I microemulsion system (8nm to 80nm, Ruckenstein *et. al*, 1975). It is apparent that current equilibrium aqueous phases contain oil are very dilute O/W microemulsions.

Ideally, it should be possible to calculate a series of R values (and thus r_h) corresponding to different salinities. In our phase behavior tests, however, the oil-water interfaces oftentimes show little if any changes, which prevent us from getting accurate and reliable readings. Nonetheless, it has been reported (Aveyard *et al.*, 1986) that for

constant surfactant concentration and temperature, R values depend on salinity, and as salinity increases R increases.

The droplet size and interfacial tension are related through inter-droplet interactions, i.e. the free energy of mixing of the droplets (Ruckenstein, 1981) and a bending energy term (Miller, 1980; Guest *et al.*, 1986). The magnitude of the bending energy depends on the difference between the "natural" and actual radii of the interface, as well as the curvature rigidity. The "natural" radius r_o (Fletcher, 1987) is that adopted by the film in the absence of entropic free energy for droplet mixing, as well as the interaction energy among the droplets. Whenever one phase is predominant, there is a deviation from r_o. The entropy effect favors the formation of a greater number of droplets with radius < r_o. At higher volume fractions of dispersed phase, droplet interactions may also modify the drop size and IFT. In the dilute microemulsion systems studied here, however, these interactions may be assumed to be negligible. If so the major contributions to IFT may well be due to the bending energy and may be written as (Aveyard *et al.*, 1988),

$$\gamma = \frac{2K}{r^2} \tag{5.8}$$

where K is a rigidity coefficient, having dimensions of energy. Eq. (5.8) can only be expected to hold if the interfacial thickness (t) is considerably smaller than r. Our concern here is to test if the equation predicts the trend in IFT with salinity with a reasonable value of K. Measured K values (Aveyard *et al.*, 1988) have been reported at plane interfaces in systems containing SDS, butanol, toluene, and aqueous NaCl. Although K is expected to depend on salt concentration, it is reported that for salinities between 8 and 10%, K/kT only varies between 0.5 and 0.75.

We might, therefore, expect that in the region of minimum IFT (where r is largest), eq. (5.8) will reasonably represent the trend in experimental data with a single value of K, at least for a given microemulsion type. In what follows, a constant value of K=0.75 is used to calculate r. The calculated r and IFT calculated from eq. (5.8), together with experimentally measured IFT values, are listed in Table 5.3. At 20wt% salinity, the drop radius is calculated to be 28.56nm, in good agreement with the hydrodynamic radii r_h (28.7nm).

Table 5.3 Experimental IFT γ_{exp}, Hydrodynamic Radii r_c, and Calculated IFT γ_{cal}, in Systems Containing *14-4-14*, Aqueous NaCl, and Dodecane at 55°C.

Salinity (wt%)	$\gamma_{exp.}$ (dyne/cm)	r (nm)	$\gamma_{cal.}$ (nm)
5	0.650	3.23	0.650
10	0.332	4.54	0.330
15	0.076	9.44	0.076
20	0.007	28.56	0.008

We now perform a simple material balance calculation. Again, considering 20wt% salinity, 0.02ml of oil is solubilized into aqueous phase, and with monodisperse droplets of radius 28.56 nm, the total interfacial area A_{tot} region can be calculated, A_{tot} $=3V_O/r_c=2.1\times10^{18}$nm^2. Divide total area by 0.75nm^2, the total number of Gemini molecules adsorbed at interface can be calculated to be 4.957×10^{-6}mol. 0.2wt% of 2ml *14-4-14* Gemini surfactant solution contains 4.963×10^{-6}mol of molecules. Apparently, all the *14-4-14* molecules are close-packed at the oil droplet surface and effectively reduce the IFT to an ultralow level.

5.6.4 Type I Microemulsion System by Conventional Surfactant

Consider now a Type I microemulsion formed by a more conventional single chain surfactant. At a comparable surfactant concentration level (~ 0.2wt%), this system

can only solubilize a limited amount of oil, similar to the scenario for Gemini surfactants. The IFT values measured for such a system is normally not ultralow. Monolayer adsorption theory would attribute this to a loose packing of surfactant molecules at the interface, or simply a larger surface area per molecule. On the other hand, the area per molecule can be estimated from eq. (5.6), provided that we have information on the drop radius r. Assuming for now that the IFT and r are still related through eq. (5.8), then higher IFT would imply smaller droplet radius, which in turn renders larger surface area A_D. It should be noted, however, that as the drop size gets smaller, the validity of eq. (5.8) is questionable since the entropy effect will come into play in determining drop size and IFT (Ruckenstein, 1981).

Nonetheless, from this qualitative analysis, it is apparent that two-phase systems formed by Gemini surfactants are capable of reducing IFT to an ultralow level because of the tighter interfacial packing, while conventional surfactants cannot pack as tight, resulting in a smaller drop size and higher IFT. The closer packing by Gemini molecules can be ascribed to at least two facts: i) at the intramolecular level the existence of the short spacer group chemically constrains the distance between the two tails; ii) at the intermolecular level the extremely high salinity condition Gemini surfactants can withstand helps screen out the electrostatic repulsion between head groups and thus facilitate even closer packing.

5.6.5 Effect of Salt on IFT for Two-Phase Gemini Surfactant System

A thermodynamic treatment (Aveyard *et al.*, 1985) originally developed and validated for conventional surfactants (e.g. SDS, AOT) was adopted here to explore the effect of salt on interfacial tension minimum for two-phase (Type I microemulsion) systems containing Gemini surfactant / aqueous NaCl / pure hydrocarbon. More

specifically, the conditions under which IFT minima can arise will be investigated, this is of interest because only a monotonically decreasing tread was observed from experiments.

For a system containing a Gemini surfactant (Na_2R_2), pure hydrocarbon (O), and NaCl, the variation of the oil-water interfacial tension γ with surfactant molality (expressed in moles of head groups) m_R is taken to be as shown in Figure 5.19, where the plateau attained at and above the CMC (expressed in moles of head groups), e.g. points A and B, is designated γ_C. For variations in salt concentration, γ_C can potentially pass through a minimum; and the corresponding salinity is called optimal salinity. The object of the present treatment is to obtain an expression for $d\gamma_C/d\ln m_{Na}$ and to show under what circumstances this quantity will diminish (where γ_C reaches extreme value).

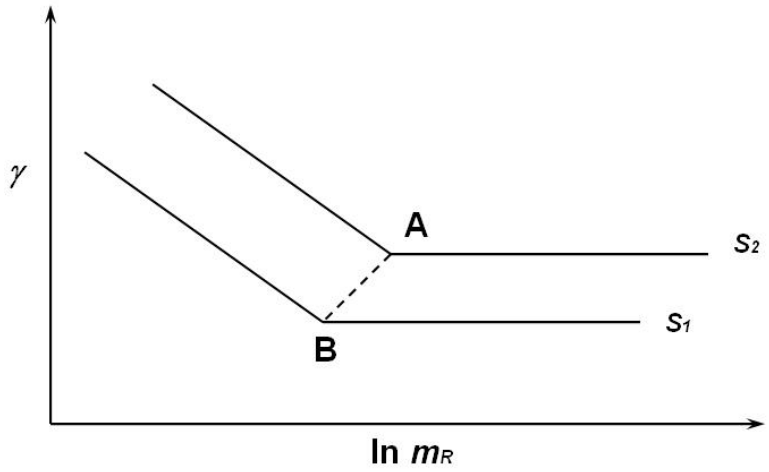

Figure 5.19 Schematic Representation of γ vs. $\ln m_R$ for Salt Concentrations of S_1 and S_2.

The changes in γ_C between points A and B (Figure 5.19) due to the addition of salt at constant temperature is given by performing complete differential of γ_C,

$$\frac{d\gamma_C}{d\ln m_{Na}} = \left(\frac{\partial\gamma_C}{\partial\ln m_{Na}}\right)_{R,T} + \left(\frac{\partial\gamma_C}{\partial\ln m_R}\right)_{Na,T} \cdot \frac{d\ln m_R}{d\ln m_{Na}} \tag{5.9}$$

The terms in parentheses on the right-hand side can be obtained from the Gibbs adsorption isotherm (Adamson *et al.*, 1997),

$$-d\gamma = RT\sum_i \Gamma_i d\ln a_i \tag{5.10}$$

where Γ_i and a_i are surface excesses and the activity of the *i*th ionic species in solution respectively. Eq. (5.10) is rewritten for the Gemini (Na_2R_2) solution containing NaCl as,

$$-d\gamma = RT\left(\Gamma_{Na} d\ln a_{Na} + \Gamma_R d\ln a_R + \Gamma_{Cl} d\ln a_{Cl}\right) \tag{5.11}$$

Here we treat one Gemini as two surfactant monomers (e.g. Na_2R_2=2NaR). Differentiating eq. (5.11) with respect to molar concentration of Na^+ m_{Na}, we obtain,

$$\begin{aligned}\frac{-1}{RT}\left(\frac{\partial\gamma}{\partial\ln m_{Na}}\right)_{R,T} &= \Gamma_{Na} + \Gamma_{Na}\left(\frac{\partial\ln f_{Na}}{\partial\ln m_{Na}}\right)_{R,T} + \Gamma_R\left(\frac{\partial\ln f_R}{\partial\ln m_{Na}}\right)_{R,T} \\ &\quad + \Gamma_{Cl}\left[\frac{m_{Na}}{m_{Cl}} + \left(\frac{\partial\ln f_{Cl}}{\partial\ln m_{Na}}\right)_{R,T}\right]\end{aligned} \tag{5.12}$$

where *f* are the molar activity coefficients.

Tajima (1971) experimentally measured the chloride adsorption on the surface of aqueous solutions containing SDS and varying amounts of NaCl, using direct radiotracer method. Γ_{Cl} was found to be very small or even slightly negative, as might be expected for a surface coated with a monolayer of adsorbed sulfate groups. For the present study of Gemini surfactants having double sulfate head groups ($2R^-$), it would be reasonable to assume Γ_{Cl} is effectively zero at the interface. Also the electroneutrality at the interface requires $\Gamma_{Na}=\Gamma_R$, therefore, eq. (5.12) may be written as,

$$\frac{-1}{RT}\left(\frac{\partial\gamma}{\partial \ln m_{Na}}\right)_{R,T} = \Gamma_R\left[1+\left(\frac{\partial \ln f_{Na}}{\partial \ln m_{Na}}\right)_{R,T}+\left(\frac{\partial \ln f_R}{\partial \ln m_{Na}}\right)_{R,T}\right]$$
$$= \Gamma_R\left[1+\frac{1}{2}\left(\frac{\partial \ln f_{Na}^2 f_R^2}{\partial \ln m_{Na}}\right)_{R,T}\right] = \Gamma_R\left[1+2\left(\frac{\partial \ln f_{\pm}^{Na_2R_2}}{\partial \ln m_{Na}}\right)_{R,T}\right] \quad (5.13)$$

where $f_{\pm}^{Na_2R_2}$ is the mean ionic activity coefficient ($=\sqrt[4]{f_{Na}^2 \cdot f_R^2}$) of Gemini Na_2R_2. For a more concise form, eq. (5.13) can rewritten as,

$$\frac{-1}{RT}\left(\frac{\partial\gamma}{\partial \ln m_{Na}}\right)_{R,T} = \Gamma_R\left[1+\left(\frac{\partial \ln f_{Na}}{\partial \ln m_{Na}}\right)_{R,T}+\left(\frac{\partial \ln f_R}{\partial \ln m_{Na}}\right)_{R,T}\right]$$
$$= \Gamma_R\left[1+2\left(\frac{\partial \ln f_{\pm}^{NaR}}{\partial \ln m_{Na}}\right)_{R,T}\right] \quad (5.14)$$

$f_{\pm}^{NaR}$ is the mean ionic activity coefficient of the "monomer" NaR from the Gemini Na_2R_2. In presence of the swamping amount of salt, it is reasonable to assume that $f_{\pm}^{NaR} = f_{\pm}^{NaCl}$ (Tajima, 1971 and Aveyard *et al.*, 1985).

The second term in parentheses in eq. (5.9) can also be obtained from eq. (5.11) assuming as before that $\Gamma_{Cl}=0$, and is given as,

$$\frac{-1}{RT}\left(\frac{\partial\gamma}{\partial \ln m_R}\right)_{Na,T} = \Gamma_R + \Gamma_R\left(\frac{\partial \ln f_R}{\partial \ln m_R}\right)_{Na,T} + \Gamma_{Na}\left(\frac{\partial \ln f_{Na}}{\partial \ln m_R}\right)_{R,T} \quad (5.15)$$

again, we have $\Gamma_{Na}=\Gamma_R$,

$$\frac{-1}{RT}\left(\frac{\partial\gamma}{\partial \ln m_R}\right)_{Na,T} = \Gamma_R\left[1+2\left(\frac{\partial \ln \ln f_{\pm}^{NaR}}{\partial \ln m_R}\right)_{Na,T}\right] \quad (5.16)$$

In the vicinity of the CMC and in the presence of a large excess of salt, the term $f_{\pm}^{NaR}$ is determined by the salt and so one may assume that $\partial \ln f_{\pm}^{NaR} / \partial \ln m_R$ is negligible.

Combining eqs. (5.9), (5.14) and (5.16), we have,

$$-\frac{d\gamma_C}{d\ln m_{Na}} = RT\Gamma_R\left[1+2\left(\frac{\partial \ln f_{\pm}^{NaCl}}{\partial \ln m_{Na}}\right)_{R,T}+\frac{d\ln CMC}{d\ln m_{Na}}\right] \tag{5.17}$$

where $f_{\pm}^{NaR}$ has been replaced by $f_{\pm}^{NaCl}$ as stated before. Inspection of eq. (5.17) shows that for minimum γ_C,

$$2\left(\frac{\partial \ln f_{\pm}^{NaCl}}{\partial \ln m_{Na}}\right)_{R,T}+\frac{d\ln CMC}{d\ln m_{Na}} = -1 \tag{5.18}$$

Depending on the relative magnitudes of two terms, three different scenarios can be expected for a γ_C versus m_{Na} plot (Aveyard *et al.*, 1985): i) no minimum; ii) a shallow minimum; iii) a very sharp minimum. From the foregoing discussion, it appears that whether or not a minimum tension is observed with respect to salt concentration depends on the magnitude of $d\text{InCMC}/dm_{Na}$, given that $\partial \ln f_{\pm}^{NaCl}/\partial \ln m_{Na}$ is provided. When a minimum does occur, the activity coefficient term is an important factor in determining the salt concentration at which it does so.

In general terms, the form of the γ_C against salt concentration curves arise from the competing effects on the tension when salt is added. At constant m_R, salt addition lowers γ_C according to eq. (5.14). On the other hand, m_R is reduced leading, at constant salt concentration, to an increase in γ_C (Figure 5.19). The form of the γ_C against m_{Na} curves predicted by (5.17) may be obtained by integration with respect to $\text{In}m_{Na}$. At constant Γ_R and temperature, this produces,

$$-\gamma_C = RT\Gamma_R\left(\ln m_{Na}+2\ln f_{\pm}^{NaCl}+\ln CMC\right)+const. \tag{5.19}$$

This requires knowledge of $\partial \ln f_{\pm}^{NaCl} / \partial \ln m_{Na}$ and a very careful determination of the variation of CMC with m_{Na}. For the current study, $f_{\pm}^{NaCl}$ at 55°C has been interpolated from reported experimental data at 25°C and 100°C (Zemaitis *et al.*, 1986).

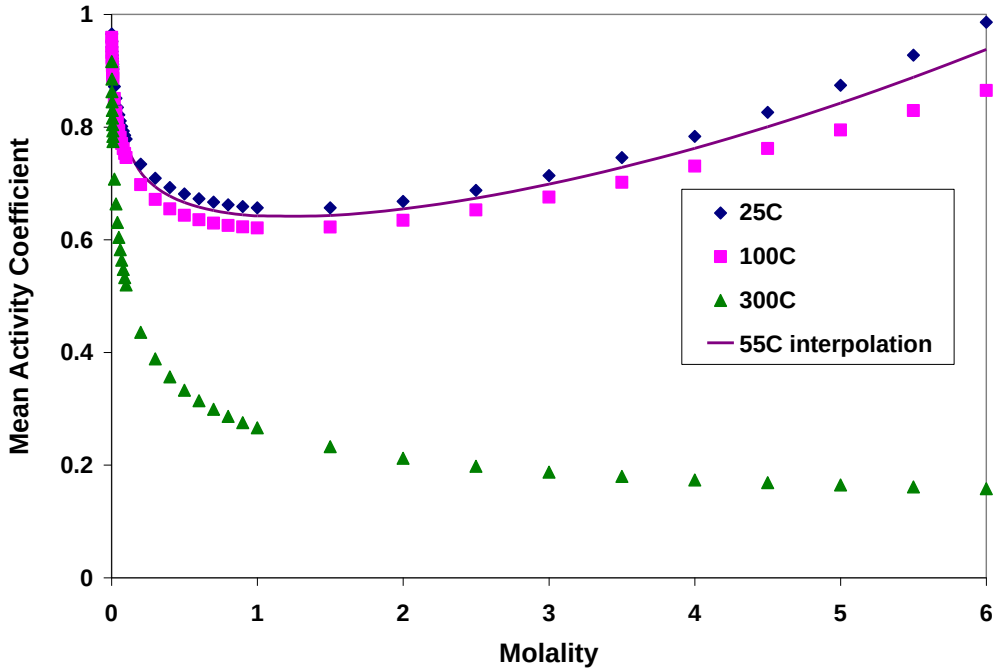

Figure 5.20 Mean Activity for NaCl at different Temperature (data from Zemaitis *et al.*, 1986). (Data at 55°C is interpolated from 25°C and 100°C)

Values of $f_{\pm}^{NaCl}$ at 25°C and below 1M was fitted with a cubic polynomial by Aveyard (1985) and used for a conventional surfactant AOT. For current study, however, data beyond 1M should be used and fitted to a new cubic in Inm_{Na},

$$2\ln f_{\pm}^{NaCl} = 0.1353\left(\ln m_{Na}\right)^3 - 0.0026\left(\ln m_{Na}\right)^2 - 0.0083\ln m_{Na} - 0.8858 \quad (5.20)$$

It can be seen from Figure 5.21 that $2\partial \ln f_{\pm}^{NaCl} / \partial \ln m_{Na}$ is positive and monotonically increasing with m_{Na}. From eq. (5.18), it is apparent that unless $|d\text{InCMC}/dm_{Na}|$ is at least 1, no minimum γ_C appears possible using sodium chloride.

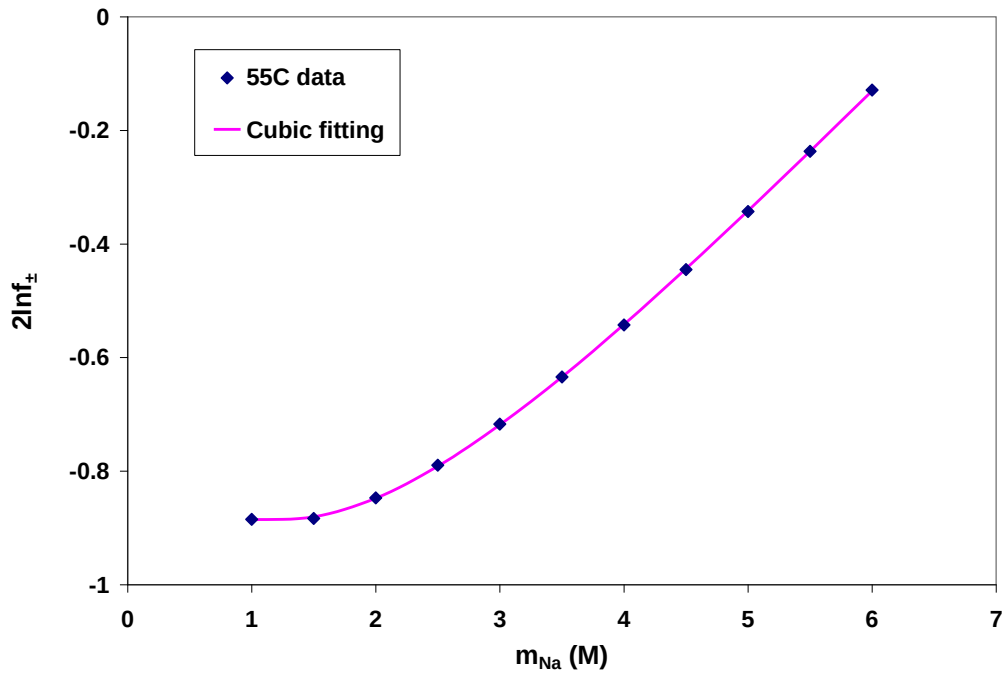

Figure 5.21 Plot of $f_{\pm}^{NaCl}$ vs. m_{Na} by eq. (5.20) for Salinities Greater than 1M.

Furthermore, it was proposed that (Aveyard *et al.*, 1985),

$$\ln CMC = \left(\frac{d \ln CMC}{d \ln m_{Na}} \right) \ln m_{Na} + d_1 \tag{5.21}$$

Combining the above relations, we get:

$$\gamma_C = -RT\Gamma_R \left(\begin{array}{c} 0.1353\left(\ln m_{Na}\right)^3 - 0.0026\left(\ln m_{Na}\right)^2 \\ + \left(0.9917 + \dfrac{d \ln CMC}{d \ln m_{Na}} \right) \ln m_{Na} \end{array} \right) + C_1 \tag{5.22}$$

where constant C_1 is the tension at m_{Na}=1. Eq. (5.22) shows that the form of γ_C curves will be determined primarily by the values of Γ_R and the CMC term.

To test how well eq. (5.19) fits the experimental IFT data for the current system consisting of *14-4-14* / dodecane / NaCl, the variation of CMC with m_{Na} must be carefully determined. IFT measurement results are shown below in Figure 5.22.

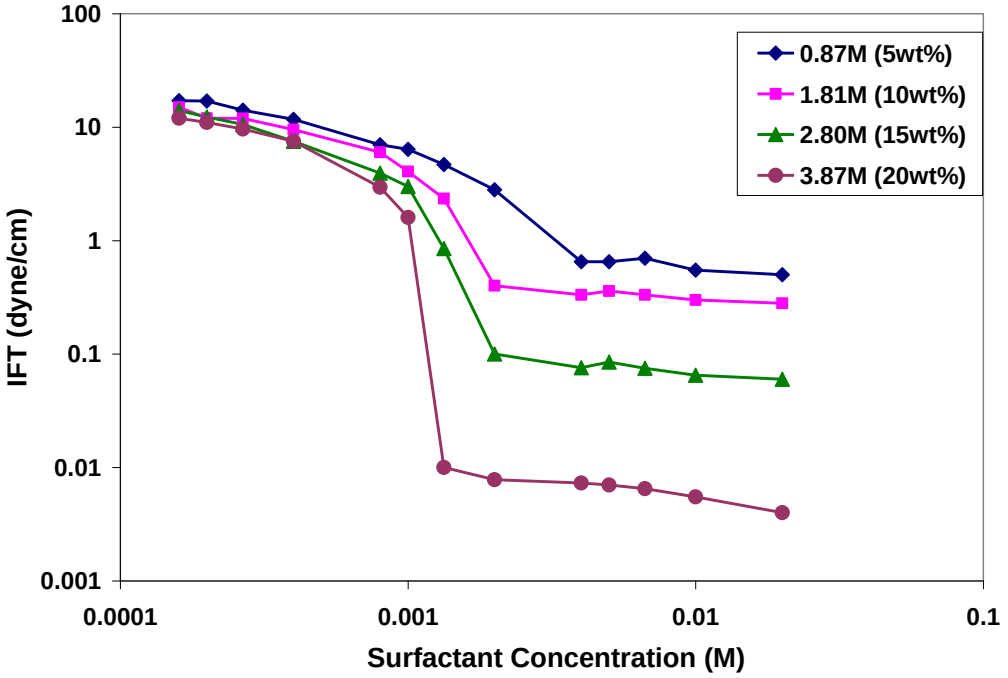

Figure 5.22 IFT Determination of CMC of *14-4-14* in the Presence of NaCl and Excess Dodecane Phase at 55°C.

Table 5.4 Experimental IFT and CMC, in Systems Containing *14-4-14*, NaCl and Dodecane at 55°C.

Salinity (wt%)	Morality m_{Na}	γ_{exp} (dyne/cm)	CMC (mM)
5	0.873	0.6502	0.0026
10	1.806	0.3324	0.0019
15	2.802	0.0757	0.0015
20	3.865	0.0075	0.0013

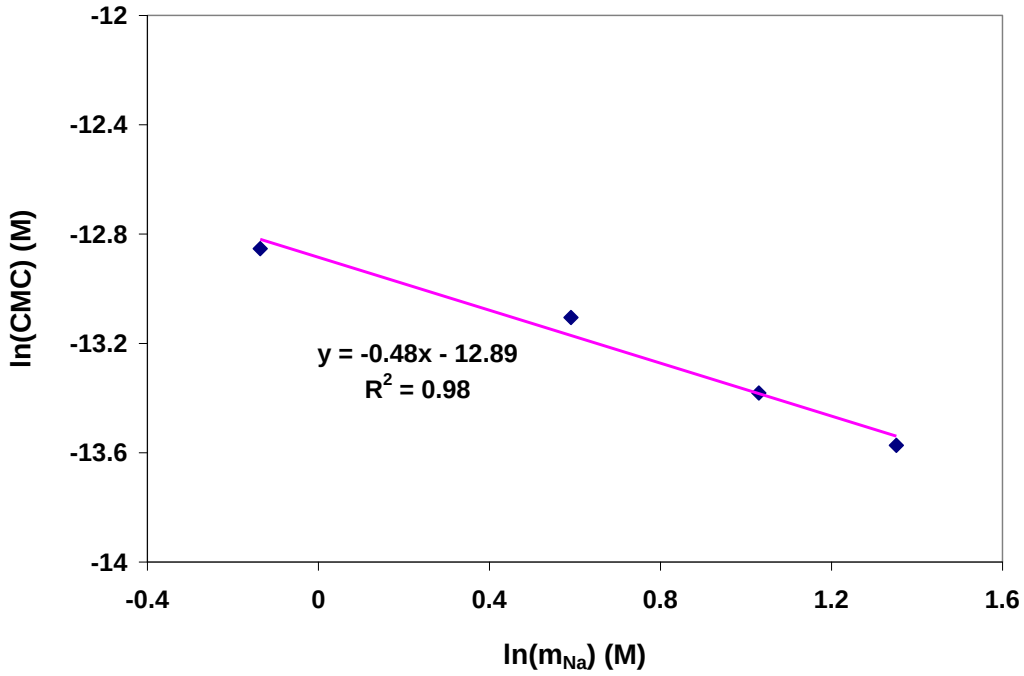

Figure 5.23 Dependence of *14-4-14* CMC on Counter-ion Concentration.

The variation of CMC with salt concentration as shown in Figure 5.23 can be described by the following linear relation:

$$\ln CMC = -0.48 \ln m_{Na} - 12.89 \tag{5.23}$$

$|d\ln\text{CMC}/dm_{Na}|$ determined for *14-4-14* is only 0.48, as discussed above, this value cannot satisfy eq. (5.18),, therefore, a minimum of γ_C is probably not possible for this surfactant with variation of NaCl concentration, at least for the salinity range investigated in this section.

For *14-4-14* Gemini surfactant system, Γ_R as mentioned before can be obtained from the slope of the curves in Figure 5.22, and the resulted values for different salinities are quite close, and is thus taken to be a constant of 2.23×10^{-6}mol/m^2, which corresponds to an area per surfactant molecule of about 0.75 nm^2 (recall section 5.5.2). The full curve in Figure 5.24 is obtained from eq. (5.22) with a constant C_1 of 0.6256 mN/m. The

magnitude of C_1 has been chosen to give the best fit shown. The agreement between experimental IFTs and the curve predicted by eq. (5.22) is at least satisfactory in terms of general trend and order of magnitude. There are however still significant discrepancies which are most likely due to the assumptions that Γ_{Cl} is zero and $f_{\pm}^{NaR} = f_{\pm}^{NaCl}$.

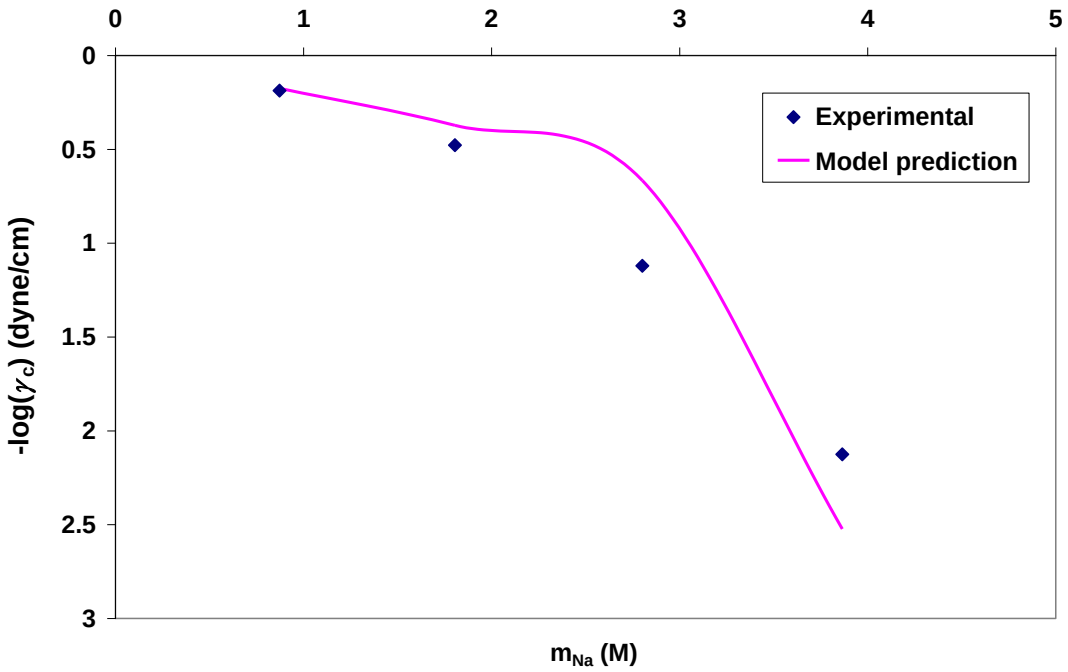

Figure 5.24 Variation of IFT with Salt Concentration at 55°C. (full line from eq. (5.22)).

The monotonically decreasing trend in Figure 5.24 verifies the statement that an IFT minimum is probably not possible for the salinity range investigated here. Moreover, for lower salinity range ($m_{Na} \leq 1$M), Aveyard showed that the maximum value $-2\left(\partial \ln f_{\pm}^{NaCl} / \partial \ln m_{Na}\right)$ is about 0.18, and since -$d$lnCMC/dm_{Na} is only 0.48, eq. (5.18) still cannot be satisfied,, therefore, it is not possible for *14-4-14* systems to reach minimum IFT using NaCl. This statement is again in agreement with our experimental observation.

5.7 SUMMARY

The anionic Gemini surfactants synthesized in the current study have shown their extraordinary tolerance to salinity and/or hardness. Even with extremely high concentration of NaCl (up to 20wt%) and/or $CaCl_2$ (up to 5wt%) present in solution, no phase separation or precipitation of any kind was observed for all the samples prepared. Ultra-low IFT values were observed towards the higher end of the salinity and/or hardness range for Gemini surfactants. Gemini surfactants can thus be potentially used and perform better in higher salinity (more than 10% TDS) and higher temperature (higher than 200 F) environments, which are commonly encountered in oil reservoirs around the world. The molecular interaction between the Gemini and conventional surfactants provide mutual benefits that contribute to aqueous stability and interfacial activity. This leads to a new possibility of making use of Gemini surfactants as co-solvents that help the solubility of the main surfactants, or as co-surfactants that help bring out the best performance of the surfactant mixture.

ULIFT is caused by monolayer adsorption of surfactant molecules at an oil-water interface. The fact that Gemini surfactants can pack more closely at the interface helps the system to reach ULIFT despite a low solubilization ratio. On the other hand, conventional surfactants cannot form an interfacial packing as compact as Geminis, which result in larger surface area per molecule, smaller microemulsion droplet radius and higher interfacial tension. The closer packing by Gemini molecules can be ascribed to at least two facts: i) intramolecular level: the existence of the short spacer group chemically constrains the distance between the two halves; ii) intermolecular level: the extremely high salinity condition Gemini surfactants can withstand helps screen out the electrostatic repulsion between head groups and thus facilitate even closer packing.

A thermodynamic treatment proposed by Aveyard for conventional surfactant systems was adopted here for Gemini surfactants. The *14-4-14* molecule was taken as an example for more in-depth analysis. Starting from Gibbs adsorption isotherm, a condition for the existence of minimum IFT value was derived. Variations of CMC with salt concentration were quantified using IFT measurements and incorporated into the model. The agreement between experimental IFTs and the curve predicted by the model is satisfactory in terms of the general trend and the order of magnitude. The discrepancies are most likely due to the assumptions that go into the model derivation. It appears from the current analysis that a minimum IFT is not possible for the current *14-4-14* / aqueous NaCl / dodecane system, which is in agreement with our experimental observations.

Chapter 6: Rheological Behavior of Anionic Gemini Surfactant in Aqueous Solutions

6.1 INTRODUCTION

Many commercial products used in various industry applications are formulations that contain surfactants. Surfactants are included in these formulations in most cases for their ability to lower the surface or interfacial tension. As shown in previous chapters, Gemini surfactants are superior to conventional surfactants in interfacial tension reduction. Another aspect in which Gemini surfactants could bring significant improvement is the flow behavior of a surfactant-containing formulation. This aspect is crucial for many chemical engineering processes involving mixing, pumping, or extruding. Gemini surfactants introduce new structural variables to control the rheology of surfactant-based formulations.

It is known that surfactant molecules will self-assemble into aggregates in aqueous solution above the critical micelle concentration. In general, the aggregates are round, globular micelles. Under appropriate conditions of concentration, salinity, temperature, presence of counter-ions, etc., spherical micelles can undergo a transition to form flexible wormlike micelles (Cates *et al.*, 1990; Clausen *et al.*, 1992; Lin *et al.*, 1992 & 1994; Walker, 2001; Yang, 2002). The most widely studied micellar solution is CTAB. Halide anions associate only moderately with surfactant cations, and the micellar growth is thus gradual. However, with anions that associate strongly with surfactant cations, such as salicylate ($C_6H_4(OH)COO^-$), wormlike micelles grow rapidly at low surfactant and salt concentrations because salicylate counter-ions can penetrate between the head groups into the hydrophobic interior of micelles and effectively screen the repulsions between head groups. The rheological behavior exhibited by these systems is viscoelastic and

analogous to that observed in polymer solutions. Cryo-TEM images of these solutions clearly show the transition of globular to wormlike or threadlike micelles (Clausen *et al.*, 1992; Lin *et al.*, 1992 & 1994).

Gemini surfactants are created by the covalent linking of two "conventional" surfactants via a spacer. They provide novel and interesting opportunities in investigating surfactant aggregation behaviors. Aqueous solutions of some dimeric surfactants with short spacers can have a very high viscosity at relatively low surfactant concentration whereas the solution of the corresponding monomer remains its low viscosity (Zana, 2002).

In the assemblies formed by Gemini surfactants, the arrangement of the head groups at the interface separating the aqueous phase and the micelle hydrophobic core is very different from that of conventional surfactants. In solutions of conventional surfactants, the head groups are randomly distributed on the micellar surface. The distribution of distances between head groups on these surfaces is a maximum at a thermodynamic equilibrium distance d_T (Figure 6.1a), determined by the competing forces at play in micelle formation. With Gemini surfactants, however, the distribution becomes bimodal (Danino *et al.*, 1995). The head group distance distribution function exhibits a maximum at the thermodynamic distance d_T and another narrow maximum at a distance d_s which corresponds to the length of the spacer (Figure 6.1b). This length depends on the number of atoms in the spacer and its conformation. The bimodal distribution of head group distances and the effect of the chemical linkage on the packing of surfactant alkyl chains in the micelle core are expected to strongly affect the curvature of surfactant layers, and thus the micelle shape and the properties of the solution.

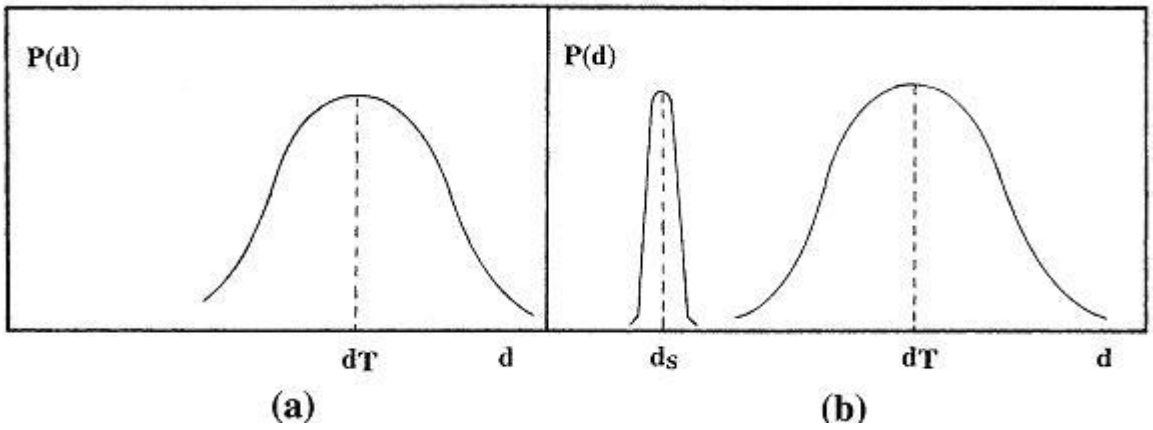

Figure 6.1: Schematics of Head Group Distance Distribution in Micelles of a Conventional Surfactant (a) and of a Gemini Surfactant (b) (Danino *et al.*, 1995).

From a energy viewpoint, the end-cap energy (the energy required to create two end-caps by breaking a spherical micelle) in Gemini surfactant systems can be quite large due to the bulkiness of the twin hydrophobic tails that pack more easily in the cylindrical part of the micelles than in the hemispherical end-caps, thus favoring the growth of longer micelles. Most reports and papers have focused on bis-(ammonium bromide), the most thoroughly studied series of cationic Gemini surfactants.

This chapter deals with solutions of anionic Gemini surfactants with a short spacer, since these molecules represent the most interesting rheological properties. Viscosity measurements are carried out on aqueous micellar solutions of the anionic Geminis synthesized in-house. Effects of surfactant structure and concentration, temperature, additives, and shear rate are investigated.

6.2 GROWTH OF WORMLIKE MICELLES

Even in dilute solution, surfactant self-assemblies can be of different shapes: spherical or cylindrical micelles and vesicles. Complex fluids of long cylindrical micelles share many common structural and dynamical characteristics with polymeric fluids.

Wormlike micelle solutions have been used as thickeners in the oil industry (Maitland, 2000). The rheology of threadlike micelles in solution has been studied (Cates *et al.*, 1990; Rehage *et al.*, 1991) and reviewed (Walker, 2001). Wormlike micelles can be obtained with all kinds of conventional surfactants, but their formation generally requires the presence of salt, co-surfactant, or lipophilic counter-ions. Cylindrical micelles can be obtained with Gemini surfactants in the absence of any additive. The tendency of the micelles to grow is controlled by molecular structure parameters: spacer length (or carbon number *s*) and alkyl chain length (or carbon number *m*).

Micellization is a reversible association process. Wormlike micelles are, therefore, continuously breaking and merging. They are "equilibrium polymers", which means that their average lengths depend on concentration, temperature, and any other thermodynamic state variables. The early models of micellar growth, which neglected inter-micellar interactions, account well for the variation of the average micelle size with the surfactant concentration C and temperature T (Mukerjee, 1972; Israelachivili *et al.*, 1976; Missel *et al.*, 1980).

For large micelles formed by nonionic surfactants, the stepwise self-association model predicts an exponential equilibrium distribution of micelle lengths:

$$C(L) \propto \exp\left(-\frac{L}{\bar{L}}\right) \tag{6.1}$$

where $C(L)$ is the concentration of micelles of length L. The average micelle length, $\bar{L}$ increases with concentration according to,

$$\bar{L} \approx C^{1/2} \exp\left(\frac{E_c}{2kT}\right) \tag{6.2}$$

where E_c is the end-cap energy. It corresponds to the excess energy associated to the larger curvature in the two hemispherical end caps of a micelle. It is also twice the energy necessary to break a wormlike micelle in two and is, therefore, also referred to as scission energy. For dilute solutions of nonionic surfactants, E_c is independent of the aggregation number *N*. It is the enthalpic driving force of growth of wormlike micelles.

For ionic surfactant micelles in salt-free solution, the scission energy contains an electrostatic contribution (repulsion) that favors the breaking of the micelles. This contribution decreases upon increasing concentration of the surfactant or adding salt, due to the screening of the electrostatic interaction. This means that adding salt leads to an increase of the micelle length. The ionic strength dependence of $\bar{L}$ and E_c and the overall growth of charged wormlike micelles, from very dilute to more concentrated regimes, have been described theoretically (Odijk, 1989; Eriksson, 1990). Starting from a very low concentration, three regimes characterize the growth (Mackintosh *et al.*, 1990).

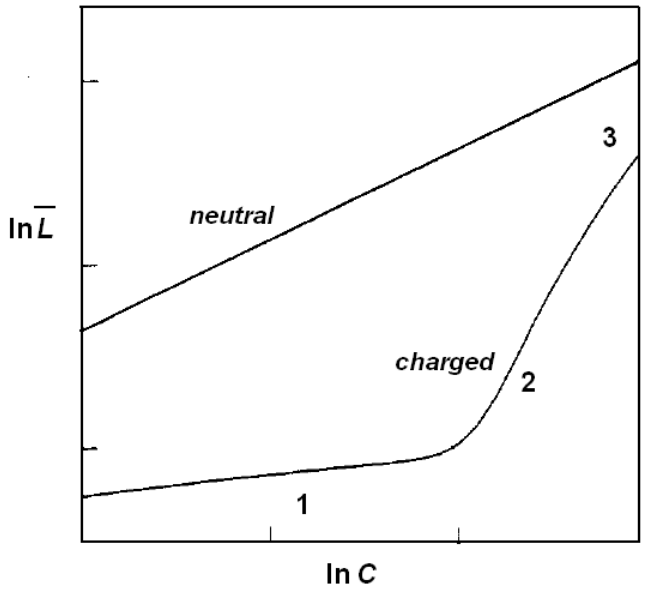

Figure 6.2: Schematics of the Concentration Dependence of the Average Length of Wormlike Micelles (Mackintosh *et al.*, 1990).

At very low concentration such that the Debye length κ is longer than $\bar{L}$, the growth rate is low and the micelles are nearly spherical and monodisperse. As the concentration increases, a sharp crossover to a rapid growth regime occurs when $\bar{L}$ becomes larger than κ. As in the case of neutral micelles, the distribution is large, but the characteristic size $\bar{L}$ grows faster than for neutral micelles. In the third regime, at high concentration, the growth can be characterized by an effective power law, with an exponent close to ½ as for neutral surfactant solutions.

6.3 MATERIALS AND METHODS

As described in Chapter 2, a series of Gemini surfactants of the type referred to below as *m-s-m* were synthesized. The samples used in current study were carefully purified by recrystallization of the crude products in dichloromethane (DCM) twice. Products were checked by ^{1}H NMR spectroscopy at 500 MHz, using D_2O as solvent.

Gemini surfactant solutions were prepared by diluting stock Gemini solution in deionized (DI) water and stirred on a magnetic stirrer at a constant temperature until the product totally dissolved into the solvent. Viscosities of Gemini surfactant solutions were measured by ARES LS-1 (shown in Figure 6.3) from TA Instruments. The ARES is equipped with a thermostat bath for temperature control. This rheometer is suitable for low-viscosity fluid. It measures the torque generated by the sample in response to either an oscillatory or steady-shear strain deformation. The double-wall Couette geometry was used because it can handle low viscosity fluids and it enables the use of relatively small sample volumes.

Figure 6.3: ARES LS-1 Rheometer.

6.4 RHEOLOGY TESTS

As steady-mode tests, transient and steady shear measurements were conducted to quantify accurate steady shear viscosities of various Gemini solutions, while two dynamic-mode tests, strain and frequency sweeps, were performed to investigate viscoelastic properties. The details for each test are described below.

6.4.1 Strain-Controlled Transient Test

The transient test accurately measures the steady-state properties at a constant shear rate during the selected time duration. Four separate zones (where the user defines a shear rate and its time duration) can be programmed to investigate stress growth; time required to reach steady-state flow behavior; and relaxation before and after steady shear. The major purpose of our measurements is to obtain an accurate viscosity at a specific

shear rate. The test is typically run for a shear rate of $10s^{-1}$, with a time-zone schedule of 10-second pause, 50-second measurement, and 10-second pause. The shear steady viscosity at a specific shear rate is obtained by taking an average of the values in the plateau region.

6.4.2 Steady-Rate Test

The steady-rate test was performed to generate flow curves for the fluid sample. This test is conducted by varying magnitudes of steady shear rate, at constant temperature to measure steady viscosities. The shear deformation varies from 0.1 to $1000s^{-1}$, with a 10-second delay before and after measurement, as well as a 10s measurement duration to obtain accurate readings.

6.4.3 Dynamic Strain Sweep Test

The dynamic strain sweep test performs successive measurements at logarithmic step increases in strain, while holding frequency and temperature constant, to determine the limits of the linear viscoelasticity and torque levels. In our experiments, the sweeps are conducted over the range of strain between 1 and 200% at a frequency of 10rad/s to make sure the sample is in the linear viscoelastic region during oscillatory measurements.

6.4.4 Dynamic Frequency Sweep Test

The dynamic frequency sweep test was performed to investigate viscoelastic behavior of samples in the specified range of oscillatory frequencies. Similar to strain sweep, successive measurements at logarithmic step increases in frequency were conducted at constant strain and temperature. At the strain chosen within the linear viscoelastic region in the previous dynamic sweep test, the sweeps were performed over the frequency range between 0.01 and 10rad/s.

6.5 RESULTS AND DISCUSSION

Dilute solutions of ionic and nonionic conventional surfactants usually behave as Newtonian liquids with viscosities only slightly greater than that of water. In contrast to these simple fluids, some Gemini surfactants solutions can exhibit significant viscosity (Zana, 2002). The viscosity of the Gemini surfactant solution is greatly related to the size, shape and organization of micelles in solution, which strongly depend upon the actual packing parameters (Israelachvili *et al.*, 1976) in the micellar assembly. There are many factors that will affect the packing parameters, and thus the viscosity of Gemini surfactants solutions.

6.5.1 Surfactant Concentration

The variation of the viscosity of *14-2-14* solution with surfactant concentration in the absence of added salt at the shear rate of $10s^{-1}$ at $30^{o}C$ is shown in Figure 6.4.

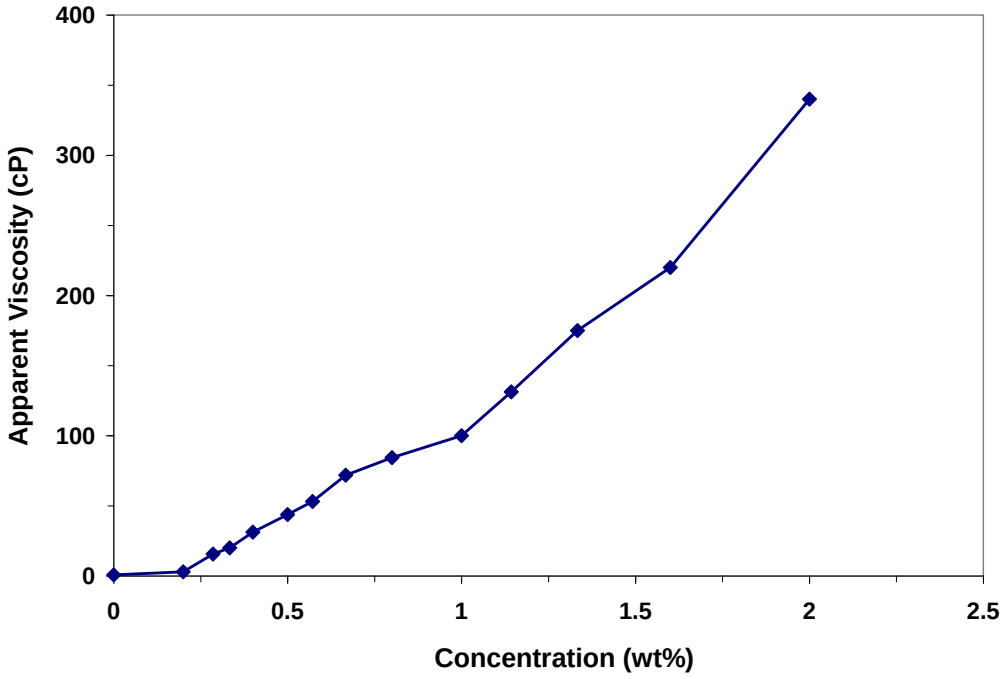

Figure 6.4: Apparent Viscosity Growth of *14-2-14* Solution at $10s^{-1}$ and $30^{o}C$.

The viscosities of dilute conventional surfactant solutions without salt are usually only slightly greater than that of water. However, as can be seen from Figure 6.4, the *14-2-14* solution exhibits high viscosity with increasing surfactant concentration. The turning (or takeoff) point for viscosity growth in the above figure seems to be around 1wt%. Before the turning point, the viscosity increases with concentration moderately, after the turning point, however, the viscosity increases much faster.

The rheological behavior of this system is analogous to that observed for aqueous polymer solutions. Similar trends were also found for the cationic bis-quaternary ammonium Gemini surfactant with a short spacer (Groswasser *et al.*, 2000). For cationic Geminis, the formation of wormlike micelles and entanglement of micelles has been proposed to cause the high viscosity (Han *et al.*, 2004). More recently, the viscosity behavior an anionic Gemini surfactant (ditetradecyldibenzene disulfonate) was studied by Du *et al.* (2007). Their *14-4-14* dibenzene disulfonate Gemini shows a comparable viscosity range and response to concentration. TEM was used to visualize the shape of the micelles at different concentrations, and the viscosity behavior was attributed to the changes of micelle structures/shapes.

Figure 6.5 below is a more complete picture of the viscosity behavior of the current series of sulfate Gemini surfactants. It is apparent that the turning points for *16-4-16* and *18-4-18* are around 1.3wt%. The turning point of *18-2-18* is around 1wt%. And the turning points for 20^{+}-*2*-20^{+} and 20^{+}-*4*-20^{+} are about the same and around 0.5wt%. It is clear that the ability of Gemini surfactants to viscosify solutions improves with alkyl chain length.

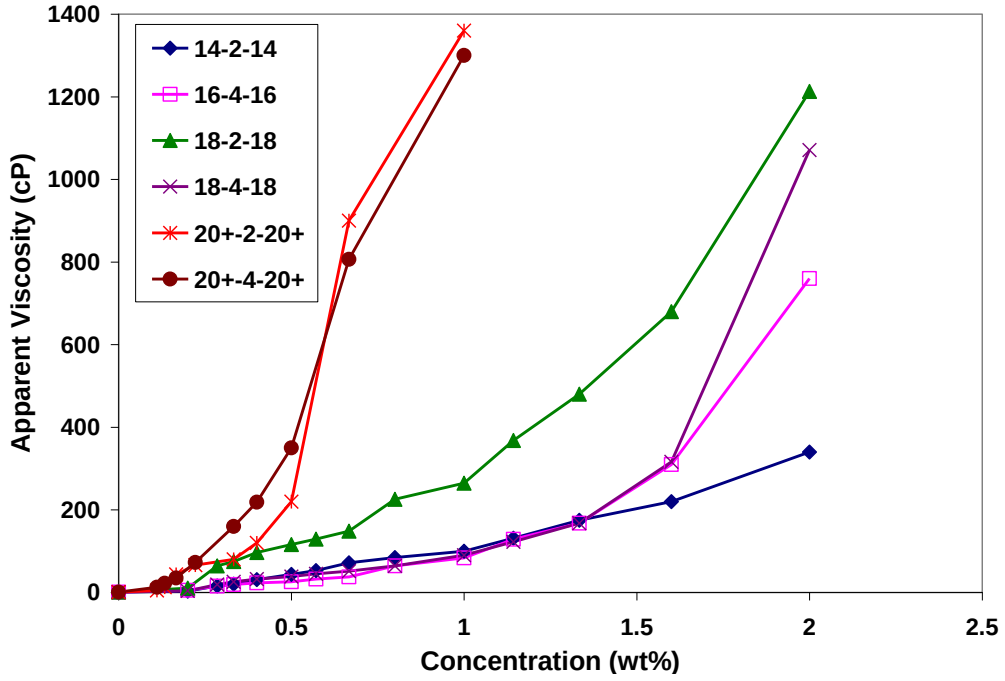

Figure 6.5: Apparent Viscosities of Gemini Solution at $10s^{-1}$ and $30^{o}C$ (linear-scale).

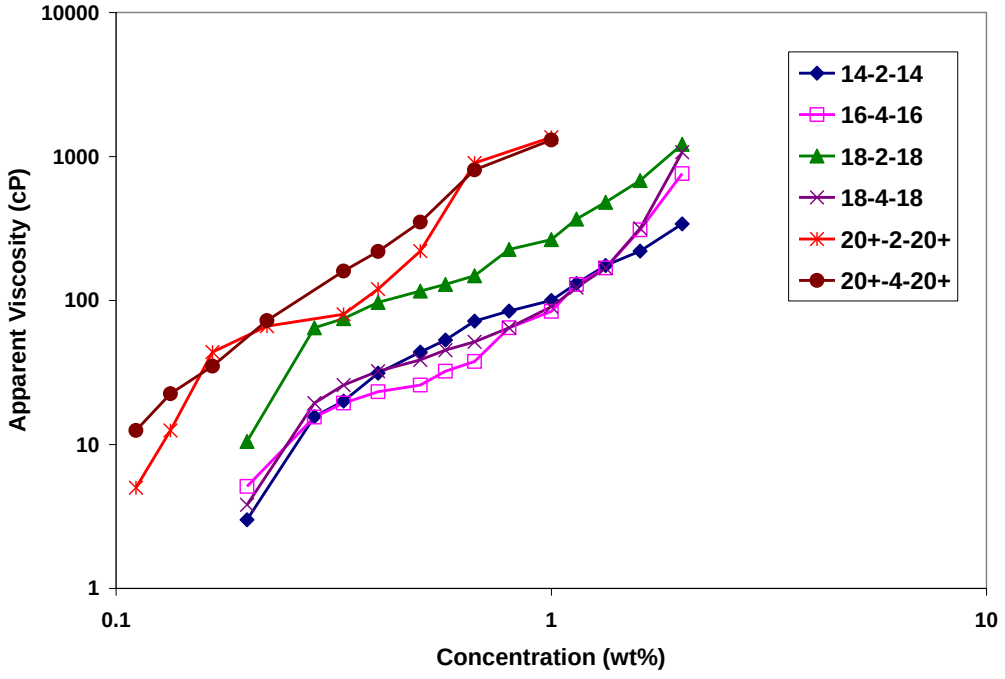

Figure 6.6: Apparent Viscosities of Gemini Solution at $10s^{-1}$ and $30^{o}C$ (log-scale).

The fact that the solution viscosities only increase dramatically when the surfactant concentration reaches certain turning point value C^* reminds us the intersecting point of regions 1 and 2 in Figure 6.2 for ionic surfactants. Thus Figure 6.5 is replotted on a log-log scale in Figure 6.6. Comparing Figure 6.6 with Figure 6.2, for most Gemini surfactants, we do see changes of slope along their corresponding curves, as suggested by the ideal scenario for ionic surfactants outlined in Figure 6.2. The changes, however, are sometimes very small and could almost be neglected, just like the trend for nonionic surfactants. This can be qualitatively explained using the degree of ionization α results obtained from Chapter 3. α values for the entire series of sulfate Geminis lie in-between 0.1 to 0.2. Such a low ionization level near the micelle surface renders a low surface charge density, and these micelles behave similar to those formed by nonionic surfactants.

We propose here a possible picture of micellar structure change that might have caused the viscosity behavior of sulfate Gemini solutions. At low concentration, the micelles are spherical for surfactants with a shorter spacer. However, with an increase in concentration, there is a spherical-to-wormlike micelle transition. The spherical-to-wormlike micelle transition is not abrupt. Both types of micelles may coexist over a range of concentrations. With a further increase in concentration, the number of spherical micelles per unit volume decrease and more and more wormlike micelles form. When the majority of the surfactant is in wormlike micelles, the solutions exhibit viscous behavior as a result of micellar entanglement and the formation of transient micellar networks.

6.5.2 Spacer Group

The viscosities of Gemini surfactants are heavily influenced by the spacer group. A shorter spacer group seems to promote viscosity growth in general as seen in Figure

6.5 and Figure 6.6. It is generally accepted that high viscosity can only be observed for Geminis with shorter spacers (*s* = 2-4) (In *et al.*, 2000; Han *et al.,* 2004). For surfactants with longer spacers, the surface area per surfactant molecule occupied by head groups must be larger than that with a shorter spacer, i.e., there is a smaller packing parameter, which will facilitate the formation of spherical micelles rather than wormlike micelles. With an increase in spacer length, the tendency of spherical micelles formation increases. If the spacer is too long, then the wormlike micelles will not form even at high concentrations. In such cases the viscosity of the Gemini solution remains low.

Gemini surfactants with short spacers may result in the formation of aggregates that are less curved than those formed by the corresponding surfactant monomers with an increase in concentration and the aggregate curvature will also decrease with the increase alkyl chain length *m*. The electron micrographs of a 12.3g/L *12-2-12* (cationic) solution showed entangled wormlike micelles several microns long (Zana *et al.*, 1993; Danino *et al.*, 1995; Groswasser *et al.*, 2000). With increasing *s*, the sequence of structures found for the *12-s-12* series was thus: elongated micelles $\rightarrow$ spheroidal micelles $\rightarrow$ vesicles (Danino *et al.*, 1995). Danino *et al.* (1995) also investigated the micelles of *16-s-16* by Cryo-TEM and found that wormlike micelles, vesicles and bilayer membrane fragments coexisted in 9g/L *16-3-16* solution; entangled wormlike micelles , some open membranes and spheroidal micelles in 34g/L *16-4-16* solution; spherical and slightly elongated micelles in 40g/L 16-6-16 solutions. The sequence of structures of *16-s-16* micelles upon increasing s is: vesicles + elongated micelles $\rightarrow$ elongated micelles $\rightarrow$ spheroidal micelles.

6.5.3 Solution Temperature

Figure 6.7 illustrates the effect of temperature on the viscosities of Gemini surfactant solutions at 0.2wt% concentration and a shear rate of $10s^{-1}$. It is obvious that the solution viscosity shows a strong dependence on temperature.

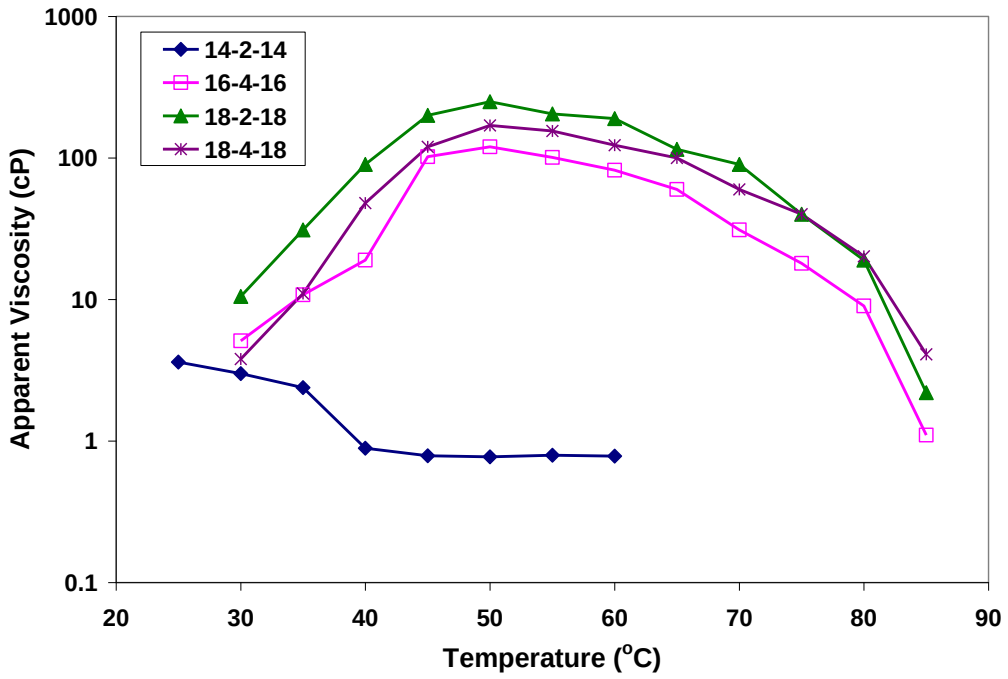

Figure 6.7: Apparent Viscosities of Gemini Surfactant Solution vs. Temperature at 0.2wt% and $10s^{-1}$.

The viscosity of a solution normally decreases with an increase in temperature. This is observed in the current study for the case of *14-2-14*, which has higher viscosity at room temperature (25°C); the viscosity continues to drop as solution temperature goes up, and the viscosity is reduced to the same level as that of the solvent when the temperature exceeds about 50°C. For Gemini surfactants, *16-4-16*, *18-2-18*, and *18-4-18*, however, the viscosity variations with temperature are quite unusual. Starting from room temperature, the viscosity of the solution increases with temperature, and there is a peak

when the temperature reaches about 48-52^{o}C. After this point, the viscosity of the solution goes back to the normal trend and decreases as temperature goes up. In the end, the solution viscosities were close to that of the solvent water. Similar rheological behavior has been observed in conventional surfactant systems (cationic, Mendes *et al.*, 1997; and anionic, Tobita *et al.*, 1997), as well as cationic Gemini surfactants (Han *et al.*, 2004), and were explained by the formation and breaking of wormlike micelles.

At first, it was suspected that the peaking and the decreasing viscosities of sulfate Gemini surfactants might be caused by the chemical instability of sulfate head groups at elevated temperature. But this still does not help explain the unusual increase of viscosity at lower temperature. Moreover, a rheology study by Du *et al.* (2007) using a disulfonate anionic Gemini revealed a similar increasing $\rightarrow$ peaking $\rightarrow$ decreasing viscosity variation as the solution was gradually heated up. This is surprising since sulfonates are much more stable than sulfates within the temperature range of interest. And the micrograph of the 0.2 wt% solution at 65^{o}C shown in Du's study suggests that wormlike micelles turn completely into spherical micelles at that temperature.

Viscosity is a macroscopic representation of the microstructures existing in solution. Therefore, the viscosity variations with temperature are likely to indicate micellar structure changes, and these changes have been successfully visualized using modern microscopy imaging tools (Han *et al.*, 2004; Du *et al.*, 2007). We propose a new picture of micellar structure change that is responsible for the viscosity variation of Gemini solutions as temperature increases. With an increase in temperature, the vesicles or bilayer membrane fragments in the Gemini surfactants system will gradually transit into worm-like micelles and at about 50^{o}C the wormlike micelles take predominance. When the temperature is higher than 50^{o}C, some wormlike micelles will turn into vesicles or spherical micelles, so the network structure is destroyed and the viscosity decreases

with temperature. In the end, viscosity of the solution is almost similar to that of solvent when the temperature is about 85^{o}C. Thus, the viscosity variation with temperature is also related to the changes of micelle shapes.

6.5.4 Shear Rate

When large strains or strain rates are allowed, the rheological behavior is extremely diversified, shear fields being able to induce all kinds of structures, especially in equilibrium structures like long chain polymers (Delshad *et al.*, 2008; Kim *et al.*, 2010) and micelles (Richtering, 2001). Nonlinear rheology of viscoelastic surfactant (VES) solutions has been recently reviewed (Richtering, 2001). Both shear thinning and shear thickening have been experimentally observed for aqueous solutions of the most thoroughly studied cationic Gemini surfactant *12-2-12* (Oda *et al.*, 1997; Oelschlaeger *et al.*, 2002; Weber *et al.*, 2002). Shear thickening is observed for solutions of *12-2-12* for a small concentration window (0.1wt% - 1.8wt%) when the shear rate reaches a critical value $\dot{\gamma}_c$, which is in turn related to the average micelle length. It should be noted, however, that shear thickening depends strongly on the shear and temperature history of the sample (Berret *et al.*, 2000). And it is not a universal behavior for cationic Gemini surfactants (Han *et al.*, 2004).

In our study here, we measured the solution viscosities subjected to a range of shear rates. Figure 6.8 shows the rheological behavior of *16-4-16* solutions (at 30^{o}C) at three different surfactant concentrations and over a wide range of shear rates ($0.1s^{-1}$ – $800s^{-1}$). A classic shear thinning behavior was observed for all concentrations investigated, with a monotonic decreasing viscosity as shear rate increases. Shear-induced thickening was not observed over these concentration and shear rate ranges.

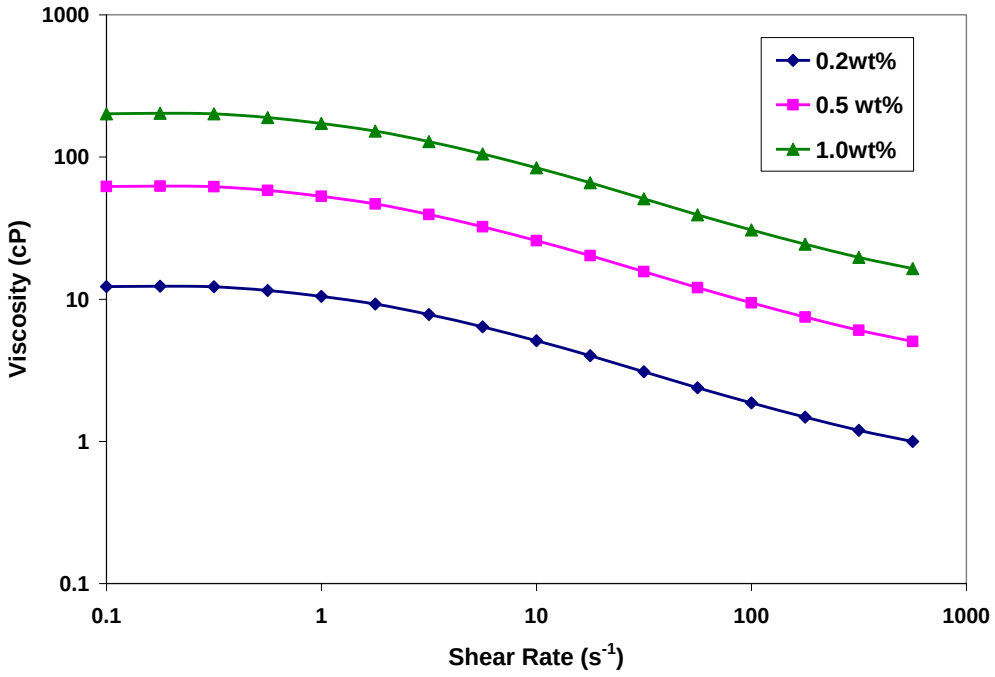

Figure 6.8: Shear Rate Dependence of *16-4*-16 Solution Viscosities at Three Different Concentrations at 30°C.

From Figure 6.8, it is found that *16-4-16* and other members of the current series of Gemini surfactants have an extraordinary ability to viscosify aqueous solutions. At 1.0wt% and a low shear rate of $1s^{-1}$, the viscosity is about 170cP. Recall the unusual temperature response in Figure 6.7, and the fact that all measurements were conducted at 30°C, this high viscosifying capability might disappear under high temperature conditions. More specifically, if we were to fit a power-law model to the viscosity data beyond $1s^{-1}$ for the 1.0wt% case in Figure 6.8, we get $\mu = K\dot{\gamma}^{n-1}$, where $K = 193.5$, $n = 0.6077$. With the high value of K and deviation of n from 1, Gemini surfactant solutions obviously exhibit stronger non-Newtonian properties, as compared to the more Newtonian behavior of most conventional surfactant solutions. The shear-thinning behavior may result from the microstructure change of micelles when the solution is subjected to shear forces.

Figure 6.9 compares the rheological behaviors of aqueous solutions of three different Geminis, all at 1wt% concentration and a temperature of 30°C.

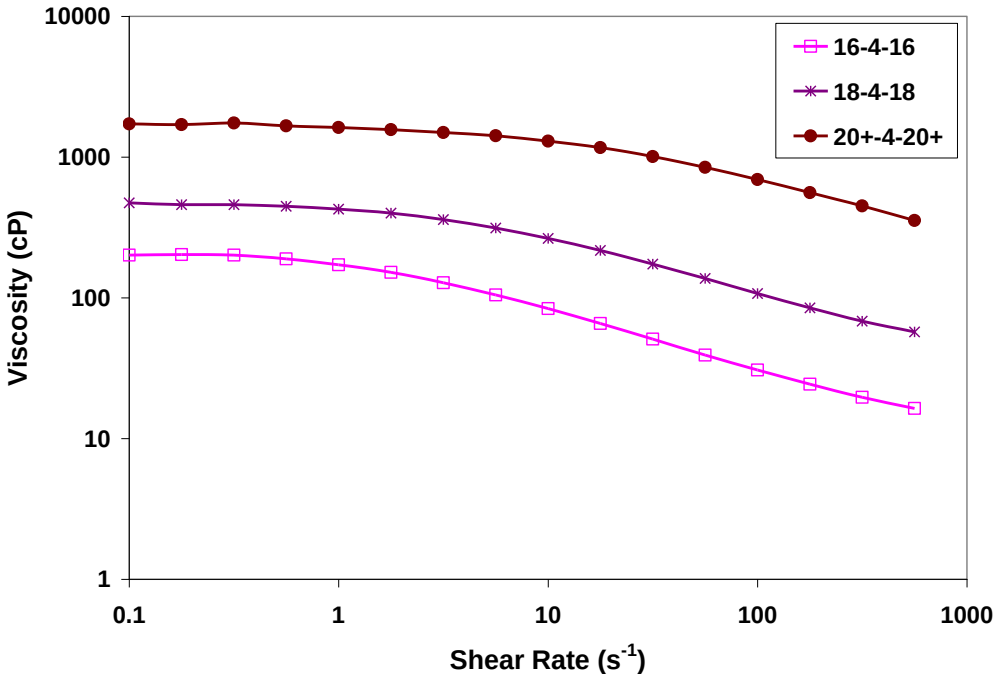

Figure 6.9: Shear Rate Dependence of Solution Viscosities for Three Different Gemini Surfactants at 1wt% and 30°C.

Again only shear-thinning response is seen here and all Gemini solutions show very high viscosity at this temperature and low shear. Also notice that molecules with longer alkyl chains seem to be able to maintain a high viscosity level for a wider shear rate range. This is consistent with our observation from Figure 6.5 that surfactants with longer alkyl chains show higher abilities to viscosify the solution than the ones with shorter chains.

6.5.5 Oscillating Shear Measurements

A strain sweep was performed at frequency of 10rad/s before the test to make sure the sample was in the linear viscoelastic region during oscillating measurements.

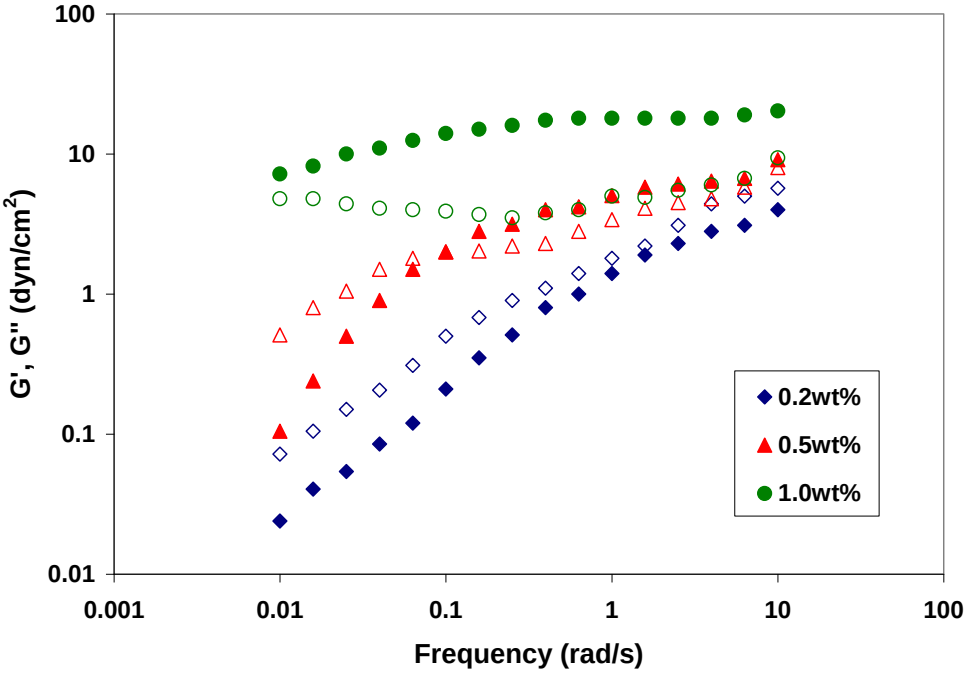

Figure 6.10: Variations of G' (filled symbols) and G'' (open symbols) with Frequency in 16-4-16 Solutions at 30°C.
* The symbols represent 0.2wt% (diamonds), 0.5wt% (triangles), and 1wt% (circles).

The elastic modulus *G'* (storage modulus) and viscous modulus *G''* (loss modulus) of 16-4-16 solutions at different concentrations are shown in Figure 6.10. Both moduli increase with concentration, and for the 0.2wt% solution, the viscous modulus *G''* is always above the elastic modulus *G'* in the examined frequency range, while *G''* is always below *G'* for the solution at 1wt%, which shows very strong elastic behavior. The two moduli intersect in the case of 0.5wt% solution, and the sample exhibits elastic behavior at high frequency, whereas at low frequencies the sample shows a viscous behavior (*G''* exceeds *G'*). This successive change in relative magnitude of elastic and

viscous moduli with increasing surfactant concentration seems to suggest a micellar structure transition from low to high concentration, and agree well with the viscosity measurements shown in Figure 6.6 and Figure 6.8.

6.4.6 Effect of Salt

The addition of salt to surfactant solutions has long been known as an effective way to promote micellar structure changes, which oftentimes are represented macroscopically by a substantial increase in solution viscosity. We have observed high viscosity in pure Gemini aqueous solutions without any salt present. A surfactant concentration scan was repeated on *16-4-16* solutions at 30°C after 6000ppm NaCl was added into the solution. The measured viscosity values are shown in Figure 6.11 for both cases, i.e. pure aqueous solution and saline solution at 6000ppm salinity.

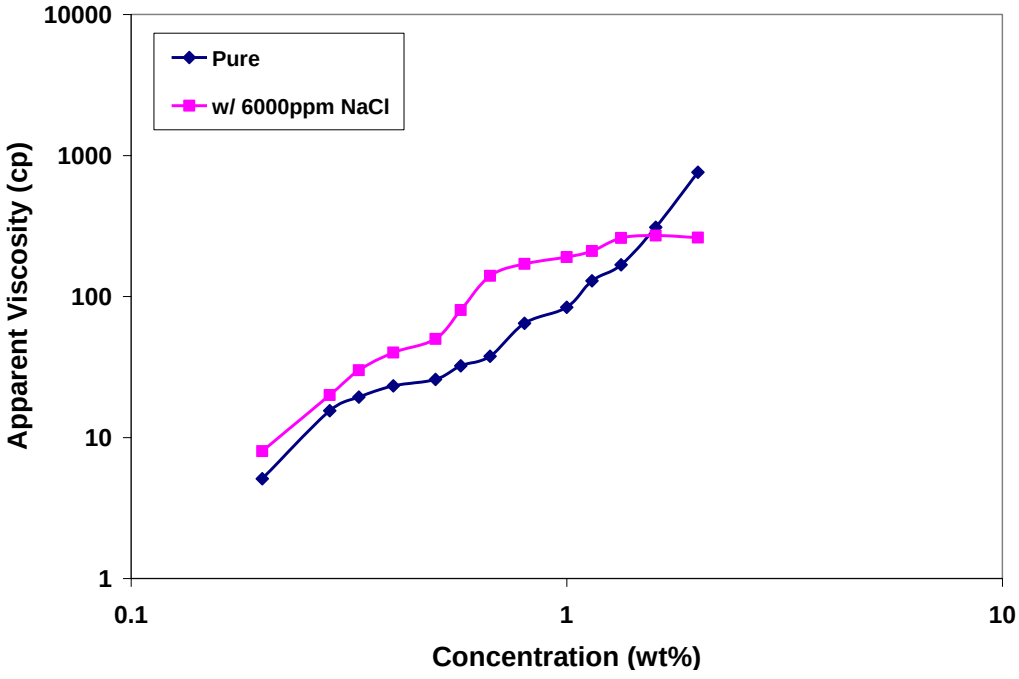

Figure 6.11: Effect of Salt on the Rheology of *16-4-16* Solutions at 30°C and $10s^{-1}$.

With the added salt present in solution, we observe earlier viscosity growth and higher viscosity values over a wide range of surfactant concentration. And finally, towards the higher end of the concentration range, the viscosity growth slows down and stabilizes. A similar trend was observed with solutions of cationic Gemini *12-3-12*, in presence of 0.1M KBr (Zana and Xia, 2004), moreover the turning point (takeoff point of viscosity) was actually reduced by an order of magnitude in that case. The detailed viscosity behavior of Gemini solution with added salt is yet to be further explored. Hong *et al.* (2011) reported a monotonic decreasing viscosity trend when more and more NaCl was added into cationic *14-2-14* solutions.

6.6 SUMMARY

Gemini surfactants with short spacers are capable of giving rise to high solution viscosities at fairly low concentrations, possibly due to the formation of wormlike micelles in solution. These structures bring about interesting rheological properties. The viscosities of solutions increase with increasing concentration, and surfactants with longer alkyl chains and shorter spacer groups have a better ability to viscosify solutions. For some of the sulfate Gemini surfactants, the solution viscosities undergo an unusual maximum with increasing temperature, and then drop down to almost solvent viscosities at higher temperature. All the Gemini solutions show classic shear-thinning behavior within the concentration and shear rate ranges investigated. A transition to more elastic behavior was also observed at higher surfactant concentration. All the rheological behavior observed can be tied back to the unique micellar structure changes observed in Gemini surfactants in aqueous solution.

Chapter 7: Thermodynamic Modeling of Micelle Formation and CMC for Anionic Gemini Surfactants

7.1 INTRODUCTION

Studying surfactant self-assembly in aqueous media from a molecular thermodynamic perspective allows a quantitative prediction of the aggregation behavior of surfactants. Starting from molecular structure and solution condition, such treatment combines the general thermodynamic principles of self-assembly with detailed molecular models for various contributions to the free energy of aggregation. As the direct output, the aggregation behavior of surfactants can be predicted. For the modeling of conventional surfactants, there have been two main advancements in recent years: the original model proposed by Nagarajan and Ruckenstein (1991), and further development from Srinivasan and Blankschtein (2003).

Nagarajan and Ruckenstein (1991) used an approximate analytical solution to the Poisson-Boltzmann equation derived by Evans and Ninham (1983) to calculate the ionic head group interactions. The key assumption in their approach is that the ionic surfactants are fully dissociated and the free counter-ions are present only in the electrical diffuse layer surrounding the micelle, which is at a distance δ away from the hydrophobic core surface. The δ values were estimated to the best of the authors' knowledge based on the size of the ionic head group and the hydrated counter-ion.

Srinivasan and Blankschtein (2003) made an effort to incorporate the effect of counter-ion binding on micelle formation. In their formulations, the counter-ions are allowed to bind onto the micelle surface. The influence of bound counter-ions on various contributions to the free energy of micellization was analyzed. Their model accounted an

important aspect of ionic surfactant aggregation behavior, but ignored the ion specific interactions between head group and counter-ion.

More recently, Moreira and Firrozabadi (2009, 2010) presented an updated model and focused on specific ion effects. More specifically, the counter-ions, released by the surfactant heads and any added electrolytes, are assumed either to bind to the micelle surface or to be distributed in the diffuse region. The charged head groups and counter-ions in the Stern layer are assumed to form solvent-shared ion pairs. They also included ionic specificity in different contributions, including decrease in solubility of hydrocarbons in electrolyte solutions, finite size effect of ions adsorbed at the micellar surface of charge, and mixing entropy due to adsorption of different types of ions, as well as effect of salt addition on solution dielectric constant and density.

For Gemini surfactants, despite the considerable progress recently in the study of their aqueous micellar solutions and extensive experimental data, there has been little effort made so far to set up a model that can adequately describe the effects of the covalent connection by a spacer and head group / counter-ion interaction during micellization. The only attempt made on model development for Gemini surfactants was by Camesano and Nagarajan (2000), for a series of cationic Gemini surfactants. Their model considered various free energy contributions arising from the inclusion of a spacer group into the surfactant structure. The counter-ion binding effect was, however, not properly accounted for, neither was the effect of salt on different solution properties.

Unlike charged solid surfaces, the micelle surface is porous and non-uniform and the micelles are transient, fluctuating entities. This indicates that the surfactant heads are rather widely distributed outside the micelle core. It is thus certainly possible for some counter-ions to penetrate into the Stern layer and accumulate between surfactant heads causing partial neutralization of the charged micellar surface. And this is exactly what we

have observed from conductivity measurements in Chapter 3. The fact that our measured degree of ionization values all lie between 0.1 to 0.2 suggests substantial counter-ion binding taking place at the micelle surface for the current series of Gemini surfactants. This will apparently affect the head group / counter-ion interactions and the arrangement of head groups at the surface, as well as the overall packing of surfactant molecules. A molecular model of micellization that allows for the presence of bound counter-ions within the Stern layer of ionic surfactant micelles is, therefore, needed to capture the complete electrostatic effects associated with the charged micelle-aqueous solvent interface.

In this chapter, we aim to develop a model that keeps the simplicity of the molecular thermodynamic modeling approach introduced by Camesano and Nagarajan (2000) and incorporate the binding effect between head group and counter-ion. Moreover, instead of employing lengthy and complicated optimization algorithms, our model greatly simplifies the computational procedure for minimizing the total Gibbs free energy by utilizing many experimentally measured parameters that are otherwise treated as optimization variables, for instance the degree of ionization α (Moreira *et al.*, 2010).

7.2 THERMODYNAMICS OF MICELLIZATION

Consider a surfactant aqueous solution composed of N_W water molecules, N_{sA} Gemini surfactant (A) molecules, and N_{add} ionic pairs of an inorganic salt at temperature T and pressure p. The total Gibbs free energy of the solution is the sum of two contributions: the free energy of formation G_f and the free energy of mixing G_m:

$$G = G_f + G_m \tag{7.1}$$

When globular micelles form, usually they are narrowly dispersed in size. , therefore,, we use the maximum-term approximation as has been routinely employed in the calculations of micellar solutions (Nagarajan, 1991 & 2003; Moreira *et al.*, 2009 & 2010). This can also be interpreted as implying that the aggregates constitute a pseudophase in equilibrium with the single dispersed surfactant molecules. Then, we may write the free energy of formation as:

$$G_f = N_W \mu_W^o + N_{1A} \mu_{1A}^o + \sum_i N_i^{free} \mu_i^o + N_g \mu_g^o \tag{7.2}$$

where μ_l^o is the standard state chemical potential of the species *l*. The subscript *W* refers to water, 1*A* to the singly dispersed surfactant, *i* to inorganic ions from the dissociation of ionic surfactants and added salts, and *g* to the aggregate containing *g* surfactant molecules. N_{1A} stands for the number of surfactant monomers in solution. N_i^{free} is the number of ionic species *i* free in solution. N_g denotes the number of micelles composed of *g* surfactant molecules. The standard state chemical potential of water is defined here as pure water. The standard states of all species other than water are taken as those corresponding to infinitely dilute solution conditions.

The free energy of mixing under the maximum term approximation is:

$$G_m = kT\left(N_W \ln X_W + N_{1A} \ln X_{1A} + \sum_i N_i^{free} \ln X_i^{free} + N_g \ln X_g \right) \tag{7.3}$$

where *k* is the Boltzmann constant, and X_l is the mole fraction of the species *l*:

$$X_l = \frac{N_l}{N_W + N_{1A} + \sum_i N_i^{free} + N_g}, \text{ for } l = W,\ 1\text{A},\ i,\ g \tag{7.4}$$

The mass balance equations are:

$$N_{sA} = N_{1A} + gN_g \tag{7.5}$$

$$N_i = N_i^{free} + g\left(2\beta_i\right)N_g, \quad \text{for } i = 1,2,3,4,... \tag{7.6}$$

We assume that the counter-ions may adsorb at the monolayer formed by surfactant head groups. The number of counter-ions of species *j* adsorbed to the micelle, per surfactant molecule in the micelle, is referred to as the degree of counter-ion binding and is denoted by $2\beta_j$ (β_j = 1-α, the fraction of micellar charge neutralized; the factor 2 accounts for the fact that one Gemini molecule contains two head groups).

Let z_A be the valence of the ionic polar head of the surfactant and z_i is the valence the counter-ion, where $z_i = z_1$ if the ionic surfactant is anionic and $z_i = z_2$ if the ionic surfactant is cationic. If the surfactant is anionic, $z_A < 0$, then $N_1 = \left|z_A/z_1\right| N_{sA}$ and N_2=0. And, if the surfactant is cationic, $z_A > 0$, then $N_2 = \left|z_A/z_2\right| N_{sA}$ and N_1=0. In current study, we account for the presence of one inorganic salt in the mixture. Let C_{add} be the molar concentration of inorganic salt added. Assuming that the volume of the solution is primarily determined by the volume of water, one may use the following relation to calculate the number of ion pairs in the mixture N_{add}:

$$N_{add} = \frac{C_{add} N_W M_W}{\rho_{sol}} \tag{7.7}$$

where M_W is the molecular weight of water and ρ_{sol} is the density of the electrolyte solution. Using the mass balance equations, eq. (7.5) and eq. (7.6) into eq(7.2):

$$G_f = N_W \mu_W^o + \left(N_{sA} - gN_g\right)\mu_{1A}^o + \sum_i \left(N_i - 2g\beta_i N_g\right)\mu_i^o + N_g \mu_g^o \tag{7.8}$$

Substituting eq. (7.8) and eq. (7.3) into eq. (7.1):

$$G = N_W \mu_W^o + N_{sA} \mu_{1A}^o - gN_g \mu_{1A}^o + \sum_i N_i \mu_i^o - \sum_i 2g\beta_i N_g \mu_i^o + N_g \mu_g^o + kT\left(N_W \ln X_W + N_{1A} \ln X_{1A} + \sum_i N_i^{free} \ln X_i^{free} + N_g \ln X_g \right) \quad (7.9)$$

Since some of the terms of the expression above depend on fixed variables, we define *G*' as:

$$\begin{aligned} G' &= G - N_W \mu_W^o - N_{sA} \mu_{1A}^o - \sum_i N_i \mu_i^o \\ &= -gN_g \mu_{1A}^o - \sum_i 2g\beta_i N_g \mu_i^o + N_g \mu_g^o \\ &\quad + kT\left(N_W \ln X_W + N_{1A} \ln X_{1A} + \sum_i N_i^{free} \ln X_i^{free} + N_g \ln X_g \right) \end{aligned} \quad (7.10)$$

Reorganizing the expression above and dividing by *kT*:

$$\frac{G'}{kT} = \frac{gN_g}{kT}\left(\frac{\mu_g^o - g\mu_{1A}^o - \sum_i 2g\beta_i \mu_i^o}{g} \right) + N_W \ln X_W + N_{1A} \ln X_{1A} + \sum_i N_i^{free} \ln X_i^{free} + N_g \ln X_g \quad (7.11)$$

Define,

$$\Delta\mu_g^o = \frac{\mu_g^o - g\mu_{1A}^o - \sum_i 2g\beta_i \mu_i^o}{g} \quad (7.12)$$

$\Delta\mu_g^o$ is the difference in the standard chemical potentials between a surfactant molecule present in an aggregate that contains *g* surfactant molecules and $2\beta_i$ adsorbed counter-ions, and singly dispersed surfactants and dissolved ions in water. $\Delta\mu_g^o$ is referred to as the free energy of micellization, which not only depends on the surfactant type, but also on *g*, $2\beta_i$, X_{1A}, C_{add}, aggregate shape, and salt type. The term $\sum 2g\beta_i \mu_i^o$ in eq. (7.12)

represents the contribution from the counter-ion binding effect, which is not properly accounted for in classical studies from Nagarajan (1991).

By using the above definition of $\Delta\mu_g^o$, eq. (7.11) can be rewritten as:

$$\frac{G'}{kT} = gN_g \frac{\Delta\mu_g^o}{kT} + N_W \ln X_W + N_{1A} \ln X_{1A} + \sum_i N_i^{free} \ln X_i^{free} + N_g \ln X_g \qquad (7.13)$$

It is worth noting that the above equation is a more general and complete description of a Gemini surfactant solution containing electrolytes. The inclusion of inorganic ion species here in our study is one step further in modeling the reality (partial dissociation at micellar surface of charge), as compared to the approach adopted by Camesano and Nagarajan.

If the surfactant concentration is lower than the CMC, then *G*' is:

$$\frac{G'}{kT} = N_W \ln X_W + N_{1A} \ln X_{1A} + \sum_i N_i \ln X_i \qquad (7.14)$$

The addition of salts may result in micellar change from spherical to rod-like shape above a certain concentration. The free energy of micellization is defined differently for rod-like micelles. For surfactant concentration range near CMC, however, rod-like micelles are not typically formed and will not be discussed in this study.

7.3 GEOMETRICAL RELATIONS

The critical micelle concentration and the average aggregation number can be precisely estimated by computing the concentrations of the aggregates using the size distribution equation as described earlier. To proceed further and calculate the aggregation behavior of the surfactants, models for the standard free energy differences associated with micelle formation are necessary. This, in turn, requires the specification

of the shapes of the aggregates and of their geometrical characteristics (Israelachvili, 1976 & 2011).

The hydrophobic interiors of the surfactant aggregates are constituted of the surfactant tails. Regardless of the shape an aggregate assumes, no point within the aggregate can be farther away from the aggregate core-water interface than the extended surfactant tail length, denoted as l_{sA}. This implies that at least one dimension of the surfactant micelles should be confined within the limit of $2l_{sA}$ (Tanford, 1973; Israelachvili, 2011). For smaller, spherical micelles, this means the radius of the spherical micelle cannot exceed l_{sA}. When micelles cannot pack into spheres anymore, namely, for aggregation number for which a spherical aggregate will have a radius larger than l_s, and if at the same time the rod-like micelles are not yet favored, small globular aggregates that are not much larger than the largest sphere should form. Israelachvili *et al.* (2011) have suggested globular shapes generated via ellipses of revolution for aggregates in the transition region between spheres and sphero-cylinders.

7.3.1 Spherical Micelles

Small micelles are considered spherical with a radius of the hydrophobic core R_c smaller than or equal to l_{sA} For spherical micelles containing g surfactant molecules, the total volume of the aggregate, V_g, and the aggregate surface area, A_g, are given by:

$$V_g = \frac{4}{3}\pi R_c^3 = 2gv_{sA} \tag{7.15}$$

$$A_g = 4\pi R_c^2 = 2ga \tag{7.16}$$

Notice here that a factor of 2 arises due to the symmetric structure of Gemini surfactants. Here, v_{sA} denotes the half volume of the entire hydrophobic moiety, including

two tail groups and possibly part of the spacer group. For simplicity, we approximate v_{sA} by considering only the single hydrophobic tail of the molecule and similarly, a is defined as the surface area of the aggregate per head group. A geometrical ratio P that characterizes the average molecular packing in the aggregates is defined via the expression:

$$P = V_g / A_g R_c = v_{sA} / a R_c = 1/3 \tag{7.17}$$

The geometrical packing ratio defined by Israelachvili, $v_{sA} / a l_{sA}$, will always be less than equal to 1/3 since $R_c \le l_{sA}$.

7.3.2 Globular Micelles

The micelles whose sizes are moderately larger than allowed by the spherical shape are considered globular, and their average geometrical characteristics are computed as ellipsoids. Since one of dimensions of any aggregate is determined by the extended tail length of the surfactant tail, the semi-minor radius is taken to be R_c=l_{sA}, and the semi-major radius is denoted by b. Note that when b is greater than $3l_{sA}$, the aggregation number will become so large that the micelle has to take on a more elongated configuration, and globule model is not sufficient to describe the geometry. For globular micelles though, R_c and b are related through the eccentricity E of the ellipsoid by:

$$E = \sqrt{1 - \left(R_c / b\right)^2} \tag{7.18}$$

The total volume of the hydrophobic core of the aggregate can be computed from,

$$V_g = \frac{4}{3} \pi R_c^2 b = 2 g v_{sA} \tag{7.19}$$

and the total surface area of the hydrophobic core of the aggregate can be computed from,

$$A_g = 2\pi R_c^2 \left[1 + \frac{\sin^{-1} E}{E(1-E^2)^{1/2}} \right] = 2ga \tag{7.20}$$

Further, the packing factor P for the globular aggregate is given by,

$$P = V_g / A_g R = v_{sA} / aR_c \tag{7.21}$$

Obviously, P will always be great than 1/3.

7.3.3 Molecular Volume and Tail Length Calculations

The molecular volume of the surfactant tail containing n_c carbon atoms is calculated from the group contributions of n_c-2 methylene groups, the terminal methyl group and a -CH- group on the other end.

$$v_{sA} = v_{CH_3} + v_{CH} + (n_c - 2)v_{CH_2} \tag{7.22}$$

These group molecular volumes are estimated from the density data available (Daubert *et al.*, 1988) for aliphatic hydrocarbons. At 25°C, the molecular volume of a methylene group is estimated to be $26.9\,\text{Å}^3$ while that of a methyl group is estimated to be $54.6\,\text{Å}^3$, and that of -CH- to be $20.5\,\text{Å}^3$ (Rand *et al.*, 1968). With available temperature dependency data on methyl and methylene groups, the molecular volumes are calculated from the following relations, while volume of -CH- group is kept constant:

$$v_{CH_3} = 54.6 + 0.124(T - 298) \tag{7.23}$$

$$v_{CH_2} = 26.9 + 0.0146(T - 298) \tag{7.24}$$

where T is in Kelvin. The extended length of the surfactant tail l_s at 198 K has been calculated by Tanford (1973) using a group contribution of 1.265 Å for the methylene and -CH- groups, and 2.765 Å for the methyl group:

$$l_{sA} = 1.50 + 1.265 n_c \tag{7.25}$$

Temperature dependency of l_{sA} is neglected due to absence of relevant information and very small volumetric expansion of the surfactant tail over the range of temperature of interest.

In principle, the presence of different functional groups (e.g. -O-) could affect the free energy terms. The assumption here is that the contribution from these groups will be minor as compared to the much longer polymethylene tail chains, therefore, in all cases, the role of the functional group in a much more complicated Gemini structure is taken to be comparable to that of a $-CH_2-$ unit.

7.4 FREE ENERGY OF MICELLIZATION FOR GEMINI SURFACTANTS

In the molecular thermodynamic modeling approach, the free energy change associated with the formation of the surfactant aggregate is expressed as the sum of several free energy contributions, all of which can be computed given the chemical structure of the various micellar components and the solution conditions:

$$\begin{aligned}\frac{\left(\Delta\mu_g^o\right)_{\text{total}}}{kT} = &\frac{\left(\Delta\mu_g^o\right)_{\text{tr}}}{kT} + \frac{\left(\Delta\mu_g^o\right)_{\text{def}}}{kT} + \frac{\left(\Delta\mu_g^o\right)_{\text{pack}}}{kT} + \frac{\left(\Delta\mu_g^o\right)_{\text{steric}}}{kT} \\ &+ \frac{\left(\Delta\mu_g^o\right)_{\text{int}}}{kT} + \frac{\left(\Delta\mu_g^o\right)_{\text{cover}}}{kT} + \frac{\left(\Delta\mu_g^o\right)_{\text{ent}}}{kT} + \frac{\left(\Delta\mu_g^o\right)_{\text{ionic}}}{kT}\end{aligned} \tag{7.26}$$

For Gemini surfactants, special modifications based on Camesano's study (2000) are made to account for free energy contributions arising from the inclusion of spacer

group. These contributions originate from the fact that a) the spacer shield the hydrophobic core from contact with water, b) the spacer constrains the distance between the head groups, thus imposing non-uniformity charge density at the aggregate interface, c) the spacer prevents the two linked tails from having a packing conformation inside the micelle identical to that of analogous unlinked single chain surfactants, and d) the spacer can be partially buried inside the micelle core provided its length and the molecular interactions allows it.

Besides the aforementioned free energy terms from the spacer group, our current model includes the counter-ion binding effect at the micelles surface of charge as shown in eq. (7.12). A free energy term accounting for the mixing between head groups and counter-ions is also added to the original Nagarajan model. The counter-ions are allowed either to bind onto the micelle surface or to be distributed in the diffuse region (Figure 7.1). The fraction of the counter-ions bound is modeled as being intercalated among the surfactant heads at the micellar surface of charge (dotted line in Figure 7.1). The remaining counter-ions are distributed according to Boltzmann equation in the diffuse region, which lies beyond the Stern layer of steric exclusion. The accumulation of the surfactant coion (e.g. Cl^-) in the Stern layer is negligible due to the strong electrostatic repulsion by the charge of the head groups. More specifically, we assume that the counter-ions adsorbed onto the micelle surface of charge preserve their freedom. The head groups and the bound counter-ions are considered to be arranged randomly and any possible ordering effects are ignored. In the diffuse layer, all the ions are treated as point charges having no physical excluded volume except for a minimum distance of to the charged micelle surface in the context of the Stern layer model.

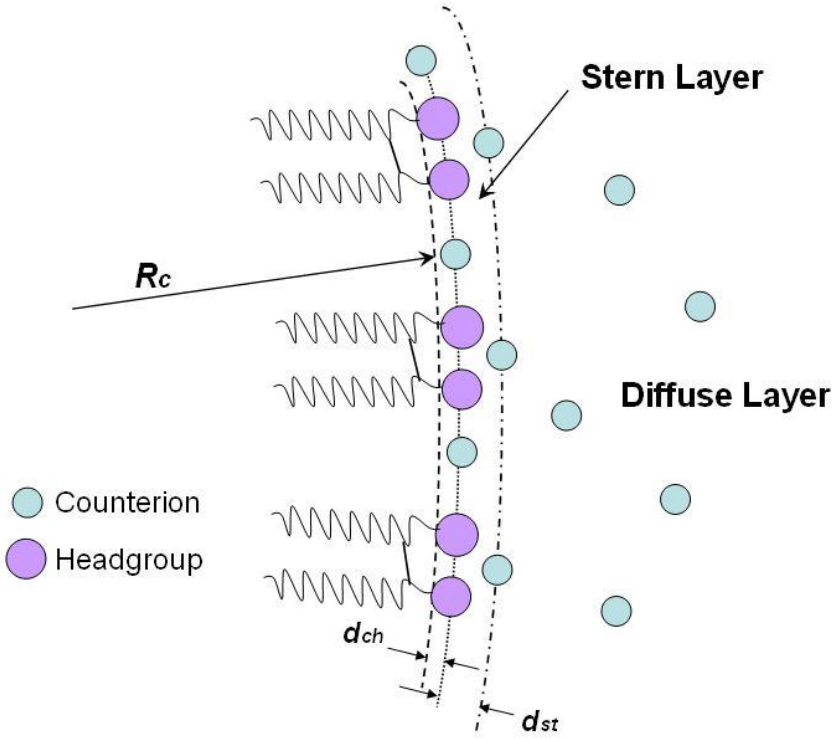

Figure 7.1 Schematics of the Micelle Interfacial Region (Srinivasan *et al.*, 2003). The dashed line marks the radius of the hydrocarbon core (R_c). The adsorbed counter-ions and surfactant head groups are located on the micelle surface of charge represented by the dotted line (R_c+d_{ch}). The Stern surface is represented by the dash-dot line and is located at a distance d_{st} from the micelle surface of charge.

For the ionic free energy calculation, the original Poisson-Boltzmann equation (PBE) is solved for two distinctive scenarios that correspond to experimental conditions under which critical micelle concentrations (CMC) were measured in previous chapters: i) dilute and pure (without any salt addition) solution with Gemini surfactant concentration near CMC, for which the PBE can be linearized and the solution is expressed in modified Bessel functions; ii) Gemini surfactant solutions near CMC with addition of large amount of electrolyte (e.g. NaCl, and $C_{add} \geq 0.1\,\mathrm{M}$), for which an

approximate analytical solution is built upon the work by Evans and Ninham (1983) and modified to take the counter-ion binding effect into account.

Explicit expressions are presented in the following subsections for each of the free energy contributions in terms of the molecular characteristics of the surfactant. For more detailed discussions of these terms, one can refer to Camesano (2000) and Moreira's (2010) papers.

7.4.1 Transfer Free Energy of the Surfactant Tail

When aggregation occurs, the hydrophobic tail of the surfactant is transferred from its contact with water to the hydrophobic core of the aggregate. A negative contribution to the free energy of aggregation accompanies the transfer process. The transfer free energy $\left(\Delta\mu_g^o\right)_{\text{tr}}$ depends on the temperature T, the number of methyl and methylene groups in the tails, as well as the solution condition.

The addition of salts to the aqueous solution decreases the solubility of hydrocarbons. Carale *et al.* (1994) decompose the transfer of surfactant tails from the aqueous salt solution to bulk hydrocarbon liquid into two steps: (1) the transfer of the tail from the aqueous salt solution to water, and (2) the subsequent transfer of the tail from water to the micelle's interior.

$$\frac{\left(\Delta\mu_g^o\right)_{\text{tr}}}{kT} = \frac{\left(\Delta\mu_g^o\right)_{s/w}}{kT} + \frac{\left(\Delta\mu_g^o\right)_{w/hc}}{kT} \tag{7.27}$$

The free energy change in the first transfer step is estimated using the McDevit-Long theory (McDevit and Long, 1952) and the second transfer step can be estimated from solubility data of hydrocarbons in water.

$$\frac{\left(\Delta\mu_g^o\right)_{s/w}}{kT} = -k_s C_{add} \tag{7.28}$$

where k_s is the salting-out constant which depends on a particular salt. Moreira (2010) reported the k_s values for some common salts.

Table 7.1 Salting-Out Constants from Moreira (2000).

Salt	k_s **(L/mol)**	**Salt**	k_s **(L/mol)**
LiCl	0.141	KBr	0.119
NaCl	0.195	KI	0.066
KCl	0.166	NaF	0.254
CsCl	0.088	SO_4^{2-}	0.155

The transfer free energy of the surfactant tail from water to a liquid hydrocarbon state can be estimated from independent experimental data regarding the solubility of hydrocarbons in water (Abraham *et al.*, 1984 & 1988). The expressions for the methylene and methyl group contribution to the free energy of transfer of an aliphatic tail as a function of temperature (absolute) from pure water are

$$\left(\Delta\mu_g^o\right)_{w/hc,\mathrm{CH_3}} \Big/ kT = 3.38\ln T + 4064/T - 44.13 + 0.02595T \tag{7.29}$$

$$\left(\Delta\mu_g^o\right)_{w/hc,\mathrm{CH_2}} \Big/ kT = 5.85\ln T + 896/T - 36.15 + 0.0056T \tag{7.30}$$

The contribution from a -CH- group is assumed to close to that of a methylene group,

$$\left(\Delta\mu_g^o\right)_{w/hc,\mathrm{CH}} \approx \left(\Delta\mu_g^o\right)_{w/hc,\mathrm{CH_2}} \tag{7.31}$$

For Gemini surfactants, the contribution from both tails should be taken into account, as well as the contribution from the portion of the spacer buried within the hydrophobic core. The number of methylene units of the spacer buried in the micelle core is denoted by s_{core}. It is estimated as the difference between the total number of methylene

groups in the spacer s and the minimum number of groups necessary to connect the two head groups separated by the distance $a^{1/2}$, l_{CH2} being the length of a methylene group,

$$s_{\text{core}} = s - a^{1/2} / l_{\text{CH}_2} \tag{7.32}$$

For double chained molecules, intramolecular interactions between the chains exist even in their singly dispersed state, therefore, for such molecules, the transfer free energy of the second tail needs to be estimated. The same estimate is used for the contribution from the buried part of the spacer. A factor accounting for the second tail group, $f_{\text{sec-tail}}$, is introduced here. More specifically, for our in-housed synthesized Gemini surfactants, the total transfer free energy is calculated by including the contributions from the (n_c-2) methylene groups and the terminal methyl group, as well as the other terminal -CH- group of each tail, and the buried methylene groups in the spacer:

$$\begin{aligned}\frac{\left(\Delta\mu_g^o\right)_{\text{tr}}}{kT} = (1+ f_{\text{sec-tail}})\left[\frac{\left(\Delta\mu_g^o\right)_{w/hc,\text{CH}_3}}{kT} + \frac{\left(\Delta\mu_g^o\right)_{w/hc,\text{CH}}}{kT} + (n_c - 2)\frac{\left(\Delta\mu_g^o\right)_{w/hc,\text{CH}_2}}{kT}\right] \\ + f_{\text{sec-tail}} s_{\text{core}} \frac{\left(\Delta\mu_g^o\right)_{w/hc,\text{CH}_2}}{kT} - k_s C_{add}\end{aligned} \tag{7.33}$$

A universal $f_{\text{sec-tail}}$ of 0.6 was used by Nagarajan *et al.* (1991) for different surfactant systems. Theoretically, the value could be affected by the surfactant structure. The two hydrocarbon chains on the same molecule tend to associate with each other so that the hydrocarbon-water interface is reduced. As will be seen later, a decent match for critical micelle concentrations for the current series of Gemini surfactants is achieved by correlating $f_{\text{sec-tail}}$ with surfactant tail and spacer lengths in a linear fashion.

$$f_{\text{sec-tail}} = c \cdot n_c + d \cdot s + e \tag{7.34}$$

c and d are negative constants. Eq. (7.34) is based on the idea that when the surfactant molecule get larger or the spacer group gets shorter, the hydrophobic interaction between the tail chains become stronger, and they will behave more towards a single tail and show less impact on the transfer free energy (as $f_{\text{sec-tail}}$ decreases in eq. (7.33))

7.4.2 Tail Deformation Free Energy

The configurations of the hydrophobic chains in micellar structures are severely constrained (Dill and Flory, 1981) by the spacing filling requirements of the chain segments and the continuity of the chains, as well as by the aggregate geometry. Dill and Flory treated the micelle packing problem using lattice representation for the interior of the aggregate and by considering the placement of the surfactant chains on this lattice. The advantage of a lattice method is that it naturally includes the excluded volume effect and there will be no overlap in space of two different segments. Nagarajan and Ruckenstein (1991) built upon the lattice picture an expression for the free energy due to constrained conformations of the surfactant tail for an aggregate core region. One can refer to their paper for detailed derivation.

It is, however, important to reiterate the physical picture that defines the scope of their model. The use of a lattice requires the specification of the size of the segment which can be placed on the lattice without any orientation constraints. As suggested by Dill and Flory, a suitable segment is that which contains about 3.6 methylene groups. Correspondingly, the linear dimension of a lattice site, denoted by l, is taken equal to about $4.6\,\text{Å}$. This linear dimension also represents the typical spacing between alkane molecules in the liquid state, and hence, l^2 equals the cross-sectional area of a polymethylene chain. And l^3 equals the volume of 3.6 methylene group. Since the volume of the methyl group is twice that of a methylene group, a surfactant tail that contains n_c-1

methylene groups and a terminal methyl group is considered as made up of N segments, where $N = (n_c + 1)/3.6$. One end of the surfactant tail, namely that attached to the polar head group is constrained to be located at the aggregate-water interface. The other end (the terminal methyl group) is free to occupy any position in the entire volume of the aggregate as long as a uniform segment density (Tanford, 1973; Menger, 1979) can be maintained within the aggregate core. Obviously, the chains will be locally deformed in order to satisfy both the packing and the uniform density constraints. The conformational free energy per surfactant tail can be determined by calculating the integral of this local deformation energy over the entire volume of the aggregate.

The packing and deformation free energy expression for spherical and globular micelles is given by:

$$\frac{\left(\Delta\mu_g^o\right)_{\text{def}}}{kT} = 2\left(\frac{9P\pi^2 R_c^2}{80Nl^2}\right) \tag{7.35}$$

for spherical aggregates. The factor 2 arises because there are two tails per molecule. P is the packing parameter defined in previous section.

7.4.3 Packing Free Energy

Equation (7.35) is formulated for conventional surfactant molecules and it does consider the fact that two tails coexist in one Gemini molecule. However, the problem is further complicated by the spacer group. When the spacer is short, it forces the two tails of the molecule to be closer to one another, assuming conformations different from those of two independent molecules unconnected by the spacer, therefore, an additional packing free energy contribution beyond the above deformation energy is necessary to account for the constraint imposed by the spacer. Using the Semenov model (Nagarajan, 1991) for chain segment distribution as a function of the distance from core-water

interface, one can calculate the area occupied by the methylene segments near the core-water interface. This effective area is:

$$a_{eff} = \frac{v_{sA}}{\eta \pi R_c} \tag{7.36}$$

where η is a shape-dependent constant equal to 0.28 for spheres and globules; v_{sA} is the molecular volume of a surfactant tail. R_c is the radius of the sphere or globule. This effective area available for two unconnected chains is not available to the two tails of Gemini molecule because of their connectivity via the spacer. The ratio between the effective area for unconnected chains and the area allowed by the spacer for the connected chains is taken as a measure of the additional packing restriction imposed by the spacer. For a spacer containing *s* methylene groups, the center to center distance of head group is $(s+1)l_{CH_2}$, and this is used to calculate the area allowed by the spacer. On this basis, the following expression is used for the additional packing free energy

$$\frac{\left(\Delta\mu_g^o\right)_{\text{pack}}}{kT} = \ln\left(\frac{a_{eff}}{\left[(s+1)l_{CH_2}\right]^2}\right) \tag{7.37}$$

This free energy contribution is largest for spherical micelles, less for cylindrical micelles, and yet smaller for lamellar aggregates. When $\left[(s+1)l_{CH_2}\right]^2 \geq a_{eff}$, the spacer is long enough to allow the two tails to have conformations equivalent to those of unconnected chains and hence, this contribution ceases to be relevant.

7.4.4 Head group Steric Interactions

The steric free energy contribution accounts for steric interactions between surfactant head groups and adsorbed counter-ions at the micelle-water interface. The

molecules at the micelle surface are treated as components of an ideal localized monolayer:

$$\frac{\left(\Delta\mu_g^o\right)_{\text{steric}}}{kT} = -\left(1+\sum_j 2\beta_j\right)\ln\left(1-\frac{2a_A+\sum_j 2\beta_j a_{h,j}}{2a}\right) \tag{7.38}$$

where a_A and $a_{h,j}$ are the effective cross-sectional areas of the hydrated head group of surfactant A and of the hydrated counter-ions j, respectively; and a is the surface area of the hydrophobic core per surfactant head group. Head group and counter-ions are modeled here as hard spheres occupying areas a_A and $a_{h,j}$ at the micelle core-water interface. Eq. (7.35) reflects the fact that the presence of the bound counter-ions along with the surfactant heads at the micelle surface leads to an increase in the steric repulsions.

Besides the dependence of the effective cross sectional area of the head group on the molecular structures, Moreira and Firoozabadi (2010) showed that the type of the counter-ion at the interfacial region also affects this cross-sectional area a_A. They further proposed that the effective cross-sectional area of the head group is estimated as:

$$a_A = \sum_j \frac{N_j}{\sum_k N_k} a_{A,j} \tag{7.39}$$

where the j and k stand for the counter-ions present in solution. $a_{A,j}$ is the effective cross-sectional area of the head group for the pair composed of surfactant A and counter-ion j. Assume that the head group of the surfactant is spherical, then the radius of the surfactant head group, $r_{A,j}$, can be used to calculate the cross-sectional area, $a_{A,j}$. The estimated effective head group radii are listed in Table 7.2.

Table 7.2 Effective Radius of Head group, $r_{A,j}$ (in nm, from Moreira *et al.*, 2010).

Counter-ion	Alkyl Sulfate	Alkyl Carboxylate
Li^+	0.270	0.254
Na^+	0.273	0.250
K^+	0.277	0.244
Rb^+	0.281	0.242
Counter-ion	**Alkyl trimethylammonium**	**Alkyl Pyridinium**
F^-	0.17	0.21
Cl^-	0.20	0.24
Br^-	0.23	0.26
I^-	0.26	0.30

The cross-sectional area of the counter-ions is obtained from knowledge of the hydrated ionic radii and again the assumption that they are spherical. The counter-ion radii are listed in Table 7.3.

Table 7.3 Hard Sphere Radii of Hydrated Ions (from Moreira, *et al.*, 2000).

ion	$r_{h,j}$ (nm)
Li^+	0.238
Na^+	0.184
K^+	0.123
Rb^+	0.118
F^-	0.166
Cl^-	0.121
Br^-	0.118
I^-	0.119

7.4.5 Formation of Hydrophobic Core-Water Interface

The formation of surfactant aggregates generates an interface between the hydrophobic core region consisting of the surfactant tails and the surrounding water molecules. The free energy associated with the formation of this interface can be taken

into account as the product of the area of the interface and the macroscopic interfacial tension of the aggregate core-water interface.

$$\frac{\left(\Delta\mu_g^o\right)_{\text{int}}}{kT} = \frac{2\sigma_{agg}\left(a - a_A\right)}{kT} \tag{7.40}$$

where σ_{agg} is the macroscopic interfacial tension between bulk hydrocarbon and the aqueous salt solution. a_A can be obtained from eq. (7.39) and radii listed in Table 7.4. The factor 2 arises because there are two head groups per molecule and the free energy is expressed per molecule.

The interfacial tension σ_{agg} is taken equal to the interfacial tension between the aliphatic hydrocarbon of the same molecular weight as the surfactant tail and the surrounding water. The interfacial tension σ_{agg} can be calculated in terms of the surface tensions σ_A of the aliphatic surfactant tail and σ_{salt} of the electrolyte solution via the relation interpolated from experimental data of water/hydrocarbon interfacial tension (Moreira *et al.*, 2000):

$$\sigma_{agg} = 0.7562\left(\sigma_A + \sigma_{salt}\right) - 0.4906\sqrt{\sigma_A\sigma_{salt}} \tag{7.41}$$

where the surface tension is in mN/m. Assume that a linearity variation of the hydrocarbon-aqueous salt solution interfacial tension with salt concentration, similar to the linearity in the variation of the aqueous salt solution surface tension with salt concentration (Weissenborn *et al.*, 1996; Ali *et al.*, 2009). With this in mind, the following relation between σ_{salt} and C_{add} is obtained:

$$\sigma_{salt} = \sigma_W + \left(\frac{d\sigma}{dC_{add}}\right)C_{add} \tag{7.42}$$

The values for $d\sigma/dC_{add}$ are listed in Table 7.5. The experimentally measured surface tension of water as a function of temperature (Vargaftik *et al.*, 1983) can be correlated by the expression:

$$\sigma_w = 235.8\left(1-\frac{T}{647.15}\right)^{1.256}\left[1-0.625\left(1-\frac{T}{647.15}\right)\right] \tag{7.43}$$

where the surface tension is given in dyne/cm and the temperature in Kelvin. The surface tension σ_A can be correlated against the molecular weight of the aliphatic hydrocarbons to within 2% accuracy by the relation (Girifalco *et al.*, 1957)

$$\sigma_A = 35.0 - 325M_{sA}^{-2/3} - 0.098(T-298) \tag{7.44}$$

where M_{sA} the molecular weight of the surfactant tail, T is in Kelvin, and σ_A is expressed in dyne/cm.

Table 7.5 Variation of Surface Tension with Salt Molarity (Weissenborn *et al.*, 1996)

Salt	$d\sigma/dC_{add}$ **(mN/(m M))**
LiCl	2.20
NaCl	2.10
KCl	1.84
KBr	1.425
NaF	2.34
NaBr	1.89

7.4.6 Coverage Free Energy

An additional coverage free energy arises since a part of the spacer is present at the micellar surface, replacing the micelle core-water contact by the micelle core-spacer contact. This extra coverage is a function of the spacer length, and is calculated by assuming a projected area for the spacer on the core surface,

$$\frac{\left(\Delta\mu_g^o\right)_{\text{cover}}}{kT} = \frac{\left(\sigma_{SP} - \sigma_{agg}\right)}{kT} \cdot \left[\left(s - s_{\text{core}}\right) l_{\text{CH}_2} L\right] \tag{7.45}$$

Here, σ_{SP} is the interfacial tension between the spacer and the micelle core (assuming to be zero due to HC-HC contact). The factor (σ_{SP}-σ_{agg}) denotes the interfacial tension difference associated with the displacement of water by the spacer at the core surface. The factor [(s-s_{core})$l_{\text{CH2}}L$] represents the projected area of the spacer covering the micelle surface. Here, L is the close-packed distance between polymethylene chains (0.46 nm), and (s-s_{core})l_{CH2} is the length of the polymethylene spacer.

7.4.7 Head group-Counter-ion Mixing Entropy

This contribution accounts for the entropic gain associated with the mixing of the surfactant heads and the bounded counter-ions at the micelle surface. The ionic heads and bound counter-ions are considered to be arranged randomly on the micelle surface.

$$\frac{\left(\Delta\mu_g^o\right)_{\text{ent}}}{kT} = \ln\left(\frac{1}{1+\sum_j 2\beta_j}\right) + \sum_j 2\beta_j \ln\left(\frac{2\beta_j}{1+\sum_j 2\beta_j}\right) \tag{7.46}$$

7.4.8 Ionic Interactions between Head groups

The free energy of the double layer is equal to the amount of work performed in building up the double layer around the colloidal particle by a reversible and isothermal process. The ionic free energy contribution is accounted for by the double layer free energy of an isolated charged particle (Derjaguin, 1940):

$$\frac{\left(\Delta\mu_g^o\right)_{\text{ionic}}}{kT} = \frac{a_{ch}}{kT}\int_0^{\sigma_o} \phi_o\left(\sigma\right) d\sigma \tag{7.47}$$

where σ_o is the surface charge density at the surface of charge, ϕ_o is the electrical potential at the micellar surface of charge, and a_{ch} is the surface area per surfactant molecule at the micelle surface of charge:

$$a_{ch} = \frac{4\pi R_{ch}^2}{g} \tag{7.48}$$

The radius of the micelle surface of charge, R_{ch}, is calculated using:

$$R_{ch} = R_c + d_{ch} \tag{7.49}$$

The distance between the hydrocarbon core and the center the ionic surfactant head, d_{ch}, is estimated from molecular structure of the surfactant and is given in Table 7.6.

Table 7.6 Distance between the Hydrocarbon Core and the Center of Charge of the Head group (Moreira, *et al.*, 2010)

Surfactant Head group	d_{ch} **(nm)**
alkyl sulfate	0.4
alkyl carboxylate	0.2
alkyl trimethylammonium	0.1
alkyl pyridinium	0.1

Most thermodynamic models available in the literature (Nagarajan *et al.*, 1991; Evans *et al.*, 1983) deal with conventional surfactants and assume complete dissociation between surfactant head group and counter-ion, therefore, this surface change density term is simply, $\sigma_o = e/a_{ch}$. For our current model, the ionic binding effect will be taken into account at the surface of charge, the surface charge density is, therefore:

$$\sigma_o = \frac{e\left(z_A + \sum 2z_j\beta_j\right)}{a_{ch}} \tag{7.50}$$

where e is elementary charge, z_A is the valence of the surfactant head group (z_A=-2 for anionic Geminis), and z_j is the valence of the counter-ion j. For Gemini surfactants, z_A=-2, z_j=1 for sodium salt. $2\beta_j$ denotes the number of counter-ions of species j adsorbed to the micelle, per surfactant molecule in the micelle.

The electrical potential at the surface of charge ϕ_o is determined by solving the Poisson-Boltzmann equation which in spherical coordinates and SI units is given by:

$$\nabla^2\phi = \frac{d^2\phi}{dr^2} + \frac{2}{r}\frac{d\phi}{dr} = -\frac{\sigma(r)}{\varepsilon} \tag{7.51}$$

In the above equation ϕ is the self-consistent electrical potential. The electrical potential depends on the spatial distance from the micelle particle r. $\varepsilon=\varepsilon_o=\varepsilon_{sol}$ is the dielectric constant. And ε_o and ε_{sol} are vacuum permittivity and dielectric constant of the solvent, respectively. The dielectric constant ε_{sol} is the static dielectric constant of the saline solution. In the limit of low salt concentration the dependence of ε_{sol} upon salt concentration can be approximated by a linear relationship:

$$\varepsilon_{sol} = \varepsilon_W + \delta_{salt} C_{add} \tag{7.52}$$

ε_W is available from experimental measurements. For pure water at temperatures ranging from 273.15 to 373.15K:

$$\varepsilon_W = -1.0677 + 306.4670\exp\left(-4.52\times10^{-3}T\right) \tag{7.53}$$

δ_{salt} in eq. (7.52) is a known as the dielectric decrement given in Table 7.7.

$\sigma(r)$ in eq. (7.51) is the charge density at distance r, which is related to the ion number density by:

$$\sigma = \sum_i z_i e n_i \tag{7.54}$$

z_i is the change number of species i; e is the elementary charge. n_i is the number density of species i that obeys Boltzmann statistics:

$$n_i = n_i^{\infty} e^{-\frac{z_i e \phi}{kT}} \tag{7.55}$$

n_i^{∞} is the ion concentration infinitely far (bulk phase) from the charged interface. The total ionic concentration n_i^{∞} is related to the molar concentration c_i^{∞} by the relation,

$$n_i^{\infty} = 10^3 N_{Av} c_i^{\infty} \tag{7.56}$$

where N_{Av} is the Avogadro number.

Table 7.7 Dielectric Decrements δ_{salt} (Giese *et al.*, 1970).

	F^-	Cl^-	Br^-	I^-
Li^+	-11.77	-13.07	-13.57	-14.57
Na^+	-9.17	-11.27	-11.87	-13.07
K^+	-8.67	-9.67	-10.37	-10.77
Rb^+	-7.77	-8.87	-9.07	-10.07
Cs^+	-7.37	-7.87	-8.27	-8.67

For a spherical micelle immersed in an electrolyte solution, combing eqs. (7.51) and (7.54), we get:

$$\frac{d^2\phi}{dr^2} + \frac{2}{r}\frac{d\phi}{dr} = -\sum_i \frac{z_i e n_i^{\infty}}{\varepsilon} \exp\left(-\frac{z_i e \phi}{kT}\right) \tag{7.57}$$

Eq. (7.57) is a second-order differential equation with two boundary conditions. The first boundary condition is that the potential vanishes at infinity, i.e., far away from the charged interface:

$$\lim_{r\to\infty}\phi = 0 \tag{7.58}$$

The second boundary condition gives information about the charged surface. Here, by knowing the charge density at the interface, the electrical field at the interface is calculated to be:

$$\nabla\phi\big|_{r=R_{ch}} = -\frac{\sigma}{\varepsilon} \tag{7.59}$$

This nonlinear PBE (Poisson-Boltzmann equation) is difficult to solve and does not follow the principle of linear superposition for the relationship between the number of charges and the strength of the potential field. Luckily for our application only two special cases of eq. (7.57) are relevant, namely: i) pure and dilute (C_{sA} on the order of 10^{-4}M) Gemini surfactant solutions with no salt added, corresponding to experimental conditions encountered in Chapter 3, CMC measurements using conductivity meter; ii) dilute Gemini surfactant solutions with moderate amount of salt (e.g. $0.1 \le [\mathrm{NaCl}] \le 0.5\mathrm{M}$) added (Chao *et al.*, 1985), corresponding to some of the experiments conducted in Chapter 4. Derivations of solutions to both scenarios are outlined in the Appendices F and G, respectively.

Scenario I: Pure and Dilute Gemini Solutions

For scenario I, due to the low ion concentration in the aqueous solution, eq. (7.57) can be linearized and simplified to the Debye-Hückel equation. The solution has the following form:

$$u(x) = t\frac{x_o^2}{1+x_o}\frac{e^{(x_o-x)}}{x} \tag{7.60}$$

where u is the reduced electric potential, $u=e\phi/KT$; and x is the reduced distance $x=\kappa r$. t has the following expression:

$$t = \frac{e\sigma}{\varepsilon\kappa kT} \tag{7.61}$$

κ is the inverse Debye length, and for Gemini surfactants, it can expressed in,

$$\kappa = \sqrt{\frac{6\times10^3 e^2 N_{Av} C_{1A}}{\varepsilon kT}} \tag{7.62}$$

C_1 is the molar concentration of singly dispersed Gemini surfactant molecules (in mol/L). $K_v(x)$ is the modified Bessel function of the second kind of order v.

The analytic expression for the electrostatic free energy is derived by performing an isothermal charging process (see detailed derivation in Appendix F)

$$\frac{\left(\Delta\mu_g^o\right)_{\text{ionic}}}{kT} = \frac{a_{ch}\sigma_o^2}{2\varepsilon\kappa kT}\frac{\kappa R_{ch}}{1+\kappa R_{ch}} \tag{7.63}$$

Scenario II: Dilute Gemini Solutions with Salt

For scenario II, we assume a moderate concentration of 1:1 type electrolyte (swamping amount compared with surfactant concentration) in the aqueous solution, as a result, the PBE is rearranged into a special form (see Appendix G) and the ionic free energy can be expressed using,

$$\left.\frac{\left(\Delta\mu_g^o\right)_{\text{ionic}}}{kT}\right|_{sph} = \frac{2a_{ch}\sigma_o}{e}\left[\begin{array}{l}\ln\left(\frac{t_o}{2}+\left[1+\left(\frac{t_o}{2}\right)^2\right]^{1/2}\right)-\left(\frac{2}{t_o}\right)\left(\left[1+\left(\frac{t_o}{2}\right)^2\right]^{1/2}-1\right)\\ -\frac{2C}{\kappa t_o}\ln\left(\frac{1}{2}+\frac{1}{2}\left[1+\left(\frac{t_o}{2}\right)^2\right]^{1/2}\right)\end{array}\right] \tag{7.64}$$

The curvature correction term C depends on the geometry of the aggregate and equals $2/R_{ch}$ for spheres and 0 for planar structures. Also,

$$t_o = \frac{e\sigma_o}{\varepsilon\kappa kT} \tag{7.65}$$

and,

$$\kappa = \sqrt{\frac{2\times10^3 e^2 N_{Av} C_{add}}{\varepsilon kT}} \tag{7.66}$$

The surface change density σ based on eq. (7.50) takes into account the counter-ion binding happening at the surface of charge, the underlying assumption to that is a uniformly distributed change density across the spherical micelle surface.

When a short spacer is introduced into the molecular structure, just like the tail groups, the two ionic groups of a Gemini molecule are forced to be closer to one another than they are to the charged groups of adjacent single chain molecules, resulting in a non-uniform charge distribution at the micellar surface. Such a change in surface charge distribution occurs when the extended length of the spacer sl_{CH_2} is less than the mean thermodynamic distance between head groups $a^{1/2}$. The non-uniformity in charge distribution has two additional affects. First, since the nearest charges on the neighboring molecules are farther apart compared to the uniform charge distribution case, the actual electrostatic repulsion energy is reduced by the non-uniform charge distribution. Second, the increased concentration of charges locally in the non-uniform charge distribution case will lead to more counter-ions in the proximity of the head groups. This further reduces the electrostatic repulsive energy in the case of the non-uniform charge distribution. A semi-empirical correction factor F (Camesano *et al.*, 2000) is used to account for the non-uniformity effect and calculate the electrostatic interaction energy to be $(1-F)\left(\Delta\mu_g^o\right)_{\text{ionic}}$, with F given by,

$$F = \left(1 - \frac{sl_{CH_2}}{a^{1/2}}\right)^{\upsilon} \lambda \tag{7.67}$$

The correction factor, $1\text{-}sl_{CH_2}/a^{1/2}$ takes into account the dependence of ionic interaction energy on the distance between the charges (sl_{CH_2} for the non-uniform case compared to $a^{1/2}$ for the uniform case). It is then scaled to account for the curvature of the micelle surface using the ratio λ between the electrostatic free energies calculated for spherical and planar systems assuming uniform charge distributions,

$$\lambda = \frac{\left(\Delta\mu_g^o\right)_{\text{ionic, curved}}}{\left(\Delta\mu_g^o\right)_{\text{ionic, planar}}} \tag{7.68}$$

The exponent υ in eq. (7.67) is an empirical constant that is added to represent the counter-ion condensation at the micellar surface. A constant of 0.9 was used in Camesano's (2000) study, with the constraint that this exponent is used as a universal constant for all Gemini surfactants irrespective of the tail lengths, spacer lengths, and spacer structures. When $sl_{CH_2} >> a^{1/2}$, the charges are uniformly distributed, and $F = 0$.

7.5 COMPUTATIONAL SCHEME

7.5.1 Molecular Constants

Calculations for molecules of the type: *m-s-m* are carried out in the current study for tail lengths of m = 14 to ~23. The free energy model given above was used in the calculations for this series of molecules. Estimates of molecular constants appearing in the above free energy expressions are available from earlier works on conventional surfactants (Nagarajan *et al.*, 1991; Srinivasan *et al.*, 2003; Moreira *et al.*, 2010), such as the molecular volume v_{sA} and extended length l_{sA} of the surfactant tail, the effective cross-sectional area of the hydrated sulfate head groups a_A and that of the hydrated counter-ions

$a_{h,j}$. The usage of all these material properties and constants is illustrated in a detailed working example in Appendix H.

7.5.2 Degree of Ionization

The knowledge of the degree of ionization, α (=1-β) is a prerequisite for the current modeling approach. α values are determined from conductivity measurements in Chapter 3 for pure and dilute Gemini surfactants (Scenario I). For cases where there presents moderate amount of salt in the solution, it is difficult to determine the α values from experiments. The change in slope is typically not seen in the conductivity vs. concentration plot due to the fact that conductivity contribution from the salt itself predominates over the entire concentration range, provided that surfactant concentration is not too high. If we assume, however, that swamping amount of counter-ions Na^+ present in the solution, the dissociation of head groups and Na^+ from the surfactant will greatly suppressed considering the association/dissociation dynamics taking place at the micellar surface of charge. It is, therefore, reasonable and safe to assume that α is fairly small (close to 0 for the extreme). And as will be seen later, it actually provides reasonable estimates on the CMC values for Gemini solutions with salt added. An alternative modeling approach when the degree of ionization is unknown is to treat α (or β) as an independent variable in the Gibbs free energy minimization process, in addition to g and N_g. This will obviously further complicate the optimization process and oftentimes render unreasonable values for α (Moreira *et al.*, 2010). For simplicity, a sufficiently small value of α will be used in the current study when dealing with electrolyte addition.

7.5.3 Gibbs Free Energy Minimization

In order to find the minimum of the total Gibbs free energy of a system consisting of N_W water molecules, N_{sA} Gemini surfactant A molecules, and N_{add} ionic pairs of an inorganic salt at temperature T and pressure p, we proceed with the following algorithm. First, eq. (7.13) is minimized with respect to the independent variables, g and N_g, subject to the material balance constraint under the maximum term approximation (eqs. (7.5) and (7.6)). The result of the minimization of eq. (7.13) is compared with the result of eq. (7.14) and the minimum of the total Gibbs free energy is determined as well as the aggregation number, g, and the number of aggregates in solution N_g.

7.5.4 Calculating the CMC

In order to compare the model predictions to experimental data, we calculate the CMC by constructing a plot of X_{1A} versus the total concentration X_{tot} ($=X_{1A}+gX_g$). The Gibbs free energy minimization is performed for different values of total surfactant concentration. The plot is marked by a change in slope as the concentration reaches the CMC, and an extrapolation procedure is used to determine the total concentration at the CMC ($X_{tot}=X_{CMC}$). Then, the CMC is calculated by the following expression (Moreira *et al.*, 2010):

$$CMC(\text{mM}) = \frac{1000}{\left[\left(\frac{1-X_{CMC}}{X_{CMC}}\right)\left(\frac{M_W}{\rho_{sol}}\right)+\nu_{sA}N_{Av}10^{-24}\right]} \tag{7.69}$$

where v_{sA} is in nm^3 and ρ_{sol} in kg/m^3. The density of the electrolyte solution ρ_{sol} in kg/m^3 for the temperature T in Kelvin is given by (Novotny *et al.*, 1988):

$$\rho_{sol} = \rho_W + AC_{add} + BC_{add}\left(T - 273.15\right) + CC_{add}\left(T - 273.15\right)^2 + DC_{add}{}^{1.5} + EC_{add}{}^{1.5}\left(T - 273.15\right) + FC_{add}{}^{1.5}\left(T - 273.15\right)^2 \quad (7.70)$$

where A through F are specific constants for each salt and the values are provided in Table 7.8, and ρ_W is the water density in kg/m^3 fro the temperature T in Kelvin:

$$\rho_W = 999.65 + 0.20438\left(T - 273.15\right) - 0.06174\left(T - 273.15\right)^{1.5} \quad (7.71)$$

Table 7.8 Constants for Equation (7.70) (Novotny *et al.*, 1988)

Salt	$A\times10^{-2}$	$-B\times10$	$C\times10^{3}$	$-D$	$E\times10^{2}$	$-F\times10^{-4}$
LiCl	0.2446	0.5505	0.8671	0.7927	1.169	1.761
NaCl	0.4485	0.9634	0.6136	2.712	1.009	0
KCl	0.4971	0.7150	0.6506	2.376	0	0
CsCl	1.327	1.511	1.251	3.113	4.181	3.319
KBr	0.9057	1.876	1.425	4.019	5.985	4.092
NaF	0.4940	2.985	3.365	4.752	16.22	18.72
NaBr	0.8362	1.872	1.353	2.847	4.791	3.413

7.6 RESULTS AND DISCUSSION

We apply the model to single Gemini surfactants in water. All seven sulfate Gemini molecules are considered: *14-2-14*, *14-4-14*, *16-4-16*, *18-2-18*, *18-4-18*, *20*$^+$*-2-20*$^+$, and *20*$^+$*-4-20*$^+$. The calculated critical micelle concentrations (CMC) are compared with experimental data. For all molecules listed above, we also present results of CMC values at three different temperatures, 30^{o}C, 40^{o}C, and 60^{o}C (experimental data also available from Chapter 3). The effect of salt concentration on the predicted CMC and comparison with lab results (Chapter 4) are discussed as well for 0, 0.01, and 0.05M of NaCl in aqueous solution.

7.6.1 Influence of Free Energy Contributions on Aggregation

Some general information can be extracted from the free energy model even without performing detailed calculations. For Gemini surfactant molecules, a major contributor to the spontaneous formation of aggregates is the negative transfer free energy. However, the transfer free energy does not depend on the size of the micelle (as can be seen in eq. (7.33)) and thus has no influence on the shape of the aggregate. Two other negative contributions to the free energy come from the coverage and mixing terms, which are also independent of the aggregate size (eq. (7.45) and eq. (7.46)). And when these contributions are large enough in magnitude to ensure that the total free energy change on micellization is negative, the aggregated state of surfactant will be favored compared to the singly dispersed state.

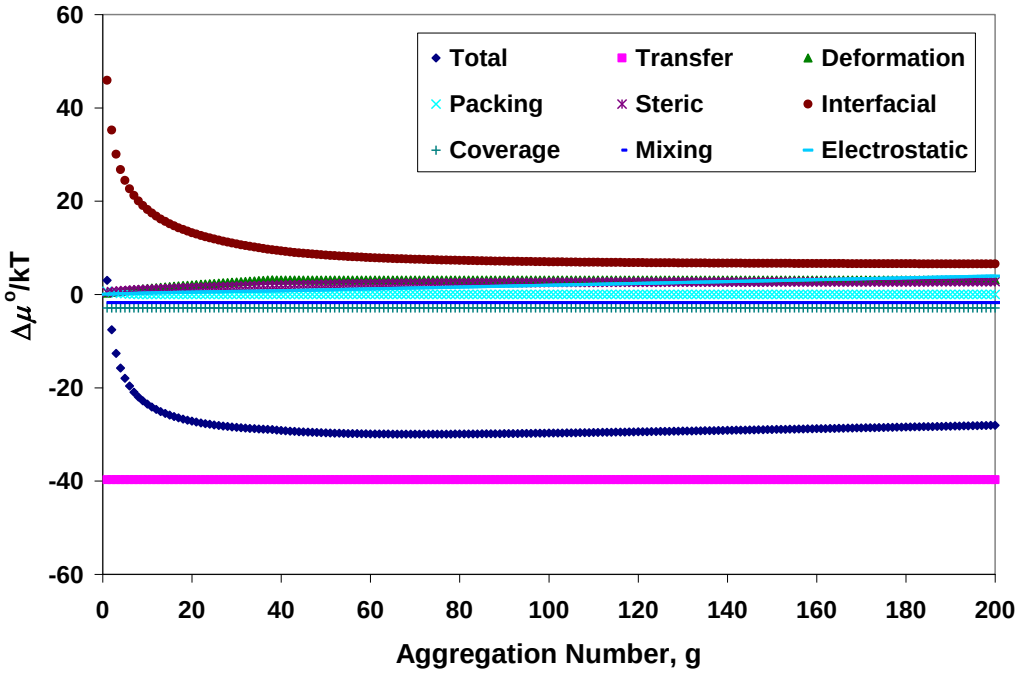

Figure 7.2: Dependence of Individual Free Energy Contributions on Micelle Aggregation Number for *14-4-14* at 30°C.

The calculated individual contributions to the free energy are compared as functions of the micelle aggregation number to determine which terms favor micellar growth (see Figure 7.2 and a zoom-in plot in Figure 7.3).

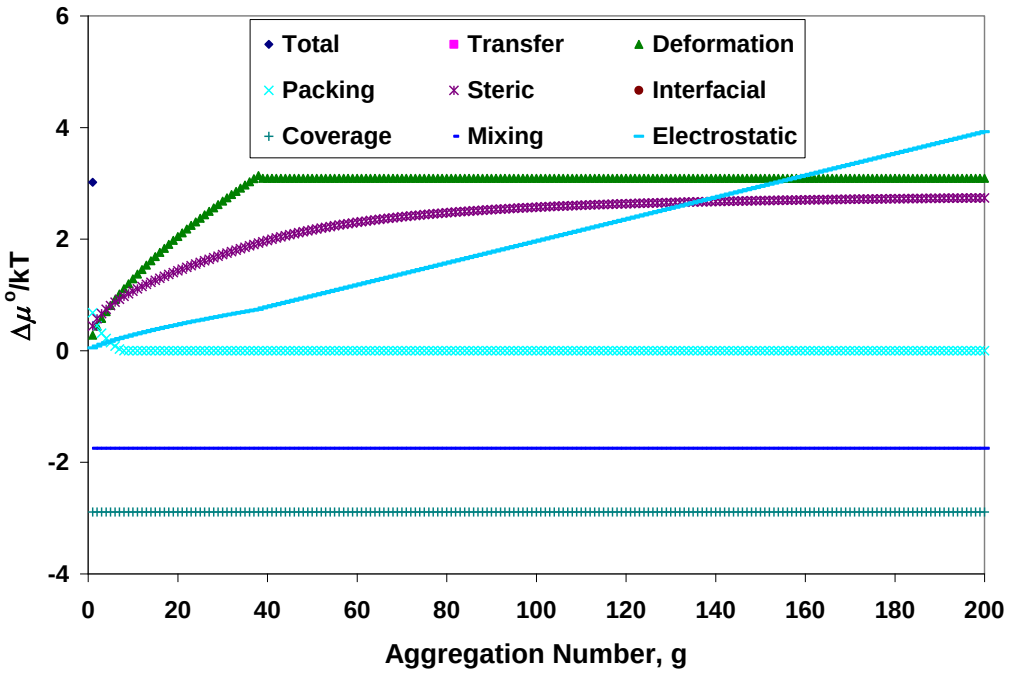

Figure 7.3: Expanded View on Some of the Contributions in Figure 7.2.

The formation of aggregates is made possible by the negative transfer, coverage and mixing free energies. Among the remaining positive free energy contributions, the aggregate core-water interfacial free energy decreases with increasing aggregation number. This is due to the decrease in the area per molecule of the hydrophobic core of the aggregate with increasing aggregation number. This free energy thus favors the growth of aggregates to large sizes. The extra packing free energy also favors the growth since it decreases as micelle size increases. The remaining free energy contributions like surfactant tail deformation energy, the steric repulsion between head groups, and the

ionic interactions between the head groups at the surface of charge increase with increasing aggregation number. These free energy contributions limit the aggregates to finite sizes. All the free energy contributions, however, affect the magnitude of the CMC.

A special note needs to be made here regarding the ionic (electrostatic) free energy term. Compared to the study by Camesano and Nagarajan (2000), the ionic term in the current study is smaller in magnitude. This could be attributed to the fact that we consider counter-ion binding (supported by experimental measurements of rather small α values) taking place at the micellar surface of charge, which effectively reduced the net charge density as compared to Camesano's model where the head groups and counter-ions are assumed to be completely dissociated. As a result, the electrostatic repulsion in the current study is rather small, which favors the aggregation process. And as can be seen later, the micelle aggregation numbers, as a result of the reduced electrostatic repulsion, are much larger in current study than those predicted by Camesano. And our predicted aggregation numbers are more in line with the values reported in the literature for various kinds of Gemini surfactants (Zana and Xia, 2004).

Results in Figure 7.3 suggests that the deformation of the surfactant tails, the steric interaction between surfactant head groups (in presence of counterions), and the ionic interaction energy are the dominant terms in deciding the size and shape micelles will form. Although these free energy contributions are important in the case of conventional ionic surfactants as well (Nagarajan *et al.*, 1993), the existence of spacer in Gemini structure and the severe counter-ion binding taking place in solution make these interaction energies more important because (i) the steric interaction has a higher magnitude when the spacer is short or counter-ions are present in the surface of charge, both of which rending a more ordered structure at micellar surface; (ii) the extra packing contribution arising from the connectivity of the tails via the spacer increases as the

aggregate gets larger; (iii) the ionic interaction energy has a lower magnitude when the spacer is short, or when more counter-ions bind with head groups at surface of charge, but it gets stronger as the effective surface area per surfactant molecule decreases due to the growth of micelle. The coverage term related to the spacer and the mixing term related to the counter-ion binding, while not affecting size and shape, do lower the CMC by making aggregation favorable at a lower concentration.

7.6.2 Origin of Ultra-low CMC

In the framework of current molecular thermodynamic model, there are three negative free energy terms contributing to the formation of micellar structures. In terms of absolute magnitude however, the transfer free energy is the largest free energy term for all the molecules studied. The ultralow CMC of Gemini surfactants can, therefore, be traced to the much larger magnitude of the transfer free energy stemming from both tail chains in one single molecule (see Figure 7.4). The buried part of the spacer can also contribute to this transfer free energy drop when the spacer is long, although none of the molecules examined in the present study had spacers long enough to permit a buried portion (s_{core} in eq. (7.33) was always zero). The mixing of the head groups and counter-ions at the micellar surface of charge also contributes to the aggregation of surfactant monomers. The net result is a much lower free energy per one Gemini molecule, therefore,, even if the free energy per chain (or head group) of a Gemini surfactant is probably still comparable to that of its monomeric counterpart, the free energy per molecule is significantly lower for the Gemini case, implying a much lower CMC.

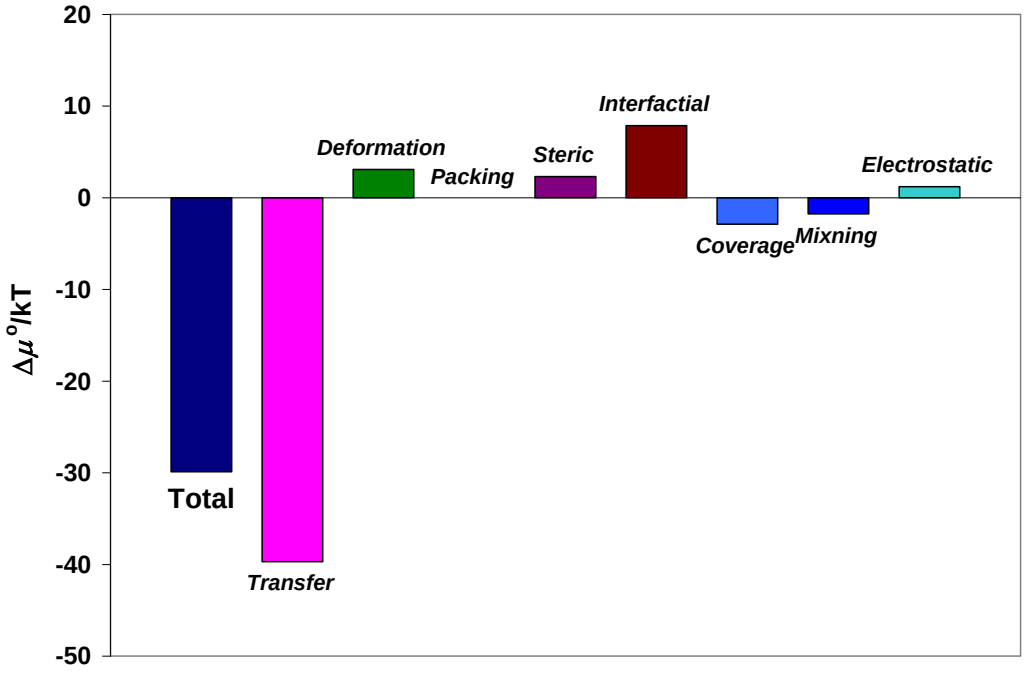

Figure 7.4: Comparison Between Different Free Energy Terms at Optimal Configuration, $g_{\text{opt}} = 61$, for *14-4-14* Sulfate Gemini Surfactant at 30°C.

Now if we take a closer look at the numerical value of the calculated total free energy, $\left(\Delta\mu_g^o\right)_{\text{total}} \big/ kT = -29.89$, then the free energy of micellization per mole of surfactants can be calculated as:

$$\begin{aligned} \Delta G_M^o &= \left[\left(\Delta\mu_g^o\right)_{\text{total}} \big/ kT\right] \cdot N_{Av} kT \\ &= -29.89 \times 8.314 \times 303.15 = -75.33 \text{ kJ/mol} \end{aligned} \tag{7.72}$$

Recalling now from Chapter 3, we also calculated a free energy of micellization, but based upon CMC and degree of ionization results obtained from conductivity measurements, and for *14-4-14* at 30°C we have $\Delta G_M^o = -78.54$ kJ/mol (Table 3.8). The two free energy values are in good agreement with each other, showing the self-consistency and reliability of our experimental and modeling approaches.

7.6.3 Critical Micelle Concentration Prediction

Recall from section 7.4.1, we introduce an alkyl chain length n_c and spacer length s dependent factor $f_{\text{sec-tail}}$ to account for the contribution to transfer free energy from the second alkyl tail in a Gemini molecule:

$$f_{\text{sec-tail}} = c \cdot n_c + d \cdot s + e \tag{7.73}$$

Camesano (2000) used a set of coefficients, c=d=0 and e=0.6 in her study. In our current model, c and d are negative constants to account for the consideration that when the tail chain gets longer or the spacer group gets shorter, the hydrophobic interaction between the tail chains will naturally become stronger. As a result, the tail chains tend to get closer to each other. The net effect is that they will behave more like a 'combined single tail' rather than two separate chains. This 'combined single tail' will apparently have less impact on the transfer free energy.

Coefficients c, d and e in eq. (7.73) are obtained by correlating $f_{\text{sec-tail}}$ with n_c and s for different Gemini surfactants, where $f_{\text{sec-tail}}$ is determined by matching modeled and experimental CMC values.

Table 7.9 $f_{\text{sec-tail}}$ Determined by Matching Modeled and Experimental CMCs at 30°C.

Surfactant	n_c	s	$f_{\text{sec-tail}}$
C_{14}-C_2-C_{14}	14	2	0.9155
C_{14}-C_4-C_{14}	14	4	0.7590
C_{16}-C_4-C_{16}	16	4	0.6758
C_{18}-C_2-C_{18}	18	2	0.7121
C_{18}-C_4-C_{18}	18	4	0.6010
C_{20+}-C_2-C_{20+}	~23	2	0.4788
C_{20+}-C_4-C_{20+}	~23	4	0.3828

The final expression for $f_{\text{sec-tail}}$ in all the modeling work has the following form:

$$f_{\text{sec-tail}} = -0.4495n_c - 0.06185s + 1.64982 \qquad (7.74)$$

R^2 for using eq. (7.74) to correlate $f_{\text{sec-tail}}$ data listed in Table 7.9 is over 0.99. All the prediction results are obtained based on a $f_{\text{sec-tail}}$ calculated from eq. (7.74).

The predicted CMC values compare reasonably well with experimental data as a function of alkyl tail chain length for both *m-2-m* and *m-4-m* series of sulfate Geminis at temperatures of 30°C, as shown in Figure 7.5.

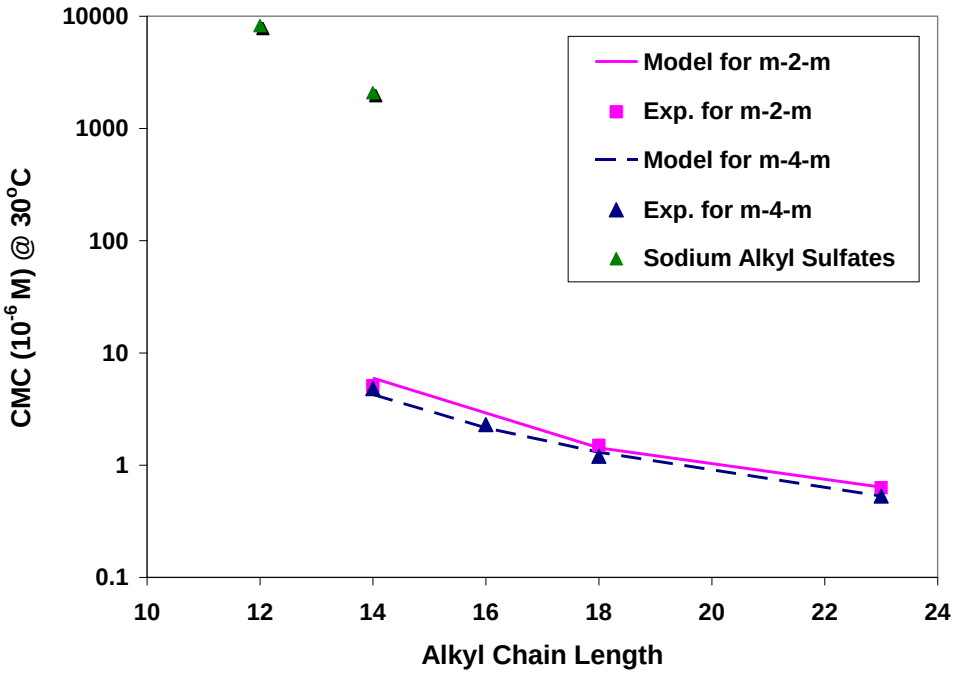

Figure 7.5: Modeled vs. Experimental CMC Values of Sulfate Geminis at 30°C.

Due to the increasing hydrophobicity, CMC decreases with longer tail chain length. It can be observed that the CMCs of Gemini surfactants are orders of magnitude lower than those of the corresponding single-chained sodium alkyl sulfates. The CMC comparison between model and experiments is also carried out at two other temperatures, 40°C and 60°C, as shown in Figure 7.6 and Figure 7.7, respectively. The results at 40°C

are fairly satisfactory, whereas when the temperature is increased up to 60°C, we see an overestimation of CMC from the model over the entire range of alkyl chain length. The impact of temperature on all the input parameters and various free energy terms probably needs further investigation. On the other hand, one should also understand that the CMC is typically not a specific concentration point; rather a narrow range of concentrations and its value oftentimes depends on the experimental techniques and procedure. This could be another possible reason for the discrepancies observed here.

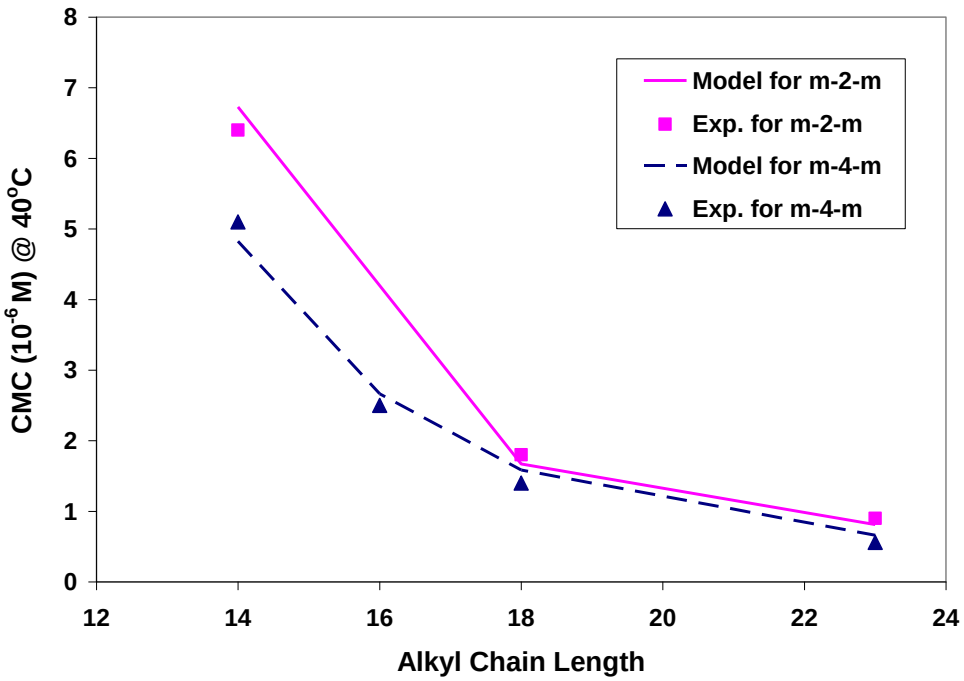

Figure 7.6: Modeled vs. Experimental CMC Values of Sulfate Geminis at 40°C.

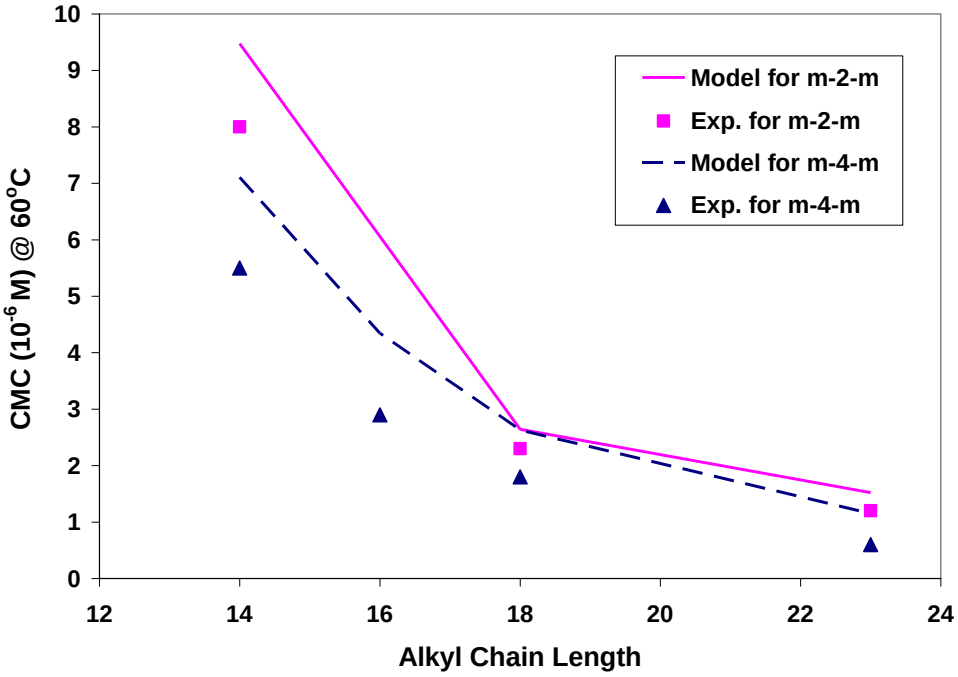

Figure 7.7: Modeled vs. Experimental CMC Values of Sulfate Geminis at 60°C.

7.6.4 Micelle Aggregation Number

For all the sulfate Gemini surfactants, globular aggregates are predicted to form. The aggregation numbers reported in Figure 7.8 and Figure 7.9 correspond to a surfactant concentration of 5×10^{-4} M. The aggregation numbers do not change with changing surfactant concentration which implies that they are narrowly dispersed. This observation agrees with our maximum term approximation. The aggregation number increases as the number of carbon atoms in the tail increases over the entire n_c range investigated. One other observation is that shorter spacer group (-2-) gives rise to larger aggregation number, which has been experimentally verified for many types of cationic and nonionic Gemini surfactants (Zana and Xia, 2004). As the spacer gets shorter, the chemical bonding provided by the spacer helps overcome the electrostatic repulsion between the head groups, which favors the aggregation and growth of micellar structures.

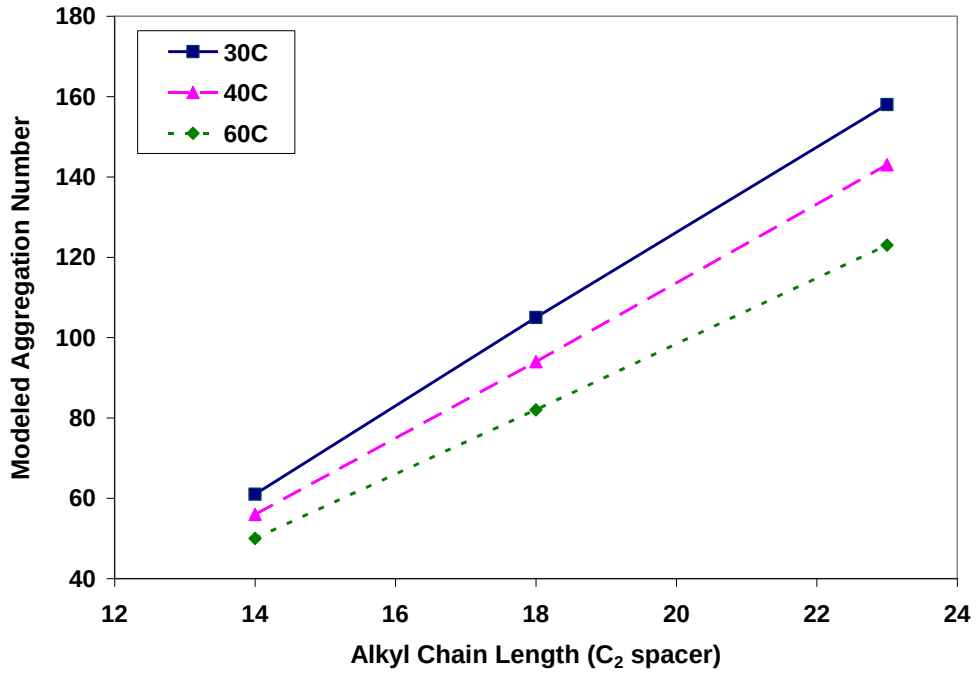

Figure 7.8: Predicted Aggregation Number for Sulfate Geminis with -2- Spacer.

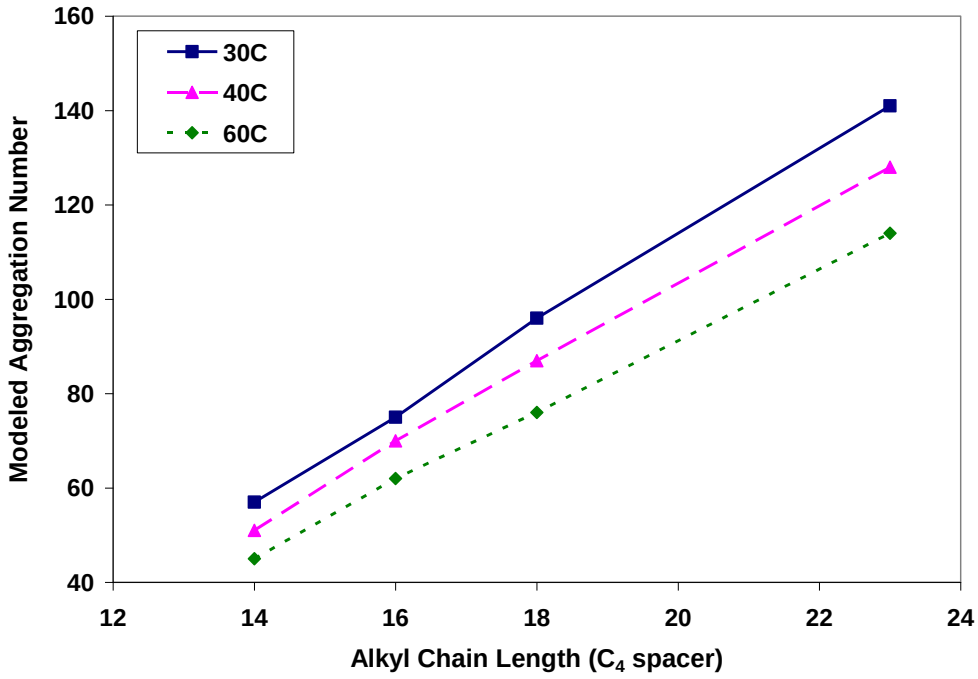

Figure 7.9: Predicted Aggregation Number for Sulfate Geminis with -4- Spacer.

As mentioned earlier, our predicted micellar aggregation number values are much greater than those from Camesano's paper, and are actually more in line with reported aggregation number ranges from the literature (typically 50-180 from Zana and Xia, 2004). As temperature increases, solubility of surfactant monomers is improved, as well as the disassociation rate of the micelles already present in solution, therefore,, the aggregation number shows a decreasing trend with rising temperature.

7.6.5 Addition of Electrolytes

To evaluate the effect of salt on CMC, we apply the model to calculate the CMCs of two sulfate Gemini surfactants, *14-4-14* and *18-4-18* in presence of NaCl, and present the comparison between our model and experimental data from Chapter 4 in Figure 7.10.

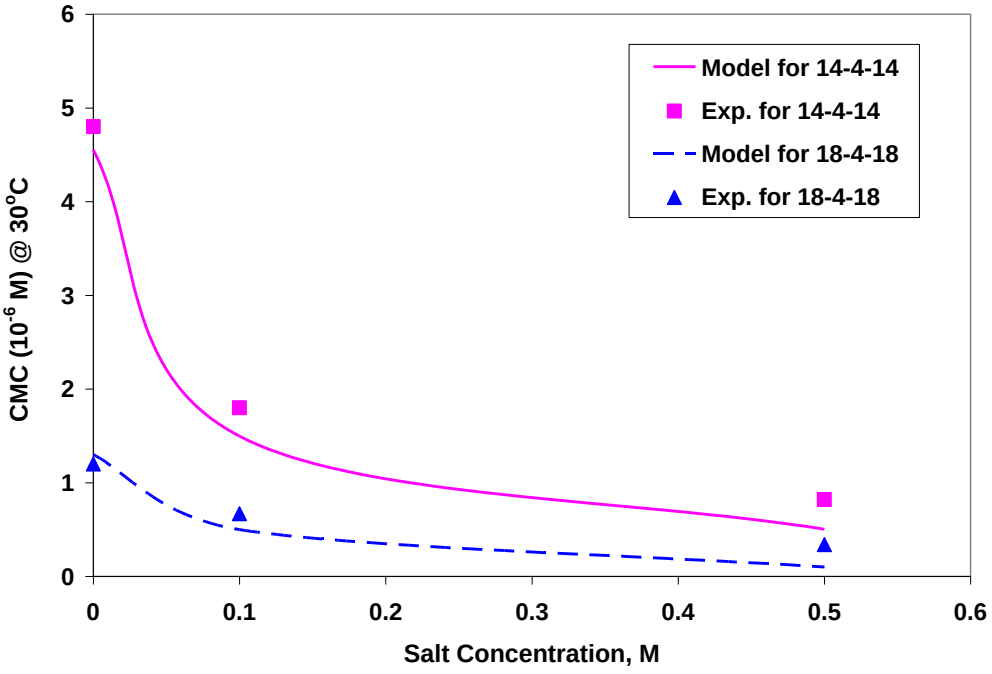

Figure 7.10: Calculated and Experimental CMC Values as a Function of Salt Concentration for *14-4-14* and *18-4-18* at 30°C.

As can be seen here, the agreement on CMC values at low electrolyte concentrations is good, but as the salt concentration increases, the agreement weakens. Notice in Table 7.10 that the aggregation number g_{opt} shows a sudden jump when 0.1M of NaCl is present in the solution, this is somewhat expected. The electrostatic repulsion between head groups diminish in this case, allowing larger aggregates to from.

Table 7.10 CMC, g_{opt}, and Micelle Shaper Predicted from Current Model with Salt Addition in Solutions, for *14-4-14* and *18-4-18* at 30°C.

Surfactant	**Salt Conc. (M)**	**CMC Modeled (10^{-6}M)**	**CMC Exp. (10^{-6}M)**	g_{opt}	**Micelle Shape**
14-4-14	0	4.55	4.80	57	Globular
	0.1	1.50	1.80	104	Globular
	0.5	0.50	0.82	104	Globular
18-4-18	0	1.30	1.2	96	Globular
	0.1	0.50	0.67	175	Cannot predict
	0.5	0.10	0.34	186	Cannot predict

It is worth reiterating that two simplified and extreme cases are used for ionic free energy calculation in the current study to avoid troublesome numerical solution of the Poisson-Boltzmann equation, one tailored for dilute and pure Gemini solutions, and the other for solutions with moderate concentration of electrolyte present. The deviation (especially at high salt concentration) observed here seems to agree with what have been reported by Moreira (2010) in their study of conventional single chain surfactants, even though a finite difference scheme was used to solve the nonlinear PBE in their case and the numerical solution should, 'theoretically' speaking, be able to cover the entire larger salinity range. Possible explanations to the loss in agreement at high NaCl concentration include: (i) change in micellar shape due to high salt concentration, which is not captured in the current spherical/globular micelle model (see Table 7.10), and this is particularly true when the model tries to predict micelle shape of the longer chain Gemini, *18-4-18*;

(ii) limitation of PBE itself for higher electrolyte concentration conditions; (iii) other neglected non-electrostatic potentials (Moreira, 2010).

7.7 SUMMARY

A predictive model of surfactant self-assembly in aqueous solution is developed to study the micellization properties of our in-house synthesized sulfate Gemini surfactants. The model is able to predict the CMC values for our Gemini surfactants with varying tail lengths. The effects of temperature and salinity of solution are also incorporated into the model for investigating more realistic cases.

We present a molecular thermodynamic model for ionic Gemini surfactant solutions that takes into account of the head group-counter-ion binding effect. Two simplified solutions to the Poisson-Boltzmann equation are utilized to study the aggregation behavior of Gemini surfactants under corresponding experimental conditions. The thermodynamic model properly predicts the CMC of all surfactants synthesized. The application scope of current model can be expanded to investigate other surfactants or factors of interest in the micellization process.

SECTION II: DESIGN AND IMPLEMENTATION OF A PILOT SCALE ALKALINE / SURFACTANT / POLYMER FLOOD

Chapter 8: Development of Surfactant Formulations for Field Pilot

Recent oil prices are currently encouraging a tremendous growth in the study of chemical enhanced oil recovery (Manrique *et al.*, 2010; Hirasaki *et al.*, 2011). The vast amount of residual oil left behind after secondary recovery efforts are becoming increasingly appealing due to high demand and the price of oil. Chemical flooding has been studied for over half a century now. However, never have the conditions encouraging its growth been as good as right now. These conditions include new, improved technology and oil prices high enough to make implementation economical.

The second section of this dissertation studies chemical formulation design and implementation for an oilfield where, after the results of these studies, a pilot is being carried out. The purpose of **Chapter 8** is to develop and test a surfactant formulation for the Brookshire Dome field ASP pilot. **Chapter 9** discusses pilot execution plan and on-site pilot implementation. **Chapter 10** is a summary of field operations and oil production results throughout the project, as well as lessons learned from the pilot study.

8.1 CATAHOULA SAND INFORMATION

8.1.1 Geology and Petrophysics of Pilot Area

The Catahoula sand lies in the Brookshire Dome filed in Texas. The field is about 35 miles to the west of Houston, off I-10. Discovered in 1996, the field is a piercement salt dome containing two main sands, the Catahoula and Plunk sands. Oil is found in the caprock above the salt dome (~3500ft). The Catahoula net sand ranges in thickness from 50 to 70ft thick within the pattern (Figure 8.11). A spinner survey run on the injector (Martin 24) suggests some degree of heterogeneity. An inverted five-spot pattern was chosen for the pilot (highlighted area in Figure 8.10). It comprises four producers (Martin 34, 37, 10A and 12) and a central well (Martin 24) converted for chemical injection. The

short producer-to injector distance enables early flood response and ensures completion of the field trial within a relatively short period of time.

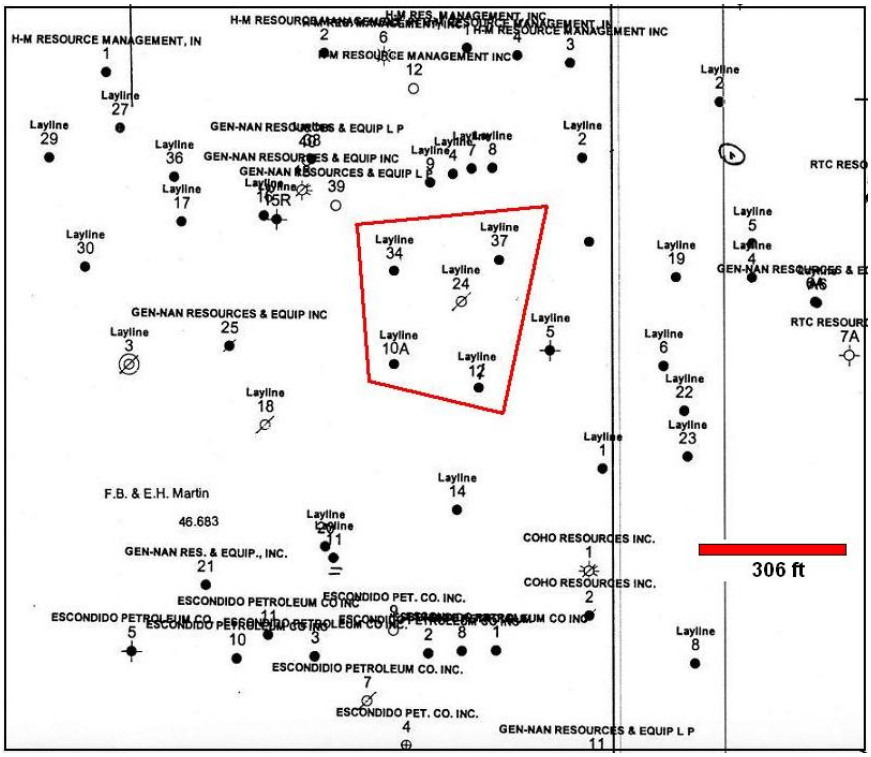

Figure 8.10: Well Locations in Brookshire Dome Field (pilot pattern in red box).

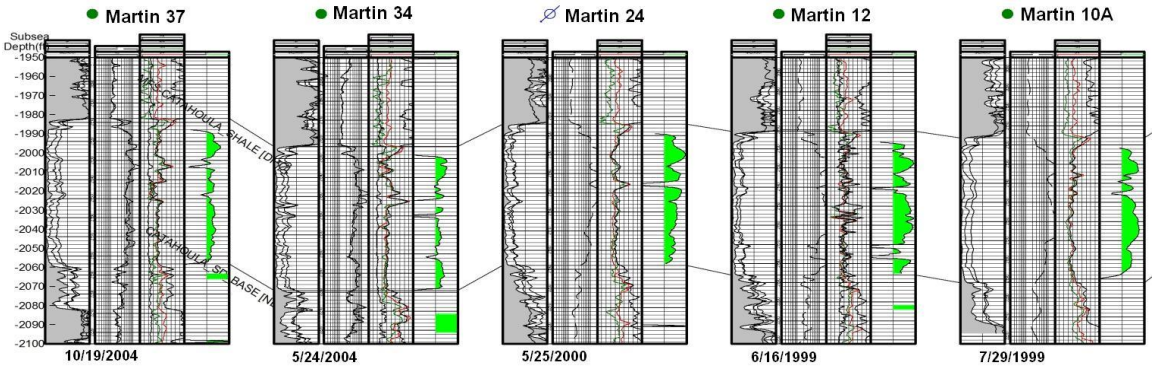

Figure 8.11: Lateral Continuity of the Catahoula Sand within the Pattern (Injector: Martin 24; Producers: Martin 37, 34, 12 and 10A).

8.1.2 Crude Oil and Brine

The crude oil is light to medium, ~30° API (lab measured density of 0.8762 g/cc @ 20°C), acidic and reactive. The viscosity was measured to be around 28cP at the reservoir temperature of 130°F (55°C). Because the Catahoula sand is a fairly shallow formation, the temperature is moderate, 130°F (55°C), and thus sulfate surfactants can be used for the ASP formulation.

The formation brine has a low salinity (~7000 to 8000ppm) and is fairly fresh. This poses a challenge for the surfactant selection process since most commercial surfactant systems have optimum salinities in the 20,000 to 35,000ppm range. Table 8.1 shows the composition of a typical field water sample.

For lab testing purposes, the sulfate ions were removed to avoid precipitation issues at lab conditions. The synthetic version of this brine is referred to as Synthetic Brookshire Brine (SBB). SBB was prepared based on the composition of heater treater water, and by mixing appropriate amounts of $CaCl_2$, $MgCl_2 \cdot 6H2O$, $NaHCO_3$, and NaCl in DI water. The Table below was used for preparing 1L SBB.

Table 8.1: Composition of Field Water Samples (from Heater Treater).

Ion	Conc., mg/L	MW	Charge	Conc., meq/ml*
Ca^{2+}	88.80	40	2	0.00444
Mg^{2+}	8.40	24	2	0.00070
Na^{+}	2678.00	23	1	0.11643
Cl^{-}	3920.00	35.5	1	0.11042
SO_4^{2-}	10.60	96	2	0.00022
HCO_3^{-}	659.00	61	1	0.01080
Sr^{2+}	2.10	88	2	0.00005
Total	7366.90	---	---	0.24307

Table 8.2: Mixing Sheet for Preparing 1L SBB (TDS = 7360.74 mg/L).

Compound	Mass (g/L)
$CaCl_2$	0.246
$MgCl_2 \cdot 6H2O$	0.070
$NaHCO_3$	0.907
NaCl	6.174
DI	992.602

Table 8.3: Composition of SBB (TDS = 7360.74 mg/L).

Ion	Conc., mg/L	MW	Charge	Conc., meq/ml*
Ca^{2+}	88.80	40	2	0.00444
Mg^{2+}	8.40	24	2	0.00070
Na^{+}	2678.00	23	1	0.11643
Cl^{-}	3926.54	35.5	1	0.11061
SO_4^{2-}	0	96	2	0
HCO_3^{-}	659.00	61	1	0.01080
Sr^{2+}	0	88	2	0
Total	7360.74	---	---	0.24325

8.1.3 Field Core Samples

A good quality reservoir core is of key importance to the evaluation of candidate chemical formulations through coreflood experiments. Lack of reservoir core oftentimes poses challenges to laboratory evaluation of the ASP formulation. Unfortunately for this project, only poor quality sidewall cores were available. These core plugs were obtained from offset wells outside the pilot area. They were delivered either broken apart or severely contaminated by drilling mud (very muddy looking). Figure 8.12 shows a picture of two plug samples. One relatively 'cleaner' sample was sent to Core Laboratories for mineralogy (XRD) analysis and the results are listed in Table 8.4.

Figure 8.12: Core Plugs from the Field (broken apart and muddy looking).

Table 8.4: X-Ray Diffraction Analysis of Core Sample at 2468' Depth (from CoreLab).

		Depth (ft)	
		2468'	**2468' re-run**
Bulk Mineralogy (%)	Quartz	81	91
	Plagioclase	4	3
	K-Feldspars	4	3
	Calcite	1	Trace
	Barite	1	Trace
	Pyrite	Trace (<0.5%)	Trace
	Total Clay	9	3
Clay Mineralogy (%)	Kaolinite	1	Trace
	Chlorite	Trace	Trace
	Illite	2	1
	MXL I/S*	6	2
	% Smectite in MXL I/S*	60-70	60-70

About 15 grams of sample was sent out for the XRD work, and two independent runs were performed by CoreLab. The results are questionable from at least two aspects: 1) the inconsistency in quartz and clay contents between the two runs; 2) the

inconsistency between high content of smectite and the fact that the permeability is several hundred millidarcies with over 30% porosity. One possible explanation to these inconsistencies could be bentonite contamination which causes a high smectite (or bentonite) content. Due to the poor quality of these core plugs, coreflood experiments were only conducted with Berea sandstone cores, as will be discussed in later sections.

8.2 PHASE BEHAVIOR MEASUREMENTS

The methodology for using phase behavior and aqueous stability tests to find an optimum surfactant, co-solvent and alkali concentrations is described by many researchers (Levitt, 2006; Jackson, 2006; Flaaten, 2007; Sahni, 2009; Yang, 2010; Dean, 2011; Solairaj, 2011; Walker, 2011) here at UT. This description explains how different formulations were evaluated, and how the best candidates were identified.

Formulations were given the name B-###, signifying Brookshire and the number of the experiment. Many different surfactants, co-surfactants, and co-solvents were used during the phase behavior evaluation phase. Propoxylate and ethoxylate are abbreviated PO and EO respectively. Internal olefin sulfonate is abbreviated IOS. Unless otherwise noted PO-sulfates and IOSs were Stepan branded surfactants.

Lot numbers of chemicals changed over time during these experiments. This led to certain phase behavior changes of formulations even though the same chemicals were used. For instance different TDA-9PO-SO_4 lots were delivered by Stepan and the phase behavior changed for various reasons including different tri-decyl alcohol feed stocks and different activities with varying amount of solvent in the delivered surfactant. This also happened many times with the C_{15-18}IOS manufactured by Stepan. It is, therefore, very important to keep track of different batches of chemicals used in every set of experiments.

After reviewing the background information on the reservoir and its fluid characteristics, the goal was to develop an inexpensive ASP formulation with suitable characteristics as discussed in detail below.

8.2.1 Initial Screening and Oil Activity (B-1 to B-16)

Since Brookshire reservoir is a light (to medium) oil reservoir, for the initial screening, Petrostep S1 (Neodol®C_{16-17}-7PO-SO_4) and similar molecules, e.g. Alfoterra L167-7S (C_{16-17}-7PO-SO_4) and Alfoterra L145-8S (C_{14-15}-8PO-SO_4) (Alfoterra surfactants from Sasol) where tried out as main surfactants with Petrostep S2 (C_{15-18}IOS) as the co-surfactant and IBA as the co-solvent. These surfactants have been shown in the past to work with many light oil reservoirs. Both salinity and sodium carbonate (Na_2CO_3) scans were done on the above samples. However, the formulation with Alfoterra L167-7S formed high viscosity microemulsions. Also, some formulations had an aqueous stability limit lesser than the optimum salinity. For most formulations, the optimum salinity (around 30,000 to 50,000 ppm) was found to be much higher than that of SBB (7360 ppm). The solubilization curves for one formulation with Alfoterra L167-7S are shown in Figure 8.13.

It should be noted that phase behavior plots do not exist for many experiments due to an inability to read interfaces often attributed to undesirable long equilibration times. Sometimes, the chemical formulation was not a good fit for this oil and there was no solubilization, just a transition from Type I to Type II. When optimum salinities are mentioned without a phase behavior plot, the value came from qualitative observations of lowest interfacial tension when the fluids are mixed to form an emulsion in a pipette.

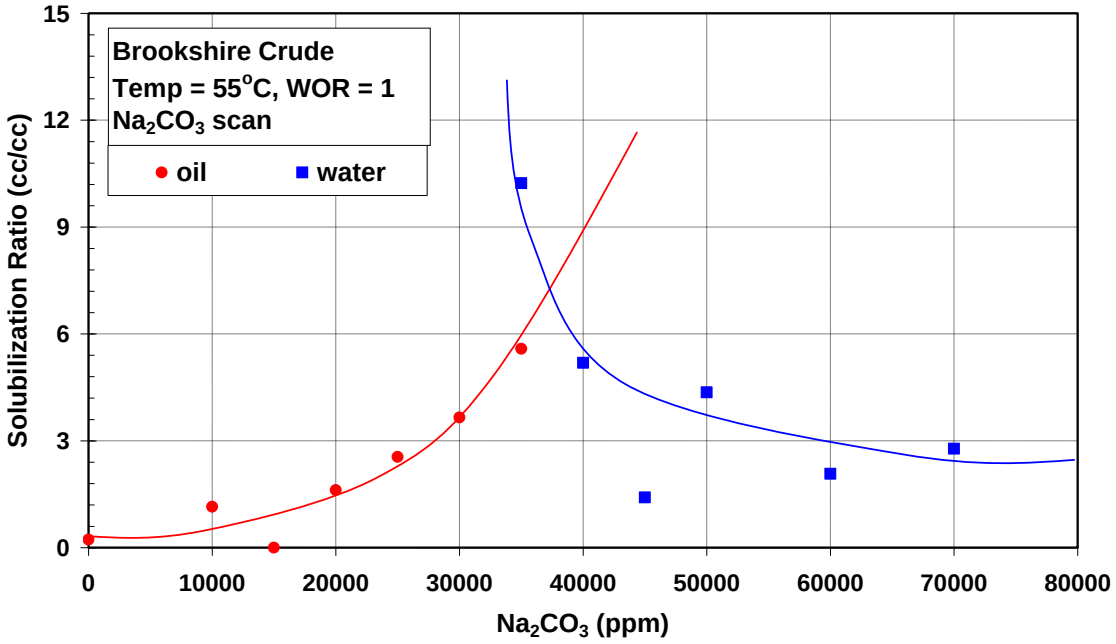

Figure 8.13: B-3 Solubilization Plot after One Month Settling at WOR=1 (1.5wt% Alfoterra L167-7S + 0.5wt% Petrostep S-2 + 2wt% IBA).

To check whether the oil is reactive or not, the above experiment using Alfoterra L167-7S and Petrostep S2 with 2% IBA as the co-solvent was repeated at a water oil ratio (WOR) of 4. The solubilization plot at this water oil ratio is shown in Figure 8.14. It can be seen that the optimum salinity has shifted lightly from 3.7wt% Na_2CO_3 to 4.2% Na_2CO_3 showing that the oil is reactive. Therefore, the addition of Na_2CO_3 will help promote soap generation and prevent surfactant adsorption.

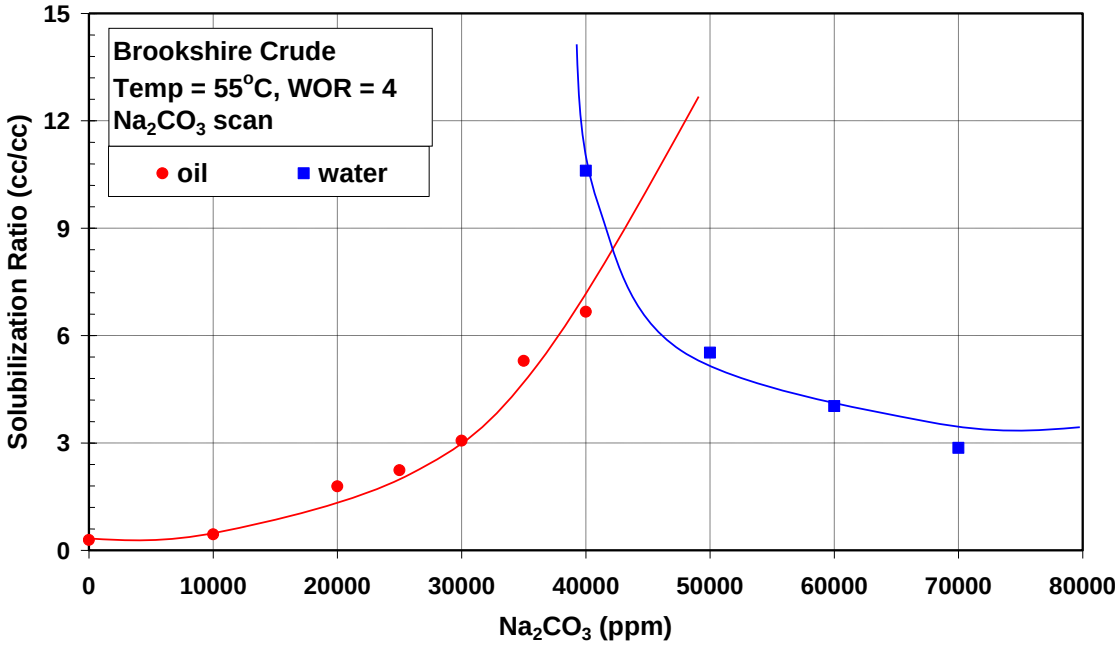

Figure 8.14: B-4 Solubilization Plot after 20 Days Settling at WOR = 4(1.5wt% Alfoterra L167-7S + 0.5 wt% Petrostep S-2 + 2wt% IBA).

The crude oil activity is more evident when one visually compares the phase behavior pipettes of a salinity (SBB) scan with those of a sodium carbonate (Na_2CO_3) scan. Figure 8.15 and Figure 8.16 show such a comparison. The salinity scan in Figure 8.15 shows only Type I microemulsion with a clear aqueous phase at the bottom. However, if Na_2CO_3 is used in the scan, the aqueous phase in all pipettes becomes the brownish messy looking phase shown in Figure 8.16, which is a direct result of soap generation and promoted solubilization by alkali addition.

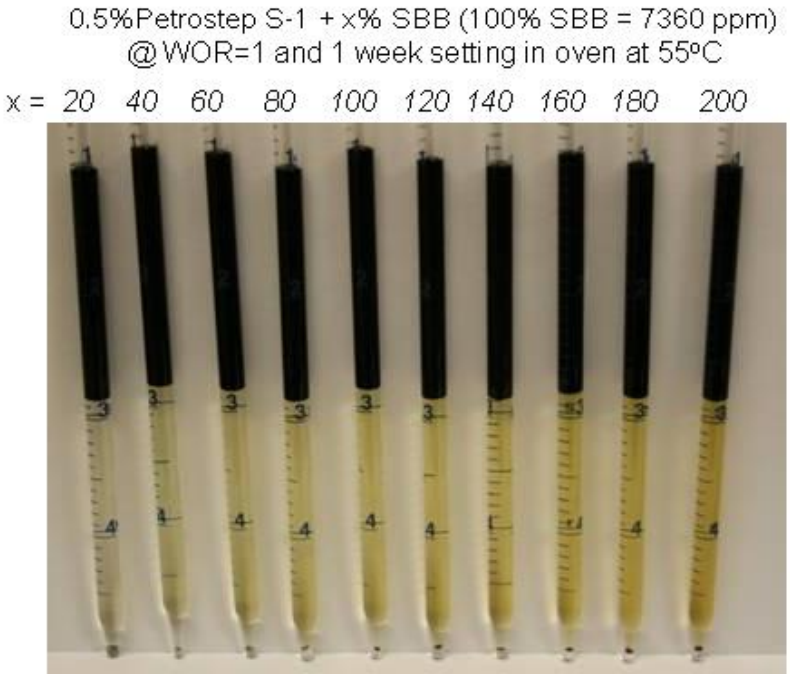

Figure 8.15: B-11 Phase Behavior Pipettes after 1 Week Settling.

Figure 8.16: B-12 Phase Behavior Pipettes after 1 Week Settling

Table 8.5: Summary of Group 1 (Alcohol Ether Sulfates) Surfactant Screening.

Exp. No.	Surfactant		Co-surfactant		Co-solvent		Scan	WOR	Aqueous Limit	Optimum Salinity	Comment
	Name (Structure)	wt%	Name (Structure)	wt%	Name	wt%					
B-1	Petrostep S-1 (C16-17 7PO SO4)	1.50	Petrostep S-2 (C15-18 IOS)	0.50	IBA	2.0	SBB	1	all clear	4%	Type I→III→II
B-2	Alfoterra L67-7S (C16-17 7PO SO4)	1.50	Petrostep S-2 (C15-18 IOS)	0.50	IBA	2.0	SBB	1	all clear	3.85%	Type I→III→II
B-3							Na_2CO_3	1	all clear	3.7%	Type I→III→II
B-4							Na_2CO_3	4	all clear	4.2%	Type I→III→II
B-5	Petrostep S-1 (C16-17 7PO SO4)	0.50	---		IBA	0.0	SBB	1	all clear	---	Type I
B-6							Na_2CO_3		all clear	---	Aqueous phase: messy & opaque; Oil phase: different from original
B-7	Petrostep S-1 (C16-17 7PO SO4)	0.50	---		IBA	1.0	SBB	1	all clear	---	Type I
B-8							Na_2CO_3		all clear	---	Aqueous phase: messy & opaque; Oil phase: different from original
B-9	Petrostep S-1 (C16-17 7PO SO4)	0.50	---		IBA	2.0	SBB	1	all clear	---	Type I
B-10							Na_2CO_3		all clear	---	Aqueous phase: messy & opaque; Oil phase: different from original
B-11	Alfoterra 145-8S (C14-15 8PO SO4)	0.50	---		IBA	0.0	SBB	1	all clear	---	Type I
B-12							Na_2CO_3		1.6%	---	Aqueous phase: messy & opaque; Oil phase: different from original
B-13	Alfoterra 145-8S (C14-15 8PO SO4)	0.50	---		IBA	1.0	SBB	1	all clear	---	Type I
B-14							Na_2CO_3		1.6%	---	Aqueous phase: messy & opaque; Oil phase: different from original
B-15	Alfoterra 145-8S (C14-15 8PO SO4)	0.50	---		IBA	2.0	SBB	1	all clear	---	Type I
B-16							Na_2CO_3		1.6%	---	Aqueous phase: messy & opaque; Oil phase: different from original

8.2.2 Alkyl Benzene Sulfonate (ABS) Trials (B-17 to B-26)

The surfactant formulations tested above all rendered optimum salinities much higher than the formation brine and the solubilization ratios less than target (at least 10). Therefore, in an effort to bring down the optimum salinity to within the range of the synthetic Brookshire brine (SBB), alkyl benzene/toluene sulfonates, which are known to give low optimal salinities, were tested. A series of experiments using different alkyl benzene/toluene sulfonates was conducted. Low concentrations of 0.2% surfactant were used and Neodol 25-12 (C_{12-15}-12EO) was used as the co-solvent (or non-ionic co-surfactant) in each case. The following surfactants were tried out:

- ORS-41HF (Alkylaryl Sulfonate)
- Petrostep A-1 (C15-18 Branched Alkyl Benzene Sulfonate)
- Petrostep A-6 (C16-18 Branched Alkyl Xylene Sulfonate)
- Petrostep M-2 (C16-18 Branched Alkyl Benzene Sulfonate)
- ORS-47HF (C15.8 Alkyl Benzene Sulfonate)
- Shell C16 (C16 Xylene Sulfonate)

Some of these surfactants, however, are known to give low aqueous solubilities. For instance, ORS-41HF (trade name ORS-## from Oil Chem Technology) was tested with 0.1, 0.2, 0.3 and 0.4wt% of Neodol 25-12 as the co-solvent and it was found that it requires at least 0.3wt% Neodol 25-12 for reasonable aqueous stability. All other surfactants were tried out with 0.2wt% co-solvent and were found to have reasonable aqueous stability limits as shown in Table 8.6. However, the phase behavior experiments on the above formulations resulted in optimum salinities far below the TDS of SBB. In fact, all samples in the salinity range from 1300ppm TDS to 7360ppm TDS formed Type II systems.

Table 8.6: Summary of Group 2 (ABS) Surfactant Screening.

Exp. No.	Surfactant		Co-solvent		Scan	WOR	Aqueous Limit	Optimum Salinity	Comment
	Name (Structure)	wt%	Name (Structure)	wt%					
B-17	Petrostep S-1 (C16-17 7PO SO4)	0.20	Neodol 25-12 (C12-15 12EO)	0.10	SBB	1	2680 ppm	---	Extremely low optimum salinity, all Type II
B-18	ORS-41HF (Alkylaryl Sulfonate)	0.20	Neodol 25-12 (C12-15 12EO)	0.10	SBB	1	<1340 ppm	---	
B-19	ORS-41HF (Alkylaryl Sulfonate)	0.20	Neodol 25-12 (C12-15 12EO)	0.20	SBB	1	1340 ppm	---	
B-20	ORS-41HF (Alkylaryl Sulfonate)	0.20	Neodol 25-12 (C12-15 12EO)	0.30	SBB	1	7360 ppm	---	
B-21	ORS-41HF (Alkylaryl Sulfonate)	0.20	Neodol 25-12 (C12-15 12EO)	0.40	SBB	1	7360 ppm	---	
B-22	ORS-41HF (Alkylaryl Sulfonate)	0.20	Neodol 25-12 (C12-15 12EO)	0.20	SBB	1	3680 ppm	---	
B-23	Petrostep A-6 (C16-18 BAXS)	0.20	Neodol 25-12 (C12-15 12EO)	0.20	SBB	1	3680 ppm	---	
B-24	Petrostep M-2 (C16-18 BABS)	0.20	Neodol 25-12 (C12-15 12EO)	0.20	SBB	1	5350 ppm	---	
B-25	ORS-47HF (C15.8 ABS)	0.20	Neodol 25-12 (C12-15 12EO)	0.20	SBB	1	7360 ppm	---	
B-26	Shell C16 (C16 AXS)	0.20	Neodol 25-12 (C12-15 12EO)	0.20	SBB	1	3345 ppm	---	

8.2.3 Surfactant Mixture and New Molecules (B-27 to B-40)

Two different approaches were then employed in order to obtain an intermediate to low optimum salinity: a) mixing Group 1 (alcohol ether sulfates) and Group 2 (ABS) surfactants to adjust the optimum condition; b) looking into other molecules that have easily tailored structures (by manipulating PON or alkyl chain length). Table 8.7 summarizes these efforts.

Experiments B-27 to B-32 were trials using surfactant mixtures. Unfortunately, many of the test tubes did not even show any volume of middle phase, it was difficult to identify optimum salinities and quantify solubilization ratios. A C_{13}-13PO-SO_4 molecule was then tested for both SBB and Na_2CO_3 scans. With this surfactant, a large volume of middle phase microemulsion was observed within a short period of time and was fairly stable over time. The optimum salinity was relatively low compared to other systems tested before. The aqueous stability was marginally acceptable but could be further improved. Therefore, it was determined that Petrostep S8-D (and other structurally similar molecules) would be used as the primary surfactant and detailed formulation optimization should be planned and conducted accordingly. Figure 8.17 and Figure 8.18 below show the phase behavior pipettes of B-33 and B-34 after 3 weeks' settling in the oven. Notice in Figure 8.18 (Na_2CO_3 scan) at 1.4wt%, almost all the originally oil and water phases were solubilized into the huge middle phase, indicating an extremely high solubilization ratio and ultralow interfacial tension.

Table 8.7: Summary of Group 3 (Surfactant Mixtures or New Molecules) Surfactant Screening.

Exp. No.	Surfactant		Co-surfactant		Co-solvent		Scan	WOR	Aqueous Limit	Optimum Salinity	Comment
	Name (Structure)	wt%	Name (Structure)	wt%	Name (Structure)	wt%					
B-27	Petrostep S-1 (C16-17 7PO SO4)	0.20	ORS-41HF (Alkylaryl Sulfonate)	0.20	Neodol 25-12 (C12-15 12EO)	0.20	SBB	1	all clear	---	Type I→II, very little middle phase
B-28	Alfoterra L67-7S (C16-17 7PO SO4)	0.20	ORS-41HF (Alkylaryl Sulfonate)	0.20	Neodol 25-12 (C12-15 12EO)	0.20	SBB	1	all clear	---	Type I→II, very little middle phase
B-29	Petrostep S-2 (C15-18 IOS)	0.20	ORS-41HF (Alkylaryl Sulfonate)	0.20	Neodol 25-12 (C12-15 12EO)	0.20	SBB	1	all clear	---	Type I→III→II
B-30	Petrostep S-1 (C16-17 7PO SO4)	0.30	Petrostep A-1 (C15-18 BABS)	0.10	IBA	0.00	SBB	1	1.84%	---	Type I→II, very little middle phase
B-31					IBA	1.00			2.21%	2.58%	Type I→III→II
B-32					IBA	2.00			---	2.58%	Type I→III→II
B-33	Petrostep S8-D (Sasol TDA 13PO SO4)	0.50	---		IBA	0.0	SBB	1	all clear	---	All Type I
B-34							Na_2CO_3		1.40%	1.4%	Type I→III→II, σ*~150
B-35	Petrostep S8-D (Sasol TDA 13PO SO4)	0.50	---		IBA	1.0	SBB	1	all clear	---	All Type I
B-36							Na_2CO_3		1.40%	1.4%	Type I→III, σ*~150
B-37	Petrostep S8-D (Sasol TDA 13PO SO4)	0.50	---		IBA	2.0	SBB	1	all clear	---	All Type I
B-38							Na_2CO_3		1.20%	1.4%	Type I→III, σ*~150
B-39	Petrostep S3-A (C20-24 IOS Shell feedstock)	0.50	---		IBA	0.0	SBB	1	<3680 ppm	---	Type I→II
B-40					IBA	1.0			3680 ppm	---	Type I→II

Figure 8.17: B-33 Phase Behavior Pipettes after 3 Weeks' Settling.

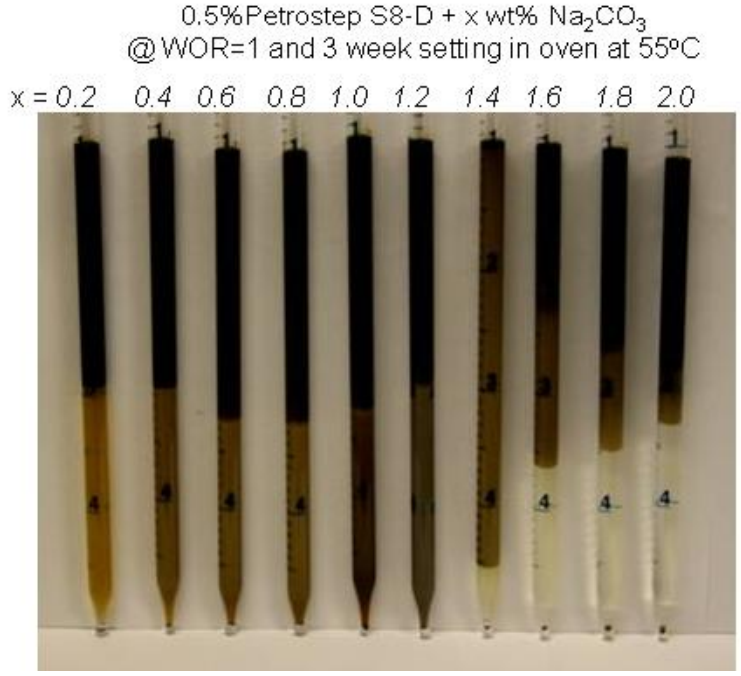

Figure 8.18: B-34 Phase Behavior Pipettes after 3 Weeks' Settling.

8.2.4 Formulation Optimization (B-41 to B-91)

After identifying TDA (C13) PO sulfate as the primary surfactant, more tests were performed to determine relevant formulation parameters, including TDA feedstock selection (Sasol vs. Exxal), optimal HLB of the molecule (PO number adjustment), effective (and economic) surfactant concentration, co-solvent type and concentration, as well as impact of WOR (activity map). Table 8.8 is a complete summary of aqueous stability and phase behavior tests conducted for formulation optimization.

Several general observations can be made from these fifty sets of experiments:

- Formulations with Petrostep S8-D as the primary surfactant take longer time to reach equilibrium and often give rise to gel or macroemulsion formation;
- Petrostep S13 surfactant series performs in general better than Petrostep S8 series, in terms of faster equilibration and a more fluid interface. This is possibly due to different tridecyl alcohol feed stocks used to make the surfactants (Sasol vs. Exxal TDA);
- Within the aqueous stability limit, adding polymer into the aqueous phase does not change the phase behavior (optimum salinity and solubilization ratio);
- Phase behavior does not change much with surfactant concentration reduced to 0.2wt%, which is very beneficial in terms of project economics;
- At least 0.1wt% of Neodol 25-12 is needed in the formulation to achieve desirable aqueous stability; too much Neodol, on the other hand, causes optimum salinity to increase drastically. Co-solvent concentration should, therefore, be carefully controlled;
- Coexistence of divalent ions (Ca^{2+}, Mg^{2+}) with carbonate ions does not severely affect aqueous stability because of their low concentrations; the

stability is further secured when sufficient co-solvent is added; EDTA could be added to ensure a clear surfactant slug injection in the field;

- Oil concentration scan shows that as WOR goes up, the optimum salinity increases and solubilization ratio in general decreases. The activity map (Figure 8.29 and Figure 8.30) shows a negative slope;
- Petrostep S13-B and S13-C perform comparably well at low concentration, with S13-C offering a lower optimum salinity and slightly higher solubilization ratio.

Based on the information collected, the proposed formulation for the coreflood experiment contains 0.3wt% Petrostep S13-C, 0.1wt% Neodol 25-12, and 1wt% Na_2CO_3. Phase behavior pipettes and solubilization plots of several formulations tested in this section are shown in Figure 8.19 to Figure 8.28.

Table 8.8: Summary of Screening Experiments for Formulation Optimization.

Exp. No.	Surfactant		Co-solvent		Scan	WOR	Aqueous Limit	Optimum Salinity	Comment
	Name (Structure)	wt%	Name (Structure)	wt%					
B-41	Petrostep S8-D (Sasol TDA 13PO SO4)	0.50	Neodol 25-12 (C12-15 12EO)	1.0	SBB	1	all clear	---	All Type I
B-42					Na_2CO_3	1	all clear	---	Na_2CO_3 up to 2wt% Aqueous phase looks messy
B-43					Na_2CO_3	1	all clear	3.6%	Na_2CO_3 up to 4wt%; at 3.6% Type III observed; aqueous phase looks messy; σ*~80
B-44	Petrostep S8-B (Sasol TDA 7PO SO4)	0.5	Neodol 25-12 (C12-15 12EO)	1.0	SBB	1	all clear	---	All Type I
B-45					Na_2CO_3	1	all clear	> 4.0%	Na_2CO_3 up to 4wt%; at 4.0% Type III observed; aqueous phase looks messy; σ*~80
B-46	Petrostep S8-D (Sasol TDA 13PO SO4)	0.50	---		Na_2CO_3	4	all clear	1.1%	Na_2CO_3 up to 4wt% in 100% SBB; at 0.8% Type III observed; σ*~80
B-47						1	all clear	0.9%	Na_2CO_3 up to 4wt% in 100% SBB; at 0.8% Type III observed; σ*~30
B-48	Petrostep S8-D (Sasol TDA 13PO SO4)	1.00	Neodol 25-12 (C12-15 12EO)	1.0	Na_2CO_3	4	all clear	3.8%	Na_2CO_3 up to 4wt% in 100% SBB; at 3.6% Type III observed; σ*~30
B-49						1	all clear	3.6%	Na_2CO_3 up to 4wt% in 100% SBB; at 2.8% Type III observed; σ*~110
B-50	Petrostep S8-D (Sasol TDA 13PO SO4)	0.50	IBA	1.0	Na_2CO_3	4	all clear	0.8%	Na_2CO_3 up to 4wt% in 100% SBB; at 0.8% Type III observed; σ*~40
B-51						1	all clear	---	Na_2CO_3 up to 4wt% in 100% SBB; at 1.2% Type III observed

Table 8.8: Summary of Screening Experiments for Formulation Optimization (Cont.).

Exp. No.	Surfactant		Co-solvent		Scan	WOR	Aqueous Limit	Optimum Salinity	Comment
	Name (Structure)	wt%	Name (Structure)	wt%					
B-52	Petrostep S8-D (Sasol TDA 13PO SO4)	0.50	Neodol 25-12 (C12-15 12EO)	1.0	Na_2CO_3	4	all clear	---	Na_2CO_3 up to 4wt% in 100% SBB; aqueous phase looks messy
B-53						1		3.0%	Na_2CO_3 up to 4wt% in 100% SBB; at 2.8% Type III observed; σ*~70
B-54	Petrostep S8-D (Sasol TDA 13PO SO4)	0.50	---		SBB	4	---	---	Up to 500% SBB in 1% Na_2CO_3; at 100% SBB Type III observed
B-55						1		---	Up to 500% SBB in 1% Na_2CO_3; at 100% SBB Type III observed
B-56	Petrostep S8-D (Sasol TDA 13PO SO4)	1.00	---		SBB	4	---	---	Up to 500% SBB in 1.4% Na_2CO_3; at 50% SBB Type III observed
B-57						1		---	Up to 500% SBB in 1.4% Na_2CO_3
B-58	Petrostep S8-D (Sasol TDA 13PO SO4)	0.50	IBA	1.0	SBB	4	all clear	---	Up to 500% SBB in 1 % Na_2CO_3; at 100% SBB Type III observed
B-59						1		---	Up to 500% SBB in 1% Na_2CO_3 at 50% SBB Type III observed
B-60	Petrostep S8-D (Sasol TDA 13PO SO4)	0.50	Neodol 25-12 (C12-15 12EO)	1.0	SBB	4	all clear	---	Up to 500% SBB in 1% Na_2CO_3; aqueous phase looks messy
B-61						1		3.18%	Up to 500% SBB in 1 % Na_2CO_3; at 400% SBB Type III observed; σ*~90
B-62	Petrostep S8-D (Sasol TDA 13PO SO4)	0.50	Neodol 25-12 (C12-15 12EO)	0.20	Na_2CO_3	1	1.5%	---	Na_2CO_3 up to 5wt%
B-63		0.30					2.0%		
B-64		0.20					2.5%		

Table 8.8: Summary of Screening Experiments for Formulation Optimization (Cont.).

Exp. No.	Surfactant		Co-solvent		Scan	WOR	Aqueous Limit	Optimum Salinity	Comment
	Name (Structure)	wt%	Name (Structure)	wt%					
B-65	Petrostep S13-B (Exxal TDA 7PO SO4)	0.50	Neodol 25-12 (C12-15 12EO)	0.20	Na_2CO_3	1	2.5%	2.5%	Na_2CO_3 up to 5wt%; σ*~70
B-66						1.5	3.0%	2.65	Na_2CO_3 up to 5wt%; σ*~105
B-67						2.33	3.0%	3.5%	Na_2CO_3 up to 5wt%; σ*~47
B-68						4	3.5%	4.45%	Na_2CO_3 up to 5wt%; σ*~28
B-69						9	4.0%	> 5%	Na_2CO_3 up to 5wt%
B-70	Petrostep S13-B (Exxal TDA 7PO SO4)	0.50	Neodol 25-12 (C12-15 12EO)	0.20	Na_2CO_3	4	3.0%	4.45%	With polymer added; up to 5% Na_2CO_3; σ*~28
B-71						1		2.1%	With polymer added; up to 5% Na_2CO_3; σ*~66
B-72	Petrostep S13-B (Exxal TDA 7PO SO4)	0.30	Neodol 25-12 (C12-15 12EO)	0.20	Na_2CO_3	1	---	---	Na_2CO_3 up to 5wt%; gel formation
B-73		0.20						1.85%	Na_2CO_3 up to 5wt%; σ*~85
B-74	Petrostep S13-C (Exxal TDA 9PO SO4)	0.50	Neodol 25-12 (C12-15 12EO)	0.20	Na_2CO_3	1	3.0%	2.0%	Na_2CO_3 up to 5wt%; σ*~135
B-75		0.30					3.5%	1.95%	Na_2CO_3 up to 5wt%; σ*~92
B-76		0.20					3.5%	---	Na_2CO_3 up to 5wt%

Table 8.8: Summary of Screening Experiments for Formulation Optimization (Cont.).

Exp. No.	Surfactant		Co-solvent		Scan	WOR	Aqueous Limit	Optimum Salinity	Comment
	Name (Structure)	wt%	Name (Structure)	wt%					
B-77	Petrostep S13-C (Exxal TDA 9PO SO4)	0.50	Neodol 25-12 (C12-15 12EO)	0.20	Na_2CO_3	1.5	2.5%	2.3%	Na_2CO_3 up to 5wt%; σ*~125
B-78						2.33	2.8%	2.6%	Na_2CO_3 up to 5wt%; σ*~85
B-79						4	3.0%	3.5%	Na_2CO_3 up to 5wt%; σ*~180
B-80						9	3.0%	4.6%	Na_2CO_3 up to 5wt%; σ*~70
B-81	Petrostep S13-B (Exxal TDA 7PO SO4)	0.30	Neodol 25-12 (C12-15 12EO)	0.10	Na_2CO_3	1	3.0%	2%	Na_2CO_3 up to 5wt%; σ*~145
B-82	Petrostep S13-C (Exxal TDA 9PO SO4)	0.30	Neodol 25-12 (C12-15 12EO)	0.10	Na_2CO_3	1	3.0%	2%	Na_2CO_3 up to 5wt%; σ*~150
B-83	Petrostep S13-B (Exxal TDA 7PO SO4)	0.25	Neodol 25-12 (C12-15 12EO)	0.20	Na_2CO_3	1	2.8%	2.7%	Na_2CO_3 up to 5wt%; σ*~75
	Petrostep S13-C (Exxal TDA 9PO SO4)	0.25							
B-84	Petrostep S13-B (Exxal TDA 7PO SO4)	0.10	Neodol 25-12 (C12-15 12EO)	0.10	Na_2CO_3	1	3.0%	1.38%	Na_2CO_3 up to 5wt%; σ*~380
	Petrostep S13-C (Exxal TDA 9PO SO4)	0.10							

Table 8.8: Summary of Screening Experiments for Formulation Optimization (Cont.).

Exp. No.	Surfactant		Co-solvent		Scan	WOR	Aqueous Limit	Optimum Salinity	Comment
	Name (Structure)	wt%	Name (Structure)	wt%					
B-85	Petrostep S13-B (Exxal TDA 7PO SO4) Petrostep S13-C (Exxal TDA 9PO SO4)	0.15 0.15	Neodol 25-12 (C12-15 12EO)	0.10	Na_2CO_3	1	3.0%	1.9%	Na_2CO_3 up to 5wt%; σ*~100
B-86	Petrostep S13-B (Exxal TDA 7PO SO4) Petrostep S13-C (Exxal TDA 9PO SO4)	0.15 0.15	Neodol 25-12 (C12-15 12EO)	0.20	Na_2CO_3	1	3.5%	2.0%	Na_2CO_3 up to 5wt%; σ*~230
B-87	Petrostep S13-B (Exxal TDA 7PO SO4) Petrostep S13-C (Exxal TDA 9PO SO4)	0.10 0.10	Neodol 25-12 (C12-15 12EO)	0.10	Na_2CO_3	1	3.5%	0.9%	Na_2CO_3 up to 4wt% in 100% SBB; σ*~380
B-88	Petrostep S13-B (Exxal TDA 7PO SO4) Petrostep S13-C (Exxal TDA 9PO SO4)	0.15 0.15	Neodol 25-12 (C12-15 12EO)	0.10	Na_2CO_3	1	3.5%	0.75%	Na_2CO_3 up to 4wt% in 100% SBB; σ*~210
B-89	Petrostep S13-B (Exxal TDA 7PO SO4) Petrostep S13-C (Exxal TDA 9PO SO4)	0.15 0.15	Neodol 25-12 (C12-15 12EO)	0.20	Na_2CO_3	1	3.0%	1.2%	Na_2CO_3 up to 4wt% in 100% SBB; σ*~210

Table 8.8: Summary of Screening Experiments for Formulation Optimization (Cont.).

Exp. No.	Surfactant		Co-solvent		Scan	WOR	Aqueous Limit	Optimum Salinity	Comment
	Name (Structure)	wt%	Name (Structure)	wt%					
B-90	Petrostep S13-B (Exxal TDA 7PO SO4)	0.30	Neodol 25-12 (C12-15 12EO)	0.10	Na_2CO_3	1	3.0%	1.3%	Na_2CO_3 up to 4wt% in 100% SBB; σ*~95
B-91	Petrostep S13-C (Exxal TDA 9PO SO4)	0.30	Neodol 25-12 (C12-15 12EO)	0.10	Na_2CO_3	1	3.0%	1.0%	Na_2CO_3 up to 4wt% in 100% SBB; σ*~220

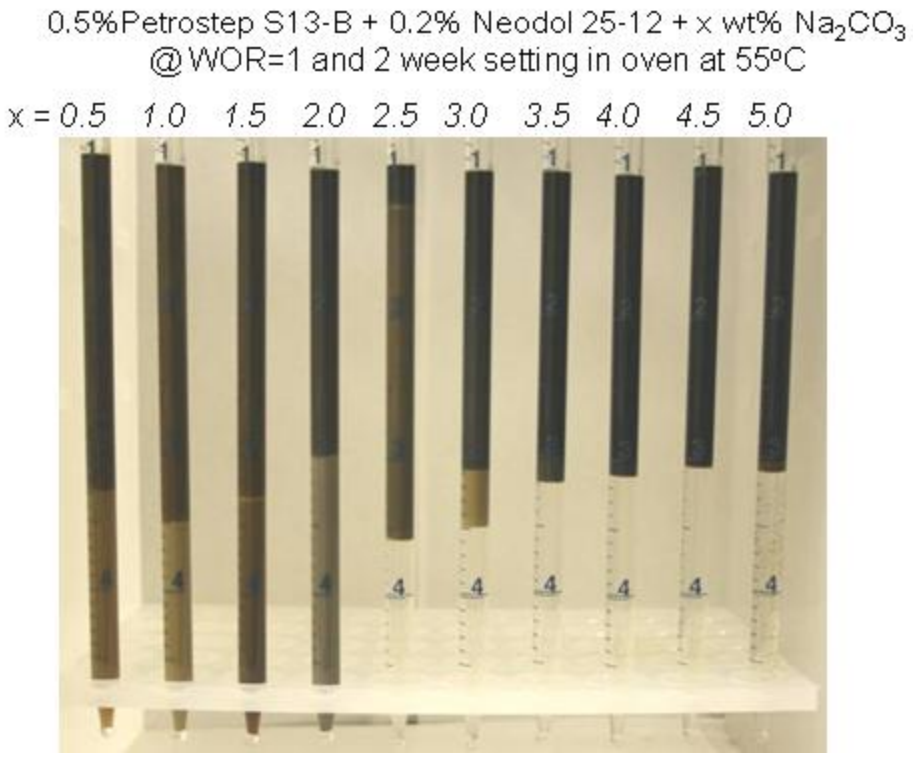

Figure 8.19: B-65 Phase Behavior Pipettes after 2 Weeks' Settling.

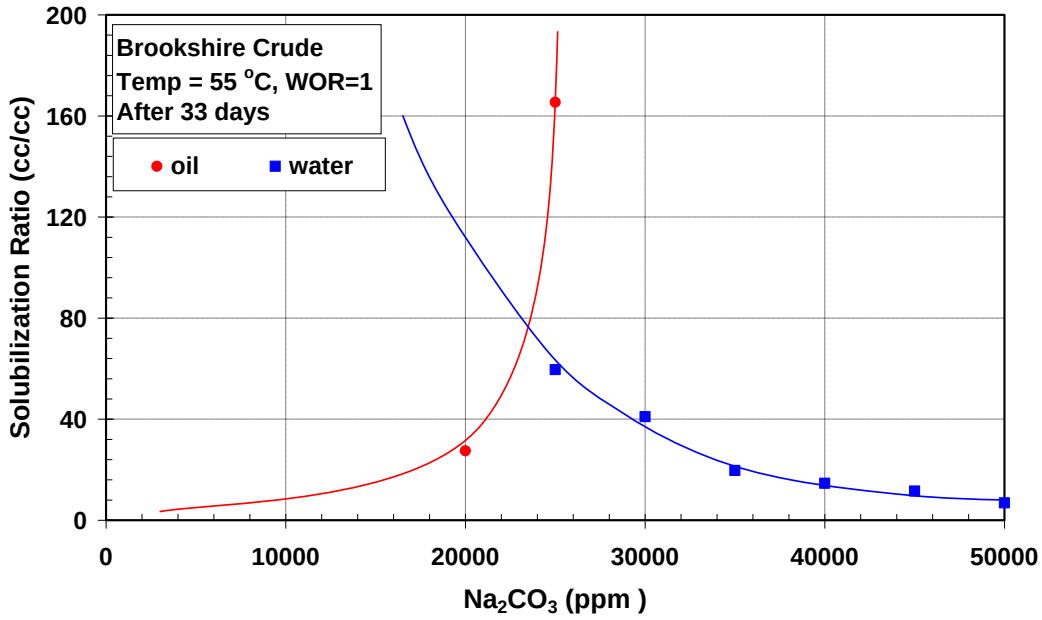

Figure 8.20: B-65 Solubilization Plot after 33 Days Settling at WOR = 1 (0.5 wt% Petrostep S13-B + 0.2 wt% Neodol 25-12).

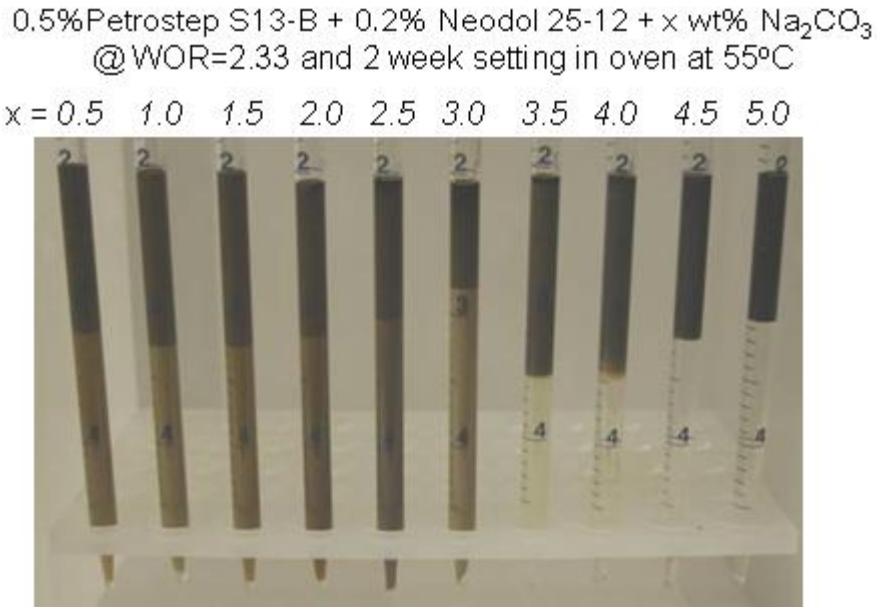

Figure 8.21: B-67 Phase Behavior Pipettes after 2 Weeks' Settling.

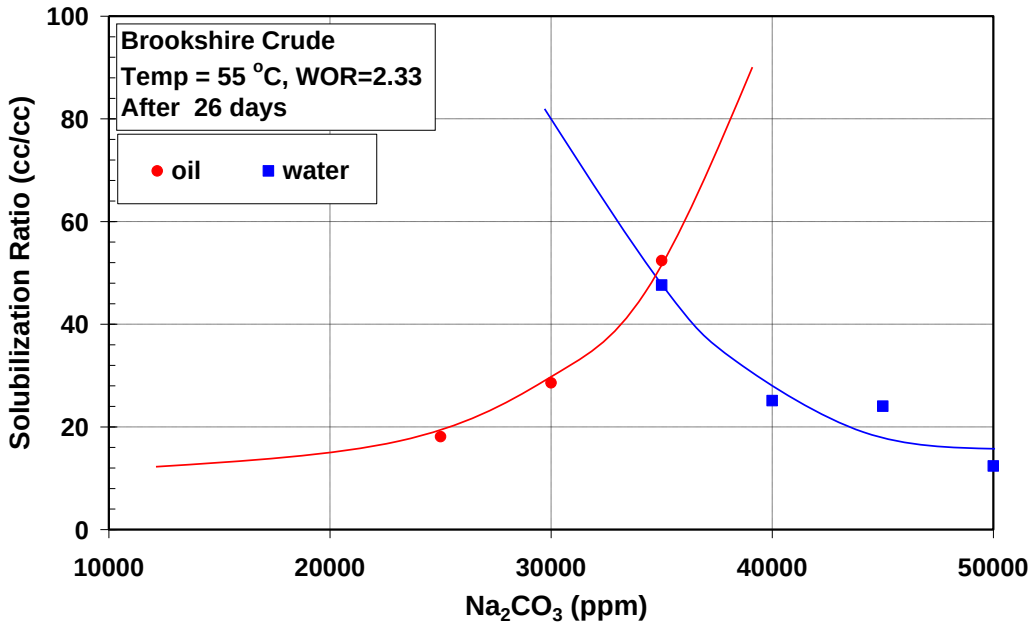

Figure 8.22: B-67 Solubilization Plot after 26 Days Settling at WOR = 2.33 (0.5 wt% Petrostep S13-B + 0.2 wt% Neodol 25-12).

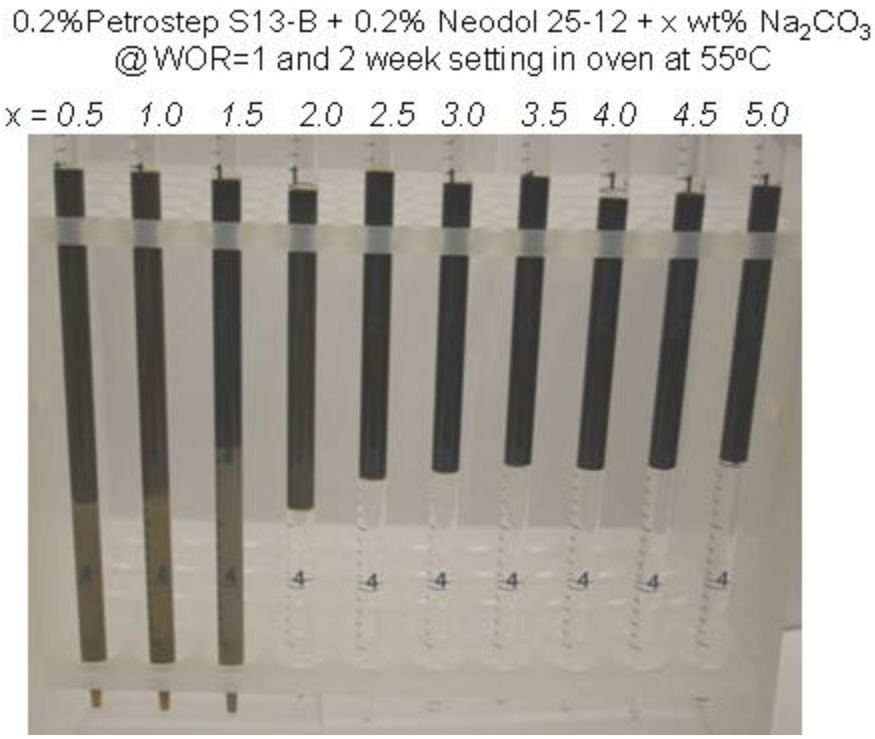

Figure 8.23: B-73 Phase Behavior Pipettes after 2 Weeks' Settling.

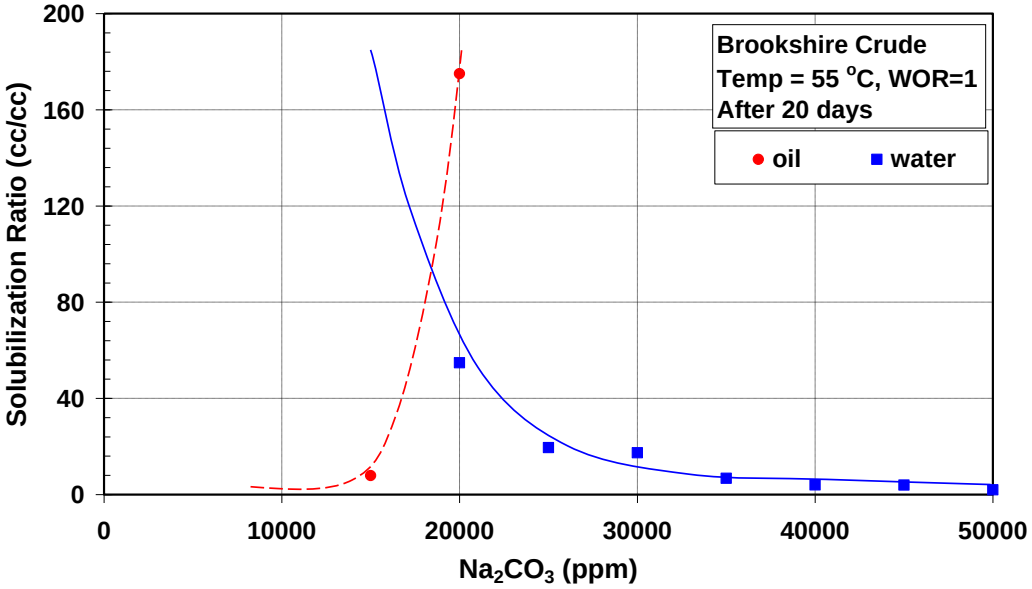

Figure 8.24: B-73 Solubilization Plot after 20 Days Settling at WOR = 1 (0.2 wt% Petrostep S13-B + 0.2 wt% Neodol 25-12).

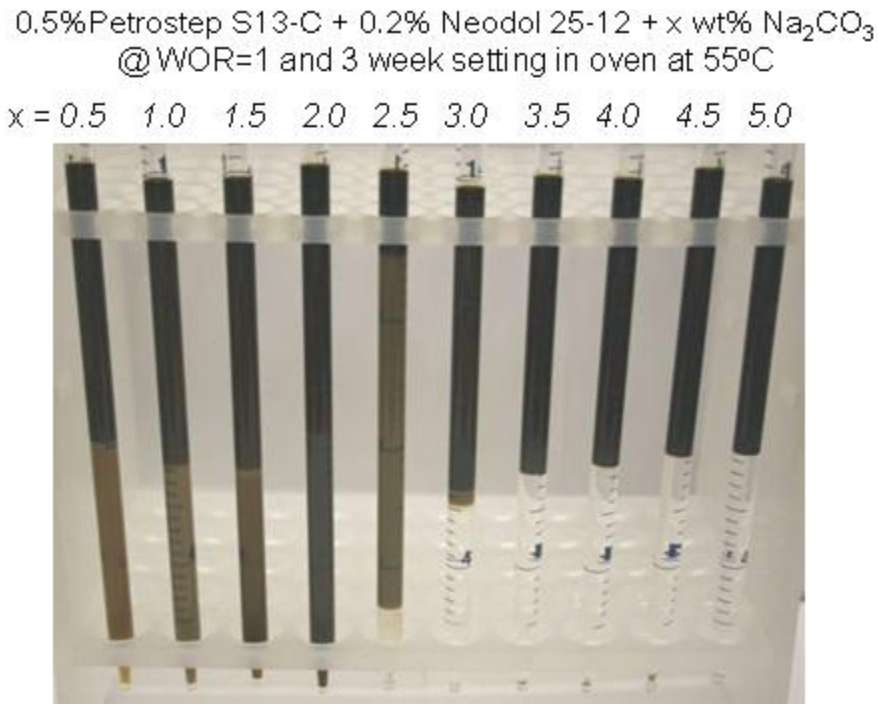

Figure 8.25: B-74 Phase Behavior Pipettes after 3 Weeks' Settling.

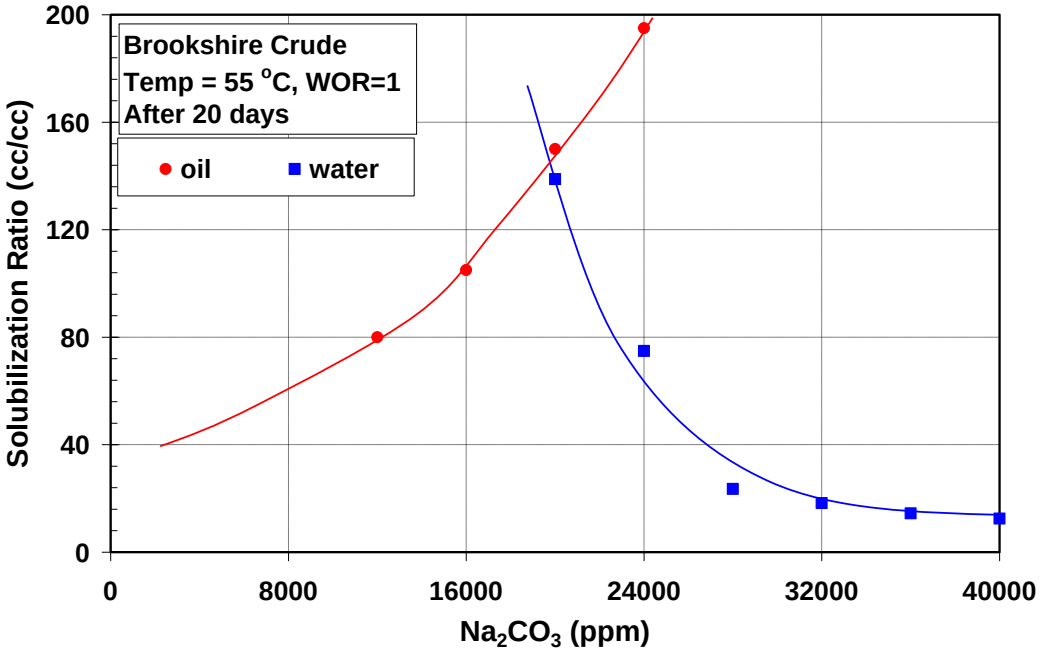

Figure 8.26: B-74 Solubilization Plot after 20 Days Settling at WOR = 1 (0.5 wt% Petrostep S13-C + 0.2 wt% Neodol 25-12).

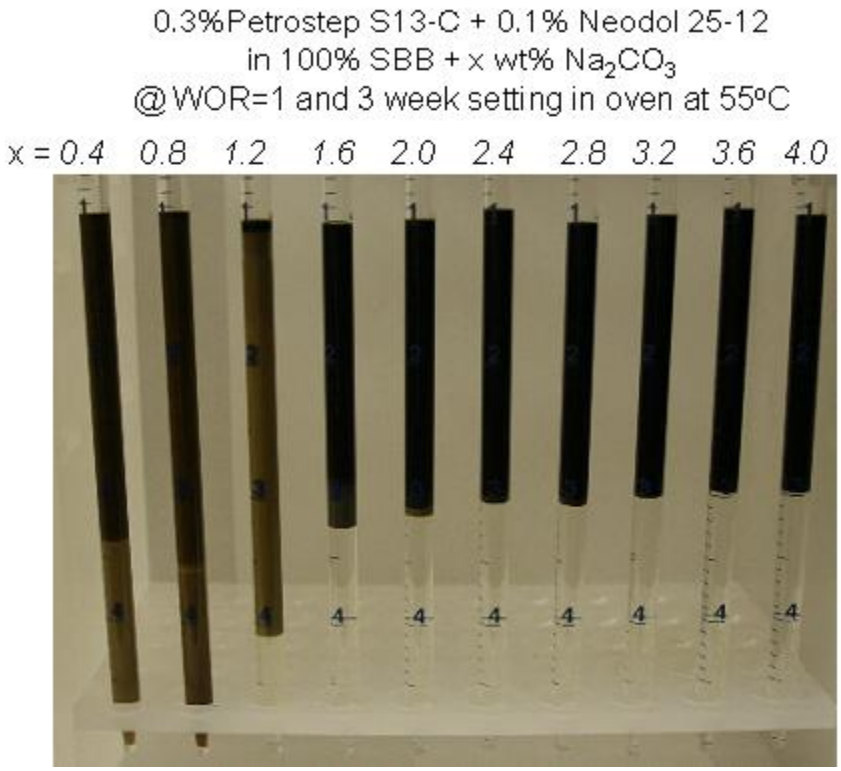

Figure 8.27: B-91 Phase Behavior Pipettes after 3 Weeks' Settling.

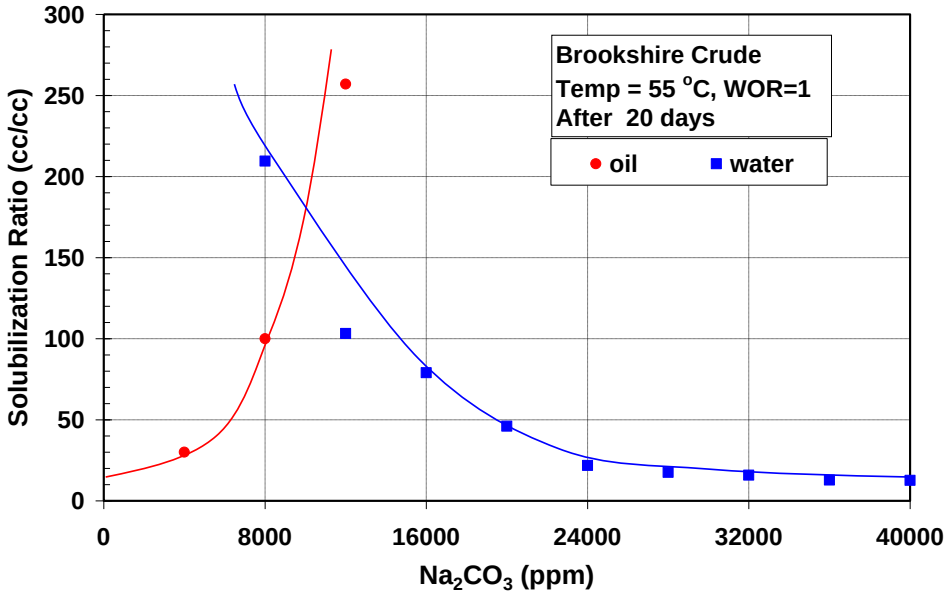

Figure 8.28: B-91 Solubilization Plot after 20 Days Settling at WOR = 1 (0.3wt% Petrostep S13-C + 0.1 wt% Neodol 25-12).

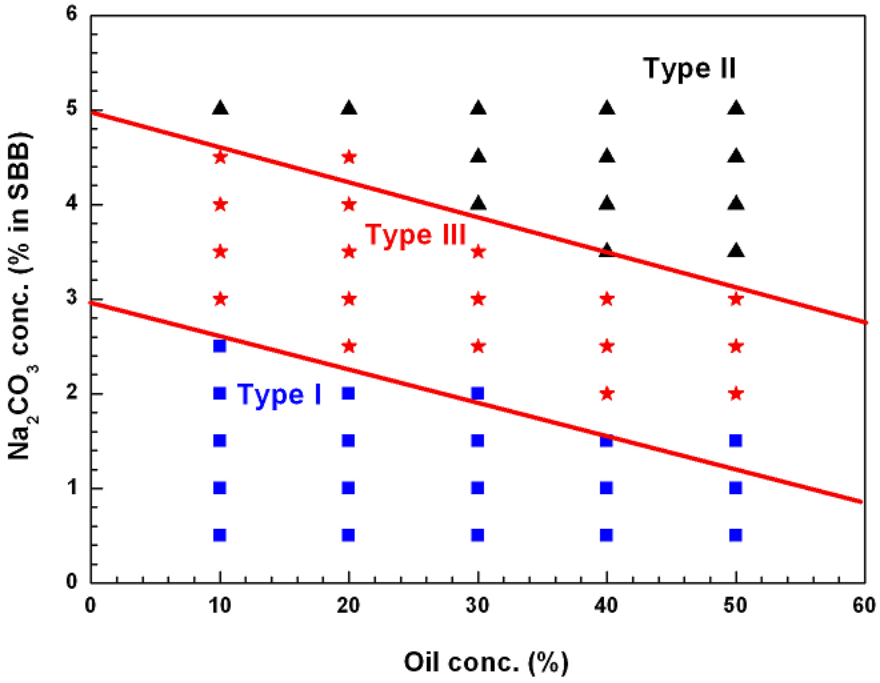

Figure 8.29: Activity Map for 0.3wt% Petrostep S13-B + 0.1 wt% Neodol 25-12.

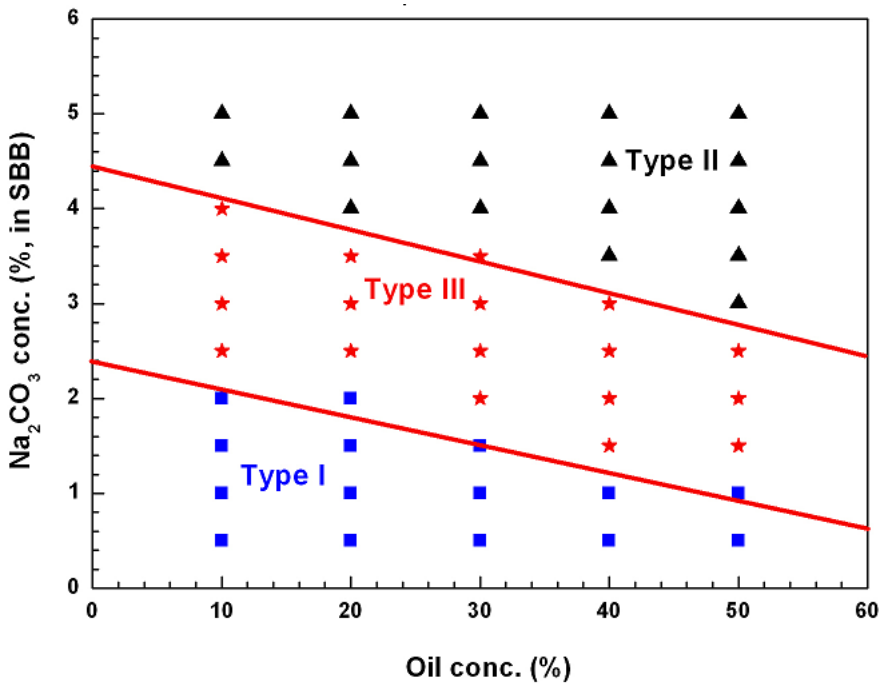

Figure 8.30: Activity Map for 0.3wt% Petrostep S13-C + 0.1 wt% Neodol 25-12.

8.3 COREFLOOD EXPERIMENTS

Coreflood experiments are conducted to test the performance of the optimal formulation in an idealized laboratory setting. Coreflooding procedures are well documented in many theses and papers published earlier (Levitt *et al.*, 2006 & 2009; Jackson *et al.*, 2006; Flaaten *et al.*, 2007 & 2008; Zhao *et al.*, 2008; Yang *et al.*, 2010; Dean, 2011; Solairaj, 2011; Walker, 2011).

8.3.1 Experimental Equipment

The experimental setup was built upon an existing system designed by Dr. Choi in his study of polymer transport properties (Choi, 2008). A LC-5000 syringe pump (ISCO Inc.) was used to inject the fluids at a constant rate. The pump was filled with mineral oil to displace the fluid in the columns into core. It can pump in the range between 0 to 400ml/hr, with maximum 500ml storage capacity. A Hassler-type steel core holder was chosen to safely operate at high pressure. A glass column was used for aqueous fluid (brine, surfactant slug or polymer drive) injection under lower pressure. A high pressure steel column was used for the oil flood experiment. The pressure drops for different sections across the core are measured by pressure transducers (Model DP15-30, Validyne Engineering Corp.) In order to confirm the proper operation of pressure transducers, the pressure drop across the entire core was also measured and compared with the sum of three pressure drops. The lines connected to the core should be flushed with DI water in order to remove any air bubbles and transducers should be calibrated prior to experiment. The effluents from the core were collected at regular intervals with a fraction collector (Retriever II, ISCO Inc.). The signals from the pressure transducers were collected and transformed by a data collector (Model MCI-20, Validyne Engineering Corp.) and the data were displayed in real time using LabVIEW 8.0 (National Instruments). Heating tape

with a temperature controller (Thermo Scientific) was used together with fiberglass cloth insulation to provide the desired experimental core flood temperature.

8.3.2 Coreflood Description

The coreflood procedure includes a method of core preparation and assembly, brine flooding, oil flooding, water flooding and chemical flooding, collecting and analyzing the effluent samples. This section describes the flooding procedure.

Brine Flood

After finishing core preparation and assembly, the core was vacuum saturated and flushed with synthetic formation brine. The objective of this brine flooding was to determine the absolute brine permeability. Several pore volume of formation brine was injected at a flow rate 2-4ml/min into the core until pressure stabilized. The pressure drop was recorded to determine the average absolute brine permeability of the core.

Oil Flood

After brine flooding, oil flooding was conducted at high injection pressure at the reservoir temperature. The main purpose of the oil flooding is to determine initial oil saturation, residual water saturation, effective oil permeability, and the relative oil permeability. Prior to oil flooding, the crude was filtered by a 0.45μm filter paper at reservoir temperature. Oil flooding was conducted under a constant pressure to saturate the pore volume with oil and obtain accurate residual water saturation. Approximately, 1.5PV of oil was injected. The effluent fluids were collected in 100ml burettes and the volume of displaced water was the volume of saturated oil inside the core. Oil flooding was continued until the water cut was less than 1% and pressure stabilized.

Water Flood

Oil flooding was followed by water flooding with filtered synthetic injection brine. Water flooding was conducted in order to determine the residual oil saturation, effective water permeability, and relative water permeability. Approximately 1.5PV of synthetic brine was injected into the core at low constant flow rate (0.4-0.5 ml/min) to achieve residual oil saturation after water flooding. The effluent fluids were collected in a burette and water flooding was stopped when the oil cut was less than 1% and pressure stabilized.

Chemical Flood

A chemical (ASP) slug was injected after water flooding in order to check the performance of the formulation by measuring the incremental recovery of residual oil in the core (tertiary recovery). Typically, 0.3-0.5PV of ASP slug was injected into the core at reservoir temperature and followed by approximately 1.5-2.0PV polymer drive. Chemical flooding was performed at a constant flow rate of about 1-2ft/day and the flooding was performed until no more emulsion was produced. The effluent fluids were collected by a fraction collector for estimating the oil-water ratio and for further analyses. Oil recovery and residual oil saturation were determined after chemical flooding by material balance and measuring volumes of oil produced.

8.3.3 Quality and Mobility Control for Polymer

In order to properly test the surfactants, proper quality control steps must be taken to ensure that no problems arise due to the polymer. Therefore, several checks need to be in place regarding the polymer.

High quality, properly hydrated polymer must be used. In order to test the quality of polymer, all polymer solutions must have their filtration ratio measured. The filtration

ratio was measured at 15psi using a 1.2μm filter paper. The filtration ratio checks to ensure that the last volumes of polymer flow out at the same rate as the volumes of polymer near the beginning of the test. It is therefore a measure of the plugging occurring during polymer flow. The filtration ratio is expressed as,

$$F.R. = \frac{t_{200ml} - t_{180ml}}{t_{80ml} - t_{60ml}} \tag{8.1}$$

This check ensures that no large, contaminated, or improperly mixed polymer is filtering out causing the polymer flow rate to decrease with time as a polymer filter cake builds up on the filter paper. The quality control cut-off is a filtration ratio of 1.2. Any polymer sample with a filtration ratio above 1.2 is not used for coreflooding.

Proper mobility control must be achieved with the correct concentration of polymer. This is done following these steps:

1). In order to select the correct concentration, the inverse of the estimated maximum oil bank mobility (i.e. necessary slug viscosity) is calculated using Corey exponents of 2, water and oil viscosities, and water and oil endpoint relative permeabilities. Notice that this estimation is on the more conservative side. A more aggressive approach is to use an estimated oil bank saturation to evaluate the required apparent slug viscosity. Polymer drive viscosity should be higher or equal to surfactant slug viscosity to prevent viscous fingering.

$$\mu_{app} = \frac{1}{\lambda_t} = \frac{1}{\left(\frac{k_w}{\mu_w} + \frac{k_o}{\mu_o}\right)} \tag{8.2}$$

2). An existing polymer database can be used to give a close estimation of the range of polymer concentration necessary with a given salinity and hardness

at a given temperature. The desired viscosity is achieved typically at a target shear rate of $10s^{-1}$, due to flooding rates and common ranges of permeabilities.

3). Several samples are made over a range of polymer concentration close to the estimated value. The samples must have the correct salinity hardness, and they should also contain all chemicals when designing the slug. Viscosities (from a rheometer) at $10s^{-1}$ can be plotted as a function of polymer concentration. The polymer concentration can then be selected from a fitted curve and used when mixing the slug.

8.3.4 Brookshire Coreflood GB-2

The surfactant formulation (0.3wt% Petrostep S13-C, 0.1wt% Neodol 25-12, and 1wt% Na_2CO_3 in 100% SBB) was tested in a sandstone coreflood experiment at reservoir temperature to verify that it is effective at recovering residual oil. The standard laboratory protocol is to test a new chemical formulation in an outcrop rock such as Berea sandstone before testing it in the reservoir rock. Berea sandstone cores are often employed in experiments because of their consistent properties, and also because of the fact that many surfactant floods have been done using Berea that serve as a useful benchmark.

GB-2 Core Data

A Berea sandstone core was weighted and its dimensions (length and diameter) were measured. The closed system for the core holder was prepared by shutting off the valves and pulling vacuum overnight. The core was then saturated with pure CO_2 gas, twice at 30 minute intervals, at the beginning of vacuum evacuation to effectively eliminate any air trapped in the pores of the core. The core was then saturated by imbibing 0.45μm filtered SBB. The pore volume was calculated by subtracting the dead

volume of the closed system (the amount of brine saturated in unnecessary parts, such as valves or lines) from the total amount of imbibed brine. The porosity is given by,

$$\phi = \frac{V_p}{V_b} = \frac{\Delta V - V_{dead}}{\pi d^2 L/4} \tag{8.3}$$

The core properties of the GB-2 coreflood experiment are shown below in Table 8.9. The permeability values are listed in Table 8.10. These values are calculated from pressure data and flow rates after flooding experiments. The flooding experiments consisted of brine flooding, oil flooding, water flooding, chemical flooding, and finally followed by polymer flooding. Then the oil permeability and relative oil permeability, 437md and 0.89 respectively, are acquired after the oil flood at the residual water saturation. Initial oil saturation of 0.64 is calculated using the volume of oil from the core. After water flooding with synthetic brine, a water permeability of 58.4md and a relative water permeability of 0.119, and residual oil saturation of 0.314 were measured. Oil saturation data for the GB-2 core are shown in Table 8.11.

Table 8.9: Berea Core Properties for Coreflood GB-2.

Core	**GB-2**
Source	Berea Sandstone
Mass (g)	310.6
Porosity	0.2014
Length (cm)	29.067
Diameter (cm)	2.54
Area (cm^2)	5.067
Temperature (^oC)	55
Pore Volume (ml)	29.66

Table 8.10: Permeability and Relative Permeability Values of Berea Core GB-2.

Absolute Brine Permeability, k_{brine} (md)	491
Oil Permeability, k_{oil} (md)	437
Water Permeability, k_{water} (md)	58.4
Relative Oil Permeability, k_{ro}^{o} (end point)	0.89
Relative Water Permeability, k_{rw}^{o} (end point)	0.119

Table 8.11: Saturation Data for Berea Core GB-2.

Initial Oil Saturation, S_{oi}	0.64
Residual Water Saturation, S_{wr}	0.36
Residual Oil Saturation, S_{orw}	0.314

GB-2 Brine Flood

Initially GB-2 core was saturated with SBB and then flooded with SBB to measure the brine permeability. The composition of SBB was described in previous sections. The brine flood was done at a rate of 2.64ml/min and the pressure data measured is shown in Figure 8.31. The measured absolute permeability is again 491md.

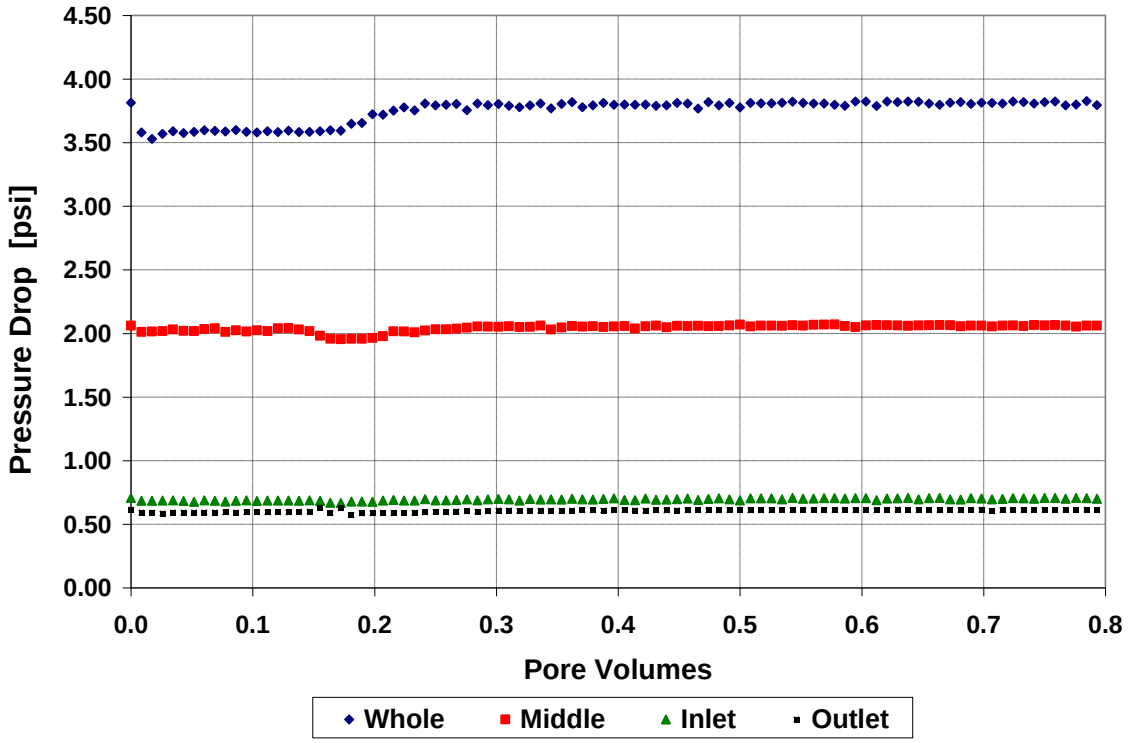

Figure 8.31: GB-2 Brine Flood Pressure (q = 2.64ml/min, μ_w = 0.54cP).

GB-2 Oil Flood

The crude was filtered through a 0.45μm filter paper under a pressure of 50psi at reservoir temperature. Prior to the oil flood, filtered oil viscosity was measured by a rheometer at the reservoir temperature (28cP at $10s^{-1}$). Then, the oil flood experiment was conducted with 1.5-2 pore volumes of filtered oil. The flood was continued until the water cut was less than 1%. The oil permeability to residual water was calculated to be 437md and the relative endpoint permeability of oil was 0.89. The initial oil saturation after oil flood was 0.64, for a residual water saturation of 0.36. The pressure data is shown for the GB-2 oil flood in Figure 8.32.

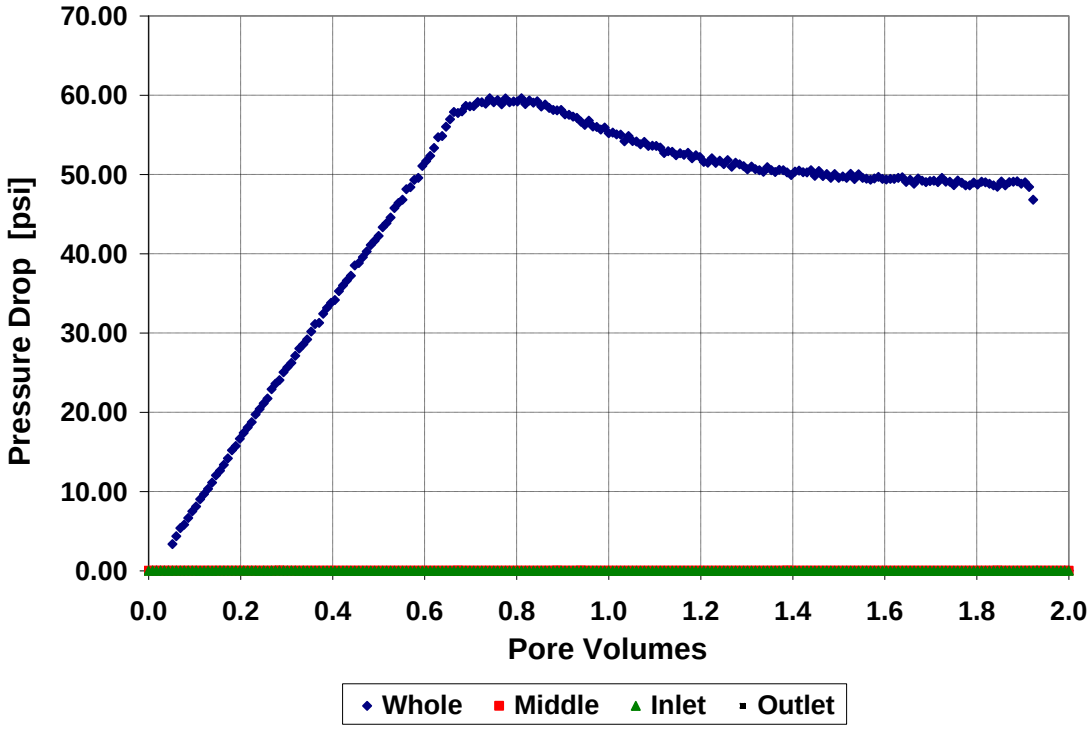

Figure 8.32: GB-2 Oil Flood Pressure (q = 0.54ml/min, μ_o = 28cP).

GB-2 Water Flood

The core was water flooded with SBB at a flow rate of 0.054ml/min until the produced oil cut was less than 1%. The pressure data for GB-2 water flood is illustrated in Figure 8.33. After 1.4 PV of water flood, residual oil saturation was obtained to be 0.314. The permeability of water was evaluated to be 58.4md, corresponding to endpoint relative permeability of 0.119.

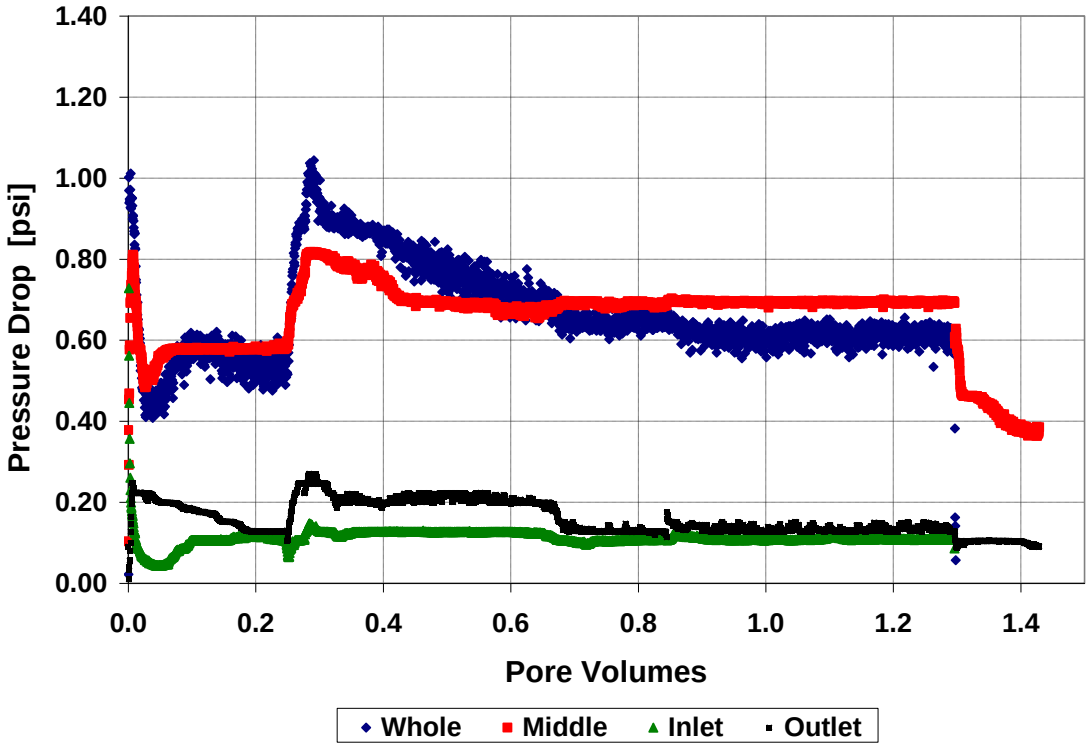

Figure 8.33: GB-2 Water Flood Pressure (q = 0.054ml/min, μ_w = 0.54cP).

GB-2 Chemical Flood Desgin

The chemical flood is designed using data from the phase behavior, aqueous stability, activity diagram, and polymer viscosity experiments. The phase behavior and solubilization plot for the optimal formulation (0.3wt% Petrostep S13-C, 0.1wt% Neodol 25-12, and 1wt% Na_2CO_3 in 100% SBB) are illustrated from Figure 8.27 and Figure 8.28. The aqueous stability test was conducted with Flopaam^{TM} 3330S polymer (SNF Floerger). The designed viscosity was estimated from the inverse of the minimum total mobility as described in eq. (8.2). Figure 8.34 below illustrates relative permeability curves calculated using Corey model and values from Table 8.10 and Table 8.11. An oil bank saturation of 0.5 requires the apparent viscosity for the slug to be at least 18cP

(based on eq. (8.2) and Corey Model). Polymer drive should have a viscosity greater than the slug viscosity.

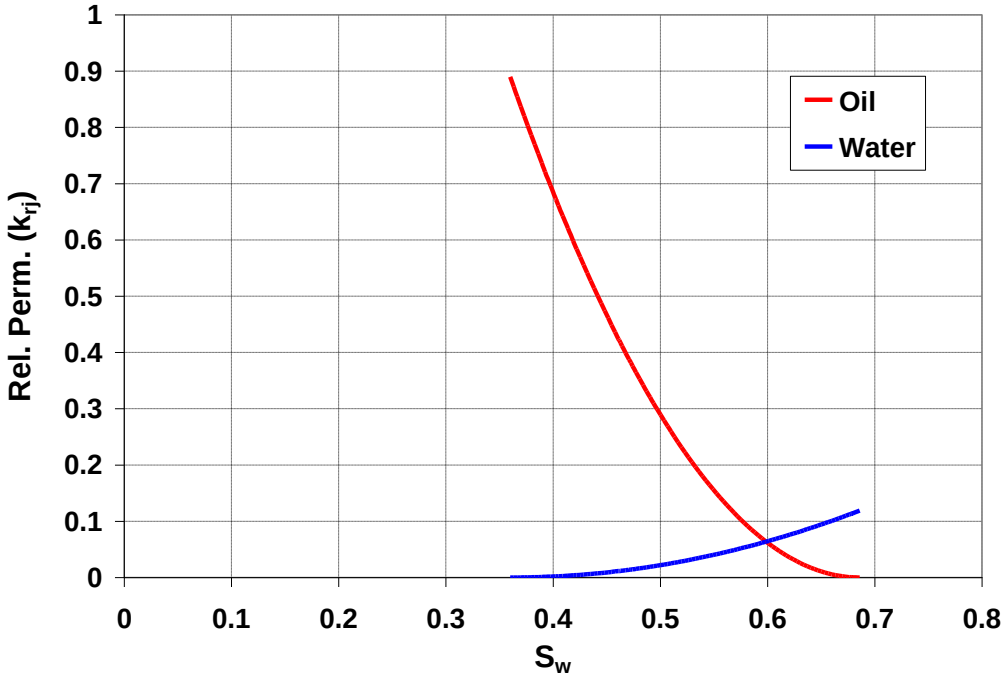

Figure 8.34: Corey Model Estimation of Relative Permeability (n = 2).

The concentrations of polymer for the ASP slug and polymer drive were determined based on the polymer viscosity experiments at reservoir temperature show in Figure 8.35.

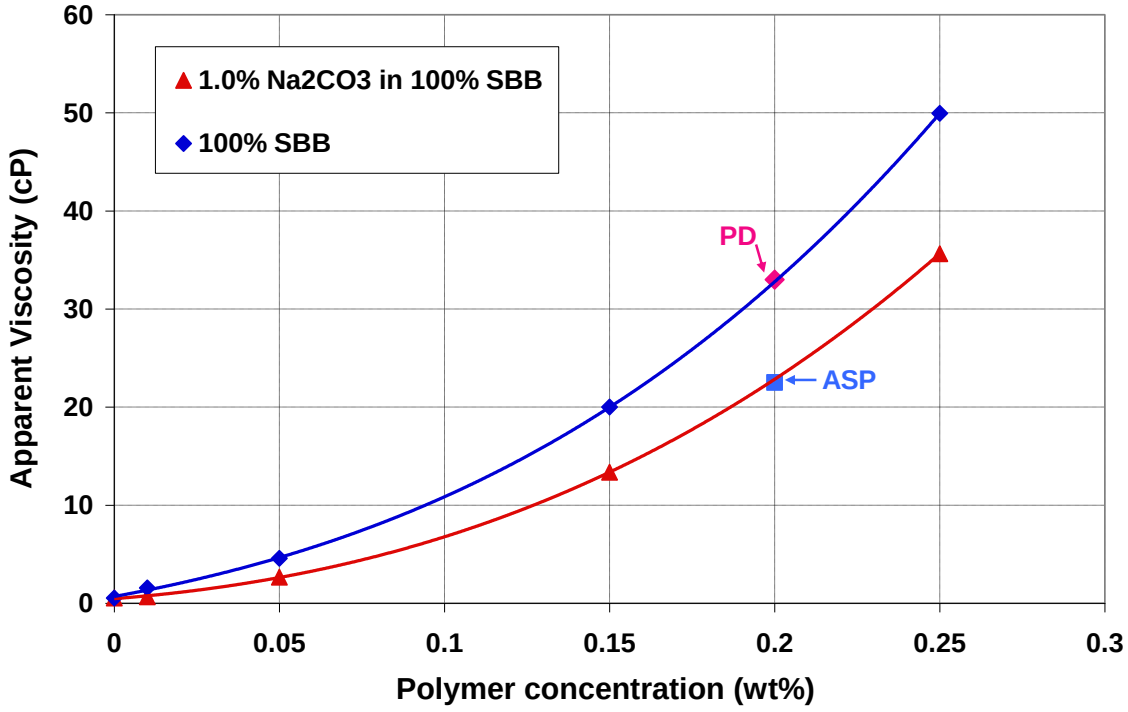

Figure 8.35: Polymer Viscosities for GB-2 at 55°C and $10s^{-1}$.

As can be seen in the figure, at 0.2wt% (2000ppm) polymer concentration, ASP slug will have a viscosity of 23cP, which is greater than oil bank apparent viscosity (18cP). And the polymer drive will have a more than sufficient value of 32cP. All the measured fluid viscosities at reservoir temperature are listed in Table 8.12. Characteristics and chemical composition for the ASP slug and polymer drive for coreflood experiment GB-2 are tabulated in Table 8.13 and Table 8.14 respectively.

Table 8.12: Fluid Viscosities Measured at 55°C and $10s^{-1}$.

Brine Viscosity (cP)	0.54
Crude Oil Viscosity (cP)	28
ASP Slug Viscosity (cP)	23
Polymer Drive Viscosity (cP)	32

Table 8.13: Alkali Surfactant Polymer Slug Data for GB-2 Coreflood.

Pore Volume Injected (PV)	0.3
Petrostep S-13C (C_{13}-9PO-SO_4)	0.3%
Neodol 25-12 (C_{12-15}-12EO)	0.1%
Sodium Carbonate (ppm)	10000
TDS (ppm)	17360
Floppam 3330S (ppm)	2000
Front Velocity (ft/day)	2
Slug Viscosity (cP)	23

Table 8.14: Polymer Drive Data for GB-2 Coreflood.

Polymer Drive Injected (PV)	2
TDS (ppm)	7360
Floppam 3330S	2000
Front Velocity (ft/day)	2
Drive Viscosity (cP)	32

GB-2 Chemical Flood Recovery

A 0.3PV ASP slug with 2000ppm Floppam 3330S polymer concentration (23cP) was injected at 2 ft/day followed by a polymer drive with 2000ppm 3330S (32cP) at the same rate. Figure 8.36 below shows the pressure data for the chemical flood process. The oil breakthrough occurred at 0.3PV and the emulsion breakthrough occurred at 0.88PV. The total oil recovery was calculated to be 92% of residual oil. A high oil cut (around 50%) was observed and most of the free oil was recovered before emulsion breakthrough. The residual oil saturation after the chemical flood was 2.5%.

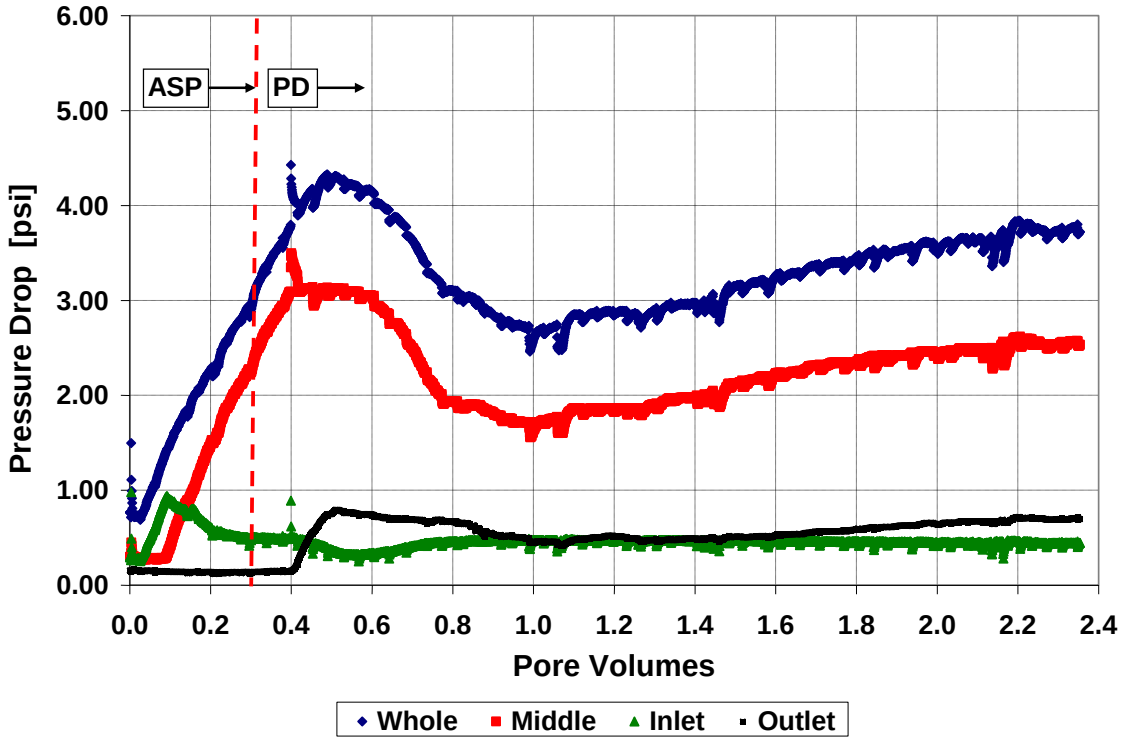

Figure 8.36: GB-2 ASP Pressure (q = 0.04ml/min).

Figure 8.37 shows the oil recovery data for the GB-2 coreflood. Effluent pH was measured periodically using a pH meter. Figure 8.38 shows the effluent pH and emulsion cut history during the chemical flood. It seems that alkali and surfactant (contained in the emulsion phase) were able to travel together and thus provide optimum condition inside the core, which obviously resulted in high oil recovery. Since the coreflood was not performed on a reservoir core, the surfactant retention was not measured in current experiment. Based on the high oil recovery and highly reactive crude oil, it was believed that the retention level would be quite low (Solairaj *et al.*, 2012b).

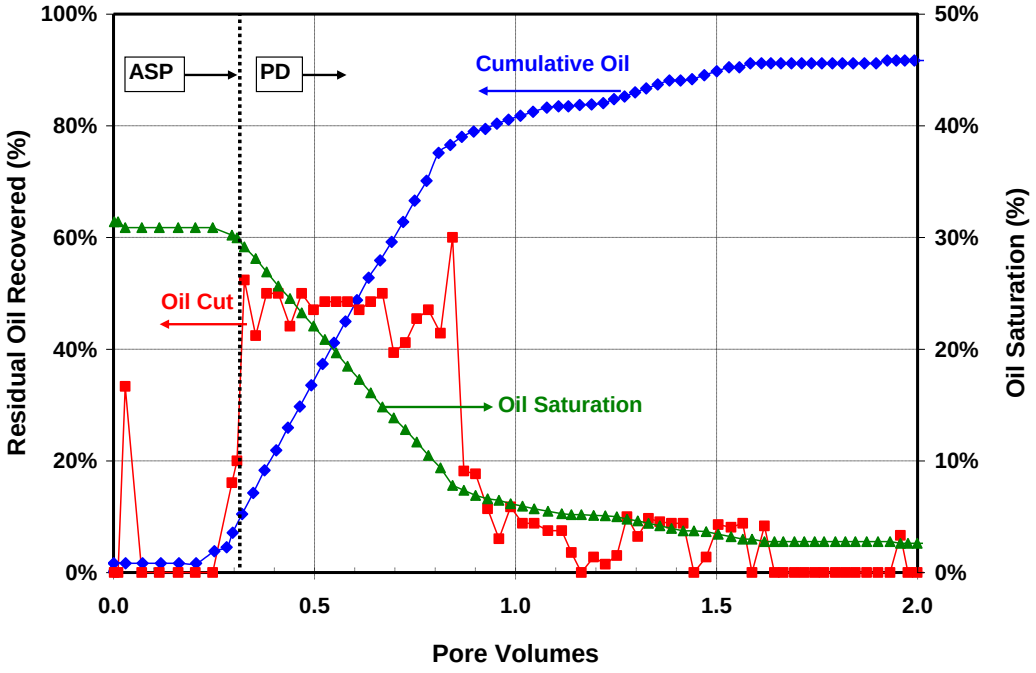

Figure 8.37: GB-2 Oil Recovery.

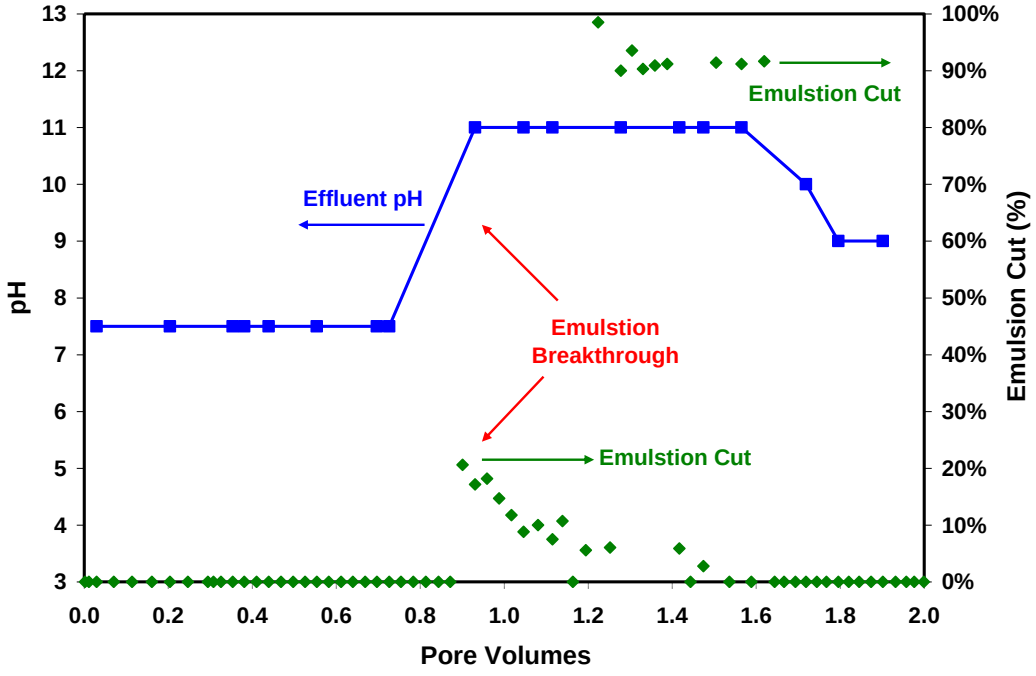

Figure 8.38: GB-2 Effluent pH and Emulsion Cut.

8.4 SUMMARY

A systematic laboratory design study was carried out to identify, test, and verify the optimum chemical formulation for the Brookshire Dome ASP flood pilot project. The optimum ASP formulation (0.3wt% Petrostep S13-C, 0.1wt% Neodol 25-12, and 1wt% Na_2CO_3 in 100% SBB, with 2000 ppm 3330S) successfully recovered over 90% waterflood residual oil in a Berea sandstone coreflood. The poor quality of core plugs from the field prevented us from conducting coreflood experiments using reservoir core, which leaves some uncertainties in the design process.

Chapter 9: Pilot-Scale ASP Flood Design

This chapter presents modeling and simulation of a pilot scale ASP flood. The primary goal of the simulation was to optimize the field scale performance by simulating and comparing various injection and operating strategies.

The University of Texas Chemical Compositional Simulator, UTCHEM (Delshad *et al.*, 1996; UTCHEM, 2000; Hourshad, 2008) is used for modeling the ASP process. The simulator is a 3D multi-component chemical flooding simulator. Various physical and chemical phenomena modeled include microemulsion phase behavior and interfacial tension models, compositional phase viscosity models, phase trapping models, three-phase relative permeability models that depend on trapping number, chemical adsorption models, and polymer rheology models. It is worth stressing from the onset of this chapter that setting up a UTCHEM ASP simulation is quite an involved process. Invaluable guidance and inputs from Mr. Faiz Veedu, Mr. Abhinav Sharma and Dr. Delshad are greatly appreciated.

9.1 COREFLOOD HISTORY MATCHING

9.1.1 Phase Behavior: Experiments and Modeling

Before the pilot simulations were started, phase behavior and laboratory coreflood data were used to estimate as many simulation parameters as possible. Phase behavior experiments identify surfactants with acceptably high oil solubilization, rapid coalescence time, and minimal tendency to form liquid crystals, gels, or macroemulsions. Solubilization ratio diagrams are routinely used to represent the phase behavior. They provide an understanding of the sensitivity of the surfactant solution behavior to additional electrolytes. They also provide information on the electrolyte concentrations at

which a transition from Type I to Type III to Type II is observed. The salinity at which the transition occurs from Type I to Type III is called lower critical salinity (CSEL) and the salinity at which transition occurs from Type III to Type II is called upper critical salinity (CSEU). In addition, these diagrams provide information on the solubilization of the oil in the middle phase and the optimum salinity.

As discussed in Chapter 8, numerous surfactant / co-solvent / alkali / polymer combinations were tested to examine both the aqueous and microemulsion phase behavior using the field crude oil, and the best formulation was selected for testing in coreflood experiment. Alkali (Na_2CO_3) was added into synthetic Brookshire brine (SBB) to increase the pH and thereby reduce the surfactant adsorption. With the reactive Brookshire crude, one other primary use of alkali is to react with naphthenic acids in the crude oil to produce in-situ hydrophobic surfactant or soap. It also adds ionic strength along with SBB to bring the salinity up to optimum value. The surfactant formulation identified from Chapter 8 consists of 0.3wt% Petrostep S13-C (Exxal TDA-9PO-SO_4), 0.1wt% Neodol 25-12 (C_{12-15}-12EO).

Figure 9.1 shows the data of phase behavior experiment done on the above surfactant system where the oil concentration is fixed at WOR=1 (50% oil and 50% water). The optimum salinity observed from the surfactant phase behavior was 1% Na_2CO_3 in SBB (0.310meq/ml salinity in total). One thing worth noting is the salinity calculation employed here. Both Na_2CO_3 and background brine salinity contribute to the total salinity, and thus they should both be considered in modeling phase behavior. The phase behavior is modeled in UTCHEM using Hand's rule of bimodal curve (UTCHEM, 2000). The equations derived from Hand's model for phase behavior calculations are solved using the height of bimodal curve as input parameters, which in UTCHEM are HBNC70, HBNC71 and HBNC72, representing the height of bimodal curve at zero,

optimum and twice optimum salinity conditions. The values of these parameters are obtained by matching the laboratory measured phase behavior data. This matching step is crucial to get the height of bimodal curve (HBNC) parameters and the salinity window (CSEL and CSEU) which are to be used for coreflood modeling and further to conduct pilot scale simulations. UTCHEM batch mode simulations were conducted by Mr. Faiz Veedu to predict the phase behavior of the current surfactant system. The curves in Figure 9.1 are UTCHEM simulated results. Figure 9.2 shows the phase behavior match at 30% oil concentration. Table 9.1 lists the phase behavior parameters used to obtain these matches.

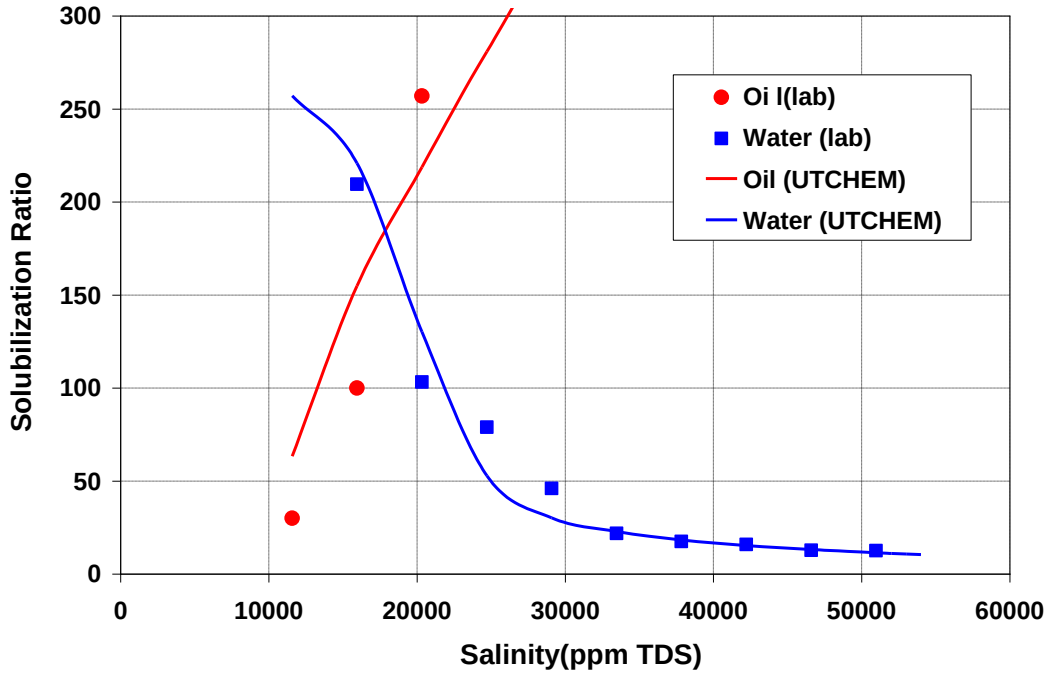

Figure 9.1: Phase Behavior Match for 50% Oil Concentration.

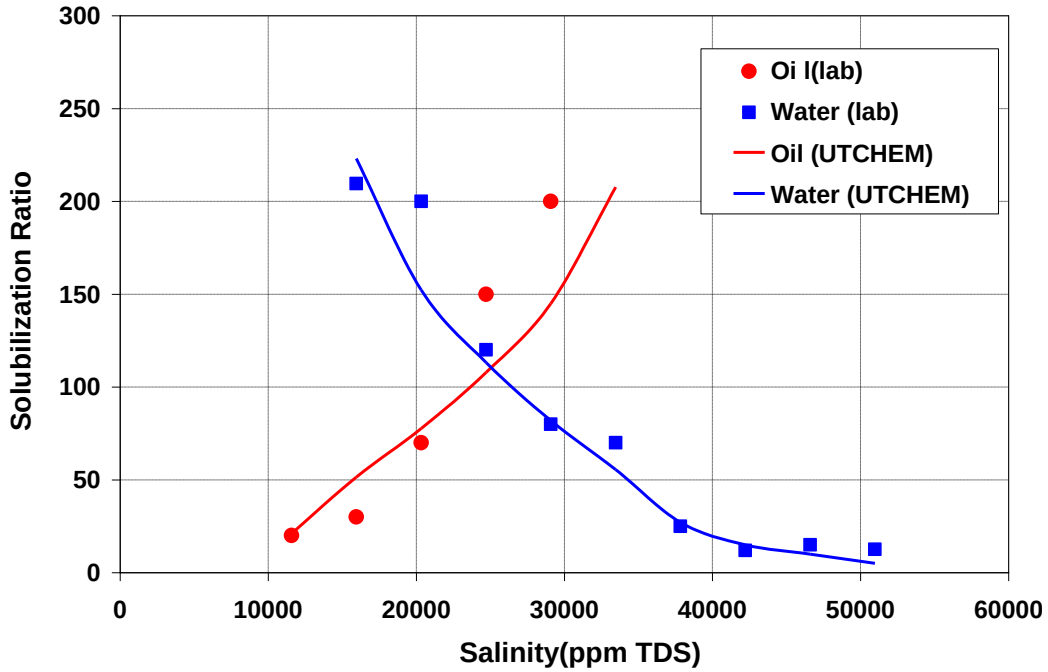

Figure 9.2: Phase Behavior Match for 30% Oil Concentration.

Table 9.1 Phase Behavior Parameters to Match the Experimental Data Shown in Figure 9.1 and Figure 9.2.

Height of Binodal Curve at Zero Salinity, HBNC70	0.007
Height of Binodal Curve at Optimum Salinity, HBNC71	0.002
Height of Binodal Curve at Twice Optimum Salinity, HBNC71	0.007

9.1.2 Polymer Rheology Modeling

The basic idea of adding polymer is to provide a viscosity of about 20cP in the surfactant slug (see Chapter 8) and greater than 20cP in the polymer drive. To achieve this in the slug at 0.310meq/ml total salinity, 2000ppm Floppam 3330S was added. Moreover, for the polymer drive, 2000ppm 3330S was used to provide about 30cP viscosity at 0.243meq/ml. Figure 9.3 through Figure 9.5 present a comparison of polymer lab data along with the UTCHEM model under reservoir conditions at various concentrations, salinities and shear rates.

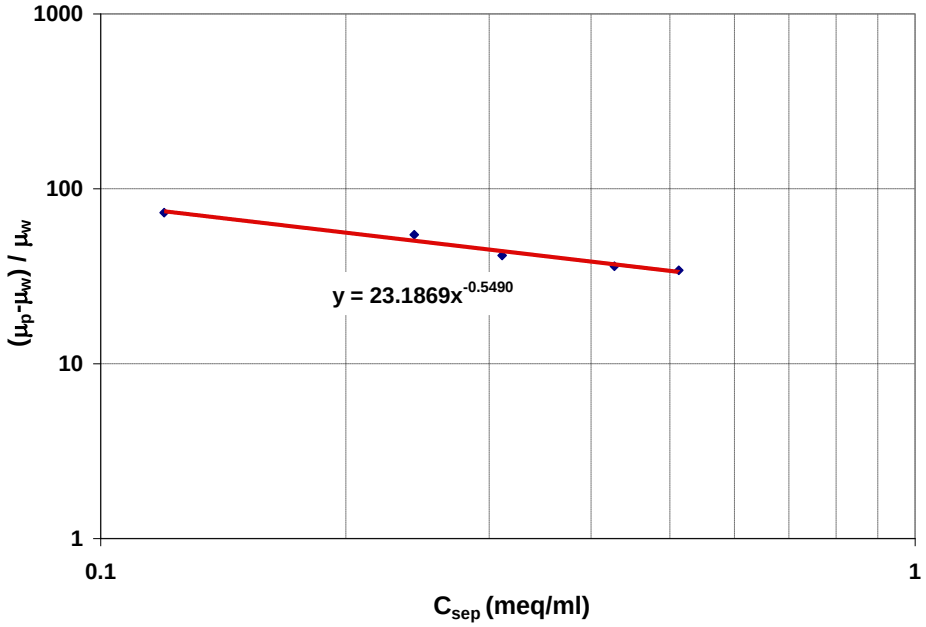

Figure 9.3: UTCHEM Model Fit to Lab Data: Viscosity vs. Salinity (2000ppm Floppam 3330S at 55°C).

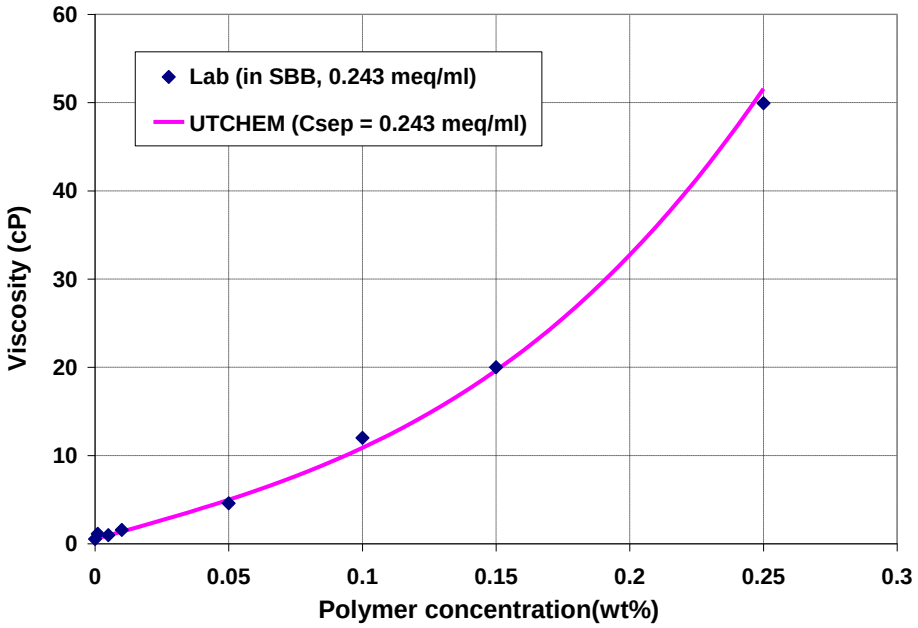

Figure 9.4: UTCHEM Model Fit to Lab Data: Viscosity vs. Concentration (Floppam 3330S in SBB of 0.243meq/ml at 55°C).

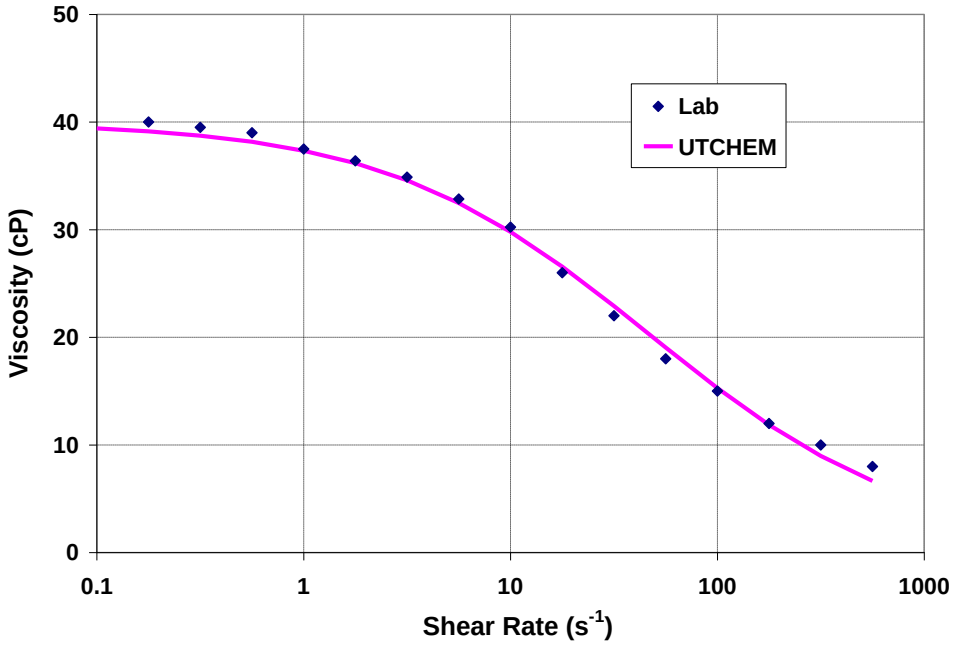

Figure 9.5: UTCHEM Model Fit to Lab Data: Viscosity vs. Shear Rate (2000ppm Floppam 3330S in 100% SBB at 55°C).

9.1.3 Geochemical Input Data

The UTCHEM geochemistry model (Hourshad, 2008) is based on a local thermodynamic equilibrium assumption to compute the detailed composition of the reservoir rock and fluids in the presence of reactions among the injected species and reservoir rock and fluids. The reactions include aqueous electrolytes chemistry, precipitation / dissolution of minerals, ion-exchange reactions with the matrix, and the reaction of acidic components of the oil with bases in the aqueous solution.

A preprocessor called EQBATCH can be used for UTCHEM to calculate the initial equilibrium state of the reservoir. EQBATCH writes the output data in a format similar to the geochemical input data of UTCHEM, so it can be directly pasted into the input for UTCHEM. Formation brine composition and elemental concentration, pH, temperature, acid number of the crude oil and some knowledge about the rock and its

minerals are all important data for EQBATCH calculation. The UTCHEM geochemical input for current simulation model was kindly provided by Mr. Faiz Veedu and Mr. Abhinav Sharma from EQBATCH calculations.

9.1.4 Coreflood Simulation

As discussed in Chapter 8, the ASP formulation was tested in coreflood experiment. About 92% of the waterflood residual oil was recovered. This coreflood was simulated to estimate various simulation parameters needed to simulate the ASP pilot. The UTCHEM model parameters for phase behavior data, surfactant, relative permeability (Figure 9.6), capillary desaturation curve (Figure 9.7), and polymer viscosity dependence on salinity / polymer concentration / shear rate are listed in Table 9.3. The adsorption parameters for polymer were obtained by assuming a maximum polymer adsorption and using core properties. The adsorption parameters of surfactant were obtained by matching coreflood results using UTCHEM simulation.

Table 9.2 Review of Core and Fluid Properties for GB-2 Coreflood.

Core & Fluid Properties (from Chapter 8)	
Porosity	0.2014
Absolute Permeability (md)	491
Temperature (^{o}F)	131
Length (cm)	29.067 (0.9536ft)
Diameter (cm)	2.54 (0.0833ft)
Residual Water Saturation, S_{wr}	0.36
Residual Oil Saturation, S_{orw}	0.314
Water Endpoint Relative Perm., k^{o}_{rw}	0.119
Oil Endpoint Relative Perm., k^{o}_{ro}	0.89
Water Viscosity (cP)	0.54
Oil Viscosity (cP)	28

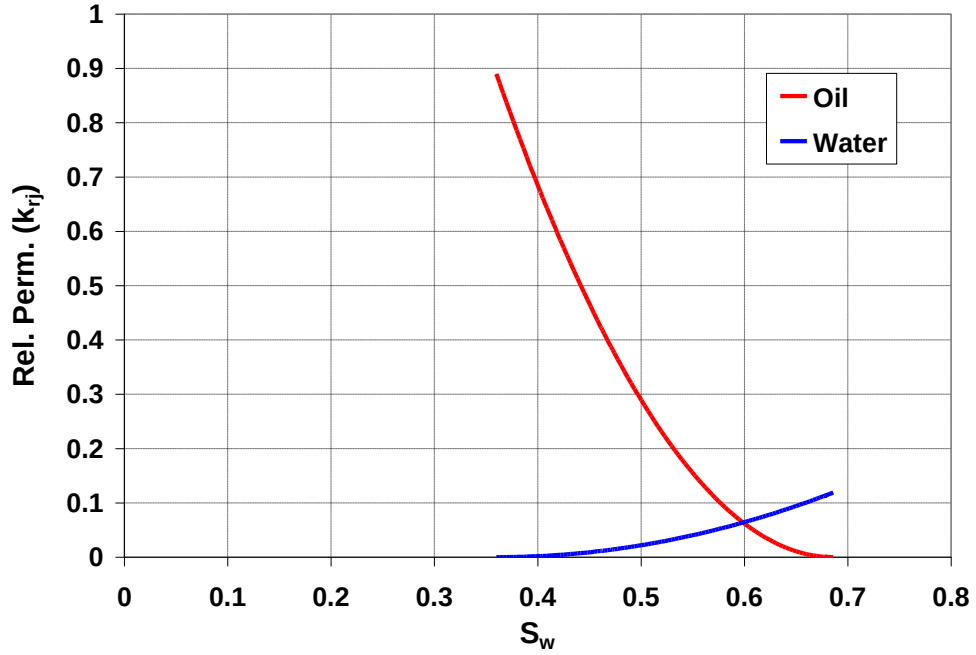

Figure 9.6: Relative Permeability Curves used in UTCHEM Coreflood Simulation.

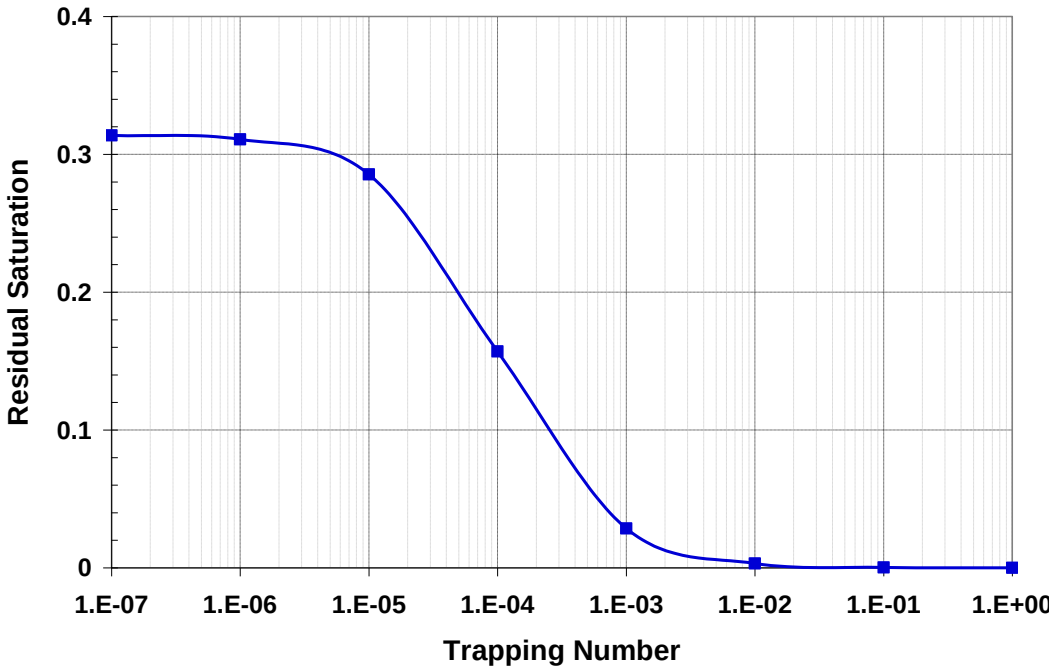

Figure 9.7: Capillary Desaturation Curve for Oil in Simulation Model.

Table 9.3 Summary of Simulation Inputs for GB-2 Coreflood.

Simulation Inputs	
Simulation Model Dimension (ft)	0.9536 × 0.07385 × 0.07385
Number of Grid Blocks in X, Y, Z	100 × 1 × 1
Capillary Desaturation Parameters for Water, Oil, ME	1865, 10000, 364.2
Intercept of Binodal Curve at Zero, OPT., and 2OPT. Salinities (HBNC70 – HBNC72)	0.007, 0.002, 0.007
CMC (volume fraction)	0.001
Type III Salinity Window (CSEL, CSEU, COPT)	0.25, 0.60, 0.31
Interfacial Tension Parameters for Huh's Model (CHUH, AHUH)	0.3, 10
Log10 of Oil/Water Interfacial Tension (XIFTW)	1.3
Compositional Phase Viscosity Parameters for ME (ALPHAV1 - ALPHAV5)	1.0, 2.0, 0.5, 0.5, 0.5
Parameters to Calculate Polymer Viscosity (AP1, AP2, AP3)	71.473, 2, 1630.083
Salinity Dependence of Polymer Viscosity (SSLOPE)	-0.5490
Shear Rate Dependence of Polymer Viscosity (GAMMAC, POWN, GAMHF)	4.0, 1.68, 46.86
Permeability Reduction Factors (BRK, CRK)	100, 0.015
Relative Perm. Exponent of Water	2.0
Relative Perm. Exponent of Oil	2.0
Physical Dispersion Coefficient for Water, Oil, ME (ALPHAL1-3, ALPHAT1-3)	0.02, 0.002
Surfactant Adsorption Parameters (AD31, AD32, B3D)	2.7, 0.1, 1000
Polymer Adsorption Parameters (AD41, AD42, B4D)	3.9, 0, 100

Figure 9.8 through Figure 9.10 show the match between the simulation and measured data for the GB-2 coreflood. As shown in Figure 9.8, oil breakthrough occurs

at about 0.28PV with an oil cut of about 50%, which is in close agreement with experimental observations. The cumulative oil recovery was also satisfactorily matched.

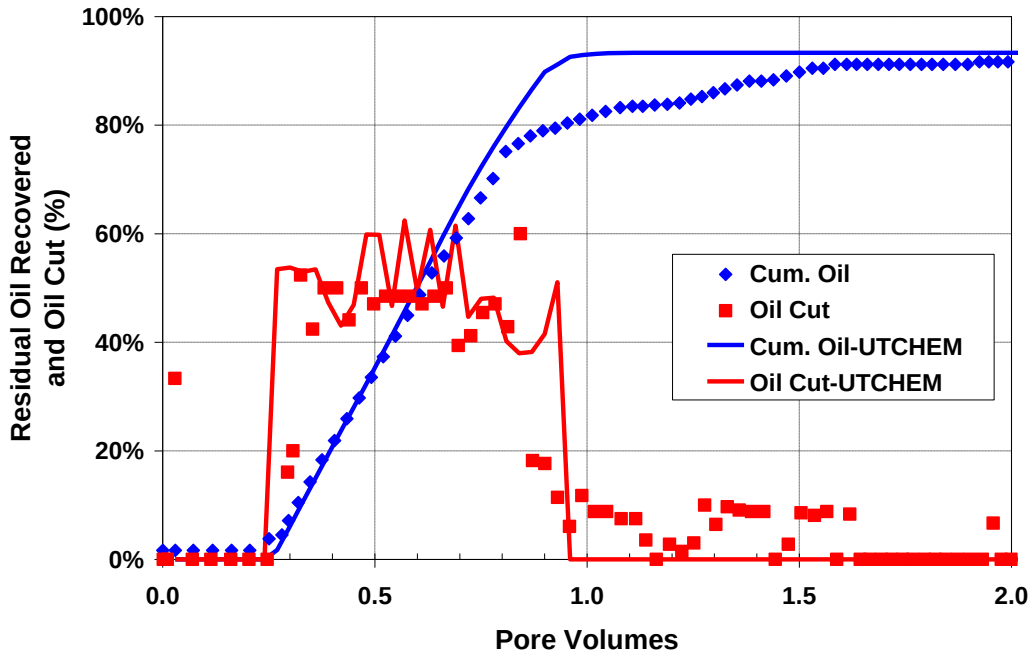

Figure 9.8: Comparison of Simulated and Measured Oil Recovery and Oil Cut for GB-2 Coreflood.

Figure 9.9 shows a good match between the simulation and measured data for the effluent pH. Winsor Type III salinity region at 0.5PV of injection is shown in Figure 9.10, which is bounded by CSEU and CSEL. This is a good illustration of how Type III region is affected by the chemical propagation in the core. The effective salinity passes through the Type III region in the middle of the core and return back to Type I, which gives a negative salinity gradient to the system (at least partially). An ultra-low interfacial tension (less than 0.001dyne/cm) is achieved when the salinity passes through the Type III region. Also shown in the plot is the oil concentration. It is clearly shown that a substantial oil bank is formed in the core.

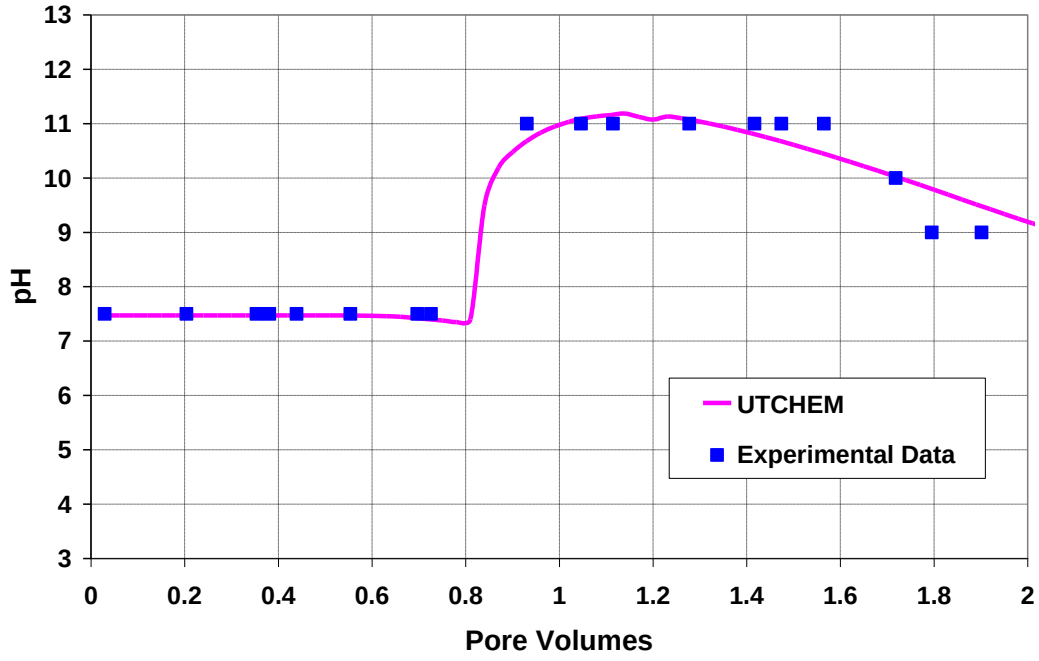

Figure 9.9: Comparison of the Effluent pH between UTCHEM and Experimental Data for GB-2 Coreflood.

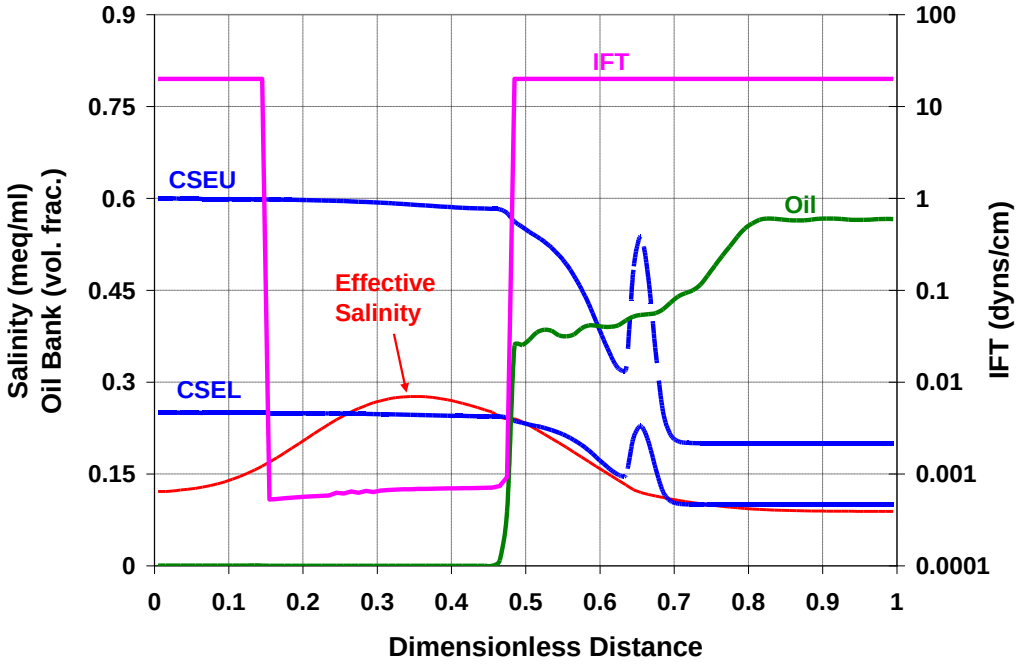

Figure 9.10: Simulated Salinity, IFT and Oil Saturation for GB-2 at 0.5 PV.

9.2 PILOT SCALE SIMULATION STUDY

Before the simulation results are presented for this section, it is imperative to discuss the reservoir and the simulation model. A detailed geological model for the Catahoula sand was built using data from logs from each well and from data collected as a part of the pilot such as flowing spinner surveys and an inter-well tracer test program.

9.2.1 Simulation Model Setup

The inverted five-spot pattern and associated peripheral producers (shown as the red-boxed area in Figure 9.11) represents the area of interest and is a part of ~ 50acre simulation model. In theory a direct five spot is preferable, as it enables a better fluid confinement. But too large a quantity of chemicals would probably be wasted outside the pattern and the success of the pilot would hinge heavily on the behavior of the center producer. To our knowledge, the pattern is not confined by any geological boundaries (at least not nearby). Field production history suggests a strong aquifer charge with a preferential flow direction of SW to NE (red arrows in Figure 9.11).

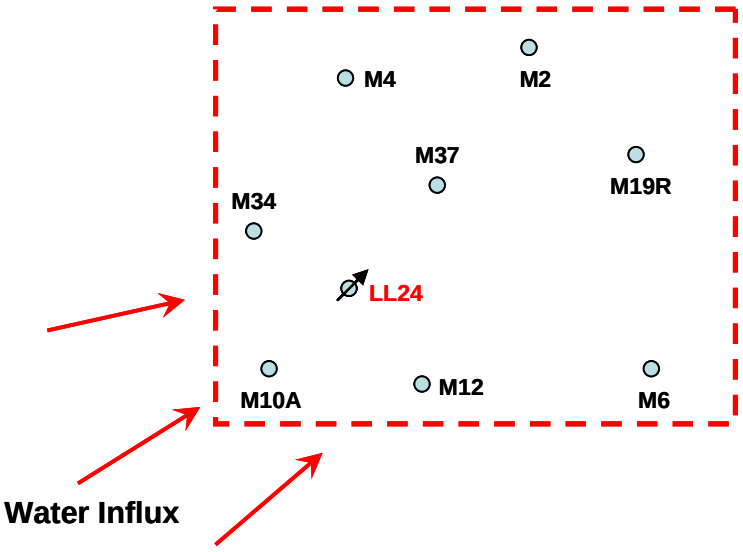

Figure 9.11: Areal View of the Well Placement in the Simulation Model.

Pattern Volume Calculation

Pattern volume calculation was conducted by geologists from Layline Petroleum. And this is a key piece of information for evaluating project economics, as well as interpreting pilot results later on. The pilot pattern was divided into 17 sub-polygons for area and volume calculations as shown in Figure 9.4. Porosity is taken to be a constant of 0.33, and the original oil saturation in the reservoir is 0.75. A formation volume factor for oil is taken to be 1.05. Volume averaged net pay thickness if 49.6 ft.

Table 9.4 Areal and Volumetric Calculations for Pilot Pattern.

Polygon No.	Avg. Net Pay (ft)	Area (acre)	Pore Volume (bbl)	OOIP (STB)
1	48	0.004	519	371
2	48.5	0.074	9215	6582
3	49.5	0.181	22933	16381
4	50.5	0.113	14626	10447
5	51.5	0.120	15866	11333
6	52.5	0.105	14128	10092
7	53.5	0.085	11703	8359
8	54	0.025	3507	2505
9	53.5	0.012	1666	1190
10	54	0.008	1050	750
11	48.5	0.108	13437	9598
12	47.5	0.103	12585	8989
13	46.5	0.127	15107	10791
14	45.5	0.040	4712	3366
15	44.5	0.026	3005	2146
16	43.5	0.022	2442	1744
17	43	0.007	809	578
Total		1.16	147310	105222

Spinner Survey

A spinner survey was conducted by Layline Petroleum (the Operator) on the injector well (Martin 24). The perforated interval (72 ft in total) runs from 2118ft down to

2190ft, as shown in Figure 9.12 (left). With an average net pay thickness of 49.6ft, the average net-to-gross (NTG) is about 0.70. It appeared during the test that the injected fluid predominantly entered the reservoir through the top 12ft of perforations with less fluid going to the bottom layers. Based on the change in slope of the flow profile (fraction of flow going into each section of sand), it would be more realistic to further divide the perforation interval into thinner layers as shown in Figure 9.12 (right). The top layers have higher permeability than the bottom layers. Furthermore, a water injectivity of 1.8bpd/psi was reported from the field during the tracer test injection. Based on this, an average (arithmetic) permeability of 125md was estimated with an assumed relative permeability value of 0.12 (same as Berea core data). Individual layer permeability can then be estimated combining spinner survey information.

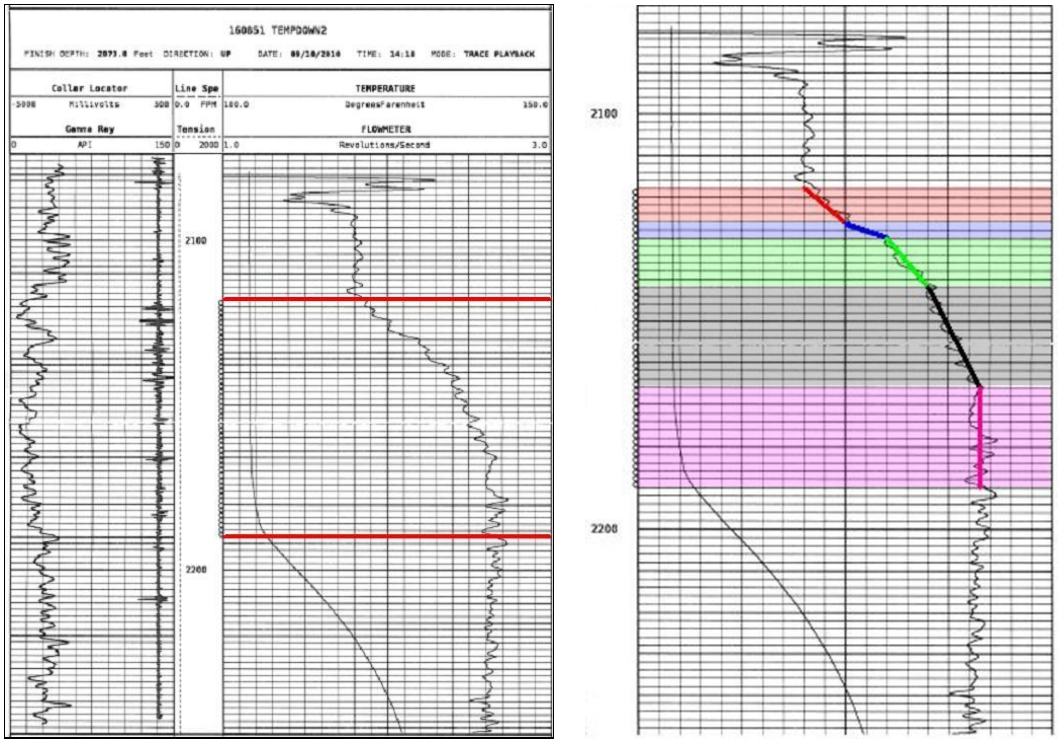

Figure 9.12: Spinner Survey Results Provided by Weatherford.

Two different layering and gridding schemes were implemented in the current study, the coarser (5-layer) and the refined (9-layer) grids. The layer division of the coarser model was based upon Figure 9.12 (right). The individual layer properties, including thickness, x-direction permeability, total grid block number and cell dimensions in x, y, z directions of this model are listed in Table 9.5 and Table 9.6. For simplicity, the net pay thickness was used directly as layer thickness in the simulation. For both gridding schemes, we assume $k_y/k_x = 1$, $k_z/k_x = 0.2$, and $\phi = 0.33$.

Table 9.5 5-Layer Model: Individual Layer Properties.

Layer No.	Thickness (ft)			k_x (md)
	Gross	NTG	Net (model)	
1	8	0.7	5.6	250
2	4		2.8	500
3	12		8.4	167
4	24		16.8	100
5	24		16.8	20

Table 9.6 5-Layer Model: Reservoir Size and Dimensions.

Simulation Model Volume (ft × ft × ft)	2010.86 × 1355.14 × 50.4
Number of Grid Blocks in x, y, z	61 × 43 × 5
Cell Dimensions in x (ft)	18 × 43.71; 30 × 21.855; 13 × 43.71
Cell Dimensions in y (ft)	8 × 43.71; 24 × 14.57; 11 × 43.71
Cell Dimensions in z (ft)	8, 4, 12, 24, 24
Pattern Pore Volume (bbl)	150097
Initial Oil Saturation, S_{oi}	0.75
Residual Oil Saturation to WF, S_{orw}	0.4

The more refined 9-layer model was used to investigate the layering effect on simulation results. As can be seen from Table 9.8 and Table 9.10, smaller cell dimension (in x-y plane) within the pattern area was also implemented in this model with the intention to better capture the near wellbore flow behavior.

Table 9.7 9-Layer Model: Individual Layer Properties.

Layer No.	Thickness (ft)			k_x (md)
	Gross	NTG	Net (model)	
1	4		2.8	250
2	4		2.8	250
3	4		2.8	350
4	6		4.2	167
5	6	0.7	4.2	167
6	12		8.4	100
7	12		8.4	100
8	12		8.4	50
9	12		8.4	50

Table 9.8 9-Layer Model: Reservoir Size and Dimensions.

Simulation Model Volume (ft × ft × ft)	2010.86 × 1355.14 × 50.4
Number of Grid Blocks in x, y, z	80 × 59 × 9
Cell Dimensions in x (ft)	17 × 43.71; 51 × 14.57; 12 × 43.71
Cell Dimensions in y (ft)	7 × 43.71; 42 × 14.57; 10 × 43.71
Cell Dimensions in z (ft)	3 × 2.8; 2 × 4.2; 4 × 8.4
Pattern Pore Volume (bbl)	150097
Initial Oil Saturation, S_{oi}	0.75
Residual Oil Saturation to WF, S_{orw}	0.4

Multi-well Tracer Test

A multi-well bromide tracer study was conducted in the pilot area for a better understanding of inter-well communication in the reservoir. As mentioned earlier, a strong aquifer charge exists in the pilot area. In the simulation model, influx and efflux due to the aquifer were modeled by SW water injection (4 additional injectors) and NE production wells (5 additional producers). It was hoped that tracer test results could also help better quantify the influence of the aquifer.

In the field, 54 barrels of sodium bromide tracer were introduced at concentration of ~50,000ppm and rate of ~1500bpd into the injector, Martin 24. After this initial injection, liquid samples were collected for 70 days from eight offset producing wells and sent to TIORCO laboratory for bromide concentration analysis by ion chromatography. The production wells represented in this study include Martin 2, 4, 6, 10A, 12, 19, 34, and 37 (see Figure 8.1 and Figure 9.11). In general, wells with consistent bromide concentrations 5ppm over baseline are considered to have obvious breakthrough, while wells with 1-4ppm over baseline must be investigated further for other variables before breakthrough can be determined. Figure 9.13 shows the tracer breakthrough profiles on all the monitoring wells.

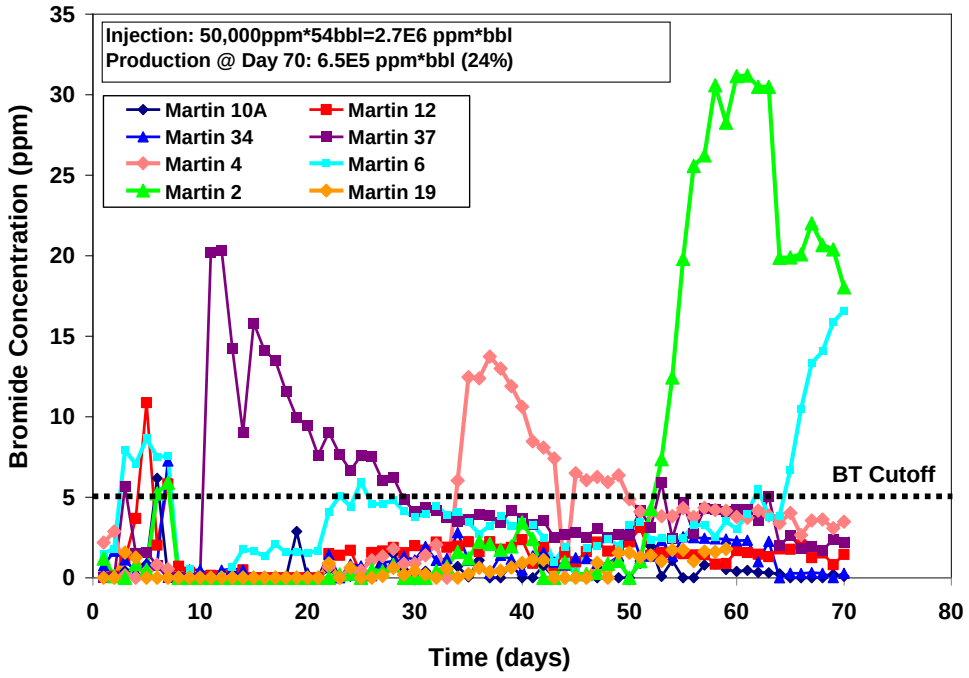

Figure 9.13: Detailed Bromide Tracer Response for All Monitoring Wells 70 Days after Injection.

The field data is quite noisy. Bromide breakthrough was initially observed in production well Martin 37 about 10 days after injection. Tracer breakthrough occurred 35 days after injection in Martin 4, 50 days in Martin 2, and 65 days in Martin 6. Breakthrough was not observed in production wells Martin 10A, 12, 19, or 34 until 70 days after injection. Recall the well locations in the field from Figure 9.11, it would appear that tracer tends to breakthrough earlier in producers (Martin 37, 4, and 2) to the north of the injector (Martin 24), which clearly shows the influence of the aquifer influx. The breakthrough of Martin 6 right after these wells is quite puzzling and seems to suggest the existence of high-perm conduit between the injector and Martin 6. On day 70, the tracer recovery was only about 24%. Although the final recovery would definitely be higher since bromide was still being produced on Martin 2 and 6 at that time, such a low recovery could possibly be attributed to the poor chemical confinement in the pilot area.

Due to the complexity of the breakthrough profile, it was decided to focus the matching effort on the breakthrough time and concentration of Martin 37 well, which is the nearest producer to the injector. The locations and constrains (rate or pressure) of the auxiliary wells (for simulating the aquifer influx) were adjusted to obtain the match shown in Figure 9.14 below. The match was obtained using a 5-layer model. No substantial improvement can be obtained with the 9-layer model. Tracer breakthrough occurs on Martin 37 after 10 days and reaches a peak concentration of 20ppm, which is in good agreement with field data considering the simplicity of the current layer cake model. Martin 4 and 2 also breakthrough fairly early, but the peak concentrations are quite different than the field measurements. A few of the possible reasons for the inconsistency between the field data and simulated results may be fractures, behind pipe flow, thief zones, and other reservoir characterization uncertainties. Nonetheless, a

decision was made at this point to move forward with the simplified layer-cake model for pilot-scale waterflood and ASP flood simulations.

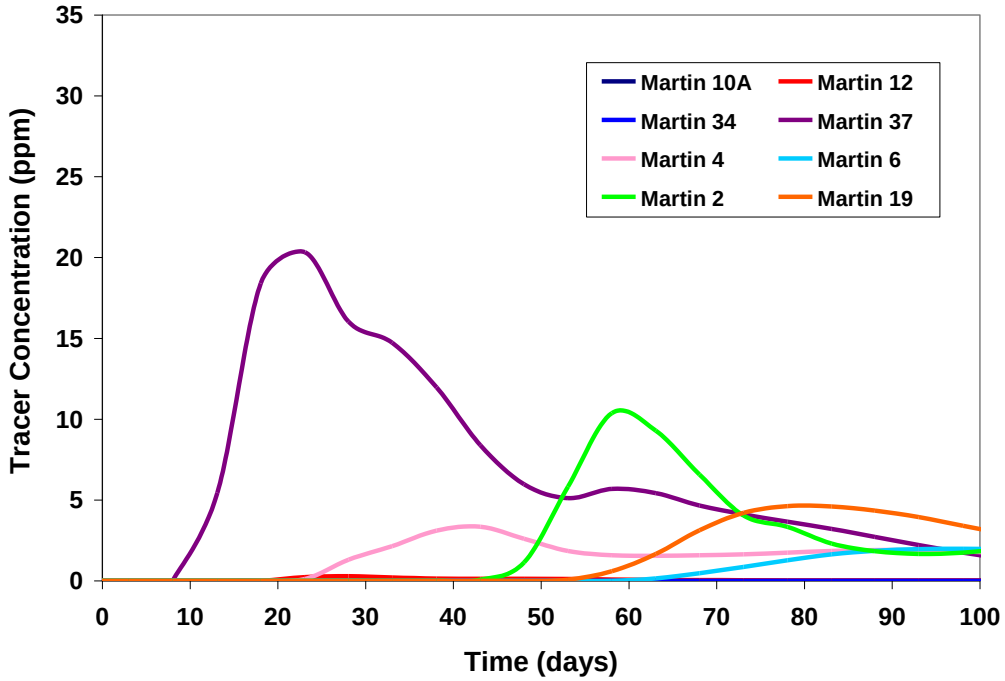

Figure 9.14: Tracer Concentration Response Simulated using UTCHEM.

9.2.2 Waterflood

Brookshire Dome field was discovered in 1996 and has been water flooded for about 15 years prior to the ASP pilot implementation. Due to the reservoir layering, the oil saturation is probably very non-uniform, with some of the layers potentially at residual oil saturation, especially the top high-perm layers. Since no detailed oil distribution information was available, a 15-year waterflood was simulated prior to chemical flooding to establish initial oil saturation in the reservoir. The very limited information regarding reservoir rock properties forced us to use relevant data from the Berea coreflood model.

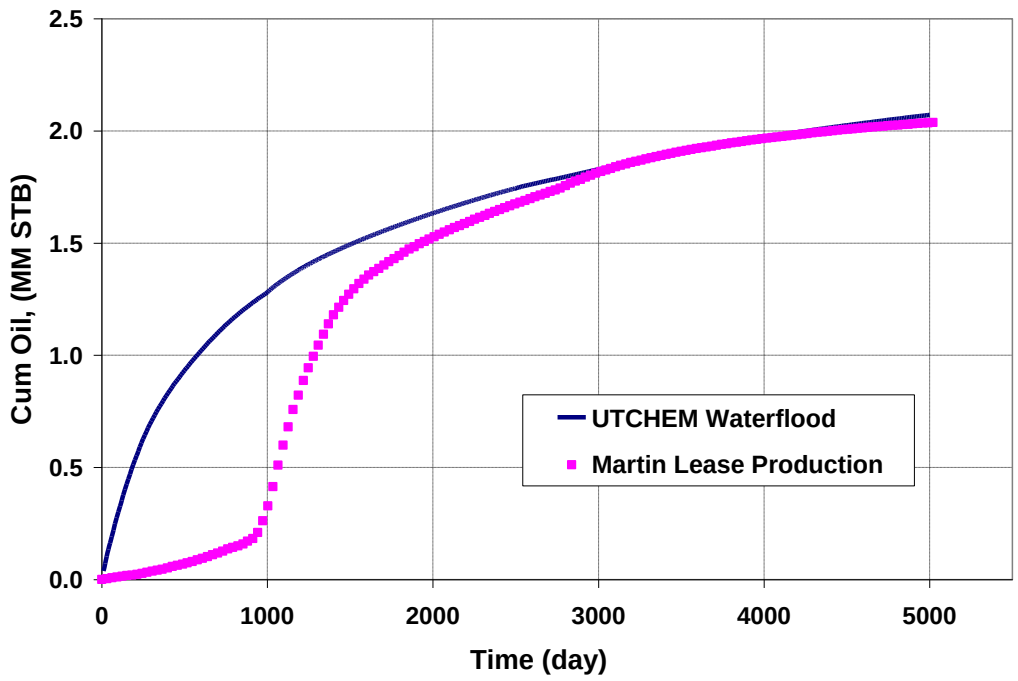

Figure 9.15: Tracer Concentration Response Simulated using UTCHEM. Note that the simulation assumes all the wells produce from day 1 while in reality the wells were drilled over a period of time.

Figure 9.15 shows a cumulative oil production comparison between UTCHEM waterflood simulation and field production data. The model was able to predict the cumulative oil production of about 2 million STB from all producers in the model, which is well in line with the field production data. The rapid increase of oil production was due to extensive field development during that period of time, whereas simulation model already has all the wells in place from the very beginning. After 15 years of production, all the wells in the pilot area are producing at very high water cut (>99%). The average oil saturations within each layer for both models are listed in Table 9.9 and Table 9.10.

Table 9.9 5-Layer Model: S_o and Oil in Place after 5000 Days of Waterflood.

Layer No.	S_o After WF	H (ft)	PV (bbl)	Oil Present after WF (bbl)
1	0.4466	5.6	16677	7403
2	0.4380	2.8	8339	3611
3	0.4289	8.4	25016	11452
4	0.4427	16.8	50032	24831
5	0.4515	16.8	50032	29739
Sum (bbl)		50.4	150097	77036

Table 9.10 9-Layer Model: S_o and Oil in Place after 5000 Days of Waterflood.

Layer No.	S_o After WF	H (ft)	PV (bbl)	Oil Present after WF (bbl)
1	0.4466	2.8	8339	3724
2	0.4380	2.8	8339	3652
3	0.4289	2.8	8339	3576
4	0.4427	4.2	12508	5537
5	0.4515	4.2	12508	5647
6	0.4818	8.4	25016	12053
7	0.5057	8.4	25016	12651
8	0.5933	8.4	25016	14842
9	0.6030	8.4	25016	15085
Sum (bbl)		50.4	150097	76768

The post-waterflood S_o distributions in different layers are shown in Figure 9.16 for the 5-layer model. Clearly the top layers have lower oil saturation, whereas the bottom low-perm layers have more mobile oil left due to poor sweep. Permeability contrast determines that top layers would be preferentially water flooded. Notice for wells M2, 19, and 6, the bottom layer oil saturation is still quite high even after extensive waterflooding. Aside from the poor sweep just mentioned, the fact these wells are relatively closer to the closed simulation boundary may also contributes to the possibly 'false' oil accumulation, although this affect has been partially alleviated by five other producers (for simulating aquifer influx) placed near the model boundary. Based on this

consideration, the production from the peripheral producers will not be counted as cumulative oil produced in the following sections. Only production from the in-pattern producers, namely M34, 37, 10A, and 12, will be counted and presented. This is likely to underestimate the total production from lease area, but provide unambiguous evaluation of the pilot performance, since all the area and volume calculations are made based upon the pilot pattern.

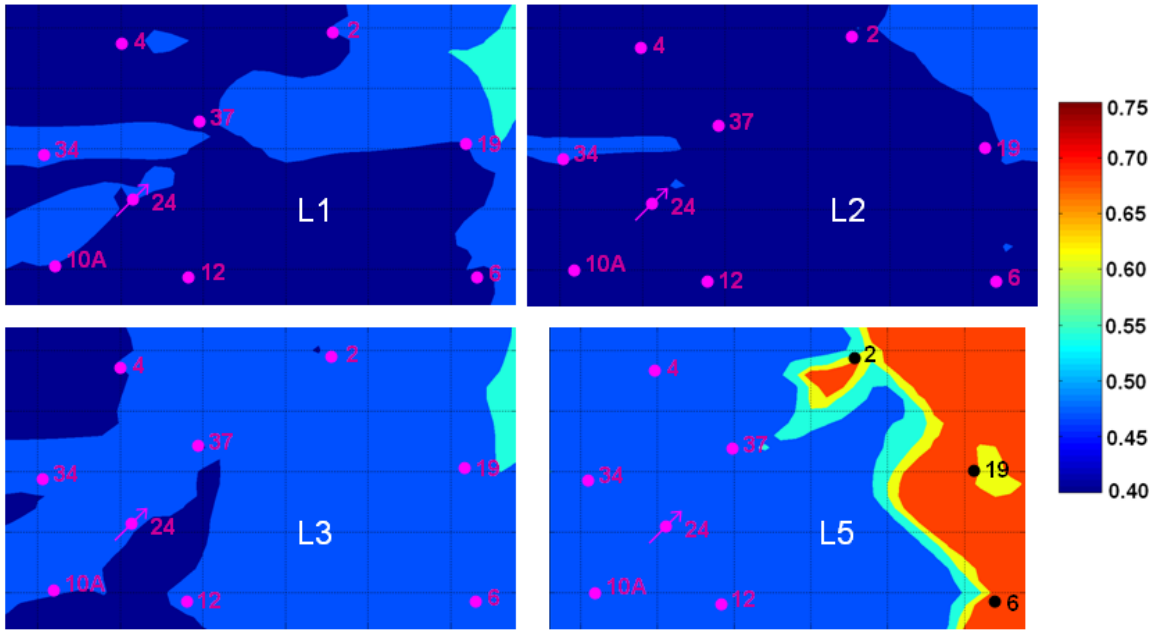

Figure 9.16: Areal View of Post-Waterflood Oil Saturation of Layer 1, 2, 3, and 5 for Coarser Model (5-layer).

9.2.3 General Operating Strategy Comparison (w/ 5-Layer Model)

Unless otherwise specified, all the wells within the pattern are rate constrained. And the rates are specified based on tracer test conditions. Martin 24 is injecting at 1500bpd and the producers are producing at rates specified in the table below. Wells

located on the south side of the pattern, namely M10A and M12 are producing at higher rates to counterbalance the influence of the aquifer influx.

Table 9.11 Producer Rates for Base Case Simulation (from tracer test).

Well No.	Rate (bpd)	Well No.	Rate (bpd)
M4	266	M34	260
M2	308	M37	290
M19	600	M10A	500
M6	442	M12	600

The ASP slug injection (started after waterflooding) lasts for 0.3PV or about 30 days. The formulation injected is the same as in coreflood experiments and simulations. About 0.7PV polymer drive was injected after the ASP slug and this period of injection lasts for 100 days. Water post-flush was conducted after the polymer drive and this lasts for 500 days. Sensitivity simulation runs (see later section) showed that 2000ppm polymer can only provide marginal mobility control. For all later studies, the concentration was raised to 4000ppm 3330S. In the field (see Chapter 10), higher MW polymer FP 3430S was used to maintain high viscosity but at a lower concentration. Table 9.12 lists various operating strategies evaluated in this section using the 5-layer model.

Table 9.12 Different Strategies Investigated in this Section.

Case #	Description
1	Base case ASP flood (30 days ASP slug + 70 days polymer drive)
2	2X ASP injection (doubling the size of slug and drive, 60+140)
3	ASP bottom injection (injecting into bottom layer)
4	Polymer pre-flush + ASP (100 days of polymer first, then ASP)
5	ASP double production rates (doubling the rates on all producers)

Case 1: Base Case ASP Flood

The cumulative oil recovery and oil production rate of Case 1 (base case ASP) is shown in Figure 9.17. The cumulative oil recovery after 500 days is 21,085bbl. The maximum total oil production rate predicted by UTCHEM is about 235bpd. Due to the close well spacing in the pattern, oil bank breakthrough occurs in all the wells within 30 days. The maximum oil rate occurs at about 80 days. It can be seen that the oil bank is still being produced even after the polymer drive is injected (100 days). After about 290 days since the start of the slug injection, the water cut goes back to 99%. Hence, no more incremental oil recovery is counted after that. Chemical cost per barrel of oil produced in this case is about $21.35/bbl (assuming $2/lb surfactant, $1.45/lb co-solvent, $1.48/lb polymer, $0.15/lb alkali, and $1.5/lb EDTA).

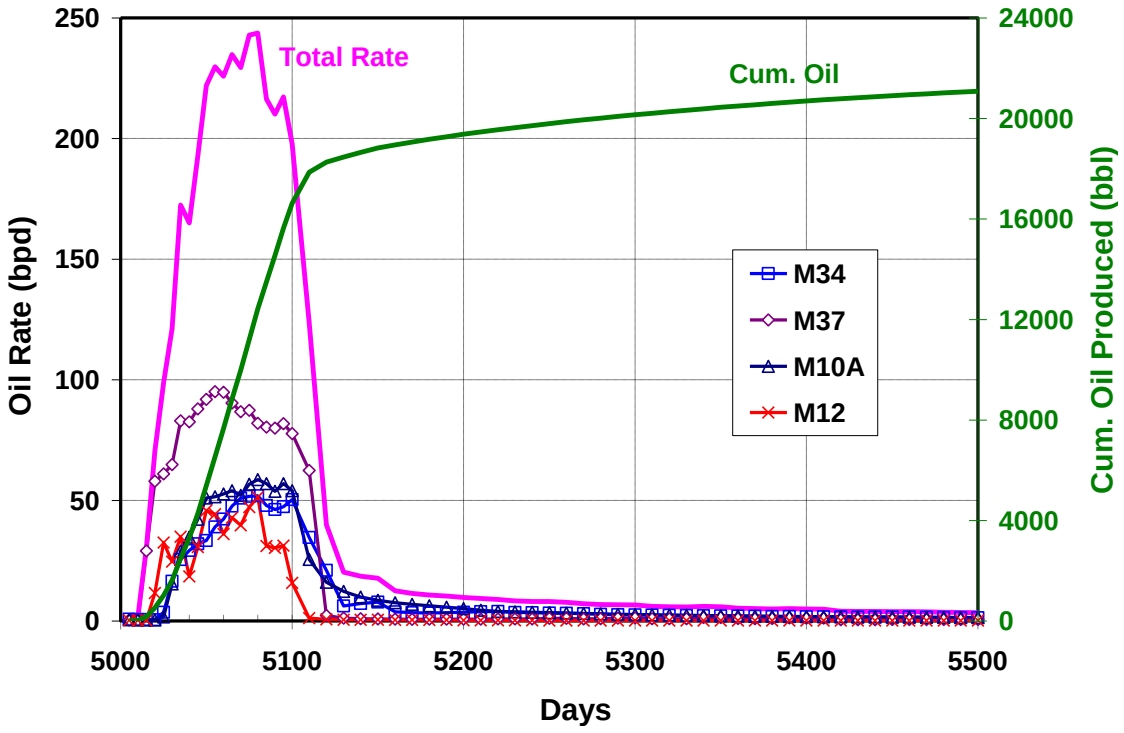

Figure 9.17: Cumulative Oil Recovery and Oil Production Rate for Case 1 (base case ASP injection).

Oil saturation distribution at the end of the ASP flood is shown in Figure 9.18 below. In the top three layers (high-perm), waterflood residual oil has been effectively recovered inside the pilot pattern, rending near zero residual oil saturation. Due to the permeability contrast, however, most chemicals only go into the high-perm top layers, leaving the bottom layer essentially untouched by chemicals, and at high oil saturation.

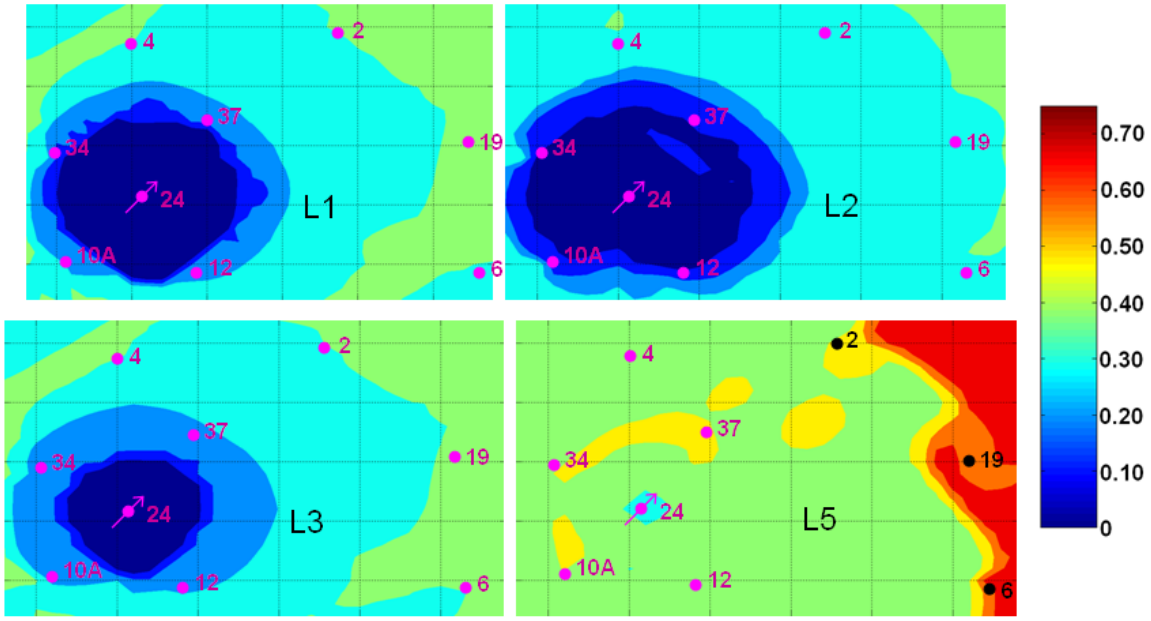

Figure 9.18: Areal View of Post Chemical Flood Oil Saturation of Layer 1, 2, 3, and 5 for Case 1 (base case ASP injection).

Case 2: 2X ASP Injection

Chemical cost accounts for a major part of the expense during a chemical flood; hence, optimizing the injected chemical mass is crucial. In Case 2, the injected the chemical mass is doubled (denoted as 2X ASP) for comparison with the base case. The cumulative oil recovery and oil production rate curves are shown in Figure 9.19. The cumulative oil recovery after 500 days is 34,252 bbl due to more chemical mass injected. The maximum total oil production rate predicted by UTCHEM is about 270bpd. Similar

to Case 1, oil bank breakthrough occurs in all the wells within 30 days. The maximum oil rate occurs at about 70 days. After about 260 days since the start of the slug injection, the water cut goes back to 99%. Both chemical cost and oil production for this case are different from Case 1. Cost per barrel of oil produced is probably a better metric for economic comparison. For Case 2, this number is $26.30/bbl, which is higher than Case 1. In the meantime however, quite some more oil has been produced in this case; with the high oil price these days, the economics of this scenario could still be quite attractive. In the field execution phase, the decision was made to stick to the original 1X ASP injection plan due to project economics; and depending on field performance, further expansion of the project can be carried out accordingly.

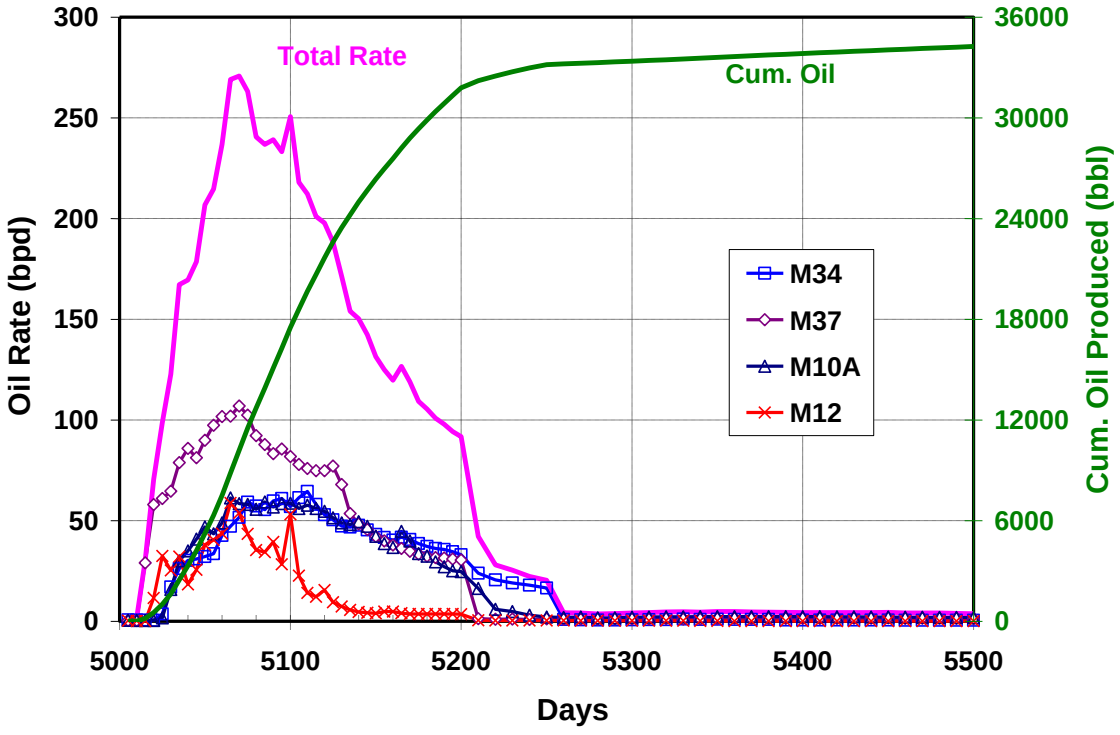

Figure 9.19: Cumulative Oil Recovery and Oil Production Rate for Case 2 (2X ASP injection).

Oil saturation distribution at the end of the ASP flood is shown in Figure 9.20 below. In the top three layers (high-perm), near zero residual oil zone is further expanded in this case due to more chemical injection. And chemicals start to penetrate into the low-perm bottom layer. The oil saturation of the near injector region has been effectively reduced.

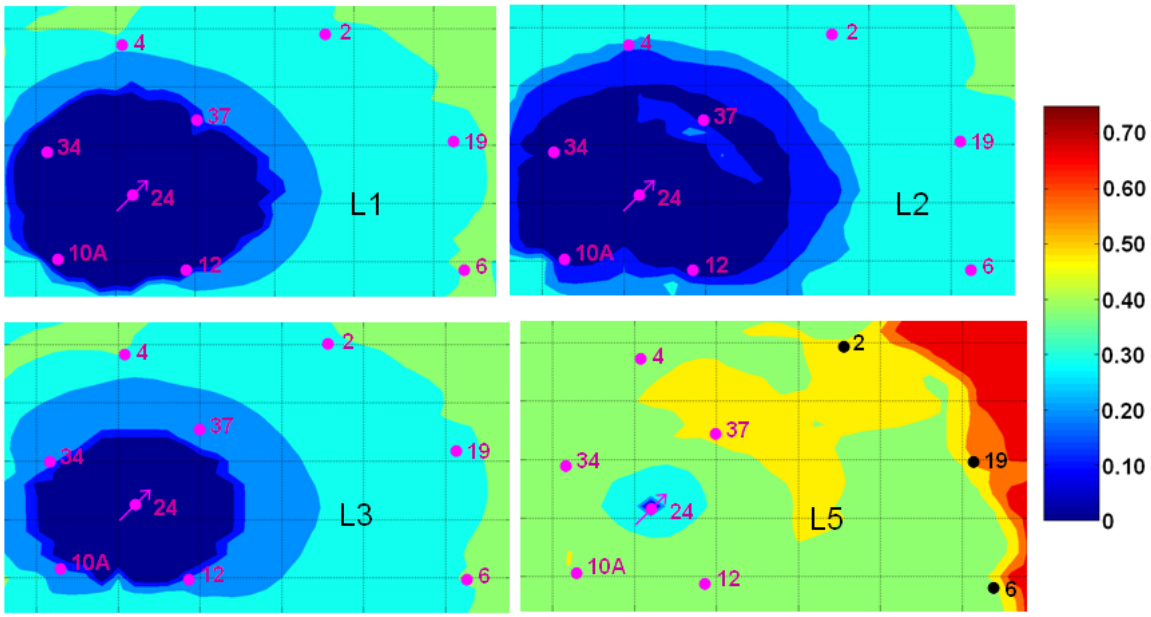

Figure 9.20: Areal View of Post Chemical Flood Oil Saturation of Layer 1, 2, 3, and 5 for Case 2 (2X ASP injection).

Case 3: ASP Bottom Injection

As discussed before, oil saturations in the bottom layers are much higher than the top layers after the waterflood due to unfavorable permeability contrast. If more chemicals can be directed into the bottom layers, higher recovery can be expected. Two possible solutions are proposed: 1) injecting chemicals only into the bottom layer by blocking out the rest of the perforation interval, as discussed in this section; 2) injecting a small portion of polymer before the ASP slug for conformance control and enhancing

cross flow in the vertical direction. The cumulative oil recovery and oil production rate of Case 1 (base case ASP) is shown in Figure 9.21.

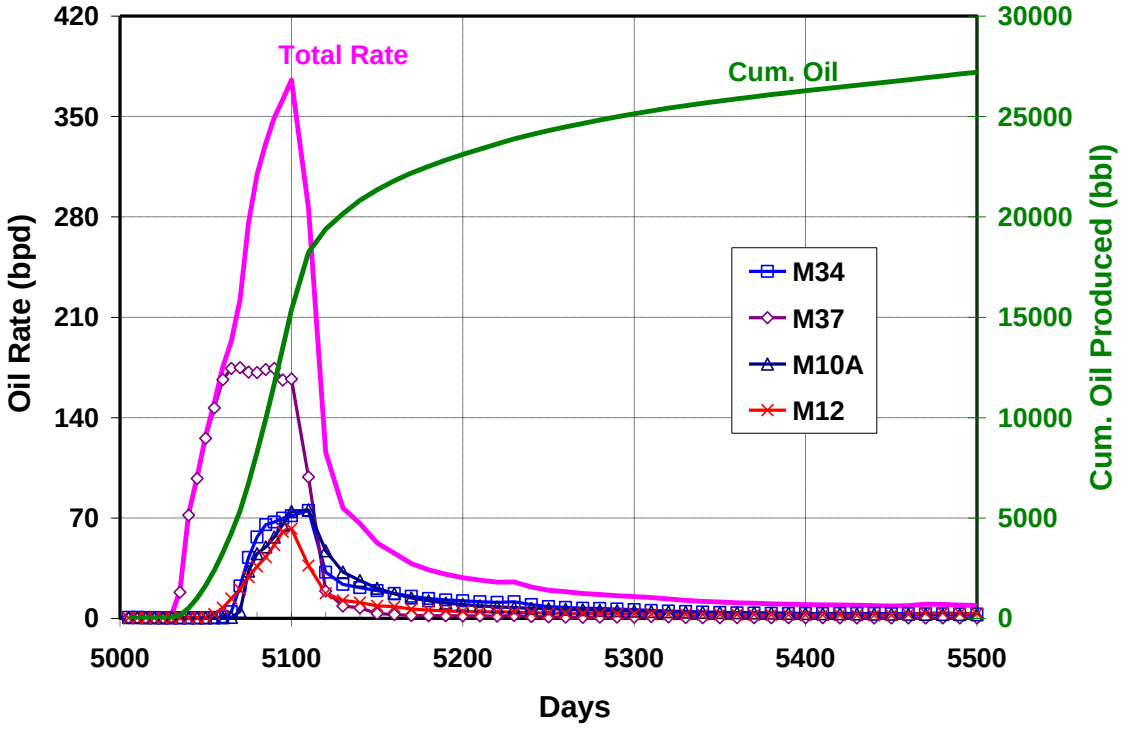

Figure 9.21: Cumulative Oil Recovery and Oil Production Rate for Case 3 (ASP bottom layer injection).

The cumulative oil recovery after 500 days is 27,203 bbl. The maximum total oil production rate predicted by UTCHEM is about 375 bpd. Oil bank breakthrough at M37 occurs after about 35 days of injection. After 70 days, all the other wells show substantial oil production. The maximum oil rate occurs at about 100 days. After about 320 days since the start of the slug injection, the water cut goes back to 99%. Chemical cost per barrel of oil produced in this case is about $16.55/bbl, which is much more attractive than Case 1 and Case 2. However, a practical concern for this scenario would be the fluid injectivity, considering the low permeability in the bottom layer. Simulation result

suggests an injection pressure way above formation parting pressure if this scheme were to be implemented in the field. To make sure the chemicals can be injected in the field, this bottom injection scenario was abandoned. Figure 9.22 shows the effectiveness of this approach in recovering residual oil in low-perm bottom layers.

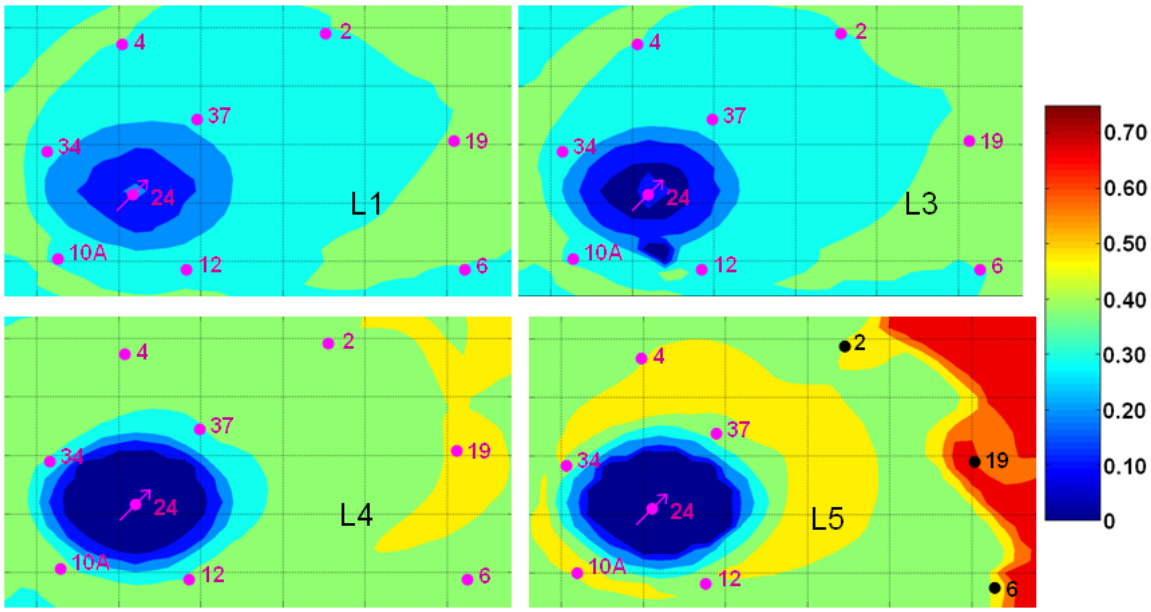

Figure 9.22: Areal View of Post Chemical Flood Oil Saturation of Layer 1, 3, 4, and 5 for Case 3 (ASP bottom layer injection).

Case 4: Polymer Pre-Flush + ASP

As discussed above, another way to possibly modify the injection profile is to utilize a polymer pre-flush. In this case, 70 days of polymer is injected before the ASP slug. The cumulative oil recovery and oil production rate are shown in Figure 9.23. The cumulative oil recovery after 500 days is 27,586 bbl. The maximum total oil production rate predicted by UTCHEM is about 565 bpd. Oil bank breakthrough occurs in all the wells after about 100 days of injection. The maximum oil rate occurs at about 120 days. After about 300 days since the start of the slug injection, the water cut goes back to 99%.

Chemical cost per barrel of oil produced in this case is about $21.48/bbl, which is comparable to base case ASP flood. In the meantime, since quite a bit more oil (~ 6500bbls) are produced with the injection of pre-flush. The overall economics for this case is better than the base case.

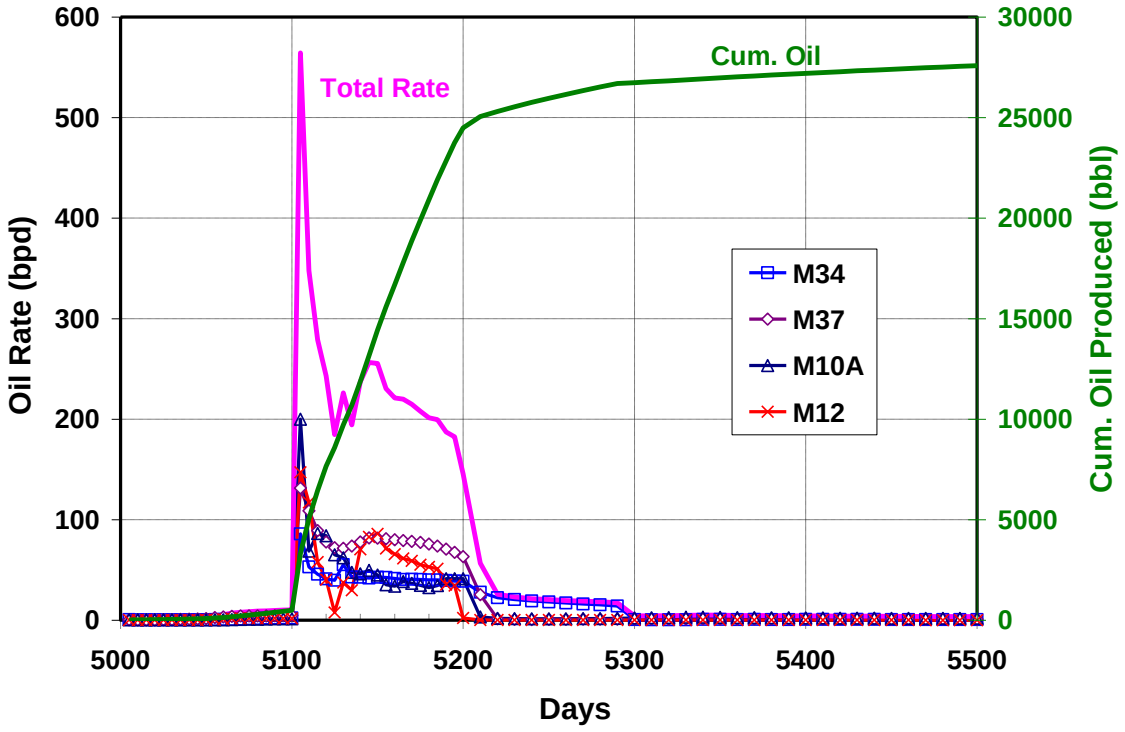

Figure 9.23: Cumulative Oil Recovery and Oil Production Rate for Case 4 (Polymer Pre-flush and ASP flood).

Figure 9.24 below shows the impact of the polymer pre-flush on sweep efficiency, especially on the bottom low-perm layer. Apparently more of the surfactant slug has been directed into the low-perm layers due to the enhanced cross flow between different layers. Hence we observe in Figure 9.23 that substantial enhancement of oil recovery is achieved with this polymer pre-flush injection scheme.

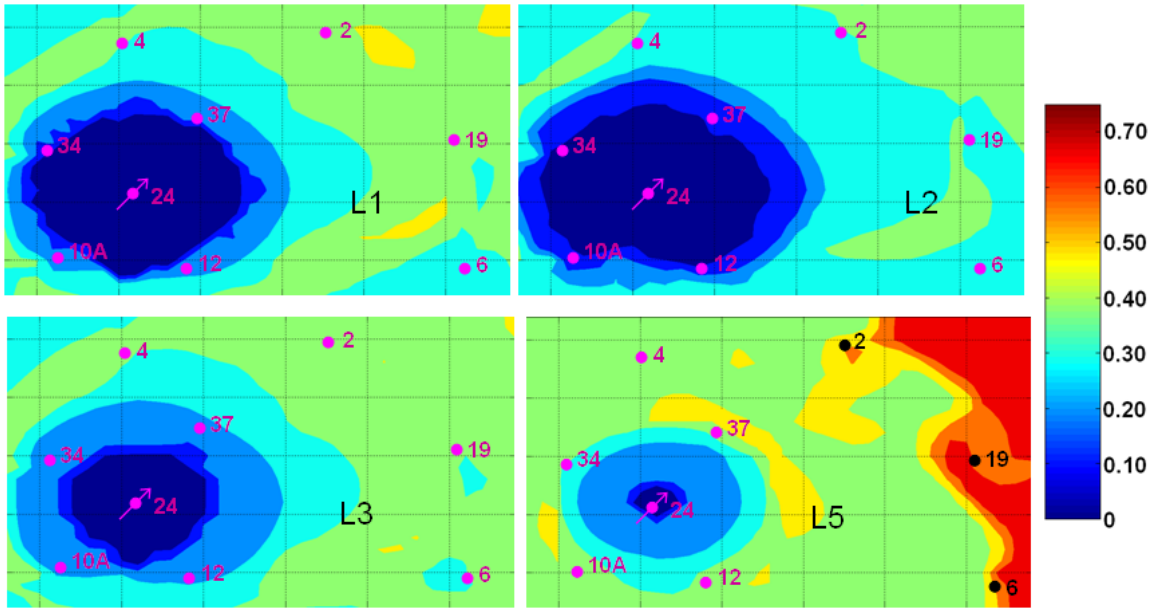

Figure 9.24: Areal View of Post Chemical Flood Oil Saturation of Layer 1, 2, 3, and 5 for Case 4 (Polymer Pre-flush and ASP flood).

Case 5: ASP with Doubled Production Rates

Considering the active aquifer influx in the pilot area, one of the concerns is the dilution of chemicals once they are injected. By producing at higher rates on the pilot producers, it is hoped that this dilution effect can be mitigated. In case 5, all the producers now are set to produce at double rates (two times the rates specified in Table 9.11). The cumulative oil recovery and oil production rate are shown in Figure 9.25. The cumulative oil recovery after 500 days is 31,400 bbl. The maximum total oil production rate predicted by UTCHEM is about 345 bpd. Oil bank breakthrough occurs in all the wells after about 30 days of injection. The maximum oil rate occurs at about 70 days. After about 230 days since the start of the slug injection, the water cut goes back to 99%. Chemical cost per barrel of oil produced in this case is about $14.33/bbl, which is apparently the best of all cases studied so far. In practice, however, there is a maximum production rate for the pumping unit used in the field. For this project, this upper limit is

600bpd. Figure 9.26 below shows the oil distribution after the ASP flood. Although producing at much higher rates in this case, the total chemicals injected remain the same as the base case, therefore, the areal impact of the slug injection is about the same as the base case.

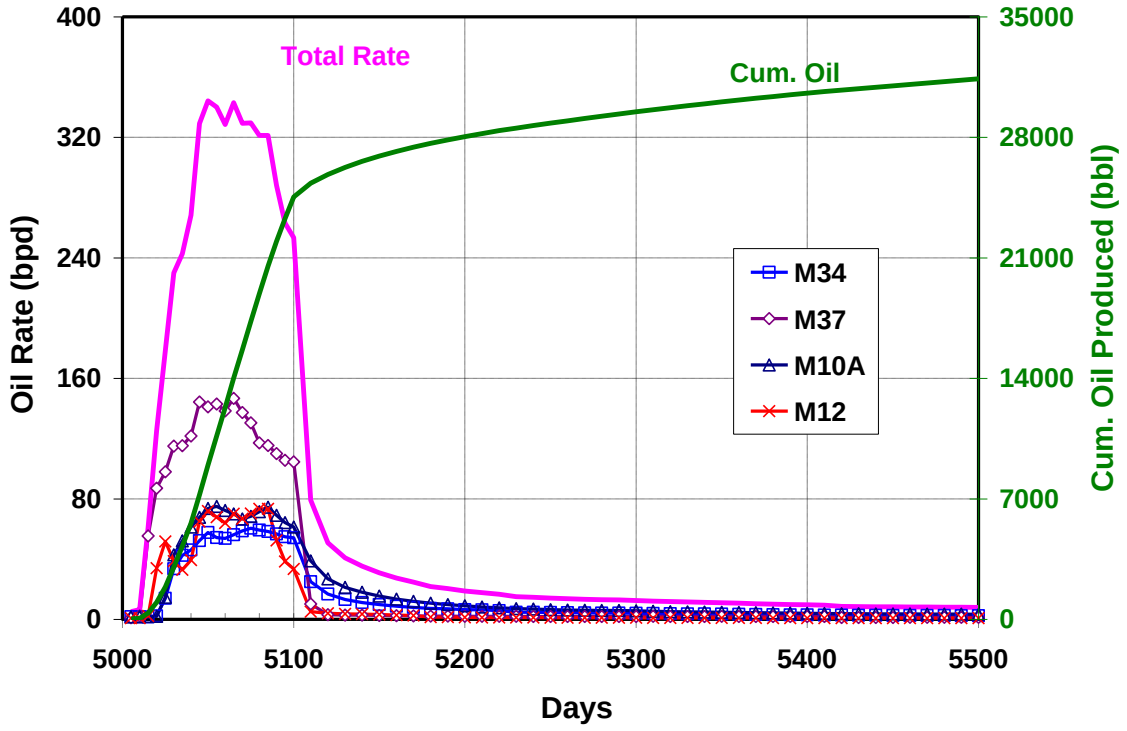

Figure 9.25: Cumulative Oil Recovery and Oil Production Rate for Case 5 (ASP with doubled production rates).

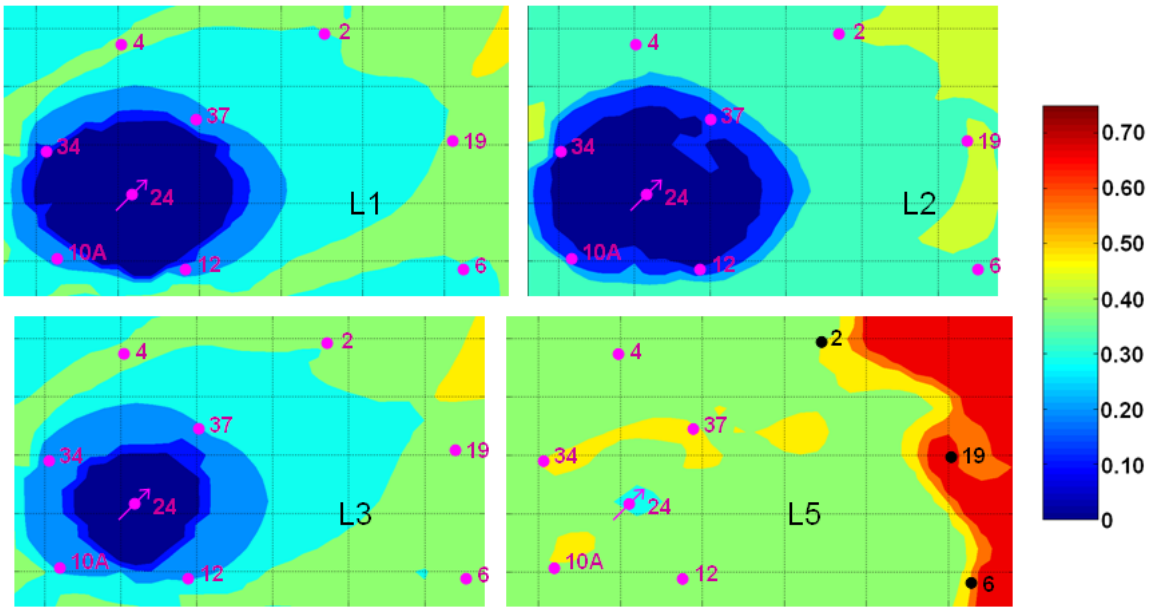

Figure 9.26: Areal View of Post Chemical Flood Oil Saturation of Layer 1, 2, 3, and 5 for Case 5 (ASP with doubled production rates).

Summary

Table 9.13 below summarizes the simulation results for all five cases studied in this section. Figure 9.27 shows the cumulative oil recovery history for these scenarios.

Table 9.13 Simulation Results Summary for Different Operating Strategies.

Case #	Brief Description	Oil Recovered (bbl)	Max. Rate (bpd)	Time to Reach 1% Water Cut (days)	Cost ($bbl)
1	ASP base case	21085	235	290	21.35
2	2X ASP	34252	270	260	26.30
3	ASP bottom inj.	27203	375	320	16.55
4	Pre-flush + ASP	27586	565	300	21.48
5	2X prod. rates	31400	345	230	14.33

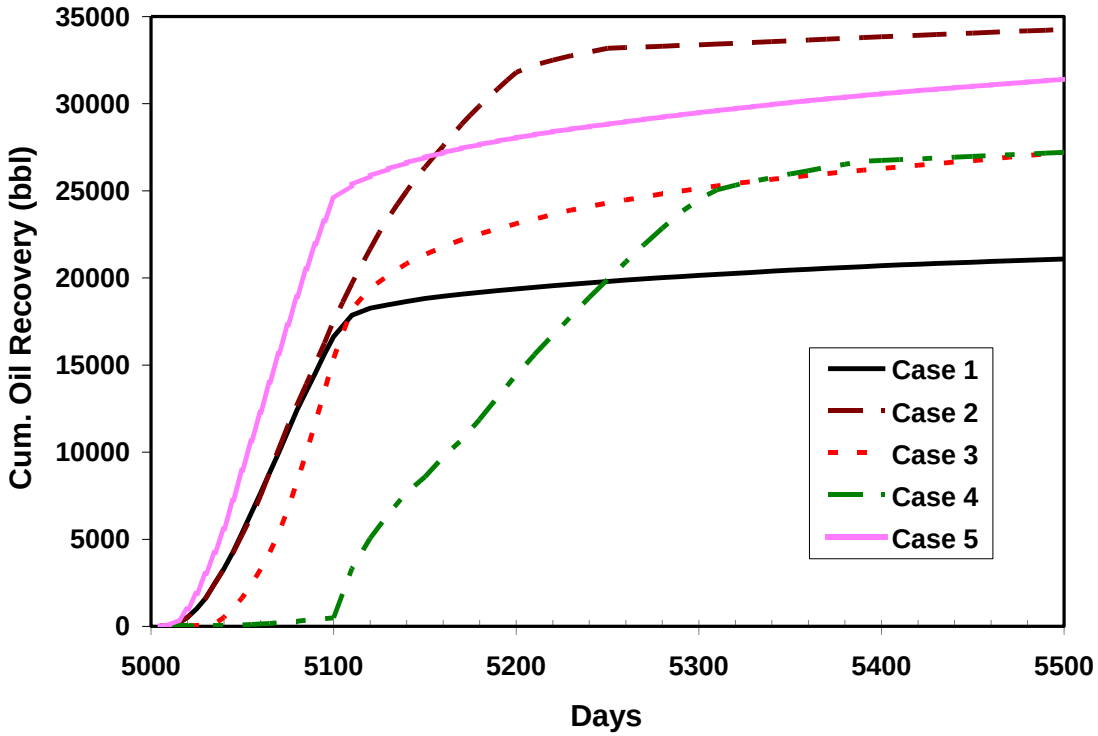

Figure 9.27: Cum. Oil Production Comparison between 5 Cases Studied.

The 5-layer pilot-scale model has been used to studied different possible operating strategies in the field. The simulation results can be used to guide field execution and some of the general observations can be summarized below:

1). Doubling the injected chemical quantity leads naturally to higher oil production, but in the meantime substantially increases the cost per incremental barrel, which is an important technical and economical metric for evaluating an EOR project. Taking into account the risk and uncertainty associated with field production, the originally planned amount of chemicals should be injected in the initial phase of the project. Follow-up injection can be planned and implemented later based on field performance;

2). A polymer pre-flush before the surfactant slug is helpful in getting the injection profile more uniform across the entire pay zone, and helps guide the chemicals into and recover oil from the bottom layers;

3). Higher production rates can indeed help counterbalance the influence of the aquifer influx, and thus should be implemented in the field when possible;

4). Injectivity could be a serious issue for the injection of viscous chemicals and the injector wellhead pressure needs to be carefully monitored at all time in the field.

9.2.4 Sensitivity Simulations for ASP Flood (w/ 9-Layer Model)

So far, some general guidelines for field operation have been obtained from pilot-scale simulation study using the 5-layer model. In this section, the refined 9-layer model is employed and various sensitivity cases are simulated with different polymer concentration, total chemical mass, and alkali consumption.

Polymer Concentration Sensitivity

The importance of polymer in the ASP flood can never be overstated (Yang *et al.*, 2010). Sufficient polymer in the flood provides good mobility control and hence, decreases the chances of fingering and bypassing mobilized oil. Moreover, in the polymer drive phase, the typically lowered salinity provides a salinity gradient for the slug.

The sensitivity of oil recovery to polymer concentration is studied through a comparison with the base case ASP simulations. The base case here is the same as Case 1 investigated in the previous section, where a concentration of 4000ppm 3330S was used in the flood. Before going into details of the sensitivity study, the results of the simulations with the 5-layer and 9-layer grid models are presented in Figure 9.28 below. The refined 9-layer model shows a higher oil production of 23,756bbls, or 2700bbls more

oil in comparison with the coarser 5-layer model. The oil recovery and daily production rate decreased with an increase in the size of the grid block. The reason for the difference in recovery as discussed by Veedu (Veedu, 2010), was the surfactant and sodium carbonate dilution in large grid blocks. The following sensitivities were based on the 9-layer base case ASP simulation, with only changes made on polymer concentration, to 2000ppm and 3000ppm.

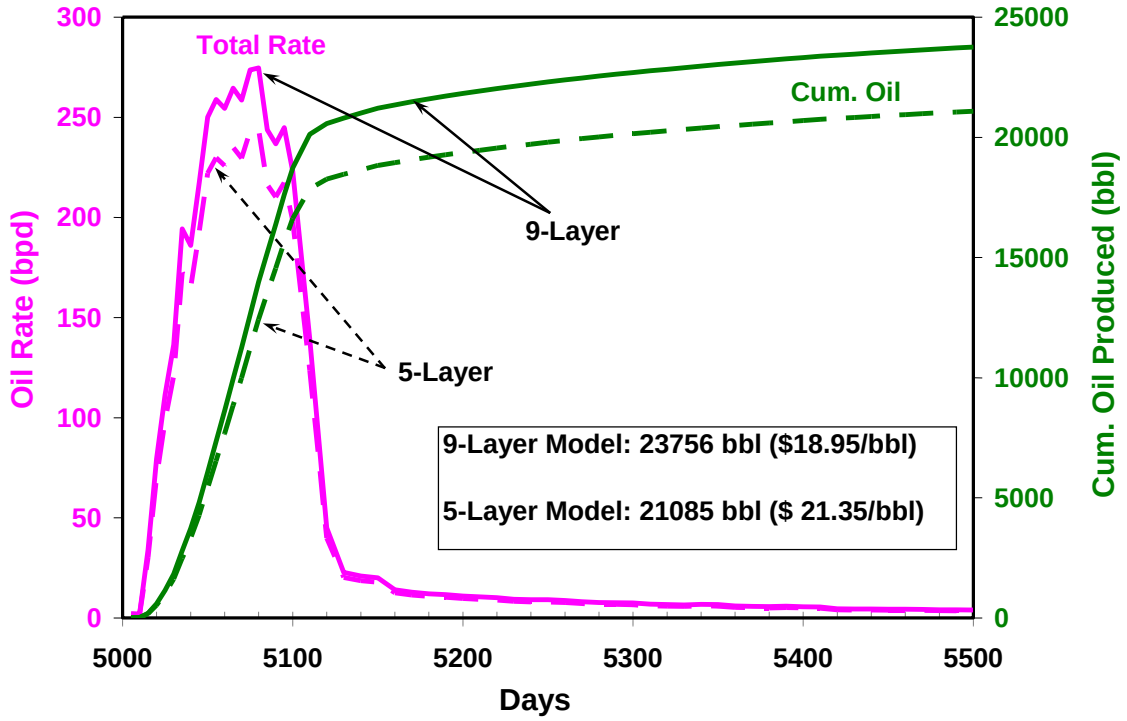

Figure 9.28: Cum. Oil Production and Total Oil Rate Comparison between 5-Layer and 9-Layer Models.

The cumulative oil recovery and oil production rate plots for these two cases are shown in Figure 9.29 to Figure 9.31. Figure 9.31 presents the cumulative oil recovery comparison for all the sensitivity cases. Clearly, as the polymer concentration is increased, the recovery increases. This can be attributed to the better mobility control due

to the higher computed grid-block concentration of polymer. Recall from the linear coreflood experiment and simulation results, where 2000ppm polymer was able to provide sufficient mobility control in a homogeneous coreflood setting. The mobility ratio during a core flood can be estimated by taking the ratio of pressure gradients in the oil bank and surfactant slug (Yang *et al.*, 2010). Judging from Figure 8.27, this ratio was very close to 1, thus the mobility control was only marginally achieved in the 1D linear core flood. In a more realistic heterogeneous pilot model (although still a much simplified one), this marginal mobility control was no longer sufficient. Therefore, 4000ppm 3330S concentration was used in all the simulation cases in the previous section to ensure an adequate mobility control. In the field, however, a higher molecular weight 3430S polymer was chosen to provide an equivalent viscosity but at a lower concentration.

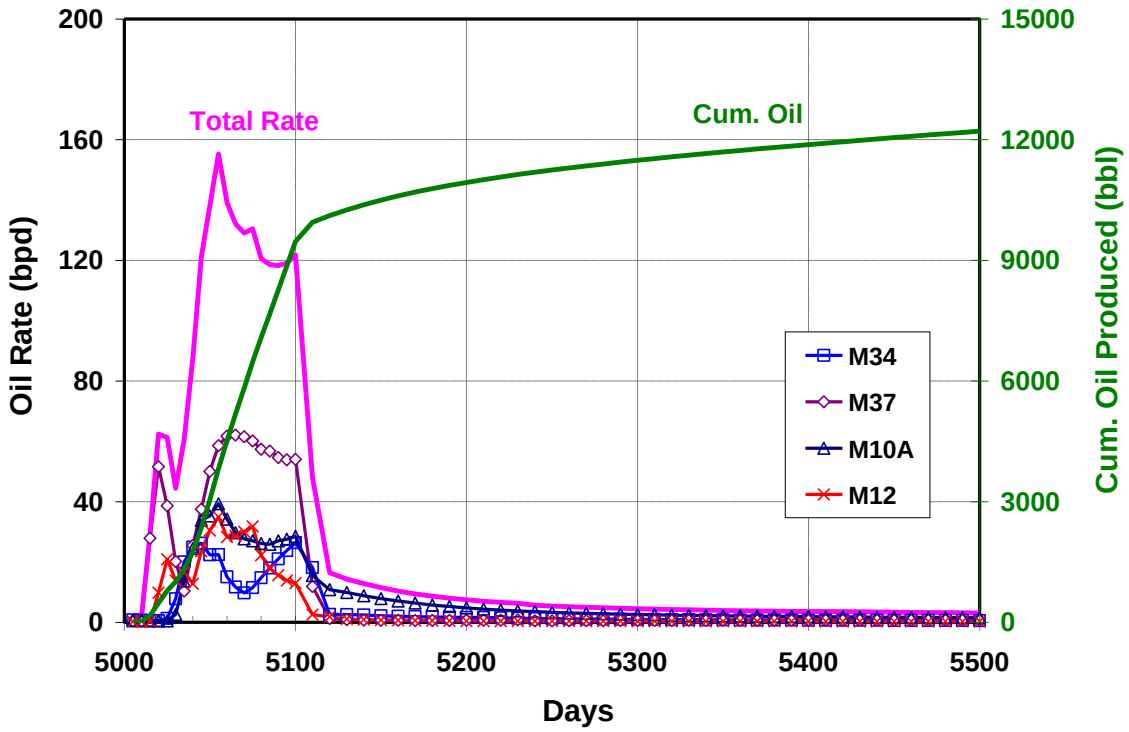

Figure 9.29: Cumulative Oil Recovery and Oil Production Rate for ASP Simulation with 2000 ppm Polymer.

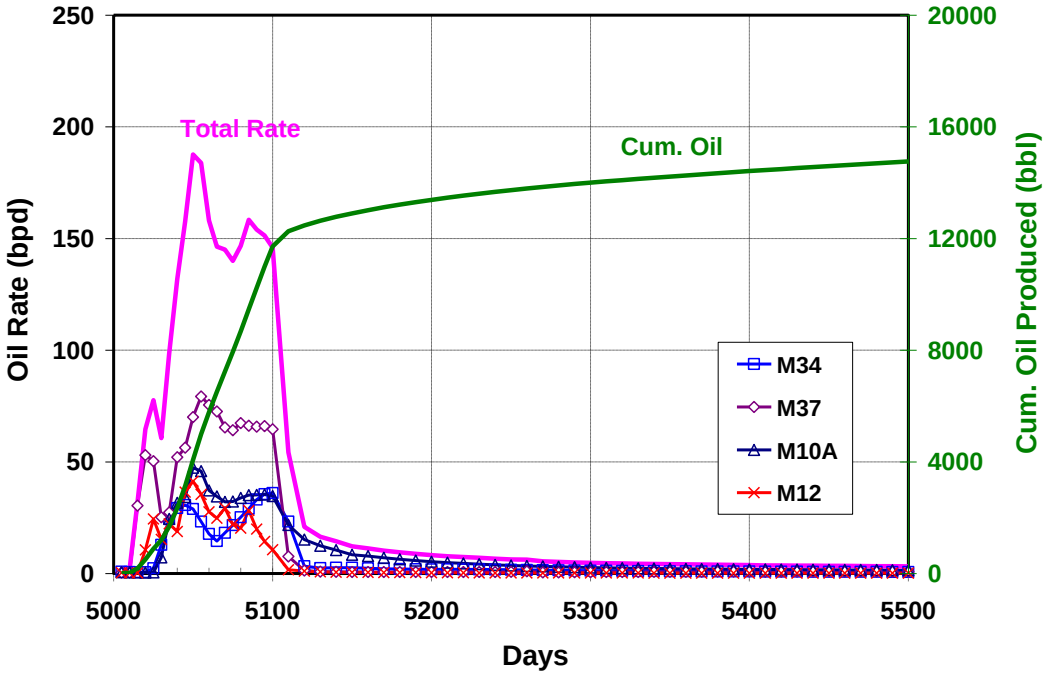

Figure 9.30: Cumulative Oil Recovery and Oil Production Rate for ASP Simulation with 3000 ppm Polymer.

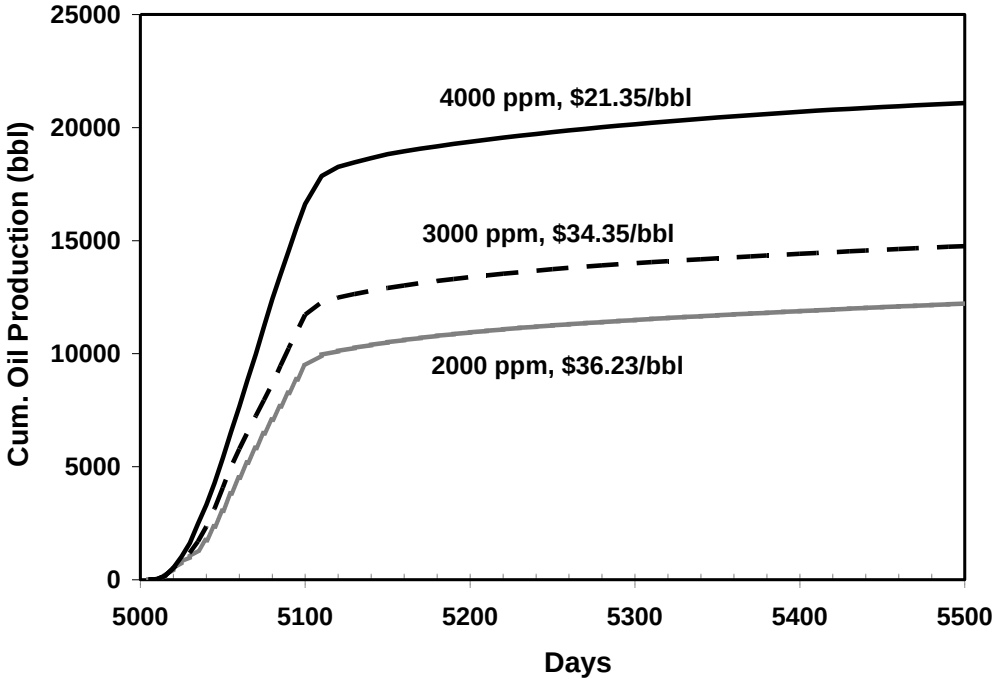

Figure 9.31: Effect of Polymer Concentration on the Recovery Results of ASP Flood.

Total Chemical Mass Sensitivity

It is important in a surfactant flood to have sufficient amount of chemicals injected to sweep the designed pilot pore volume. However, the existence of fractures near an injector, and thief zones in a pilot pattern, as well as poor fluid confinement within the pattern, result in big uncertainties in the chemical mass estimation. In this sensitivity study, the injected chemical mass is varied around that of a base case (which is equivalent to changing the swept pore volume), and the impact of this change is examined.

The base case scenario includes a 70-day polymer pre-flush, 200-day of surfactant slug (at a rate of 300 bpd), 250-day polymer drive and chase water injection till 1000 days. The injection rate in this sensitivity study was reduced to 300 bpd due to the practical concerns on polymer injectivity. All the producers were set to produce at

maximum rate of 600 bpd to counteract the dilution of aquifer influx. Different cases studied includes: 1) base case; 2) 15% less total chemical (or equivalently 15% more-than-expected swept pore volume); 3) 15% more total chemical; and 4) 30% less total chemical.

The cumulative oil recovery and oil production rate plots for these four cases are shown in Figure 9.32 to Figure 9.35. The production profiles for different cases are quite similar in terms of peak and average production rates. The main difference is the duration of the active production period.

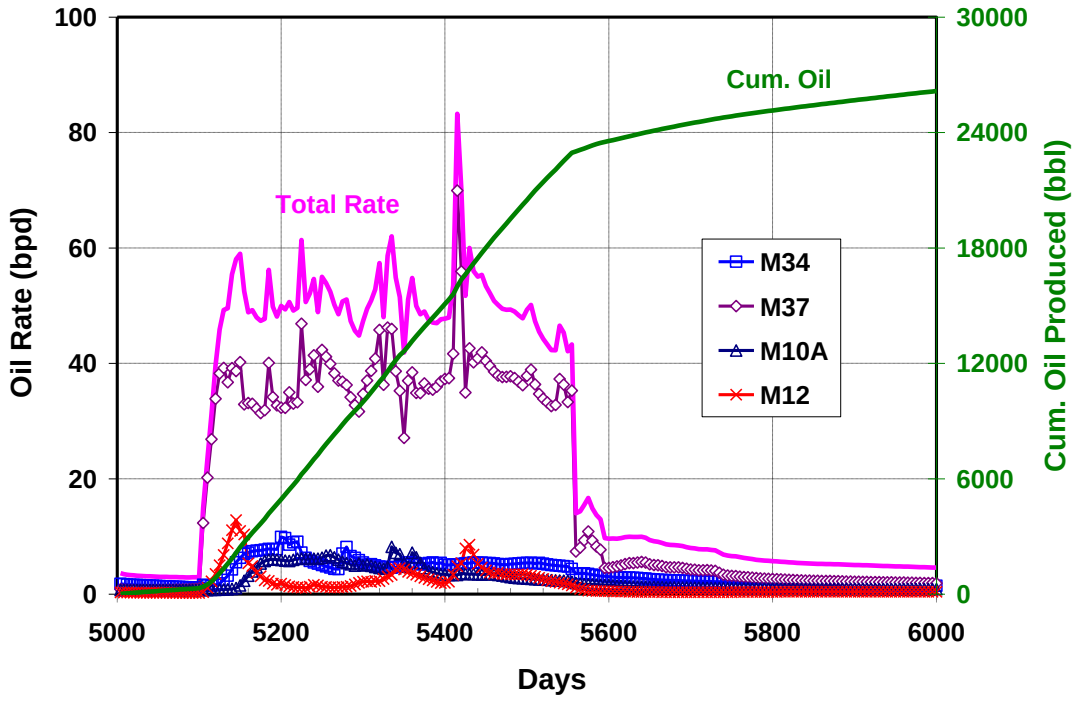

Figure 9.32: Chemical Mass Sensitivity Study: Base Case.

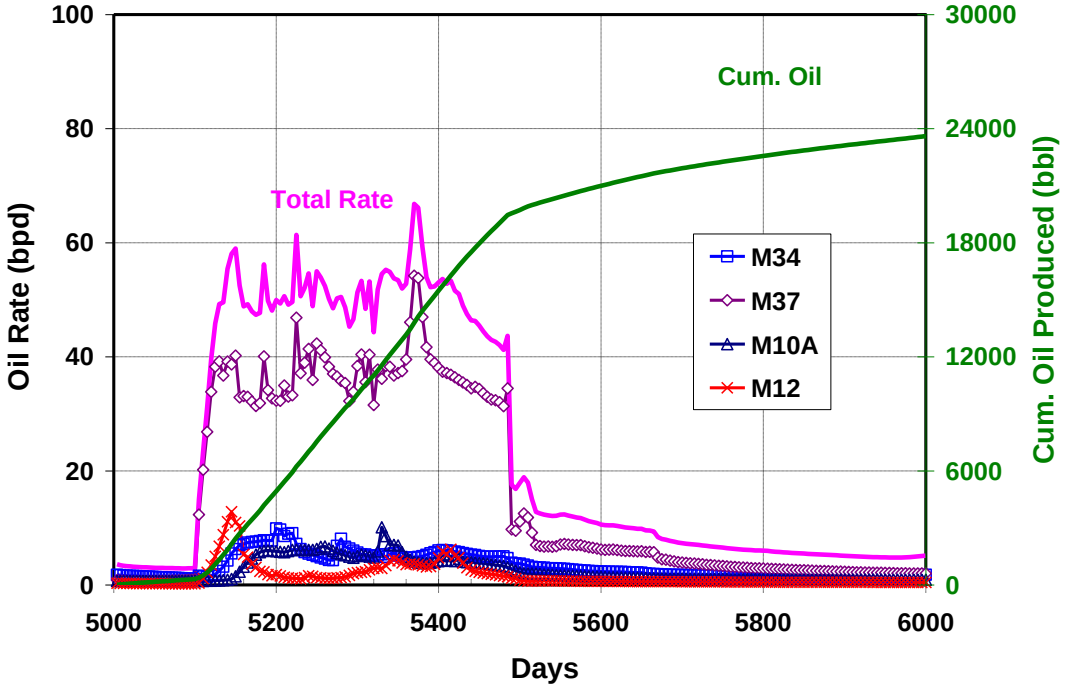

Figure 9.33: Chemical Mass Sensitivity Study: 15% Less Chemical Mass.

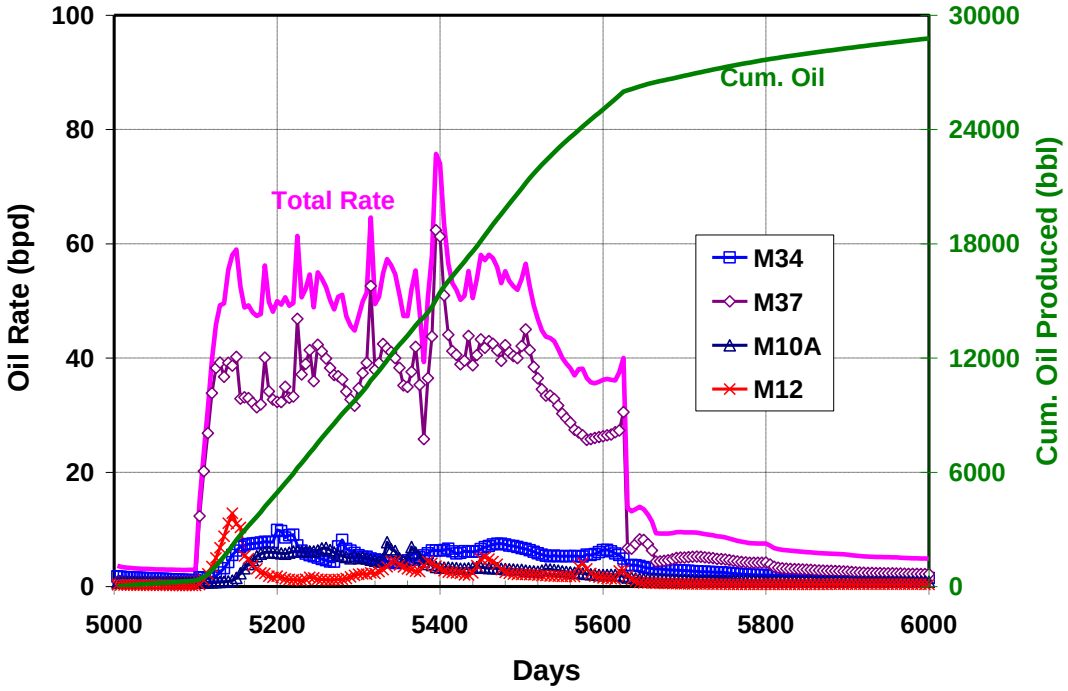

Figure 9.34: Chemical Mass Sensitivity Study: 15% More Chemical Mass.

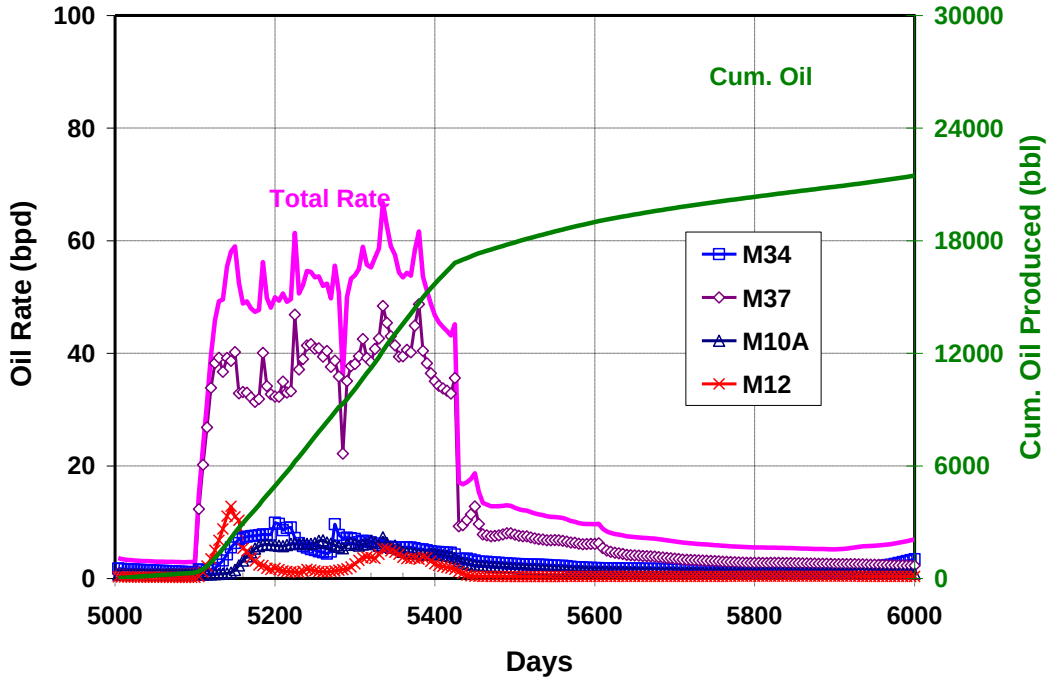

Figure 9.35: Chemical Mass Sensitivity Study: 30% Less Chemical Mass.

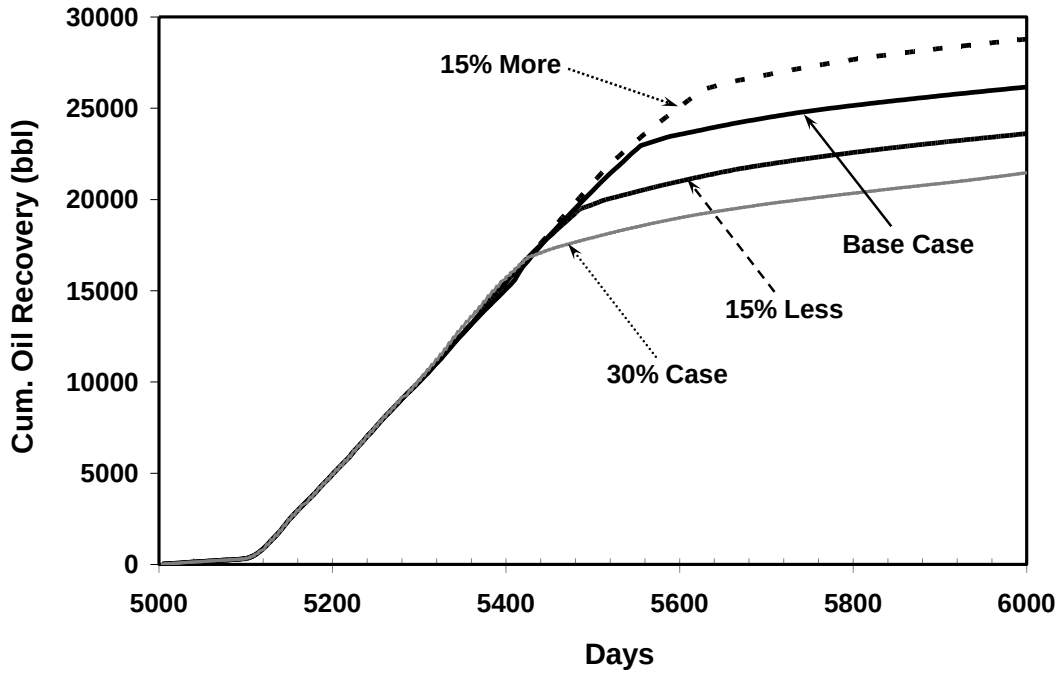

Figure 9.36: Cum. Oil Production Comparison between the Chemical Mass Sensitivity Cases.

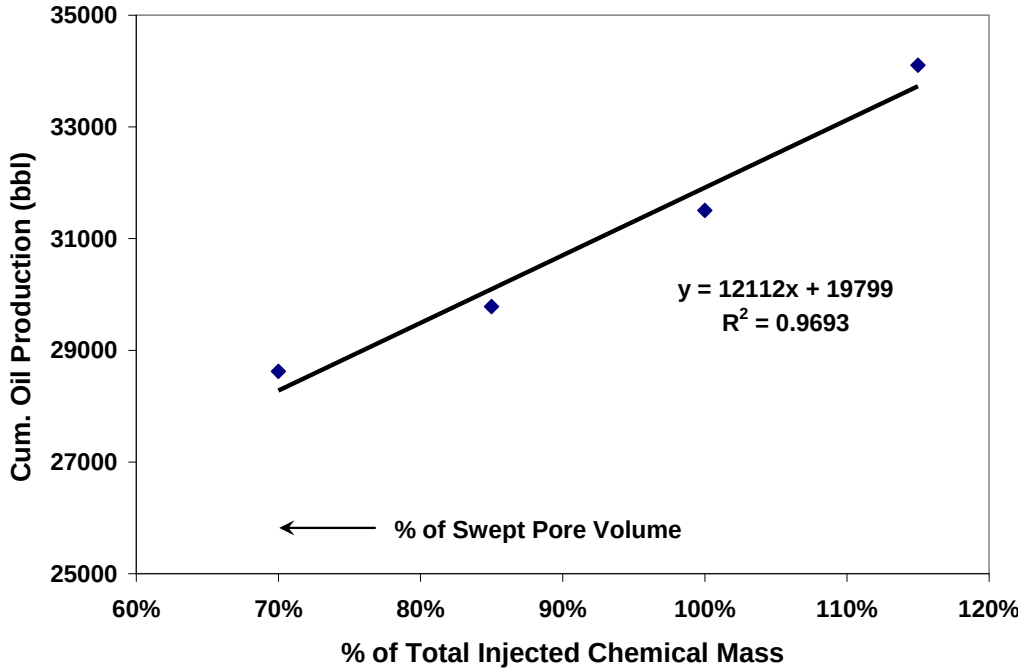

Figure 9.37: Dependence of Cum. Production on Total Injected Chemical Mass (or Swept Pore Volume).

Figure 9.36 presents the oil recovery comparison for all the simulated cases. As the total injected chemical mass is increased, the simulated oil recovery increases. The cumulative oil production shows a linear increase with total injected mass (Figure 9.37), which again is equivalent to a decrease in swept pore volume. In case where the true swept pore volume is larger than expected, the designed injection mass would be smaller than needed which results in less oil recovery. Depending on how well the swept pore volume is estimated, this impact could be quite substantial, and the associated risk should be carefully evaluated.

Alkali Consumption Sensitivity

During an ASP flood, the high pH front is retarded by geochemical reactions in the reservoir. When alkali is injected in the slug with surfactant and polymer, the

concentration of alkali must be high enough to satisfy alkali consumption and still transport with the surfactant. It is therefore very important that ASP pilots be designed taking into account the consumption of alkali in the reservoir. In case of a high level of alkali consumption, the pH front cannot be propagated at the same rate as the synthetic surfactant, thereby reducing the slug effectiveness. Large consumption of alkali also causes adverse changes total salinity if most of the alkali is consumed. Various alkali consumption/retardation mechanisms (Dean, 2011) include mixing with hard formation water in front of slug, with cations from ion exchange with clay, sodium/hydrogen base exchange, reaction with minerals that dissolve at high pH.

Novosad (1984) carried out experiments to measure the alkalinity loss resulting from cation exchange capacity (CEC) in Berea cores. They found out the CEC is between 0.1 and 0.4meq/100g rock. They noted that the cation exchange capacity was about half of the total exchange capacity. Cation exchange reactions are much more significant for large-surface-area clay contents (Mohnot *et al.*, 1987). Another cause of alkali consumption lies in the reaction of alkali with rock minerals (Sydansk, 1982). It is generally recognized (Mohammadi, 2008) that the increase of pH, temperature, and contact time with minerals increases the alkali consumption. It is, therefore, of key importance to load the ASP slug with sufficient amount of alkali for contingency, especially when the CEC condition in the reservoir is uncertain. This way the performance of the slug can be ensured even when the consumption is higher than expected. In the meantime, however, the impact of high alkali concentration on phase behavior should also be carefully evaluated. Dean (2011) performed core flood experiments on a Bentheimer sandstone of high clay content (CEC = 2meq/100g rock). For a non-reactive crude at 86^{o}C, a 0.3 PV slug of 0.7% Na_2CO_3 is more than minimum

required mass and concentration at a reasonable field flux of 0.33ft/D. When the crude oil is reactive however, alkali will also be consumed to generate soap (Hourshad, 2008).

Different alkali consumption scenarios are examined in this sensitivity study by adjusting the cation exchange capacities in the simulation model. The CEC value was changed from virtually zero to 0.15meq/ml of PV (2.8meq/100g rock, ϕ = 0.33, ρ_s = 2.65g/cc). The injection sequence consisted of 10 days of polymer pre-flush, followed by ASP slug injection. Figure 9.38 demonstrates the effect of CEC on effluent pH on two producers, M37 and M34. The fact that M37 well is closer to the injector M24 than M34 results in an earlier pH breakthrough on M37. As the CEC value becomes higher, more alkali will be consumed in the reservoir, which translates to slower propagation of the pH front, or later pH breakthrough on the producers.

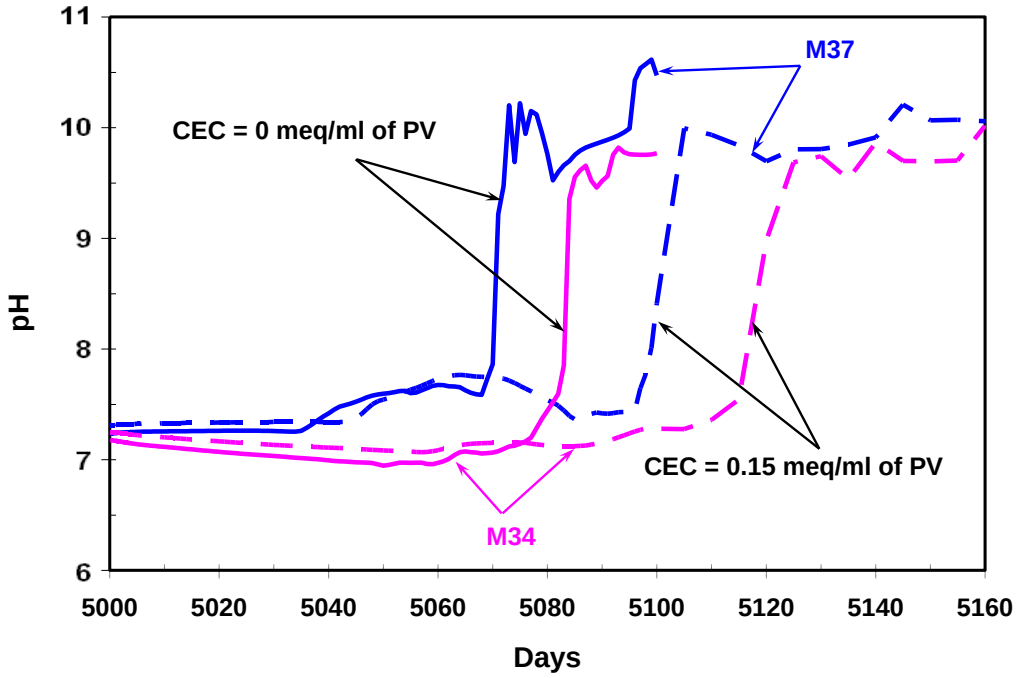

Figure 9.38: pH Breakthrough Profiles on M37 and M34 with Two Different Cation Exchange Capacities.

Hourshad (2008) preformed a 1D core flood simulation to study the alkali consumption and resulted pH frond retardation in a sandstone reservoir rock. A relatively large CEC value of 1.8meq/100g rock was used to account for high clay content in the rock. At 1PV injection volume, a spatial separation of X_D=0.4 between the pH and surfactant fronts was clearly shown from her study. Figure 9.39 above delivers the same idea for current 3D simulation, only from a temporal viewpoint. The impact of a high CEC value on the propagation of pH and surfactant fronts was evident. As the CEC value gets larger, alkali consumption goes up in the reservoir, and thus the pH front starts to lag behind the surfactant concentration front. With a CEC value of 0.15meq/ml of PV, it takes much more time for the pH to break through after the surfactant front reached the producer. This is very likely to be caused by the high CEC and a slower pH front.

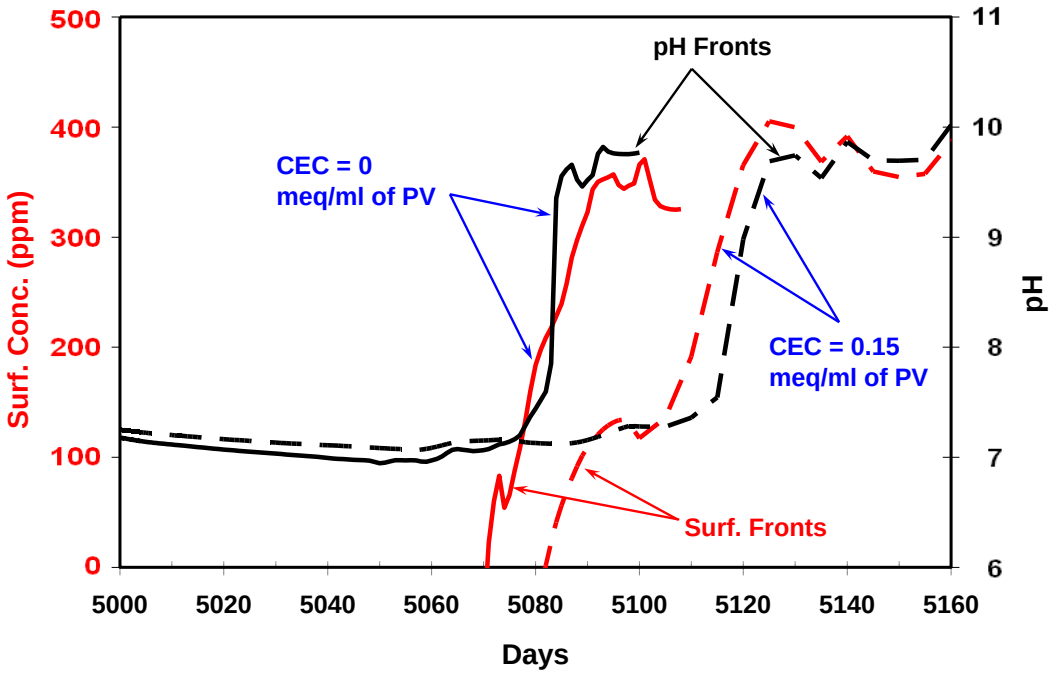

Figure 9.39: pH and Surfactant Breakthrough Profiles on M34 with Two Different Cation Exchange Capacities.

For zero or low CEC for Berea (Novosad *et al.*, 1984)), we would not expect to see significant separation between the pH and surfactant fronts with Berea sandstone, which apparently agrees with what we have seen from the Berea core flood experiment. However, the mineralogy and lithology of the Brookshire sand is quite different from Berea sample used in the lab, and the reservoir rock may contain high clay content, which in turn would dramatically change the phase behavior and optimum condition of the system. It is probably worth mentioning that pH front always breaks through in all simulation runs, even though it might take much longer time to happen. In the field (see next chapter), however, pH breakthrough has yet to be observed, even on the nearest producer.

9.3 SUMMARY AND CONCLUSIONS

The Brookshire Dome ASP pilot flood was simulated using UTCHEM. The pilot model was built upon the success of history matching lab-scale coreflood experiments. Geologic uncertainties still remain a challenge. Field inputs, including well logs, an injection well spinner survey, an inter-well tracer test, and waterflood production data, were used for setting up the pilot-scale model. Different possible operating strategies were simulated and compared with a base case scenario where a surfactant slug with a chase polymer drive was injected as done in the coreflood. Various sensitivity runs were performed on different factors impacting the project performance. Some of the more general conclusions and directions for improvement are as follows:

1. A polymer pre-flush will be helpful in getting the injection profile more uniform and thus recover oil from the bottom low-perm layers; higher production rates will help counterbalance the influence of the aquifer influx, and thus should be implemented in the field when possible; injectivity might

be an issue for chemical injections and will need careful monitoring in the field; chemical injection should be carried out following the original plan, and depending on field performance, the project can be expanded to a larger scale.

2. A pilot project is always challenged by unexpected problems and potential risks. A sensitivity study on different factors is thus very helpful and useful for project design. Mobility control is crucial to ensure the integrity of the ASP slug and the successful recovery of the mobilized oil. It is also important to recognize and be fully aware of the impact of various uncertainties on the pilot performance. Two among many others are swept pore volume estimation and alkali consumption in the pilot pattern. Sensitivity studies conducted in this chapter clearly shows how big a difference in project performance they can make.
3. The current pilot-scale geological model is over-simplified. Some of the important model inputs were best estimations based on information at hand. The poor match to the field tracer test and our inability to predict chemical injectivity pose serious questions about the accuracy of the results obtained from the model and they need to be interpreted and evaluated with extreme caution. The exact impact of natural water drive is also uncertain in the simulation model.

Chapter 10: Field Implementation and Performance Update

10.1 INTRODUCTION

A tertiary alkaline / surfactant / polymer flood was implemented from September 2011 to March 2012 in the Brookshire Dome field, Texas. Production monitoring and data collection are continuing at this time. With initial discovery of the Catahoula sand formation in 1996 and over 15 years of waterflooding and infill drilling, oil cuts are less than one percent, suggesting that the reservoir is approaching residual oil saturation to waterflood. The mature stage of the field makes it a typical candidate for the application of a chemical EOR process.

As discussed in Chapter 8, laboratory phase behavior and coreflood experiments (Chapter 8) were conducted to determine the optimal chemical formulation for the field crude oil and to provide essential parameters for a numerical simulation model (see Chapter 9). Spinner survey and an inter-well tracer test program were conducted to collect reservoir information and understand well connectivity, as well as support the interpretation of the pilot results. A field laboratory was set up onsite to monitor the quality of injected and produced fluids. We discuss in this chapter the field pilot implementation, pilot results to date, major risks associated with the pilot design, the key lessons learnt, and probably more importantly some unanswered questions encountered throughout the project.

10.2 FIELD IMPLEMENTATION

10.2.1 Field Injection Plan

The original injection plan was to inject 0.3PV of an ASP slug followed by 0.7PV of a polymer drive. The surfactant formulation contained 0.3wt% Petrostep S-13C, 0.2wt% of Tomadol 15-12 (field substitute for Neodol 25-12), and 0.8wt% of Na_2CO_3.

Notice that the co-solvent concentration was raised (from 0.1wt% in the lab) to ensure aqueous stability of the injected slug. And the alkali concentration was reduced by 0.2wt% (from 1wt% in the lab) to account for the downshift of optimum salinity observed during QC on the field surfactant batch. This decrease in alkali concentration, however, caused a possible risk of insufficient alkali injection due to high consumption. To ensure a stringent mobility control, the higher molecular weight 3430S polymer (EOR 90) was used at an average concentration (over the entire injection period) of 2700ppm. Even higher concentration of polymer was actually used due to viscosity loss when switching to new polymer batches.

In view of severe layering of the reservoir and unfavorable oil distribution (high oil saturation in bottom layers of low permeability), a polymer pre-flush was designed for injection profile control (based on simulation results from Chapter 9) and was injected in the field before the surfactant slug. The polymer concentration was tapered off in the drive phase and chase water was injected at the tail end. Table 10.1 below lists the final chemical injection design, in terms of pore volume of fluid injected and nominal concentration of chemicals.

Table 10.1 ASP Pilot Chemical Injection Design.

Injection Phase	Pore Volume	Nominal Concentration (%)		
		Alkali	Surfactant + Co-solvent	Polymer
Polymer Pre-Flush (PPF)	0.05	---	---	0.23
ASP Slug (ASP)	0.3	0.8	0.5 (w/ EDTA)	0.28
Polymer Drive (PD)	0.7	---	---	Tapered
Chase Water (CW)	continuous	---	---	---

10.2.2 Project Timeline

Table 10.2 shows the overall timeline of the project. Since the start of the project, Layline Petroleum has been proactive in executing the pilot. Laboratory experiments to select the ASP formulation and test it in corefloods were concluded in April, 2011, at the University of Texas. Numerical simulations were also done afterwards at the University of Texas (Chapter 9). Based on these test results, the chemicals were ordered. In parallel to ordering chemicals, an inter-well tracer test program was implemented in June, 2011 with the primary purpose of using tracer breakthrough data to identify communication and reservoir continuity between injection and production wells as well as quantify the impact of groundwater flow on the transport of the chemicals. Field preparation, including drilling a new producer, was completed in July, 2011. EOR equipment was delivered in August and onsite facility installation and testing started right away. Chemicals were received from TIORCO in the same month.

Table 10.2 Brookshire Dome Field ASP Pilot Timeline.

February, 2011	Surfactant Formulation Identified
April, 2011	Coreflood Test Completed
June, 2011	Field Tracer Test Completed
July, 2011	Field Preparation Completed
August, 2011	EOR Equipment Delivered
August, 2011	Chemicals Received in the Field
Sept. 2nd, 2011	**Polymer Pre-Flush (PPF) Injection Started**
Sept. 13th, 2011	**ASP Slug (ASP) Injection Started**
Jan. 3rd, 2012	**Polymer Drive (PD) Injection Started**
Feb. 24th, 2012	**Polymer Drive Completed**
April 6th, 2012	ESP Pump Installed for Production Enhancement

Chemical injection was initiated on September 2nd 2011 with a polymer pre-flush for injection profile control. ASP slug injection started on September 13th after completion of the pre-flush for 11days. On January 3rd 2012, polymer drive injection was

initiated and lasted till February 24th, which concluded the entire chemical injection sequence in the pilot. One April 6th 2012, an ESP pump was installed to reduce the backpressure on the well by lowering the fluid levels in the well. The total fluid production rate and the daily oil production showed a corresponding increase.

10.3 FIELD OPERATION

10.3.1 Injection and Production Facilities

The produced water was processed by the water treatment facilities onsite. The treated water was mixed with soda ash stock solution (delivered at 10% concentration). Surfactant, co-solvent and EDTA were added into the flow line through a chemical injection calibration system where the concentrations of each component can be carefully controlled. Polymer was delivered as sacks of powders, which were added into the polymer hopper and mixed with treated water in the mixing tank. The solution was continuously mixed for proper hydration of the polymer molecules. Finally the surfactant and polymer flow lines merged and went through a static mixer and filtration system before being injected through a triplex pump. The chemical injection calibration system and polymer mixing unit were situated in a dedicated work unit, where the ambient environment can be controlled. Such a controlled environment helps prevent phase separation of the surfactant slug and ensure proper polymer mixing. The entire pumping and mixing system can be easily monitored and adjusted through the central control panel. Figure 10.1 shows some of the surface facilities installed onsite. The EOR skid was built and installed by TIORCO based on specifications provided by Layline Petroleum and the University of Texas.

All the wells are produced by rod pumps. Their pumping schedule is based on predetermined production rate. The produced fluid from all the wells is connected to the

production facilities. As the concentration of polymer increased, the importance of maximizing retention time became important. Emulsion breakers were used for faster separation of oil and produced fluid.

Figure 10.1 Surface Facilities Installed at Pilot Location.

10.3.2 Field Laboratory Testing

Good quality control is essential for a successful pilot. There are four series of quality control checks that need to be put in place for a chemical flood pilot (Dean, 2011):

1). Periodically check surfactant phase behavior to make sure the optimum salinity and solubilization ratio are within acceptable range;

2). Polymer solution viscosity and filtration ratio should be checked frequently to ensure adequate mobility control;

3). Brine salinity and pH should also be checked for phase behavior and mobility control;

4). The aqueous stability of the ASP formulation needs to be verified to make sure that all components are soluble and form one single, stable, and clear phase.

A field laboratory was established and built on location with capabilities of testing fluid samples that were collected from injection and production wells. The quality of injection fluids is very important to pilot performance. Samples off the injection line were collected every four hours and pH and conductivity (salinity) were recorded. Polymer concentration and viscosity were also recorded on samples taken from the mixing tank. The filtration ratio of the injected polymer solutions was also checked periodically (typically twice a day). The surfactant and co-solvent delivered to the field were tested in the research lab at the University of Texas for pre-pilot quality control. The performance of the field batch (surfactant and co-solvent) was consistent with the one used previously in lab screening, except for a slight shift of optimum salinity from 1% to 0.8% Na_2CO_3 (see solubilization plot in Figure 10.2). Polymer samples were also frequently sent to research lab for rheology checks using a state-of-the-art rheometer. Inconsistency of viscosity at target concentration (Figure 10.3) was indeed observed, and adjustments (increased polymer concentration during slug injection) were made in the field. Chemical injection quantity and pressure was also monitored and recorded on a daily basis. On the producer side, produced fluid was monitored by collecting wellhead samples from all the pilot wells. And the samples were analyzed for oil cuts, the presence of surfactant and polymer and pH. Wells outside the pilot area were also monitored for chemical breakthrough.

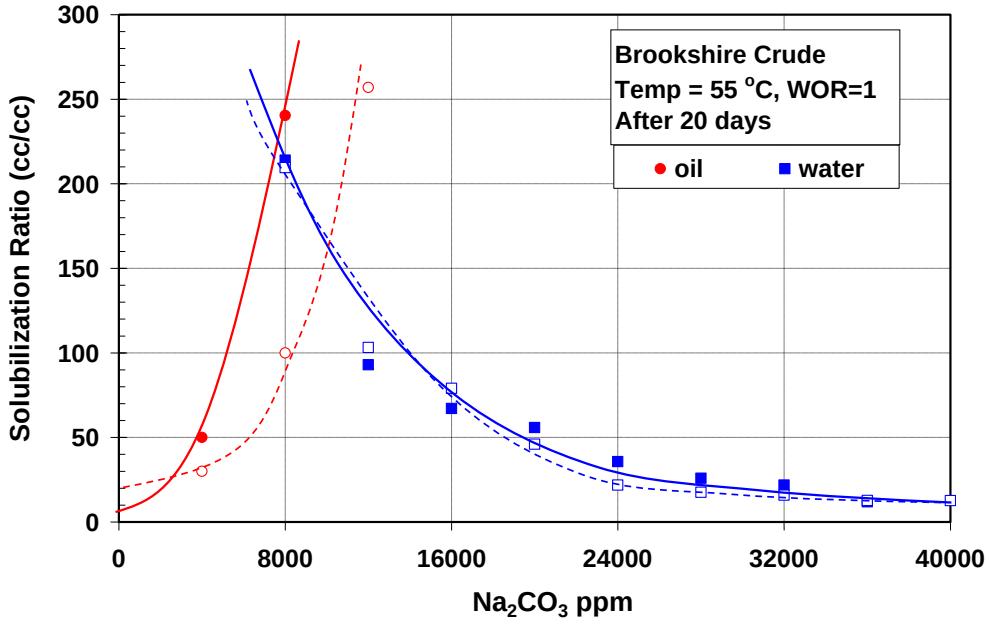

Figure 10.2 Solubilization Plot Comparison between Field QC Test (solid lines & filled symbols) and Original Lab Results (dash lines & open symbols) (0.3wt% Petrostep S13-C + 0.1 wt% Neodol 25-12).

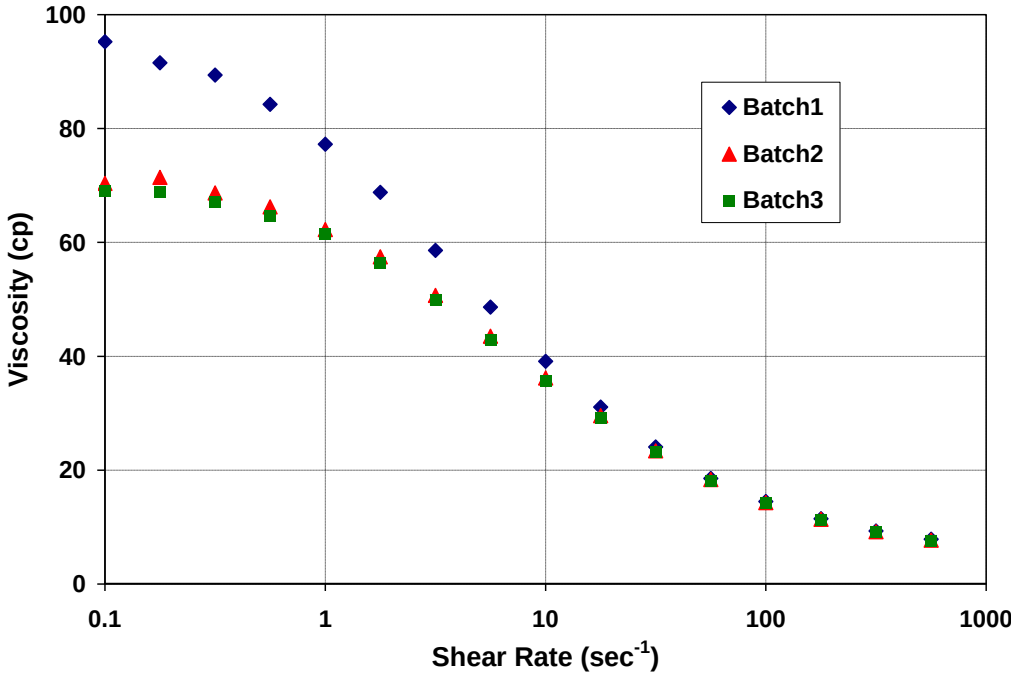

Figure 10.3 QC Viscosity Measurements of Different 3430S Polymer (EOR90) Batches (@ 2500 ppm & 55°C).

10.4 FIELD OBSERVATIONS AND RESULTS

10.4.1 Injection Data

Prior to chemical injection, one of the major concerns in the field was the injectivity reduction due to viscous fluid injection, which is a potential problem in EOR operations (Qu, 1998; Jain, 2012; Sharma, 2012). The field injection permit was specified at 1055 psi maximum wellhead pressure to prevent fracturing the formation. Both theoretical and numerical calculations suggested a low injectivity of ~ 0.2 bpd/psi under this pressure if 2000ppm polymer were to be injected. The plot shown in Figure 10.4 was based on a theoretical calculation conducted using equation (8.3-9) in Lake's EOR book (1989). Any injection rate greater than 500 bpd was expected to result in injection above this pressure limit.

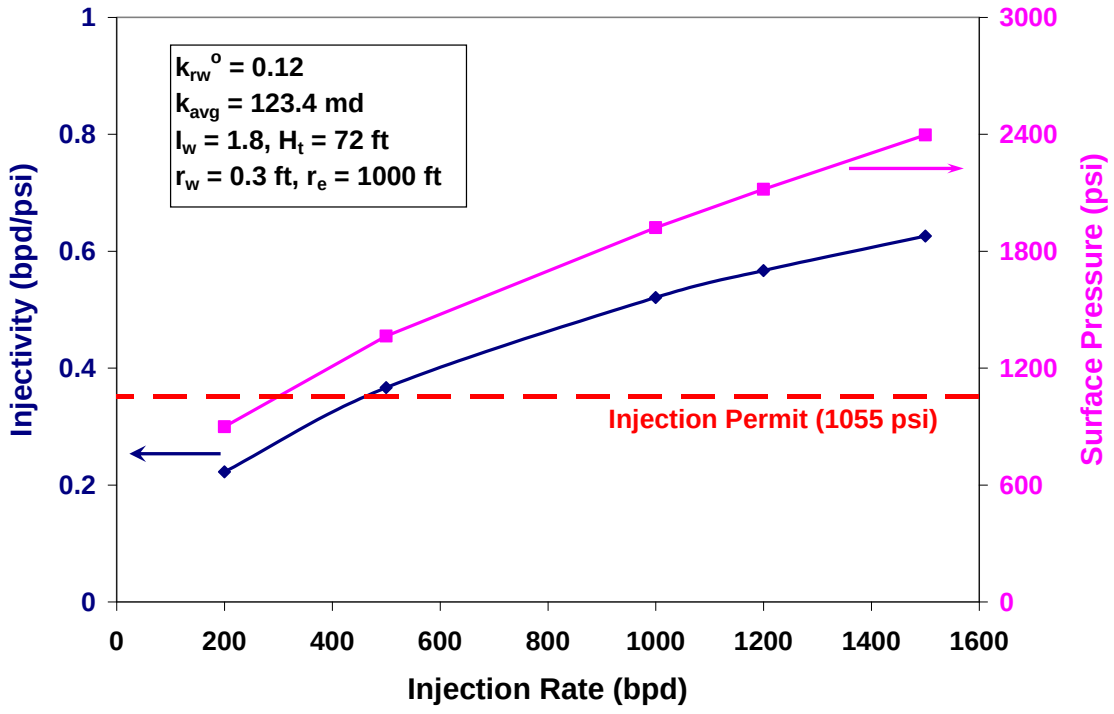

Figure 10.4 Theoretical Calculation of Polymer Injectivity and Surface Pressure.

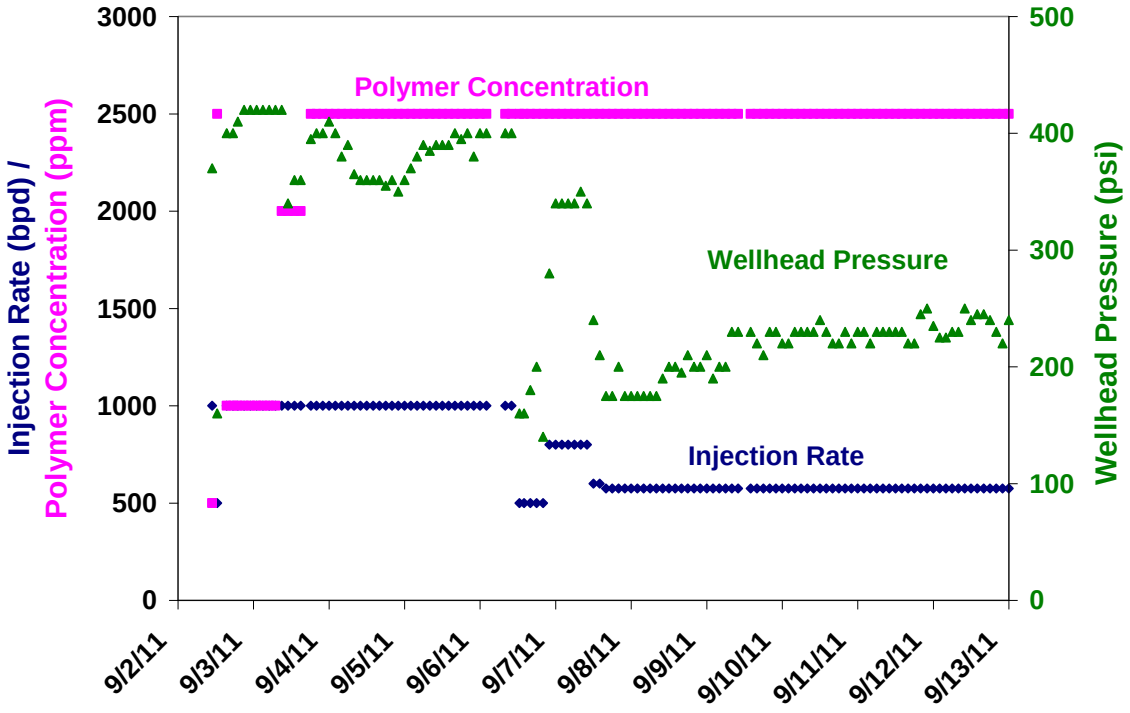

Figure 10.5 Polymer Pre-Flush (PPF) Injection Data.

As a result of this calculation, at the onset of polymer pre-flush (PPF), as shown in Figure 10.5 (the first data point), low concentration of polymer (1000ppm, ~ 12cP at surface temperature) was injected at a fairly low rate (500bpd), with the intention to carefully monitor the injectivity and identify any issues. The surface pressure was found actually to be quite low at 370psi, resulting in a high injectivity of 2.7bpd/psi, which was almost the same as the water injectivity. With this surprisingly high injectivity, the polymer concentration was steadily increased to 2500ppm (~ 70cP measured at the surface), and the injection rate was increased adjusted to 500bpd. As shown in Figure 10.5, throughout the polymer pre-flush, the injection pressure remained well below the permitted injection pressure. And the corresponding change of pressure with rate rendered an almost constant injectivity, despite of the fact that polymer concentration and injection rate were both frequently adjusted. Since the injection was done way below

parting pressure, pre-existing fractures were suspected to be present in the injector and were likely responsible for this very high injectivity.

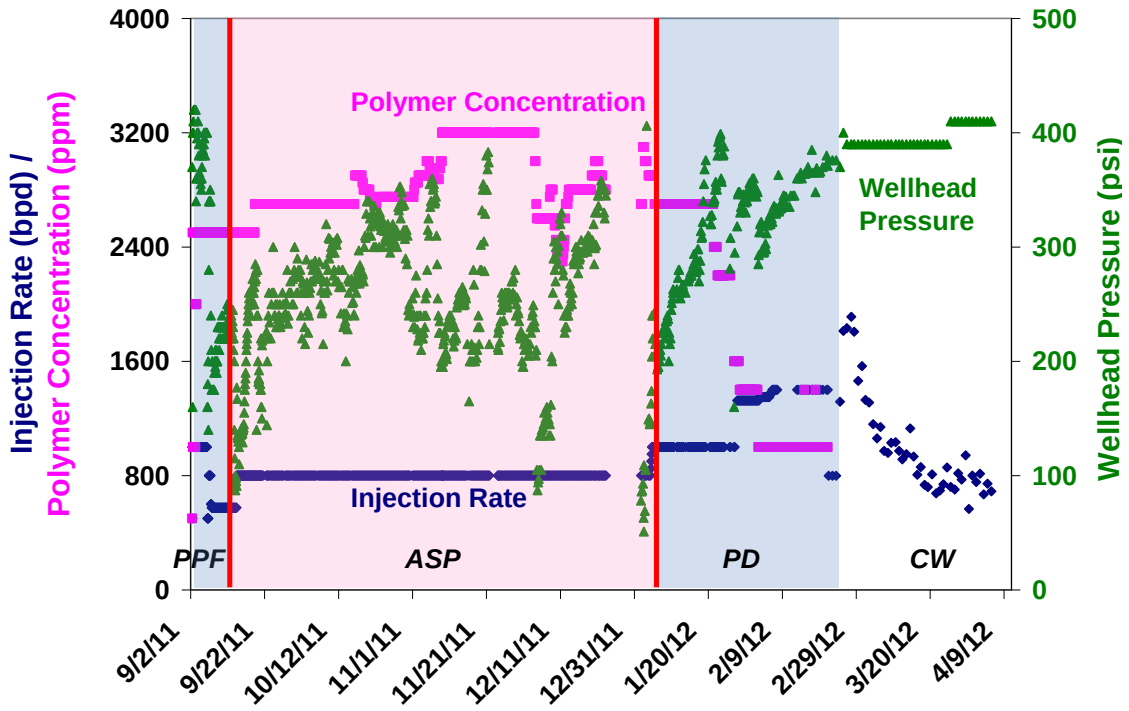

Figure 10.6 Injection Data throughout the Entire Chemical Injection Sequence (PPF: polymer pre-flush; ASP: surfactant slug; PD: polymer drive; CW: chase water).

This lower-than-expected wellhead pressure was maintained throughout the entire injection sequence, as shown in Figure 10.6. This abnormal injectivity response was recently studied numerically in our group (Lee, 2012). Various factors, including perforation density, shear rate coefficient (in rheological model), sand layer thickness (out-of-zone injection), near wellbore gird block size, and fracture growth, and their impacts on well injectivity were investigated. While improvement on matching field data was achieved by adjusting certain parameters, the agreement was still not satisfactory,

indicating a more complicated mechanism controlling the process. This aspect will need a more in-depth study and may never be completely resolved.

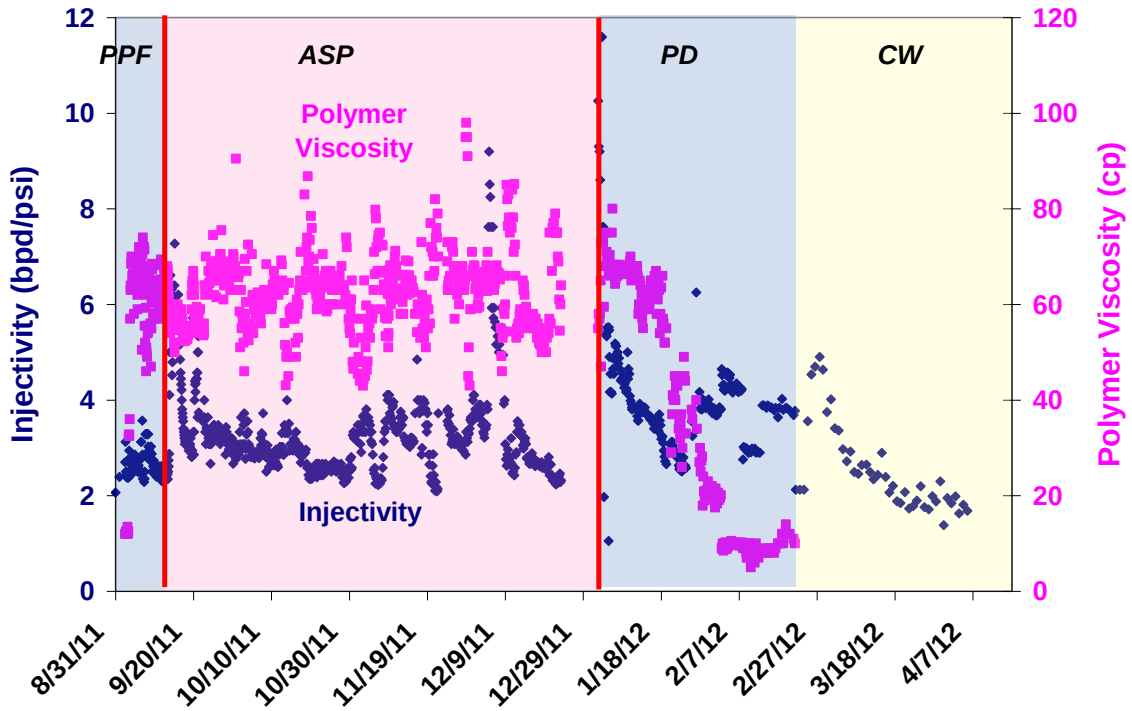

Figure 10.7 Injectivity and Polymer Viscosity Profiles throughout the Chemical Injection Sequence.

Figure 10.7 shows the corresponding injectivity and polymer viscosity data throughout the same time period. The injectivity here is calculated by simply dividing the wellhead pressure from the injection rate (assuming a hydrostatic reservoir pressure and neglecting frictional loss). The polymer viscosity reported here was measured on samples taken from the polymer mixing tank (before blending with surfactant, co-solvent and alkali) at surface temperature. For the ASP slug due to higher total salinity (1% Na_2CO_3 + brine salinity), the actually injected fluid viscosity will be lower, roughly two thirds of the reported polymer viscosity based on results from Chapter 8. The polymer viscosity

was maintained throughout the pre-flush and ASP slug injection, and was gradually tapered down in the final polymer drive. The injectivity remained almost constant around 2.5 bpd/psi, especially during the ASP slug injection.

10.4.2 Residual Oil Mobilization

Upon contact with the residual oil, the synthetic surfactant and in-situ generated soap work together and start to solubilize the oil and dramatically bring down interfacial tension. The residual oil can then be mobilized and removed from pore space. This process was observed as evidenced by a sharp increase in fluid injectivity observed at the onset of surfactant slug injection, as shown in Figure 10.8 (well injectivity and polymer viscosity).

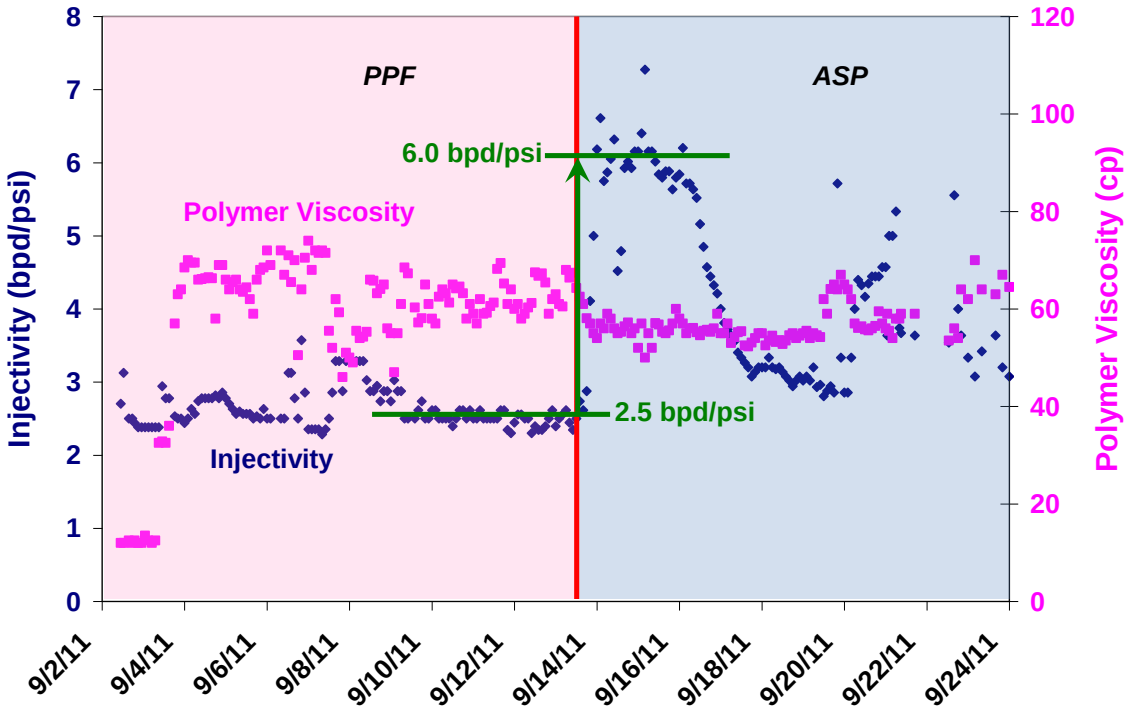

Figure 10.8 Field Injectivity Response at the Onset of ASP Slug Injection: Indication of Oil Mobilization.

ASP slug injection was initiated at 14:00 hours on September 13th, as can be seen from figure above, almost right after the surfactant injection, the injectivity increased from 2.5bpd/psi to roughly 6 bpd/psi, and actually peaked at 7.5bpd/psi at one point. Although this may be partly due to a viscosity drop when switching from polymer pre-flush to the ASP slug, this decrease was not sufficient to explain the 2.4 times injectivity increase. Recalling the injectivity equation, one other variable could potentially change and affect injectivity is the relative permeability of the aqueous phase. Due to the mobilization of residual oil by slug injection, the residual oil saturation was reduced. This resulted in an increase in the aqueous phase saturation and led to a higher relative permeability to the ASP slug, which showed up as a sharp drop of injection pressure (Figure 10.6), and as a sudden jump on the injectivity plot. Figure 10.8 unambiguously shows the oil mobilization capability of the injected surfactant formulation.

10.4.3 Chemical Detection

Chemical detection from the produced fluids is also important for pilot interpretation. Injected chemicals are effective indicators suggesting off pattern / zone fluid loss. Produced fluid samples were checked frequently for injected chemicals. The turbidity test and titration method used for polymer and surfactant detection in the field could only provide rough estimates of breakthrough times and concentrations. The polymer and surfactant breakthrough sequence seems to follow that of the tracer test. Polymer was the first chemical to be detected. Surfactant has also been detected in the Martin 37. No high pH fluid, however, has been observed in the produced fluid thus far, which suggests quite possibly an unfavorable separation of pH and surfactant fronts. This separation is detrimental to the entire process due to altered phase behavior (poor oil solubilization and high interfacial tension) and higher surfactant loss. Possible reasons to

such separation include high alkali consumption due to higher than expected clay content, as well as fluid loss from the pattern.

10.4.4 Field Production Response

During ASP slug injection, the injection rate was maintained at 800 bpd. Later on during the polymer drive phase, as the polymer concentration was progressively decreased the injection rate was increased accordingly (shown in Figure 10.6). On the producer side, as can be seen from Figure 10.9, the two wells on the south side of the pilot, Martin 10A and Martin 12, were set at a maximum production rate (total fluid) of 500bpd, whereas Martin 34 and Martin 37, situated on the north side, were set at lower rates initially but raised to higher rates later on (especially Martin 37).

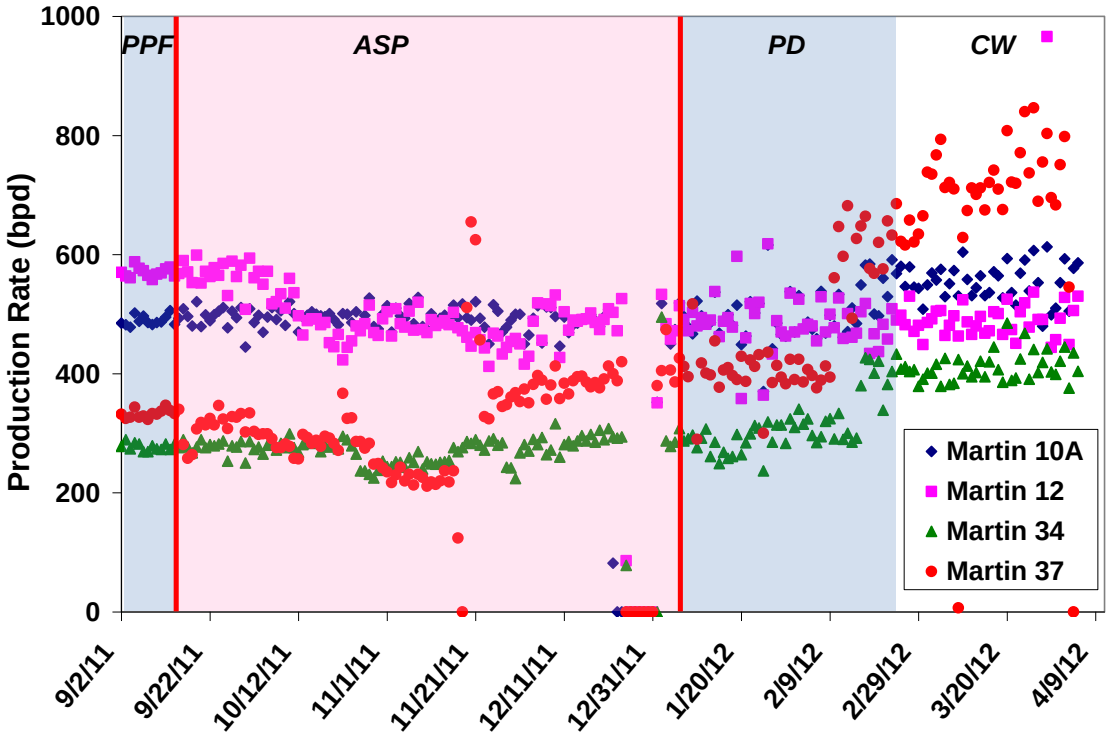

Figure 10.9 Daily Fluid Production Rate of the Four Producers in the Pattern since Polymer Pre-Flush.

By pulling fluid faster on the south side of the pilot, the initial intention was to counterbalance the influence of the natural water influx (SW to NE), and to distribute injected chemicals more evenly within the pattern area. Later on, it was discovered that polymer showed up at Martin 6 well outside the pattern (consistent with tracer response). A high-perm conduit was suspected to exist between the injector and Martin 6. A decision was made at that point to bump up the production rate on the Martin 37 well (nearest to injector) and thus pull more fluid out from in-pattern producers. This way the impact of the high-perm thief zone can probably be weakened.

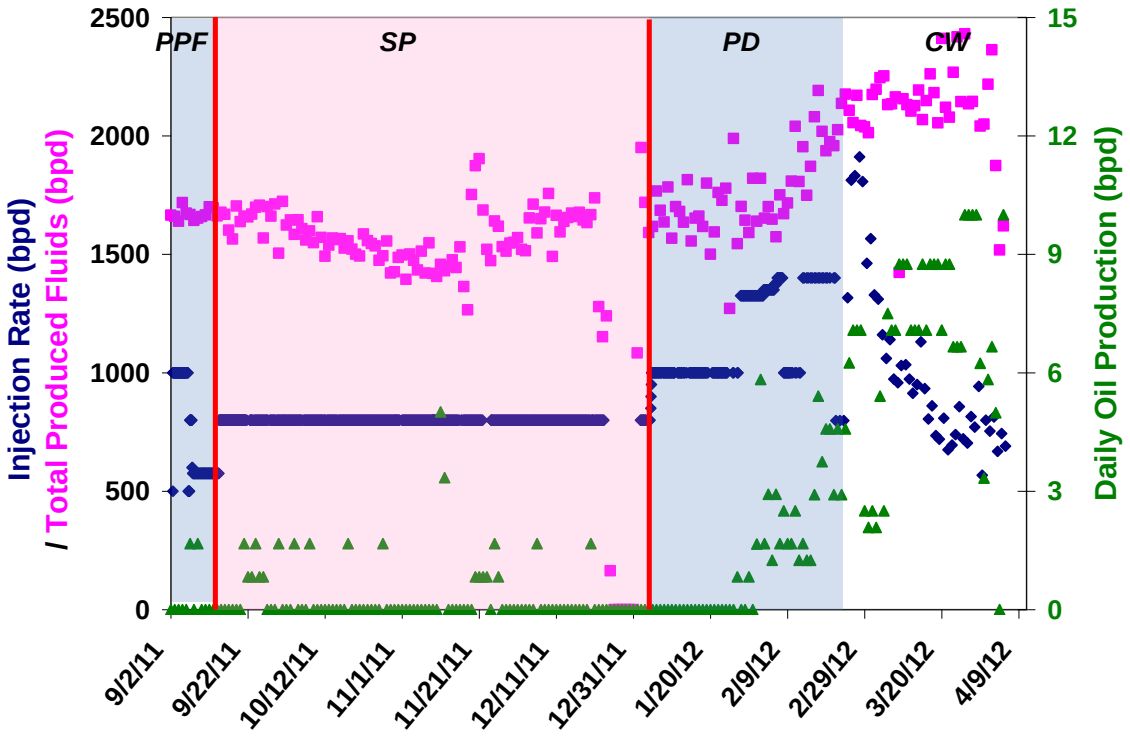

Figure 10.10 Pilot Injection and Production Rates, along with Daily Oil Production for Wells in Pattern.

Figure 10.10 plots the total injection and production rates from pilot wells, along with daily oil production rate from the four pilot producers combined. The total injection

volume is always much lower than the total fluid produced due to 1) the rate constraints put in place on the wells; and 2) the fact that a strong natural aquifer is continuously charging the reservoir. No appreciable oil production enhancement was observed throughout the ASP slug injection period. The daily oil rate, however, started to pick up roughly half way through the polymer drive injection, and has continued to grow.

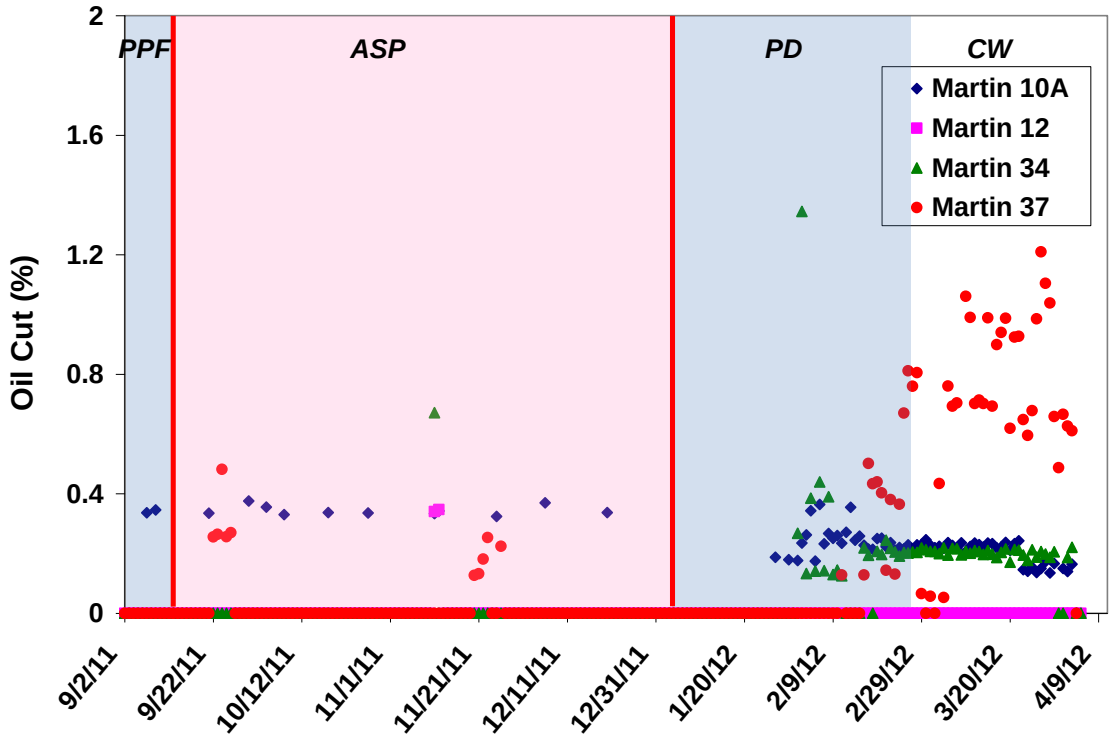

Figure 10.11 Daily Oil Cut of the Four Producers in the Pattern since Polymer Pre-Flush.

Figure 10.11 shows the oil cut on individual pilot producers since the start of the pre-flush. No appreciable oil cut increase was observed throughout the ASP slug injection period. Oil production (oil cut), however, started to pick up roughly half way through the polymer drive injection, and has continued to grow. Martin 37 well shows the strongest response, with oil cut rising from zero to about 1.5%. This is in agreement with

tracer response and the fact that M37 is the closest well to the injection. The stronger production response on M37 seems to correlate well with the higher production rate imposed on this well towards the end.

To date, the pilot oil production has been far below expectation. Three out of four (M10A, M12 and M34) producers within the pattern have not shown EOR oil response. However, if we include the other wells in the lease area especially those up-dip producers that showed early tracer breakthrough (e.g. M2, M4 and M6), a lease-area EOR oil response can be clearly seen as shown in Figure 10.12 below.

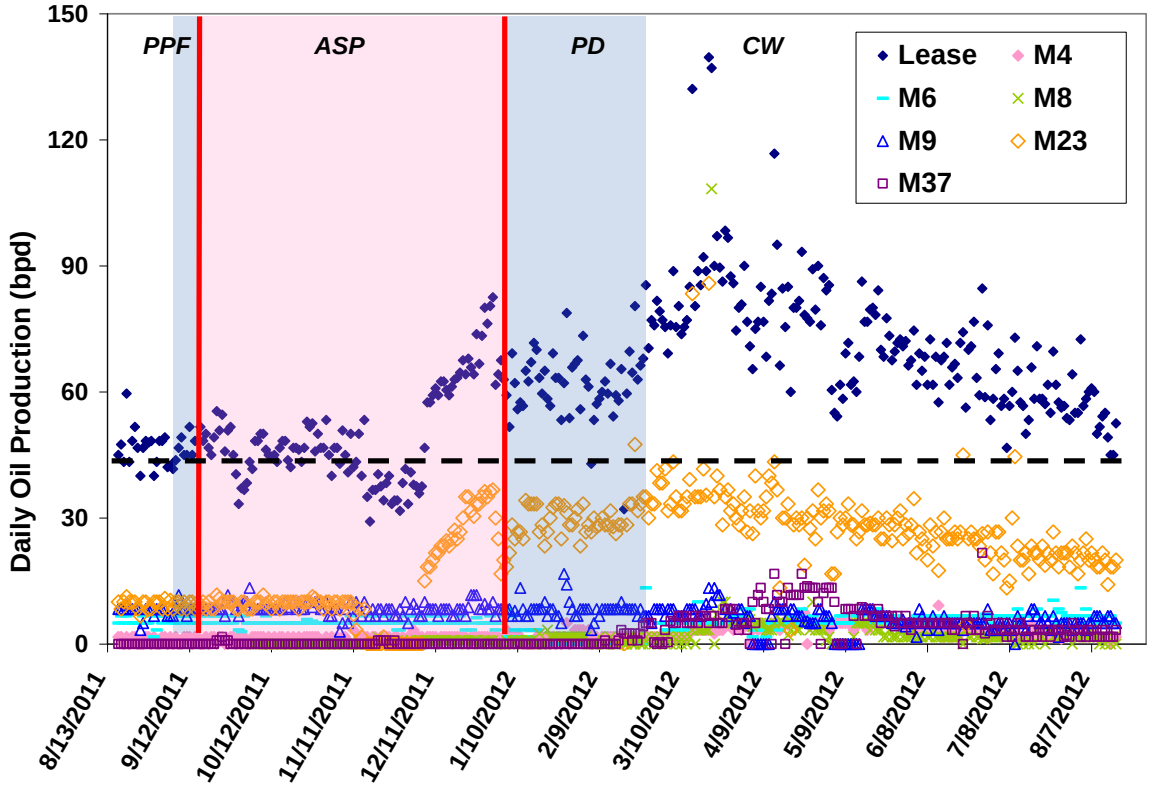

Figure 10.12 Daily Oil Production for the Entire Martin Lease and Wells Showing EOR Responses.

For the first 100 days (Sept. 2nd to Dec. 11th), the lease-area total daily production remained constant and formed a production baseline at about 40 bpd. Towards the end of ASP injection period, the oil production started to increase and actually peaked over 100 bpd. The average oil rate since then is about 70 bpd, with an increase of 30 bpd due to EOR chemical injection and ESP installation. The field production monitoring is still ongoing at this time. The total lease-area EOR oil production can be calculated by simply integrating all the oil produced above the production baseline, as shown in Figure 10.13 below.

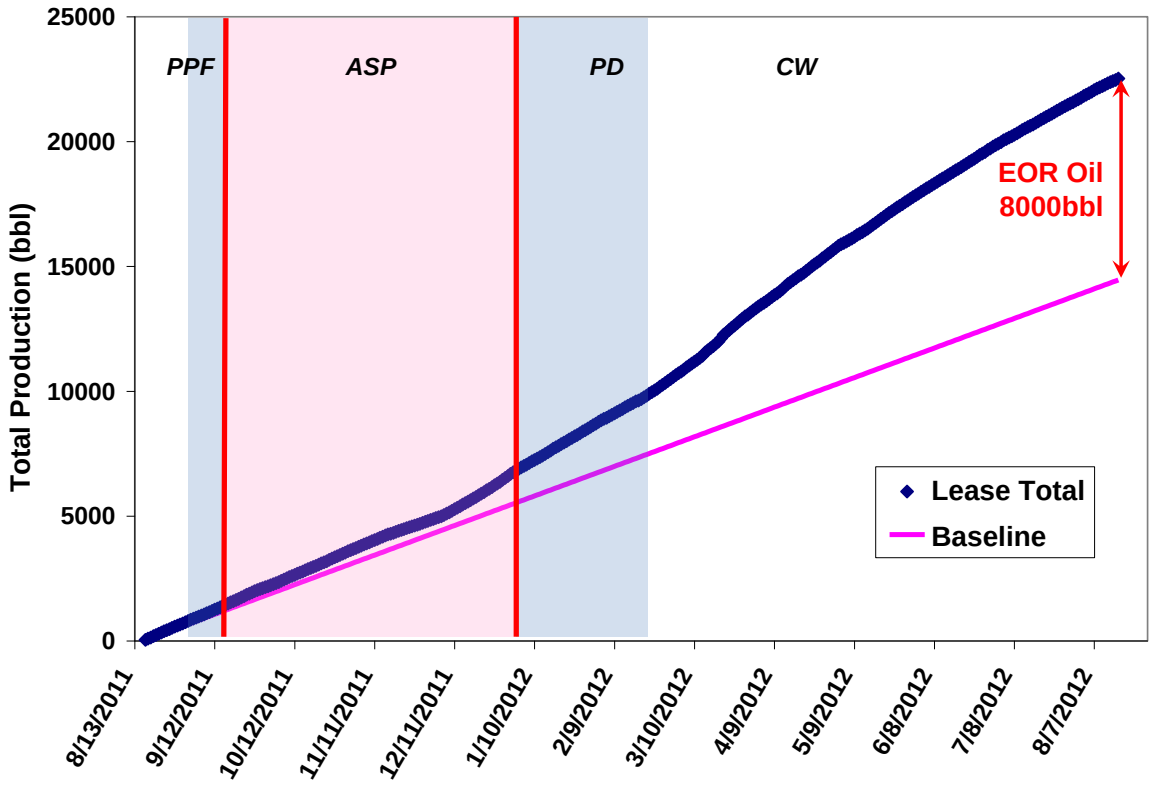

Figure 10.13 Total Lease-Area Oil Production and Baseline (8000bbl EOR oil produced as of 08/16/2012).

As of August 16 of this year, a total of 8,000 barrels (EOR oil) have been produced over the entire lease. With a total lease production of 22,500 barrels, EOR chemical injection has increased the lease production by 55% (from its baseline of 14500bbl). Another interesting observation from Figure 10.12 is that the wells that have shown EOR responses seem to be the ones (or close to them) showed early tracer breakthroughs.

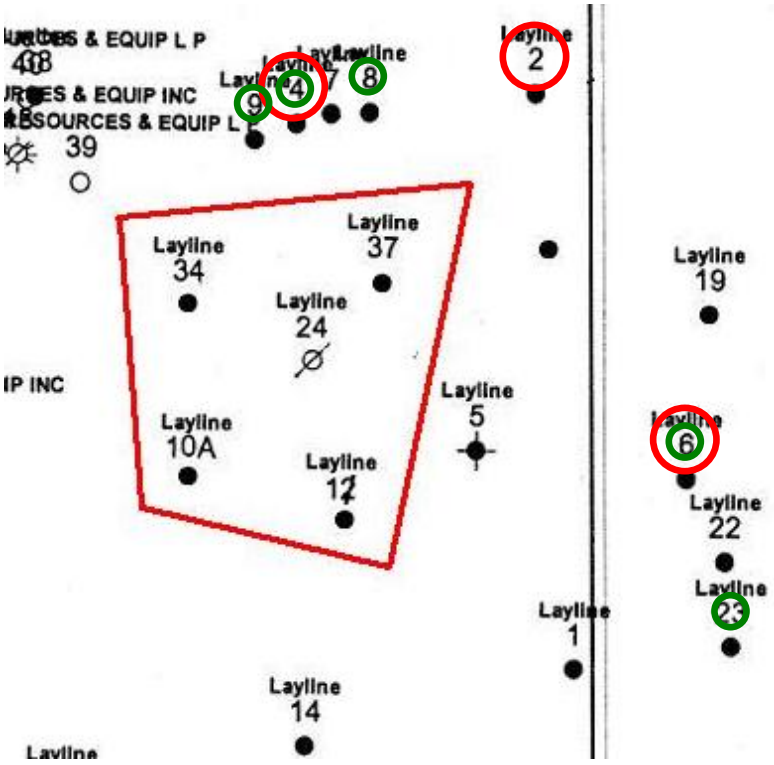

Figure 10.14 Producers that a) Showing EOR Responses (green circles) and b) Showed Early Tracer Breakthroughs (red circles).

Figure 10.14 above clearly marks the wells that are showing EOR responses now and wells that showed early tracer breakthroughs during inter-well tracer test. There are clearly quite some overlaps between the two groups of wells. This shows again the

importance of the tracer test in understanding fluid flow in the reservoir and in facilitating interpretation of field data and results.

10.5 PILOT RISKS AND UNCERTAINTIES

There are many factors that can greatly affect the performance of an EOR pilot. Dean (2011) conducted a comprehensive review of the potential risks associated with chemical floods. Not all of the factors are applicable to the Brookshire pilot. The following is a list of possible problems that may affect the results from this pilot.

10.5.1 Out-of-Zone Fluid Flow & Poor Confinement

The injected mass of surfactant and polymer injected is based on an estimated swept pore volume. An underestimated volume could result in insufficient surfactant injection. Thus it would be impossible for the slug to reach the producers. This can occur if injection occurs out of the target zone due to the presence of fractures or unanticipated flow behind pipe. Each of these scenarios can adversely affect the pilot performance since not enough of the injected fluids would be injected into the target zone. Based on a polymer injectivity study conducted in our group (Lee, 2012), the injectivity cannot be matched with existing models unless the injected fluids are being injected out of zone. This may suggest unexpected behind pipe flow since the injection pressures are well below fracturing pressures.

Poor confinement of chemicals within the pilot area also adversely affects the project performance, since effectively less chemical would go into the target reservoir volume. This typically occurs if there is a good bit of fluid flux into and out of the pilot pattern. The low overall tracer recovery, only about 24% recovered, suggests fluid loss from the pattern. Earlier breakthrough on some of the out-of-pilot (and faraway)

producers (for instance, Martin 6 well) seems to suggest the existence of a thief zone and more severe heterogeneity in the area than suggested by well logs.

10.5.2 Unexpectedly High Chemical Injectivity

The injectivity response observed in the field is extremely puzzling in the sense that it is completely unexpected and much higher than both analytical and simulation predictions. The injected fluid viscosity and the filtration ratio were constantly monitored. The viscosity remains at the target level throughout the project. Thus the high injectivity was probably not due to poor injection fluid quality (lower than expected viscosity), although other degradation processes (such as exposure to oxygen of some sulfite in fluid) could occur during polymer pumping and transport in the reservoir. Fracturing the injector is also not a possibility since the wellhead pressures were so much below the fracture gradient. The most likely explanation of the high injectivity is out of zone injection of the chemicals due to unexpected behind pipe flow or transport of the injected chemicals through natural fractures (or a thief zone) towards the Martin 6 and Martin 23 wells. This would result in the EOR chemicals being injected only into certain areas of the formation, leading to poor overall oil recovery.

10.5.3 Higher Chemical Retention

Higher-than-expected surfactant retention will result in lower oil recovery and less favorable economics. The best way to prevent this from happening is to do realistic and accurate coreflood experiments with representative reservoir core under reservoir conditions. This unfortunately could not be accomplished for the Brookshire Dome project due to the poor quality of core plugs form the field. One way to reconcile this in the field is to inject more than sufficient surfactant so that even a higher than expected retention will not cause problems. For the Brookshire pilot, larger than designed pore

volume (0.4 vs. 0.3PV) of surfactant slug was actually injected due to the fact that the surfactant retention in the reservoir is a bit of an unknown.

An increase in alkali consumption together with surfactant adsorption may be another possible reason for the pilot performance. Common solutions includes pre-flooding the reservoir to unload the clays of divalent cations, increasing the alkali concentration and / or changing to a surfactant that is more tolerant to divalent ions. Accurate mineralogy information needs to be collected. A core plug from an adjacent lease was sent for XRD analysis for Brookshire project. The results, however, were not self-consistent, which made the clay content estimation even more difficult. In the field, no high-pH (~ 10 to 11) fluid sample has been detected so far in any producer, whereas surfactant breakthrough was interpreted to have occurred on the adjacent Martin 37 well. The separation of pH and surfactant fronts seems to suggest higher alkali consumption in the reservoir, which delayed the pH front propagation in the reservoir. This situation was particularly undesirable since proper phase behavior, and thus oil mobilization, depends on the presence of both the alkali (in-situ soap generation) and the synthetic surfactant. It seems as if this may be a likely reason for the poor oil recovery seen in the pilot.

Simulations conducted to explore the impact of clay content on oil recovery (using UTCHEM) do not indicate any significant detrimental effects.

10.5.4 Viscous Microemulsion Formation

In the classic Winsor (1954) microemulsion theory, the formation of Type III (or middle phase) microemulsion is of key importance for achieving ultra-low IFT. The flow behavior of microemulsion phase also has direct impact on surfactant flood performance (Bennett, 1981; Walker, 2012; Solairaj, 2012). High microemulsion viscosity will significantly increase surfactant retention; adversely affect mobility control requirements

and oil recovery results. Careful visual inspection of the middle phase is, therefore, very important during phase behavior screening. By using a branched main surfactant (Levitt *et al.*, 2006) and a hydrophilic co-solvent (Sahni *et al.*, 2010), the current surfactant formulation showed improved phase behavior and reduced microemulsion viscosity. The data in Figure 10.15 show the low shear microemulsion viscosities at two C_{23} values.

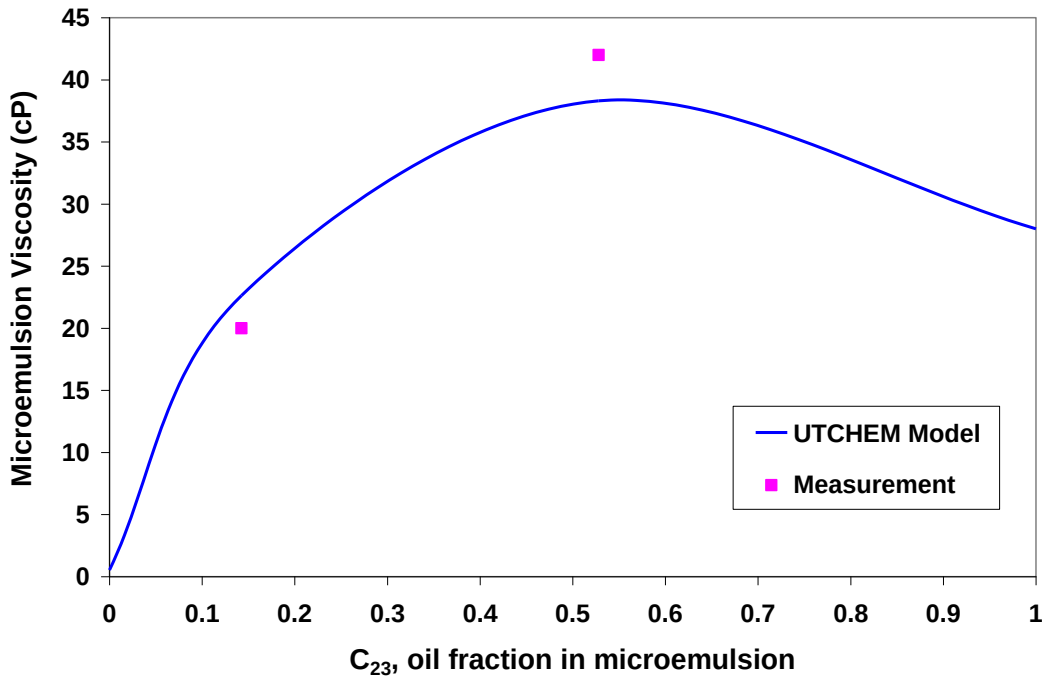

Figure 10.15 Experimental and Modeled Microemulsion Viscosity at 55°C vs. C_{23}.

In UTCHEM simulations, microemulsion viscosity is modeled by a liquid phase viscosity model (UTCHEM, 2000), where the required input parameters are determined by matching lab measured viscosities at different compositions. The microemulsion viscosity varies between the brine (left) and oil (right) viscosity boundaries. Where C_{23} equals zero, the viscosity is the brine viscosity. When C_{23} equals one, the viscosity is the oil viscosity. At about 0.5 C_{23}, the microemulsion viscosity shows a maximum of about

43cP. As can be seen from Figure 10.15, the UTCHEM model is able to predict lab measured microemulsion viscosities using solubilization parameters from phase behavior tests. There are, however, other complexities to this problem.

The non-Newtonian behavior of the microemulsion phase, as shown in Figure 10.16, cannot be captured in the UTCHEM model. Similar behavior has been reported elsewhere (Bennett, 1981; Walker, 2012).

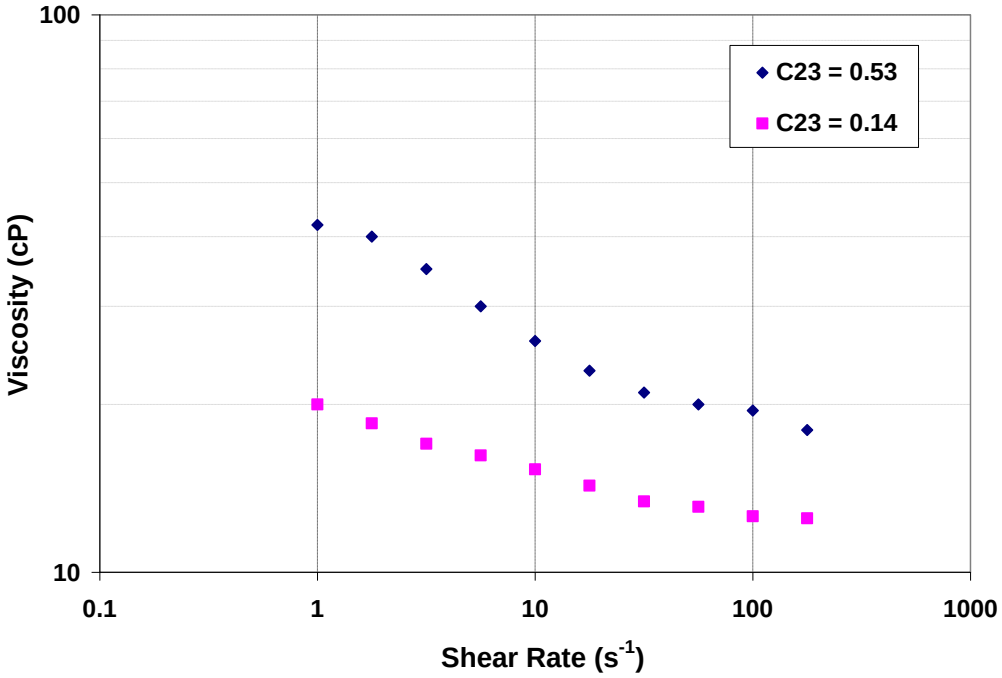

Figure 10.16 Non-Newtonian Behavior of Microemulsion Viscosity at 55°C.

Consider the different mixing condition in a phase behavior pipette and the pore space of a reservoir rock, the microemulsion viscosity could be quite different from lab measurements. A more viscous microemulsion will cause a much more serious problem in the field than in a 1D linear core flood. On the more "open" reservoir scale, the viscous microemulsion phase may act as a "diverting agent" to the injected fluid behind if

mobility control is not ensured. As a result, phase trapping and high surfactant retention will lead to poor oil recovery. The fact that the injectivity remained almost constant (see Figure 10.7) during slug and drive injection seems to suggest the possibility that the injected fluid was trying to avoid the high viscosity microemulsion zone, since otherwise a steady drop of injectivity would be observed.

The fact that the pilot area is subject to the influence of a strong water drive may make the situation even worse. The dilution caused by this huge water influx on the polymer drive may jeopardize the designed mobility ratio. Without a proper mobility control by the drive, the mobilized and viscous oil bank (and/or microemulsion bank) cannot be efficiently driven to the producers leading to bypassing and re-entrapment.

10.5.5 Low Initial Oil Saturation

The economics of any tertiary EOR process are very sensitive to the remaining oil saturation in the target zone. The waterflood residual oil saturation should ideally be determined as accurately as possible before planning the EOR pilot, using method such as single well chemical tracer test (SWCTT). For a small scale pilot project such as the Brookshire Dome pilot it is not cost effective to conduct such a test. It is very unlikely that this was the reason for the poor pilot performance. The increase in injectivity at the start of EOR chemical injection indicates that the waterflood residual oil was being displaced by the injected chemicals from the near wellbore region.

10.6 SUMMARY AND CONCLUSIONS

An ASP flood in a mature waterflooded field was implemented in the Brookshire Dome field, Texas. Chemical injection in the field went smoothly without any injectivity issues as was originally feared. The injectivity remained remarkably stable throughout the flood even when injection rates and polymer concentration was changed. The

unexpectedly high injectivity suggests the presence of fractures in the injector or unconstrained fracture growth induced by injection. This could lead to fluid loss to out-of-pattern zones, and viscosity breakdown in the wellbore. All these could severely impair the pilot performance. The mobilization of waterflood residual oil by the surfactant slug (formation of an oil bank) was clearly indicated by the drastic increase of injectivity upon ASP slug injection. Production rates on the pilot producers were adjusted in real time based on field observation and response. Field production has been well below expectation to date. EOR responses were, however, clearly seen in the lease-area oil production plot. Martin 37 started to show 1 to 2% oil cut on towards the end of the polymer flood. EOR responses were observed in peripheral producers that have previously shown early tracer breakthrough.

The technical accomplishments of this pilot project include:

1. A systematic and successful laboratory design process was carried out in the research lab at the University of Texas. The four-step design approach, composed of a) process and material selection; b) formulation optimization; c) coreflood validation; 4) lab-scale simulation, could be easily transferred to other EOR projects. The optimal formulation recovered over 90% residual oil in a Berea coreflood. Lab-scale simulation models accurately history matched the coreflood experiment and were set up to simulate the pilot flood.
2. Pilot-scale simulation model was set up based on available information in hand. Different injection and operating strategies were investigated, as well as the sensitivities of project economics to various design parameters. A field execution plan was proposed based on the results of this simulation study.
3. A surface facility conceptual design was put together based on the practical needs and conditions in the field. All field preparations, on-site equipment

installation, chemical ordering and delivering were carried out in a timely and efficient manner. Flood injection was completely without any major issues. Good field management ensured a smooth operation and effective communication with different parties involved.

4. Residual oil mobilization and accumulation oil in front of surfactant slug (formation of oil bank) were clearly shown by drastic increase of injectivity upon ASP slug injection. Production rates on the pilot producers were adjusted in real time based on field observation and response. The overall EOR response has been below our expectation. A lease-area EOR oil response, however, has clearly been observed, with a total EOR production of 8,000bbl to date.

There are many factors, risks, and uncertainties involved in the field trial that could impact the final performance. A more thorough investigation needs to be conducted when more data and information are collected from the field. Some of key lessons learned throughout the project include:

1. Good quality reservoir core is crucial to the design process, and should be collected and used whenever possible for more realistic (compared to Berea) coreflood experiments. Invaluable information could, therefore, be obtained. Chemical (surfactant and alkali) consumption in the reservoir can be much better estimated since such knowledge is of key importance to the design process. Endpoint relative permeability and residual phase saturation are two other (among many) important sets of parameters can more accurately estimated using reservoir core, and they are absolutely crucial in simulation studies.

2. For ASP processes that make use of alkali and naphthenic acid reaction to generate soap, the phase behavior and thus oil solubilization capacity of the chemical formulation are always greatly impacted by the amount of alkali present in the system. By itself, the synthetic surfactant can seldom render optimal phase behavior. It is, therefore, imperative that sufficient synthetic surfactant and alkali always coexist in the system. However, in rocks with high clay content, alkali could be consumed very quickly which leads to a separation between surfactant and pH (alkali) fronts. Then the system is no longer optimum and loses its ability to mobilize residual oil. Therefore, it is important to monitor surfactant breakthrough and pH values of effluent from corefloods and produced fluids in the field. It is necessary oftentimes to add more alkali to compensate higher than expected consumption in the reservoir.
3. Mobility ratio is a key parameter in a successful APS flood design. This is especially important when considering the possibility of highly viscous and non-Newtonian microemulsion formation in the reservoir. Careful laboratory characterization of microemulsion rheology is, therefore, of key importance. An improved rheology model could help better understand the flow behavior of the microemulsion phase in the reservoir. Mobility control in the field could be much more complicated, especially when the injected chemicals are subject to a strong water drive. The impact of natural water flow should be studied and the ASP design needs to be adjusted accordingly.
4. All numerical simulations are based upon assumptions. This is particularly true when building the geological model. By no means can a successfully lab-scale history match on a coreflood guarantee the quality of a field-scale run. The results need to be interpreted with extreme caution.

5. Polymer injectivity has long been researched, yet most simulation models today have a hard time matching the injectivity in the field. Better and probably more fundamental understanding of various injectivity related issues is needed.

Alkaline/surfactant/polymer flooding normally involves a complicated design process even at the laboratory scale. When applied in the field, the complexities and risk levels grow exponentially. Brookshire Dome field represents a typical candidate for ASP flooding in mature oilfields in the US. Many of the unanswered questions from this project are, therefore, very representative of what other fields will encounter:

1. Why is the polymer injectivity so high in the field?
2. How do we implement better fluid confinement (vertically and areally) in complicated geologic settings?
3. How can we better estimate chemical consumption in the reservoir? How can we simulate this more accurately?
4. How can we better understand the impact of natural aquifers on chemical injection? How do we design the chemical injection program to ensure proper mobility control under these circumstances?

Chapter 11: Conclusions

11.1 ANIONIC GEMINI SURFACTANT DEVELOPMENT

A systematic laboratory development program was planned and carried out in our lab on the synthesis, characterization, modeling and EOR specific testing for a new family of anionic surfactants that has great potential for EOR applications. The following conclusions can be made from current study:

- By utilizing a two-step stable reaction scheme, a new series of anionic Gemini surfactants of various structures was successfully synthesized in our lab. ^{1}H and ^{13}C NMR spectroscopy is employed for chemical characterization. All products exhibited spectroscopic properties that are in agreement with those expected for the desired structures. (Chapter 2)
- Anionic Gemini surfactants with a range of different structures (C_{14} to C_{24} chain length, -C_2- and -C_4- spacers, sulfate and carboxylate head groups) are all strongly hydrophilic, with Krafft temperatures below room temperature (20˚C). The hydrophilicity is expected to come from the two ionic head groups and multiple ether groups in the structure. (Chapter 3)
- The CMC values for anionic Gemini surfactants are about two to three orders of magnitude lower than the corresponding conventional surfactants. Important thermodynamic parameters (ΔG_M^o, ΔH_M^o and ΔS_M^o) of the micellization process are determined using experimental data. The significantly more negative ΔG_M^o for Gemini surfactant drives the micellization process and results in ultralow CMC. The micellization process of Gemini surfactants is primarily entropy driven. (Chapter 3)

- Surface tension measurements suggest that Gemini surfactants have higher tendency to spontaneously adsorb at the air-water interface, and thus are more efficient in reducing surface tension. Changes made on alkyl chain length, electrolyte concentration and type of anionic head group can help adjust the HLB balance at air-water interface, rendering better surface performance in terms of lowering surface tension and obtaining closer molecular packing. (Chapter 4)
- A series of static adsorption tests were conducted using adsorbents disaggregated from Berea sandstone. The Langmuir adsorption model is found capable of capturing the general trend of the adsorption isotherm for Gemini surfactant. Gemini surfactant shows lower maximum adsorption density than the corresponding conventional single chain surfactant. Lower adsorption can be achieved by decreasing the solution salinity. Longer alkyl chain and spacer group on the other hand promote adsorption due to reduced solubility and stronger interactions with solid surface. (Chapter 4)
- The anionic Gemini surfactants have shown their extraordinary tolerance to salinity and/or hardness. Ultra-low IFT values are reached under these harsh conditions for Type I microemulsion systems, at very low surfactant concentrations. Gemini surfactant can potentially be used and may perform better in more hostile environments. The stronger molecular interaction between the Gemini and conventional surfactants offers synergy that promotes aqueous stability and interfacial activity. They can be used as co-solvents that help the solubility of the main surfactants, or as co-surfactants that help bring out the best performance of the surfactant mixture. (Chapter 5)
- Anionic Gemini surfactants with short spacers are capable of giving rise to high viscosifying capabilities at fairly low concentrations. The viscosities of solutions

increase with the increasing of concentration, and surfactants with longer alkyl chains and shorter spacer groups have higher ability in viscosification. For some of the sulfate Gemini surfactants, the solution viscosities undergo an unusual maximum with increase of temperature, and then drop down to almost solvent viscosities at higher temperature. All the Gemini solutions show classic shear-thinning behavior within the concentration and shear rate ranges investigated. A transition to more elastic behavior of the solution was also observed at higher surfactant concentration. All these rheological behaviors can be tied back to the unique micellar structure changes by Gemini surfactants in aqueous solution. (Chapter 6)

- A molecular thermodynamic model is developed for anionic Gemini surfactants to study their aggregation behavior in solution. The model takes into account of the head group-counter-ion binding effect and utilizes two simplified solutions to the Poisson-Boltzmann equation. It properly predicts the CMC of the surfactants synthesized and can be easily expanded to investigate other factors of interest in the micellization process. (Chapter 7)

The remarkable abilities of Gemini surfactants to influence interface and solution properties are fully demonstrated from the findings listed above. And indeed they have great potential of being applied in EOR processes. It should be recognized in the meantime that more work needs to be done before any concrete conclusion can be made regarding the feasibility of applying Gemini surfactants in real world applications. Some of the recommended areas for future research include:

- Conduct more in-depth analysis of the experimental data collected from IFT and phase behavior tests; and perform more validation study for the theory proposed

to explain the absence of IFT minimum in salinity scans for current series of Gemini surfactants.

- Synergy between Gemini and conventional surfactants have been evidenced in this dissertation, however more work should be planned and carried out in a systematic manner, since this might be the best way of utilizing Gemini surfactants in practical formulations.
- As shown in this dissertation, Gemini surfactants are capable of reducing oil-water IFT to ultralow level, the phase behavior test results, on the other hand, are quite different from conventional systems that can produce ULIFT and renders high oil recovery in corefloods. Therefore coreflood experiments must be conducted with Gemini surfactant formulations to examine the oil recovery potential of two-phase (Type I microemulsion) surfactant flooding. This is a key step towards more practical applications for these novel surfactants.
- Dynamic adsorption behavior of Gemini surfactants can also be studied from coreflood experiments. Compared to static adsorption tests, dynamic data are more useful and offer quantitative information regarding surfactant loss during a more realistic flooding process. This is especially important when we propose to use these novel molecules at very low concentrations.
- Microscopic imaging experiments should be conducted on Gemini aqueous solutions to help visualize various micellar structures. Direct evidence of our proposed theory of micellar structure change can be provided and better and fundamental understanding of Gemini solution behavior can be gained.
- Rheological properties of current series of Gemini surfactants are very interesting. Testing program should be planned and designed to examine the feasibility of utilizing these molecules in some more specific application areas, such as

viscosifying agent (substitute for polymer), or hydraulic fracturing fluids (like other VES fluids).

- The thermodynamic model proposed in this dissertation aims to study the onset of Gemini surfactant aggregation and to predict CMC values under different solution conditions. This model could easily be expand to study more solution behaviors, for instance, to predict aggregation shape and structure at higher surfactant concentrations and thus help us better understand the viscosity behavior of these molecules. The model can also be modified to study oil-water-surfactant system and predict solubilization behaviors.
- Other possible applications for Gemini surfactants can also be investigated, for instance, good foaming ability has been reported for cationic Gemini surfactants, and therefore the possibility of using current series of anionic Gemini surfactants as foam stabilizers can also be examined.
- Other synthesizing routes can be explored. Current method of synthesizing Gemini surfactant is fairly stable and straightforward; the limitation however is the availability of starting materials like long-chain epoxides. Synthesis route that starts from even simpler and more abundant feedstock chemicals will be more attractive from both practical and economical standpoints.

11.2 ASP PILOT DESIGN PROJECT

A systematic laboratory design was carried out to optimize the chemical formulation for an ASP pilot flood. Lab-scale simulation model accurately history matched the coreflood experiment and sets up foundation for pilot-scale numerical study. Different operating strategies were investigated using a pilot-scale model, as well as the sensitivities of project economics to various design parameters. A field execution plan

was proposed based on the results of the simulation study. A surface facility conceptual design was put together based on the practical needs and conditions in the field. Positive production responses have been observed from several nearby producers, and are under careful monitoring. More specifically, the technical accomplishments of this pilot project include:

- A systematic and successful laboratory design process was carried out in research lab at the University of Texas. The four-step design approach, composed of a) process and material selection; b) formulation optimization; c) coreflood validation; 4) lab-scale simulation, could be easily transferred to other EOR projects. The optimal formulation recovered over 90% residual oil from Berea coreflood. Lab-scale simulation model accurately history matched the coreflood experiment and set up foundation for pilot-scale numerical study.
- Pilot-scale simulation model was set up based on available information in hand. Different operating strategies were investigated, as well as the sensitivities of project economics to various design parameters. A field execution plan was proposed based on the results of this simulation study.
- A surface facility conceptual design was put together based on the practical needs and conditions in the field. All field preparations, on-site equipment installation, chemical ordering and delivering were carried out in a timely and efficient manner. Flood injection was completely without any major issues. Good field management ensured a smooth operation and an effective communication with different parties involved.
- Residual oil mobilization and accumulation oil in front of surfactant slug (formation of oil bank) were clearly shown by drastic increase of injectivity upon ASP slug injection. Production rates on the pilot producers were adjusted in real

time based on field observation and response. Daily oil rate started to increase about half way through the polymer drive and is still continuing to grow. Production responses were observed on Martin 34 and 37, two of more close-by producers to the injector, as expected and suggested by the tracer test. Martin 37 starts to show stronger oil production on towards the end.

There are many factors, risks, and uncertainties involved in the field trial that could impact the final performance. More thorough investigation needs to be conducted when more data and information are collected from the field. Some of key lessons learned throughout the project, among others, include:

- Good quality reservoir core is crucial to the design process, and should be collected and used whenever possible for more realistic (compared to Berea) coreflood experiment. Invaluable information could therefore be obtained. Chemical (surfactant and alkali) consumption in the reservoir can be much better estimated. And such knowledge is of key importance to the design process. Endpoint relative permeability and residual phase saturation are two other (among many) important sets of parameters can more accurately estimated using reservoir core, and they are absolutely crucial in simulation studies.
- For ASP processes that make use of alkali and naphthenic acid reaction to generate soap, the phase behavior and thus oil solubilization capacity of the chemical formulation are always greatly impacted by the amount of alkali present in the system. By itself, the synthetic surfactant can seldom render optimal phase behavior. It is therefore imperative that sufficient synthetic surfactant and alkali always coexist in the system. However, in rocks with high clay content, alkali could be consumed very quickly which leads to a separation between surfactant and pH (alkali) fronts. Then the system is no longer optimum and loses its ability

to mobilize residual oil. Therefore, it is important to monitor surfactant breakthrough and pH values of effluents from coreflood and produced fluids in the field. It is necessary oftentimes to add more alkali to compensate higher than expected consumption in the reservoir.

- Mobility ratio is a key parameter to a successful APS flood design. This is especially important when considering the possibility of highly viscous and non-Newtonian microemulsion formation in the reservoir. Careful laboratory characterization of microemulsion rheology is therefore of key importance. Improved rheology model could help better understand the flow behavior of microemulsion phase in the reservoir.
- All numerical simulations are based upon assumptions. This is particularly true when building the geological model. Lack of good reservoir cores in most cases makes the situation even worse. By no means can a successfully lab-scale history match on a coreflood guarantee the quality of a field-scale run. The results need to be interpreted with extreme caution.
- The injection of chemicals marks the beginning of a flood. But oftentimes even this starting point cannot be well understood. Polymer injectivity has long been a hot research topic, and yet most simulation models today have hard time matching the injectivity in the field. Better and probably more fundamental understanding of various injectivity related issues is most definitely needed.

Alkaline/surfactant/polymer flooding normally involves an extremely complicated design process even on the laboratory scale. When applied in the field, the complexities and risk levels grow exponentially. Brookshire Dome field represents a typical candidate for ASP flooding in mature oilfields in the US. Many of the unanswered questions from

this project are therefore very representative, and they need immediate attentions from both the academia and the industry:

5. Why is the polymer injectivity so high usually in the field? Is there anything more fundamental we are missing in modeling?
6. How do we implement better fluid confinement in more and more complicated geologic settings?
7. How can we better estimate chemical consumption in the reservoir? How can we simulate them more accurately?

How can we better understand natural aquifer charge? How do we design the chemical injection and how do we ensure proper mobility control under these circumstances?

APPENDICES

Appendix A: Key Techniques in Gemini Surfactant Synthesis

A.1 Reaction Monitoring Using TLC

Real-time monitoring is of key importance to the success of chemical reactions. After the reaction chamber is properly set up, more efforts need to be focused on carefully monitoring the reaction progression. Thin-layer chromatography (TLC) was used for following the course of reactions in all experiments. TLC plates were acquired from EMD Chemicals Inc., which are manufactured by coating a thin, uniform layer of silica gel onto a glass microscope slide. The silica gel is the stationary phase, while the solvent mixture is the mobile phase. A TLC operation generally includes: 1) spotting the plates; 2) developing the plate; 3) staining and visualization.

A.1.1 Spotting the Plates

7. Dissolve (separately) a small portion of the starting material and the unknown mixture (taken out of the reaction flask) into different vials (A and B) that contain hexane (*n*-C_6) and ethyl acetate (EA) solvent mixtures. The dissolved solution should contain about 1-2% of the substance. The polarity of the solvent can be easily adjusted by changing the volume ratio (5:1 ratio of *n*-C_6 vs. EA for initial trial). For our reaction, there will be two solutions prepared at this time (Solution A: long chain epoxide for RXN1, intermediate diol for RXN2; Solution B: unknown mixture for both reactions).
8. In order to keep track of where the sample is applied, it is important to clearly mark the TLC plate before spotting. Draw a straight baseline approximately 1cm from the bottom of the plate. Then draw three small ticks (#1 through 3) through the lines and make sure the ticks are evenly distributed on the line. (see in Figure A.39a)

9. Dip the capillary spotter into Solution A (starting material). The solution should rise up into the capillary tube.
10. Touch the capillary onto #1 tick mark on TLC plate briefly. The compound will then run out and form a small spot. The spot should be kept as small as possible (typically no larger than 2 mm in diameter). Blow gently on the spot to evaporate the solvent. This will build up a concentration of the compound. (see in Figure A.39b)
11. Repeat steps 3 and 4 for Solution B (reaction mixture) on #2 tick mark.
12. Co-spot Solutions A and B on #3 tick mark.

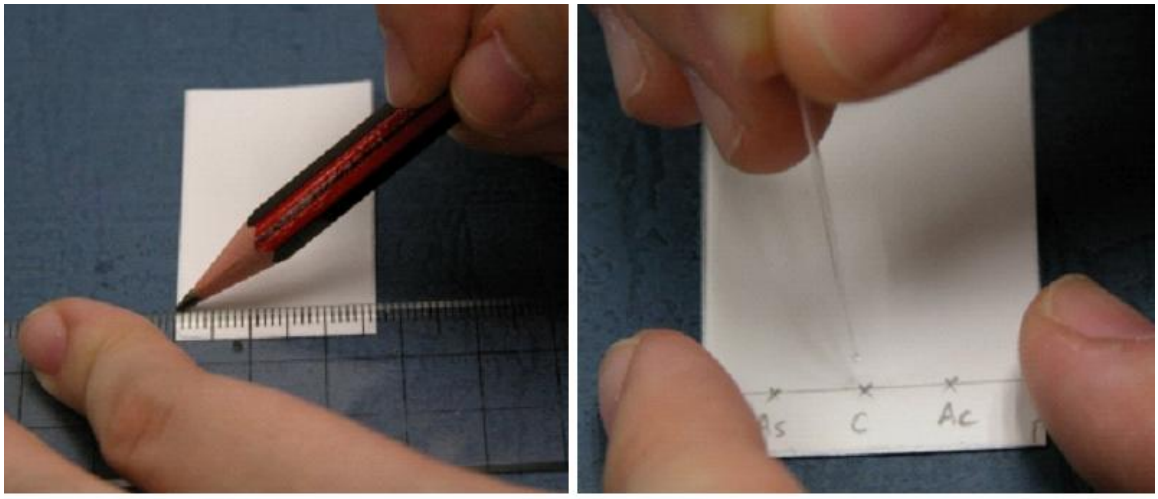

a *b*

Figure A.39: Marking the Starting Line and Points on the TLC Plate (a); Spotting the TLC Plate with a Capillary Tube (b).

A.1.2 Developing the Plate

1. Take a 100ml glass container, line the sides of it with filter paper, and cover with a lid.

2. Pour some solvent mixture into the container, and tilt the bottle so that the solvent wets the filter paper. Put no more that ¼ inch of solvent at the bottom. This helps saturate the air in the bottle with solvent and stops the evaporation from the plate.
3. Place the plate in the developing chamber. Make sure the solvent in the bottle does not touch the spot on the plate; otherwise the spot will dissolve away into the solvent.
4. Cover the bottle with the lid. The solvent will travel up the plate. When the solvent goes about 90% of the way up the plate, quickly take the plate out of the bottle and mark the solvent front with a pencil. Drain the solvent from it, and blow gently on the plate till all of the solvent is gone.

A.1.3 Staining and Visualization

Once the TLC plate has been developed, it is necessary to aid the visualization of the plate with a staining procedure since most organic compounds are colorless. Phosphomolybdic acid (PMA) is sensitive to most functional groups even at low concentrations, and it is therefore chosen in our study. It will stain most functional groups. To use the stain, pick up the dried TLC plate with a pair of tweezers and dip it into the PMA stain, making sure to cover the area from the baseline to the solvent front. Completely dry the back of the plate with a paper towel. TLC plates treated with PMA will appear as a light green color. It is necessary to heat TLC plates in order to activate the stain for visualization. Hold the plate just about the barrel of a heat gun. Watch closely for the spot to appear and make sure the plate is not overheated.

A.2 CRUDE PRODUCTS EXTRACTION

Extraction is the process where we selectively take the crude product out of the reaction mixture using a solvent. Aqueous washings are done to remove water soluble impurities (e.g. NaCl in our reactions) from the products. It is crucial to follow the proper experimental protocols for effective and successful extraction of the crude product for further reaction work-up.

1. Dissolve the reaction mixture in ether, which can be easily removed on the rotary evaporator. A 125ml size separatory funnel is used in the experiment to accommodate all the solvent and wash liquid.
2. Transfer the diluted reaction mixture (dissolvent in 150ml ether) from the reaction flask to the clean sep. funnel. Wash the flask with ether thoroughly.
3. Wash the organic phase with DI water to remove inorganic impurities, NaCl and unreacted HCl in our case. The volume of DI water is one third (50ml) of the organic phase. And repeat a wash two to three times.
4. When shaking the mixture in a separatory funnel, it is important to vent the funnel regularly by holding it upside-down, pointing it up to the back of the fume hood, then opening the stopcock. This will help release any pressure that has built up during mixing (see Figure A.40a).
5. Additionally, to avoid an emulsion (a fog of particles) phase from forming, shake the funnel gently. Sometimes, it is necessary to continue the rocking and inverting motions 30 to 100 times to get a phase separation.
6. Finish with a brine (saturated NaCl solution) wash. This helps disrupt any emulsion and will “dry” the organic layer by extracting water that may have dissolved in the organic phase.

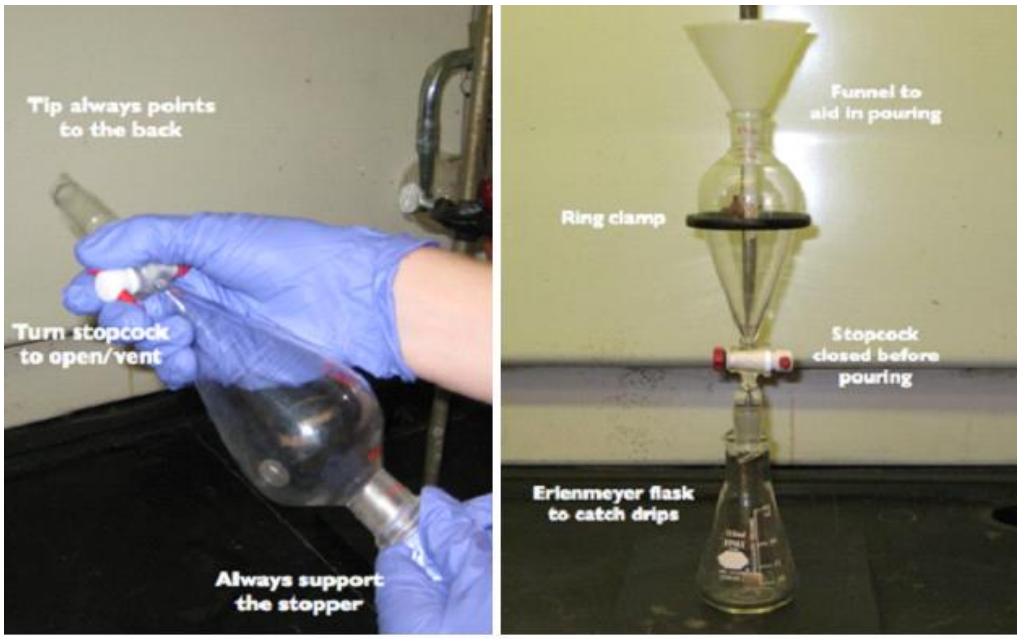

Figure A.40: Venting a Separatory Funnel (a); Extraction Setup (b).

7. Put the sep. funnel in an iron ring and remove the glass stopper.
8. Open the stopcock, and drain the bottom layer into a flask. Close the stopcock, swirl the funnel gently and see if any more bottom layer forms. If so, collect it. If not, collect the top layer in another flask. It is common practice to extract the organic layer for 2 to 3 times and combine all the organic liquids.
9. Dry the organic layer. After removing the solution from the aqueous phase, a drying agent is added to remove all traces of water. This is Na_2SO_4 in our experiments. It will bind to any water remaining in the organic solution, forming clumps when it reacts. A decent amount of drying agent should be added, but as long as some solid is not clumped, no more needs to be added.
10. Filter the solution into a large round bottom flask using a Buchner funnel and filter paper under mild vacuum.

A.3 SOLVENT REMOVAL USING ROTOVAP

After extraction and washing, the crude product is now separated out from the mixture, but still dissolved in ether, which needs to be removed by evaporation. Rotary evaporator (or rotovap, shown in Figure A.41) is used for solvent removal.

Figure A.41: Buchi R-114 Rotary Evaporator.

To start the rotovapping operation:

1. Make sure the sample-sucking inlet stopcock is closed off. Empty the receiving flask. Reattach the socket joint flask to the ball joint on the condenser, and use the special clip to hold the flask to the condenser outlet.
2. Starting the cooling water flowing (gently) through the condenser.
3. Make sure the round bottom jointware flask fits the rotovap.
4. Slowly, angle the flask so it is parallel to the join of the rotovap. Make sure that the flask is no more than half-full.

5. Connect the flask to the joint on the rotovap. Start the motor that spins the flask.
6. Slowly establish a vacuum in the rotovap. Jack down the flask into the heating bath.

In ending a rotovapping operation, it is always first turning off the heat, then breaking vacuum, and then stopping the spinning. Whenever taking the flask off the rotovap, always:

1. Jack up the flask away from the heating bath first.
2. Slowing let air into the rotovap by turning on the sample-sucking inlet stopcock.
3. Turn off the spinner motor and remove the flask.
4. Turn off water aspirator which establishes the vacuum in the rotovap.
5. Turn off the cooling water.

A.4 PURIFICATION FROM RECRYSTALLIZATION

Recrystallization is the primary method for purifying the crude product in current study, and therefore is of key importance to the quality and quantity of the final product that can be collected from the experiment. The principle behind recrystallization is that the amount of solute that can be dissolved by a solvent increases with temperature. The solute must be relatively insoluble in the solvent at room temperature but much more soluble in the solvent at higher temperature. Dichloromethane (CH_2Cl_2, DCM) is used in our experiments as the solvent.

There are three major steps in the recrystallization process: dissolving the solute in the solvent, collecting the solute crystals by vacuum filtration, and, finally, drying the resulting crystals.

A.4.1 Dissolving the Crude Product in the Solvent

1. Transfer the crude product from round bottom flask into a 125-ml Erlenmeyer flask. Heat a large quantity of DCM to the boiling point (39.6 °C). And slowly add the hot solvent to the sample in the Erlenmeyer.
2. Heat the beaker containing the solute and continue adding boiling solvent incrementally until all of the solute has just been dissolved.
3. Let the Erlenmeyer flask and hot solution cool. Slow cooling gives best crystals. After the flask cools and it is just warm to the touch, then put the flask in an ice-water bath to cool.

A.4.2 Vacuum Filtration

1. Get a piece of filter paper large enough to cover all the holes in the bottom plate of the Buchner funnel, and yet not curl up the sides of the funnel. Clamp a suction flask to a ring stand.
2. Apply the maximum amount of suction possible using the water aspirator. This will make the paper stick to the plate.
3. Swirl and pour the crystals and solvent slowly and directly into the center of the filter paper.
4. Some crystals may have been left behind in the beaker. Use a very small amount of the same cold recrystallization solvent and a spatula to remove any crystals.
5. When the crystals have been collected and washed, allow the aspirator to run for several minutes so that the crystals have an opportunity to dry.

A.4.3 Drying the Crystals

1. When the crystals have been dried as much as possible in the Buchner funnel, use a spatula to remove them to a beaker. This will ensure that the crystals are not contaminated by filter paper fibers as they dry.
2. After removing all the crystals from the filter paper, remove the filter paper and scrape any remaining crystals from the funnel.
3. Spreading the crystals out in a beaker will provide for the most efficient drying as the crystals will have a maximum of exposed surface area.
4. When the crystals are dried, weigh a vial, put in the product, and weigh the vial again. Subtracting the weight of the vial from the latter measurement gives the weight of the product.

A.5 NMR SAMPLE PREPARATION

Nuclear magnetic resonance (NMR) is used in current study to help identify the structures of many compounds, by studying the peaks of NMR spectra. Since the crude product is in solid or semi-solid form, it needs to be dissolved into a solvent without affecting the measurements. For the intermediate diol compound, deuterated chloroform is used as the solvent. For the Gemini surfactant, deuterated water is used. To prepare a NMR sample of the crude product:

1. Place approximately 10mg of the product into a vial.
2. Dissolve the product in about 1ml of deuterated solvent.
3. Get a disposable pipette and a little rubber bulb, and construct a narrow medicine dropper. Use this to transfer the sample from the vial to the NMR tube. Make sure the liquid level is not much higher than about 3-4cm.
4. Cap the tube and record sample number. Have the NMR of the sample taken.

A.6 NMR SPECTRA INTERPRETATION

There are three things to look for in a NMR spectrum. First, the chemical shift reveals information regarding the type of proton that is giving the signal (so called chemical environment). Second, the integration of peaks tells us how many equivalent protons are giving the signal. Finally, the splitting pattern implies what is next to the proton giving the signal.

A.6.1 Chemical Shift

It is important to understand trend of chemical shift in terms of NMR interpretation. Chemical shift is associated with the Larmor frequency of a nuclear spin to its chemical environment. Tetramethylsilan [TMS; $(CH_3)_4Si$] is generally used for standard to determine chemical shift of compounds (δ_{TMS} = 0ppm). In other words, frequencies for chemicals are measured for a ^1H or ^{13}C nucleus of a sample from the ^1H or ^{13}C resonance of TMS. TMS is chosen as the internal standard for all analyses due to the fact that most other proton signals from any sample fall at lower frequencies than that of the protons in TMS. The proton NMR chemical shift is affect by nearness to electronegative atoms (O, N, halogen.) and unsaturated groups(C=C, C=O, aromatic). Electronegative groups move to the down field (left; increase in ppm). ^1H chemical shift play a role in identifying many functional groups. Figure A.42 indicates important example to figure out the functional groups. Figure A.43 shows typical ^{13}C chemical shift regions of the major chemical class.

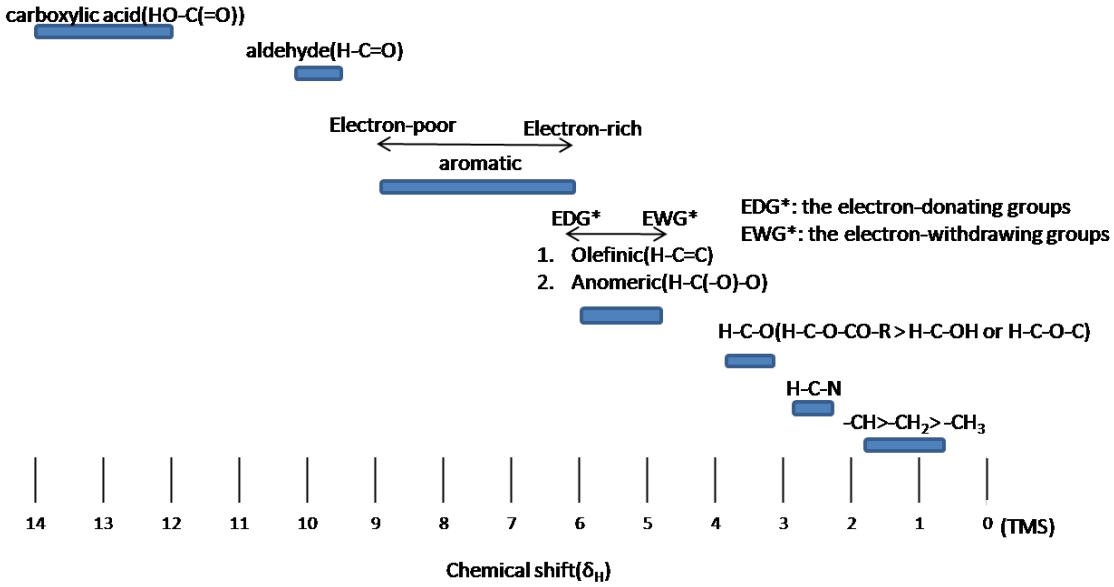

Figure A.42: ^{1}H Chemical Shift Ranges for Organic Compound.

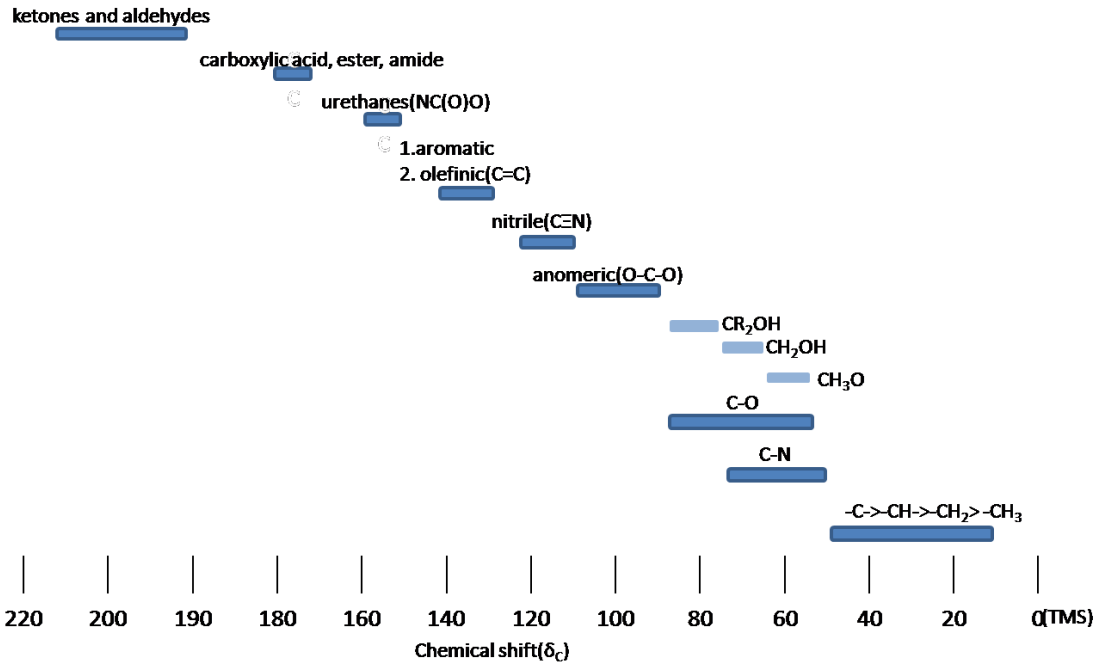

Figure A.43: ^{13}C Chemical Shift Ranges for Organic Compound.

A.6.2 Integration

The integration of the area under the peak is directly proportional to the number of equivalent protons giving that signal. Therefore, by calculating the area, we estimate how many protons there are. Usually, we need to know something about the compound to be able to use this knowledge because the first integration is set to 1 proton and everything else is relative to that area under the curve.

A.6.3 Splitting Pattern

The splitting pattern is dependent on the number of equivalent protons on the carbon next door. Chemical equivalent protons do not result in spin-spin splitting. If the protons next door are non-equivalent, then more complex splitting patterns occur (for example, doublet of triplets). The spitting is a very essential part to obtain exact information about the number of the neighboring protons. The maximum of distance for splitting is three bonds. When a proton splits, the proton's chemical shift is determined in the center of the splitting lines.

Appendix B: Conductivity Measurements for Gemini Surfactants

B.1 *14-4-14*

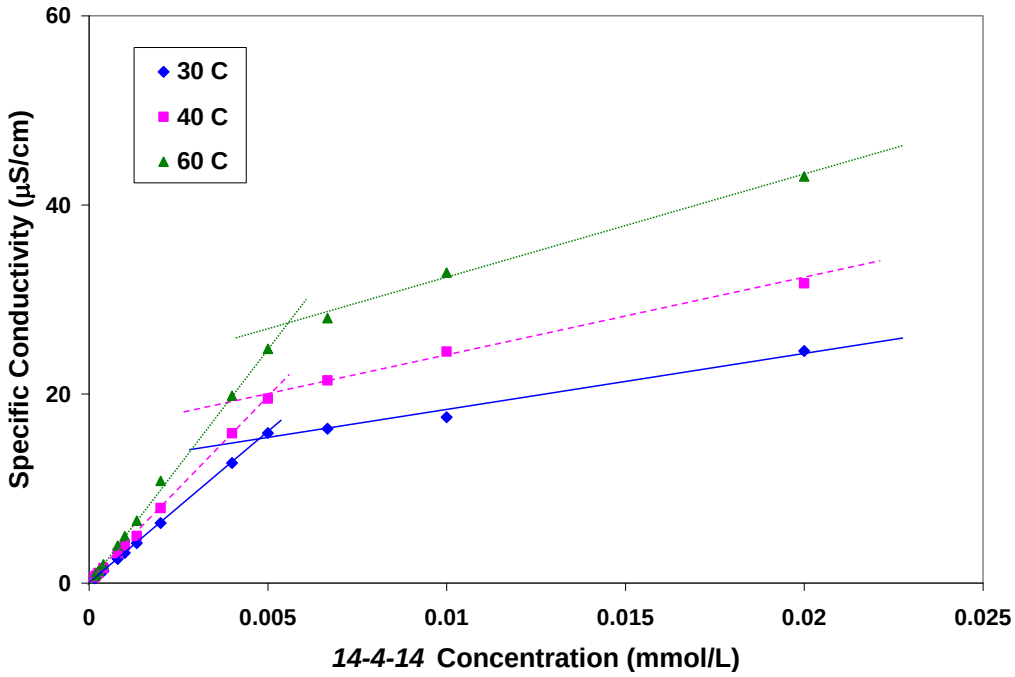

Figure B.14: Electrical Conductivity (in μS/cm) v.s. *14-4-14* Concentration.

Table B.21: CMC of *14-4-14* at Various Temperatures.

Temp.	CMC (10^{-3} mM)	m_1	m_2	α
30˚C	4.8	3175.4	576.189	0.1815
40˚C	5.1	3961.31	791.765	0.1999
60˚C	5.5	4955.47	1085.86	0.2191

Table B.22: Thermodynamic Parameters of *14-4-14* at Different Temperatures.

Temp.	In(CMC)	ΔG_M^o (kJ/mol)	ΔH_M^o (kJ/mol)	ΔS_M^o (J/mol/K)
30˚C	-12.247	-78.54	-1.05	255.59
40˚C	-12.186	-79.61	-6.64	233.01
60˚C	-12.111	-82.94	-18.12	194.55

B.2 *16-4-16*

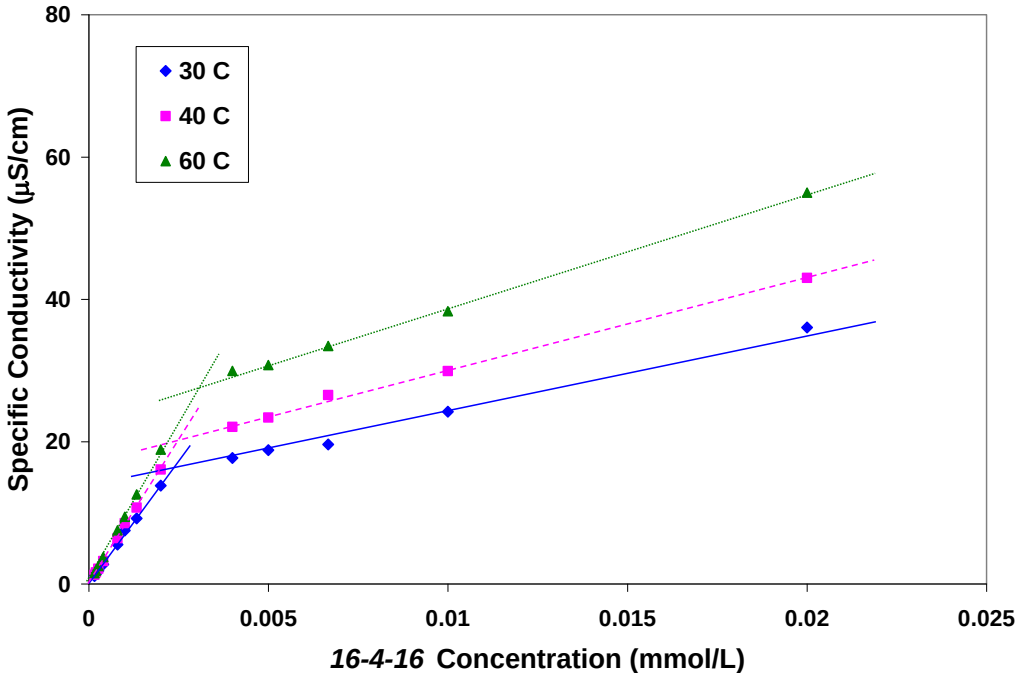

Figure B.15: Electrical Conductivity (in μS/cm) v.s. *16-4-16* Concentration.

Table B.23: CMC of *16-4-16* at Various Temperatures.

Temp.	CMC (10^{-3} mM)	m_1	m_2	α
30˚C	2.3	6901.48	1080.6	0.1566
40˚C	2.5	8039.45	1308.65	0.1628
60˚C	2.9	9434.1	1616.44	0.1713

Table B.24: Thermodynamic Parameters of *16-4-16* at Different Temperatures.

Temp.	In(CMC)	ΔG_M^o (kJ/mol)	ΔH_M^o (kJ/mol)	ΔS_M^o (J/mol/K)
30˚C	-12.983	-84.97	-7.76	254.70
40˚C	-12.899	-86.79	-13.93	232.68
60˚C	-12.751	-90.67	-26.78	191.77

B.3 *18-2-18*

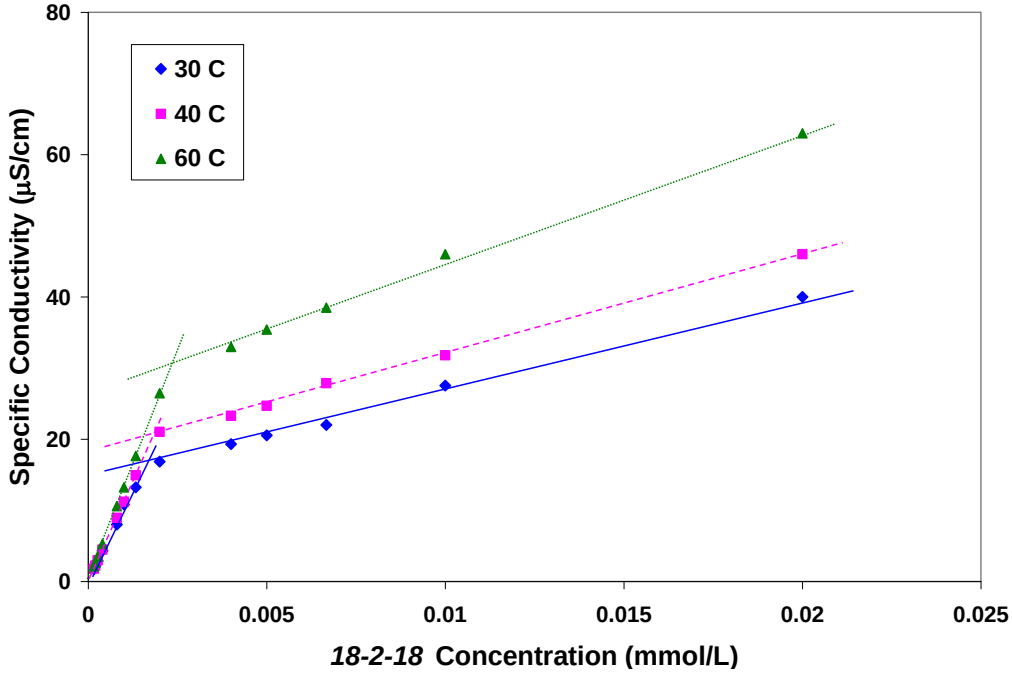

Figure B.16: Electrical Conductivity (in μS/cm) v.s. *18-2-18* Concentration.

Table B.25: CMC of *18-2-18* at Various Temperatures.

Temp.	CMC (10^{-3} mM)	m_1	m_2	α
30˚C	1.5	10817.1	1231.04	0.1138
40˚C	1.8	11192.9	1420.49	0.1269
60˚C	2.3	13235.8	1839.42	0.139

Table B.26: Thermodynamic Parameters of *18-2-18* at Different Temperatures.

Temp.	In(CMC)	ΔG_M^o (kJ/mol)	ΔH_M^o (kJ/mol)	ΔS_M^o (J/mol/K)
30˚C	-13.410	-90.61	-21.31	228.58
40˚C	-13.228	-91.42	-28.37	201.35
60˚C	-12.983	-94.58	-43.21	154.17

B.4 *18-4-18*

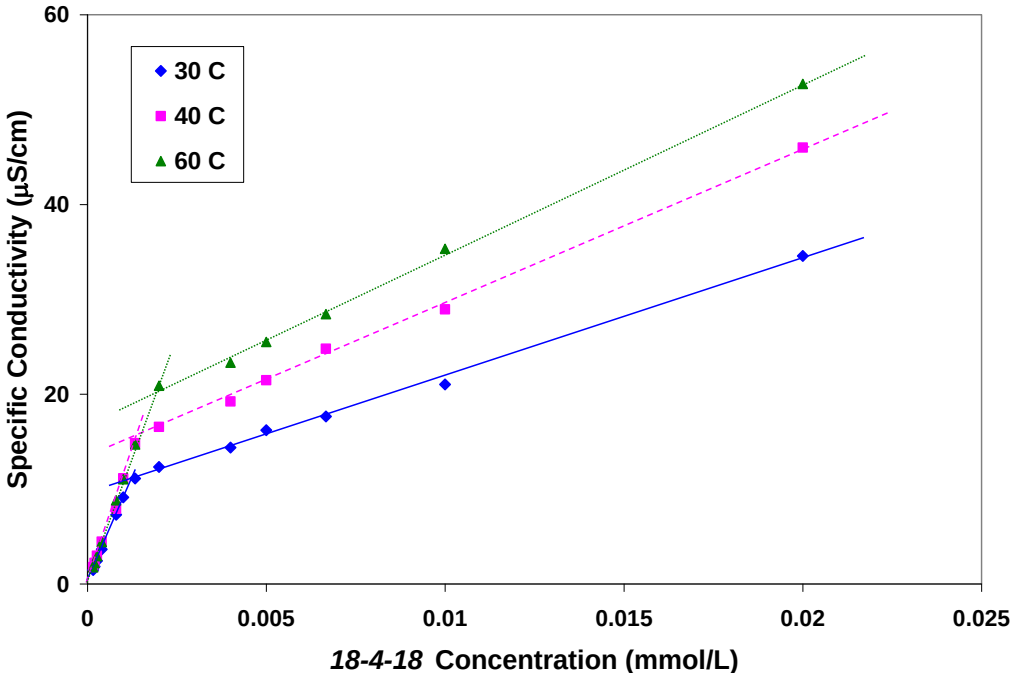

Figure B.17: Electrical Conductivity (in μS/cm) v.s. *18-4-18* Concentration.

Table B.27: CMC of *18-4-18* at Various Temperatures.

Temp.	CMC (10^{-3} mM)	m_1	m_2	α
30˚C	1.2	9120.92	1226.32	0.1345
40˚C	1.4	11125.6	1635.71	0.147
60˚C	1.8	11025.7	1766.69	0.1602

Table B.28: Thermodynamic Parameters of *18-4-18* at Different Temperatures.

Temp.	In(CMC)	ΔG_M^o (kJ/mol)	ΔH_M^o (kJ/mol)	ΔS_M^o (J/mol/K)
30˚C	-13.633	-90.82	-19.78	234.34
40˚C	-13.479	-91.88	-26.67	208.26
60˚C	-13.228	-94.95	-41.10	161.65

B.5 *20^{+}-2-20^{+}*

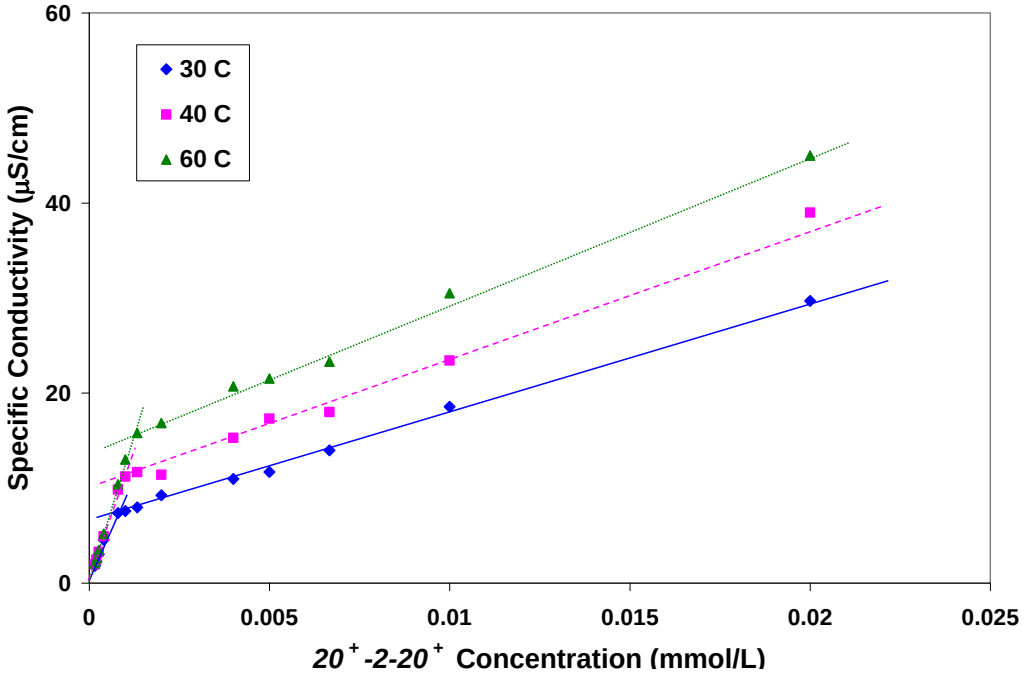

Figure B.18: Electrical Conductivity (in μS/cm) v.s. *20^{+}-2-20^{+}* Concentration.

Table B.29: CMC of *20^{+}-2-20^{+}* at Various Temperatures.

Temp.	**CMC (10^{-3} mM)**	**m_1**	**m_2**	α
30˚C	0.63	11379.6	1127.04	0.099
40˚C	0.90	12306.8	1357.27	0.1095
60˚C	1.2	12995.8	1564.1	0.1202

Table B.30: Thermodynamic Parameters of *20^{+}-2-20^{+}* at Different Temperatures.

Temp.	**In(CMC)**	ΔG_M^o **(kJ/mol)**	ΔH_M^o **(kJ/mol)**	ΔS_M^o **(J/mol/K)**
30˚C	-14.278	-97.68	-35.47	205.23
40˚C	-13.921	-97.58	-43.48	172.76
60˚C	-13.633	-100.83	-60.37	121.43

B.6 *20⁺-4-20⁺*

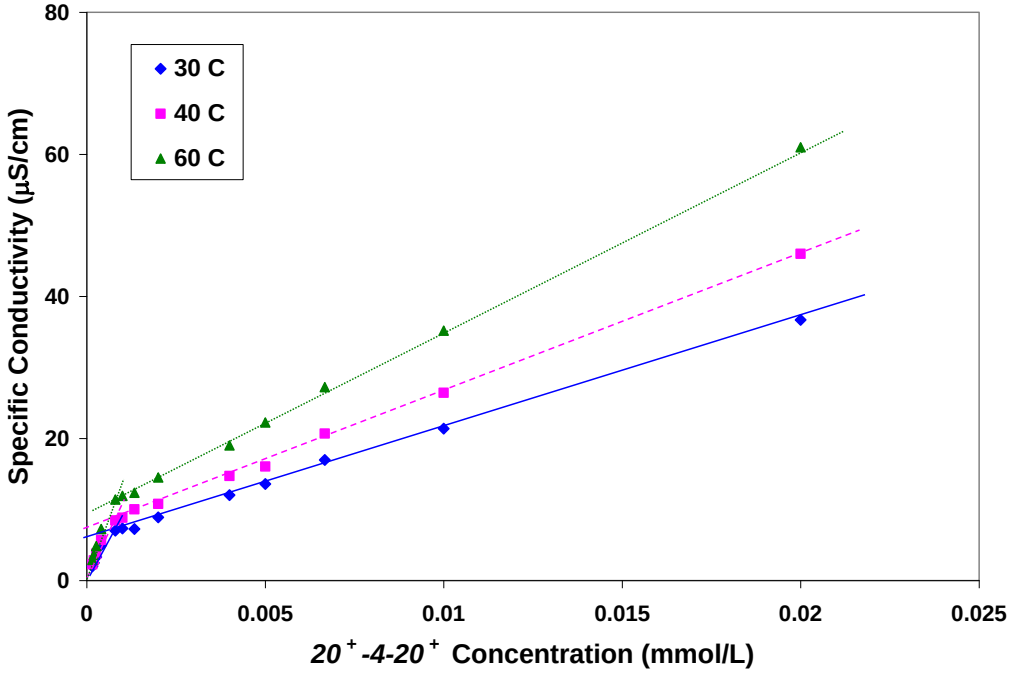

Figure B.19: Electrical Conductivity (in μS/cm) v.s. *20⁺-4-20⁺* Concentration.

Table B.31: CMC of *20⁺-4-20⁺* at Various Temperatures.

Temp.	CMC (10^{-3} mM)	m_1	m_2	α
30˚C	0.53	12449	1561.48	0.1254
40˚C	0.56	14270.4	1955.17	0.137
60˚C	0.6	18141.5	2583.25	0.1424

Table B.32: Thermodynamic Parameters of *20⁺-4-20⁺* at Different Temperatures.

Temp.	In(CMC)	ΔG_M^o (kJ/mol)	ΔH_M^o (kJ/mol)	ΔS_M^o (J/mol/K)
30˚C	-14.450	-97.07	-0.28	319.29
40˚C	-14.395	-99.05	-6.10	296.84
60˚C	-14.326	-104.45	-18.23	258.80

B.7 *18-4-18 2COONA*

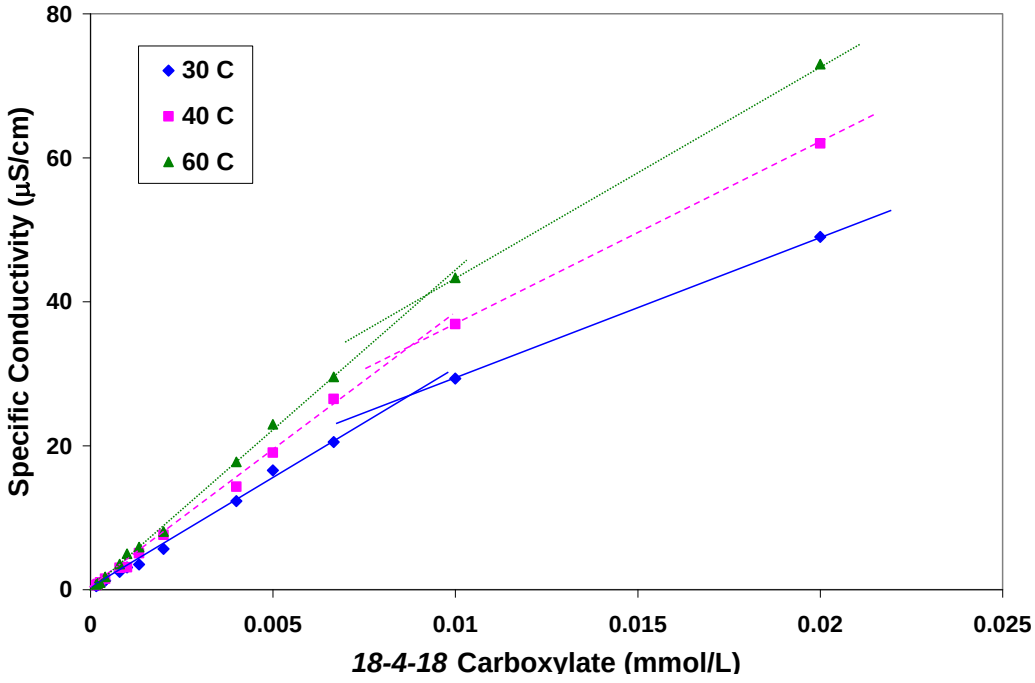

Figure B.20: Electrical Conductivity (in μS/cm) v.s. *18-4-18 2COONa* Concentration.

Table B.33: CMC of *18-4-18 2COONa* at Various Temperatures.

Temp.	CMC (10^{-3} mM)	m_1	m_2	α
30˚C	8.7	3075.44972	1968.45907	0.6401
40˚C	9.1	3805.96757	2510.61423	0.65967
60˚C	9.3	4434.3172	2968.30374	0.6694

Table B.34: Thermodynamic Parameters of *18-4-18 2COONa*.

Temp.	In(CMC)	ΔG_M^o (kJ/mol)	ΔH_M^o (kJ/mol)	ΔS_M^o (J/mol/K)
30˚C	-11.652	-49.26	2.43	170.48
40˚C	-11.607	-49.56	-1.05	154.94
60˚C	-11.585	-52.04	-8.12	131.84

B.8 *20^{+}-4-20^{+} 2COONA*

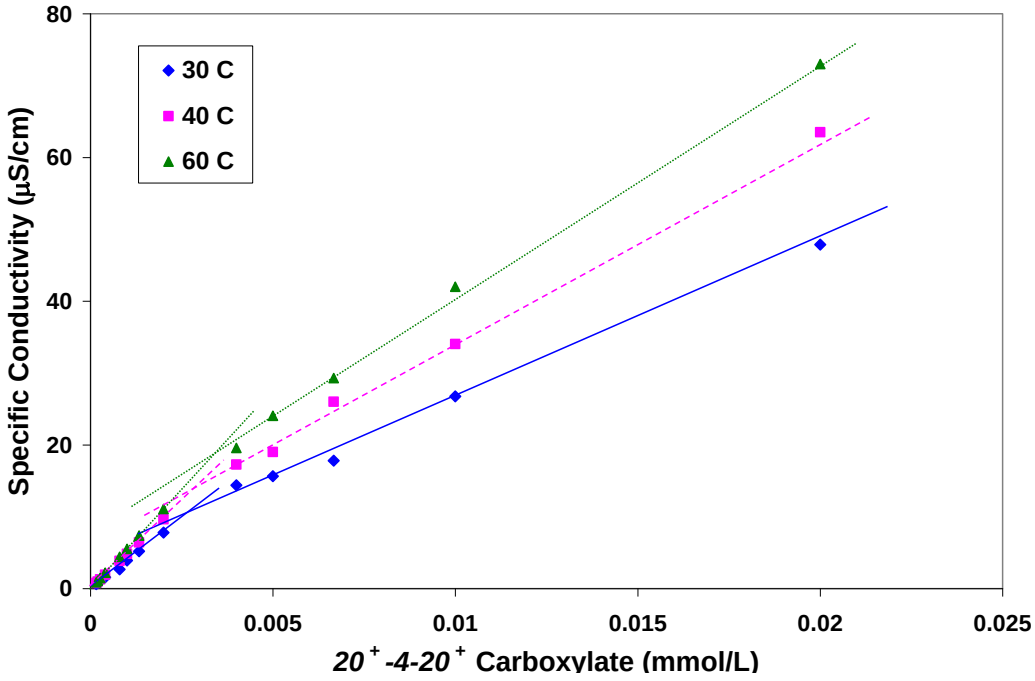

Figure B.21: Electrical Conductivity (in μS/cm) v.s. *20^{+}-4-20^{+} 2COON*a Concentration.

Table B.35: CMC of *20^{+}-4-20^{+} 2COON*a at Various Temperatures.

Temp.	CMC (10^{-3} mM)	m_1	m_2	α
30˚C	2.7	3898.11	2223.99	0.5705
40˚C	3.0	4824.83	2795.62	0.5794
60˚C	3.4	5539.77	3262.94	0.5890

Table B.36: Thermodynamic Parameters of *20^{+}-4-20^{+} 2COON*a.

Temp.	In(CMC)	ΔG_M^o (kJ/mol)	ΔH_M^o (kJ/mol)	ΔS_M^o (J/mol/K)
30˚C	-12.822	-58.57	-5.08	176.47
40˚C	-12.717	-59.44	-9.29	160.16
60˚C	-12.592	-61.97	-18.02	131.91

Appendix C: Working Principle of du Nouy Ring Tensiometer

The du Nouy ring method (du Nouy, 1925) for the determination of surface tension is very widely used. It is convenient because of the experimental procedure necessary to obtain a good degree of accuracy can be made very simple. The central features of the tensiometer are a ring, capable of being wetted, suspended horizontally in the surface of a liquid, and some device to measure the force necessary to separate ring and liquid. So that the applied force may be changed gradually, a torsion balance is often used. In much of the early work, the maximum pull on the ring was thought to equal the surface tension according to $mg=4\pi R\gamma$, where mg is the maximum upward force applied to a ring of inner radius R. The quantity m is the maximum weight of liquid raised above the free surface of the liquid. Harkins and Jordan (Lyklema, 2000) showed that this equation could be seriously in error because the meniscus formed by the ring was not of the same form as that formed by a plate. They further derived a correction factor, F, that must be applied so that $mg=4\pi R\gamma/F$. The factor F is found to be a function of R^3/V and of R/r, where V is the volume of liquid raise above the plane surface by the maximum pull of the ring, and r is the radius of the wire of which the ring is made. The physical significance of the correction factor is best understood by reference to Figure C.1 which shows three successive stages of pulling a ring from the surface of a liquid.

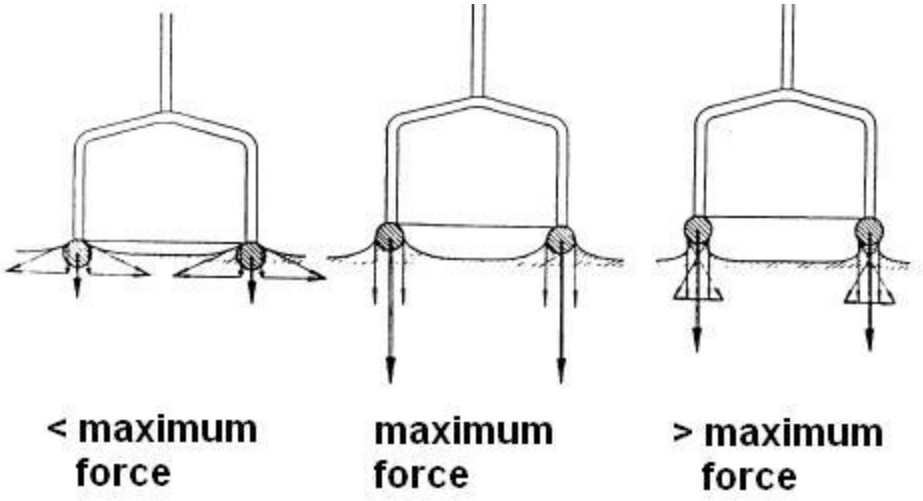

Figure C.1 Stages in Measurement with the Ring.

Provided that the wire is completely wetted, the meniscus begins to form as a force, *f*, is applied. When lifting the ring, the tension is acting along its wetted line. The resultant, due to the force acting on the ring, reaches a maximum as soon as the tangent on the point of wetting is vertical to the surface. This maximum is measured and so it is not normally necessary, as is often done, to raise the ring until interruption. Besides the resultant of the tension, the hydrostatic weight of the liquid volume underneath the ring has to be measured. This additional force must be eliminated by the correction factor.

Appendix D: Surface Tension Measurements for Gemini Surfactants

D.1 *14-4-14*

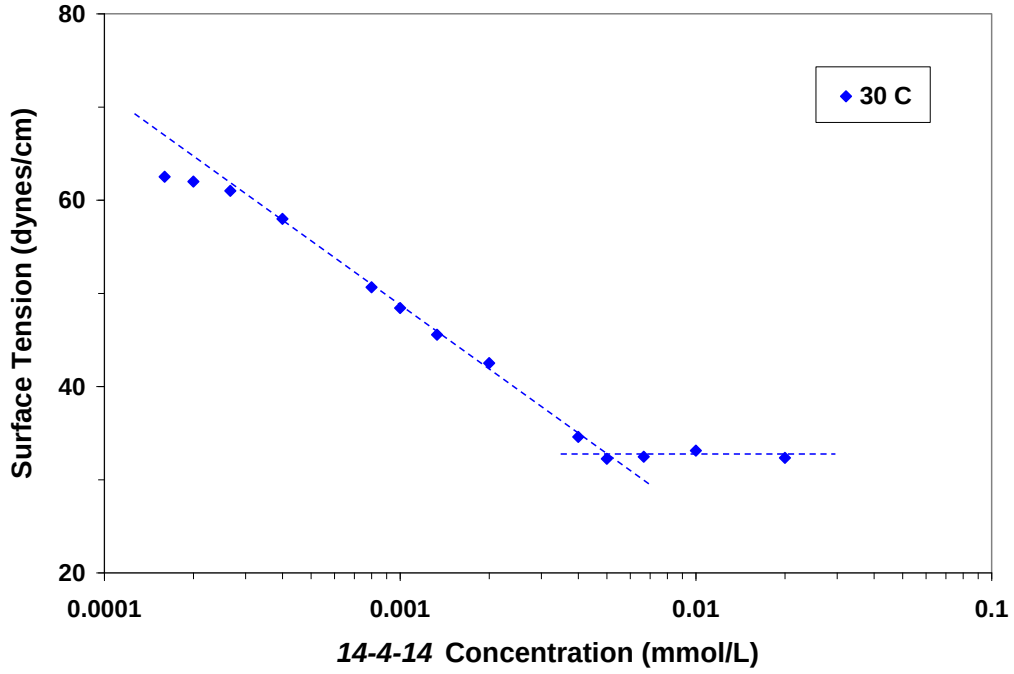

Figure D.23: Surface Tension vs. *14-4-14* Concentration at 25°C.

Table D.37: Surface Properties of *14-4-14* in Water at 25°C.

CMC (10^{-3} mM)	γ_{CMC} **(dynes/cm)**	$\Gamma_{max} \times 10^{10}$ **(mol/cm^2)**	a_{min} **($\dot{A}^2$)**	pC_{20}	**CMC /C_{20}**	ΔG^0_{ad} **(kJ/mol)**
4.9	32.56	1.98	84	6.12	6.47	-101.41

D.2 *16-4-16*

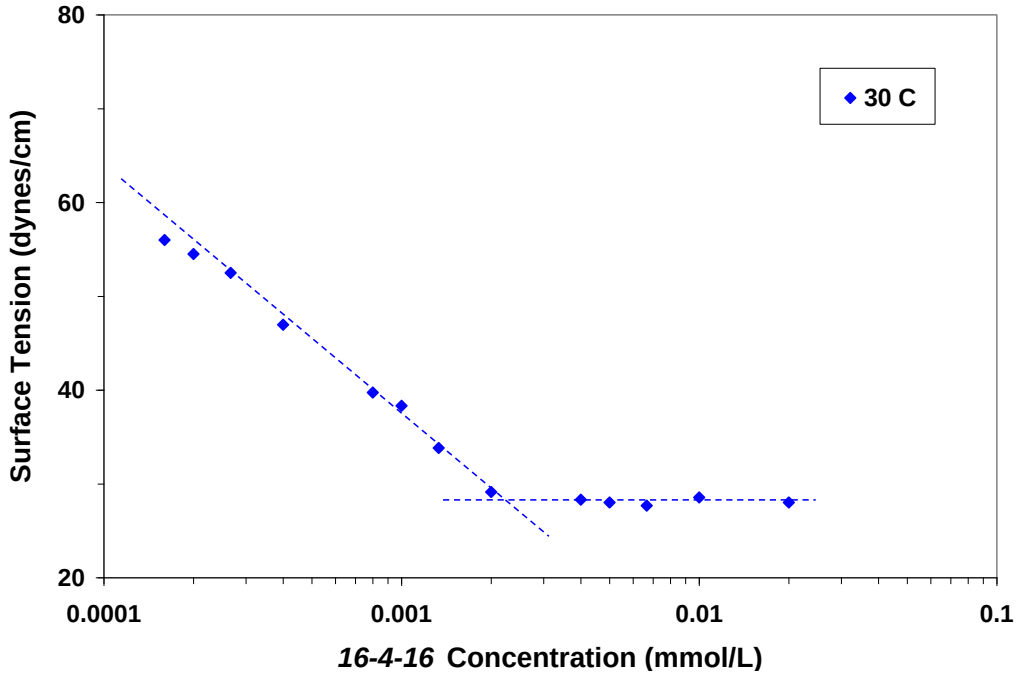

Figure D.24: Surface Tension vs. *16-4-16* Concentration at 25°C.

Table D.38: Surface Properties of *16-4-16* in Water at 25°C.

CMC (10^{-3} **mM**)	γ_{CMC} **(dynes/cm)**	$\Gamma_{max} \times 10^{10}$ **(mol/cm^2)**	a_{min} **(Å^2)**	pC_{20}	**CMC /C$_{20}$**	ΔG^0_{ad} **(kJ/mol)**
2.2	28.02	2.30	72	6.53	7.38	-104.71

D.3 *18-2-18*

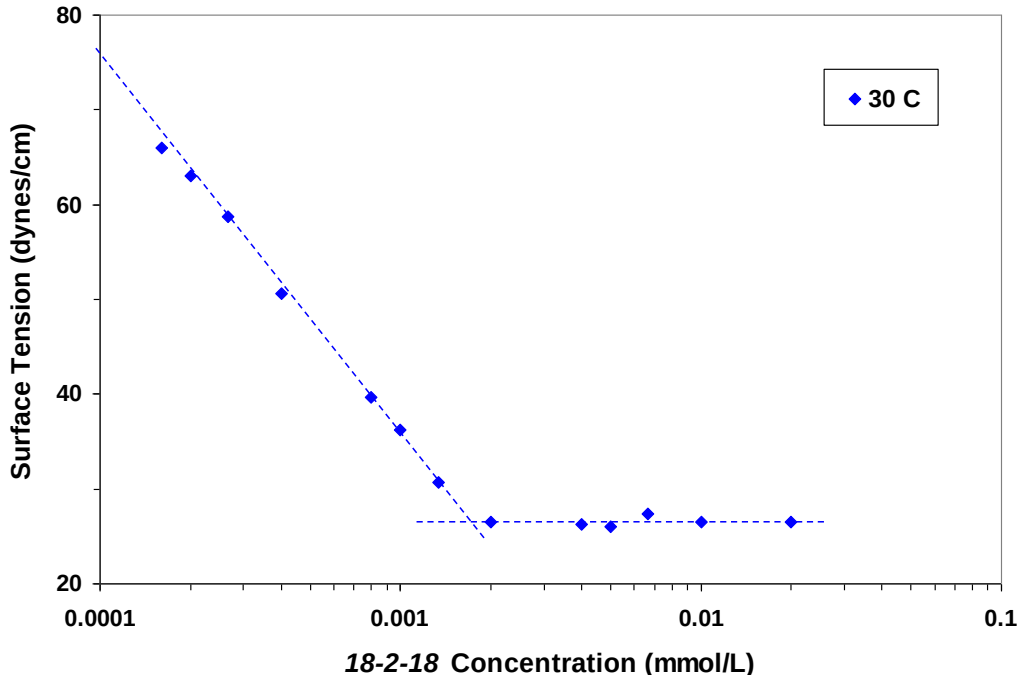

Figure D.25: Surface Tension vs. *18-2-18* Concentration at 25°C.

Table D.39: Surface Properties of *18-2-18* in Water at 25°C.

CMC (10^{-3} **mM**)	γ_{CMC} **(dynes/cm)**	$\Gamma_{max} \times 10^{10}$ **(mol/cm^2)**	a_{min} **(Å^2)**	pC_{20}	**CMC /C$_{20}$**	ΔG^0_{ad} **(kJ/mol)**
1.7	26.5	3.45	48	6.39	4.14	-100.19

D.4 *18-4-18*

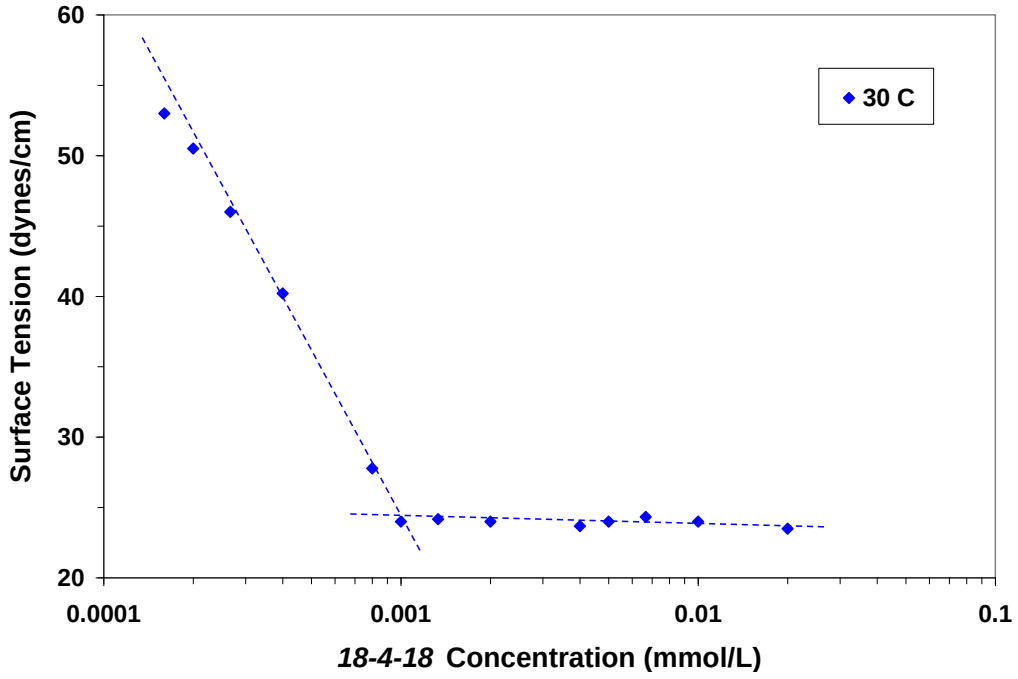

Figure D.26: Surface Tension vs. *18-4-18* Concentration at 25°C.

Table D.40: Surface Properties of *18-4-18* in Water at 25°C.

CMC **(10^{-3} mM)**	γ_{CMC} **(dynes/cm)**	$\Gamma_{max} \times 10^{10}$ **(mol/cm^2)**	a_{min} **($\dot{A}^2$)**	pC_{20}	**CMC /C_{20}**	ΔG^0_{ad} **(kJ/mol)**
1.0	24.02	3.36	49	6.70	4.98	-103.96

D.5 *20⁺-2-20⁺*

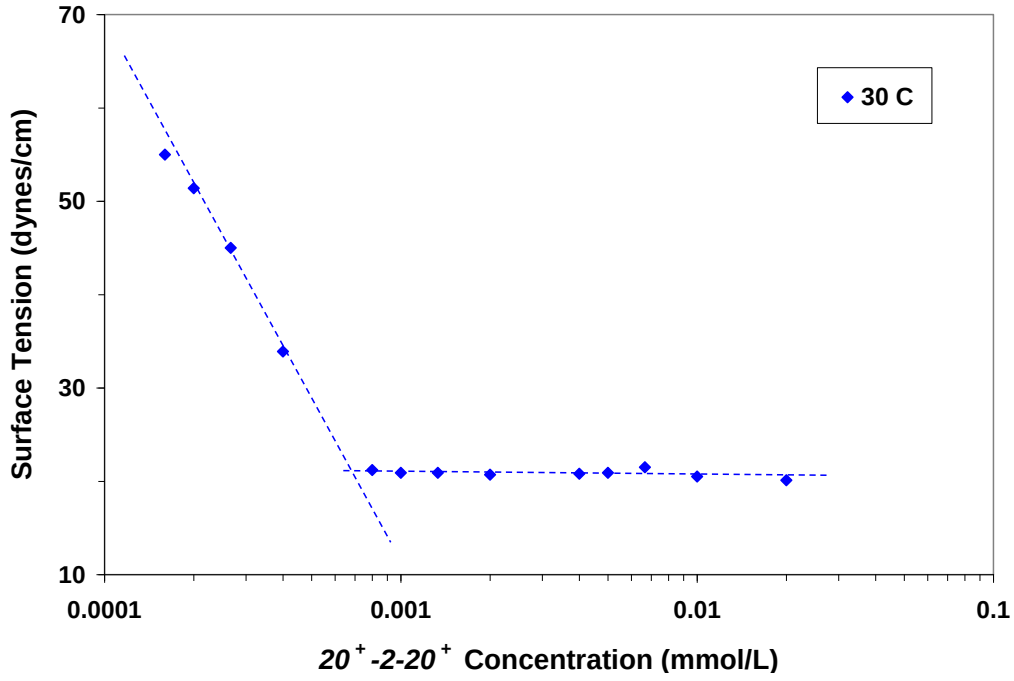

Figure D.27: Surface Tension vs. *20⁺-2-20⁺* Concentration at 25°C.

Table D.41: Surface Properties of *20⁺-2-20⁺* in Water at 25°C.

CMC (10^{-3} mM)	γ_{CMC} **(dynes/cm)**	$\Gamma_{max} \times 10^{10}$ **(mol/cm²)**	a_{min} **(Å²)**	pC_{20}	**CMC /C₂₀**	ΔG^0_{ad} **(kJ/mol)**
0.67	20.91	5.0	33	6.70	3.33	-102.0

D.6 *20⁺-4-20⁺*

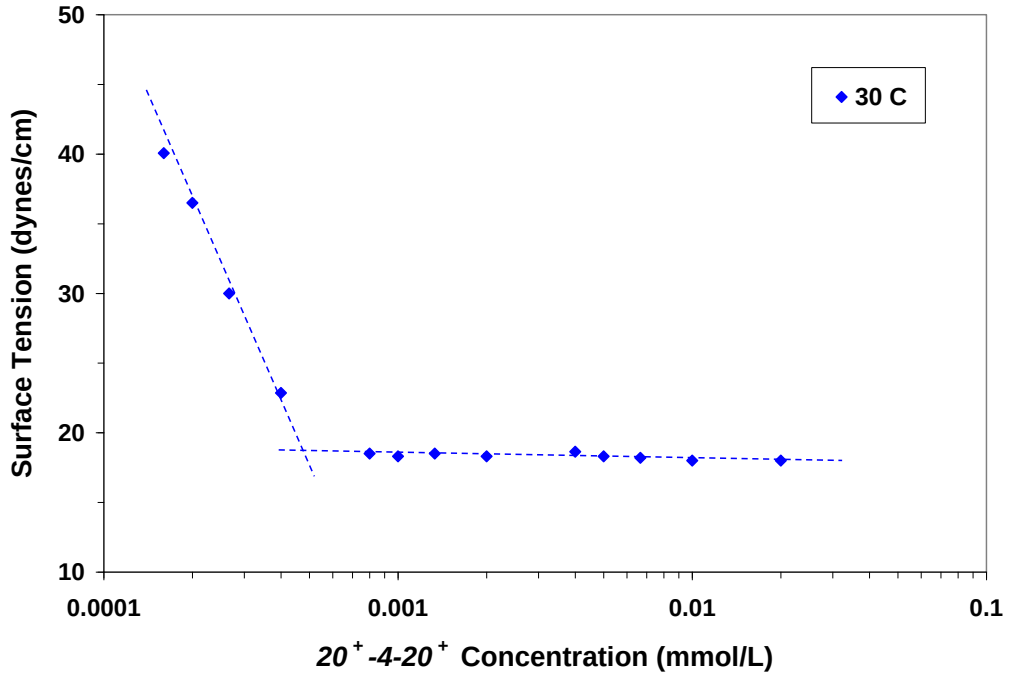

Figure D.28: Surface Tension vs. *20⁺-4-20⁺* Concentration at 25°C.

Table D.42: Surface Properties of *20⁺-4-20⁺* in Water at 25°C.

CMC (10^{-3} mM)	γ_{CMC} **(dynes/cm)**	$\Gamma_{max} \times 10^{10}$ **(mol/cm²)**	a_{min} **($\dot{A}^2$)**	pC_{20}	**CMC /C_{20}**	ΔG^0_{ad} **(kJ/mol)**
0.5	18.30	4.05	41	7.00	5.01	-106.47

D.7 *18-4-18 2COONA*

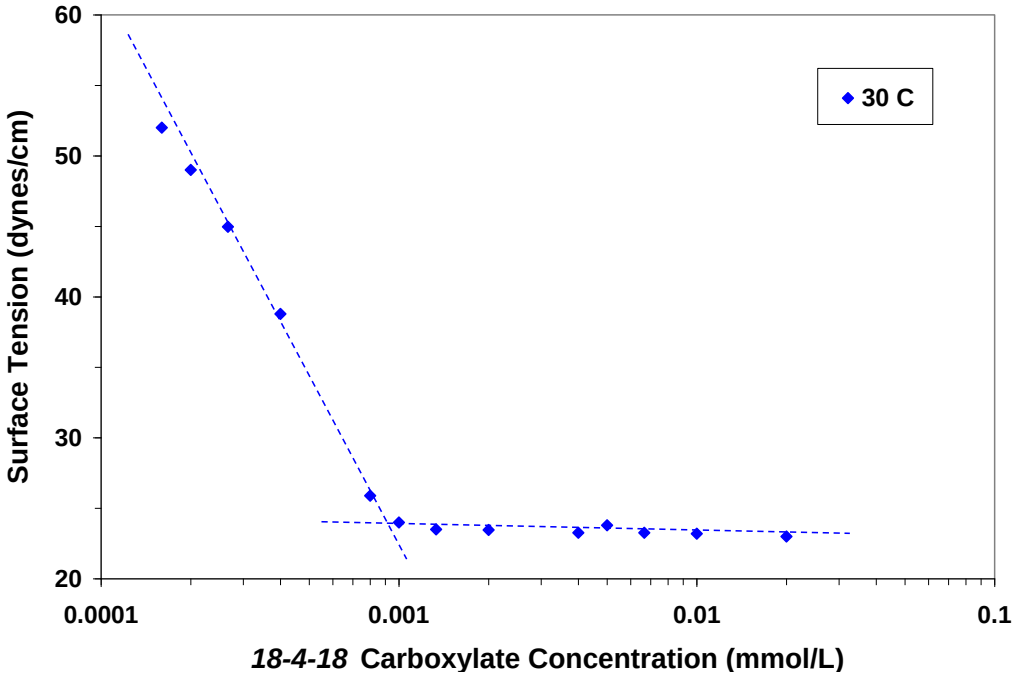

Figure D.29: Surface Tension vs. *18-4-18 2COONa* Concentration at 25°C.

Table D.43: Properties of *18-4-18 2COONa* in Water at 25°C.

CMC **(10^{-3} mM)**	γ_{CMC} **(dynes/cm)**	$\Gamma_{max} \times 10^{10}$ **(mol/cm^2)**	a_{min} **($\dot{A}^2$)**	pC_{20}	**CMC /C_{20}**	ΔG^0_{ad} **(kJ/mol)**
0.93	23.27	3.45	48	6.73	5.00	-104.19

D.8 *20^{+}-4-20^{+} 2COONA*

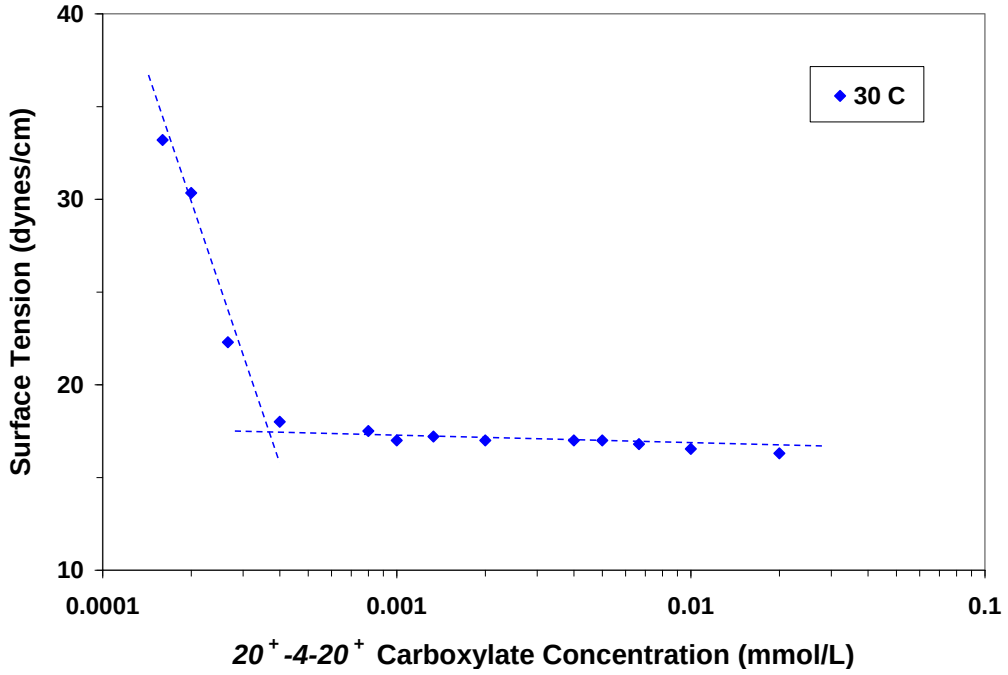

Figure D.30: Surface Tension vs. *20^{+}-4-20^{+} 2COONa* Concentration at 25°C.

Table D.44: Surface Properties of *20^{+}-4-20^{+} 2COONa* in Water at 25°C.

CMC (10^{-3} mM)	γ_{CMC} **(dynes/cm)**	$\Gamma_{max} \times 10^{10}$ **(mol/cm^2)**	a_{min} **($\dot{A}^2$)**	pC_{20}	**CMC /C_{20}**	ΔG^0_{ad} **(kJ/mol)**
0.35	17.03	4.22	39	7.15	4.97	-108.04

Appendix E: Laboratory Interfacial Tension and Phase Behavior Tests

E.1 Working Principle of Spinning Drop Tensiometer

Several classical methods for measuring interfacial tensions are limited to values larger than 0.1mN/m, e.g. Wilhelmy plate and drop-volume techniques. Convenient methods allowing the measurement of low interfacial tension include the sessile-drop technique, the surface laser light scattering method and the so-called spinning-drop technique.

The spinning-drop is a relatively simple method for obtaining interfacial tensions by the measurement of the shape of a liquid drop in a more dense liquid contained in a horizontal tube rotating about its long axis. When a closed vessel, containing a liquid and a drop of a lighter immiscible liquid, is rotated about a horizontal axis, the drop will take up an equilibrium position on the axis of rotation because of the pressure caused by the centrifugal force. As the rotation frequency is increased, the drop will elongate until finally it is in the form of a cylinder with rounded ends. For each speed of rotation the drop will come to an equilibrium shape dictated by rotation forces and opposing interfacial tension forces.

The spinning drop geometry can typically be described by configuration shown in Figure E.1, in which the rotation takes place about x-axis, and y-axis denotes the distance from the rotation axis. The bubble shape exhibits symmetry about x-axis. The centrifugal acceleration is $\omega^2 y$ (ω is the rotational velocity), and it increases with the distance from the axis. Under high rotational speed, the natural gravity effect can be safely neglected. Hence the influence of the density difference between the two fluids increases with the distance from the axis and produces a pull of the interface toward the axis, which results in the elongation of the drop along x-axis. On the other hand, the interfacial tension

acting on the air-water interface tends to minimize the surface area, i.e. to make the drop shape more spherical.

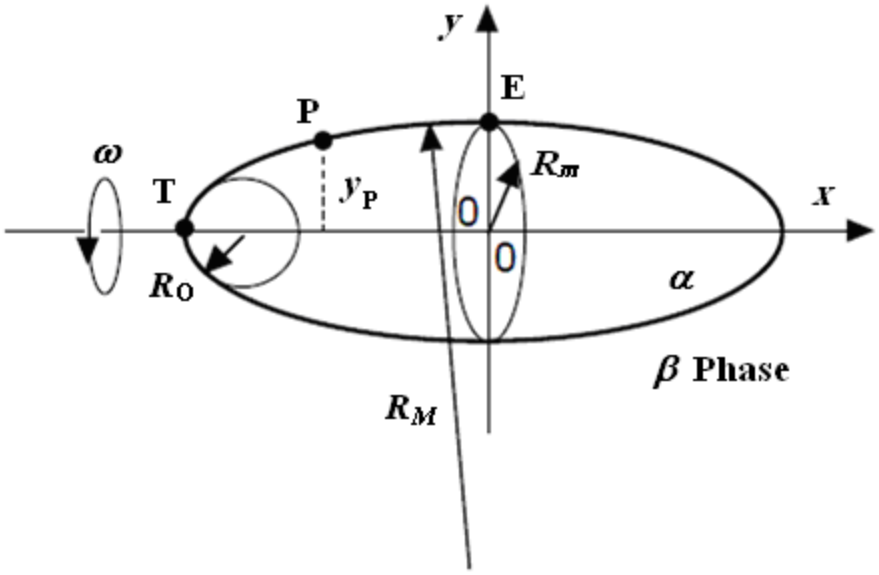

Figure E.1 Geometry of a Spinning Droplet of Liquid α in Liquid β.

For an elongated air bubble, the central part of which can typically approximated by a cylinder, i.e. the radius of curvature at equator point E (R_M) in the plane of paper is much larger that the radius of the slice cut (R_m), so that the curvature at point E may be approximated by the inverse of the radius of the cylinder ($1/R_m$). This approximation has been shown to be valid whenever the length of the bubble is at least 4 times its diameter.

The densities of the phases are ρ_α and ρ_β (with $\rho_\alpha < \rho_\beta$ and $\Delta\rho = \rho_\beta - \rho_\alpha$) and R_o is the radius of curvature at the tip of the bubble. Let p_T be the pressure (reference) at point T on the axis at the tip of the bubble, and p be the pressure at any (P) point at the interface, located at distance "y_P" of the axis. The classical Pascal's formula to calculate

the pressure difference between two points located in the same phase ($\Delta p = \rho g h$) is still valid if the centrifugal acceleration ($\omega^2 y_P/2$) replaces gravity g. In phase α,

$$p_\alpha = p_{\alpha T} + \rho_\alpha \omega^2 y_P^2/2 \tag{E.1}$$

In phase β,

$$p_\beta = p_{\beta T} + \rho_\beta \omega^2 y_P^2/2 \tag{E.2}$$

By difference,

$$p_\alpha - p_\beta = p_{\alpha T} - p_{\beta T} - \Delta\rho\omega^2 y_P^2/2 \tag{E.3}$$

Because of the concavity toward phase α, $p_\alpha > p_\beta$ at any point of the interface, and according to Laplace equation:

$$p_\alpha - p_\beta = 2\gamma H = \gamma\left[\frac{1}{y\sqrt{1+y'^2}} - \frac{y''}{\left(\sqrt{1+y'^2}\right)^3}\right] \tag{E.4}$$

H is the average curvature, i.e., $H = [1/R_1 + 1/R_2]/2$ where R_1 and R_2 are the principal (minimum and maximum) radii of curvature. y' and y'' are the first and second derivatives of y with respect to x. In the expression in brackets, the first term is the curvature along a circle centered on the axis (not equal to "y" because the radius of curvature is measured along the normal vector, and thus is equal to y only if $y' = 0$), and the second one is the curvature of the generating curve, i.e., the curve shown in the plane of Figure E.1.

Because of the axial symmetry at the tip T, both radii of curvature are equal and the average curvature $H_T = (1/R_o + 1/R_o)/2$, hence:

$$p_\alpha - p_\beta = 2\gamma H_T = 2\gamma / R_o \tag{E.5}$$

By substituting eqs. (7.12) and (E.5) in (E.3), an equation in 'y' is attained. At any point P of the interface:

$$2\gamma / R_o - \Delta\rho\omega^2 y_P^2 / 2 = \gamma \left[\frac{1}{y\sqrt{1+y'^2}} - \frac{y''}{\left(\sqrt{1+y'^2}\right)^3} \right] \tag{E.6}$$

By using dimensionless variables $X = x_P/R_o$, $Y = y_P/R_o$ and scaling parameter $K=\Delta\rho\omega^2 R_o^3/2\gamma$ and by multiplying by "y_P" and substituting in eq. (E.6), the following equation is attained:

$$2Y - KY^3 = \frac{d}{dY}\left(\frac{Y}{\sqrt{1+Y'^2}} \right) \tag{E.7}$$

by integration,

$$Y^2 - KY^4/4 = \left(\frac{Y}{\sqrt{1+Y'^2}} \right) + const \tag{E.8}$$

At the tip of the drop (point T) ($Y = 0$), hence $const = 0$.

Applying eq. (E.8) at the equator of the drop (point E) where Y is maximum (Y_m) and where the derivative $Y' = 0$.

$$Y_m^2 - KY_m^4/4 = Y_M \tag{E.9}$$

By applying eq. (E.8) at point E where $Y' = 0$,

$$2Y_m - KY_m^3 = \frac{dY}{dY} = 1 \tag{E.10}$$

Combining eqs. (E.9) and (E.10),

$$Y_m = 3/2,\ y_m = R_m = 1.5R_o \tag{E.11}$$

and,

$$K = 16/27 = \Delta\rho\omega^2 R_o^3/2\gamma \tag{E.12}$$

Substitute R_o by R_m from eq. (E.11),

$$\gamma = \Delta\rho\omega^2 R_m^3/4 \tag{E.13}$$

in which the units are all in SI or any consistent system. R_m is the radius of the drop at equator (E) as indicated in Figure E.1. In practice a more elongated drop is used which really looks like a cylinder, but it is worth remarking that the hemisphere at the tip of the drop has not the same radius than the cylinder at the center as indicated in Figure E.2 (R_o = 2/3 R_m). This is due to the fact that the centrifugal acceleration is not constant, but increases with the distance from axis.

It is worth noting that eq. (E.13) does only require the evaluation of a distance (bubble radius at center) and not the estimation of a curvature, which would implies the estimation of the first and second derivative of the shape of the bubble, a much more difficult problem. It is also worth noting that in this method the bubble is not in contact with a solid surface, hence no contact angle has to be measured or estimated.

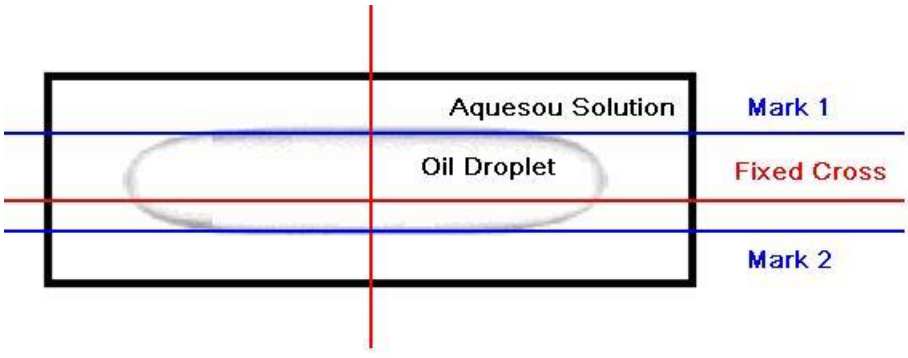

Figure E.2: Cylindrical Elongated Drop Curvature Radii.

Finally the formula indicates that low tension will be associated with small radius, i.e., an elongated drops and slow rotational velocity, whereas high tension would require a high rotational velocity and the drop might not be elongated enough to fall in the case for eq. (E.13) . This method is thus appropriate to measure low tensions, typically below 1 mN/m, and down to ultralow values (μN/m or less) found in surfactant-oil-water systems containing microemulsions. In practice the spinning tube, often a capillary of internal diameter equal or less than 2 mm, produces a lens effect than blows up the drop size, and a correction has to be applied to estimate the real radius. The tension may be calculated for non elongated drops, by numerically solving the equation set without having to estimate the curvature.

E.2 USE OF SPINNING DROP TENSIOMETER

The tensiometer consists of a high speed rotating capillary tube (2mm ID) open at one end. The tube in its housing is pivoted and sealed so that the open ends rotate inside the chamber, and its middle section is observable through the windows. Illumination of the capillary is with a stroboscope 'in-phase' with the rotation of the tube. A microscope with a magnifying eyepiece is used to determine the drop diameter.

E.2.1 Cleaning

For good results with interfacial tension measurements, it is imperative to start with a clean apparatus. The four basic items which contact the aqueous and/or oil phases, tube, septum, cap (o-ring) and syringe, need to be thoroughly cleaned before any measurements take place. A typical flushing sequence for the tube includes: i) many tube volumes of distilled water; ii) several volume of acetone (about 5 ml should be sufficient); iii) oil-dissolving solvent like hexane; iii) another acetone washing; and finally iv) many more volumes of water.

E.2.2 Loading

The filling of surfactant solution into the tube, and subsequent loading of oil droplet into the solution are intricate operations that require lots of practice beforehand. First, the needle of the surfactant syringe is inserted to the tube bottom and moved upward as the tube is filled. The needle should be held against the tube wall so that bubbling is avoided. Next, a syringe containing oil and equipped with the appropriate-sized needle is prepared. Then, quickly insert the needle into the tube, and gently force out a small air bubble or oil droplet by moving the syringe plunger with a twisting motion. And finally, seat the tube into the cap by pressing it firmly into a solution-filled cap. Clean the excess solution outside the tube.

E.2.3 Reading

Reading drops is made considerably easier if the machine is running at an appropriate speed for the drop in question. And this would also allow for very high accuracy. Drops can usually be kept near the center of the tube by careful adjustment on the leveling screws. Reading is usually done about once an hour, though there are occasionally times when more or less frequent readings are desirable. For low interfacial tension systems, solubilization could result in intermediate drop composition when the two phases are not pre-equilibrated (Cayias *et al.*, 1975). It is therefore of key importance to be able to tell when the system reaches equilibrium, especially when the oil and aqueous samples are not pre-equilibrated prior to the experiment, which is the case for most of our IFT measurements. In current study, the droplets are considered to be at equilibrium when three consecutive width readings agree to within about ±0.001cm, suggested by the instruction manual. As will be seen later, by implementing this equilibrium criterion, the interfacial tensions obtained from non-equilibrated system are in close agreement with those from the pre-equilibrated system for a range of salinities.

E.2.4 Calculation

The most commonly used relation for calculating interfacial tension by spinning drop method is the Vonnegut's equations (Cayias *et al.*, 1975),

$$\gamma = \Delta\rho\omega^2 R_m^3/4, \text{ in dynes/cm} \tag{E.14}$$

in which $\Delta\rho$ is the density difference of the two fluids, in g/cc; ω is the angular velocity of the spinning tube, in rad/s; and R_m is the radius of the center portion (cylinder) of the bubble or droplet. It should be noted that equation above is only strictly valid for infinite long drop (see Appendix E). Practically when the maximum drop length $l_{\max}$ and radius $r_{\max}$ satisfy $l_{\max} \geq 8r_{\max}$, the equation is considered appropriate.

E.3 PHASE BEHAVIOR TEST

E.3.1 Phase Behavior Pipettes Preparation

A phase behavior experiment involves mixing certain portion of an aqueous surfactant solution, saline water, and oil phase in an array of pipettes. The array of pipettes serves to create a salinity gradient, where different volumes of saline water are added to each pipette to render different salinities. Equal volumes of pre-mixed surfactant solutions are then added to each pipette.

Contact of concentrated electrolyte stock with surfactant stock could adversely affect performance. To mitigate this risk, the electrolyte stock is added first, and followed by DI water. The surfactant stock is then added. Oil phase is the last component added after aqueous stability and aqueous fluid levels are recorded.

Prior to adding oil phase to the pipette, an aqueous stability assessment determines the clarity and homogeneity of all aqueous mixtures. As a quick screening during phase behavior test, aqueous fluids are agitated after being dispensed into pipettes,

and then allowed to settle for one hour. The fluids in the phase behavior array are visually inspected, and the salinity is recorded where cloudiness and/or phase separation occurs.

After assessing aqueous stability and adding oil phase, the ends of pipettes are sealed with a Benzomatic® flame torch. Following the heat-sealing, the pipettes are allowed time to cool before being slowly inverted several times to allow the oil and aqueous phase mix. The greater contact area provided by the inversion is more representative of the mixing taking place at pore-scale.

E.3.2 Measurements and Observations

Prepared pipettes are then kept in convection oven at a specified temperature (55^{o}C). The visual and quantitative assessment of microemulsion properties and phase interfaces are conducted periodically after the pipettes are prepared.

A qualitative, visual inspection of the phase behavior pipettes is used to assess the presence of gel or macroemulsion and the fluidity of interfaces. The pipettes are inverted couple of more times when a small accumulation of gel/macroemulsion at the interface is observed. Careful observations of droplet size and behavior when the pipettes are gently mixed can be used to infer interfacial activity.

Pipettes that have free-flowing interfaces are quantified to calculate phase volumes. Measurements of phase interface levels are interpolated to the nearest 0.01ml using the markings on the pipettes. Further analyzing and comparing these volumes and volume fractions with respect to salinity can help determine the optimal condition.

E.3.3 Microemulsion Characterization

Solubilization of oil and water phases with respect to available surfactant forms the basis of the solubilization ratio parameter used for microemulsion characterization. After pipettes have been incubated and measured over a period of time, microemulsion

could be sampled from the pipettes for interfacial tension measurements using the spinning drop tensiometer. A comparison can then be made between IFT values obtained from Chun Huh equation and spinning drop measurements.

Appendix F: Analytical Solution to the Linearized Poisson-Boltzmann Equation for Diluted and Pure Gemini Solutions

For predicting CMC values of pure (without any salt addition) and dilute Gemini surfactant solutions (C_{sA} on the order of 10^{-4}M, conditions encountered in Chapter 3), the ion concentration will be extremely low that the original Poisson-Boltzmann equation (PBE) can be linearized using a first order Taylor series approximation for the exponential function ($e^x = 1 + x$ for $0 < x \ll 1$). Debye and Hückel (Adamson, 1997) argued that this approximation holds at large distances between ions, which is the same as saying that the concentration is low. Lastly, they claim that the addition of more terms in the expansion has little effect on the final solution. Thus:

$$\begin{aligned} -\sum_i \frac{z_i n_i^\infty}{\varepsilon} \exp\left(-\frac{z_i e\phi}{kT}\right) &\approx -\sum_i \frac{z_i e n_i^\infty}{\varepsilon}\left(1 - \frac{z_i e\phi}{kT}\right) \\ &= -\left(\sum_i \frac{z_i e n_i^\infty}{\varepsilon} - \sum_i \frac{z_i^2 e^2 n_i^\infty \phi}{\varepsilon kT}\right) \end{aligned} \tag{F.1}$$

The PBE is transformed to:

$$\nabla^2 \phi = \sum_i \frac{z_i^2 e^2 n_i^\infty \phi}{\varepsilon kT} \tag{F.2}$$

notice that the first summation in eq. (F.1) is zero due to electroneutrality, $\sum z_i e n_i^\infty = 0$.

Factor out the scalar potential and assign the leftovers to κ^2:

$$\kappa^2 = \sum_i \frac{z_i^2 e^2 n_i^\infty}{\varepsilon kT} \tag{F.3}$$

κ^{-1} is the Debye length. Debye and Hückel recognized the importance of the parameter in their paper and characterize it as a measure of the thickness of the ion atmosphere.

For a monovalent anionic surfactant molecule, $z_A : z_1$, $z_A = -1$ and $z_1 = 1$, at infinite distance away from the charged surface, $n_A^\infty = n_1^\infty = 1000 C_{1A} N_{Av}$. Then,

$$\kappa^2 = \frac{z_A^2 e^2 n_A^\infty}{\varepsilon kT} + \frac{z_1^2 e^2 n_1^\infty}{\varepsilon kT} = \frac{2 \times 10^3 e^2 N_{Av} C_{1A}}{\varepsilon kT} \tag{F.4}$$

Eq. (F.4) is widely used for analysis relevant to 1:1 electrolyte or surfactant. C_{1A} is the molar concentration for singly dispersed surfactant molecules,

$$C_{1A} = \begin{cases} CMC, & C_{sA} \geq CMC \\ C_{sA}, & C_{sA} < CMC \end{cases} \tag{F.5}$$

For anionic Gemini surfactant, we have $z_A = -2$ and $z_1 = 1$, at infinite distance away from the charged surface, $n_1^\infty = 2 n_A^\infty = 1000 \left(2 C_{1A} \right) N_{Av}$. Then,

$$\kappa^2 = \frac{z_A^2 e^2 n_A^\infty}{\varepsilon kT} + \frac{z_1^2 e^2 n_1^\infty}{\varepsilon kT} = \frac{6 \times 10^3 e^2 N_{Av} C_{1A}}{\varepsilon kT} \tag{F.6}$$

With eq. (F.3), the original PBE (in SI unit) is reduced to a form of the Helmholtz equation:

$$\nabla^2 \phi = \frac{d^2 \phi}{dr^2} + \frac{2}{r} \frac{d\phi}{dr} = \kappa^2 \phi \tag{F.7}$$

The boundary conditions are again the requirement of a vanishing electric field far from the aggregate and the Gauss law at the micelle surface:

$$\lim_{r \to \infty} \phi = \lim_{r \to \infty} \nabla \phi = 0 \tag{F.8}$$

$$\nabla \phi \big|_{r = R_{ch}} = -\frac{\sigma}{\varepsilon} \tag{F.9}$$

Introducing the following dimensionless variables:

$$u = \frac{e\phi}{kT},\ x = \kappa r \tag{F.10}$$

From eqs. (F.7) to (F.9), we have:

$$\frac{d^2u}{dx^2} + \frac{2}{x}\frac{du}{dx} = u \tag{F.11}$$

$$\left.\frac{du}{dx}\right|_{x\to\infty} = 0 \tag{F.12}$$

$$\left.\frac{du}{dx}\right|_{x=x_o} = -t \equiv -\frac{e\sigma}{\varepsilon\kappa kT} \tag{F.13}$$

t is the reduced variable related to the surface charge density; and $x_o = \kappa R_{ch}$. Using the substitution $\omega(x) = x^{1/2}u(x)$, eq. (F.11) s rewritten as,

$$x^2\frac{d^2\omega}{dx^2} + x\frac{d\omega}{dx} - \left(x^2 + \frac{1}{4}\right)\omega = 0 \tag{F.14}$$

Eq. (F.14) is the modified Bessel equation with a general solution of:

$$\omega(x) = C_1 I_{1/2}(x) + C_2 K_{1/2}(x) \tag{F.15}$$

where $I_{1/2}(x)$ and $K_{1/2}(x)$ are the modified Bessel functions of order $1/2$ of the first and second kind, respectively. Thus the general solution to eq. (F.11) is:

$$u(x) = C_1 x^{-1/2} I_{1/2}(x) + C_2 x^{-1/2} K_{1/2}(x) \tag{F.16}$$

The boundary conditions eq. (F.12) and eq. (F.13) give $C_1 = 0$ and $C_2 = tx_o^{1/2} \big/ K_{3/2}\left(x_o^{1/2}\right)$, respectively, and hence the particular solution is:

$$u(x) = t\left(\frac{x_o}{x}\right)^{1/2} \frac{K_{1/2}(x)}{K_{3/2}(x_o)} \tag{F.17}$$

Consider the following relations for the modified Bessel function of the second kind:

$$K_{1/2}(z) = \sqrt{\frac{\pi}{2z}} e^{-z} \tag{F.18}$$

$$K_{3/2}(z) = K_{1/2+1}(z) = \frac{1}{z} K_{1/2}(z) + K_{-1/2}(z) = \frac{1+z}{z} K_{1/2}(z) \tag{F.19}$$

in which we utilize the reflection relation $K_{1/2}(z) = K_{-1/2}(z)$ Then,

$$u(x) = t \frac{x_o^2}{1+x_o} \frac{e^{(x_o - x)}}{x} \tag{F.20}$$

The analytic expression for the electrostatic free energy is derived by performing an isothermal charging process,

$$\begin{aligned} \left.\frac{\left(\Delta\mu_g^o\right)_{\text{ionic}}}{kT}\right|_{sph} &= \frac{a_{ch}}{kT}\int_0^{\sigma_o} \phi_o(\sigma')\, d\sigma' = \frac{a_{ch}\varepsilon\kappa kT}{e^2}\int_0^{t_o} u(x_o)\, dt \\ &= \frac{a_{ch}\varepsilon\kappa kT}{2e^2}\frac{K_{1/2}(x_o)}{K_{3/2}(x_o)} t_o^2 = \frac{a_{ch}\sigma_o^2}{2\varepsilon\kappa kT}\frac{\kappa R_{ch}}{1+\kappa R_{ch}} \end{aligned} \tag{F.21}$$

A similar analysis could be done for the case of planar micellar structure, with a solution in the form of:

$$\left.\frac{\left(\Delta\mu_g^o\right)_{\text{ionic}}}{kT}\right|_{pla} = \frac{a_{ch}\sigma_o^2}{2\varepsilon\kappa kT}\frac{K_{-1/2}(x_o)}{K_{1/2}(x_o)} = \frac{a_{ch}\sigma_o^2}{2\varepsilon\kappa kT} \tag{F.22}$$

Appendix G: Approximate Solution to the Nonlinear PBE for Gemini Solutions at High Electrolyte Concentrations

Consider a spherical micelle of radius R_{ch} immersed in a 1:1 type of electrolyte, e.g. NaCl, $z_3 = 1,\ z_4 = -1$. For Gemini surfactant, $z_A = -2$ and $z_1 = 1$, at infinite distance away from the charged surface, the surfactant monomers are assumed to completely dissociated, we then have:

$$\begin{aligned} n_1^\infty &= 2n_A^\infty = 2\times 10^3 N_{Av} c_{1A}^\infty \\ n_3^\infty &= n_4^\infty = 10^3 N_{Av} C_{add} \end{aligned} \tag{G.1}$$

Substituting eq. (F.1) into the original PBE,

$$\begin{aligned} \frac{d^2\phi}{dr^2} + \frac{2}{r}\frac{d\phi}{dr} &= -\frac{e}{\varepsilon}\left[\begin{array}{l} z_A n_A^\infty \exp\left(-\dfrac{z_A e\phi}{kT}\right) + z_1 n_1^\infty \exp\left(-\dfrac{z_1 e\phi}{kT}\right) \\ + z_3 n_3^\infty \exp\left(-\dfrac{z_3 e\phi}{kT}\right) + z_4 n_4^\infty \exp\left(-\dfrac{z_4 e\phi}{kT}\right) \end{array}\right] \\ &= \frac{4\pi e}{\varepsilon}\left[\begin{array}{l} n_1^\infty\left[\exp\left(\dfrac{2e\phi}{kT}\right) - \exp\left(-\dfrac{e\phi}{kT}\right)\right] \\ + n_3^\infty\left[\exp\left(\dfrac{e\phi}{kT}\right) - \exp\left(-\dfrac{e\phi}{kT}\right)\right] \end{array}\right] \end{aligned} \tag{G.2}$$

With high concentration of salt ($0.1 \le [\mathrm{NaCl}] \le 0.5\mathrm{M}$) added into the aqueous solution, $n_1^\infty / n_3^\infty \gg 100$ considering the CMC values for the Gemini molecules synthesized. Therefore, the first term in the square bracket on RHS of eq. (G.2) can be safely neglected to get,

$$\frac{d^2\phi}{dr^2} + \frac{2}{r}\frac{d\phi}{dr} = \frac{en_3^\infty}{\varepsilon}\left[\exp\left(\frac{e\phi}{kT}\right) - \exp\left(-\frac{e\phi}{kT}\right)\right] = \frac{2en_3^\infty}{\varepsilon}\sinh\left(\frac{e\phi}{kT}\right) \tag{G.3}$$

in which $n_3^\infty = 1000 C_{add} N_{Av}$. With again the same sets of boundary conditions,

$$\lim_{r\to\infty}\phi = \lim_{r\to\infty}\nabla\phi = 0 \tag{G.4}$$

$$\nabla\phi\big|_{r=R_{ch}} = -\frac{\sigma}{\varepsilon} \tag{G.5}$$

Similar to what we have done in Appendix A, introducing two dimensionless variable u and x:

$$u = \frac{e\phi}{kT},\ x = \kappa r \tag{G.6}$$

where the Debye screening constant for a 1:1 type of electrolyte is,

$$\kappa^2 = \left(\frac{z_3^2 e^2 n_3^\infty}{\varepsilon kT} + \frac{z_4^2 e^2 n_4^\infty}{\varepsilon kT}\right) = \frac{2\times 10^3 e^2 N_{Av} C_{add}}{\varepsilon kT} \tag{G.7}$$

Then eqs. (G.3) to eq. (G.5) become,

$$\frac{d^2u}{dx^2} + \frac{2}{x}\frac{du}{dx} = \sinh u \tag{G.8}$$

$$\left.\frac{du}{dx}\right|_{x=\kappa R_{ch}} = -t \equiv -\frac{e\sigma}{\varepsilon\kappa kT} \tag{G.9}$$

Writing the dimensionless surface potential $u_o = u\left(\kappa R_{ch}\right)$, the approximate solution of eq. (G.8) and (G.9) gives to the first order in $\left(\kappa R_{ch}\right)^{-1}$ (an accuracy of about 5% for $\kappa R_{ch} = 0.5$) (Evans, *et al.*, 1983 & 1984),

$$z = \cosh\left(\frac{u_o}{2}\right) = \left[\left(1+\frac{2}{\kappa R_{ch}}\right)^2 + \frac{t^2}{4}\right] - \frac{2}{\kappa R_{ch}} \tag{G.10}$$

Since $\sinh\left(u_o/2\right) = \sqrt{\left(z^2-1\right)}$, the surface potential is then,

$$u_o = 2\ln\left[\cosh\left(\frac{u_o}{2}\right)+\sinh\left(\frac{u_o}{2}\right)\right] = 2\ln\left[z+\sqrt{\left(z^2-1\right)}\right] \tag{G.11}$$

Given u_o, one can then calculate the electrostatic part of the surface Gibbs free energy per surfactant molecule by using (Evans *et al.*, 1983):

$$\left.\frac{\left(\Delta\mu_g^o\right)_{\text{ionic}}}{kT}\right|_{sph} = \frac{a_{ch}}{kT}\int_0^{\sigma_o}\phi_o\left(\sigma'\right)d\sigma' = \frac{a_{ch}\sigma}{e}\frac{1}{t}\int_0^{t_o}u\left(x_o\right)dt$$

$$= \frac{2a_{ch}\sigma_o}{e}\left[\begin{array}{l}\ln\left(\frac{t_o}{2}+\left[1+\left(\frac{t_o}{2}\right)^2\right]^{1/2}\right)-\left(\frac{2}{t_o}\right)\left(\left[1+\left(\frac{t_o}{2}\right)^2\right]^{1/2}-1\right)\\ -\frac{2C}{\kappa t_o}\ln\left(\frac{1}{2}+\frac{1}{2}\left[1+\left(\frac{t_o}{2}\right)^2\right]^{1/2}\right)\end{array}\right] \tag{G.12}$$

$$\left.\frac{du}{dx}\right|_{x=x_o} = -t \equiv -\frac{e\sigma}{\varepsilon\kappa kT} \tag{G.13}$$

In the curvature correction term, C depends no the geometry of the aggregate and equals $2/R_{ch}$ for spheres and 0 for planar structure. Comparing eq. (G.13) with eq. (11) in Evans' original paper, one might notice that these two equations differ by a factor of $a_{ch}\sigma_o/e$. For Gemini surfactants, we consider the counterion binding effect at micelle surface of charge, then $\sigma_o = e\left(z_A+\sum z_j\beta_j\right)/a_{ch}$. For conventional monovalent surfactants, $\sigma_o = e/a_{ch}$, this factor reduces to unity.

Equation Section (Next)

Appendix H: Working Example for Computing Free Energy of Micellization

In this section, a detailed example is provided on how to calculate different free energy contributions for the Gemini surfactant micellization process. The program for Gibbs free energy minimization follows the same procedure.

Consider a dilute and pure (no salt addition, $C_{add} = 0$) solution of sulfate Gemini surfactant C_{14}-C_4-C_{14}. The solution temperature is 30°C (303.15K). CMC and degree of ionization values reported in Chapter 3 are 4.8×10^{-6} mol/L (M) and 0.1815, respectively.

H.1 GEOMETRICAL RELATIONS

H.1.1 Molecular Volume and Tail Length

At temperature of 303.15K,

$$\begin{aligned} v_{CH_3} &= 54.6 + 0.124(T - 298) \\ &= 54.6 + 0.124\times(303.15 - 298) = 55.22 \text{ Å}^3 \end{aligned} \tag{H.1}$$

$$\begin{aligned} v_{CH_2} &= 26.9 + 0.0146(T - 298) \\ &= 26.9 + 0.0146\times(303.15 - 298) = 26.973 \text{ Å}^3 \end{aligned} \tag{H.2}$$

$$v_{CH} = 20.5 \text{ Å}^3 \tag{H.3}$$

For C_{14}-C_4-C_{14}, $n_c = 14$, $s = 4$.

$$\begin{aligned} v_{sA} &= v_{CH_3} + v_{CH} + (n_c - 2)v_{CH_2} \\ &= 55.22 + 20.5 + (14 - 2)\times 26.973 = 399.396 \text{ A}^3 \end{aligned} \tag{H.4}$$

$$l_{sA} = 1.50 + 1.265 n_c = 1.50 + 1.265\times 14 = 19.21 \text{ Å} \tag{H.5}$$

H.1.2 Maximum Aggregation Number for Spherical Micelles $g_{sph,\max}$

By enforcing $R_c = l_{sA} = 19.21\ \text{A}$, we can calculate the maximum aggregation number for spherical micelles $g_{sph,\max}$ as:

$$g_{sph,\max} = \text{Int}\left(\frac{2\pi l_{sA}^3}{3v_{sA}}\right)+1 = \text{Int}\left(\frac{2\pi \times 19.21^3}{3\times 399.396}\right)+1 = 38 \tag{H.6}$$

Therefore, if the aggregation number g exceeds $g_{sph,\max} = 38$, the micelle will assume the globular shape. Take $g_1 = 35$ and $g_2 = 45$ as two comparing cases, and all the geometric parameters should be computed with proper equations.

H.1.3 Spherical Micelles ($g_1 = 35$, $R_c \le l_{sA}$)

For $g = 35 < g_{sph,\max}$, the micelle will be spherical, then

$$R_c = \left(\frac{3gv_{sA}}{2\pi}\right)^{1/3} = \left(\frac{3\times 35\times 399.396}{2\pi}\right)^{1/3} = 18.828\ \text{Å} \tag{H.7}$$

$$a = \frac{2\pi R_c^2}{g} = \frac{2\pi \times 18.828^2}{35} = 63.6386\ \text{Å}^2 \tag{H.8}$$

$$P = 1/3 \tag{H.9}$$

H.1.4 Globular Micelles ($g_2 = 45$, $R_c = l_{sA}$)

For $g = 45 > g_{sph,\max}$, the micelle will be globular, $R_c = l_{sA} = 19.21\ \text{Å}$.

$$b = \frac{3gv_{sA}}{2\pi R_c^2} = \frac{3\times 45\times 399.396}{2\pi \times 19.21^2} = 23.2543\ \text{Å} \tag{H.10}$$

$$E = \sqrt{1-\left(R_c/b\right)^2} = \sqrt{1-\left(19.21/23.2543\right)^2} = 0.5635 \tag{H.11}$$

$$a = \frac{\pi R_c^2}{g}\left[1+\frac{\sin^{-1}E}{E(1-E^2)^{1/2}}\right] = \frac{\pi \times 19.21^2}{45}\left[1+\frac{\sin^{-1}(0.5635)}{0.5635\times(1-0.5635^2)^{1/2}}\right] = 58.8932 \text{ Å}^2 \quad \text{(H.12)}$$

$$P = v_{sA}/aR_c = \frac{399.396}{58.8932\times 19.21} = 0.3530 \quad \text{(H.13)}$$

H.2 FREE ENERGY OF MICELLIZATION FOR GEMINI SURFACTANTS

H.2.1 Transfer Free Energy of the Surfactant Tail

$$\frac{\left(\Delta\mu_g^o\right)_{\text{tr}}}{kT} = \frac{\left(\Delta\mu_g^o\right)_{s/w}}{kT} + \frac{\left(\Delta\mu_g^o\right)_{w/hc}}{kT} \quad \text{(H.14)}$$

$$\frac{\left(\Delta\mu_g^o\right)_{s/w}}{kT} = -k_s C_{add},\ k_s^{NaCl} = 0.195 \text{ L/mol} \quad \text{(H.15)}$$

For pure Gemini surfactant solution, this term drops out. At 303.15K,

$$\begin{aligned}\frac{\left(\Delta\mu_g^o\right)_{w/hc,\text{CH}_3}}{kT} &= 3.38\ln T + \frac{4064}{T} - 44.13 + 0.02595T \\ &= 3.38\times\ln 303.15 + \frac{4064}{303.15} - 44.13 + 0.02595\times 303.15 \\ &= -3.5433\end{aligned} \quad \text{(H.16)}$$

$$\begin{aligned}\frac{\left(\Delta\mu_g^o\right)_{w/hc,\text{CH}_2}}{kT} &= 5.85\ln T + \frac{896}{T} - 36.15 + 0.0056T \\ &= 5.85\times\ln 303.15 + \frac{896}{303.15} - 36.15 + 0.0056\times 303.15 \\ &= -1.4638\end{aligned} \quad \text{(H.17)}$$

$$\frac{\left(\Delta\mu_g^o\right)_{w/hc,\mathrm{CH}}}{kT} \approx \frac{\left(\Delta\mu_g^o\right)_{w/hc,\mathrm{CH_2}}}{kT} = -1.4638 \tag{H.18}$$

$$s_{\mathrm{core}} = s - a^{1/2}/l_{\mathrm{CH_2}}, \text{ for } s > a^{1/2}/l_{\mathrm{CH_2}} \tag{H.19}$$

For $g = 35 < g_{sph,\max}$, $a = 63.6386\ \text{Å}^2$,

$$s < a^{1/2}/l_{\mathrm{CH_2}} = 6.3062,\ s_{\mathrm{core}} = 0 \tag{H.20}$$

For $g = 45 > g_{sph,\max}$, $a = 58.8932\ \text{Å}^2$,

$$s < a^{1/2}/l_{\mathrm{CH_2}} = 6.0666,\ s_{\mathrm{core}} = 0 \tag{H.21}$$

Take $f_{\text{sec-tail}} = 0.6$, we then have:

$$\begin{aligned}\frac{\left(\Delta\mu_g^o\right)_{\mathrm{tr}}}{kT} &= (1+f_{\text{sec-tail}})\left[\frac{\left(\Delta\mu_g^o\right)_{w/hc,\mathrm{CH_3}}}{kT} + \frac{\left(\Delta\mu_g^o\right)_{w/hc,\mathrm{CH}}}{kT} + (n_c-2)\frac{\left(\Delta\mu_g^o\right)_{w/hc,\mathrm{CH_2}}}{kT}\right] \\ &\quad + f_{\text{sec-tail}} s_{\mathrm{core}} \frac{\left(\Delta\mu_g^o\right)_{w/hc,\mathrm{CH_2}}}{kT} - k_s C_{add} \\ &= (1+0.6)\left[-3.5433-1.4638-(14-2)\times 1.4638\right] = -36.1158\end{aligned} \tag{H.22}$$

H.2.2 Tail Deformation Free Energy

$$\frac{\left(\Delta\mu_g^o\right)_{\mathrm{def}}}{kT} = 2\left(\frac{9P\pi^2 R_c^2}{80NL^2}\right),\ L = 4.6\ \text{Å} \tag{H.23}$$

in which, $N = l_{sA}/L = 19.21/4.6 = 4.1761$.

For $g = 35 < g_{sph,\max}$, $P = 1/3$,

$$\frac{\left(\Delta\mu_g^o\right)_{\text{def}}}{kT} = 2\left(\frac{3\pi^2 \times 18.828^2}{80 \times 4.1761 \times 4.6^2}\right) = 2.9695 \tag{H.24}$$

For $g = 45 > g_{sph,\max}$, $P = 0.3530$,

$$\frac{\left(\Delta\mu_g^o\right)_{\text{def}}}{kT} = 2\left(\frac{9 \times 0.3530\pi^2 \times 19.21^2}{80 \times 4.1761 \times 4.6^2}\right) = 3.2739 \tag{H.25}$$

H.2.3 Tail Deformation Free Energy

$$\frac{\left(\Delta\mu_g^o\right)_{\text{pack}}}{kT} = \ln\left(\frac{a_{eff}}{\left[(s+1)l_{\text{CH}_2}\right]^2}\right), \text{ for } \left[(s+1)l_{\text{CH}_2}\right]^2 < a_{eff} \tag{H.26}$$

$$a_{eff} = \frac{v_{sA}}{\eta\pi R_c}, \ \eta = 0.28 \tag{H.27}$$

For $g = 35 < g_{sph,\max}$, $R_c = 18.828$ Å,

$$a_{eff} = \frac{399.396}{0.28\pi \times 18.828} = 24.1152 \text{ Å}^2 \tag{H.28}$$

$$\left[(s+1)l_{\text{CH}_2}\right]^2 = \left(5 \times 1.265\right)^2 = 40.0056 > a_{eff} \tag{H.29}$$

For $g = 45 > g_{sph,\max}$, $R_c = 19.12$ Å,

$$a_{eff} = \frac{399.396}{0.28\pi \times 19.21} = 23.6357 \text{ Å}^2 \tag{H.30}$$

$$\left[(s+1)l_{\text{CH}_2}\right]^2 = \left(5 \times 1.265\right)^2 = 40.0056 > a_{eff} \tag{H.31}$$

$$\frac{\left(\Delta\mu_g^o\right)_{\text{pack}}}{kT} = 0 \tag{H.32}$$

H.2.4 Head Group Steric Interactions

$$\frac{\left(\Delta\mu_g^o\right)_{\text{steric}}}{kT} = -\left(1+\sum_j \beta_j\right)\ln\left(1-\frac{2a_A+\sum_j \beta_j a_{h,j}}{2a}\right) \tag{H.33}$$

The area terms, a_A and a, are expressed per head group. The factor 2 is included to account for the fact that one Gemini molecule has two head groups. Noticing that β_j is expressed per surfactant molecule. Since only one type of counterion present in the solution, e.g. Na^+,

$$\frac{\left(\Delta\mu_g^o\right)_{\text{steric}}}{kT} = -\left(1+\beta_{Na^+}\right)\ln\left(1-\frac{2a_A+\beta_{Na^+}a_{h,Na^+}}{2a}\right) \tag{H.34}$$

$$a_A = a_{A,Na^+} = \pi r_{A,Na^+}^2 = \pi\times 2.73^2 = 23.414\ \text{Å}^2 \tag{H.35}$$

$$a_{h,Na^+} = \pi r_{h,Na^+}^2 = \pi\times 1.84^2 = 10.6362\ \text{Å}^2 \tag{H.36}$$

$$\beta_{Na^+} = 1-\alpha_{Na^+} = 1-0.1815 = 0.8185 \tag{H.37}$$

For $g = 35 < g_{sph,\max}$, $a = 63.6386\ \text{Å}^2$,

$$\frac{\left(\Delta\mu_g^o\right)_{\text{steric}}}{kT} = 1.0425 \tag{H.38}$$

For $g = 45 > g_{sph,\max}$, $a = 58.8932\ \text{Å}^2$,

$$\frac{\left(\Delta\mu_g^o\right)_{\text{steric}}}{kT} = 1.1596 \tag{H.39}$$

H.2.5 Formation of Hydrophobe Core-Water Interface

$$\frac{\left(\Delta\mu_g^o\right)_{\text{int}}}{kT} = \frac{2\sigma_{agg}\left(a - a_A\right)}{kT} \tag{H.40}$$

$$\sigma_{agg} = 0.7562\left(\sigma_A + \sigma_{salt}\right) - 0.4906\sqrt{\sigma_A\sigma_{salt}} \tag{H.41}$$

$$\sigma_{salt} = \sigma_W + \left(\frac{d\sigma}{dC_{add}}\right)C_{add},\ \left(\frac{d\sigma}{dC_{add}}\right)_{NaCl} = 2.10 \text{ mN/m/M} \tag{H.42}$$

$$\begin{aligned}\sigma_w &= 235.8\left(1-\frac{T}{647.15}\right)^{1.256}\left[1-0.625\left(1-\frac{T}{647.15}\right)\right] \\ &= 235.8\left(1-\frac{303.15}{647.15}\right)^{1.256}\left[1-0.625\left(1-\frac{303.15}{647.15}\right)\right] \\ &= 71.1981 \text{ mN/m}\end{aligned} \tag{H.43}$$

$$\sigma_{salt} = \sigma_W + \left(\frac{d\sigma}{dC_{add}}\right)C_{add} = 71.1981 \text{ mN/m/M} \tag{H.44}$$

$$\begin{aligned}\sigma_A &= 35.0 - 325M_{sA}^{-2/3} - 0.098(T - 298.15) \\ &= 35.0 - 325\times 196.3721^{-2/3} - 0.098(303.15 - 298.15) \\ &= 24.8903 \text{ mN/m}\end{aligned} \tag{H.45}$$

$$\begin{aligned}\sigma_{agg} &= 0.7562\left(\sigma_A + \sigma_{salt}\right) - 0.4906\sqrt{\sigma_A\sigma_{salt}} \\ &= 0.7562\times\left(24.8903 + 71.1981\right) - 0.4906\sqrt{24.8903\times 71.1981} \\ &= 52.0093 \text{ mN/m}\end{aligned} \tag{H.46}$$

$$\frac{\left(\Delta\mu_g^o\right)_{\text{int}}}{kT} = \frac{2\sigma_{agg}\left(a - a_A\right)}{kT} \tag{H.47}$$

For $g = 35 < g_{sph,\max}$, $a = 63.6386\ \text{Å}^2$,

$$\begin{aligned}\frac{\left(\Delta\mu_g^o\right)_{\text{int}}}{kT} &= \frac{2\sigma_{agg}\left(a - a_A\right)}{kT} \\ &= \frac{2\times 52/1000\times\left(63.6386 - 23.414\right)/10^{20}}{1.38/10^{23}\times 303.15} = 9.9968\end{aligned} \tag{H.48}$$

For $g = 45 > g_{sph,\max}$, $a = 58.8932\ \text{Å}^2$,

$$\begin{aligned}\frac{\left(\Delta\mu_g^o\right)_{\text{int}}}{kT} &= \frac{2\sigma_{agg}\left(a - a_A\right)}{kT} \\ &= \frac{2\times 52/1000\times\left(58.8932 - 23.414\right)\times 10^{-20}}{1.38\times 10^{-23}\times 303.15} = 8.8175\end{aligned} \tag{H.49}$$

H.2.6 Coverage Free Energy

$$\begin{aligned}\frac{\left(\Delta\mu_g^o\right)_{\text{cover}}}{kT} &= \frac{\left(\sigma_{SP} - \sigma_{agg}\right)}{kT}\cdot\left[\left(s - s_{\text{core}}\right)l_{\text{CH}_2}L\right] \\ &= -\frac{52/1000\times\left[\left(4-0\right)\times 1.265\times 4.6\times 10^{-20}\right]}{1.38\times 10^{-23}\times 303.15} = -2.8923\end{aligned} \tag{H.50}$$

H.2.7 Head group-Counterion Mixing Entropy

$$\begin{aligned}\frac{\left(\Delta\mu_g^o\right)_{\text{ent}}}{kT} &= \ln\left(\frac{1}{1+\sum_j \beta_j}\right) + \sum_j \beta_j \ln\left(\frac{\beta_j}{1+\sum_j \beta_j}\right) \\ &= \ln\left(\frac{1}{1+0.8185}\right) + 0.8185\times\ln\left(\frac{0.8185}{1+0.8185}\right) = -1.2514\end{aligned} \tag{H.51}$$

H.2.8 Ionic Interactions between Head groups

$$\frac{\left(\Delta\mu_g^o\right)_{\text{ionic}}}{kT} = \frac{a_{ch}}{kT}\int_0^{\sigma_o}\phi_o\left(\sigma\right)d\sigma \tag{H.52}$$

$$R_{ch} = R_c + d_{ch},\ d_{ch} = 4\ \text{Å} \tag{H.53}$$

For $g = 35 < g_{sph,\max}$, $R_c = 18.828\ \text{Å}$,

$$R_{ch} = R_c + d_{ch} = 18.828 + 4 = 22.828\ \text{Å} \tag{H.54}$$

$$a_{ch} = \frac{4\pi R_{ch}^2}{g} = \frac{4\pi \times 22.828^2}{35} = 187.102\ \text{Å}^2 \tag{H.55}$$

a_{ch} is defined per Gemini molecule.

$$\sigma_o = \frac{e\left(z_A + \sum z_j\beta_j\right)}{a_{ch}} = \frac{1.6022\times10^{-19}\times\left(-2+0.8185\right)}{187.102\times10^{-20}} = -0.1012\ \text{C/m}^2 \tag{H.56}$$

For $g = 45 > g_{sph,\max}$, $R_c = 19.21\ \text{Å}$,

$$R_{ch} = R_c + d_{ch} = 19.21 + 4 = 23.21\ \text{Å} \tag{H.57}$$

$$a_{ch} = \frac{4\pi R_{ch}^2}{g} = \frac{4\pi \times 23.21^2}{45} = 150.435\ \text{Å}^2 \tag{H.58}$$

$$\sigma_o = \frac{e\left(z_A + \sum z_j\beta_j\right)}{a_{ch}} = \frac{1.6022\times10^{-19}\times\left(-2+0.8185\right)}{150.435\times10^{-20}} = -0.1258\ \text{C/m}^2 \tag{H.59}$$

$$\varepsilon_{sol} = \varepsilon_W + \delta_{salt}C_{add},\ \delta_{salt}^{NaCl} = -11.27 \tag{H.60}$$

$$\varepsilon_W = -1.0677 + 306.4670 \exp\left(-4.52\times10^{-3}T\right) = 76.7892 \tag{H.61}$$

$$\varepsilon_{sol} = \varepsilon_W + \delta_{salt} C_{add} = 76.7892 \tag{H.62}$$

$$\varepsilon = \varepsilon_o \varepsilon_{sol} = 8.85419\times10^{-12} \times 76.7892 = 6.7991\times10^{-10} \text{ F/m} \tag{H.63}$$

Assuming solution is at critical micelle concentration, $C_{1A} = CMC = 4.6\times10^{-6}$ M

$$\begin{aligned} \kappa &= \sqrt{\frac{6\times10^3 e^2 N_{Av} C_{1A}}{\varepsilon kT}} \\ &= \sqrt{\frac{6\times10^3 \times \left(1.6022\times10^{-19}\right)^2 \times 6.022\times10^{23} \times 4.8\times10^{-6}}{6.79906\times10^{-10} \times 1.38\times10^{-23} \times 303.15}} \\ &= 1.2245\times10^7 \text{ 1/m} \end{aligned} \tag{H.64}$$

For $g = 35 < g_{sph,\max}$, $R_{ch} = 22.828$ A, $a_{ch} = 187.102$ A^2

$$\frac{\left(\Delta\mu_g^o\right)_{\text{ionic}}}{kT} = \frac{a_{ch}\sigma_o^2}{2\varepsilon\kappa kT} \frac{\kappa R_{ch}}{1+\kappa R_{ch}} = 7.4728 \tag{H.65}$$

$$F = \left(1 - \frac{sl_{\text{CH}_2}}{a^{1/2}}\right)^{\upsilon} \lambda = \left(1 - \frac{4\times1.265}{63.6386^{1/2}}\right)^{0.9} \times 0.02719 = 0.0110 \tag{H.66}$$

$$\left.\frac{\left(\Delta\mu_g^o\right)_{\text{ionic}}}{kT}\right|_{\text{true}} = \frac{\left(\Delta\mu_g^o\right)_{\text{ionic}}}{kT} \cdot \left(1 - F\right) = 7.3907 \tag{H.67}$$

For $g = 45 > g_{sph,\max}$, $R_{ch} = 23.21$ A, $a_{ch} = 150.435$ A^2

$$\frac{\left(\Delta\mu_g^o\right)_{\text{ionic}}}{kT} = \frac{a_{ch}\sigma_o^2}{2\varepsilon\kappa kT} \frac{\kappa R_{ch}}{1+\kappa R_{ch}} = 9.4455 \tag{H.68}$$

$$F = \left(1 - \frac{sl_{\mathrm{CH_2}}}{a^{1/2}}\right)^{\upsilon} \lambda = \left(1 - \frac{4 \times 1.265}{58.8932^{1/2}}\right)^{0.9} \times 0.02763 = 0.0105 \tag{H.69}$$

$$\left.\frac{\left(\Delta\mu_g^o\right)_{\mathrm{ionic}}}{kT}\right|_{\mathrm{true}} = \frac{\left(\Delta\mu_g^o\right)_{\mathrm{ionic}}}{kT} \cdot \left(1 - F\right) = 9.3464 \tag{H.70}$$

H.3 TOTAL FREE ENERGY OF MICELLIZATION

$$\begin{aligned}\frac{\left(\Delta\mu_g^o\right)_{\mathrm{total}}}{kT} = {} & \frac{\left(\Delta\mu_g^o\right)_{\mathrm{tr}}}{kT} + \frac{\left(\Delta\mu_g^o\right)_{\mathrm{def}}}{kT} + \frac{\left(\Delta\mu_g^o\right)_{\mathrm{pack}}}{kT} + \frac{\left(\Delta\mu_g^o\right)_{\mathrm{steric}}}{kT} \\ & + \frac{\left(\Delta\mu_g^o\right)_{\mathrm{int}}}{kT} + \frac{\left(\Delta\mu_g^o\right)_{\mathrm{cover}}}{kT} + \frac{\left(\Delta\mu_g^o\right)_{\mathrm{ent}}}{kT} + \frac{\left(\Delta\mu_g^o\right)_{\mathrm{ionic}}}{kT}\end{aligned} \tag{H.71}$$

For $g = 35 < g_{sph,\max}$,

$$\begin{aligned}\frac{\left(\Delta\mu_g^o\right)_{\mathrm{total}}}{kT} = {} & \left(-36.1157\right) + \left(2.9695\right) + \left(0\right) + \left(1.0425\right) \\ & + \left(9.9968\right) + \left(-2.8923\right) + \left(-1.2514\right) + \left(7.3907\right) \\ = {} & -18.860\end{aligned} \tag{H.72}$$

For $g = 45 > g_{sph,\max}$,

$$\begin{aligned}\frac{\left(\Delta\mu_g^o\right)_{\mathrm{total}}}{kT} = {} & \left(-36.1157\right) + \left(3.2739\right) + \left(0\right) + \left(1.1596\right) \\ & + \left(8.8175\right) + \left(-2.8923\right) + \left(-1.2514\right) + \left(9.3465\right) \\ = {} & -17.6620\end{aligned} \tag{H.73}$$

Apparently, under current condition, a micelle with aggregation number of 35 has a more negative free energy and therefore will be a favored configuration over a larger aggregate with $g = 45$.

Nomenclature

a	surface area of the aggregate per head group
a_A	effective cross-sectional areas of the hydrated head group of surfactant A
$a_{A,j}$	effective cross-sectional area of the head group for the pair composed of surfactant A and counter-ion j
a_{ch}	surface area per surfactant molecule at the micelle surface of charge
$a_{h,j}$	effective cross-sectional areas of the hydrated head group of the hydrated counter-ions j
a_i	activity of component i in the bulk phase
$a_{\min}$	minimum area per molecule at the surface
a_π	activity of the surfactant in the aqueous phase at a surface pressure of π
A	area of the electrodes, in Chapter 3
A_{CO}	cohesive energy (per unit interfacial area) of the surfactant with oil
A_{CW}	cohesive energy (per unit interfacial area) of the surfactant with water
A_D	area occupied by a surfactant molecule at the drop surface
A_g	aggregate surface area
A_{hh}	cohesive energy between the hydrophilic portions
A_{ll}	cohesive energy between the lipophilic portions
$A_{\min}$	minimum molar area of the surfactant
A_{OO}	cohesive energy of the solvent molecules in oil
A_{WW}	cohesive energy of the solvent molecules in water
C	molar concentration, in Chapter 3
C	IFT constant, approximately 0.3dyne/cm, in Chapter 5
$C(L)$	concentration of micelles of length L

C_o surfactant concentrations before adsorption tests

C_1 molar concentration of singly dispersed Gemini surfactant molecules

C_{20} surfactant concentration that reduces the surface tension by 20mN/m

C_{add} salt concentration

C_π molar concentration of surfactant in the aqueous phase at a surface pressure of π

d_{ch} distance between the hydrocarbon core and the center the ionic surfactant head

d_s narrow maximum in head group distance distribution function

d_T thermodynamic equilibrium distance between head groups

E eccentricity of globular micelle

E_c end-cap energy

f molar activity coefficients

f_i activity coefficient of component i

$f_{\text{sec-tail}}$ factor accounting for contribution from the second tail group

$f_{\pm}^{Na_2R_2}$ mean ionic activity coefficient of Gemini Na_2R_2

F semi-empirical correction factor to account for the non-uniformity effect

F.R. filtration ratio

g_i HLB number for a functional group

G electrical conductance, in Chapter 3

G Gibbs free energy, in Chapter 4

G' elastic / storage modulus

G'' viscous / loss modulus

G_f free energy of formation

G_m free energy of mixing

$\bar{L}$ average micelle length / size

k Boltzmann constant

k_{brine} absolute brine permeability

k_{oil} oil permeability

k_s salting-out constant

k_{water} water permeability

k_{ro}^{o} relative oil permeability

k_{rw}^{o} relative water permeability

K rigidity coefficient

K_m monomer-micelle equilibrium constant

K_v modified Bessel function of the second kind of order v

l distance between electrodes

l_{CH2} length of a methylene group

l_{sA} extended surfactant tail length

m_{Na} molar concentration of Na^+

m_R surfactant molality expressed in moles of head groups

M mass of the adsorbents used in the adsorption test

M_{sA} molecular weight of the surfactant tail

M_W molecular weight of water

n_i number density of species i in aqueous solution

n_i^{∞} ion concentration infinitely far (bulk phase) from the charged interface

n^o optimum aggregation number

N segment number of a surfactant tail in lattice theory

N_{1A} number of surfactant monomers in solution

N_{add} number of ionic pairs of an inorganic salt

N_{Av} Avogadro number

N_C capillary number

N_g number of micelles composed of g surfactant molecules

N_i^{free} number of ionic species i free in solution

N_{sA} number of Gemini surfactant molecules

N_W number of water molecules

P geometrical ratio

$r_{A,j}$ radius of the surfactant head group

r_c monodisperse oil droplet radius, in Chapter 5

r_e equilibrium globule radius, in Chapter 3

r_h hydrodynamic radius

r_o natural radius

R electrical resistance, in Chapter 3

R Winsor R ratio, in Chapter 5

R_c radius of the hydrophobic core

R_{ch} radius of the micelle surface of charge

s_{core} number of methylene units of the spacer buried in the micelle core

S_d entropy of dispersion of the globules in the continuous medium of the microemulsion

S_{oi} initial oil saturation

S_{orw} residual oil saturation

S_{wr} residual water saturation

T absolute temperature

T_K Krafft point temperature

u reduced electric potential

v Darcy velocity of the displacing fluid

v_- numbers of anions pre formula unit of electrolyte

v_+ numbers of cations pre formula unit of electrolyte

v_c molecular volume of the continuous phase

v_o molecular volume of an oil molecule

v_{sA} half volume of the entire hydrophobic moiety

V volume of surfactant solution used in the test

V_b bulk volume

V_g total volume of the aggregate

V_p pore volume

x reduced distance

x_i mole fraction of component i

X_l mole fraction of the species l

X_{tot} total surfactant concentration

z valency of ions

z_A valence of the ionic polar head of the surfactant

z_i valence the counter-ion

α degree of micelle ionization

δ distance of the electrical diffuse layer from the hydrophobic core surface

δ_{salt} dielectric decrement

ϕ_o electrical potential at the micellar surface of charge

κ inverse Debye length

μ viscosity of the displacing fluid, in Chapter 1

μ_{app} apparent viscosity of oil bank

μ_i chemical potential of the component *i*, in Chapter 7

μ_o oil viscosity

μ_w water viscosity

π surface pressure

υ empirical constant added to represent the counter-ion condensation at micellar surface

β fraction of micellar charge neutralized

γ interfacial tension

γ_a surface free energies per unit area of the pure liquid *a*

γ_{ab} *a-b* interaction energy per unit area across the interface

γ_{CMC} minimum surface tension at CMC

γ_{mo} microemulsion-oil interfacial tension

γ_{mw} microemulsion-water interfacial tension

γ_{ow} oil-water interfacial tension

Γ surface excess density

Γ_{max} maximum (or saturated) adsorption density

ε dielectric constant

ε_o vacuum permittivity

ε_{sol} dielectric constant of the solvent

θ fraction of surface area that is covered by surfactant

λ molar conductivity

λ_o limiting molar conductivity

ρ_{sol} density of the electrolyte solution

σ electrical conductivity, in Chapter 3

σ solubilization ratio, in Chapter 5

σ_A surface tension of the aliphatic surfactant tail

σ_{agg} macroscopic interfacial tension between bulk hydrocarbon and the aqueous salt solution

σ_o surface charge density at the surface of charge

σ_{salt} surface tension of the electrolyte solution

σ_{SP} interfacial tension between the spacer and the micelle core

ω moles of water per liter

ϕ_v volume fraction of the dispersed phase per unit microemulsion volume

Δf_e free energy for the entropy of dispersion of the globules in the continuous phase

ΔG_M^o change in Gibbs free energy of micellization

$\Delta G_{\mathrm{ad}}^{\mathrm{o}}$ standard free energies change upon adsorption

ΔH_M^o change in enthalpy of micellization

ΔS_M^o change in entropy of micellization

$\Delta \mu_g^o$ free energy of micellization

Bibliography

Abraham, M.H., and Matteoli, E., The Temperature Variation of the Hydrophobic Effect, Journal of the Chemical Society, Faraday Transactions 1, 84 (1988), 1985-2000.

Abraham, M.H., Thermodynamics of Solution of Homologous Series of Solutes in Water, Journal of the Chemical Society, Faraday Transactions 1, 80 (1984), 153-181.

Achouri, M.El, Infante, M.R., Izquierdo, F., et al., Synthesis of Some Cationic Gemini Surfactants and Their Inhibitive Effect on Iron Corrosion in Hydrochloric Acid Medium, Corrosion Science, 43 (2001), 19-35.

Achouri, M.El, Kertit, S., Gouttaya, H.M., et al., Corrosion Inhibition of Iron in 1 M HCl by Some Gemini Surfactants in the Series of Alkanediyl-bis-(Dimethyl Tetradecyl Ammonium Bromide), Progress in Organic Coatings, 43 (2001), 267-273.

Adamson, A.W., and Gast, A.P., Physical Chemistry of Surfaces, 6th Ed., 1997, Wiley New York.

Adkins, S., Arachchilage, G.W., Solairaj, S., Lu, J., Weerasooriya, U., and Pope, G.A., Development of Thermally and Chemically Stable Large-Hydrophobe Alkoxy Carboxylate Surfactants, Paper SPE 154256, presented at the SPE Improved Recovery Symposium, Tulsa, Oklahoma, 14-18 April, 2012.

Adkins, S., Liyanage, P. J., Arachchilage, G.W., Mudiyanselage, T., Weerasooriya, U., and Pope, G.A., A New Process for Manufacturing and Stablizing High-Performance EOR Surfactants at Low Cost for High Temperature, High Salinity Oil Reservoirs, SPE 129923, presented at the SPE Improved Recovery Symposium, Tulsa, Oklahoma, 25-28 April, 2010.

Aguiar, H.B., Strader, M.L., Beer, A.G.F., and Roke, S., Surface Structure of Sodium Dodecyl Sulfate Surfactant and Oil at the Oil-in-Water Droplet Liquid/Liquid Interface: A Manifestation of a Nonequilibrium Surface State, The Journal of Physical Chemistry B, 115 (2011), 2970-2978.

Ali, K., Shaha, A.A., and Bilal, S., Surface Tensions and Thermodynamic Parameters of Surface Formation of Aqueous Salt Solutions: III. Aqueous Solution of KCl, KBr and KI, Colloids and Surfaces A, Physicochemical and Engineering Aspects, 337 (2009), 194-199.

Aniansson, E.A.G., Wall, S.N., Almgren, M., et al., Theory of the Kinetics of Micellar Equilibria and Quantitative Interpretation of Chemical Relaxation Sudies of Micellar Solutions of Ionic Surfactants, Journal of Physical Chemistry, 80 (1976), 905-922.

Aswal, V.K., De, S., Goyal, P.S., et al., Micellar Structures of Dimeric Surfactants with Phosphate Head Groups and Wettable Spacers: A Small-Angle Neutron Scattering Study, Physical Review E, 59 (1999), 3116-3122.

Aswal, V.K., De, S., Goyal, P.S., et al., Small-Angle Neutron Scattering Study of Micellar Structures of Dimeric Surfactants, Physical Review E, 57 (1998), 776-783.

Atkins, P.W., and Paula, J. de, Physical Chemistry, 7th Ed., 2002, Oxford University Press.

Austad, T., and Milter, J., Surfactant Flooding in Enhanced Oil Recovery, Book Chapter in "Surfactants Fundamentals and Applications in the Petroleum Industry" by Schramm, L.L.., Cambridge University Press, 2000, 203-249.

Austad, T., Fjlde, I., and Rolfsvag, T.A., Adsorption V. Nonequilibrium Competitive Adsorption of Polydisperse Ethoxylated Sulfonates onto Clay-Containing Cores and Kaolinite, Journal of Petroleum Science and Engineering, 6 (1992), 277-287.

Aveyand, R., Binks, B.P., Clark, S., and Mead, J., Interfacial Tension Minima in Oil-Water-Surfactant Systems: Behavior of Alkane-Aqueous NaCl Systems Containing Aerosol OT, Journal of the Chemical Society, Faraday Transactions I, 82 (1986), 125-142.

Aveyand, R., Binks, B.P., Lawless, T.A., and Mead, J., Nature of the Oil-Water Interface and Equilibrium Surfactant Aggregates in Systems Exhibiting Low Tensions, Canadian Journal of Chemistry, 66 (1988), 3031-3037.

Aveyard, R., Binks, B.P., and Mead, J., Interfacial Tension Minima in Oil + Water + Surfactant Systems, Effect of Salt, Temperature and Alkane in Systems Containing Ionic Surfactants, Journal of the Chemical Society, Faraday Transactions I, 81 (1985), 2177.

Barnes, J.R., Smit, J.P., Smit, J.R., Shpakoff, P.G., and Raney, K.H., Development of Surfactants for Chemical Flooding at Difficult Reservoir Conditions, Paper SPE 113313, presented at the SPE Improved Recovery Symposium, Tulsa, Oklahoma, 19-23 April, 2008.

Baviere, M., Ruaux, E., and Defives, D., Sulfonate Retention by Kaolinite at High pH-Effect of Inorganic Anions, SPE Reservoir Engineering, 8 (1993), 123-127.

Becher, P., Hydrophile-Lipophile Balance: History and Recent Developments Langmnir Lecture - 1983, Journal of Dispersion Science and Technology, 5 (1984), 81-96.

Bennett, K.E., Davis, H.T., Macosko, C.W., and Scriven L.E., Microemulsion Rheology: Newtonian and Non-Newtonian Regimes, Paper SPE 10061, presented at the SPE ATCE, San Antonio, Texas, 5-7 October, 1981.

Benrraou, M., Bales, B.L., and Zana, R., Effect of the Nature of the Counter-ion on the Properties of Anionic Surfactants. 1. CMC, Ionization Degree at the CMC and Aggregation Number of Micelles of Sodium, Cesium, Tetramethylammonium, Tetraethylammonium, Tetrapropylammonium, and Tetrabutylammonium Dodecyl Sulfates, Journal of Physical Chemistry B, 107 (2003), 13432-13440.

Berger, P.D., and Lee, C.H., New Anionic Alkylaryl Surfactants Based on Olefin Sulfonic Acids, Journal of Surfactants and Detergents, 5 (2002), 39-4.

Berger, P.D., and Lee, C.H., Ultro-Low Concentration Surfactants for Sandstone and Limestone Floods, Paper SPE 75186, presented at the SPE/DOE Improved Oil Recovery Symposium, Tulsa, Oklahoma, 13-17 April, 2002.

Berret, J.F., Gamez-Corrales, R., Lerouge, S., and Decruppe, J.P., Shear-Thickening Transition in Surfactant Solutions: New Experimental Features from Rheology and Flow Birefringence, The European Physical Journal E, 2 (2000), 343-350.

Bersworth, F.C., and Verona, N.J., Washing Composition, US Patent 2524218, 1946.

Blair, C.M., and Lehmann, S., Process for Increasing Productivity of Subterranean Oil-Bearing Strata, US Patent 2356205, 1942.

Blokhus, A.M., Hoiland, H., Gjerde, M.I., and Ersland, E.K., Adsorption of Sodium Dodecyl Sulfate on Kaolin from Different Alcohol-Water Mixtures, Journal of Colloid and Interface Science, 179 (1996), 625-627.

Bohmer, M.R., Koopal, L.K., Adsorption of Ionic Surfactants on Variable-Charge Surfaces. 1. Charge Effects and Structure of the Adsorbed Layer, Langmuir, 8 (1992), 2649-2659.

Bourrel, M., and Chambu, C., The Rules for Achieving High Solubilization of Brine and Oil by Amphiphilic Molecules, SPE Journal, 23 (1983), 327-338.

Bourrel, M., and Schechter, R.S., Microemulsions and Related Systems: Formulation, Solvency, and Physical Properties, Marcel Dekker, Inc., New York, NY, 1988.

Bourrel, M., Verzaro, F., and Chambu, C., Effect of Oil Type on Solubilization by Amphiphiles, SPE Reservoir Engineering, 2 (1987), 41-53.

Bunton, C.A., Robinson, L.B., Schaak, J., and Stam, M.F., Catalysis of Nucleophilic Substitutions by Micelles of Dicationic Detergents, The Journal of Organic Chemistry, 36 (1971), 2346-2350.

Camesano, T.A., and Nagarajan, R., Micelle Formation and CMC of Gemini Surfactants: a Thermodynamic Model, Colloids and Surfaces A, 167 (2000) 165-177.

Carale, T.R., Pham, Q.T., and Blankschtein, D., Salt Effects on Intramicellar Interactions and Micellization of Nonionic Surfactants in Aqueous Solutions, Langmuir, 10 (1994), 109-121.

Cates, M.E., and Candau, S.J., Statics and Dynamics of Worm-Like Surfactant Micelles, Journal of Physics: Condensed Matter, 2 (1990), 6869-6892.

Cayias, J.L., Schechter, R.S., and Wade, W.H., The Measurement of Low Interfacial Tension via the Spinning Drop Technique. Adsorption at Interfaces ACS Symposium Series, 8 (1975), 234-247.

Cazabat, A.M., Langevin, D., Meunier, J., and Pouchelon, A., Critical Behavior in Microemulsions, Advances in Colloid and Interface Science, 16 (1982), 175-199.

Chan, K.S., and Shah, D.O., The Molecular Mechanism for Achieving Ultra Low Interfacial Tension Minimum in a Petroleum Sulfonate / Oil / Brine System, Journal of Dispersion Science and Technology, 1 (1980), 55-95.

Chatterjee, J., Nikolov, A., and Wasan, D.T., Measurement of Ultralow Interfacial Tension with Application to Surfactant-Enhanced Alkaline Systems, Industrial and Engineering Chemistry Research, 37 (1998), 2301-2306.

Chen, H., Han, L., Luo, P., and Ye, Z., The Interfacial Tension Between Oil and Gemini Surfactant Solution, Surface Science, 552 (2004), 53-57.

Chen, H., Han, L., Luo, P., and Ye, Z., The Ultralow Interfacial Tensions Between Crude Oils and Gemini Surfactant Solutions, Journal of Colloid and Interface Science, 285 (2005), 872-874.

Chen, H., Ye, Z., Han, L., and Luo, P., Temperature-Induced Micelle Transition of Gemini Surfactant in Aqueous Solution, Surface Science, 601 (2007), 2147-2151.

Choi, S.K., pH Sensitive Polymers for Novel Conformance Control and Polymer Flooding Applications, PhD Dissertation, The University of Texas at Austin, Austin, Texas, 2008.

Clausen, T.M., Vinson, P.K., Minter, J.R., et al., Viscoelastic Micellar Solutions: Microscopy and Rheology, The Journal of Physical Chemistry, 96 (1992), 474-484.

Dam, Th., Engberts, J.B.F.N., Karthauser, J., et.al, Synthesis, Surface Properties and Ol Solubilisation Capacity of Cationic Gemini Surfactants, Colloids and Surfaces A: Physicochemical and Engineering Aspects, 118 (1996), 41-49.

Danino, D., Talmon, Y., and Zana, R., Alkanediyl-Bis(Dimethylalkylammonium Bromide) Surfactants (Dimeric Surfacants). 5. Aggregation and Microstructure in Aqueous Solutions, Langmuir, 11 (1995), 1448-1456.

Daubert, T.E., and Danner, R.P., Physical and Thermodynamic Properties of Pure Chemicals; AICE; Hemisphere Publishing Corp.: New York, 1988.

De Groote, M., Flooding Process for Recovering Fixed Oil From Subterranean Oil-Bearing Strata, US Patent 1823440, 1930.

De Groote, M., Flooding Process for Recovering Oil From Subterranean Oil-Bearing Strata, US Patent 1823429, 1929.

Dean, R.M., Selection and Evaluation of Surfactants for Field Pilots, MS Thesis, The University of Texas at Austin, Austin, Texas, 2011.

Delshad, M., Kim, D.H., Magbagbeola, O.A., et al., Mechanistic Interpretation and Utilization of Viscoelastic Behavior of Polymer Solutions for Improved Polymer-

Flood Efficiency, Paper SPE 113620, presented at SPE ATCE, Houston, Texas, 2-5 October, (2008).

Delshad, M., Pope, G., and Sepehrnoori, K., A Compositional Simulator for Modeling Surfactant Enhanced Aquifer Remediation 1. Formulation, Journal of Contaminant Hydrology, 23 (1996), 303-327.

Derjaguin, B.V., On the Repulsive Forces between Charged Colloid Particles and on the Theory of Sow Coagulation and Stability of Lyophobe Sols, Transactions of the Faraday Society, 35 (1940), 203-215.

Devinsky, F., Lacko, I., Bittereova, F., and Tomeckova, L., Relationship Between Structure, Surface Activity, and Micelle Formation of Some New Bisquaternary Isosteres of 1,5-Pentanediammonium Dibromides, Journal of Colloid and Interface Science, 114 (1986), 314-32.

Dill, K.A., and Flory, P.J., Molecular Organization in Micelles and Vesicles, PNAS, 78 (1981), 676-680.

Diz, M., Manresa, A., Pinazo, A., et al., Synthesis, Surface Active Properties and Antimicrobial Activity of New Bis-quaternary Ammonium Compounds, Journal of the Chemical Society, Perkin Transactions 2, 8 (1994), 1871-1876.

Du, X., Li, L., Lu, Y., and Yang, Z., Unusual Viscosity Behavior of a Kind of Anionic Gemini Surfactant, Colloids and Surfaces A: Physicochemical and Engineering Aspects, 308 (2007), 147-149.

Duivenvoorde, F.L., Feiters, M.C., Gaast, S.J., and Engberts, B.F.N., Synthesis and Properties of Di-n-dodecyl-Alkyl Bisphosphate Surfactants, 13 (1997), 3737-3743.

Eriksson, J.C., and Ljunggren, S., Model Calculations on the Transitions between Surfactant Aggregates of Different Shapes, Langmuir, 6 (1990), 895-904.

Estroff, L.A., and Hamilton,A.A., Effective Gelation of Water Using a Series of Bis-urea Dicarboxylic Acids, Angewandte Chemie International Edition, 39 (2000), 3447-3450.

Esumi, K., Goino, M., Koide, Y., Adsorption and Adsolubilization by Monomeric, Dimeric, or Trimeric Quaternary Ammonium Surfactant at Silica/Water Interface, Journal of Colloid and Interface Science, 183 (1996), 539-545.

Evans, D.F., and Ninham, B.W., Ion Binding and the Hydrophobic Effect, Journal of Physical Chemistry, 87 (1983), 5025-5032.

Evans, D.F., and Wennerstrom, H., The Colloidal Domain: Where Physics, Chemistry, Biology, and Technology meet, 1994, VCH Publishers, Inc.

Evans, D.F., Mitchell, D.J., and Ninham, B.W., Ion Binding and Dressed Micelles, Journal of Physical Chemistry, 88 (1984), 6344-6348.

Fjlde, I., Austad, T., Milter, J., Adsorption VII. Dynamic Adsorption of a Dual Surfactant System onto Reservoir Cores at Seawater Salinities, Journal of Petroleum Science and Engineering, 13 (1995), 193-201.

Flaaten, A.K., Experimental Study of Microemulsion Characterization and Optimization in Enhanced Oil Recovery: A Design Approach for Reservoirs with High Salinity and Hardness, MS Thesis, The University of Texas at Austin, Austin, Texas, 2007.

Flatten, A.K., Nguyen, Q.P., Pope, G.A., and Zhang, J., A Systematic Laboratory Approach to Low-Cost, High-Performance Chemical Flooding, Paper SPE 113469, presented at the Symposium on Improved Oil Recovery, Tulsa, Oklahoma, 19-23 April, 2008.

Fletcher, P.D.I., Galal, M.F., and Robinson, B.H., Structural Study of Aerosol-OT-Stabilised Microemulsions of Glycerol Dispersed in n-Heptane, Journal of the Chemical Society, Faraday Transactions I, 80 (1984), 3307-3314.

Fletcher, P.D.I., Interfacial Tension Between Microemulsion and Excess Dispersed Phases, Chemical Physics Letters, 141 (1987), 357-360.

Foster, W.R., A Low-Tension Waterflooding Process, Journal of Petroleum Technology, 25 (1973), 205-210.

Franses, E.I., Puig, J.E., Talmon, Y., et al., Roles of Liquid Crystals and Micelles in Lowering Interfacial Tension, The Journal of Physical Chemistry, 84 (1980), 1547-1556.

Gale, W.W., and Sandvik, E.I., Tertiary Surfactant Flooding: Petroleum Sulfonate Composition-Efficacy Studies, SPE Journal, 13 (1973), 191-199.

Giese, K., Kaatze, U., and Pottel, R., Permittivity and Dielectric and Proton Magnetic Relaxation of Aqueous Solutions of the Alkali Halides, Journal of Physical Chemistry, 74 (1970), 3718-3725.

Girifalco, L.A., and Good, R.J., A Theory for the Estimation of Surface and Interfacial Energies. I. Derivation and Application to Interfacial Tension, Journal of Physical Chemistry, 61 (1957), 904-909.

Grosmaire, L., Chorro, M. Chorro, C., et al., Alkanediyl-Bis (Dimethyl-alkylammonium Bromide) Surfactants: 9. Effect of the Spacer Carbon Number and Temperature on the Enthalpy of micellization, Journal of Colloid and Interface Science, 246 (2002), 175-181.

Groswasser, A.B., Zana, R., and Talmon, Y., Sphere-to-Cylinder Transition in Aqueous Micellar Solution of a Dimeric (Gemini) Surfactant, The Journal of Physical Chemistry B, 104 (2000), 4005-4009.

Gu, X.P., Ikeda, I., and Okahara, M., Synthesis of Glycol Diglycidyl Ethers Using Phase-Transfer Catalysis, Synthetic Communications, 15 (1985), 649-651.

Guest, D., and Langevin, D., Light Scattering Study of a Multiphase Microemulsion System, Journal of Colloid and Interface Science, 112 (1986), 208-220.

Hait, S.K., and Moulik S.P., Gemini Surfactants: A Distinct Class of Self-Assembling Molecules, Current Science, 82 (2002), 1101-1111.

Hall, A.C., Interfacial Tension and Phase Behavior in Systems of Petroleum Sulfonate / Brine / n-Alkane, Colloids and Surfaces, 1 (1980), 209-228.

Han, L., Chen, H., and Luo, P., Viscosity Behavior of Cationic Gemini Surfactants with Long Alkyl Chains, Surface Science, 564 (2004), 141-148.

Hanna, H.S., Somasundaran, P., Physico-Chemical Aspects of Adsorption at Solid/Liquid Interfaces. II. Mahogany Sulfonates/Berea Sandston, Kaolinite, Book Chapter in "Improved Oil Recovery by Surfactant and Polymer Flooding" by Shah, D.O., and Schechter, R.S., Academic Press Inc., 1977, 253-274.

Hato, M., and Shinoda, K., Krafft Points of Calcium and Sodium Dodecylpoly(oxyethylene) Sulfates and Their Mixtures, The Journal of Physical Chemistry, 77 (1973), 378-381.

Healy, R.N., Reed, R.L., and Stenmark, D.G., Multiphase Microemulsion Systems, SPE Journal, 16 (1976), 147-160.

Hirasaki, G.J., Miller, C.A., and Puerto, M., Recent Advances in Surfactant EOR, SPE Journal, 16 (2011), 889-907.

Holbrook, O.C., Surfactant-Water Secondary Recovery Process, US Patent 3006411, 1958.

Hong, C., Tang, F., Liu, B., et al., Researches on Rheologic Property of Gemini Surfactants and Polymer Compound System, Chinese Journal of Oil and Gas Technology, 33 (2011), 124-127.

Huh, C., Interfacial Tension and Solubilizing Ability of a Microemulsion Phase That Coexists with Oil and Brine, Journal of Colloid and Interface Science, 71 (1979), 408-426.

In, M., Bec, V., Aguerre-Chariol, O., and Zana, R., Quaternary Ammonium Bromide Surfactant Oligomers in Aqueous Solution:? Self-Association and Microstructure, Langmuir, 16 (2000), 141-148.

Israelachivili, J.N., Mitchell, D.J., and Ninham, B.W., Theory of Self-Assembly of Hydrocarbon Amphiphiles into Micelles and Bilayers, Journal of the Chemical Society, Faraday Transactions 2, 72 (1976), 1525-1568.

Israelachvili, J.N., Intermolecular and Surface Forces; Academic Press, 3rd ed. 2011.

Jackson, A.J., Experimental Study of the Benefits of Sodium Carbonate on Surfactants for Enhanced Oil Recovery, MS Thesis, The University of Texas at Austin, Austin, Texas, 2006.

Jain, A.K., Dhawan, A.K., and Misra, T.R., ASP Flood Pilot in Jhalora (K-IV) - A Case Study, Paper SPE 153667, resented at the SPE Oil and Gas India Conference and Exhibition, Mumbei, India, 28-30 March, 2012.

Jones, R.A.L., Soft Condensed Matter, 2002, Oxford University Press.

Jordan, M.M., Sorbie, K.S., Yuan, M.D., etc, Static and Dynamic Adsorption of Phosphonate and Polymeric Scale Inhibitors onto Reservoir Core from Laboratory Tests to Field Application, Paper SPE 29002, presented at the SPE International Symposium on Oilfield Chemistry, San Antonio, Texas, 14-17 February (1995).

Kang, K., Kim, H., and Lim, K., Effect of Temperature on Critical Micelle Concentration and Thermodynamic Potentials of Micellization of Anionic Ammonium Dodecyl Sulfate and Cationic Octadecyl Trimethyl Ammonium Chloride, Colloids and Surfaces A: Physicochemical and Engineering Aspects, 189 (2001), 113-121.

Kern, F., Lequeux, F., Zana, R., and Candau, S.J., Dynamical Properties of Salt-Free Viscoelastic Micellar Solutions, Langmuir, 10 (1994), 1714-1723.

Kim, D.H., Lee, S., Ahn, C.H., et al., Development of Viscoelastic Property Database for EOR Polymers, Paper SPE 129971, presented at the SPE Improved Recovery Symposium, Tulsa, Oklahoma, 24-28 April, 2010.

Kim, H., and Lim, K., A Model on the Temperature Dependence of Critical Micelle Concentration, Colloids and Surfaces A: Physicochemical and Engineering, 235 (2004), 121-128.

Klevens, H.B., Structure and Aggregation in Dilute Solutions of Surface Active Agents, Journal of the American Oil Chemists' Society, 30 (1953), 74-80.

Lake, L.W., Enhanced Oil Recovery, 1989, Prentice-Hall, Inc.

Lee, K., Impact of Fracture Creation and Growth on Well Injectivity and Reservoir Sweep during Waterflooding and Chemical EOR Processes, PhD Dissertation, The University of Texas at Austin, Austin, Texas, 2012.

Levitt, D. B., Jackson, A. C., Heinsen, C. Britton, L. N., Malik, T., Dwarakanath, V., and Pope, G.A., Identification and Evaluation of High-Performance EOR Surfactants, SPE Reservoir Evaluation and Engineering, 12 (2009), 243-253.

Levitt, D.B., Experimental Evaluation of High Performance EOR Surfactants for a Dolomite Oil Reservoir, MS Thesis, The University of Texas at Austin, Austin, Texas, 2006.

Levitt, D.B., Jackson, A.C., Heinson, C., Britton, L.N., and Pope, G.A., Identification and Evaluation of High Performance EOR Surfactants, Paper SPE 100089, presented at the Symposium on Improved Oil Recovery, Tulsa, Oklahoma, 22-26 April, 2006.

Li, F., and Rosen, M.J., Adsorption of Gemini and Conventional Cationic Surfactants onto Montmorillonite and the Removal of Some Pollutants by the Clay, Journal of Colloid and Interface Science, 224 (2000), 265-271.

Li, X. Hu, Z., Zhu, H., etc., Synthesis and Properties of Novel Alkyl Sulfonate Gemini Surfactants, Journal of Surfactants and Detergents, 13 (2010), 353-359.

Lin, Z., Cai, J.J., Scriven, L.E., and Davis, H.T., Spherical-to-Wormlike Micelle Transition in CTAB Solutions, The Journal of Physical Chemistry, 98 (1994), 5984-5993.

Lin, Z., Scriven, L.E., and Davis, H.T., Cryogenic Electron Microscopy of Rodlike or Wormlike Micelles in Aqueous Solutions of Nonionic Surfactant Hexaethylene Glycol Monohexadecyl Ether, Langmuir, 8 (1992), 2200-2205.

Liyanage, P.J., Solairaj, S., Arachchilage, G.W., Linnemeyer, H.C., Kim, D., Weerasooriya, U., and Pope, G.A., Alkaline Surfactant Polymer Flooding using a Novel Class of Large Hydrophobe Surfactants, Paper SPE 154274, presented at the SPE Improved Recovery Symposium, Tulsa, Oklahoma, 14-18 April, 2012.

Lu, J., Britton, C., Solairaj, S., Liyanage, P.J., Kim. D., Adkins, S., Arachchilage, G.W., Weerasooriya, U., and Pope, G.A., Novel Large-Hydrophobe Alkoxy Carboxylate Surfactants for Enhanced Oil Recovery, Paper SPE 154261, presented at the SPE Improved Recovery Symposium, Tulsa, Oklahoma, 14-18 April, 2012a.

Lu, J., Goudarzi, A., Chen, P., Kim. D., Britton, C., Delshad, M., Mohanty, K.K., Weerasooriya, U., and Pope, G.A., Surfactant Enhanced Oil Recovery from Naturally Fractured Reservoirs, Paper SPE 159979, presented at the SPE ATCE, San Antonio, Texas, 8-10 October, 2012b.

Mackintosh, F.C., Safran, S.A., and Pincus, P.A., Equilibrium Size Distribution of Charged 'Living' Polymers, Journal of Physics: Condensed Matter, 2 (1990), SA359-SA364.

Maitland, G.C., Oil and Gas Production, Current Opinion in Colloid and Interface Science, 5 (2002), 301-311.

Mannhardt, K., Schramm, L.L., and Novosad, J.J., Adsorption of Anionic and Amphoteric Foam-Forming Surfactants on Different Rock Types, Colloids and Surfaces, 68 (1992), 37-53.

Manrique, E., Thomas, C., Ravikiran, R., etc., EOR: Current Status and Opportunities, Paper SPE 130113, presented at the SPE Improved Recovery Symposium, Tulsa, Oklahoma, 24-28 April, 2010.

Masuyama, A., Endo, C., Takeda, S., et al., Ozone-Cleavable Gemini Surfactants. Their Surface-Active Properties, Ozonolysis, and Biodegradability, Langmuir, 16 (2000), 368-373.

McDevit, W.F., and Long, F.A., The Activity Coefficient of Benzene in Aqueous Salt Solutions, Journal of the American Chemical Society, 74 (1952), 1773-1777.

Melrose, J.C., and Brandner, C.F., The Role of Capillary Forces in Determining Microscopic Displacement Efficiency for Oil Recovery by Waterflooding, Journal of Canadian Petroleum Technology, 13 (1974), 54-62.

Mendes, E., Narayanan, J., Oda, R., et al., Shear-Induced Vesicle to Wormlike Micelle Transition, The Journal of Physical Chemistry B, 101 (1997), 2256-2258.

Menger, F.J., and Keiper, J.S., Gemini Surfactants, Angewandte Chemie International Edition, 39 (2000), 1906-1920.

Menger, F.M., and Littau, C.A., Gemini Surfactants: A New Class of Self-Assembling Molecules, Journal of the American Chemical Society, 115 (1993), 10083-10090.

Menger, F.M., and Littau, C.A., Gemini Surfactants: Synthesis and Properties, Journal of the American Chemical Society, 113 (1991), 1451-1452.

Menger, F.M., On the Structures of Micelles, Accounts on Chemical Research, 12 (1979), 111-117.

Miller, C.A., and Neogi, P., Thermodyamics of Microemulsions: Combined Effects of Dispersion Entropy of Drops and Bending Energy of Surfactant Films, AIChE Journal, 26 (1980), 212-220.

Miller, D.J., von Halasz, S.P., Schmidt, M., et al., Dual Surfactant Systems for Enhanced Oil Recovery at High Salinities, Journal of Petroleum Science and Engineering, 6 (1991), 63-72.

Missel, P.J., Mazer, N.A., Benedek, G.B., et al., Thermodynamic Analysis of the Growth of Sodium Dodecyl Sulfate Micelles, Journal of Physical Chemistry, 84 (1980), 1044-1057.

Mohammadi, H., Mechanistic Modeling, Design, and Optimization of Alkaline / Surfactant / Polymer Flooding, PhD Dissertation, The University of Texas at Austin, Austin, 2008.

Mohnot, S.M., Bae, J.H., and Foley, W.L., A Study of Mineral/Alkali Reactions, SPE Reservoir Engineering, 2 (1987), 653-663.

Moreira, L., and Firoozabadi, A., Molecular Thermodynamic Modeling of Specific Ion Effects on Micellization of Ionic Surfactants, Langmuir, 26 (2010), 15177-15191.

Moreira, L.A., and Firoozabadi, A., Thermodynamic Modeling of the Duality of Linear 1-Alcohols as Cosurfactants and Cosolvents in Self-Assembly of Surfactant Molecules, Langmuir, 25 (2009), 12101-12113.

Mukerjee, P., and Mysels, K.J., Critical Micelle Concentrations of Aqueous Surfactant Systems, National Bureau of Standards, NSRDS-NBS 36, 1971.

Mukerjee, P., Size Distribution of Small and Large Micelles: Multiple Equilibrium Analysis, Journal of Physical Chemistry, 76 (1972), 565-570.

Murata, Y., Sugihara, G., Fukushima, K., et al., Study of the Micelle Formation of Sodium Deoxycholate. Concentration Dependence of Carbon-13 Nuclear Magnetic Resonance Chemical Shift, Journal of Physical Chemistry, 86 (1982), 4690-4694.

Nagarajan, R. and Ruckenstein, E., Theory of Surfactant Self-Assembly: a Predictive Molecular Thermodynamic Approach, Langmuir, 7 (1991), 2934-2969.

Nagarajan, R., Theory of Micelle Formation. Chapter 1 in Structure-Performance Relationships in Surfactants, Surfactant Science Series, 112 (2002), edited by Kunio Esumi, Minoru Ueno, 2nd ed., revised and expanded. Marcel Dekker, New York.

Nelson, R.C., Lawson, J.B., Thigpen, D.R., and Stegemeier, G.L., Cosurfactant-Enhanced Alkaline Flooding, Paper SPE 12672-MS, presented at the SPE Enhanced Oil Recovery Symposium, Tulsa, Oklahoma, 15-18 April, 1984.

Novosad, Z., and Novosad, J., Determination of Alkalinity Losses Resulting From Hydrogen Ion Exchange in Alkaline Flooding, SPE Journal, 24 (1984), 49-52.

Novotny, P., and Sohnel, O., Densities of Binary Aqueous Solutions of 306 Inorganic Substances, Journal of Chemical and Engineering Data, 33 (1988), 49-55.

Oda, R., Huc, I., Candau, S.,J., Gemini Surfactants as New, Low Molecular Weight Gelators of Organic Solvents and Water, Angewandte Chemie International Edition, 37 (1998), 2689-2691.

Oda, R., Penizza, P., Schmutz, M., and Lequeux, F., Direct Evidence of the Shear-Induced Structure of Wormlike Micelles:? Gemini Surfactant 12-2-12, Langmuir, 13 (1997), 6407-6412.

Odijk, T., Ionic Strength Dependence of the Length of Charged Linear Micelles, Journal of Physical Chemistry, 93 (1989), 3888-3889.

Oelschlaeger, Cl., Waton, G., Candau, S.J., and Cates, M.E., Structural, Kinetics, and Rheological Properties of Low Ionic Strength Dilute Solutions of a Dimeric (Gemini) Surfactant, Langmuir, 18 (2002), 7265-7271.

Oida, T., Nakashima, N., Nagadome, S., et al., Surfactant Adsorption and Micelle Formation of Mixed Surfactant Systems in Water. III. A Comparison Between Cationic Gemini/Cationic and Cationic Gemini/Nonionic Combinations, Journal of Oleo Science, 52 (2003), 509-522.

Okano, T., Egawa, N., Fujiwara, M., and Fukuda, M., Sulfonated Fatty Acid Esters: II. Solution Behavior of Sulfonated Fatty Acid Polyethylene Glycol Esters, Journal of the American Oil Chemists' Society, 73 (1996), 31-37.

Pallas, N.R., Harrison, Y., An Automated Drop Shape Apparatus and the Surface Tension of Pure Water, Colloids and Surfaces, 43 (1990), 169-194.

Paria, S., Khilar, K.C., A Review on Experimental Studies of Surfactant Adsorption at the Hydrophilic Solid-Water Interface, Advances in Colloid and Interface Science, 110 (2004), 75-95.

Perez, L, Torres, J.L., Manresa, A., et al., Synthesis, Aggregation, and Biological Properties of a New Class of Gemini Cationic Amphiphilic Compounds from Arginine, bis(Args), Langmuir, 12 (1996), 5296-5301.

Perez, L., Pinazo, A., and Rosen, M.J., Surface Active Properties at Equilibrium of Novel Gemini Cationic Amphiphilic Compounds from Arginine, bis (args), Langmuir, 14 (1998), 2307-2315.

Pope, G.A., Wu, W., Narayanaswaymy, G., Delshad, M., Sharma, M.M., and Wang, P., Modeling Relative Permeability Effects of Gas-Condensate Reservoirs with a New Trapping Model, SPE Reservoir Evaluation and Engineering, 3 (2000), 171-178.

Pouchelon, A., Chatenay, D., Meunier, J. and Langevin, D., Origin of Low Interfacial Tension in Systems Involving Microemulsion Phases, Journal of Colloid and Interface Science, 82 (1981), 418-422.

Preiss, U., Jungnickel, C., Thoming, J., et al., Predicting the Critical Micelle Concentrations of Aqueous Solutions of Ionic Liquids and Other Ionic Surfactants, Chemistry, 15 (2009), 8880-8885.

Puig, J.E., Franses, E.I., and Miller, W.G., Relation of Phase Behavior to Interfacial Tensions of Mixed Surfactant Systems, Journal of Colloid and Interface Science, 89 (1982), 441-45.

Puig, J.E., Mares, M.T., Miller, W.G., and Franses, E.I., Mechanism of Ultralow Interfacial Tensions in Dilute Surfactant - Oil - Brine Systems, Colloids and Surfaces, 16 (1985), 139-152.

Qu, Z., Zhang, Y., Zhang, X., P., and Dai, J., A Successful ASP Flooding Pilot in Gudong Oil Field, Paper SPE 39613, resented at the SPE/DOE Improved Oil Recovery Symposium, Tulsa, Oklahoma, 19-22 April, 1998.

Rand, R.P., and Luzzati, V., X-Ray Diffraction Study in Water of Lipids Extracted from Human Erythrocytes, Biophyscial Journal, 8 (1968), 125-137.

Rapaport, M.J., Patch Testing in Japanese Subjects, Contact Dermatitis, 11 (1984), 93-97.

Rehage, H., and Hoffmann, H., Viscoelastic Surfactant Solutions: Model Systems for Rheological Research, Molecular Physics, 74 (1991), 933-973.

Reisberg, J., and Doscher, T.M., Interfacial Phenomena in Crude-Oil-Water Systems, Producers Monthly, 20 (1956), 28-49.

Richtering, W., Rheology and Shear Induced Structures in Surfactant Solutions, Current Opinion in Colloid and Interface Science, 6 (2001), 446-450.

Rist, O., and Carlsen, P.H.J., Synthesis of New Geminal Surfactants, Synthetic Communications, 29 (1999), 749-754.

Rosen, M.J., and Aronson, S., Standard Free Energies of Adsorption of Surfactants at the Aqueous Solution/Air Interface from Surface Tension Data in the Vicinity of the Critical Micelle Concentration, Colloids and Surfaces, 3 (1981), 201-208.

Rosen, M.J., and Li, F., The Adsorption of Gemini and Conventional Surfactants onto Some Soil solids and the Removal of 2-Naphthol by the Soil Surfaces, Journal of Colloid and Interface Science, 234 (2001), 418-424.

Rosen, M.J., and Song, L.D., Dynamic Surface Tension of Aqueous Surfactant Solutions 8. Effect of Spacer on Dynamic Properties of Gemini Surfactant Solutions. Journal of Colloid and Interface Science, 179 (1996) 261-268.

Rosen, M.J., and Tracy, D.J., Gemini Surfactants, Journal of Surfactants and Detergents, 1 (1998), 547-554.

Rosen, M.J., Geminis: A New Generation of Surfactants, Chemtech, 23 (1993), 30-33.

Rosen, M.J., Mathias, J.H., and Davenport, L., Aberrant Aggregation Behavior in Cationic Gemini Surfactants Investigated by Surface Tension, Interfacial Tension, and Fluorescence Methods, Langmuir, 15 (1999), 7340-7346.

Rosen, M.J., Surfactants and Interfacial Phenomena, 2004, John Wiley & Sons Inc.

Rosen, M.J., Zhu, Z.H., and Gao, T., Synergism in Binary Mixture of Surfactants 11. Mixtures Containing Mono- and Disulfonated Alkyl- and Diakyldiphenylethers, Journal of Colloid and Interface Science, 157 (1993), 254-259.

Ruckenstein, E., and J.C. Chi, Stability of Microemulsions, Journal of the Chemical Society, Faraday Transactions 2: Molecular and Chemical Physics, 71 (1975), 1690-1707.

Ruckenstein, E., Evaluation of the Interfacial Tension Between a Microemulsion and the Excess Dispersed Phase, SPE Journal, 21 (1981), 593-602.

Sahni, V., Dean, R.M., Britton, C., Kim, D., Weerasooriya, U., and Gary, P.A., The Role of Co-Solvents and Co-Surfactants in Making Chemical Floods Robust, Paper SPE 130007, presented at the SPE Improved Recovery Symposium, Tulsa, Oklahoma, 24-28 April, 2010.

Sahni, V., Experimental Evaluation of Co-solvents in Development of High Performance Alkali/Surfactant/Polymer Formulations for Enhanced Oil Recovery, M.S. Thesis, The University of Texas at Austin, Austin, Texas, 2009.

Saita, S., Solubilization Properties of Polymer-Surfactant Complexes, Journal of Colloid and Interface Science, 24 (1967), 227-234.

Salager, J.L., Bourrel, M.U., Schechter, R.S., and Wade, W.H., Mixing Rules for Optimum Phase-Behavior Formulations of Surfactant/Oil/Water Systems, SPE Journal, 19 (1979), 271-278.

Sandler, S.I., Chemical, Biochemical and Engineering Thermodynamics, 4th Ed., 2006, Wiley New York.

Scamehorn, J.F., Schechter, R.S., and Wade, W.H., Adsorption of Surfactants on Mineral Oxide Surfaces from Aqueous Solutions. Part 1. Isomerically Pure Anionic Surfactants, Journal of Colloid and Interface Science, 85 (1982), 463-478.

Scriven, L.E., Equilibrium Bicontinuous Structure, Nature, 263 (1976), 123-125.

Shahidzadeh, N., Bonn, D., and Meunier, J., Dynamics of Spontaneous Emulsification for Fabrication of Oil in Water Emulsions, Langmuir, 16 (2000), 9703-9708.

Sharma, A., Azizi-Yarand, A., Clayton, B., etc., The Design and Execution of an Alkaline-Surfactant-Polymer Pilot Test, Paper SPE 154318, resented at the 18th SPE Improved Oil Recovery Symposium, Tulsa, Oklahoma, 14-18 April, 2012.

Shukla, D., and Tyagi, V.K., Anionic Gemini Surfactants: A Distinct Class of Surfactants, Journal of Oleo Science, 55 (2006), 215-226.

Silverstein, T.P., The Real Reason Why Oil and Water Don't Mix, Journal of Chemical Education, 75 (1998), 116-118.

Sjoblom, J., Encyclopedic Handbook of Emulsion Technology, 2001, Marcel Dekker New York.

Solairaj, S., Britton, C., Kim, D., Weerasooriya, U., and Pope, G.A., Measurement and Analysis of Surfactant Retention, Paper SPE 154247, presented at the SPE Improved Recovery Symposium, Tulsa, Oklahoma, 14-18 April, 2012b.

Solairaj, S., Britton, C., Lu, J., Kim, D., Weerasooriya, U., and Pope, G.A., New Correlation to Predict the Optimum Surfactant Structure for EOR, Paper SPE 154262, presented at the SPE Improved Recovery Symposium, Tulsa, Oklahoma, 14-18 April, 2012a.

Solairaj, S., New Method of Predicting Optimum Surfactant Structure for EOR, MS Thesis, The University of Texas at Austin, Austin, Texas, 2011.

Somasundaran, P., Ananthapadmanabhan, K.P., and Viswanathan, K.V., Adsorption of Sulfonate on Kaolinite and Alumina in the Presence of Gypsum, Paper SPE 11781-MS, presented at the SPE Oilfield and Geothermal Chemistry Symposium, Denver, Colorado, 1-3 June (1983).

Somasundaran, P., Huang, L., Adsorption / Aggregation of Surfactants and Their Mixtures at Solid-water Interfaces, Advances in Colloid and Interface Science, 88 (2000), 179-208.

Somasundaran, P., Krishnakumar, S., Adsorption of Surfactants and Polymer at the Solid-water Interface, Colloids and Surfaces A: Physicochemical and Engineering Aspects, 123-124 (1997), 491-513.

Somasundaran, P., Shrotri, S., Huang, L., Thermodynamics of Adsorption of Surfactants at Solid-water Interfaces, Pure and Applied Chemistry, 70 (1998), 621-626.

Song, L.D., and Rosen, M.J., Surface Properties, Micellization, and Premicellar Aggregation of Gemini Surfactants with Rigid and Flexible spacers, Langmuir, 12 (1996), 1149-1153.

Srinivasan, V., and Blankschtein, D., Effect of Counter-ion Binding on Micellar Solution Behavior: 1. Molecular?Thermodynamic Theory of Micellization of Ionic Surfactants, Langmuir, 19 (2003), 9932-9945.

Srinivasan, V., and Blankschtein, D., Effect of Counter-ion Binding on Micellar Solution Behavior: 1. Prediction of Micellar Solution Properties of Ionic Surfactant?Electrolyte Systems, Langmuir, 19 (2003), 9946-9961.

Stache, H., Anionic Surfactants: Organic Chemistry, Surfactant Science Series, Vol. 56, 1995, Marcel Dekker, New York.

Stegemeier, G.L., Mechanisms of Entrapment and Mobilization of Oil in Porous Media, in Improved Oil Recovery by Surfactant and Polymer Flooding, Shah, D.O. and Schechter, R.S. (eds.), Academic Press, New York, 1977.

Sugihara, G., Miyazono, A. Nagadome, S., et al., Adsorption and Micelle Formation of Mixed Surfactant Systems in Water II: A Combination of Cationic Gemini-type Surfactant with MEGA-10, Journal of Oleo Science, 52 (2003), 449-461.

Sun, Z. Zhang, J., and Zhu, H., Research of Composite Oil Displacing Agent Based on Novel Sulfonate Gemini Surfactant, Fine and Specialty Chemicals, 14 (2006), 65-67.

Sun, Z., Zhang, J., Xia, J., Zhang, Y., and Zhu, H., Development of Two Novel Composite Oil Displacement Agents Based on Petroleum Sulfonate, Journal of China University of Petroleum, 31 (2007), 135-138.

Sydansk, R.D., Elevated-Temperature Caustic/Sandstone Interaction: Implications for Improving Oil Recovery, SPE Journal, 22 (1982), 453-462.

Taber, J.J., Dynamic and Static Forces Required to Remove a Discontinuous Oil Phase from Porous Media Containing Both Oil and Water, SPE Journal, 9 (1969), 3-12.

Tajima, K., Radiotracer Studies on Adsorption of Surface Active Substance at Aqueous Surface. III. The Effects of Salt on the Adsorption of Sodium Dodecylsulfate, Bulletin of the Chemical Society of Japan, 44 (1971), 1767-1771.

Tan, Z., Study on Characteristics and Salt-Endurance Activity of Gemini Surfactant, Fine and Specialty Chemicals, 14 (2006), 50-54.

Tan. Z., and Yuan, X., Synthesis of New Anionic Gemini Surfactants, Fine Chemicals, 23 (2006), 945-949.

Tan. Z., Han, D., and Yang, P., The Properties and Application Prospect in Enhanced Oil Recovery of Gemini Surfactant, Oilfield Chemistry, 20 (2003), 187-191.

Tanford, C., The Hydrophobic Effect: Formation of Micelles and Biological Membranes; Wiley: New York, 1973.

Tang, S., Wang, L., Hao, M., Lai, Y., and Yue, Q., Study of Surface Activity and Displacement Efficiency of Gemini Surfactant (C12-2-12 2Br-1), Drilling and Production Technology, 30 (2007), 127-129.

Tang, X. Pu, W., and Yang, Y., Laboratory Study on Static Adsorption Properties of Cationic Gemini Surfactants, Advances in Fine Petrochemicals, 6 (2005), 12-15.

Tobita, K., Sakai, H., Kondo, Y., et al., Thermoresponsive Viscoelasticity of Sodium 1-Oxo-1-[4-(tridecafluorohexyl)phenyl]-2-hexanesulfonate Aqueous Solutions, Langmuir, 13 (1997), 5054-5055.

Tsubone, K., Ogawa, T., and Mimura, K., Surface and Aqueous Properties of Anionic Gemini Surfactants Having Dialkyl Amide, Carboxyl, and Carboxylate Groups, Journal of Surfactants and Detergents, 6 (2003), 39-46.

Tsubone, K., The Interaction of an Anionic Gemini Surfactant with Conventional Anionic Surfactants, Journal of Colloid and Interface Science, 261 (2003), 524-528.

UTCHEM-9, Volume II: Technical Documentation for UTCHEM 9.0, A Three-Dimensional Chemical Flooding Simulator, The University of Texas at Austin, Texas, 2000.

Vargaftik, N.B., Volkov, B.N., and Voljak, L.D., International Tables of the Surface Tension of Water, Journal of Physical and Chemical Reference Data, 12 (1983), 817-820.

Veedu, F.K., Scale-up Methodology for Chemical Flooding, MS Thesis, The University of Texas at Austin, Austin, Texas, 2010.

Wade, W.H., Morgan, J.C., Schechter, R.S., et al., Interfacial Tension and Phase Behavior of Surfactant Systems, SPE Journal, 18 (1978), 242-252.

Walker, D.L, Britton, C., Kim, D., Dufour, S. Weerasooriya, U., and Pope, G.A., The Impact of Microemulsion Viscosity on Oil Recovery, Paper SPE 154275, presented at the SPE Improved Recovery Symposium, Tulsa, Oklahoma, 14-18 April, 2012.

Walker, D.L. Experimental Investigation of the Effect of Increasing the Temperature of ASP Flooding, M.S. Thesis, The University of Texas at Austin, Austin, Texas, 2011.

Walker, L.M., Rheology and Structure of Worm-Like Micelles, Current Opinion in Colloid and Interface Science, 6 (2001), 451-456.

Wang, H., Yang, Y., Zhang, G., and Wu, X., Applied Prospects of New Type of Gemini Surfactant in Tertiary Oil Recovery, Petroleum Geology and Recovery Efficiency, 10 (2003), 59-61.

Wang, H., Zhang, L.P., Zhang, L.S., Ni, H., and Wu, X., Synthesis of Gemini Surfactant DTDPA and Its Application to EOR Technology, Journal of Zhejiang University Science Edition, 34 (2007), 665-668.

Weber, V., and Schosseler, F., Shear-Thickening in Salt-Free Aqueous Solutions of a Gemini Cationic Surfactant: A Study by Small Angle Light Scattering, Langmuir, 18 (2002), 9705-9712.

Weissenborn, P.K., and Pugh, R.J., Surface Tension of Aqueous Solutions of Electrolytes: Relationship with Ion Hydration, Oxygen Solubility, and Bubble Coalescence, Journal of Colloid and Interface Science, 184 (1996), 550-563.

Wesson, L.L., Harwell, J.H., Surfactant Adsorption in Porous Media, Book Chapter in "Surfactants Fundamentals and Applications in the Petroleum Industry" by Schramm, L.L.., Cambridge University Press, 2000, 121-158.

Wettig, S.D., and Verrall, R.E., Thermodynamic Studies of Aqueous m-s-m Gemini Surfactant Systems, Journal of Colloid and Interface Science, 235 (2001), 310-316.

Widom, B., Interfacial Tensions of Three Fluid Phases in Equilibrium, Journal of Chemical Physics, 62 (1975), 1332-1336.

Winsor, P.A., Binary and Multicomponent Solutions of Amphiphilic Compounds. Solubilization and the Formation, Structure, and Theoretical Significance of Liquid Crystalline Solutions, Chemical Review, 68 (1968), 1-40.

Winsor, P.A., Hydrotropy, Solubilization and Related Emulsification Processes, Transactions of the Faraday Society, 44 (1948), 376-398.

Winsor, P.A., Solvent Properties of Amphiphilic Compounds, Butterworths, London, 1954.

Yang, H., Britton, C., Liyanage, P.J., Solairaj, S., Kim, D., Nguyen, Q., Weerasooriya, U., and Pope, G.A., Low-cost, High-performance Chemicals for Enhanced Oil Recovery, Paper SPE 129978, presented at the SPE Improved Recovery Symposium, Tulsa, Oklahoma, 24-28 April, 2010.

Yang, H., Development of Improved ASP Formulation for Reactive and Non-reactive Crude Oils, MS Thesis, The University of Texas at Austin, Austin, Texas, 2010.

Yang, H.T., Development of Improved ASP Formulation for Reactive and Non-reactive Crude Oils, MS Thesis, The University of Texas at Austin, Austin, Texas, 2010.

Yang, J., Viscoelastic Wormlike Micelles and Their Applications, Current Opinion in Colloid and Interface Science, 7 (2002), 276-281.

Yang, Y., Li, Y., Pu, W., Hu, Q., Zhou, M., and Zhao, J., Study Advances of Gemini Surfactants, Petroleum Geology and Recovery Efficiency, 12 (2005), 67-70.

Yang, Y., Pu, W., Liu, Y., Zhou, M., and Hu, X., Study of Interfacial Tension Between NNMB/NAPS Binary System and Crude Oil, Journal of Southwest Petroleum Institute, 28 (2006), 68-70.

Ye, Z., Zhang, F., Han, L., Luo, P. Yang, J., and Chen, H., The Effect of Temperature on the Interfacial Tension Between Crude Oil and Gemini Surfactant Solution, Colloids and Surfaces A: Physicochemical and Engineering Aspects, 322 (2008), 138-141.

Yue, Q., Tang, S., Zhu, Z. and Hao, M., A New Sulphate Gemini Surfactant for Oil and Gas Recovery, Fault-Block Oil and Gas Field, 15 (2008), 52-53.

Zaitoun, A., Fonseca, C. Berger, P., Bazin, B., and Monin, N., New Surfactant for Chemical Flood in High-Salinity Reservoir, Paper SPE 80237, resented at the SPE International Symposium on Oilfield Chemistry, Houston, Texas, 5-7 February, 2003.

Zana, R., and Levy, H., Mixed Micellization of Cetyltrimethylammonium Bromide and an Anionic Dimeric (Gemini) Surfactant in Aqueous Solution, Langmuir, 13 (1997), 402-408.

Zana, R., and Talmon, Y., Dependence of Aggregate Morphology on Structure of Dimeric Surfactants, Nature, 362 (1993), 228-230.

Zana, R., and Xia, J., Gemini Surfactants: Synthesis, Interfacial and Solution-Phase Behavior, and Applications, Surfactant Science Series, 117 (2004), Marcel Dekker, New York.

Zana, R., Critical Micellization Concentration of Surfactants in Aqueous Solution and Free Energy of Micellization, Langmuir, 12 (1996), 1208-1211.

Zana, R., Dimeric (Gemini) Srfactants: Effect of the Spacer Group on the Association Behavior in Aqueous Solution, Journal of Colloid and Interface Science, 248 (2002), 203-220.

Zana, R., Dimeric and Oligomeric Surfactants. Behavior at Interfaces and in Aqueous Solution: A Review, Advances in Colloid and Interface Science, 97 (2002), 205-253.

Zana, R., Ionization of Cationic Micelles: Effect of the Detergent Sructure, Journal of Colloid and Interface Science, 78 (1980), 330-337.

Zana, R., Levy, H., and Kwetkat, K., Mixed Micellization of Dimeric (Gemini) Surfactants and Conventional Surfactants. I. Mixtures of an Anionic Dimeric

Surfactant and of the Nonionic Surfactants C12E5 and C12E8, Journal of Colloid and Interface Science, 197 (1998), 370-376.

Zana, R., Talmon, Y., Dependence of Aggregate Morphology on Structure of Dimeric Surfactants, Nature, 362 (1993), 228-230.

Zemaitis, J.F., Clark, D.M., Rafal, M., and Scrivner, N.C., Handbook of Aqueous Electrolyte Thermodynamics, Theory and Application, Willey & Sons Inc., New York, 1986.

Zhang, J., Nguyen, Q.P., Flatten, A.K., and Pope, G.A., Mechanisms of Enhanced Natural Imbibition with Novel Chemicals, Paper SPE 113453, presented at the Symposium on Improved Oil Recovery, Tulsa, Oklahoma, 19-23 April, 2008.

Zhang, J., Ravikiran, R., Freiberg, D., Thomas, C., ASP Formulation Design for Heavy Oil, Paper SPE 153570, presented at the SPE Improved Recovery Symposium, Tulsa, Oklahoma, 14-18 April, 2012.

Zhang, Y. Zhu, H., Xia, J., and Sun, Z., Synthesis of Sulfonate Gemini Surfactant and Its Application in Tertiary Oil Recovery, Journal of Bejing Jiao-Tong University, 31 (2007), 100-104.

Zhao, P, Jackson, A.C., Britton, C., and Pope, G.A., Development of High-Performance Surfactants for Difficult Oils, Paper SPE 113432, presented at the Symposium on Improved Oil Recovery, Tulsa, Oklahoma, 19-23 April, 2008.

Zhu, Y., Masuyama, A., and Okahara, M., Preparation and Surface Active Properties of Amphipathic Compounds with Two Sulfate Groups and Two Lipophilic Alkyl Chains, Journal of the American Oil Chemists' Society, 67 (1990), 459-463.

Zhu, Y., Masuyama, A., Kirito, Y., and Okahara, M., Preparation and Properties of Double- or Triple- Chain Surfactants with Two Sulfonate Groups Derived from N-Acyldiethanolamins, Journal of the American Oil Chemists' Society, 68 (1991), 539-543.

Zhu, Y., Masuyama, A., Kirito, Y., Okahara, M., and Rosen, M.J., Preparation and Properties of Glycerol-Based Double or Triple- Chain Surfactants with Two Hydrophilic Ionic Groups, Journal of the American Oil Chemists' Society, 69 (1992), 626-632.

Zhu, Y., Masuyama, A., Kobata, Y., Nakatsuji, Y., and Rosen, M.J., Double-Chain Surfactants with Two Carboxylate Groups and Their Relation to Similar Double-Chain Compounds, Journal of Colloid and Interface Science, 158 (1993), 40-45.